

A CHOLERA METAPOPOPULATION MODEL INTERLINKING MIGRATION WITH INTERVENTION STRATEGIES — A CASE STUDY OF ZIMBABWE (2008–2009)

ABHISHEK SENAPATI*, TRIDIP SARDAR[†]
and JOYDEV CHATTOPADHYAY*,[‡]

**Agricultural and Ecological Research Unit
Indian Statistical Institute
203, B.T. Road, Kolkata 700108, India*

*[†]Department of Mathematics, Dinabandhu Andrews College
Baishnabghata, P.O. Garia, Dist. 24 Paraganas (S)
Kolkata, West Bengal 700084, India*

[‡]joydev@isical.ac.in

Received 26 July 2018

Accepted 18 February 2019

Published 13 May 2019

Cholera is a water-borne disease and a major threat to human society affecting about 3–5 million people annually. A considerable number of research works have already been done to understand the disease transmission route and preventive measures in spatial or non-spatial scale. However, how the control strategies are to be linked up with the human migration in different locations in a country are not well studied. The present investigation is carried out in this direction by proposing and analyzing cholera meta-population models. The basic dynamical properties including the *domain* basic reproduction number are studied. Several important model parameters are estimated using cholera incidence data (2008–2009) and inter-provincial migration data from Census 2012 for the five provinces in Zimbabwe. By defining some migration index, and interlinking these indices with different cholera control strategies, namely, promotion of hand-hygiene and clean water supply and treatment, we carried out an optimal cost effectiveness analysis using optimal control theory. Our analysis suggests that there is no need to provide control measures for all the five provinces, and the control measures should be provided only to those provinces where in-migration flow is moderate. We also observe that such selective control measures which are also cost effective may reduce the overall cases and deaths.

Keywords: Cholera; Metapopulation Model; Optimal Control; Parameter Estimation; Sensitivity.

1. Introduction

Cholera is a water-borne disease that emerges from *Vibrio cholerae* bacterium. This deadliest disease made its first appearance in a devastating form in Bengal and the Ganges river delta in September 1817.¹ During the period 1829–1975, apparently six more cholera outbreaks happened in many countries of Asia and Africa.² Very recently, countries like Zimbabwe (2008–2009), Nigeria (2010), Haiti (2010–2011),

Vietnam (2009), Ghana (2011), Venezuelan (2011) have faced serious cholera outbreaks and millions of deaths have been reported. To restrain future outbreak in these cholera affected countries, a better understanding on disease transmission routes is required.

Mathematical models are effective in describing different epidemiological scenarios. In the literature, several mathematical and computational models can be found that explore the cholera transmission and its prevention.^{3–18} Capasso *et al.*³ developed a mathematical model to study the cholera epidemic occurred in 1973 in the European Mediterranean region. Codeço⁴ extended the model of Capasso *et al.*³ to study the role of aquatic reservoir on the persistence of endemic cholera. Hartley *et al.*⁵ incorporated hyper-infectious state of cholera bacterium in the model to explain the exponential growth of cholera epidemics. Neilan *et al.*⁷ explored the optimal effect of treatment, vaccination and sanitation for the two cholera endemic regions: Calcutta and Bogra. Qualitative behaviors of cholera epidemic models have been well analyzed in Refs. 8–12, etc. However, these studies lack in capturing the spatial spread of cholera. Recently, inclusion of spatial factors into epidemiological models receive great attention.^{19–23} It is obvious that human demographic features and disease-related parameters vary over the geographical regions.²⁴ Naturally, it is preferable to encompass spatial arrangement into epidemic models. Space can be included in the model either in continuous or in discrete way.^{24,25} Reaction–diffusion model arises when the spatial context is assumed to be continuous.^{26,27} On the other hand, division of space into discrete patches leads to metapopulation models.^{24,25} Reaction–diffusion models assume that the species under consideration move randomly which is not that much realistic for human population.^{19,28} In case of metapopulation model, the discrete regions (patch) are connected through migration of human population in a patterned way which is more realistic for epidemiological studies. In recent years, several studies have been carried out in disease dynamics metapopulation models (patch model setup) (see Refs. 25; 29–39, etc. and the references therein). In the context of cholera disease dynamics metapopulation model, a lot of works have also been done (Refs. 28–42, etc). Njagarah *et al.*²⁸ formulated a two-patch cholera model and studied the effect of unrestricted migration of human in disease invasion. A mathematical model of cholera in patchy environment with both human and water movements is formulated by Eisenberg *et al.*² Bertuzzo *et al.*⁴¹ studied the role of hydrology and population distribution along the water network in disease elimination. Robertson *et al.*⁴² proposed a 2-patch cholera model with common water source and explored the effect of transmission heterogeneity in final outbreak size and the efficacy of intervention strategies. However, very few authors have explored the effect of different intervention measures for controlling the cholera epidemic in patchy environment. Kelly *et al.*⁴³ investigated the impact of spatial arrangement on the spread and management strategies of cholera outbreak. They studied the effect of vaccination strategy in two spatial settings: linear arrangement and hub arrangement. Knipf⁴⁴ described how the role

of different control strategies can be investigated by using target reproduction number and type reproduction number in a metapopulation epidemic model. She also showed that variations in human migration rate between the patches can be useful in preventing outbreak. To the best of our knowledge, no study has been carried out to explore how the implementation of control strategies could be linked up with human mobility. In this study, we attempt to investigate a possible connection between intervention strategies and human migration with an aim not to provide intervention strategies to all the provinces but to the province(s) where in-migration and/or out-migration flow is higher in compare to the other provinces.

In Sec. 2, we formulate a cholera model in a patchy environment. Some epidemic threshold quantities of the model (2.1) are discussed in Sec. 3. In Sec. 4, mathematical properties of the model (2.1) are analyzed. Section 5 is devoted to the aspect of sensitivity analysis. We calibrate our model to cholera data (weekly cumulative cases and deaths) for five provinces of Zimbabwe in Sec. 6. In Sec. 7, we introduce some indices related to human movement between provinces. To study the consequences of control strategies, an extended version of our model is presented in Sec. 8. An optimal cost effectiveness study of two cholera interventions in different human migration scenarios is executed in Sec. 9. This paper ends with a brief discussion (Sec. 10) on the results obtained from our study.

2. Formulation of Model

Several mathematical models are studied the transmission dynamics of cholera. Capasso *et al.*³ formulated a mathematical model by considering two compartments: infected human population and bacterial population. Codeço⁴ modified the model of Capasso *et al.* by including the susceptible population. Hartley *et al.*⁵ extended the model of Codeço⁴ by incorporating the hyper infectious state of bacteria into the model. However, Sardar *et al.*⁴⁵ modified the model of Ref. 5 by including variable human population size, cholera-related death rate and the effect of natural immunity loss to cholera in a time-periodic environment. All the above said models did not consider the spatial heterogeneity. We basically extended the model of Sardar *et al.*⁴⁵ in patchy environment setting. That is, instead of assuming the whole space under considered as homogeneous we divided the whole space into discrete regions and formulated a set of ordinary differential equations for each region. We also consider explicit human migration in the model to get a better insight of the realistic situation. To incorporate the human migration in the model, generally two types of approaches are considered: (i) Lagrangian approach and (ii) Eulerian approach.^{32,46} In Lagrangian approach, the daily migration or commuting-type migration of human are considered. On the other hand, the life-time migration or long term migration are considered in Eulerian approach. However, in this study, we have only the inter-provincial migration data of Zimbabwe, which are life-time

or long term in nature.⁹ Therefore, we adopt the Eulerian approach to incorporate the human migration in our model.

The model in this study is developed by considering human migration between patches in a meta-population setting. The model is based on the following assumptions:

- We consider n patches representing n distinct provinces. The total population is distributed over these n provinces depending on their geographical locations. The patches are connected through human migration.
- Human population from different patches shares a common water source.^{42,48}
- We do not consider the bacterial migration through hydrological links.^{42,48}

Let, S_i , I_i , R_i denote the number of humans in patch i ($1 \leq i \leq n$) who are susceptible to, infectious with, and recovered from cholera, respectively. Susceptible human is recruited at a constant rate in the population and receive infection through bacteria after consuming contaminated water. After some course of time, infected population get natural recovery from the infection. However, human population do not get permanent recovery from the infection, after some time, they again become susceptible. Infected individuals discharge hyper infectious cholera bacterium into the water sources during the infectious period. We assume that the rates of migration between the patches of human population depend on the epidemiological status of individuals and they do not change their disease status during movement. Let m_{ij}^X for $X = S, I, R$ are the constant migration rates from patch j to patch i for $i \neq j$ of susceptible, infectious, recovered human population respectively, with $m_{ii}^X = 0$ for $i = 1, 2, \dots, n$. The migration rate matrices $M^X = [m_{ij}^X]$ for $X = S, I, R$ are assumed to be irreducible, which means all the patches are strongly connected. However, in general, the migration data are available as the total number of population migrated from one patch to another in a given duration of time. The data usually does not contain the exact number of susceptible, infected or recovered individuals migrated from one patch to another. Therefore, we assume that for each patch p_s, p_i, p_r are the proportions of susceptible, infected, and recovered individual respectively who migrated to the other patches. As the p_s, p_i, p_r are proportions of the total individual, they are related by the equation $p_s + p_i + p_r = 1$. Thus, the migration rates m_{ij}^X are given by $m_{ij}^X = p_X m_{ij}$ for $X = S, I, R$, where m_{ij} denotes the migration rate of the total human population from patch j to patch i .

The bacterial population (i.e., *Vibrio cholerae*) is divided into two states namely, hyper-infectious bacterial population and low-infectious bacterial population.⁵ The concentrations of hyper-infectious vibrios and low-infectious vibrios in the contaminated water source are denoted by B_H and B_L , respectively. Bacterial population decays from hyper infectious state to low infectious state at a constant rate. The provinces considered in this study share a common water source (ZINWA),⁴⁹ and hence we do not consider the bacterial movement between the patches.

Based on the above assumptions, the basic cholera meta-population model is given below:

$$\frac{dS_i}{dt} = \Lambda_i - \frac{\beta_i^H B_H}{K_H + B_H} S_i - \frac{\beta_i^L B_L}{K_L + B_L} S_i - \mu_i S_i + \sum_{j=1}^n m_{ij}^S S_j - \sum_{j=1}^n m_{ji}^S S_i + \omega_i R_i,$$

$$\frac{dI_i}{dt} = \frac{\beta_i^H B_H}{K_H + B_H} S_i + \frac{\beta_i^L B_L}{K_L + B_L} S_i - (\mu_i + \delta_i + \gamma_i) I_i + \sum_{j=1}^n m_{ij}^I I_j - \sum_{j=1}^n m_{ji}^I I_i,$$

$$\frac{dR_i}{dt} = \gamma_i I_i - (\omega_i + \mu_i) R_i + \sum_{j=1}^n m_{ij}^R R_j - \sum_{j=1}^n m_{ji}^R R_i,$$

Table 1. Description of parameters for cholera models (2.1) and (8.1).

Parameters	Description	Value	Reference
Λ_i	Human recruitment rate in patch i	$6.02 \cdot 10^{-4} (S_i(0) + I_i(0) + R_i(0)) \text{ week}^{-1}$	45
β_i^H	Transmission rate of hyper-infectious cholera bacterium in patch i	Estimated	
β_i^L	Transmission rate of low-infectious cholera bacterium in patch i	Estimated	
K_L	Half saturation constant of low-infectious bacterium	10^6 cells/ml	4, 5
K_H	Half saturation constant of high-infectious bacterium	$K_L/700 \text{ cells/ml}$	5, 63
μ_i	Death rate of Human in patch i	$3.08 \cdot 10^{-4} \text{ week}^{-1}$	53
ω_i	Rate of loss of immunity of recovered population in patch i	0.0238 week^{-1}	45, 67
δ_i	Cholera related death rate in patch i	Estimated	51
γ_i	Natural recovery rate of infected population in patch i	1.4 week^{-1}	68, 69
ξ_i	Shedding rate of cholera infected human in patch i	Estimated	
χ	Rate of decay from hyper-infectious to low-infectious bacterium	33.6 week^{-1}	63
δ_L	Death rate of vibrios in water	$\frac{7}{30} \text{ week}^{-1}$	5, 45
p_s	The proportion of migration rates for susceptible population	Estimated	
p_i	The proportion of migration rates for infected population	Estimated	
p_r	The proportion of migration rates for recovered population	Estimated using the relation $p_s + p_i + p_r = 1$	
m_{ij}^X	Migration rates of human for health status X from patch j to patch i ; X denotes S, I, R	Estimated	
θ_i	Rate of reduction in bacterial ingestion by promoting PH and CW supply in patch i	$(0-0.8) \text{ week}^{-1}$	45
α_i	Proportion of infected getting treatment in patch i	$(0-0.7) \text{ week}^{-1}$	45

The *domain* reproduction number, \mathcal{R}_0^2 of the model (2.1) is defined as follows:

$$\mathcal{R}_0 = \rho(FV^{-1}), \quad (3.1)$$

where $\rho(A)$ denotes the spectral radius of the matrix A .

We define, \mathcal{R}_l , the partial reproduction number due to low infectious bacterium and \mathcal{R}_h , the partial reproduction number due to high infectious cholera bacterium, satisfying the relation $\mathcal{R}_0 = \mathcal{R}_l + \mathcal{R}_h$.⁶ The analytical expressions of \mathcal{R}_l and \mathcal{R}_h are provided below:

$$\mathcal{R}_l = \rho(FV^{-1}|_{\beta_i^H=0}), \quad i = 1, 2, \dots, n, \quad (3.2)$$

and

$$\mathcal{R}_h = \rho(FV^{-1}|_{\beta_i^L=0}), \quad i = 1, 2, \dots, n. \quad (3.3)$$

In the following section, some basic mathematical properties of the model (2.1) are discussed (detail derivation and proofs of the theorems are given in **Supplementary**).

4. Mathematical Properties of the Model (2.1)

Lemma 1. *The system of equations (2.1) preserve the positivity of the solutions.*

Proof. For proof see **Supplementary**. □

Lemma 2. *The solutions $(S_i(t), I_i(t), R_i(t), B_H(t), B_L(t))$ of the system (2.1) are uniformly and ultimately bounded in \mathbb{R}_+^{3n+2} .*

Proof. For proof see **Supplementary**. □

Theorem 1. *There exists a unique DFE, $\mathcal{E}^0 = (S_1^0, 0, 0, S_2^0, 0, 0, \dots, S_n^0, 0, 0, 0, 0) \in \mathbb{R}_+^{3n+2}$ for the system (2.1).*

Proof. For proof see **Supplementary**. □

Theorem 2. *Suppose that the movement matrix M^I is irreducible. Then the following results hold for the system (2.1):*

- (1) *If $\mathcal{R}_0 < 1$, then the disease-free equilibrium \mathcal{E}^0 is globally asymptotically stable in Ω .*
- (2) *If $\mathcal{R}_0 > 1$, then the disease-free equilibrium \mathcal{E}^0 is unstable and the system (2.1) is uniformly persistent.*

Proof. For proof see **Supplementary**. □

Theorem 3. *Suppose that the M^I is irreducible. If $\mathcal{R}_0 > 1$, then there exists at least one endemic equilibrium for the system (2.1).*

Proof. For proof see **Supplementary**. □

Theorem 4. Assume that $M^S = M^I = M^R = 0$ and $\omega_i = 0$, for $i = 1, 2, \dots, n$. If $\mathcal{R}_0 > 1$, then the endemic equilibrium \mathcal{E}^* of (2.1) is unique and globally asymptotically stable in $\text{int}(\Omega)$ under some assumptions (see **Supplementary**).

Proof. For proof see **Supplementary**. □

Section 5 discusses the sensitivity analysis of *domain* reproduction number, \mathcal{R}_0 with the model parameters.

5. Sensitivity Analysis

We executed sensitivity analysis of *domain* reproduction number, \mathcal{R}_0 , with the model parameters. Following Ref. 50, partial rank correlation coefficients (PRCC) between the *domain* reproduction number \mathcal{R}_0 and the model parameters have been calculated. Using Latin hypercube sampling (LHS), 1000 samples were drawn for each parameter from a feasible range of the parameters. It has been observed that transmission rates of low infectious bacterium and high infectious cholera bacterium (β_i^H and β_i^L) and the shedding rates of cholera infected human (ξ_i) are significantly correlated with the *domain* reproduction number, \mathcal{R}_0 . The PRCC values of the significant parameters are listed in Table 2.

In the next section, we shall validate our model to cholera incidence (2008–2009) data obtained from five provinces of Zimbabwe.

6. Model Calibration

A massive cholera outbreak happened in Zimbabwe during the period 2008–2009. The weekly case and death data during this period are readily available in the website of WHO.⁵¹ Therefore, we have chosen the weekly data for cholera cases and deaths during the above said period in our study. We calibrated cholera meta-population model (2.1) to the weekly cumulative cholera incidence from the five provinces of Zimbabwe: Harare, Manicaland, Mashonaland Central and Mashonaland East, Mashonaland West during 2008–09. Weekly cumulative cases and deaths of cholera were obtained for the period 13th November 2008–31st July 2009 from WHO.⁵¹

Table 2. PRCC values between the *domain* reproduction number \mathcal{R}_0 and the model parameters.

Parameters	PRCC-values
$[\beta_1^H, \beta_3^H, \beta_3^L, \beta_4^H, \beta_5^H]$	[0.561, 0.509, 0.503, 0.503, 0.507]
$[\beta_1^L, \beta_3^L, \beta_3^L, \beta_4^L, \beta_5^L]$	[0.148, 0.095, 0.172, 0.087, 0.156]
$[\xi_1, \xi_2, \xi_3, \xi_4, \xi_5]$	[0.584, 0.573, 0.580, 0.571, 0.586]

6.1. Demographic data

Total number of affected population of these five provinces is taken from WHO,⁵² whereas birth and death rates are taken from The World Factbook-CIA.⁵³

6.2. Migration data

The inter-provincial migration data of the different provinces of Zimbabwe are taken from the Census Report, 2012.⁹ The data provided in Ref. 9 (Table 3.2a) are given in a matrix format. The column of this matrix indicates the province of birth of the individuals and the rows indicates the place of current residence of the individuals. Therefore, the (i, j) th entry of this matrix indicates the number of persons moving from j th province to the i th province between 2002 and 2012. The weekly migration rates between different provinces are calculated by the following formula: $m_{ij} = \frac{A_{ij}}{H_j} \times \frac{7}{365 \times 10}$, where A_{ij} is the (i, j) th entry of the inter-provincial migration matrix and H_j is the total population of the j th province.

6.3. Estimation procedure

The significant parameters which we have estimated from the data are (i) transmission rate of high and low infectious cholera bacterium (β_H^i and β_L^i , respectively), (ii) shedding rate of cholera infected human (ξ_i). The proportions of migration rates for susceptible, infected, and recovered human population in different provinces are taken as p_s, p_i , and p_r . We estimated p_s, p_i , and the relation $p_s + p_i + p_r = 1$ is utilized to estimate p_r . As the initial conditions of the model (2.1) states are uncertain, we prefer to estimate those from the data. However, the initial infected human population is taken from the data.

The cumulative cases and cumulative deaths for the j th province from the model (2.1) are given by

$$C^j(t, \theta) = C^j(0) + \int_0^t S^j(\tau)(\lambda_H^j(\tau) + \lambda_L^j(\tau))d\tau, \quad (6.1)$$

$$D^j(t, \theta) = D^j(0) + \delta_j \int_0^t I^j(\tau)d\tau, \quad j = 1, 2, \dots, 5,$$

where $\theta \in \mathbb{R}^d$ consists of all the unknown variables of the cholera model (2.1). The expressions of λ_H^j and λ_L^j are as follows:

$$\lambda_H^j = \frac{\beta_j^H B_H}{K_H + B_H},$$

$$\lambda_L^j = \frac{\beta_j^L B_L}{K_L + B_L}, \quad j = 1, 2, \dots, 5.$$

The sum of square function for the model (2.1) consists of two sum of square functions: sum of square functions for the cases and those of the deaths are given

by

$$SS_j(\theta) = SS_j^C(\theta) + SS_j^D(\theta), \quad j = 1, 2, \dots, 5 \tag{6.2}$$

where the sum of square functions for the cases and the deaths are given as follows:

$$SS_j^C(\theta) = \sum_{i=1}^N [C^j(t_i) - C(t_i, \theta)]^2, \tag{6.3}$$

$$SS_j^D(\theta) = \sum_{i=1}^N [D^j(t_i) - D(t_i, \theta)]^2, \quad j = 1, 2, \dots, 5$$

where $C^j(t_i)$ and $D^j(t_i)$ are the observed data at the t_i th week and N is the number of data points. In this study, N equals 37.

For the estimation of unknown parameters of the model (2.1), the following methodology is utilized⁴⁵:

- (1) 1000 samples were drawn for the unknown parameter set θ of the model (2.1) using the LHS technique.
- (2) We performed the nonlinear least-square method to minimize the sum of square function (6.2) with θ as initial input. Therefore, we obtain 1000 samples of $\tilde{\theta}$ after each least-square step. MATLAB-based optimizer *lsqcurvefit* (Mathworks, R2015a) was used to minimize $SS_j(\theta)$ defined in Eq. (6.2).

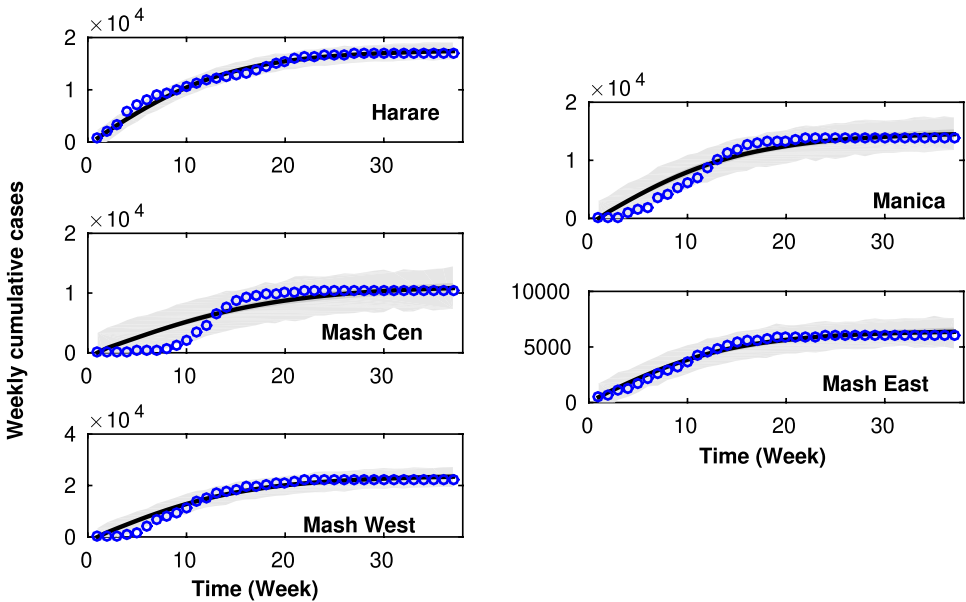


Fig. 1. Model fitting to cumulative cholera cases from five provinces of Zimbabwe. Blue circles are the discrete data points and solid black curve is model solution. Shaded region represent 95% confidence interval.

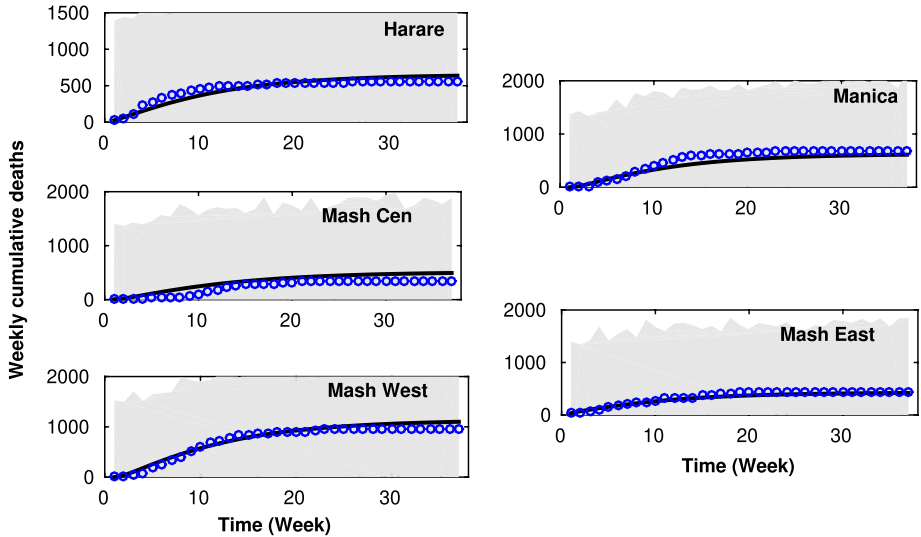


Fig. 2. Model fitting to cumulative cholera deaths from five provinces of Zimbabwe. Blue circles are the discrete data points and solid black curve is model solution. Shaded region represent 95% confidence interval.

(3) Among these 1000 samples of $\tilde{\theta}$, we choose that $\tilde{\theta}$ for which $SS_j(\theta)$ has a minimum value. Then we drew 10,000 posterior MCMC samples using Delayed Rejection Adaptive Metropolis Hastings (DRAM) algorithm^{54,55} by passing this minimum $\tilde{\theta}$ as the initial guess for the MCMC run. For the convergence of the chain, Gewekes Z-score has been examined.

Fitting of model (2.1) to cholera cases and deaths for the five provinces is depicted in Figs. 1 and 2. The estimated parameters and initial conditions of the model (2.1) are given in Tables 3 and 4. 95% confidence region is sketched around the estimated values of the parameters and the initial conditions (see Tables 3 and 4).

Table 3. Estimated parameter values of the model (2.1) for the five provinces of Zimbabwe. All data are given in the format [mean (95% CI)].

Zimbabwe province	$\beta^H(\text{week}^{-1})$	$\beta^L(\text{week}^{-1})$	$\xi(\frac{\text{cells}}{\text{mL}\cdot\text{person}\cdot\text{week}})$
Harare	1.9353E - 04 (1.6806E - 05 - 4.9551E - 04)	0.0011 (7.5791E - 04 - 0.0014)	1.8480 (1.1038 - 2.7257)
Manicaland	3.9800E - 04 (3.7264E - 05 - 7.9839E - 04)	5.9903E - 04 (2.4766E - 04 - 0.0011)	25.6696 (5.0349 - 47.9809)
Mashonaland Central	0.0013 (8.0247E - 04 - 0.0020)	1.8891E - 04 (1.4962E - 05 - 4.8585E - 04)	10.3194 (1.6044 - 26.5378)
Mashonaland East	1.1296E - 04 (8.8175E - 06 - 2.8630E - 04)	3.7414E - 04 (2.3217E - 04 - 5.3192E - 04)	10.7567 (3.4379 - 18.3966)
Mashonaland West	8.7124E - 04 (2.2158E - 04 - 0.0017)	0.0012 (7.0144E - 04 - 0.0018)	21.5661 (14.6307 - 28.7321)

Table 4. Estimated initial demographic variables of the model (2.1) for the five provinces of Zimbabwe. All data are given in the format [mean (95% CI)].

Zimbabwe province	$S(0)$ (person)	$R(0)$ (person)
Harare	1.2346E06 (1.0185E06 – 1.6141E06)	6.5145E03 (2.2263E03 – 9.7399E03)
Manicaland	1.4464E06 (1.1011E06 – 1.6511E06)	4 (2 – 6)
Mashonaland Central	7.5027E05 (5.2649E05 – 1.0156E06)	33 (13 – 47)
Mashonaland East	1.1509E06 (8.3616E05 – 1.3077E06)	328 (62 – 625)
Mashonaland West	1.0937E06 (8.4185E05 – 1.2844E06)	40 (26 – 49)

In the next section, we shall define few indices corresponding to human migration. These indices will be utilized to explore the possible link between the migration and intervention strategy.

7. Migration Index

Human migration or mobility (intercontinental, intracontinental, interregional, etc.) is technically defined as the processes through which human beings change their location in order to fulfill their purposes. Basically, migration process consists of in-migration and out-migration. In-migration means people moving into one place from another place whereas out-migration means people moving out of one place to another place.

Many authors have shown that human migration plays a key role on the spatial spread of infectious disease.^{33,44,56,57} Therefore, it is expected that, intervention strategies might be more effective if they are linked with human mobility. Implementation cost of intervention might be significantly reduced if it is targeted to those patches with high migration (in or out) rates compared to those strategies targeting all the patches. Naturally, to compare migration rates between the patches, we need to define following two indices:

- (1) **In-migration index** is denoted by \mathcal{I}_p^X and is defined by $\mathcal{I}_p^X = \frac{\sum_{j=1}^n m_{pj}^X}{n-1}$, for a particular patch p ($1 \leq p \leq n$) and for a disease status X ($X = S$ or I) of human.
- (2) **Out-migration index** is denoted by \mathcal{O}_p^X and is defined by $\mathcal{O}_p^X = \frac{\sum_{j=1}^n m_{jp}^X}{n-1}$, for a particular patch p ($1 \leq p \leq n$) and for a disease status X ($X = S$ or I) of human.

In-migration index of a patch p measures the mean proportions of individuals that visit patch p from all other patches. Out-migration index of a patch p measures the average proportions of individuals that leaves patch p . Therefore, by computing these two indices, we can compare migration rates between the patches.

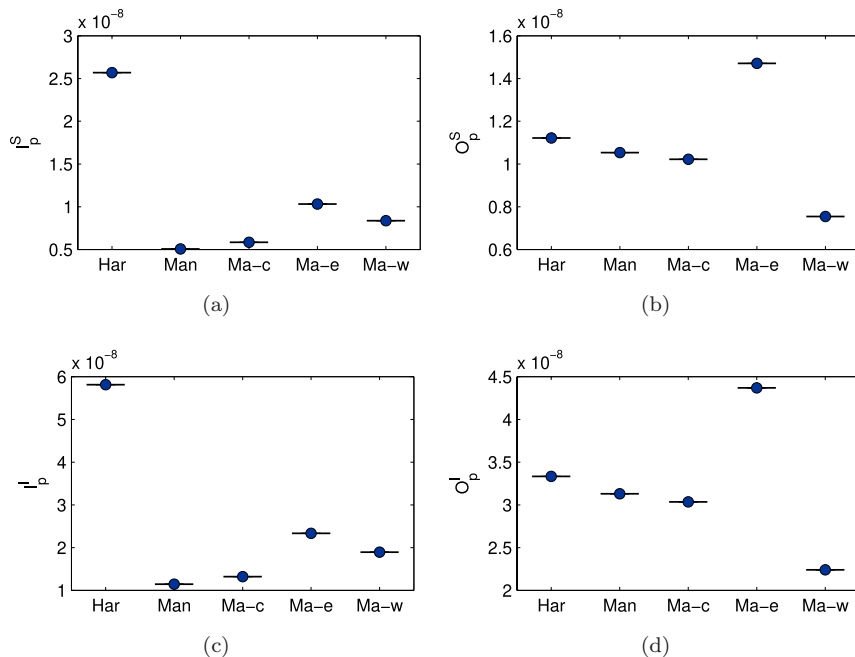


Fig. 3. In-migration indices and out-migration indices for five provinces of Zimbabwe for different epidemiological status. (a) In-migration indices for susceptible humans. (b) Out-migration indices for susceptible humans. (c) In-migration indices for infected humans. (d) Out-migration indices for infected humans. Where, Har = Harare, Man = Manicaland, Ma-c = Mashonaland Central, Ma-e = Mashonaland East, and Ma-w = Mashonaland West. Data used to draw this box and whisker plot on migration indices are taken from estimated migration rates table (see Supplementary Tables 1 and 2).

Migration indices are calculated utilizing the migration data⁹ (see Fig. 3 and Supplementary Table 4) for the patches. In-migration indices for the provinces Harare, Mashonaland East, and Mashonaland West are found to be higher than the provinces Manicaland and Mashonaland Central (see Fig. 3 and Supplementary Table 4). However, in Mashonaland East, Harare and Manicaland, the out-migration indices are found to be greater than Mashonaland Central, and Mashonaland West (see Fig. 3). In-migration index for the province Harare is found to be higher than the other provinces. This is quite natural as Harare is the capital and the most developed city in Zimbabwe.

In the next section, we shall extend the cholera model (2.1) to study the effect of two interventions namely promoting hand-hygiene, and clean water distribution and treatment.

8. Extended Model with Intervention Strategies

There are several control strategies to control cholera epidemic. Promotion of hand-hygiene, clean water supply, treatment, vaccination, sanitation are the most

studied control options in the literatures. Neilan *et al.*⁷ examined the effect of three control strategies — treatment, sanitation and vaccination — and applied it to the cholera outbreak data of Bogra and Calcutta (1900). Sardar *et al.*⁴⁵ considered four intervention strategies e.g., hand-hygiene and clean water supply, treatment, vaccination and sanitation to the Zimbabwe Cholera epidemic from 2008 to 2011. They showed that hand-hygiene, and clean water supply and treatment are more effective in comparison to other four intervention strategies. Being motivated by this result, we only adopt these two intervention strategies to study the effect of cholera control strategies on the Zimbabwe cholera epidemic. We assume that by adopting the first control strategy, the bacterial ingestion will be reduced by a fraction of $(1 - \theta_i(t))$ in each patch $i = 1, 2, \dots, n$, where $\theta_i(t)$ is the relative rate of reduction in bacterial ingestion per week in patch i by promoting hygiene practice. For the second intervention strategy, it is assumed that $\alpha_i(t)$ portion of infected people get the treatment in patch i per week. The relative rate of natural recovery of the treated people is increased by λ . The antibiotics used in the treatment process affect the excretion of the treated people.⁵⁸ Therefore, the relative shedding rate is reduced by a fraction ψ for α_i proportion of the people in patch i . Thus, the contribution of hyper-infectious bacteria coming from the treated people is given by the expression $\sum_{i=1}^n \psi \alpha_i \xi_i I_i$. The shedding rate of the $(1 - \alpha_i)$ portion untreated individual would be unchanged. Therefore, the contribution coming from the untreated people is given by $\sum_{i=1}^n (1 - \alpha_i) \xi_i I_i$.

The model (2.1) with the above two intervention strategies is now extended to the following model:

$$\begin{aligned}
 \frac{dS_i}{dt} &= \Lambda_i - (1 - \theta_i) \left[\frac{\beta_i^H B_H}{K_H + B_H} + \frac{\beta_i^L B_L}{K_L + B_L} \right] S_i - \mu_i S_i + \sum_{j=1}^n m_{ij}^S S_j \\
 &\quad - \sum_{j=1}^n m_{ji}^S S_j + \omega_i R_i, \\
 \frac{dI_i}{dt} &= (1 - \theta_i) \left[\frac{\beta_i^H B_H}{K_H + B_H} + \frac{\beta_i^L B_L}{K_L + B_L} \right] S_i - [\mu_i + \delta_i + (1 - \alpha_i) \gamma_i] \\
 &\quad + \lambda \alpha_i \gamma_i I_i + \sum_{j=1}^n m_{ij}^I I_j - \sum_{j=1}^n m_{ji}^I I_i, \\
 \frac{dR_i}{dt} &= [(1 - \alpha_i) \gamma_i + \lambda \alpha_i \gamma_i] I_i - (\omega_i + \mu_i) R_i + \sum_{j=1}^n m_{ij}^R R_j - \sum_{j=1}^n m_{ji}^R R_i, \\
 \frac{dB_H}{dt} &= \sum_{i=1}^n \psi \alpha_i \xi_i I_i + \sum_{i=1}^n (1 - \alpha_i) \xi_i I_i - \chi B_H, \\
 \frac{dB_L}{dt} &= \chi B_H - \delta_L B_L, \quad i = 1, 2, \dots, n.
 \end{aligned}
 \tag{8.1}$$

The biological interpretations and the ranges of the parameters for the cholera intervention model (8.1) are given in Table 1.

Our next job is to explore the optimal effect of two interventions by minimizing their implementation cost in different migration scenario.

9. An Optimal Cost Effectiveness Study in Different Migration Scenario

In order to determine the optimal intervention strategy/strategies i.e., the strategies for which there will be reduction of the cholera cases and deaths with minimal cost, we apply techniques of optimal control theory.⁵⁹⁻⁶¹ We construct the following cost function:

$$J(\theta_i, \alpha_i) = \int_0^T \left[A \sum_{i=1}^n \delta_i I_i + B \sum_{i=1}^n \theta_i + C \sum_{i=1}^n \alpha_i I_i + D \sum_{i=1}^n \theta_i^2 + E \sum_{i=1}^n \alpha_i^2 \right] dt. \quad (9.1)$$

Here, T denotes the number of weeks for which interventions are applied. The first term in the right-hand side of (9.1) is the cost of death due to cholera. Among the remaining four terms, the first two terms represent the costs associated with the implementation of two intervention strategies, namely hand hygiene, and clean water distribution and treatment, respectively. The last two terms (nonlinear terms) in (9.1) are the costs of interventions in emergency situations. In the expression of objective function J , A is the cost of productive time lost per premature death. The costs of percent reduction in bacterial ingestion rate by promoting hand-hygiene and water supply in normal situation and in emergency situation are denoted by B and D respectively. The costs B and D , are the costs associated in implementing the control strategy promotion of hand-hygiene and water supply in two different situations. Since the level of complicity in implementing the intervention strategy is different for the two different situations, the costs B and D are taken to be different. The costs for treatment of mild cholera cases and for severe cases are denoted by C and E , respectively. These fixed cost coefficients (i.e., A, B, C, D, E) are taken from Ref. 45. Following Ref. 45, fixed costs are transformed to subsequent intervention year costs.

A dynamical control method is used to minimize the objective function J with respect to different control parameters $\theta_i(t), \alpha_i(t)$ to determine the optimal intervention measures. Pontryagin's Maximum Principle⁶¹ is applied to solve this optimal control problem. By using this principle, the differential equation corresponding to the adjoint variables, boundary conditions, characterization of the optimal control estimates $\theta_i^*(t)$ and $\alpha_i^*(t)$ can be obtained.⁶² From Pontryagin's Maximum Principle, the representation of the control estimates is obtained in terms of the state variables and the corresponding adjoint variables. The problem of minimizing the objective functional with the respective constraints is converted by

the principle into the problem of minimizing the corresponding Hamiltonian with respect to the controls at any instant of time t . In this optimal control problem, the Hamiltonian is given by

$$\begin{aligned}
 \mathcal{H} = & \sum_{i=1}^n [A\delta_i I_i + B\theta_i + C\alpha_i I_i + D\theta_i^2 + E\alpha_i^2] \\
 & + \sum_{i=1}^n \lambda_{S_i} \left[\Lambda_i - (1 - \theta_i) \left(\frac{\beta_i^H B_H}{K_H + B_H} + \frac{\beta_i^L B_L}{K_L + B_L} \right) S_i - \mu_i S_i \right. \\
 & \left. + \sum_{j=1}^n m_{ij}^S S_j - \sum_{j=1}^n m_{ji}^S S_i + \omega_i R_i \right] \\
 & + \sum_{i=1}^n \lambda_{I_i} \left[(1 - \theta_i) \left(\frac{\beta_i^H B_H}{K_H + B_H} + \frac{\beta_i^L B_L}{K_L + B_L} \right) S_i - (\mu_i + \delta_i + (1 - \alpha_i)\gamma_i \right. \\
 & \left. + \lambda\alpha_i\gamma_i) I_i + \sum_{j=1}^n m_{ij}^I I_j - \sum_{j=1}^n m_{ji}^I I_i \right] \\
 & + \sum_{i=1}^n \lambda_{R_i} \left[((1 - \alpha_i)\gamma_i + \lambda\alpha_i\gamma_i) I_i - (\omega_i + \mu_i) R_i + \sum_{j=1}^n m_{ij}^R R_j - \sum_{j=1}^n m_{ji}^R R_i \right] \\
 & + \lambda_{B_H} \left[\sum_{i=1}^n \psi\alpha_i \xi_i I_i + \sum_{i=1}^n (1 - \alpha_i)\xi_i I_i - \chi B_H \right] + \lambda_{B_L} [\chi B_H - \delta_L B_L],
 \end{aligned} \tag{9.2}$$

where, λ_{S_i} , λ_{I_i} , λ_{R_i} , λ_{B_H} , and λ_{B_L} are the adjoint variables corresponding to state variables S_i , I_i , R_i , B_H , and B_L . The first term in the expression of Hamiltonian is the integrand of the cost function (9.1). The remaining terms are constructed by multiplying each of the adjoint variables with the corresponding right-hand side of the system of differential equations (8.1).

The set of differential equations corresponding to the adjoint variables is obtained by, $\frac{d\lambda_X}{dt} = -\frac{\partial \mathcal{H}}{\partial X}$, where $X = S_i, I_i, R_i, B_H, B_L$ and given by the following system of differential equations:

$$\begin{aligned}
 \frac{d\lambda_{S_i}}{dt} = & - \left[\lambda_{S_i} \left((1 - \theta_i) \left(\frac{\beta_i^H B_H}{K_H + B_H} + \frac{\beta_i^L B_L}{K_L + B_L} \right) - \mu_i - \sum_{j=1}^n m_{ji}^S \right) \right. \\
 & \left. + \lambda_{I_i} \left((1 - \theta_i) \left(\frac{\beta_i^H B_H}{K_H + B_H} + \frac{\beta_i^L B_L}{K_L + B_L} \right) \right) \right],
 \end{aligned}$$

$$\begin{aligned}
 \frac{d\lambda_{I_i}}{dt} &= - \left[A\delta_i + C\alpha_i - \lambda_{I_i} \left(\mu_i + \delta_i + (1 - \alpha_i)\gamma_i + \lambda\alpha_i\gamma_i + \sum_{j=1}^n m_{ji}^I \right) \right. \\
 &\quad \left. + \lambda_{R_i}((1 - \alpha_i)\gamma_i + \lambda\alpha_i\gamma_i) + \lambda_{B_H}(\psi\alpha_i\xi_i + (1 - \alpha_i)\xi_i) \right], \\
 \frac{d\lambda_{R_i}}{dt} &= - \left[\lambda_{S_i}\omega_i + \lambda_{R_i} \left(-(\omega_i + \mu_i) - \sum_{j=1}^n m_{ji}^R \right) \right], \\
 \frac{d\lambda_{B_H}}{dt} &= \sum_{i=1}^n (\lambda_{S_i} - \lambda_{I_i}) \frac{(1 - \theta_i)\beta_i^H K_H S_i}{(K_H + B_H)^2} + \chi(\lambda_{B_H} - \lambda_{B_L}), \\
 \frac{d\lambda_{B_L}}{dt} &= \sum_{i=1}^n (\lambda_{S_i} - \lambda_{I_i}) \frac{(1 - \theta_i)\beta_i^L K_L S_i}{(K_L + B_L)^2} + \lambda_{B_L} \delta_L, \quad i = 1, 2, \dots, n.
 \end{aligned}
 \tag{9.3}$$

The boundary conditions are given by $\lambda_X(T) = 0$, where $X = S_i, I_i, R_i, B_H, B_L$. The optimal control estimates are characterized as follows:

$$\begin{aligned}
 \theta_i^* &= \max(0, \min(\tilde{\theta}_i, \theta_{\max}^i)) \\
 \alpha_i^* &= \max(0, \min(\tilde{\alpha}_i, \alpha_{\max}^i)), \quad i = 1, 2, \dots, n
 \end{aligned}
 \tag{9.4}$$

where θ_{\max}^i and α_{\max}^i are the maximum efforts of the controls θ_i and α_i , respectively. The expressions of $\tilde{\theta}_i$ and $\tilde{\alpha}_i$ are obtained by equating the terms $\frac{\partial \mathcal{H}}{\partial \theta_i}$ and $\frac{\partial \mathcal{H}}{\partial \alpha_i}$ to zero, respectively. The expressions of θ_i and α_i are given as follows:

$$\begin{aligned}
 \tilde{\theta}_i &= \frac{(\lambda_{I_i} - \lambda_{S_i}) \left(\frac{\beta_i^H B_H}{K_H + B_H} + \frac{\beta_i^L B_L}{K_L + B_L} \right) S_i - B}{2D} \\
 \tilde{\alpha}_i &= \frac{[(1 - \lambda)\gamma_i(\lambda_{R_i} - \lambda_{I_i}) + (1 - \psi)\xi_i\lambda_{B_H} - C]I_i}{2E}, \quad i = 1, 2, \dots, n.
 \end{aligned}
 \tag{9.5}$$

The set of differential equations (8.1) for the state variables along with the set of differential equations (9.3) corresponding to the adjoint variables with the above control characterization (9.4) are solved numerically. The state system is solved forward in time and the adjoint system is then solved backward in time by following.⁵⁹

Due to limited resources in a cholera prone region like Zimbabwe and other developing countries, targeting a fewer regions for implementation of control strategies appears to be quite reasonable. Since the immigration and emigration between the provinces play a key role in varying population size, the migration indices defined in our study is crucial to determine the target patches. The main objective of this optimal cost effectiveness study is to provide a possible answer to the question: Is it advantageous to implement intervention strategies in fewer patches instead of all? The patches where control strategies should be implemented are identified by utilizing the migration indices. Such patches are selected on the basis of higher

in-migration index and higher out-migration index. However, to find an answer to the above-mentioned question, the optimal effect of two cholera interventions (PH and CW distribution and treatment) and their layered combinations in different scenarios depending on human mobility are studied in the following settings:

- (1) Promotion of **PH** and **CW** supply to all the five provinces.
- (2) **PH** and **CW** in three provinces — Harare (1), Manicaland (2), Mashonaland East (4) — with higher out-migration index.
- (3) **PH** and **CW** also in three provinces — Harare (1), Mashonaland East (4), Mashonaland West (5) — with higher in-migration index.
- (4) Providing treatment (**Tr**) to cholera patients in all provinces.
- (5) Providing **Tr** in the provinces 1, 2, 4.
- (6) Providing **Tr** also in the provinces 1, 4, 5.
- (7) Combinations of **PH** and **CW** with **Tr** in all the provinces.
- (8) Combinations of **PH** and **CW** with **Tr** in the provinces 1, 2, 4.
- (9) Combinations of **PH** and **CW** with **Tr** also in the provinces 1, 4, 5.

The average coverage percentages (per week) of PH and CW distributions $\hat{\theta}_i$ s and treatment $\hat{\alpha}_i$ s are estimated using the following formulas:

$\hat{\theta}_i = \frac{\int_0^T \theta_{ci}(t) dt}{T} \times 100$ and $\hat{\alpha}_i = \frac{\int_0^T \alpha_{ci}(t) dt}{T} \times 100$, where $\theta_{ci}(t)$ and $\alpha_{ci}(t)$ are the optimal rates of PH and CW distribution and treatment, respectively, for i th patch, for which the cost function J is minimum.

Cost per averted case and death for an intervention is calculated using the following formulae:

$$\text{Cost per averted case} = \frac{\text{Total cost of an intervention}}{\text{Total number of cases averted by that intervention}},$$

$$\text{Cost per averted death} = \frac{\text{Total cost of an intervention}}{\text{Total number of deaths averted by that intervention}}.$$

Dividing the cost per averted case and death by the total number of patch, the average costs are also calculated for each of the five provinces.

10. Results and Discussion

A major threat to human society is *vibrio cholerae* which has caused seven pandemics since 1817.¹ Several studies have been carried out both on non-spatial and spatial scales with an aim to reduce the burden of the diseases by implementing intervention strategies. Unfortunately, the link between human migration and intervention strategies is still missing. To fill up this gap, we proposed and analyzed cholera meta-population models (2.1) and (8.1) for having a possible link between human mobility in five provinces of Zimbabwe with intervention strategies (hand-hygiene & clean water distribution and treatment). The basic aim of such study is to point out the provinces where the interventions should be provided at a minimum implementation cost.

To establish our goal, we first estimated several important parameters of the cholera model (2.1) including the transmission rates of high and low infectious cholera bacterium (β_i^H and β_i^L , respectively) for the five provinces (see Table 3). It is observed that the average low-infectious transmission ($\beta^L = \frac{\sum_{i=1}^n \beta_i^L}{n}$) is found to be greater than the average high-infectious transmission ($\beta^H = \frac{\sum_{i=1}^n \beta_i^H}{n}$) for the five provinces. This means that the contacts of susceptible human population with the water containing hyper-infectious cholera bacterium is less frequent than the contacts with water contaminated with low-infectious cholera bacterium. This might happen due to the fact that the hyper-infectious bacteria is short lived compared to low-infectious bacterium.⁶³ However, these estimates are in accordance with the previous studies.^{6,45} Estimates for the shedding rate by infected human (ξ_i) (see Table 3) vary in 10^1 scale over the provinces which agree with the estimates given in Ref. 45. From the expression of the *domain* basic reproduction number \mathcal{R}_0 in

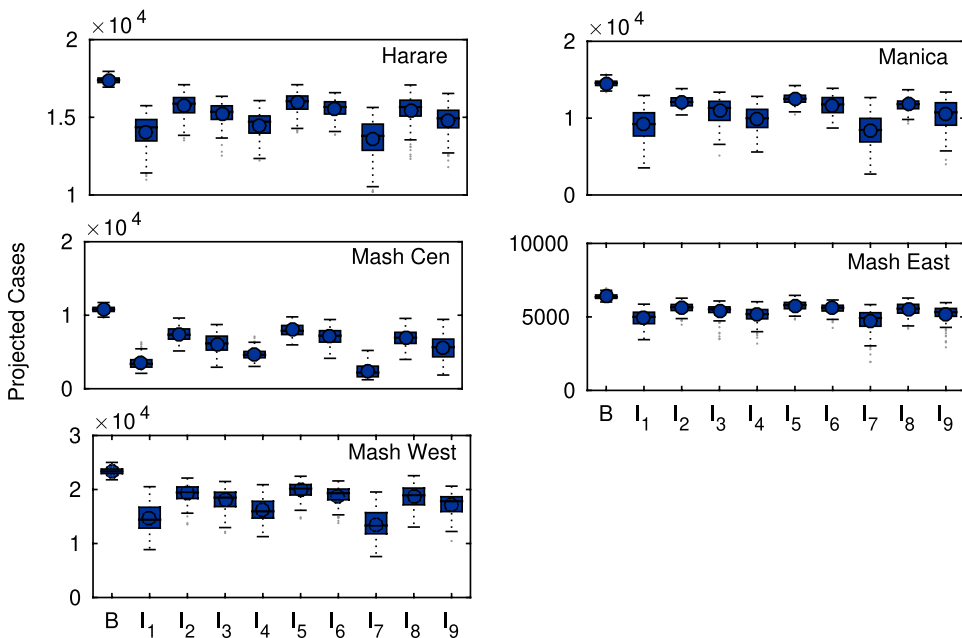


Fig. 4. Box and whisker plot of the projected cases in different provinces for different intervention settings during the epidemic in 2008–09, where, B is the base cases during 2008–09 epidemic predicted by the cholera model (2.1). I_1 = promotion hand-hygiene and clean water distribution (PH and CW) in all five provinces, I_2 = PH and CW in three provinces with higher out-migration index, I_3 = PH and CW in three provinces with higher in-migration index, I_4 = Providing treatment (Tr) to cholera patients in all provinces, I_5 = Providing Tr in three provinces with higher out-migration index, I_6 = Providing Tr in three provinces with higher in-migration index, I_7 = Combination of PH and CW with Tr in all five provinces, I_8 = Combination of PH and CW with Tr in three provinces with higher out-migration index, and I_9 = Combination of PH and CW with Tr in three provinces with higher in-migration index. This prediction is based upon estimated parameters of the model (2.1) for the five provinces (see Table 1) and minimizing the cost function J in (9.1) with respect of intervention parameters.

(3.1), it is clear that \mathcal{R}_0 depends upon several important parameters including two transmission rates (β_i^H and β_i^L) and shedding rates (ξ_i). Therefore, using estimated model parameters (see Table 3), the *domain* basic reproduction number^{2,64} \mathcal{R}_0 is found to be **1.5371 (1.2098–1.7958)**. We also estimated two partial reproduction numbers \mathcal{R}_l (**0.3520 [0.1781–0.5981]**) and \mathcal{R}_h (**1.1852 [0.7450–1.5765]**) defined in Eqs. (3.2) and (3.3) from our model. The estimated value of \mathcal{R}_h is found to be higher than \mathcal{R}_l . This indicates that in these five provinces, cholera infection is dominated by the hyper-infectious transmission. This finding agrees with the previous studies.^{6,45}

Sensitivity analysis of important parameters with the *domain* basic reproduction number (\mathcal{R}_0) suggests that transmission rates of high-infected bacterium (β_i^H) and human shedding rates (ξ_i) are positively correlated with \mathcal{R}_0 (see Table 2). Therefore, reducing these parameters may reduce the cholera transmission in these provinces.

It is observed that migration indices vary over the provinces (see Fig. 3; Supplementary Table 4). Some provinces have higher in-migration index (Harare, Mashonaland East, Mashonaland West) whereas others have higher out-migration index (Harare, Manicaland, Mashonaland East). However, for Harare, the human migration flow is found out to be moderate as it is the capital and the most populous city of Zimbabwe.

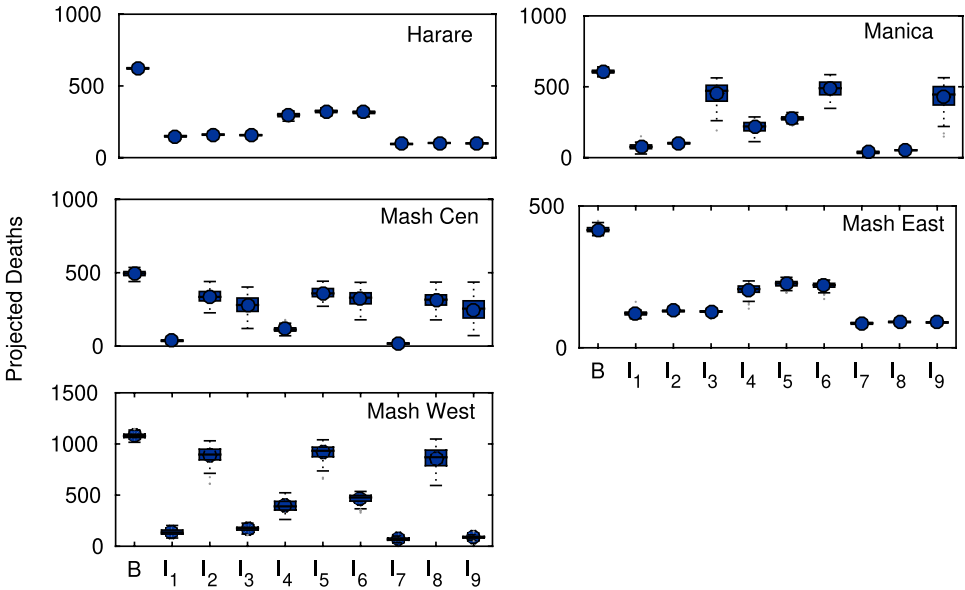


Fig. 5. Box and whisker plot of the projected deaths in different provinces for different intervention settings during the epidemic in 2008–09, where $B, I_1, I_2, I_3, I_4, I_5, I_6, I_7, I_8,$ and I_9 are same as in Fig. 4. This prediction is based upon estimated parameters of the model (2.1) for the five provinces (see Table 1) and minimizing the cost function J in (9.1) with respect of intervention parameters.

In terms of case and death reduction, the combined effect of hygiene practice and treatment is found to be advantageous if it is applied to all the five provinces (see Figs. 4 and 5 and Supplementary Tables 5 and 6). Although this intervention setting reduces maximum cases and deaths, it is not efficient in terms of its implementation cost. Carrying out this intervention in all provinces will require a total cost **0.210 (0.197–0.220)** million USD (see Supplementary Table 8). Cost per averted case and death for this intervention is found to be **7.20 (5.56–9.23)** USD and **71.86 (67.02–76.94)** USD, respectively (see Figs. 7 and 8 and Supplementary Tables 9 and 10). Our analysis suggests that the intervention that will maximize cases and deaths reduction at a minimum cost is the promotion of PH and CW distribution in the provinces with higher in-migration. Overall case reduction for this intervention is **16643 (13987–24261)** (see Fig. 4 and Supplementary Table 5) with its implementation cost being **0.087 [0.086–0.087]** million USD (see Fig. 6 and Supplementary Table 8). Overall death reduction for this intervention is **2035 (1923–2204)** (see Fig. 5 and Supplementary Table 6). Cost per averted death for this intervention is found to be **42.97 (37.76–47.72)** USD (see Fig. 8 and Supplementary Table 8). This intervention should be implemented at an average coverage of **77.6% (77.1–77.8%)** population per week (see Supplementary Table 7).

Above study implies that in terms of case and death reduction, hygiene practice would be most cost-effective among the different intervention settings if it is applied to the provinces Harare, Mashonaland East and Mashonaland West. In

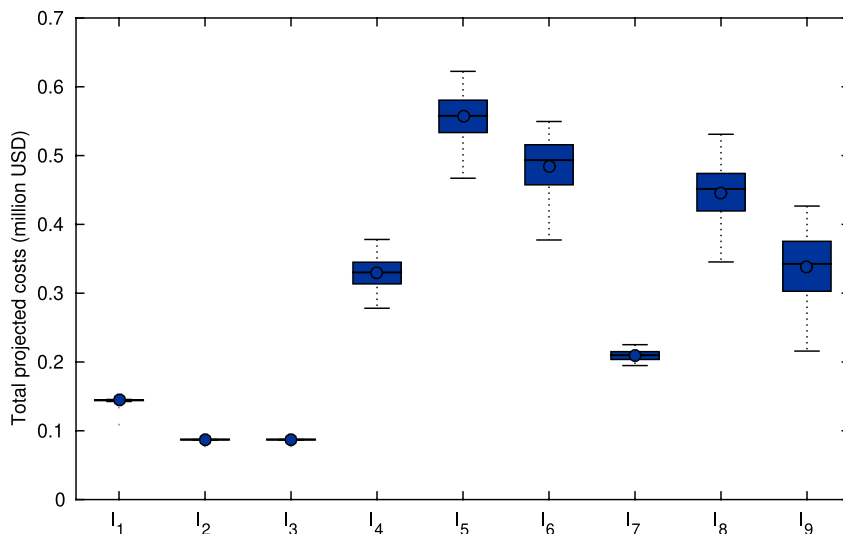


Fig. 6. Box and whisker plot of the total projected costs for implementing different intervention measures in all five provinces during the 2008–09 epidemic. Cost are provided in million USD, where, I_1 , I_2 , I_3 , I_4 , I_5 , I_6 , I_7 , I_8 , and I_9 are same interventions defined in Fig. 4. These cost of interventions are derived using the estimated parameters of the model (2.1) for the five provinces (see Table 1) and minimizing the cost function J in (9.1) with respect of intervention parameters.

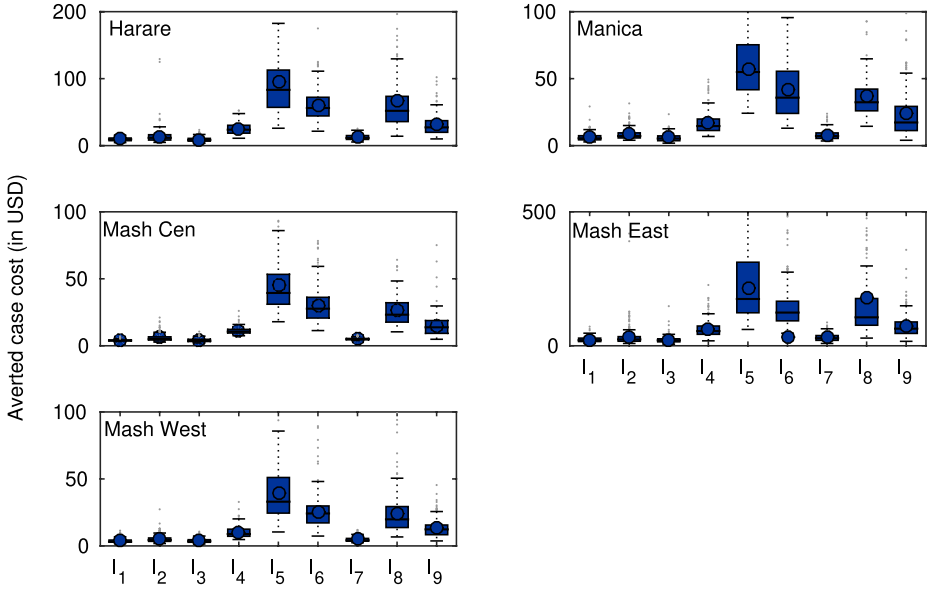


Fig. 7. Box and whisker plot of the average cost per averted case (in USD) for different intervention measures for different provinces, where, $I_1, I_2, I_3, I_4, I_5, I_6, I_7, I_8,$ and I_9 are same interventions defined in Fig. 4. Data used to draw the figure are taken from Supplementary Table 9.

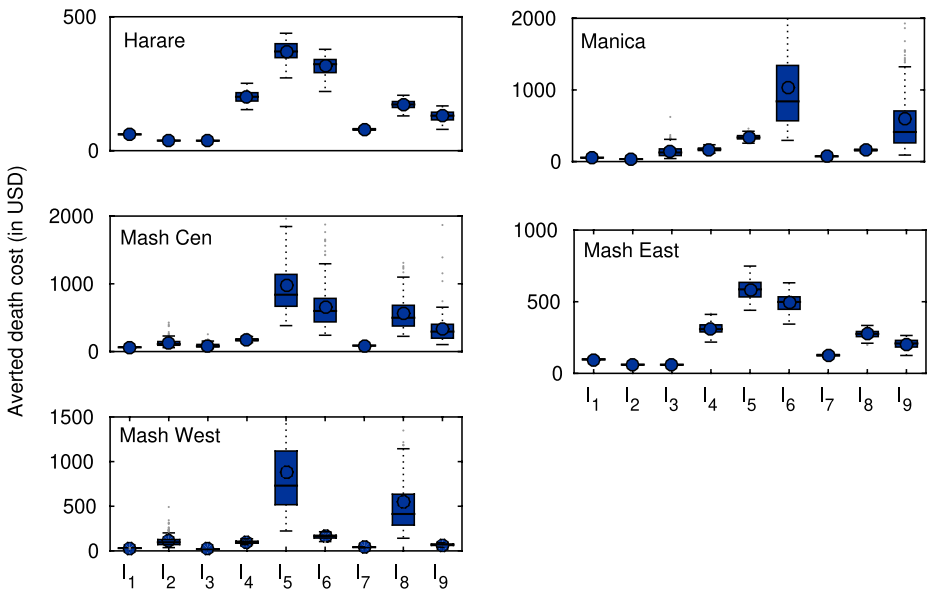


Fig. 8. Box and whisker plot of the average cost per averted death (in USD) for different intervention measures for different provinces, where, $I_1, I_2, I_3, I_4, I_5, I_6, I_7, I_8,$ and I_9 are same interventions defined in Fig. 4. Data used to draw the figure are taken from Supplementary Table 10.

these provinces, in-migration flow of human population is found to be relatively higher than the remaining two provinces. In summary, we recommend to implement hygiene practice in those provinces where the in-migration flow is moderate. Chao *et al.*⁶⁵ recommend in case of limited supply of vaccine, for epidemic cholera, coverage of 30% country's population to be targeted at high risk of exposure. We also believe that to provide control measures for all provinces is highly expensive and not easy to accommodate for developing countries and hence to control the epidemic of the country, only provide control measures for the provinces where in-migration flow is moderate. Spatially explicit models are very useful to analyze the effect of human migration in cholera transmission and also on control strategies. There is almost no scope in single-patch model setting to study the effect of control strategies that depend explicitly on space.

There are some drawbacks in our study. We consider a common water source that can be extended to a finite number of contaminated water sources (see Refs. 2, 43 and 66, etc). Cholera model considered in this study does not assume periodicity in transmission rate. We have not also used the epidemic data for all the ten provinces of Zimbabwe. We leave these extensions and modifications for our future study.

Acknowledgments

Abhishek Senapati is supported by the research fellowship from Council of Scientific & Industrial Research (Grant No: 09/093(0167)/2015/EMR-I), Government of India. The authors would like to thank the editors and anonymous reviewers for their valuable suggestions and constructive comments, which really helped to improve the presentation and quality of the paper.

References

1. Hays JN, *Epidemics and Pandemics: Their Impacts on Human History*, ABC-CLIO, 2005.
2. WHO (2014), Fact Sheet No. 107 Cholera, <http://www.who.int/mediacentre/factsheets/fs107/en/>, 2014 [Online accessed-15/09/2016].
3. Capasso V, Paveri-Fontana SL, A mathematical model for the 1973 cholera epidemic in the European Mediterranean region, *Rev Epidemet Sant Publ* **27**(2):121–132, 1979.
4. Codeço CT, Endemic and epidemic dynamics of cholera: The role of the aquatic reservoir, *BMC Infect Dis* **1**:1, 2001.
5. Hartley DM, Morris Jr JG, Smith DL, Hyperinfectivity: A critical element in the ability of *v. cholerae* to cause epidemics? *PLoS Med* **3**(1):e7, 2005.
6. Mukandavire Z, Liao S, Wang J, Gaff H, Smith DL, Morris JG, Estimating the reproductive numbers for the 2008/2009 cholera outbreaks in Zimbabwe, *Proc Natl Acad Sci USA* **108**(21):8767–8772, 2011.
7. Neilan RLM, Schaefer E, Gaff H, Fister KR, Lenhart S, Modeling optimal intervention strategies for cholera, *Bull Math Biol* **72**(8):2004–2018, 2010.
8. Xiao D, Ruan S, Global analysis of an epidemic model with nonmonotone incidence rate, *Math Biosci* **208**(2):419–429, 2007.

9. Xu R, Ma Z, Global stability of a delayed SEIRS epidemic model with saturation incidence rate, *Nonlinear Dynam* **61**(1–2):229–239, 2010.
10. Tian JP, Wang J, Global stability for cholera epidemic models, *Math Biosci* **232**(1):31–41, 2011.
11. Lubuma J, Tsanou B, Global stability of a two patch cholera model with fast and slow transmission, *Biomath Commun* **1**(1): 2014.
12. Yang J, Qiu Z, Li XZ, Global stability of an age-structured cholera model, *Math Biosci Eng* **11**(3):641–665, 2014.
13. Pascual M, Rodó X, Ellner SP, Colwell R, Bouma MJ, Cholera dynamics and El Niño-Southern oscillation, *Science* **289**(5485):1766–1769, 2000.
14. Andrews JR, Basu S, Transmission dynamics and control of cholera in Haiti: An epidemic model, *The Lancet* **377**(9773):1248–1255, 2011.
15. Sun GQ, Xie JH, Huang SH, Jin Z, Li MT, Liu L, Transmission dynamics of cholera: Mathematical modeling and control strategies, *Commun Nonlinear Sci Numer Simul* **45**:235–244, 2017.
16. Wang X, Gao D, Wang J, Influence of human behavior on cholera dynamics, *Math Biosci* **267**:41–52, 2015.
17. Posny D, Wang J, Mukandavire Z, Modnak C, Analyzing transmission dynamics of cholera with public health interventions, *Math Biosci* **264**:38–53, 2015.
18. Cai LM, Modnak C, Wang J, An age-structured model for cholera control with vaccination, *Appl Math Comput* **299**:127–140, 2017.
19. Fulford GR, Roberts MG, Heesterbeek JAP, The metapopulation dynamics of an infectious disease: tuberculosis in possums, *Theor Popul Biol* **61**(1):15–29, 2002.
20. Riley S, Large-scale spatial-transmission models of infectious disease, *Science* **316**(5829):1298–1301, 2007.
21. Balcan D, Colizza V, Gonçalves B, Hu H, Ramasco J, Vespignani A, Multiscale mobility networks and the spatial spreading of infectious diseases, *Proc Natl Acad Sci USA* **106**(51):21484–21489, 2009.
22. Belik V, Geisel T, Brockmann D, Natural human mobility patterns and spatial spread of infectious diseases, *Phys Rev X* **1**(1):011001, 2011.
23. Lloyd AL, Jansen VAA, Spatiotemporal dynamics of epidemics: synchrony in metapopulation models, *Math Biosci* **188**(1):1–16, 2004.
24. Allen LJS, Brauer F, Van den Driessche P, Wu J, *Mathematical Epidemiology*, Springer, 2008.
25. Arino J, Van den Driessche P, Metapopulation epidemic models. A survey, *Fields Inst Commun* **48**:1–13, 2006.
26. Kot M, *Elements of Mathematical Ecology*, Cambridge University Press, 2001.
27. Keeling MJ, Rohani P, *Modeling Infectious Diseases in Humans and Animals*, Princeton University Press, 2008.
28. Njagarah JBH, Nyabadza F, A metapopulation model for cholera transmission dynamics between communities linked by migration, *Appl Math Comput* **241**:317–331, 2014.
29. Wang W, Mulone G, An epidemic model in a patchy environment, *Math Biosci* **190**(1):97–112, 2004.
30. Wang W, Zhao X-Q, Threshold of disease transmission in a patch environment, *J Math Anal Appl* **285**(1):321–335, 2003.
31. Arino J, Van Den Driessche P, The basic reproduction number in a multi-city compartmental epidemic model, *Positive Systems*, pp. 135–142, Springer, 2003.
32. Arino J, Van den Driessche P, A multi-city epidemic model, *Math Popul Stud* **10**(3):175–193, 2003.

33. Salmani M, Van den Driessche P, A model for disease transmission in a patchy environment, *Discrete Continuous Dyn Syst Ser B* **6**(1):185, 2006.
34. Arino J, Portet S, Epidemiological implications of mobility between a large urban centre and smaller satellite cities, *J Math Biol* **71**(5):1243–1265, 2015.
35. Li MY, Shuai Z, Global stability of an epidemic model in a patchy environment, *Canad Appl Math Quart* **17**(1):175–187, 2009.
36. Arino J, Ducrot A, Zongo P, A metapopulation model for malaria with transmission-blocking partial immunity in hosts, *J Math Biol* **64**(3):423–448, 2012.
37. Sun GQ, Jusup M, Jin Z, Wang Y, Wang Y, Pattern transitions in spatial epidemics: Mechanisms and emergent properties, *Phys Life Rev* **19**:43–73, 2016.
38. Li L, Patch invasion in a spatial epidemic model, *Appl Math Comput* **258**:342–349, 2015.
39. Poletto C, Tizzoni M, Colizza V, Human mobility and time spent at destination: Impact on spatial epidemic spreading, *J Theor Biol* **338**:41–58, 2013.
40. Eisenberg MC, Shuai Z, Tien JH, Van den Driessche P, A cholera model in a patchy environment with water and human movement, *Math Biosci* **246**(1):105–112, 2013.
41. Bertuzzo E, Azaele S, Maritan A, Gatto M, Rodriguez-Iturbe I, Rinaldo A, On the space-time evolution of a cholera epidemic, *Water Resour Res* **44**(1):W01424, 2008.
42. Robertson SL, Eisenberg MC, Tien JH, Heterogeneity in multiple transmission pathways: Modelling the spread of cholera and other waterborne disease in networks with a common water source, *J Biol Dyn* **7**(1):254–275, 2013.
43. Kelly Jr MR, Tien JH, Eisenberg MC, Lenhart S, The impact of spatial arrangements on epidemic disease dynamics and intervention strategies, *J Biol Dyn* **10**(1):222–249, 2016.
44. Knipf D, A new approach for designing disease intervention strategies in metapopulation models, *J Biol Dyn* **10**(1):71–94, 2015.
45. Sardar T, Mukhopadhyay S, Bhowmick AR, Chattopadhyay J, An optimal cost effectiveness study on Zimbabwe cholera seasonal data from 2008–2011, *PLoS One* **8**(12):e81231, 2013.
46. Cosner C, Beier JC, Cantrell RS, Impoinvil D, Kapitanski L, Potts MD, Troyo A, Ruan S, The effects of human movement on the persistence of vector-borne diseases, *J Theor Biol* **258**(4):550–560, 2009.
47. CENSUS (2012), National Report Zimbabwe 2012, <http://www.zimstat.co.zw/sites/default/files/img/publications/Population/NationalReport.pdf>, [Online accessed-1/02/2018].
48. Shuai Z, Van den Driessche P, Modelling and control of cholera on networks with a common water source, *J Biol Dyn* **9**(Suppl 1):90–103, 2015.
49. WHO (2009). Cholera in Zimbabwe: Epidemiological Bulletin Number 5, <http://www.who.int/hac/crises/zwe/sitreps/epiarchive/en/index4.html/>, 2009 [Online accessed-15/09/2016].
50. Marino S, Hogue IB, Ray CJ, Kirschner DE, A methodology for performing global uncertainty and sensitivity analysis in systems biology, *J Theor Biol* **254**(1):178–196, 2008.
51. WHO (2008). Cholera in Zimbabwe: Epidemiological Bulletin Number 1-117, <http://www.who.int/hac/crises/zwe/sitres/epiarchive/en/index4.html/>, 2008 [Online accessed-15/09/2016].
52. WHO (2008). Cholera in Zimbabwe: Epidemiological Bulletin Number 25, http://www.602_who.int/hac/crises/zwe/sitres/epiarchive/en/index4.html/, 2008 [Online accessed-15/09/2016].

53. CIA (2009). The World Factbook, <http://www.cia.gov/library/publications/download/download2009/index.html/>, 2009 [Online accessed-15/09/2016].
54. Haario H, Saksman E, Tamminen J, An adaptive Metropolis algorithm, *Bernoulli* **7**(2):223–242, 2001.
55. Haario H, Laine M, Mira A, Saksman E, DRAM: Efficient adaptive MCMC, *Stat Comput* **16**(4):339–354, 2006.
56. Hsieh Y-H, Van den Driessche P, Wang L, Impact of travel between patches for spatial spread of disease, *Bull Math Biol* **69**(4):1355–1375, 2007.
57. Ruan S, Wang W, Levin SA, The effect of global travel on the spread of SARS, *Math Biosci Eng* **3**(1):205, 2006.
58. Saha D, Karim MM, Khan WA, Ahmed S, Salam MA, Bennish ML, Single-dose azithromycin for the treatment of cholera in adults, *N Engl J Med* **354**(23):2452–2462, 2006.
59. Lenhart S, Workman JT, *Optimal Control Applied to Biological Models*, CRC Press, 2007.
60. Donald K, *Optimal Control Theory: An Introduction*, Dover Publications, Inc., Mineola, NY, 1970.
61. Pontryagin LS, *Mathematical Theory of Optimal Processes*, CRC Press, 1987.
62. Fleming WH, Rishel RW, *Deterministic and Stochastic Optimal Control*, Springer, New York, 1975.
63. Merrell DS *et al.*, Host-induced epidemic spread of the cholera bacterium, *Nature* **417**(6889):642–645, 2002.
64. Allen LJS, Bolker BM, Lou Y, Nevai AL, Asymptotic profiles of the steady states for an SIS epidemic patch model, *SIAM J Appl Math* **67**(5):1283–1309, 2007.
65. Chao DL, Halloran ME, Longini Jr IM, Vaccination strategies for epidemic cholera in Haiti with implications for the developing world, *Proc Natl Acad Sci USA* **108**:17, 2011.
66. Tien JH, Shuai Z, Eisenberg MC, Van den Driessche P, Disease invasion on community networks with environmental pathogen movement, *J Math Biol* **70**(5):1065–1092, 2015.
67. King AA, Ionides EL, Pascual M, Bouma MJ, Inapparent infections and cholera dynamics, *Nature* **454**(7206):877–880, 2008.
68. Rahaman MM, Majid MA, Alam AKMJ, Islam MR, Effects of doxycycline in actively purging cholera patients: A double-blind clinical trial, *Antimicrob Agents Chemother* **10**(4):610–612, 1976.
69. Levine MM *et al.*, Volunteer studies of deletion mutants of *Vibrio cholerae* O1 prepared by recombinant techniques, *Infect Immun* **56**(1):161–167, 1988.

Supplementary Information

Basic Properties of the Basic Cholera Model

The proposed model is given as follows:

$$\begin{aligned} \frac{dS_i}{dt} = & \Lambda_i - \frac{\beta_i^H B_H}{K_H + B_H} S_i - \frac{\beta_i^L B_L}{K_L + B_L} S_i - \mu_i S_i + \sum_{j=1}^n m_{ij}^S S_j \\ & - \sum_{j=1}^n m_{ji}^S S_j + \omega_i R_i, \end{aligned}$$

$$\begin{aligned}
 \frac{dI_i}{dt} &= \frac{\beta_i^H B_H}{K_H + B_H} S_i + \frac{\beta_i^L B_L}{K_L + B_L} S_i - (\mu_i + \delta_i + \gamma_i) I_i \\
 &\quad + \sum_{j=1}^n m_{ij}^I I_j - \sum_{j=1}^n m_{ji}^I I_i, \\
 \frac{dR_i}{dt} &= \gamma_i I_i - (\omega_i + \mu_i) R_i + \sum_{j=1}^n m_{ij}^R R_j - \sum_{j=1}^n m_{ji}^R R_i, \\
 \frac{dB_H}{dt} &= \sum_{i=1}^n \xi_i I_i - \chi B_H, \\
 \frac{dB_L}{dt} &= \chi B_H - \delta_L B_L, \quad i = 1, 2, \dots, n.
 \end{aligned}
 \tag{S-1}$$

Lemma 1. *The system of equations (S-1) preserve the positivity of the solutions.*

Proof. To show the positivity of the solutions it is sufficient to show that each of the faces of the positive orthant cannot be crossed that means the vector field points inward on the boundary of \mathbb{R}_+^{3n+2} . We assume that at time $t = 0$ all the variables are non-negative. Now for example if we take $S_i = 0$ in the first equation of (S-1) then, $\frac{dS_i}{dt} = \Lambda_i + \sum_{j=1}^n m_{ij}^S S_j + \omega_i R_i \geq 0$, which implies that $S_i = 0$ cannot be crossed from positive to negative S_i . Similar arguments can be applied to the other variables. This proves the positivity of the solutions. \square

Lemma 2. *The solutions $(S_i(t), I_i(t), R_i(t), B_H(t), B_L(t))$ of the system (S-1) are uniformly and ultimately bounded in \mathbb{R}_+^{3n+2} .*

Proof. Let $N_i(t) = S_i(t) + I_i(t) + R_i(t)$ be the total number of human population in patch i at time t and $N = \sum_{i=1}^n N_i$ be the total human population size in all patches. Also we denote $\sum_{i=1}^n \Lambda_i = \Lambda$, $\min_{1 \leq i \leq n} \{\mu_i\} = \mu$ and $\max_{1 \leq i \leq n} \{\xi_i\} = \xi$. Now adding first $3n$ equations in (S-1),

$$\frac{dN_i}{dt} = \Lambda_i - \mu_i N_i - \delta_i I_i + \sum_{X=S,I,R} \left(\sum_{j=1}^n m_{ij}^X X_j - \sum_{j=1}^n m_{ji}^X X_i \right). \tag{S-2}$$

Now summing over i from 1 to n in (S-2) we get,

$$\frac{dN}{dt} = \sum_{i=1}^n \left[\Lambda_i - \mu_i N_i - \delta_i I_i + \sum_{X=S,I,R} \left(\sum_{j=1}^n m_{ij}^X X_j - \sum_{j=1}^n m_{ji}^X X_i \right) \right]. \tag{S-3}$$

The double summation in the above equation vanishes and since $I_i \leq N_i$, it follows that

$$\frac{dN}{dt} \leq \sum_{i=1}^n \Lambda_i - \sum_{i=1}^n \mu_i N_i \tag{S-4}$$

and thus,

$$\frac{dN}{dt} \leq \sum_{i=1}^n \Lambda_i - \min_{1 \leq i \leq n} \{\mu_i\} N. \tag{S-5}$$

Hence by standard comparison theorem, there exists $t_1 \geq 0$ such that

$$N(t) \leq \left\{ \frac{\sum_{i=1}^n \Lambda_i}{\min_{1 \leq i \leq n} \{\mu_i\}} \right\} \Rightarrow N(t) \leq \frac{\Lambda}{\mu}, \quad \text{for all } t \geq t_1. \tag{S-6}$$

By using the similar arguments for the last two equations of (S-1), $\exists t_2 \geq t_1$ and $T \geq t_1, t_2$ such that

$$B_H(t) \leq \frac{\Lambda\xi}{\chi\mu} \quad \text{for all } t \geq t_2 \tag{S-7}$$

and

$$B_L(t) \leq \frac{\Lambda\xi}{\delta_L\mu} \quad \text{for all } t \geq T. \tag{S-8}$$

Let $K = \max \left\{ \frac{\Lambda}{\mu}, \frac{\Lambda\xi}{\chi\mu}, \frac{\Lambda\xi}{\delta_L\mu} \right\}$. Thus it follows that, $N(t) \leq K, B_H(t) \leq K, B_L(t) \leq K$.

Therefore the solutions of the system (S-1) are uniformly and ultimately bounded in \mathbb{R}_+^{3n+2} . □

Corollary 1. *The region $\Omega = \{(S_i, I_i, R_i) \in \mathbb{R}_+^{3n} : N \leq \frac{\Lambda}{\mu}, B_H \in \mathbb{R}_+ : B_H \leq \frac{\Lambda\xi}{\chi\mu}, B_L \in \mathbb{R}_+ : B_L \leq \frac{\Lambda\xi}{\delta_L\mu}\}$ is invariant and attracting for system (S-1).*

Stability Analysis of the Model (S-1)

Existence of disease-free equilibrium:

Disease free equilibrium (DFE) refers to the point at which no disease persists in the population. We set $I_i = B_H = B_L = 0$ in the equation (S-1). Then the system of equation (S-1) reduces to:

$$\frac{dS_i}{dt} = \Lambda_i - \mu_i S_i + \sum_{j=1}^n m_{ij}^S S_j - \sum_{j=1}^n m_{ji}^S S_i + \omega_i R_i, \tag{S-9}$$

$$\frac{dR_i}{dt} = -(\omega_i + \mu_i) R_i + \sum_{j=1}^n m_{ij}^R R_j - \sum_{j=1}^n m_{ji}^R R_i, \quad i = 1, 2, \dots, n.$$

To find the DFE, we consider the following set of equations:

$$0 = \Lambda_i - \mu_i S_i + \sum_{j=1}^n m_{ij}^S S_j - \sum_{j=1}^n m_{ji}^S S_i + \omega_i R_i, \tag{S-10}$$

$$0 = -(\omega_i + \mu_i) R_i + \sum_{j=1}^n m_{ij}^R R_j - \sum_{j=1}^n m_{ji}^R R_i, \quad i = 1, 2, \dots, n.$$

This can be written in the matrix form as:

$$\begin{aligned} \mathcal{G}^S S - \text{diag}\{\omega_1, \omega_2, \dots, \omega_n\} R &= \Lambda, \\ \mathcal{G}^R R &= 0, \end{aligned} \tag{S-11}$$

where, $\mathcal{G}^S = \text{diag}(\mu_i + \sum_{j=1}^n m_{ji}^S) - M^S$, $\mathcal{G}^R = \text{diag}(\mu_i + \omega_i + \sum_{j=1}^n m_{ji}^R) - M^R$, M^S and M^R are the irreducible movement matrices defined in **Section 2; Main-text**, and $S = (S_1, S_2, \dots, S_n)^T$, $R = (R_1, R_2, \dots, R_n)^T$, $\Lambda = (\Lambda_1, \Lambda_2, \dots, \Lambda_n)^T$.

We see that both the matrices \mathcal{G}^S and \mathcal{G}^R have non-positive off-diagonal elements (i.e Z -sign pattern) and column sums of these matrices are also positive. Therefore both \mathcal{G}^S and \mathcal{G}^R are non-singular M -matrix and consequently possess positive inverses (1). Therefore the second equation of (S-10) has trivial solution whereas the first equation of (S-10) has a unique positive solution $S^0 \equiv (S_1^0, S_2^0, \dots, S_n^0) = (\mathcal{G}^S)^{-1} \Lambda$.

Therefore we have the following result.

Theorem 1. *There exists a unique DFE, $\mathcal{E}^0 = (S_1^0, 0, 0, S_2^0, 0, 0, \dots, S_n^0, 0, 0, 0) \in \mathbb{R}_+^{3n+2}$ for the system (S-1).*

Global stability of disease-free equilibrium

Theorem 2. *Suppose that the movement matrix M^I is irreducible. Then the following results hold for the system (S-1)*

- (1) *If $\mathcal{R}_0 < 1$, then the disease-free equilibrium \mathcal{E}^0 is globally asymptotically stable in Ω .*
- (2) *If $\mathcal{R}_0 > 1$, then the disease-free equilibrium \mathcal{E}^0 is unstable and the system (S-1) is uniformly persistent.*

Proof. To prove the above theorem we proceed as in the proof of **Theorem 5.1** in (2).

Let us denote $Z = (I_1, I_2, \dots, I_n, B_H, B_L)$. Following the **Exercise 1.2, pp. 17** in (3), the matrices FV^{-1} and $V^{-1}F$ have the same spectral radius. Thus $\mathcal{R}_0 = \rho(FV^{-1}) = \rho(V^{-1}F)$. Let $b \geq 0$ be the left eigen vector of $V^{-1}F$ corresponding to the eigen value \mathcal{R}_0 . This implies $b^T V^{-1}F = \mathcal{R}_0 b^T$.

Let us consider the following Lyapunov function

$$\mathcal{L} = b^T V^{-1} Z. \tag{S-12}$$

Differentiating \mathcal{L} along (S-1) gives,

$$\begin{aligned} \mathcal{L}' &= b^T V^{-1} Z' \\ &\leq b^T V^{-1} (F - V) Z \\ &= (\mathcal{R}_0 - 1) b^T Z \\ &\leq 0, \quad \text{if } \mathcal{R}_0 < 1. \end{aligned} \tag{S-13}$$

Utilizing the irreducibility of the matrix M^I , it can be verified that singleton $\{\mathcal{E}^0\}$ is the only invariant set where $\mathcal{L}' = 0$. Thus by LaSalle's invariance principle (4), \mathcal{E}^0 is globally asymptotically stable in (Ω) .

On the other hand if $\mathcal{R}_0 > 1$ and $Z > 0$, it follows that $(\mathcal{R}_0 - 1)b^T Z > 0$. This inequality and continuity combinedly imply that $\mathcal{L}' > 0$ in a small neighborhood of \mathcal{E}^0 in $\text{int}(\Omega)$. That means for $\mathcal{R}_0 > 1$, any solution sufficiently close to \mathcal{E}^0 will move away from \mathcal{E}^0 . Following the results of (5; 6), and using the irreducibility of the matrix M^I , the instability of \mathcal{E}^0 implies the uniform persistence of the system (S-1). □

Global stability of endemic equilibrium

Using the uniform persistence of (S-1), positive invariance of the set Ω , and also following (7; 8), the following result holds:

Theorem 3. *Suppose that the M^I is irreducible. If $\mathcal{R}_0 > 1$, then there exists at least one endemic equilibrium for the system (S-1).*

Let $\mathcal{E}^* = (S_1^*, I_1^*, R_1^*, S_2^*, I_2^*, R_2^*, \dots, S_n^*, I_n^*, R_n^*, B_H^*, B_L^*)$ denote the endemic equilibrium, where $S_i^*, I_i^*, R_i^*, B_H^*, B_L^* > 0$, for $1 \leq i \leq n$.

Following (2), we also assume that there is no human migration between the patches (i.e. $M^S = M^I = M^R = 0$) and recovered population in each patch acquired permanent immunity (i.e. $\omega_i = 0$, for $1 \leq i \leq n$).

We also assume as in ((2), Theorem 6.1) that

(A₁) There exist a family of functions $\Phi_i: (0, \frac{\Lambda}{\mu}] \rightarrow \mathbb{R}_+$, $i = 1, 2, \dots, n$ such that for all $1 \leq i \leq n$, $S_i, I_i, B_H, B_L > 0$,

$$(S_i - S_i^*)(\Phi_i(S_i) - \Phi_i(S_i^*)) > 0, \quad S_i \neq S_i^*,$$

$$\left(\frac{\lambda_H S_i \Phi_i(S_i^*)}{\lambda_H^* S_i^* \Phi_i(S_i)} - 1 \right) \left(1 - \frac{\lambda_H^* S_i^* \Phi_i(S_i) I_i}{\lambda_H S_i \Phi_i(S_i^*) I_i^*} \right) \leq 0,$$

and

$$\left(\frac{\lambda_L S_i \Phi_i(S_i^*)}{\lambda_L^* S_i^* \Phi_i(S_i)} - 1 \right) \left(1 - \frac{\lambda_L^* S_i^* \Phi_i(S_i) B_H}{\lambda_L S_i \Phi_i(S_i^*) B_H^*} \right) \leq 0,$$

where $\lambda_H = \frac{\beta_i^H B_H}{B_H + K_H}$, $\lambda_L = \frac{\beta_i^L B_L}{B_L + K_L}$, $\lambda_H^* = \frac{\beta_i^H B_H^*}{B_H^* + K_H}$, and $\lambda_L^* = \frac{\beta_i^L B_L^*}{B_L^* + K_L}$, $i = 1, 2, \dots, n$.

(A₂) For $B_H > 0$,

$$\left(\frac{B_H}{B_H^*} - 1 \right) \left(1 - \frac{B_H^*}{B_H} \right) \leq 0.$$

Theorem 4. *Suppose that the assumptions (A₁)–(A₂) hold. Assume that $M^S = M^I = M^R = 0$ and $\omega_i = 0$, for $i = 1, 2, \dots, n$. If $\mathcal{R}_0 > 1$, then the endemic equilibrium \mathcal{E}^* of (S-1) is unique and globally asymptotically stable in $\text{int}(\Omega)$.*

Proof. We shall construct a suitable Lyapunov function to prove the global stability of \mathcal{E}^* . Let,

$$\begin{aligned}
 V_i &= \int_{S_i^*}^{S_i} \frac{\Phi_i(\tau) - \Phi_i(S_i^*)}{\Phi_i(\tau)} d\tau + I_i - I_i^* - I_i^* \ln \frac{I_i}{I_i^*}, \\
 V_{n+1} &= B_H - B_H^* - B_H^* \ln \frac{B_H}{B_H^*}, \\
 V_{n+2} &= B_L - B_L^* - B_L^* \ln \frac{B_L}{B_L^*}.
 \end{aligned}
 \tag{S-14}$$

Taking the derivative of V_i along (S-1) we get,

$$\begin{aligned}
 V_i' &= \left(1 - \frac{\Phi_i(S_i^*)}{\Phi_i(S_i)}\right) S_i' + \left(1 - \frac{I_i}{I_i^*}\right) I_i' \\
 &= \left(1 - \frac{\Phi_i(S_i^*)}{\Phi_i(S_i)}\right) [\Lambda_i - (\mu_i + \lambda_H + \lambda_L)S_i] \\
 &\quad + \left(1 - \frac{I_i}{I_i^*}\right) [(\lambda_H + \lambda_L)S_i - (\mu_i + \delta_i + \gamma_i)I_i].
 \end{aligned}
 \tag{S-15}$$

Now from endemic equilibrium we have,

$$\begin{aligned}
 (\mu_i + \lambda_H^* + \lambda_L^*)S_i^* &= \Lambda_i, \\
 (\mu_i + \delta_i + \gamma_i)I_i^* &= (\lambda_H^* + \lambda_L^*)S_i^* \\
 \Rightarrow (\mu_i + \delta_i + \gamma_i)I_i &= (\lambda_H^* + \lambda_L^*)S_i^* \frac{I_i}{I_i^*} \\
 \chi B_H^* &= \sum_{i=1}^n \xi_i I_i^* \\
 \Rightarrow \chi B_H &= \sum_{i=1}^n \xi_i I_i^* \frac{B_H}{B_H^*} \\
 \delta_L B_L &= \chi B_H^* \frac{B_L}{B_L^*}
 \end{aligned}
 \tag{S-16}$$

Substituting (S-16) in (S-15) we get,

$$\begin{aligned}
 V_i' &= \left(1 - \frac{\Phi_i(S_i^*)}{\Phi_i(S_i)}\right) [\mu_i(S_i^* - S_i) + \lambda_H^* S_i^* - \lambda_H S_i + \lambda_i^* S_i^* - \lambda_L S_i] \\
 &\quad + \left(1 - \frac{I_i}{I_i^*}\right) \left[\lambda_H S_i - \lambda_H^* S_i^* \frac{I_i}{I_i^*} + \lambda_L S_i - \lambda_L^* S_i^* \frac{I_i}{I_i^*}\right]
 \end{aligned}$$

$$\begin{aligned}
 &= -\frac{\mu_i(S_i - S_i^*)}{\Phi_i(S_i)} (\Phi_i(S_i) - \Phi_i(S_i^*)) \\
 &\quad + \lambda_H^* S_i^* \left(\frac{\lambda_H S_i \Phi_i(S_i^*)}{\lambda_H^* S_i^* \Phi_i(S_i)} - 1 \right) \left(1 - \frac{\lambda_H^* S_i^* \Phi_i(S_i) I_i}{\lambda_H S_i \Phi_i(S_i^*) I_i^*} \right) \\
 &\quad + \lambda_H^* S_i^* \left(3 - \frac{\Phi_i(S_i^*)}{\Phi_i(S_i)} - \frac{\lambda_H S_i I_i^*}{\lambda_H^* S_i^* I_i} - \frac{\lambda_H^* S_i^* \Phi_i(S_i) I_i}{\lambda_H S_i \Phi_i(S_i^*) I_i^*} \right) \\
 &\quad + \lambda_L^* S_i^* \left(\frac{\lambda_L S_i \Phi_i(S_i^*)}{\lambda_L^* S_i^* \Phi_i(S_i)} - 1 \right) \left(1 - \frac{\lambda_L^* S_i^* \Phi_i(S_i) B_H}{\lambda_L S_i \Phi_i(S_i^*) B_H^*} \right) \\
 &\quad + \lambda_L^* S_i^* \left(3 - \frac{\Phi_i(S_i^*)}{\Phi_i(S_i)} - \frac{\lambda_L S_i I_i^*}{\lambda_L^* S_i^* I_i} - \frac{\lambda_L^* S_i^* \Phi_i(S_i) B_H}{\lambda_L S_i \Phi_i(S_i^*) B_H^*} - \frac{I_i}{I_i^*} + \frac{B_H}{B_H^*} \right) \\
 &\leq \lambda_L^* S_i^* \left(3 - \frac{\Phi_i(S_i^*)}{\Phi_i(S_i)} - \frac{\lambda_L S_i I_i^*}{\lambda_L^* S_i^* I_i} - \frac{\lambda_L^* S_i^* \Phi_i(S_i) B_H}{\lambda_L S_i \Phi_i(S_i^*) B_H^*} - \frac{I_i}{I_i^*} + \frac{B_H}{B_H^*} \right) \\
 &\quad + \lambda_H^* S_i^* \left(3 - \frac{\Phi_i(S_i^*)}{\Phi_i(S_i)} - \frac{\lambda_H S_i I_i^*}{\lambda_H^* S_i^* I_i} - \frac{\lambda_H^* S_i^* \Phi_i(S_i) I_i}{\lambda_H S_i \Phi_i(S_i^*) I_i^*} \right).
 \end{aligned}
 \tag{S-17}$$

The last inequality is followed from the assumption (A₁). In a similar way differentiating V_{n+1} along the equation (S-1) we get,

$$\begin{aligned}
 V'_{n+1} &= \left(1 - \frac{B_H^*}{B_H} \right) B_H' \\
 &= \left(1 - \frac{B_H^*}{B_H} \right) \left(\sum_i^n \xi_i I_i - \chi B_H \right) \\
 &= \left(1 - \frac{B_H^*}{B_H} \right) \left(\sum_i^n \xi_i I_i - \sum_i^n \xi_i I_i^* \frac{B_H}{B_H^*} \right) \\
 &= \sum_{i=1}^n \xi_i I_i^* \left(\frac{\xi_i I_i}{\xi_i I_i^*} - 1 \right) \left(1 - \frac{\xi_i I_i^* I_i}{\xi_i I_i I_i^*} \right) \\
 &\quad + \sum_{i=1}^n \xi_i I_i^* \left(2 - \frac{\xi_i I_i B_H^*}{\xi_i I_i^* B_H} - \frac{\xi_i I_i^* I_i}{\xi_i I_i I_i^*} + \frac{I_i}{I_i^*} - \frac{B_H}{B_H^*} \right) \\
 &= \sum_{i=1}^n \xi_i I_i^* \left(2 - \frac{\xi_i I_i B_H^*}{\xi_i I_i^* B_H} - \frac{\xi_i I_i^* I_i}{\xi_i I_i I_i^*} + \frac{I_i}{I_i^*} - \frac{B_H}{B_H^*} \right).
 \end{aligned}
 \tag{S-18}$$

$$\begin{aligned}
 V'_{n+2} &= \chi B_H^* \left(\frac{B_H}{B_H^*} - 1 \right) \left(1 - \frac{B_H^*}{B_H} \right) + \chi B_H^* \left(3 - \frac{B_L}{B_L^*} - \frac{B_L^* B_H}{B_L B_H^*} - \frac{B_H^*}{B_H} \right) \\
 &\leq \chi B_H^* \left(3 - \frac{B_L}{B_L^*} - \frac{B_L^* B_H}{B_L B_H^*} - \frac{B_H^*}{B_H} \right).
 \end{aligned}
 \tag{S-19}$$

The inequality follows from the assumption (A₂).

Now we consider the Lyapunov function \mathcal{V} as, $\mathcal{V} = \sum_{i=1}^n \frac{\xi_i I_i^*}{\lambda_L^* S_i^*} V_i + V_{n+1} + V_{n+2}$. Differentiating \mathcal{V} along (S-1) and using (S-17), (S-18) and (S-20) we get,

$$\begin{aligned} \mathcal{V}' &\leq \sum_{i=1}^n \frac{\xi_i I_i^*}{\lambda_L^* S_i^*} \left[\lambda_L^* S_i^* \left(3 - \frac{\Phi_i(S_i^*)}{\Phi_i(S_i)} - \frac{\lambda_L S_i I_i^*}{\lambda_L^* S_i^* I_i} - \frac{\lambda_L^* S_i^* \Phi_i(S_i) B_H}{\lambda_L S_i \Phi_i(S_i^*) B_H^*} - \frac{I_i}{I_i^*} + \frac{B_H}{B_H^*} \right) \right. \\ &\quad \left. + \lambda_H^* S_i^* \left(3 - \frac{\Phi_i(S_i^*)}{\Phi_i(S_i)} - \frac{\lambda_H S_i I_i^*}{\lambda_H^* S_i^* I_i} - \frac{\lambda_H^* S_i^* \Phi_i(S_i) I_i}{\lambda_H S_i \Phi_i(S_i^*) I_i^*} \right) \right] \\ &\quad + \sum_{i=1}^n \xi_i I_i^* \left(2 - \frac{\xi_i I_i B_H^*}{\xi_i I_i^* B_H} - \frac{\xi_i I_i^* I_i}{\xi_i I_i I_i^*} + \frac{I_i}{I_i^*} - \frac{B_H}{B_H^*} \right) \\ &\quad + \chi B_H^* \left(3 - \frac{B_L}{B_L^*} - \frac{B_L^* B_H}{B_L B_H^*} - \frac{B_H^*}{B_H} \right) \\ &\leq \sum_{i=1}^n \frac{\xi_i I_i^* \lambda_H^* S_i^*}{\lambda_L^* S_i^*} \left(3 - \frac{\Phi_i(S_i^*)}{\Phi_i(S_i)} - \frac{\lambda_H S_i I_i^*}{\lambda_H^* S_i^* I_i} - \frac{\lambda_H^* S_i^* \Phi_i(S_i) I_i}{\lambda_H S_i \Phi_i(S_i^*) I_i^*} \right) \\ &\quad + \sum_{i=1}^n \xi_i I_i^* \left(5 - \frac{\Phi_i(S_i^*)}{\Phi_i(S_i)} - \frac{\lambda_H S_i I_i^*}{\lambda_H^* S_i^* I_i} - \frac{\lambda_H^* S_i^* \Phi_i(S_i) B_H}{\lambda_H S_i \Phi_i(S_i^*) B_H^*} - \frac{\xi_i I_i B_H^*}{\xi_i I_i^* B_H} - \frac{\xi_i I_i^* I_i}{\xi_i I_i I_i^*} \right) \\ &\quad + \chi B_H^* \left(3 - \frac{B_L}{B_L^*} - \frac{B_L^* B_H}{B_L B_H^*} - \frac{B_H^*}{B_H} \right) \leq 0. \tag{S-20} \end{aligned}$$

The last inequality can be achieved by using *A.M – G.M* relation as follows:

$$\begin{aligned} &\frac{\Phi_i(S_i^*)}{\Phi_i(S_i)} + \frac{\lambda_H S_i I_i^*}{\lambda_H^* S_i^* I_i} + \frac{\lambda_H^* S_i^* \Phi_i(S_i) I_i}{\lambda_H S_i \Phi_i(S_i^*) I_i^*} \\ &\geq 3 \sqrt[3]{\frac{\Phi_i(S_i^*)}{\Phi_i(S_i)} \cdot \frac{\lambda_H S_i I_i^*}{\lambda_H^* S_i^* I_i} \cdot \frac{\lambda_H^* S_i^* \Phi_i(S_i) I_i}{\lambda_H S_i \Phi_i(S_i^*) I_i^*}} = 3, \\ &\frac{\Phi_i(S_i^*)}{\Phi_i(S_i)} + \frac{\lambda_H S_i I_i^*}{\lambda_H^* S_i^* I_i} + \frac{\lambda_H^* S_i^* \Phi_i(S_i) B_H}{\lambda_H S_i \Phi_i(S_i^*) B_H^*} + \frac{\xi_i I_i B_H^*}{\xi_i I_i^* B_H} + \frac{\xi_i I_i^* I_i}{\xi_i I_i I_i^*} \\ &\geq 5 \sqrt[5]{\frac{\Phi_i(S_i^*)}{\Phi_i(S_i)} \cdot \frac{\lambda_H S_i I_i^*}{\lambda_H^* S_i^* I_i} \cdot \frac{\lambda_H^* S_i^* \Phi_i(S_i) B_H}{\lambda_H S_i \Phi_i(S_i^*) B_H^*} \cdot \frac{\xi_i I_i B_H^*}{\xi_i I_i^* B_H} \cdot \frac{\xi_i I_i^* I_i}{\xi_i I_i I_i^*}} = 5 \end{aligned}$$

and

$$\begin{aligned} &\frac{B_L}{B_L^*} + \frac{B_L^* B_H}{B_L B_H^*} + \frac{B_H^*}{B_H} \\ &\geq 3 \sqrt[3]{\frac{B_L}{B_L^*} \cdot \frac{B_L^* B_H}{B_L B_H^*} \cdot \frac{B_H^*}{B_H}} = 3. \end{aligned}$$

It can be verified that singleton $\{\mathcal{E}^*\}$ is the largest invariant set where $\mathcal{V}' = 0$. Thus by LaSalle’s invariance principle (4), \mathcal{E}^* is globally asymptotically stable and unique in $\text{int}(\Omega)$. □

Tables

Supplementary Table 1. Migration rates for susceptible population for the five provinces. The rates are calculated using the formula $m_{ij}^s = p_s \times m_{ij}$, where m_{ij} are the migration rates between different provinces which is taken from the data (9) and $p_s [0.4185(0.3094-0.5707)]$ is estimated. Migration rates for the susceptible are given in the format [mean (95% CI)].

	Harare	Manica	Mash Cen	Mash East	Mash West
Harare	0	1.07E - 04 (7.95E - 05 - 1.46E - 04)	8.57E - 05 (6.33E - 05 - 1.16E - 04)	1.60E - 04 (1.18E - 04 - 2.19E - 04)	6.76E - 05 (4.99E - 05 - 9.22E - 05)
Manica	3.74E - 05 (2.77E - 05 - 5.11E - 05)	0	8.55E - 06 (6.32E - 06 - 1.16E - 05)	2.82E - 05 (2.09E - 05 - 3.85E - 05)	8.60E - 06 (6.36E - 06 - 1.17E - 05)
Mash Cen	3.15E - 05 (2.33E - 05 - 4.29E - 05)	9.87E - 06 (7.29E - 06 - 1.34E - 05)	0	2.74E - 05 (2.03E - 05 - 3.74E - 05)	2.70E - 05 (1.99E - 05 - 3.68E - 05)
Mash East	7.22E - 05 (5.3409E - 05 - 9.85E - 05)	4.06E - 05 (3.00E - 05 - 5.53E - 05)	3.3543E - 05 (2.4798E - 05 - 4.5742E - 05)	0	2.29E - 05 (1.69E - 05 - 3.13E - 05)
Mash West	4.64E - 05 (3.4341E - 05 - 6.33E - 05)	1.81E - 05 (1.34E - 05 - 2.48E - 05)	4.31E - 05 (3.19E - 05 - 5.88E - 05)	2.95E - 05 (2.18E - 05 - 4.02E - 05)	0

Supplementary Table 2. Migration rates for infected population for the five provinces. The rates are calculated using the formula $m_{ij}^i = p_i \times m_{ij}$, where m_{ij} are the migration rates between different provinces which is taken from the data (9) and $p_i [0.0919(0.0531-0.1659)]$ is estimated. Migration rates for the infected are given in the format [mean (95% CI)].

	Harare	Manica	Mash Cen	Mash East	Mash West
Harare	0	2.36E - 05 (1.36E - 05 - 4.26E - 05)	1.88E - 05 (1.08E - 05 - 3.39E - 05)	3.53E - 05 (2.04E - 05 - 6.37E - 05)	1.48E - 05 (8.58E - 06 - 2.68E - 05)
Manica	8.23E - 06 (4.76E - 06 - 1.48E - 05)	0	1.87E - 06 (1.08E - 06 - 3.38E - 06)	6.21E - 06 (3.59E - 06 - 1.12E - 05)	1.89E - 06 (1.09E - 06 - 3.41E - 06)
Mash Cen	6.92E - 06 (4.00E - 06 - 1.24E - 05)	2.16E - 06 (1.25E - 06 - 3.91E - 06)	0	6.03E - 06 (3.48E - 06 - 1.08E - 05)	5.93E - 06 (3.43E - 06 - 1.07E - 05)
Mash East	1.58E - 05 (9.17E - 06 - 2.86E - 05)	8.92E - 06 (5.15E - 06 - 1.60E - 05)	7.36E - 06 (4.26E - 06 - 1.32E - 05)	0	5.04E - 06 (2.91E - 06 - 9.10E - 06)
Mash West	1.02E - 05 (5.89E - 06 - 1.84E - 05)	3.99E - 06 (2.31E - 06 - 7.20E - 06)	9.48E - 06 (5.48E - 06 - 1.71E - 05)	6.49E - 06 (3.75E - 06 - 1.17E - 05)	0

Supplementary Table 3. Migration rates for recovered population for the five provinces. The rates are calculated using the formula $m_{ij}^R = p_r \times m_{ij}$, where m_{ij} are the migration rates between different provinces which is taken from the data (9) and p_r [0.4896(0.3156-0.6113)] is estimated. Migration rates for the recovered are given in the format [mean (95% CI)].

	Harare	Manica	Mash Cen	Mash East	Mash West
Harare	0	$1.25E-04$	$1.00E-04$	$1.88E-04$	$7.91E-05$
		$(8.11E-05 - 1.57E-04)$	$(6.46E-05 - 1.25E-04)$	$(1.21E-04 - 2.34E-04)$	$(5.10E-05 - 9.87E-05)$
Manica	$4.38E-05$	0	$1.00E-05$	$3.30E-05$	$1.00E-05$
	$(2.82E-05 - 5.47E-05)$		$(6.44E-06 - 1.24E-05)$	$(2.13E-05 - 4.13E-05)$	$(6.48E-06 - 1.25E-05)$
Mash Cen	$3.68E-05$	$1.15E-05$	0	$3.21E-05$	$3.15E-05$
	$(2.37E-05 - 4.60E-05)$	$(7.44E-06 - 1.44E-05)$		$(2.07E-05 - 4.01E-05)$	$(2.03E-05 - 3.94E-05)$
Mash East	$8.45E-05$	$4.74E-05$	$3.92E-05$	0	$2.68E-05$
	$(5.44E-05 - 1.05E-04)$	$(3.06E-05 - 5.93E-05)$	$(2.52E-05 - 4.8998E-05)$		$(1.73E-05 - 3.35E-05)$
Mash West	$5.43E-05$	$2.12E-05$	$5.04E-05$	$3.45E-05$	0
	$(3.50E-05 - 6.78E-05)$	$(1.37E-05 - 2.65E-05)$	$(3.25E-05 - 6.30E-05)$	$(2.22E-05 - 4.31E-05)$	

Supplementary Table 4. Different migration index of the model (S-1). Data used to derive these indices are taken from Main-Text Table 3 and Main-Text Table 4. All data are given in the format [mean (95% CI)].

	Harare	Manica	Mash Cen	Mash East	Mash West
I_S^I	$7.7973E-08$	$1.5334E-08$	$1.7725E-08$	$3.1313E-08$	$2.5392E-08$
	$(7.7973E-08 - 7.7973E-08)$	$(1.5334E-08 - 1.5334E-08)$	$(1.7725E-08 - 1.7725E-08)$	$(3.1313E-08 - 3.1313E-08)$	$(2.5392E-08 - 2.5392E-08)$
I_P^I	$4.4920E-08$	$8.8337E-09$	$1.0212E-08$	$1.8040E-08$	$1.4628E-08$
	$(4.4920E-08 - 4.4920E-08)$	$(8.8337E-09 - 8.8337E-09)$	$(1.0212E-08 - 1.0212E-08)$	$(1.8040E-08 - 1.8040E-08)$	$(1.4628E-08 - 1.4628E-08)$
C_P^S	$3.4704E-08$	$3.2586E-08$	$3.1613E-08$	$4.5499E-08$	$2.3335E-08$
	$(3.4704E-08 - 3.4704E-08)$	$(3.2586E-08 - 3.2586E-08)$	$(3.1613E-08 - 3.1613E-08)$	$(4.5499E-08 - 4.5499E-08)$	$(2.3335E-08 - 2.3335E-08)$
O_P^I	$1.9993E-08$	$1.8773E-08$	$1.8212E-08$	$2.6212E-08$	$1.3443E-08$
	$(1.9993E-08 - 1.9993E-08)$	$(1.8773E-08 - 1.8773E-08)$	$(1.8212E-08 - 1.8212E-08)$	$(2.6212E-08 - 2.6212E-08)$	$(1.3443E-08 - 1.3443E-08)$

Supplementary Table 5. Number of cases from cholera projected between November 14, 2008 to July 31, 2009, by province under base case and under each intervention scenario at an optimal rate. Data are given in the format mean (95% CI). Base cases are the cases during 2008–09 epidemic predicted by the cholera model (S-1). Where, $I_1, I_2, I_3, I_4, I_5, I_6, I_7, I_8,$ and I_9 are same interventions defined in Main-Text Fig. 4. This prediction is based upon estimated parameters of the model (S-1) for the five provinces (see Main-Text Table 3) and minimizing the cost function J with respect of intervention parameters.

	Harare	Manica	Mash Cen	Mash East	Mash West	Total
Base cases	17389 (17039 – 17754)	14538 (13874 – 15115)	10784 (10130 – 11478)	6384 (6137 – 6718)	23357 (22393 – 24329)	72453 (69573 – 75395)
I_1	14077 (11833 – 15419)	9151 (5854 – 11948)	3525 (2352 – 5103)	4916 (3936 – 5691)	14838 (11187 – 19749)	46509 (35163 – 57911)
I_2	15748 (14550 – 16718)	12094 (10861 – 13204)	7445 (5882 – 9116)	5616 (4946 – 6081)	19290 (16150 – 21602)	60194 (52391 – 64556)
I_3	15246 (14076 – 16136)	10914 (7996 – 12873)	6131 (3927 – 8018)	5423 (4711 – 5881)	18095 (14600 – 20563)	55810 (45312 – 61408)
I_4	14502 (12766 – 15657)	9916 (7250 – 12199)	4677 (3642 – 6100)	5132 (4209 – 5730)	16090 (12868 – 19411)	50317 (40737 – 55643)
I_5	15934 (14771 – 16705)	12467 (11251 – 13426)	7958 (6814 – 9209)	5751 (5175 – 6195)	19885 (17495 – 21842)	61996 (55507 – 65701)
I_6	15535 (14274 – 16310)	11622 (9424 – 13169)	7104 (4988 – 8762)	5577 (5008 – 6025)	18856 (15525 – 20681)	58695 (49222 – 63582)
I_7	13598 (10933 – 15279)	8403 (4881 – 11542)	2446 (1296 – 4694)	4765 (3567 – 5582)	13580 (9340 – 18319)	42794 (30018 – 50433)
I_8	15481 (13666 – 16585)	11751 (10437 – 13073)	6872 (4848 – 8666)	5528 (4781 – 6068)	18597 (14614 – 21549)	58231 (48347 – 63317)
I_9	14824 (13201 – 16022)	10449 (6936 – 13042)	5529 (2826 – 7759)	5223 (4225 – 5820)	17253 (13296 – 19949)	53278 (40485 – 60463)

Supplementary Table 6. Number of deaths from cholera projected between November 14, 2008 to July 31, 2009, by province under base deaths and under each intervention scenario at an optimal rate. Data are given in the format mean (95% CI). Base deaths are the deaths during 2008–09 epidemic predicted by the cholera model (S-1). Where, $I_1, I_2, I_3, I_4, I_5, I_6, I_7, I_8,$ and I_9 are same interventions defined in Main-Text Fig. 4. This prediction is based upon estimated parameters of the model (S-1) for the five provinces (see Main-Text Table 3) and minimizing the cost function J with respect of intervention parameters.

	Harare	Manica	Mash Cen	Mash East	Mash West	Total
Base deaths	663 (610 – 635)	607 (580 – 631)	495 (464 – 527)	417 (402 – 435)	1079 (1039 – 1122)	3220 (3096 – 3306)
I_1	148 (132 – 158)	76 (46 – 101)	38 (27 – 54)	121 (108 – 131)	140 (102 – 189)	523 (415 – 580)
I_2	160 (151 – 167)	102 (90 – 112)	339 (267 – 414)	129 (121 – 136)	889 (742 – 999)	1620 (1370 – 1726)
I_3	157 (148 – 164)	453 (321 – 542)	278 (170 – 370)	127 (118 – 134)	171 (135 – 195)	1185 (892 – 1383)
I_4	295 (261 – 317)	217 (152 – 272)	114 (86 – 152)	205 (174 – 225)	393 (307 – 482)	1225 (980 – 1355)
I_5	322 (300 – 337)	276 (248 – 297)	363 (310 – 421)	225 (206 – 240)	917 (801 – 1007)	2103 (1864 – 2228)
I_6	314 (389 – 330)	483 (384 – 554)	324 (220 – 404)	220 (200 – 235)	463 (374 – 513)	1804 (1467 – 1998)
I_7	95 (84 – 101)	37 (20 – 52)	18 (12 – 30)	86 (78 – 91)	68 (45 – 93)	304 (239 – 367)
I_8	102 (95 – 107)	53 (46 – 59)	312 (217 – 395)	91 (85 – 95)	856 (664 – 999)	1414 (1108 – 1654)
I_9	99 (93 – 104)	433 (278 – 547)	249 (118 – 356)	89 (82 – 93)	88 (66 – 104)	958 (637 – 1204)

Supplementary Table 7. Average coverage percentage of different interventions should be commenced between November 14, 2008 to July 31, 2009, for each province projected by the cholera model (S-1), where, I_1 = promotion hand-hygiene & clean water distribution (PH & CW) in all five provinces, I_2 = PH & CW in three provinces with higher out-migration index, I_3 = PH & CW in three provinces with higher in-migration index, I_4 = Providing treatment (Tr) to cholera patients in all provinces, I_5 = Providing Tr in three provinces with higher out-migration index, I_6 = Providing Tr in three provinces with higher in-migration index, I_7 = Combination of PH & CW with Tr in all five provinces, I_8 = Combination of PH & CW with Tr in three provinces with higher out-migration index, and I_9 = Combination of PH & CW with Tr in three provinces with higher in-migration index. Parameters used in the estimation of these coverage percentage are taken from Main-Text Table 3. All data are given in the format [mean (95% CI)].

	Harare	Manica	Mash Cen	Mash East	Mash West
I_1	77.6(77.5 – 77.8)	77.6(77.2 – 77.8)	76.07(73.4 – 77.7)	77.4(76.6 – 77.8)	77.6(77.5 – 77.8)
I_2	77.6(77.08 – 77.8)	77.6(77.1 – 77.8)	*	77.6(77.1 – 77.8)	*
I_3	77.6(77.08 – 77.8)	*	*	77.6(77.1 – 77.8)	77.6(77.1 – 77.8)
I_4	68(67.8 – 68.1)	68(67.8 – 68.1)	68(67.8 – 68.1)	68(67.8 – 68.1)	68(67.8 – 68.1)
I_5	67.9(67.4 – 68.1)	67.9(67.4 – 68.1)	*	67.9(67.4 – 68.1)	*
I_6	67.9(67.4 – 68.1)	*	*	67.9(67.4 – 68.1)	67.9(67.4 – 68.1)
I_7	77.2(75.6 – 77.8);	76.6(73.5 – 77.8);	64.6(55.8 – 74.0);	74.4(70.7 – 76.7)	77.7(77.2 – 77.8);
	68.0(67.8 – 68.1)	68.0(67.8 – 68.1)	68.0(67.8 – 68.1)	68.0(67.8 – 68.1)	68.0(67.8 – 68.1)
I_8	77.6(77.0 – 77.8);	77.6(76.9 – 77.8);	*	77.6(76.9 – 77.8);	*
	67.9(67.3 – 68.1)	67.9(67.4 – 68.1)		67.9(67.4 – 68.1)	
I_9	77.6(77.0 – 77.8);	*	*	77.4(75.8 – 77.8);	77.6(77.1 – 77.8);
	67.9(67.3 – 68.1)			67.9(67.4 – 68.1)	67.9(67.5 – 68.1)

Supplementary Table 8. Total optimal cost (in USD) and cost per averted case and death projected between November 14, 2008 to July 31, 2009, under each intervention scenario. Costs are given in the format [mean (95% CI)], where, $I_1, I_2, I_3, I_4, I_5, I_6, I_7, I_8,$ and I_9 are same interventions defined in Table 7. These costs are estimated by minimizing the cost function J defined in Sec. 9; Main-text. Parameters are used during these optimization procedure are taken from Main-Text Table 3. All data are given in the format [mean (95% CI)].

	Total Cost	Cost per averted case	Cost per averted death
I_1	1.4419E5 (1.4289E5 – 1.4534E5)	5.67 (4.41 – 7.28)	53.48 (51.10 – 55.64)
I_2	8.7045E4 (8.6049E4 – 8.7316E4)	7.86 (4.59 – 14.10)	54.74 (47.51 – 61.97)
I_3	8.7045E4 (8.6049E4 – 8.7316E4)	5.64 (3.34 – 8.76)	42.97 (37.76 – 47.72)
I_4	3.2871E5 (2.8952E5 – 3.6459E5)	15.34 (10.63 – 21.61)	165.53 (136.18 – 196.72)
I_5	5.5677E5 (5.0304E5 – 6.0485E5)	60.99 (30.10 – 106.92)	508.08 (369.50 – 648.14)
I_6	4.8478E5 (4.0541E5 – 5.3971E5)	39.22 (18.72 – 65.28)	348.78 (240.03 – 442.74)
I_7	2.0951E5 (1.9729E5 – 2.2059E5)	7.20 (5.56 – 9.23)	71.86 (67.02 – 76.94)
I_8	4.4478E5 (3.7196E5 – 5.0092E5)	37.44 (6.05 – 69.94)	250.06 (177.49 – 316.67)
I_9	3.3758E5 (2.5805E5 – 3.9918E5)	20.25 (8.85 – 38.95)	151.59 (99.89 – 200.58)

Supplementary Table 9. Average cost per averted case in different provinces projected between November 14, 2008 to July 31, 2009, under each intervention scenario, where, $I_1, I_2, I_3, I_4, I_5, I_6, I_7, I_8,$ and I_9 are same interventions defined in Supplementary Table 7. Methodology for deriving these costs are provided in Sec. 9; Main-text. Parameters are used during these cost estimation are taken from Main-Text Table 3. All data are given in the format [mean (95% CI)].

	Harare	Manica	Mash Cen	Mash East	Mash West
I_1	9.62(5.16 – 14.61)	6.24(3.28 – 10.57)	4.05(3.27 – 5.17)	23.33(11.64 – 43.68)	3.89(2.31 – 8.05)
I_2	14.04(5.64 – 26.94)	8.32(4.59 – 16.58)	5.98(3.48 – 10.80)	34.89(12.33 – 98.23)	5.27(2.44 – 11.37)
I_3	9.11(5.23 – 16.09)	5.96(2.70 – 12.12)	4.08(2.51 – 6.74)	22.52(10.21 – 43.45)	3.82(1.93 – 6.84)
I_4	25.01(13.86 – 40.57)	16.63(8.19 – 31.62)	11.04(8.32 – 14.32)	63.25(29.48 – 123.25)	10.24(5.46 – 19.37)
I_5	97.98(37.92 – 222.08)	57.75(30.15 – 125.91)	45.88(24.69 – 82.24)	216.77(73.42 – 833.74)	40.47(16.55 – 79.24)
I_6	59.68(27.59 – 103.93)	42.11(15.65 – 87.76)	30.12(14.35 – 59.64)	32.49(58.73 – 387.00)	25.73(9.89 – 46.41)
I_7	12.35(6.34 – 19.95)	7.94(4.14 – 14.65)	5.12(4.15 – 6.99)	30.87(14.59 – 54.90)	4.75(2.91 – 8.49)
I_8	68.18(21.07 – 136.03)	37.43(18.78 – 66.11)	26.56(12.63 – 45.53)	178.87(50.54 – 421.44)	24.69(8.88 – 56.71)
I_9	30.96(13.34 – 57.77)	24.02(6.79 – 59.95)	15.17(6.38 – 27.44)	74.22(24.54 – 157.66)	13.07(5.44 – 26.85)

Supplementary Table 10. Average cost per averted death in different provinces projected between November 14, 2008 to July 31, 2009, under each intervention scenario, where, $I_1, I_2, I_3, I_4, I_5, I_6, I_7, I_8,$ and I_9 are same interventions defined in Supplementary Table 7. Methodology for deriving these costs are provided in Sec. 9; Main-text. Parameters are used during these cost estimation are taken from Main-Text Table 3. All data are given in the format [mean (95% CI)].

	Harare	Manica	Mash Cen	Mash East	Mash West
I_1	60.79(58.16 – 63.00)	54.46(50.37 – 58.62)	63.33(57.79 – 68.92)	97.57(90.13 – 103.96)	30.72(28.85 – 32.86)
I_2	37.63(36.40 – 38.76)	34.51(32.55 – 36.53)	128.26(74.76 – 231.84)	60.62(56.98 – 64.30)	113.46(51.47 – 236.72)
I_3	37.35(36.23 – 38.54)	144.84(62.22 – 309.85)	88.21(53.04 – 146.70)	60.13(55.74 – 63.78)	19.18(18.03 – 20.20)
I_4	201.38(168.50 – 233.27)	171.20(130.96 – 217.28)	174.04(145.40 – 204.69)	313.02(256.44 – 374.83)	96.98(75.31 – 120.54)
I_5	370.86(309.34 – 422.77)	338.43(279.79 – 393.54)	983.28(531.36 – 1748)	585.75(475.42 – 696.74)	873.62(346.64 – 1690)
I_6	315.29(252.29 – 368.34)	1026(358 – 2266)	655.50(305.55 – 1295)	494.32(391.99 – 588.60)	159.13(113.98 – 193.56)
I_7	79.35(74.08 – 84.18)	73.62(67.09 – 79.84)	88.12(80.44 – 96.36)	126.61(116.03 – 135.52)	41.48(38.32 – 45.08)
I_8	170.91(140.12 – 195.37)	160.75(132.47 – 184.47)	566.38(267.26 – 995.13)	273.19(225.42 – 316.40)	547.92(187.30 – 1202)
I_9	129.12(98.11 – 153.47)	592.71(156.31 – 1507)	328.92(136.81 – 596.54)	206.06(155.07 – 247.76)	68.23(50.97 – 83.07)

References

- (1) Berman A, Plemmons RJ, *Nonnegative Matrices*, SIAM, 1979.
- (2) Eisenberg MC, Shuai Z, Tien JH, Van den Driessche P, A cholera model in a patchy environment with water and human movement, *Math Biosci* **246**(1):105–112, 2013.
- (3) Horn RA, Johnson CR, *Matrix Analysis*, Cambridge University Press, 2012.
- (4) LaSalle JP, *The Stability of Dynamical Systems*, Volume 25. SIAM, Philadelphia, 1976.
- (5) Freedman HI, Ruan S, Tang M, Uniform persistence and flows near a closed positively invariant set, *J Dynam Differential Equations* **6**(4):583–600, 1994.
- (6) Li MY, Graef JR, Wang L, Karsai J, Global dynamics of a SEIR model with varying total population size, *Math Biosci* **160**(2):191–213, 1999.
- (7) Smith HL, Waltman P, *The Theory of the Chemostat: Dynamics of Microbial Competition*, Volume 13. Cambridge University Press, 1995.
- (8) Bhatia NP, Szegö GP, *Dynamical Systems: Stability Theory and Applications*, Volume 35. Springer, 2006.
- (9) CENSUS (2012), National Report Zimbabwe 2012, <http://www.zimstat.co.zw/sites/default/files/img/publications/Population/NationalReport.pdf> [Online accessed-1/02/2018].



Source details

[Feedback >](#) [Compare sources >](#)

Journal of Biological Systems

Scopus coverage years: from 1996 to Present

Publisher: World Scientific

ISSN: 0218-3390 E-ISSN: 1793-6470

Subject area: [Agricultural and Biological Sciences: Agricultural and Biological Sciences \(miscellaneous\)](#) [Mathematics: Applied Mathematics](#)

[Environmental Science: Ecology](#)

Source type: Journal

[View all documents >](#)

[Set document alert](#)

[Save to source list](#)

CiteScore 2022

2.4



SJR 2022

0.436



SNIP 2022

0.597



[CiteScore](#)

[CiteScore rank & trend](#)

[Scopus content coverage](#)



Improved CiteScore methodology



CiteScore 2022 counts the citations received in 2019-2022 to articles, reviews, conference papers, book chapters and data papers published in 2019-2022, and divides this by the number of publications published in 2019-2022. [Learn more >](#)

Mathematical Study of A Memory Induced Biochemical System

Mithun Kumar Ghosh, Tridip Sardar, Xianbing Cao, and Priti Kumar Roy

Abstract—In this work, to study the effect of memory on a bi-substrate enzyme kinetic reaction, we have introduced an approach to fractionalize the system, considering it as a three-compartmental model. Solutions of the fractionalized system are compared with the corresponding integer-order model. The equilibrium points of the fractionalized system are derived analytically. Their stability properties are discussed from numerical aspect. We determine the changes of the substances due to the changes of “memory effect”. The effect is discussed critically from the perspective of product formation. We have also analyzed the memory induced system with a control measure in view of optimizing the product. Our numerical result reveals that the solutions of the fractionalized system, when it is free from memory, are in good agreement with the integer-order system. It is noticed that the effect of memory influences the reaction in the forward direction and assists in yielding the product more quickly. However, an extensive use of memory makes the system slower, but introduction of a control input makes the reaction faster. It is possible to overcome the slowness of the reaction due to the undue effect of memory by appropriate use of a control measure.

Index Terms—Bi-substrate enzymatic reaction, compartmental system, control theoretic approach, fractional-order differential equations, memory effect.

I. INTRODUCTION

ENZYMES are biological catalysts that are necessary in almost every biochemical reaction [1]. These enzymes are proteins synthesized by genes [2]. The main function of an enzyme is to catalyze the making and breaking of chemical bonds depending on an accurate sequence of amino acids and its complicated tertiary structure. The catalytic ability of enzymes increases the rate of a reaction. The enzyme is not used up in the reactions and, it does not change the equilibria of the processes [3]. This raises a new dimension of thinking towards various fields viz. physics [4], chemistry [5], biology [6], ecology [7], epidemiology [8], pharmacokinetics [9] etc. A lot of research has been done about enzymatic processes of

different chemical and biochemical transformations. Enzyme kinetics is the study of rates of these reactions to optimize the velocity of reactions, rate of intermediate complexes and products.

For a better understanding of the reaction kinetics, many authors have implemented different techniques to obtain approximate analytical solutions of the enzymatic systems [10]–[13]. Modern day literature related to enzyme activity in enzymatic processes consist of mathematical approaches to study system dynamics for optimization and quantification of product [14]. Single substrate or double substrate biochemical reactions make the approaches more interesting, of which the latter is more reasonable and important [15]–[17].

Westerlund stated in [18] that every matter has memory. Although it is debatable, a large number of theoretical physicists considered the memory function as an embedded characteristic of molecular properties, which is discussed in various domains of science and engineering branches [19]–[21]. Toledo-Hernandez et al. mentioned in [22] that biochemical reactions involve the participation of living organisms viz. enzymes. The dynamic behavior of living microorganisms not only depends on their current state conditions (e.g., substrate concentration, medium condition, etc.), but also on their previous states. They have explained this phenomena as the dynamics of the reactions that involve memory effects. Now, it is to be noted that integer-order (IO) derivatives consider only local properties (at time t) while fractional derivatives take into account the history of a process i.e., their previous states [21]. An enzymatic reaction system with IO derivatives is in general memory-less [20], [23] and hence it is unable to reflect the effect of memory. The memory effect can be incorporated in a system by introducing fractional-order ($\alpha \in (0, 1]$) derivatives as an index of memory [24] i.e., $\alpha \rightarrow 0$ indicates that the system has an ideal memory and $\alpha \rightarrow 1$ represents that the system is free from memory.

The conception of fractional calculus is first projected by Leibniz [25] in 1695. A fractional-order differential equation is considered as an alternative model to special nonlinear differential equations [26], [27]. In enzyme kinetics, Abdullah [28] employed FDEs in 2011 for modeling the Michaelis-Menten reaction in a 2-d region containing obstacles. In 2013, Alawneh [29] used the multistep generalized differential transform method to solve a time-fractional enzyme kinetics. They investigated dynamical behavior of various complex materials and systems for the benefits of more degrees of freedom and introduction of memory in the model. The drawback of both the studies was the way of introduction of memory. Both of them fractionalized the systems only by changing the order

Manuscript received June 11, 2017; accepted March 7, 2018. Recommended by Associate Editor Fei-Yue Wang. (Corresponding author: Priti Kumar Roy.)

Citation: M. K. Ghosh, T. Sardar, X. B. Cao, and P. K. Roy, “Mathematical study of a memory induced biochemical system,” *IEEE/CAA J. of Autom. Sinica*, vol. 5, no. 6, pp. 1142–1149, Nov. 2018.

M. K. Ghosh and P. K. Roy are with the Centre for Mathematical Biology and Ecology, Department of Mathematics, Jadavpur University, Kolkata 700032, India (e-mail: mkghoshjmaths@gmail.com; priti@jpu@gmail.com).

T. Sardar is with the Department of Mathematics, Dinabondhu Andrews College, Kolkata 700084, India (e-mail: tridipiitk@gmail.com).

X. B. Cao is with the College of Science, Beijing Technology and Business University, Beijing 100037, China (e-mail: xbcao3613@sina.com).

Color versions of one or more of the figures in this paper are available online at <http://ieeexplore.ieee.org>.

Digital Object Identifier 10.1109/JAS.2018.7511234

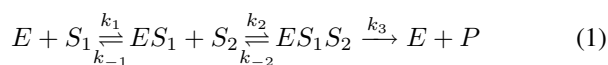
of the ordinary derivatives on the left-hand side of the ODEs. However, fractionalization of a system of two or more ODEs is not possible without violating mass balance and the system may suffer from unit inconsistencies [21], [30]. The problem is not limited to the units. The above difficulty can be removed by considering a common order of all the FDEs of the system, but it is a very particular case and makes its application restricted. Here, we present a more accurate model of a bi-substrate enzymatic reaction, where dynamics are influenced by memory.

In this article, we have introduced fractionalization of a two-substrate enzymatic reaction to study the effect of memory on it. Nonlinear FDEs cannot, in general, be solved analytically [27], but can be solved by numerical techniques [31]. The numerical solutions of the system have been studied here and compared with the integer-order system. We have also observed the dynamics of the different substances of the system by varying the order of the fractional derivatives (which signifies a measure of memory effect in a system [24]). We formulate a control based mathematical model involving the memory effect to conquer the negative effect of the extensive use of memory.

We have organized the rest of the paper as follows. In Section II, we formulate the model of a bi-substrate enzymatic reaction involving the memory effect. Some basic theoretical properties, and the existence and stability of equilibrium points are studied in Section III. In Section IV, a control theoretic approach is introduced towards the fractional-order model. The numerical results are illustrated in Section V. Finally, we have completed our article with a discussion and conclusion of the study in Section VI.

II. THE FRACTIONAL-ORDER MODEL

The schematic diagram of a two-substrate enzyme kinetic reaction, as described by Roy *et al.* [15], is given by



where S_1 , S_2 are substrates, E is the enzyme, C_1 i.e., ES_1 and C_2 i.e., ES_1S_2 are intermediate complexes and P is the product. k_1 , k_2 are the rate constants of formation of the complexes C_1 and C_2 respectively, and k_3 is the rate of product formation. The rates of dissociation of C_1 and C_2 are k_{-1} and k_{-2} respectively.

Let us denote the concentrations $[S_1]$, $[S_2]$, $[E]$, $[C_1]$, $[C_2]$ and $[P]$ by s_1 , s_2 , e , c_1 , c_2 and p respectively. From the law of mass action [10], the above enzymatic reaction (1) can be described by the following set of differential equations:

$$\begin{aligned} \frac{ds_1}{dt} &= -k_1es_1 + k_{-1}c_1 \\ \frac{ds_2}{dt} &= -k_2c_1s_2 + k_{-2}c_2 \\ \frac{de}{dt} &= -k_1es_1 + k_{-1}c_1 + k_3c_2 \end{aligned}$$

$$\begin{aligned} \frac{dc_1}{dt} &= k_1es_1 - k_{-1}c_1 - k_2c_1s_2 + k_{-2}c_2 \\ \frac{dc_2}{dt} &= k_2c_1s_2 - k_{-2}c_2 - k_3c_2 \\ \frac{dp}{dt} &= k_3c_2 \end{aligned} \quad (2)$$

with the initial conditions

$$\begin{aligned} s_1(0) &= s_{10}, s_2(0) = s_{20}, e(0) = e_0 \\ c_1(0) &= 0, c_2(0) = 0, \text{ and } p(0) = 0. \end{aligned} \quad (3)$$

From system (2), we have the following relations:

$$\begin{aligned} \frac{ds_1}{dt} - \frac{ds_2}{dt} + \frac{dc_1}{dt} &= 0 \\ \frac{ds_2}{dt} + \frac{dc_2}{dt} + \frac{dp}{dt} &= 0 \\ \frac{ds_2}{dt} + \frac{dc_2}{dt} + \frac{de}{dt} - \frac{ds_1}{dt} &= 0. \end{aligned} \quad (4)$$

Using the initial conditions (3), from (4), we have

$$\begin{aligned} s_1 - s_2 + c_1 &= s_{10} - s_{20} \\ s_2 + c_2 + p &= s_{20} \\ s_2 + c_2 + e - s_1 &= s_{20} + e_0 - s_{10}. \end{aligned} \quad (5)$$

With the help of the relations (5), system (2) can be reduced to the following three dimensional model consisting of substrates s_1 , s_2 and complex c_2 as

$$\begin{aligned} \frac{ds_1}{dt} &= -k_1(s_1 - s_2 - c_2 + s_{20} - s_{10} + e_0)s_1 \\ &\quad + k_{-1}(s_2 - s_1 + s_{10} - s_{20}), \\ \frac{ds_2}{dt} &= -k_2(s_2 - s_1 + s_{10} - s_{20})s_2 + k_{-2}c_2, \\ \frac{dc_2}{dt} &= k_2(s_2 - s_1 + s_{10} - s_{20})s_2 - k_{-2}c_2 - k_3c_2 \end{aligned} \quad (6)$$

with initial conditions,

$$s_1(0) = s_{10}, \quad s_2(0) = s_{20}, \quad c_2(0) = 0. \quad (7)$$

A. Fractionalization of the System (6)

The schematic diagram (1) can be considered as a three-compartmental model (as shown in Fig. 1) [30]. The initial stage of the reaction, where substrate S_1 is reacting with enzyme E to form the complex ES_1 , is termed as Compartment 1. Compartment 2 describes the intermediate stage where substrate S_2 is combining with ES_1 to form ES_1S_2 complex. Compartment 3 consists of the yielding of ES_1S_2 , which may either convert to the product or decompose back to the previous stage of reaction. Here, the mass flux $k_{-2}c_2$ is transferred from Compartment 3 to 2 (Fig. 1) and is common between the second and third equations of (6). We can fractionalize the system (6) as given below [30], [31]:

$$\begin{aligned} \frac{ds_1}{dt} &= -k_1(s_1 - s_2 - c_2 + s_{20} - s_{10} + e_0)s_1 \\ &\quad + k_{-1}(s_2 - s_1 + s_{10} - s_{20}), \\ \frac{ds_2}{dt} &= -k_2(s_2 - s_1 + s_{10} - s_{20})s_2 + k_{-20}^{\alpha} R D_t^{1-\alpha}(c_2), \\ \frac{dc_2}{dt} &= k_2(s_2 - s_1 + s_{10} - s_{20})s_2 \\ &\quad - k_{-20}^{\alpha} R D_t^{1-\alpha}(c_2) - k_3c_2 \end{aligned} \quad (8)$$

where $0 < \alpha \leq 1$ and ${}^R_0D_t^\alpha f(t)$ represents the Riemann-Liouville (RL) fractional derivative. In this context, it is to be noted that the memory index α was assigned between 0 to 1 in several classical systems and various engineering disciplines [27], [30], [32]–[34].

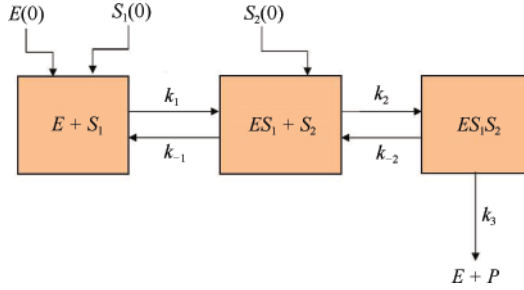


Fig. 1. Three-compartment model corresponding to the schematic diagram (1) of a bi-substrate enzymatic reaction. Rectangular boxes containing $E + S_1$, $ES_1 + S_2$ and ES_1S_2 represent Compartments 1, 2 and 3 respectively. $E(0)$, $S_1(0)$ and $S_2(0)$ are the respective initial values of E , S_1 and S_2 . k_1 , k_{-1} , k_2 and k_{-2} are the rate at which the mass fluxes are transferred from the source compartment to the targeted one as directed, where k_3 is the rate of elimination of product P and enzyme E from Compartment 3.

The unit on left-hand side of all the sub-equations of system (8) is $\text{Hour}^{-1} \cdot \text{Mol/l}$, the unit of the substances, is nothing but a number. The unit on right-hand side of the first sub-equation of (8) is also Hour^{-1} . Now, the unit of k_{-2}^α is $\text{Hour}^{-\alpha}$ and that of ${}^R_0D_t^{1-\alpha}(c_2)$ i.e., of $\frac{d^{1-\alpha}c_2(t)}{dt^{1-\alpha}}$ is $\text{Hour}^{\alpha-1}$. Thus, the unit of the term $k_{-2}^\alpha {}^R_0D_t^{1-\alpha}(c_2)$ and consequently, the right-hand side of both the second and third sub-equations of (8) is Hour^{-1} . Hence, units of all of the sub-equations of (8) remain consistent under the fractionalization process we have considered.

In order to use standard initial conditions, the Riemann-Liouville derivatives must be re-defined as Caputo fractional derivatives [22]. The relation between RL and Caputo's derivatives is given by the following equation:

$${}^R_0D_t^{1-\alpha} f(t) = {}^C_0D_t^\alpha f(t) + \frac{f(0)t^{\alpha-1}}{\Gamma(\alpha)}. \quad (9)$$

The system (8) using Caputo derivative can be expressed as follows:

$$\begin{aligned} \frac{ds_1}{dt} &= -k_1(s_1 - s_2 - c_2 + s_{20} - s_{10} + e_0)s_1 \\ &\quad + k_{-1}(s_2 - s_1 + s_{10} - s_{20}), \\ \frac{ds_2}{dt} &= -k_2(s_2 - s_1 + s_{10} - s_{20})s_2 \\ &\quad + k_{-2}^\alpha {}^C_0D_t^{1-\alpha}(c_2) + \frac{A_1 t^{\alpha-1}}{\Gamma(\alpha)}, \\ \frac{dc_2}{dt} &= k_2(s_2 - s_1 + s_{10} - s_{20})s_2 \\ &\quad - k_{-2}^\alpha {}^C_0D_t^{1-\alpha}(c_2) - k_3 c_2 - \frac{A_1 t^{\alpha-1}}{\Gamma(\alpha)} \end{aligned} \quad (10)$$

where

$$A_1 = k_{-2}^\alpha c_2(0) = 0$$

Therefore, system (10) becomes

$$\begin{aligned} \frac{ds_1}{dt} &= -k_1(s_1 - s_2 - c_2 + s_{20} - s_{10} + e_0)s_1 \\ &\quad + k_{-1}(s_2 - s_1 + s_{10} - s_{20}), \\ \frac{ds_2}{dt} &= -k_2(s_2 - s_1 + s_{10} - s_{20})s_2 + k_{-2}^\alpha {}^C_0D_t^{1-\alpha}(c_2), \\ \frac{dc_2}{dt} &= k_2(s_2 - s_1 + s_{10} - s_{20})s_2 \\ &\quad - k_{-2}^\alpha {}^C_0D_t^{1-\alpha}(c_2) - k_3 c_2. \end{aligned} \quad (11)$$

III. THEORETICAL STUDY

In this section, we have determined the equilibrium points of model (11) and discussed their stability from numerical point of view.

A. Existence of Equilibria and Stability

It is not possible to understand the stability of the equilibrium points of the system (11) directly because the fractional derivative does not satisfy Leibniz rule [35]. We apply the following transformation:

$$\begin{aligned} X &= D^\alpha s_1, \\ Y &= D^\alpha s_2 - k_{-2}^\alpha c_2, \\ Z &= D^\alpha c_2 + k_{-2}^\alpha c_2. \end{aligned} \quad (12)$$

Using the above transformation (12), system (11) is thus equivalent to the following system:

$$\begin{aligned} D^{1-\alpha} X &= -k_1(s_1 - s_2 - c_2 + s_{20} - s_{10} + e_0)s_1 \\ &\quad + k_{-1}(s_2 - s_1 + s_{10} - s_{20}), \\ D^{1-\alpha} Y &= -k_2(s_2 - s_1 + s_{10} - s_{20})s_2, \\ D^{1-\alpha} Z &= k_2(s_2 - s_1 + s_{10} - s_{20})s_2 - k_3 c_2, \\ D^\alpha s_1 &= X, \\ D^\alpha s_2 &= Y + k_{-2}^\alpha c_2, \\ D^\alpha c_2 &= Z - k_{-2}^\alpha c_2. \end{aligned} \quad (13)$$

It is sufficient to study the stability properties of system (13).

System (13) has the equilibrium points $E_1^*(0, 0, 0, 0, s_{20} - s_{10}, 0)$ for $\delta = s_{20} - s_{10} > 0$ and $E_2^*(0, 0, 0, s_1^*, 0, 0)$ for $\delta \leq 0$ where s_1^* is given by the following equation:

$$k_1 s_1^{*2} + [k_1(s_{20} - s_{10} + e_0) + k_{-1}]s_1^* + k_{-1}(s_{20} - s_{10}) = 0, \quad (14)$$

i.e., $s_1^* = \frac{-A + \sqrt{A^2 + B}}{2k_1}$, where

$$\begin{aligned} A &= k_1(s_{20} - s_{10} + e_0) + k_{-1}, \\ B &= 4k_1 k_{-1}(s_{10} - s_{20}). \end{aligned}$$

The Jacobian matrix $J_{E_1^*}$ of system (13) at E_1^* is given by

$$\begin{pmatrix} 0 & 0 & 0 & -(k_{-1} + k_1 e_0) & k_{-1} & 0 \\ 0 & 0 & 0 & k_2 \delta & -k_2 \delta & 0 \\ 0 & 0 & 0 & -k_2 \delta & k_2 \delta & -k_3 \\ 1 & 0 & 0 & 0 & 0 & 0 \\ 0 & 1 & 0 & 0 & 0 & k_{-2}^\alpha \\ 0 & 0 & 1 & 0 & 0 & -k_{-2}^\alpha \end{pmatrix} \quad (15)$$

where $\delta = s_{20} - s_{10}$.

Since α is real, it can also be an irrational number. However, there is no existing method for studying such a system with an irrational order of fractional derivatives. Therefore, we assume that $\alpha = \frac{M}{N}$ is rational, where $N > M > 0$ and $\text{gcd}(M, N) = 1$.

Therefore, the characteristic equation of the matrix $J_{E_1^*}$ is given by,

$$\Delta (J_{E_1^*} - \text{diag}([\lambda^{N-M}, \lambda^{N-M}, \lambda^{N-M}, \lambda^M, \lambda^M, \lambda^M])) = 0, \tag{16}$$

where “ Δ ” and “diag” represent the determinant and the diagonal matrix respectively [36].

Expanding the characteristic equation (16), we have

$$\lambda^{3N} + \Lambda_{11}\lambda^{2N} + \Lambda_{12}\lambda^N + \Lambda_{13}\lambda^{N(3-\alpha)} + \Lambda_{14}\lambda^{N(2-\alpha)} + \Lambda_{15} = 0 \tag{17}$$

where

$$\begin{aligned} \Lambda_{11} &= k_3 + k_2\delta + k_{-1} + k_1e_0, \\ \Lambda_{12} &= k_2k_3\delta + k_3(k_{-1} + k_1e_0) + k_1k_2e_0\delta, \\ \Lambda_{13} &= k_{-2}^\alpha, \Lambda_{14} = (k_{-1} + k_1e_0)k_{-2}^\alpha \text{ and} \\ \Lambda_{15} &= k_1k_2k_3e_0\delta. \end{aligned}$$

For $\alpha = 1$, from (17), we have

$$\lambda^3 + \eta_1\lambda^2 + \eta_2\lambda + \eta_3 = 0 \tag{18}$$

where

$$\begin{aligned} \eta_1 &= k_{-2} + k_{-1} + k_3 + k_1e_0 + k_2\delta, \\ \eta_2 &= (k_3 + k_{-2})(k_{-1} + k_1e_0) + k_2\delta(k_3 + k_1e_0), \\ \eta_3 &= k_1k_2k_3e_0\delta. \end{aligned}$$

Equation (18) is same as the characteristic equation of the integer-order system (6) for the equilibrium point $(0, \delta, 0)$.

The Jacobian matrix $J_{E_2^*}$ of system (13) at E_2^* is given by,

$$\begin{pmatrix} 0 & 0 & 0 & -\sqrt{A^2 + B} & k_1s_1^* + k_{-1} & k_1s_1^* \\ 0 & 0 & 0 & 0 & k_2(\delta + s_1^*) & 0 \\ 0 & 0 & 0 & 0 & -k_2(\delta + s_1^*) & -k_3 \\ 1 & 0 & 0 & 0 & 0 & 0 \\ 0 & 1 & 0 & 0 & 0 & k_{-2}^\alpha \\ 0 & 0 & 1 & 0 & 0 & -k_{-2}^\alpha \end{pmatrix}.$$

Proceeding as above, we have the characteristic equation of $J_{E_2^*}$ as follows:

$$(\lambda^N + \sqrt{A^2 + B})(\lambda^{2N} + \Lambda_{21}\lambda^N + \Lambda_{22}\lambda^{N(2-\alpha)} + \Lambda_{23}) = 0 \tag{19}$$

where

$$\begin{aligned} \Lambda_{21} &= k_3 - k_2(\delta + s_1^*), \\ \Lambda_{22} &= k_{-2}^\alpha, \\ \Lambda_{23} &= -k_2k_3(\delta + s_1^*). \end{aligned}$$

Arguments of the roots of the first factor of (19) are of the form $\arg(\lambda_k) = \frac{\pi}{N} + \frac{2k\pi}{N}, k = 0, 1, 2, \dots, N - 1$ and hence $|\arg(\lambda_k)| > \frac{\pi}{2N}$ for $k = 0, 1, 2, \dots, N - 1$.

Therefore, stability of E_2^* of system (13) depends upon the nature of the roots of the remaining factor of (19) as given by [36],

$$\lambda^{2N} + \Lambda_{21}\lambda^N + \Lambda_{22}\lambda^{N(2-\alpha)} + \Lambda_{23} = 0. \tag{20}$$

For $\alpha = 1$, we have, from (19)

$$(\lambda + \sqrt{A^2 + B})[\lambda^2 + [k_{-2} + k_3 - k_2(\delta + s_1^*)]\lambda - k_2k_3(\delta + s_1^*)] = 0 \tag{21}$$

which is same as the characteristic equation of the integer-order system (6) for the equilibrium point $(s_1^*, 0, 0)$. Here s_1^* is defined exactly as in (14).

IV. A CONTROL INDUCED MODEL

To determine the effect of memory towards the system, we introduce control parameter $u(t)$ into the model (11). Our aim is to get an optimum amount of the product as quick as possible. The control input $u(t)$ is used to reduce the rate of reverse reaction at the second stage satisfying $0 \leq u(t) \leq 1$. $u(t) = 1$ and 0 represent maximum and minimum use of the control measure respectively. With these assumptions, model (11) becomes:

$$\begin{aligned} \frac{ds_1}{dt} &= -k_1(s_1 - s_2 - c_2 + s_{20} - s_{10} + e_0)s_1 \\ &\quad + k_{-1}(s_2 - s_1 + s_{10} - s_{20}), \\ \frac{ds_2}{dt} &= -k_2(s_2 - s_1 + s_{10} - s_{20})s_2 \\ &\quad + (1 - u(t))k_{-20}^\alpha C D_t^{1-\alpha}(c_2), \\ \frac{dc_2}{dt} &= k_2(s_2 - s_1 + s_{10} - s_{20})s_2 \\ &\quad - (1 - u(t))k_{-20}^\alpha C D_t^{1-\alpha}(c_2) - k_3c_2 \end{aligned} \tag{22}$$

where $s_1(0) = s_{10}, s_2(0) = s_{20}$ and $c_2(0) = 0$.

Here the control measure basically stands for temperature, pressure, concentrations of the substances [7], [14] etc.. We study the effect of the control input on the system (22) from numerical point of view.

V. NUMERICAL SIMULATION

In this section, dynamics of reaction kinetics have been analyzed with the help of numerical methods. There are various methods to solve a system of fractional-order differential equations. We have used the numerical scheme given in [31] and solved our system of equations using the Matlab subroutine “lsqnonlin” and called this method as NS-lsq. Here, we have observed the solutions of the fractional-order system for $\alpha = 1$ i.e., when the system is free from the “memory effect” and compared them with the integer-order system. The stability region of equilibrium points of the system have also been studied numerically. We have compared the concentration of the substances, particularly the product, for various values of α . Consequently, we determine how the rate of formation of the substances is influenced by the “memory effect” of the system. Here the parameter values are taken from [37]–[39]. The units and recommended values of the kinetic parameters used for numerical simulation are as given in Table I.

TABLE I
VALUES OF PARAMETERS USED IN NUMERICAL CALCULATION

Parameter	Definition	Recommended value and unit
k_1	Forward rate constant for the formation of enzyme-substrate complex C_1	$2-7 \text{ (mol/l)}^{-1}\text{h}^{-1}$
k_{-1}	Rate constant for backward reaction of C_1	$0.1-3 \text{ h}^{-1}$
k_2	Forward rate constant for the formation of enzyme-product complex C_2	$2-13 \text{ (mol/l)}^{-1}\text{h}^{-1}$
k_{-2}	Rate constant for backward reaction of C_2	$2-5 \text{ h}^{-1}$
k_3	Forward rate constant for the product formation	$2-12 \text{ h}^{-1}$

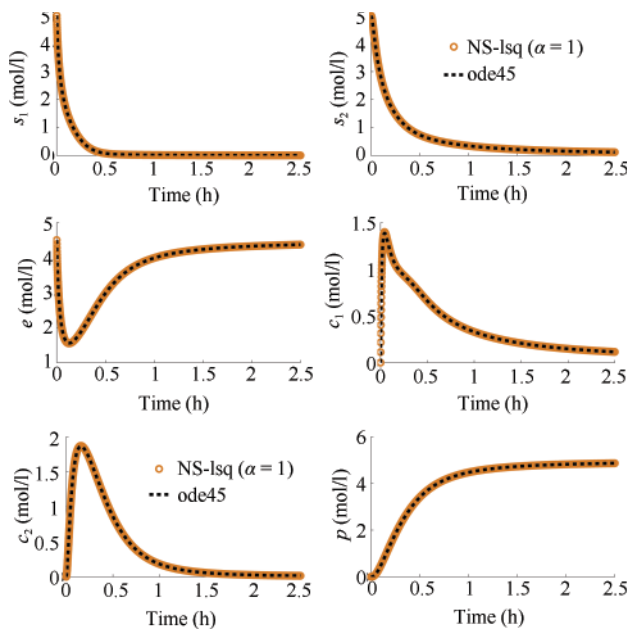


Fig. 2. Concentration profiles of the substances for integer-order system (6) (dashed line) and the fractional-order system (13) for $\alpha = 1$ (circle). The parameter values are $k_1 = 5 \text{ M}^{-1}\text{h}^{-1}$, $k_{-1} = 1 \text{ h}^{-1}$, $k_2 = 5 \text{ M}^{-1}\text{h}^{-1}$, $k_{-2} = 1 \text{ h}^{-1}$, $k_3 = 5 \text{ h}^{-1}$ and the initial values are $s_{10} = 5 \text{ M}$, $s_{20} = 5 \text{ M}$, $e_0 = 4.5 \text{ M}$ where M stands for mol/l.

A. Comparison of the Substance Profiles Obtained From the Fractional System for $\alpha = 1$ and From the Integer-order System

Fig. 2 represents the behavioral pattern of the substances for the integer-order (IO) model (6) and the fractional-order (FO) model (13) for $\alpha = 1$ simultaneously. The solutions obtained from both the systems are in good agreement with each other. Concentration of the two substrates (s_1 and s_2) decreases with the progression of the reaction. Consumption of s_1 is relatively quicker than s_2 due to faster reaction between enzyme and the primary substrate. Initially, the concentration of the enzyme decreases due to the formation of enzyme-substrate complexes c_1 and c_2 . It is recovered as the reaction progresses. Concentration of c_1 increases gradually from its initial value and it decreases with time, as

it binds with s_2 while forming the second complex. Moreover, the concentration of c_2 increases as soon as the first complex is formed, and then is decreased as time progresses due to its transformation to the product. Fig. 2 displays continuous formation of the product with time until it becomes steady.

B. Stability Region of the Equilibrium Points

The stability regions of the equilibrium points of model system (13) are studied numerically with the help of Theorem 1 of Sardar *et al.* [31] for reasonable values of the model parameters, where $\alpha \in (0, 1)$. We have observed that both equilibrium points are stable for such parameter values, and differentiating only in the time allows it to reach the steady state. Fig. 3 represents two stability regions corresponding to the equilibrium points E_1^* and E_2^* of the system (13).

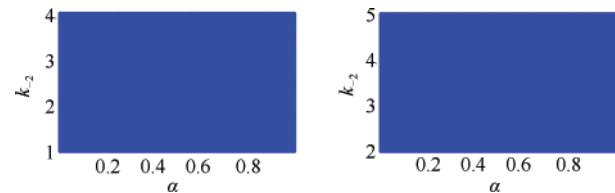


Fig. 3. Stability regions of the equilibrium points E_1^* (left panel) and E_2^* (right panel) with respect to α and k_{-2} . Other parameter values corresponding to E_1^* are taken as $k_1 = 5 \text{ M}^{-1}\text{h}^{-1}$, $k_{-1} = 1 \text{ h}^{-1}$, $k_2 = 4 \text{ M}^{-1}\text{h}^{-1}$, $k_3 = 5 \text{ h}^{-1}$, $e_0 = 2 \text{ M}$, $s_{10} = 5 \text{ M}$, $s_{20} = 6 \text{ M}$ and for E_2^* as $k_1 = 5 \text{ M}^{-1}\text{h}^{-1}$, $k_{-1} = 1 \text{ h}^{-1}$, $k_2 = 4 \text{ M}^{-1}\text{h}^{-1}$, $k_3 = 5 \text{ h}^{-1}$, $e_0 = 1 \text{ M}$, $s_{10} = 6 \text{ M}$, $s_{20} = 5 \text{ M}$.

C. Comparison Among the Concentration Profiles for Different Values of α

We have compared the dynamic profiles of the substances obtained by decreasing α values gradually to 1 and 0.7. It is to be noted that the solutions of (13) for $\alpha = 1$ correspond to the ODE system (6). Fig. 4 displays the dynamic profiles of the substances obtained from the IO system ($\alpha = 1$) and the FO system ($\alpha = 0.7$).

As the value of α reduces to 0.7, the concentrations of both the substrates (s_1 and s_2) decrease gradually. It is observed that with and without memory operator has no significant changes in the first substrate. This may be due to the fact that we do not consider memory in the first backward reaction step (see Fig. 1). The consumption of the second substrate is faster in comparison to the integer-order system. The profiles of the enzyme concentration show a faster recovery for the lower value of α . Variations in concentration of the first complex (c_1) is observed under varying α values. It is found that, the complex concentration c_1 is lower for $\alpha = 0.7$ than for $\alpha = 1$. It implies that for the lesser value of α , there exists a lower accumulation of c_1 due to its quicker conversion to the second complex by binding with the second substrate. A relatively faster accumulation of the concentration of second complex (c_2) is observed for the smaller value of α . This indicates the possibility of higher conversion of it to the product. Yielding of product is relatively faster for a lower value of α and consequently, its concentration reaches the steady state more quickly. The effect of memory assists in comparatively quicker

accumulation of c_2 and consequently, a rapid formation of the product.

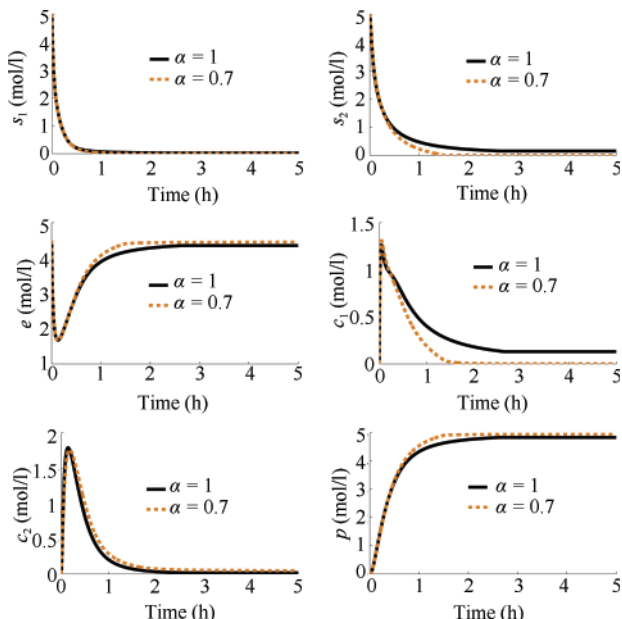


Fig. 4. Concentration profiles of the substances for the fractional-order system (13) for $\alpha = 1$ (solid line) and 0.7 (dashed line) where the parameter values are $k_1 = 5 \text{ M}^{-1}\text{h}^{-1}$, $k_{-1} = 3 \text{ h}^{-1}$, $k_2 = 6 \text{ M}^{-1}\text{h}^{-1}$, $k_{-2} = 3 \text{ h}^{-1}$, $k_3 = 5 \text{ h}^{-1}$ and the initial values are $s_{10} = 5 \text{ M}$, $s_{20} = 5 \text{ M}$, $e_0 = 4.5 \text{ M}$.

To study the effect of changes of the time taken for formation of the product due to the changes in α values, we decrease gradually the values of α as 1, 0.7 and 0.25. Fig. 5 represents the dynamic profiles of the product (p) for the aforesaid α values. Concentrations of the product are observed as 4.771 mol/l, 4.948 mol/l and 4.927 mol/l for $\alpha = 1, 0.7$ and 0.25 respectively. It is to be noted that as the α values decrease from 1 to 0.7, the formation of product becomes relatively faster than the classic case. However, it is also to be noted that, if the values of α decreased again, the time taken for the formation of product is relatively greater (Fig. 5) and consequently, the system slows down.

D. Comparison Among the Concentration Profiles for Different Values of $u(t)$

Here, we investigate the effect due to the changes of control parameter $u(t)$ to the control induced FO model (22). Fig. 6 represents the variation in the substances for $u(t) = 0, 0.4$ and 0.9. It is observed that the concentrations of both the substrates (s_1 and s_2) are decreasing more quickly for higher values of the control parameter. Accumulation of the first complex concentration (c_1) is lower for upper values of $u(t)$ due to its fast conversion into the second complex. Higher values of the control input corresponds to a more accumulation of c_2 which ultimately leads to fast formation of the product (p).

We vary the values of the control parameter as 0 and 0.6 to rise above the negative effect of extensive use of memory. Fig. 7 represents the concentration profiles of the product for the above values of $u(t)$. The rest of the parameter values are taken exactly as in Fig. 5 with $\alpha = 0.25$. Concentration of the

product (p) for $u(t) = 0$ is observed as 4.927 mol/l, which is decreasing from the value 4.948 mol/l for $\alpha = 0.7$ (see Fig. 5). While, in Fig. 7, concentration of the product for $u(t) = 0.6$ is noted as 4.973 mol/l. Thus, with proper control measures, it is possible to overcome the above mentioned negative effect.

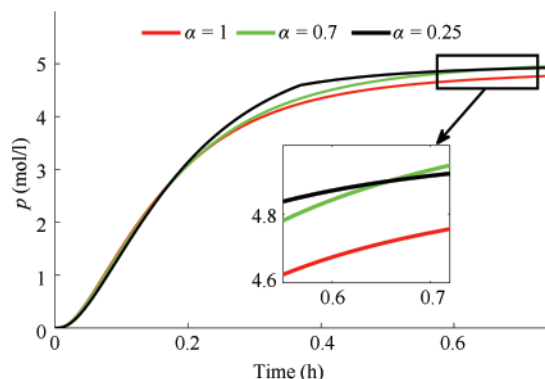


Fig. 5. Concentration profiles of the product p of system (13) for $\alpha = 1, 0.7$ and 0.25. Other parameter values are taken as $k_1 = 7 \text{ M}^{-1}\text{h}^{-1}$, $k_{-1} = 0.1 \text{ h}^{-1}$, $k_2 = 13 \text{ M}^{-1}\text{h}^{-1}$, $k_{-2} = 3 \text{ h}^{-1}$, $k_3 = 12 \text{ h}^{-1}$, $e_0 = 4.5 \text{ M}$, $s_{10} = 5 \text{ M}$, $s_{20} = 5 \text{ M}$.

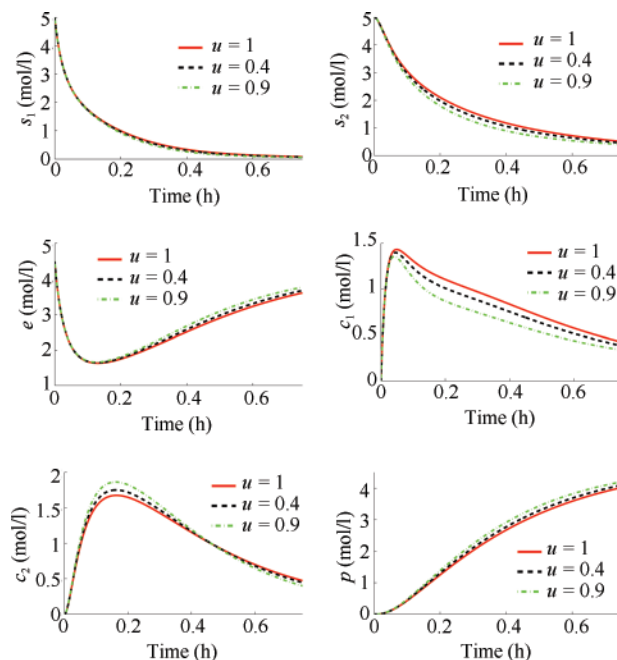


Fig. 6. Concentration profiles of the substances of (22) for $u(t) = 0, 0.4$ and 0.9. Other parameter values are taken as $k_1 = 5 \text{ M}^{-1}\text{h}^{-1}$, $k_{-1} = 2 \text{ h}^{-1}$, $k_2 = 5 \text{ M}^{-1}\text{h}^{-1}$, $k_{-2} = 2 \text{ h}^{-1}$, $k_3 = 5 \text{ h}^{-1}$, $e_0 = 4.5 \text{ M}$, $s_{10} = 5 \text{ M}$, $s_{20} = 5 \text{ M}$ and $\alpha = 0.7$.

VI. DISCUSSION AND CONCLUSION

In this study, we have presented an approach of fractionalizing a bi-substrate enzyme kinetic reaction. The fractional-order system is solved numerically, as the system is unlikely to have analytical solutions. Our numerical results reveal that the solutions of the fractional-order system for $\alpha = 1$, and the solutions of the corresponding integer-order system are overlapping. Benefits of the fractional-order model are observed from the solutions, mainly in the formation of the product.

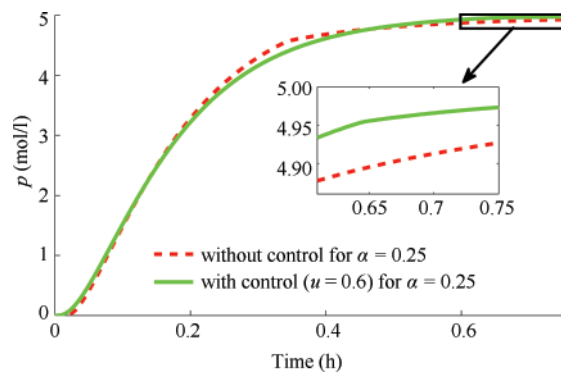


Fig. 7. Concentration profiles of the product p of system (22) for $u(t) = 0$ and 0.6. Other parameter values are taken as $k_1 = 7 \text{ M}^{-1}\text{h}^{-1}$, $k_{-1} = 0.1 \text{ h}^{-1}$, $k_2 = 13 \text{ M}^{-1}\text{h}^{-1}$, $k_{-2} = 3 \text{ h}^{-1}$, $k_3 = 12 \text{ h}^{-1}$, $e_0 = 4.5 \text{ M}$, $s_{10} = 5 \text{ M}$, $s_{20} = 5 \text{ M}$ and $\alpha = 0.25$.

In Section II, we have calculated the equilibrium points of the FO system and discussed their stability regions. Our study shows that, similar to the integer-order system, equilibrium points remain stable for a fractional-order system with a realistic range of parameters.

We have studied the changes of the concentration profiles of the substances due to the changes in α values ($\alpha = 1$ and 0.7). Lower values of α signifies a faster reaction up to certain threshold values.

We have focused on the changes of concentration of the product due to the change in α values (1, 0.7 and 0.25). The system is highly sensitive to the α values. Formation of the product is perceived relatively faster due to “memory effect.” However, extensive effect of memory makes the system slower. The results of our study can predict system dynamics with respect to optimization and quantification of the product.

The dynamical behavior of the substances is observed by varying the control input. Presence of the control parameter corresponds to a quicker reaction. The negative effect of the extensive use of memory can be recovered by proper use of a control measure.

The model can be extended by considering memory in both the backward reaction steps. One can consider the mass $k_{-1}c_1$, which is transferred from Compartment 2 to 1 similar to the way mass $k_{-2}c_2$ is transferred from Compartment 3 to 2 (see Fig. 1). In this context, with the help of relations (5), system (2) can be transformed to a three dimensional model consisting of the substrate s_1 and the complexes c_1 , c_2 . Proceeding as in Section II, one can fractionalize the model. The fractionalized model would consist of terms $k_{-10}^\alpha {}^C D_t^{1-\alpha}(c_1)$ and $k_{-20}^\beta {}^C D_t^{1-\beta}(c_2)$ of different orders without violating mass balance. Hence in this study, we may summarily conclude that the presence of the mixing parameter may show complex dynamics.

REFERENCES

- [1] R. Dutta, *Fundamentals of Biochemical Engineering*. Berlin: Springer, 2008.
- [2] I. Belgacem and J. L. Gouzé, “Global Stability of full open reversible michaelis-menten reactions,” *IFAC Proc.*, vol. 45, no. 15, pp. 591–596, 2012.
- [3] D. L. Nelson and M. M. Cox, *Lehninger Principles of Biochemistry*, 6th ed. Basingstoke: Macmillan Education, 2013.

- [4] S. Sirin, D. A. Pearlman, and W. Sherman, “Physics-based enzyme design: predicting binding affinity and catalytic activity,” *Proteins: Struct. Funct. Bioinform.*, vol. 82, pp. 3397–3409, Dec. 2014.
- [5] D. Vasic-Racki, U. Kragl, and A. Liese, “Benefits of enzyme kinetics modelling,” *Chem. Biochem. Eng. Quart.*, vol. 17, no. 1, pp. 7–18, Mar. 2003.
- [6] R. Roskoski Jr, “The ErbB/HER family of protein-tyrosine kinases and cancer,” *Pharmacol. Res.*, vol. 79, pp. 34–74, Jan. 2014.
- [7] P. K. Roy, S. Datta, S. Nandi, and F. Al Basir, “Effect of mass transfer kinetics for maximum production of biodiesel from *Jatropha Curcas* oil: a mathematical approach,” *Fuel*, vol. 134, pp. 39–44, Oct. 2014.
- [8] S. D. Thiberville, N. Moyen, L. Dupuis-Maguiraga, A. Nougairède, E. A. Gould, P. Roques, and X. De Lamballerie, “Chikungunya fever: epidemiology, clinical syndrome, pathogenesis and therapy,” *Antiv. Res.*, vol. 99, no. 3, pp. 345–370, Sep. 2013.
- [9] Y. L. Qi, D. G. Musson, B. Schweighardt, T. Tompkins, L. Jesaitis, A. J. Shaywitz, K. Yang, and C. A. O’Neill, “Pharmacokinetic and pharmacodynamic evaluation of Elosulfase Alfa, an enzyme replacement therapy in patients with morquio a syndrome,” *Clin. Pharmacokinet.*, vol. 53, no. 12, pp. 1137–1147, Dec. 2014.
- [10] J. D. Murray, *Mathematical Biology: I. An Introduction*, 3rd ed. New York: Springer, 2002.
- [11] L. A. Segel, *Mathematical Models in Molecular and Cellular Biology*. Cambridge: Cambridge University Press, 1980.
- [12] G. Varadharajan and L. Rajendran, “Analytical solution of coupled nonlinear second order reaction differential equations in enzyme kinetics,” *Nat. Sci.*, vol. 3, no. 6, pp. 459–465, May 2011.
- [13] A. Meena, A. Eswari, and L. Rajendran, “Mathematical modelling of enzyme kinetics reaction mechanisms and analytical solutions of non-linear reaction equations,” *J. Math. Chem.*, vol. 48, no. 2, pp. 179–186, Aug. 2010.
- [14] P. T. Benavides and U. Diwekar, “Optimal control of biodiesel production in a batch reactor: Part I: deterministic control,” *Fuel*, vol. 94, pp. 211–217, Apr. 2012.
- [15] P. K. Roy, S. Nandi, and M. K. Ghosh, “Modeling of a control induced system for product formation in enzyme kinetics,” *J. Math. Chem.*, vol. 51, pp. 2704–2717, Nov. 2013.
- [16] F. A. Basir, R. Bhattacharyya, and P. K. Roy, “Delay induced oscillation in a biochemical model and its control,” *Nonlin. Stud.*, vol. 22, no. 3, pp. 453–472, Aug. 2015.
- [17] R. A. Azizyan, A. E. Gevorgyan, V. B. Arakelyan, and E. S. Gevorgyan, “Mathematical modeling of uncompetitive inhibition of Bi-substrate enzymatic reactions,” *Int. Schol. Sci. Res. Innov.*, vol. 7, no. 10, pp. 974–977, 2013.
- [18] S. Westerlund, “Dead matter has memory!,” *Phys. Scrip.*, vol. 43, no. 2, pp. 174–179, 1991.
- [19] V. E. Tarasov, “Review of some promising fractional physical models,” *Int. J. Mod. Phys. B*, vol. 27, no. 9, pp. Article No. 1330005, Mar. 2013.
- [20] A. A. Stanislavsky, “Memory effects and macroscopic manifestation of randomness,” *Phys. Rev. E*, vol. 61, no. 5, pp. 4752–4759, May 2000.
- [21] J. K. Popović, M. T. Atanacković, A. S. Pilipović, M. R. Rapaić, S. Pilipović, and T. M. Atanacković, “A new approach to the compartmental analysis in pharmacokinetics: fractional time evolution of diclofenac,” *J. Pharmacokinet. Pharmacodyn.*, vol. 37, no. 2, pp. 119–134, Apr. 2010.
- [22] R. Toledo-Hernandez, V. Rico-Ramirez, G. A. Iglesias-Silva, and U. M. Diwekar, “A fractional calculus approach to the dynamic optimization of biological reactive systems. Part I: fractional models for biological reactions,” *Chem. Eng. Sci.*, vol. 117, pp. 217–228, Sep. 2014.
- [23] E. Ahmed and A. S. Elgazzar, “On fractional order differential equations model for nonlocal epidemics,” *Phys. A: Statist. Mech. Appl.*, vol. 379, no. 2, pp. 607–614, Jun. 2007.
- [24] M. L. Du, Z. H. Wang, and H. Y. Hu, “Measuring memory with the order of fractional derivative,” *Sci. Rep.*, vol. 3, pp. Article No. 3431, Dec. 2013.
- [25] M. El-Shahed and A. Alsaedi, “The fractional SIRC model and influenza A,” *Math. Probl. Eng.*, vol. 2011, pp. Article No. 480378, Aug. 2011.
- [26] S. Abbas, M. Benchohra, G. M. N’Guérékata, and B. A. Silmani, “Darboux problem for fractional-order discontinuous hyperbolic partial differential equations in Banach algebras,” *Compl. Variabl. Elliptic Equat.: Int. J.*, vol. 57, no. 2–4, pp. 337–350, 2012.

- [27] I. Podlubny, *Fractional Differential Equations*. San Diego: Academic Press, 1999.
- [28] F. A. Abdullah, "Using fractional differential equations to model the Michaelis-Menten reaction in a 2-d region containing obstacles," *Science Asia*, vol. 37, no. 1, pp. 75–78, 2011.
- [29] A. Alawneh, "Application of the multistep generalized differential transform method to solve a time-fractional enzyme kinetics," *Discr. Dyn. Nat. Soc.*, vol. 2013, pp. Article No. 592938, 2013.
- [30] A. Dokoumetzidis, R. Magin, and P. Macheras, "Fractional kinetics in multi-compartmental systems," *J. Pharmacokinet. Pharmacodyn.*, vol. 37, no. 5, pp. 507–524, Oct. 2010.
- [31] T. Sardar, S. Rana, and J. Chattopadhyay, "A mathematical model of dengue transmission with memory," *Commun. Nonlin. Sci. Numer. Simulat.*, vol. 22, no. 1–3, pp. 511–525, May 2015.
- [32] B. S. Chen, C. Y. Li, B. Wilson, and Y. J. Huang, "Fractional modeling and analysis of coupled MR damping system," *IEEE/CAA J. of Autom. Sinica*, vol. 3, no. 3, pp. 288–294, Jul. 2016.
- [33] S. Rana, S. Bhattacharya, J. Pal, G. M. N'Guerékata, and J. Chattopadhyay, "Paradox of enrichment: a fractional differential approach with memory," *Phys. A: Statist. Mechan. Appl.*, vol. 392, no. 17, pp. 3610–3621, Sep. 2013.
- [34] M. K. Ghosh, J. Pal, and P. K. Roy, "How memory regulates drug resistant pathogenic bacteria? a mathematical study," *Int. J. Appl. Comput. Math.*, vol. 3, no. S1, pp. 747–773, Dec. 2017.
- [35] V. E. Tarasov, "No violation of the Leibniz rule. No fractional derivative," *Commun. Nonlin. Sci. Numer. Simulat.*, vol. 18, no. 11, pp. 2945–2948, Nov. 2013.
- [36] M. S. Tavazoei, and M. Haeri, "Chaotic attractors in incommensurate fractional order systems," *Phys. D*, vol. 237, no. 20, pp. 2628–2637, Oct. 2008.
- [37] S. Nandi, M. K. Ghosh, R. Bhattacharya, and P. K. Roy, "Mathematical modeling to optimize the product in enzyme kinetics," *Control Cybern.*, vol. 42, no. 2, pp. 431–442, 2013.
- [38] S. Schnell and P. K. Maini, "Enzyme kinetics at high enzyme concentration," *Bull. Math. Biol.*, vol. 62, no. 3, pp. 483–499, May 2000.
- [39] S. Schnell and P. K. Maini, "A century of enzyme kinetics: reliability of the K_M and v_{max} estimates," *Comm. Theoret. Biol.*, vol. 8, no. 2–3, pp. 169–187, Mar-Jan. 2003.



Mithun Kumar Ghosh received the B.Sc. and M.Sc. degrees from the University of Calcutta, India, in 2005 and 2007 respectively. He is a member of the Centre for Mathematical Biology and Ecology, Department of Mathematics, Jadavpur University, India, and is pursuing the Ph.D. degree at the same university. His research interests focus on model formulation, analysis and control of enzymatic reactions.



Tridip Sardar graduated from the University of Calcutta, India, in 2006. He received the M.Sc. degree from IIT Kanpur, India, in 2008 and the Ph.D. degree in applied mathematics from the University of Calcutta, India, in 2015. He is currently an Assistant Professor in the Department of Mathematics, Dinabandhu Andrews College, India. His research interests include mathematical epidemiology, nonlinear dynamics, application of fractional differential equations.



Xianbing Cao received the B.S. degree in mathematics from Jishou University in 1984, the M.S. degree in probability theory from Harbin Institute of Technology in 1990, and his Ph.D. degree in stochastic control theory from the Chinese Academy of Sciences in 2002. He has been a Professor at Beijing Technology and Business University since 2003, and currently is Dean of the School of Science. His research interests include stochastic control systems, system identification and financial time series analysis.



Priti Kumar Roy is a Professor of the Department of Mathematics, Jadavpur University. He is proficient in nonlinear system dynamics and an expert in mathematical modeling. He researches infectious diseases like HIV, cutaneous leishmaniasis, filariasis and auto immune disease like psoriasis. Apart from epidemiology, he also researches on industrial mathematics on production of biodiesel from the jatropha curcus plant and its oil production optimization. Furthermore, he also researches the ecological modelling of some important ecological and environmental issues.

He has published over 100 peer reviewed publications in international and national journals on his research topics. Prof. Roy edited one book- *Insight and Control of Infectious Disease in Global Scenario* published by Intech Publishers, and is the author of Springer publication entitled *Mathematical Models for Therapeutic Approaches to Control HIV Disease Transmission*, which is published this year. He has guided 8 Ph.D. students and 8 more scholars are working under his guidance. He is the first person to supervise a thesis on mathematical models of Psoriasis. He is an eminent member of different National and International Societies like Biomathematical Society of India (BMSI), International Association of Engineers (IAENG), European Society of Clinical Microbiology and Infectious Diseases (ESCMID) and European Society for Mathematical and Theoretical Biology (ESMTB). He has completed 6 research projects as Principal Investigator, sponsored by Government of India. Prof. Roy was awarded the Best Paper Award in World Congress on Engineering 2010 held in London, UK. He was selected as an Indian Scientist under the International Collaboration/Exchange Program 2011–2012 and again in 2016 awarded by INSA. He was also awarded with Siksha Ratan award in 2012. Prof. Roy delivered invited lectures in more than 39 overseas Universities, Institutes and numerous lectures in Indian Universities.



Source details

[Feedback >](#) [Compare sources >](#)

IEEE/CAA Journal of Automatica Sinica

Scopus coverage years: from 2014 to Present

Publisher: IEEE

ISSN: 2329-9266 E-ISSN: 2329-9274

Subject area: [Mathematics: Control and Optimization](#) [Engineering: Control and Systems Engineering](#) [Computer Science: Information Systems](#)
[Computer Science: Artificial Intelligence](#)

Source type: Journal

[View all documents >](#) [Set document alert](#) [Save to source list](#)

CiteScore 2022 [i](#)
17.6

SJR 2022 [i](#)
3.218

SNIP 2022 [i](#)
3.213

CiteScore [CiteScore rank & trend](#) [Scopus content coverage](#)

i Improved CiteScore methodology x

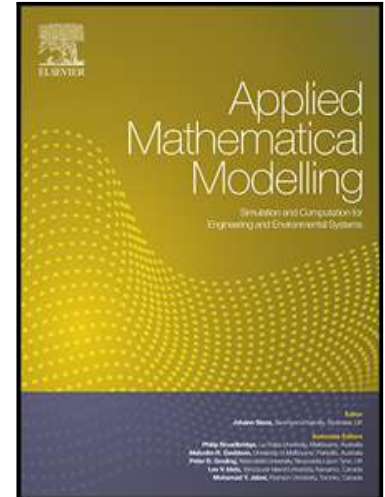
CiteScore 2022 counts the citations received in 2019-2022 to articles, reviews, conference papers, book chapters and data papers published in 2019-2022, and divides this by the number of publications published in 2019-2022. [Learn more >](#)

Accepted Manuscript

Characteristics of Rayleigh wave propagation in orthotropic magneto-thermoelastic half-space: An eigen function expansion method

Soumen Shaw , Mohamed I.A. Othman

PII: S0307-904X(18)30556-0
DOI: <https://doi.org/10.1016/j.apm.2018.11.019>
Reference: APM 12545



To appear in: *Applied Mathematical Modelling*

Received date: 14 January 2018
Revised date: 26 October 2018
Accepted date: 19 November 2018

Please cite this article as: Soumen Shaw , Mohamed I.A. Othman , Characteristics of Rayleigh wave propagation in orthotropic magneto-thermoelastic half-space: An eigen function expansion method, *Applied Mathematical Modelling* (2018), doi: <https://doi.org/10.1016/j.apm.2018.11.019>

This is a PDF file of an unedited manuscript that has been accepted for publication. As a service to our customers we are providing this early version of the manuscript. The manuscript will undergo copyediting, typesetting, and review of the resulting proof before it is published in its final form. Please note that during the production process errors may be discovered which could affect the content, and all legal disclaimers that apply to the journal pertain.

Highlights

- This problem is more general as other problem with different thermoelastic models.
- Effect of phase lag due to heat flux vector is more dominating in comparison with other phase lags.
- The secular equation magnitude increases with an increasing of wave number.
- Rayleigh wave velocity increases with the increase of wave number and magnetic field.
- The attenuation coefficient decreases with the increase of wave number and magnetic field.

ACCEPTED MANUSCRIPT

Characteristics of Rayleigh wave propagation in orthotropic magneto-thermoelastic half-space: An eigen function expansion method

Soumen Shaw¹, Mohamed I. A. Othman^{2*}

¹Department of Mathematics, IEST, Shibpur, India

²Department of Mathematics, Faculty of Science, Zagazig University, P.O. Box 44519, Zagazig, Egypt.

shaw_soumen@rediffmail.com, m_i_a_othman@yahoo.com

Abstract:

In this article, we theoretically demonstrate the characteristics of Rayleigh surface wave propagation in a homogeneous and orthotropic thermoelastic half-space in the context of three-phase-lag model of generalized thermoelasticity. The influence of magnetic field on Rayleigh wave is analyzed the framework of two-temperature model. A vector matrix differential equation is formed by employing normal mode analysis, which is then solved by the eigen function expansion method. The frequency equations in closed form are derived and the path of surface particles during Rayleigh wave propagation is found to be elliptical. The results show appreciable differences in phase velocity, attenuation coefficient and specific loss due to the presence of heat-flux phase-lag and are more dominating in comparison with other phase lags.

Keywords: Rayleigh wave; orthotropic medium; generalized thermoelasticity, three-phase-lag model; magnetic effect.

1. Introduction:

The study of surface acoustic waves in anisotropic elastic medium, especially along the surface of the earth and prediction about the nature of the earthquakes is till careworn. Consequence analysis of seismic waves gained an overriding importance to the geophysicists. Since the last century, several researchers have been devoted to analyzing the seismic waves in various types of elastic media subject to numerous external stimuli. Due to reasonably slower attenuation of energy, Rayleigh type surface waves are most destructive seismic waves that can freely propagate along the stress free surface. In general, Rayleigh waves showing non-dispersive in nature, but in stratified half-space it becomes dispersive. Rayleigh waves are characterized by elliptical motion perpendicular to the surface. In the near surface, this motion is “retrograde”, meaning that is counter-clockwise when the propagation is left-to-right. At depth, the motion can reverse to prograde. Thermoelastic response on the propagation of seismic waves is realized over amplitude as well as propagation speed. Owing to great practical applications, thermoelastic influences on the characteristics of the surface wave propagation is very significant. As the earth’s surface is

not merely a pure isotropic medium, so seismic wave propagation and its various characteristics are noteworthy in anisotropic media as well. Few authors have already been discussed some aspects of seismic wave in anisotropic medium due to various geophysical interest.

Literature concerning with thermo-elastic phenomena is enriched with the theory of propagation of thermal signals by Biot [1] in the nineteenth century. There was a long run from the uncoupled parabolic type heat conduction equation to recently developed memory dependent thermal conduction law. In this period of more than one and half a century, several developments were found to replace the earlier one. The refinements aim was to simultaneously satisfy the following conditions: (i) Finiteness of the thermal signal propagation speed, (ii) spatial propagation of thermoelastic waves without attenuation, and (iii) existence of distortion less wave forms akin to classical D'Alembert type waves. The first was due to Cattaneo [2], where a wave type heat equation was derived by postulating a new law of heat propagation to replace the classical Fourier law. Later on, Lord-Shulman [3], Green-Lindsay [4] and Green-Naghdi [5] have proposed three different theories which are the most discussed generalized heat equations in the literature.

In the process of dynamic developments of thermoelasticity theory, in the year 2007, Roychoudhuri [6] have proposed a mathematical model of propagation of thermal signals comprising with three different time delays. This model is now known as three-phase-lags (TPL) model of generalized thermoelasticity. It's claimed the superiority over earlier published models. Thermal problems in low temperatures and very high heat flux situations lagging behavior are very significant and consequently phase-lags model gets its impact over former models.

The second law of thermodynamics and its consequences on heat flow and the entropy changes in the continuum body recommends that, according to Gurtin and Williams [7, 8], the entropy changes is occurred by one temperature (thermodynamic temperature) and heat flow due to another one (conductive temperature). Based on that theory, Chen and Gurtin [9] have introduced one generalization of heat conduction law, namely, generalized thermoelasticity with two temperature theory. For further details regarding two-temperature theory and its applications one may go through the article of Shaw and Mukhopadhyay [10] and the cross references therein.

Seismic wave propagation in magneto-elastic solid with initial stresses was investigated by Yu and Tang [11]. Based on the governing equations of Yu and Tang, De and Sengupta [12, 13] have addressed the surface and interfacial waves in magneto-elastic conducting solids. Due to a wide range of application in numerous thermo-physical situations and development of electro- and magneto- sensitive elastomers, coupling between electromagnetic effects and the mechanical phenomena in continuous media has acknowledged considerably more attention in the recent literature. Great attention has been devoted inside nuclear reactors to influence its design as well

as operations and consequently to the study the electro magneto-thermoelastic coupled problems based on the generalized thermoelastic theories in non-inertial frame. The interplay of the Maxwell electromagnetic field with the motion of deformable solids is largely being undertaken by many researchers due to its possible applications to geophysical problems and certain topics in optics and acoustics. Moreover, the earth is subjected to its own magnetic field and the material of the earth may be electrically conducting. Thus, the magneto-elastic nature of the earth's material may affect the propagation of waves. Many authors have considered the propagation of electro-magneto-thermoelastic waves in an electrically and thermally conducting solids [14, 15]. During the second half of the twentieth century, great attention has been devoted to the study of electro magneto-thermoelastic coupled problems based on the generalized thermoelasticity [16, 17]. In this context, valuable information on the development of the magneto-elasticity and magneto-thermoelasticity theories is presented in a number of books [18-20].

In this article, various physical characteristics of Rayleigh surface wave propagation in an thermoelastic orthotropic half-space is being analyzed in the framework of three-phase-lags model of hyperbolic thermoelasticity theory. There is a distinguished improvement over the recently published article by Biswas and Mukhopadhyay [21] is that, though both the investigations are on anisotropic medium, we could not ignore the surrounding magnetic field within and on the earth's surface during the analysis of seismic wave, especially Rayleigh wave, propagation. In the context of two different thermo-mechanical surface boundary conditions several salient features of Rayleigh waves are identified. It is revealed that, in presence of magnetic field in the medium, the thermal time delay for heat flux into the medium has a significant impact on the attenuation of Rayleigh wave. The analytical expressions of the field functions are derived by adopting normal mode analysis followed by eigen function expansion method. The computational results for the different characteristics of waves like phase velocity, attenuation coefficient and specific loss are computed numerically and the effect of phase lags on them for various thermoelastic models are presented graphically. The applications range from geophysical problems to quantities non-destructive evaluation of mechanical structures and acoustic tomography for medical purposes.

2. Formulation of the problem:

In the reference of orthogonal Cartesian coordinate system $Oxyz$, here we consider the Rayleigh surface wave is propagating along x -axis. Consequently, a thermoelastic-plane-strain problem parallel to xz -plane in the orthotropic half-space is considered. $z = 0$ is the free surface of propagation. The reference temperature of the medium is T_0 and is assumed to be unstrained and

unstressed initially.

Without any loss of generality, here we consider the displacement components of the thermoelastic medium in the following form: $u = u(x, z, t)$, $v = 0$, $w = w(x, z, t)$.

We consider there is a uniform magnetic field with constant intensity $\mathbf{H}_0 = (0, H_0, 0)$ acts parallel to the bounding plane (taking as the direction of y – axis). The wave propagation will be influenced by the thermal field as well as by the magnetic one. The electromagnetic fields are governed by the Maxwell equations:

$$\nabla \times \mathbf{h} = \mathbf{J} + \dot{\mathbf{D}}, \quad \nabla \times \mathbf{E} = -\dot{\mathbf{B}}, \quad \nabla \cdot \mathbf{B} = 0, \quad \nabla \cdot \mathbf{D} = 0, \quad \mathbf{B} = \mu_e \mathbf{H}, \quad \mathbf{D} = \varepsilon_0 \mathbf{E} \quad (1)$$

where notations have their usual meanings and $\mathbf{h} = (0, h, 0)$ is the perturbed magnetic field.

For a perfectly conducting, slowly moving medium Ohm's law is given as $\mathbf{E} = -\dot{\mathbf{u}} \times \mathbf{B}$.

The small effect of temperature gradient on the current density vector \mathbf{J} is neglected. The dynamic displacement vector is actually measured from a steady state deformed position and the deformation is supposed to be small.

The stress-displacement-temperature relations are given as follows:

$$\tau_{xx} = c_{11}u_{,x} + c_{13}w_{,z} - \beta_1 T \quad (2)$$

$$\tau_{zz} = c_{13}u_{,x} + c_{33}w_{,z} - \beta_3 T \quad (3)$$

$$\tau_{xz} = c_{55}(u_{,z} + w_{,x}) \quad (4)$$

In which, τ_{xx} , τ_{zz} , τ_{xz} are the components of the stress tensor, c_{ij} are elastic constants, β_1 and β_3 are the thermal modulus along x -axis and z -axis respectively.

Together with the Lorentz's body force, the corresponding equations of motion in an orthotropic thermoelastic half-space can be expressed in the following manner,

$$\tau_{xx,x} + \tau_{zx,z} + F_x = \rho \ddot{u} \quad (5)$$

$$\tau_{xz,x} + \tau_{zz,z} + F_z = \rho \ddot{w} \quad (6)$$

where ρ is the mass density and an over headed dot denotes time derivative of the field functions.

The components of the magnetic intensity vector in the medium are

$$H_x = 0, \quad H_y = H_0 + h, \quad H_z = 0 \quad (7)$$

The perturbed magnetic field \mathbf{h} is small compared to the strong initial magnetic field \mathbf{H}_0 .

Then after linearization we get $\mathbf{h} = -\mathbf{H}_0 e$. (8)

where, e is the dilatation.

Now we obtain $J_x = H_0 e_{,z}$, $J_y = 0$, $J_z = -H_0 e_{,x}$ (9)

The expression of Lorentz force is given by

$$\mathbf{F}_i = \mu_e (\mathbf{J} \times \mathbf{H})_i \quad (10)$$

Now from Eq. (10), we get the components of Lorentz force as follows:

$$F_x = \mu_e H_0^2 (u_{,xx} + w_{,xz}), \quad F_z = \mu_e H_0^2 (u_{,xz} + w_{,zz}). \quad (11)$$

Consequently, in terms of displacement components, the equations of motion can be recast as follows:

$$c_{11} u_{,xx} + c_{55} u_{,zz} + (c_{13} + c_{55}) w_{,xz} - \beta_1 T_{,x} + \mu_e H_0^2 (u_{,xx} + w_{,xz}) = \rho \ddot{u} \quad (12)$$

$$(c_{13} + c_{55}) u_{,xz} + c_{55} w_{,xx} + c_{33} w_{,zz} - \beta_3 T_{,z} + \mu_e H_0^2 (u_{,xz} + w_{,zz}) = \rho \ddot{w} \quad (13)$$

The two-temperature theory in orthotropic medium can be taken as

$$T = \phi - a_1 \phi_{,xx} - a_3 \phi_{,zz} \quad (14)$$

where, T is the thermodynamic temperature above reference temperature, ϕ is the conductive temperature above reference temperature and a_1, a_3 are material parameters along x, z directions respectively.

Equation of three-phase-lag model in orthotropic medium is

$$\begin{aligned} & K_1 (1 + \tau_T \frac{\partial}{\partial t}) \dot{\phi}_{,xx} + K_3 (1 + \tau_T \frac{\partial}{\partial t}) \dot{\phi}_{,zz} + K_1^* (1 + \tau_v \frac{\partial}{\partial t}) \phi_{,xx} + K_3^* (1 + \tau_v \frac{\partial}{\partial t}) \phi_{,zz} \\ & = (1 + \tau_q \frac{\partial}{\partial t} + \frac{\tau_q^2}{2} \frac{\partial^2}{\partial t^2}) [\rho C_e \ddot{T} + T_0 (\beta_1 \ddot{u}_{,x} + \beta_3 \ddot{w}_{,z})] \end{aligned} \quad (15)$$

where, T_0 is the reference uniform temperature of the body, $K_i (i=1,3)$ are the components of the thermal conductivity, $K_i^* (i=1,3)$ are the material constant characteristic of the elastic solid, C_e is the specific heat at the constant strain, τ_q, τ_T and τ_v are the phase lags of heat flux, temperature gradient and thermal displacement gradient respectively.

3. Solution of the problem:

To solve a two dimensional thermoelastic problems, researchers are frequently adopted several

integral transform techniques. In the applications of integral transform techniques, the governing equations are to be converted into a set of ordinary differential equations. By solving those differential equations in the transformed domain and employing inverse integral transformation, the solutions of the problem can be obtained in the physical domain. However, these techniques entail a tiresome process. The crucial drawback is that, it leads the discretization and truncation errors in the process of numerical inversion, and consequently, the second sound of heat conduction could not be precisely demonstrated. To compensate the shortcomings of those above-mentioned methods, we have attempted to solve the problem of generalized thermoelasticity by employing normal mode analysis in the present context.

The normal mode analysis provides a more dulcet and analytical elucidation short of any presumed limitations on the field functions. It is pragmatic to a wide range of problems in various dissimilar branches. Presumptuous that all the field quantities are sufficiently smooth over the real line so that the normal mode analysis of the aforementioned field functions exists.

For the seismic wave propagation along x -axis, one may consider the solutions set of the Eqs. (12), (13) and (15) in the following manner:

$$\{u, w, \phi, T\}(x, z, t) = \{\bar{u}, \bar{w}, \bar{\phi}, \bar{T}\}(z) \exp[ik(x - ct)] \quad (16)$$

in which k is wave number and c represents the phase velocity.

Invoking Eq. (16), Eqs. (12) - (15) yield

$$c_{55} \frac{d^2 \bar{u}}{dz^2} - k^2 (c_{11} + \mu_e H_0^2 - \rho c^2) \bar{u} + ik (c_{13} + c_{55} + \mu_e H_0^2) \frac{d\bar{w}}{dz} - ik \beta_1 \bar{T} = 0 \quad (17)$$

$$(c_{33} + \mu_e H_0^2) \frac{d^2 \bar{w}}{dz^2} - k^2 (c_{55} - \rho c^2) \bar{w} + ik (c_{55} + c_{13} + \mu_e H_0^2) \frac{d\bar{u}}{dz} - \beta_3 \frac{d\bar{T}}{dz} = 0 \quad (18)$$

$$[ik^3 c \tau_1 K_1 - k^2 \tau_2 K_1^* + k^2 c^2 \rho C_e (1 + a_1 k^2)] \bar{\phi} + (\tau_2 K_3^* - ikc \tau_1 K_3 - a_3 k^2 c^2 \rho C_e) \frac{d^2 \bar{\phi}}{dz^2} + ik^3 c^2 \beta_1 T_0 \bar{u} + k^2 c^2 \beta_3 T_0 \frac{d\bar{w}}{dz} = 0 \quad (19)$$

$$\bar{T} = (1 + a_1 k^2 - a_3 \frac{d^2}{dz^2}) \bar{\phi} \quad (20)$$

where, $\tau_1 = \frac{1 - ikc \tau_T}{1 - ikc \tau_q - \frac{k^2 c^2 \tau_q^2}{2}}$, $\tau_2 = \frac{1 - ikc \tau_v}{1 - ikc \tau_q - \frac{k^2 c^2 \tau_q^2}{2}}$.

4. Formulation of vector matrix differential equation:

Equations (17)-(20) can be expressed in the following vector matrix differential equation:

$$\frac{dV}{dz} = AV \quad (21)$$

where, $V = [\bar{u}, \bar{w}, \bar{\phi}, \frac{d\bar{u}}{dz}, \frac{d\bar{w}}{dz}, \frac{d\bar{\phi}}{dz}]^T$

We assume that $\bar{u}, \bar{w}, \bar{\phi}, \frac{d\bar{u}}{dz}, \frac{d\bar{w}}{dz}, \frac{d\bar{\phi}}{dz} \rightarrow 0$ as $z \rightarrow \infty$

We obtain the matrix A as

$$A = \begin{bmatrix} 0 & I \\ P & Q \end{bmatrix}$$

$$\text{where, } 0 = \begin{bmatrix} 0 & 0 & 0 \\ 0 & 0 & 0 \\ 0 & 0 & 0 \end{bmatrix}, I = \begin{bmatrix} 1 & 0 & 0 \\ 0 & 1 & 0 \\ 0 & 0 & 1 \end{bmatrix}, P = \begin{bmatrix} A_{41} & 0 & A_{43} \\ 0 & A_{52} & 0 \\ A_{61} & 0 & A_{63} \end{bmatrix}, Q = \begin{bmatrix} 0 & A_{45} & 0 \\ A_{54} & 0 & A_{56} \\ 0 & A_{65} & 0 \end{bmatrix}$$

in which

$$A_{61} = \frac{-ik^3 c^2 \beta_1 T_0}{\tau_2 K_3^* - ikc\tau_1 K_3 - a_3 k^2 c^2 \rho C_e}, \quad A_{63} = \frac{k^2 \tau_2 K_1^* - ik^3 c\tau_1 K_1 - k^2 c^2 \rho C_e (1 + a_1 k^2)}{\tau_2 K_3^* - ikc\tau_1 K_3 - a_3 k^2 c^2 \rho C_e},$$

$$A_{65} = \frac{-k^2 c^2 \beta_3 T_0}{\tau_2 K_3^* - ikc\tau_1 K_3 - a_3 k^2 c^2 \rho C_e}, \quad A_{52} = \frac{k^2 (c_{55} - \rho c^2)}{c_{33} + \mu_e H_0^2 + a_3 \beta_3}, \quad A_{54} = -\frac{ik (c_{55} + c_{13} + \mu_e H_0^2) + a_3 \beta_3 A_{61}}{c_{33} + \mu_e H_0^2 + a_3 \beta_3},$$

$$A_{56} = \frac{\beta_3 (1 + a_1 k^2 - a_3 A_{63})}{c_{33} + \mu_e H_0^2 + a_3 \beta_3}, \quad A_{41} = \frac{k^2 (c_{11} + \mu_e H_0^2 - \rho c^2) - ik \beta_1 a_3 A_{61}}{c_{55}}, \quad A_{43} = \frac{ik \beta_1 (1 + a_1 k^2 - a_3 A_{63})}{c_{55}},$$

$$A_{45} = -\frac{ik \beta_1 a_3 A_{65} + ik (c_{13} + c_{55} + \mu_e H_0^2)}{c_{55}}.$$

5. Solution of vector matrix differential equation:

The characteristic equation of the aforementioned coefficient matrix A can be written in the following convenient form:

$$\lambda^6 - (A_{41} + A_{52} + A_{63} + A_{45}A_{54} + A_{56}A_{65})\lambda^4 + (A_{41}A_{63} + A_{52}A_{63} + A_{41}A_{52} - A_{43}A_{61} + A_{45}A_{54}A_{63} - A_{43}A_{54}A_{65} + A_{41}A_{56}A_{65} - A_{45}A_{56}A_{61})\lambda^2 + A_{43}A_{52}A_{61} - A_{41}A_{52}A_{63} = 0 \quad (22)$$

As the characteristic polynomial is an even degree polynomial, very often, the corresponding Eigen values of the matrix A are expressed in the following symmetrical form:

$$\lambda = \pm\lambda_1, \lambda = \pm\lambda_2, \lambda = \pm\lambda_3 \quad (23)$$

Therefore, the right Eigen vector $\vec{X} = [X_1, X_2, X_3, X_4, X_5, X_6]^T$ corresponding to Eigen value λ can be written as

$$\mathbf{X} = \begin{bmatrix} \lambda^2 (A_{45}A_{56} + A_{43}) - A_{43}A_{52} \\ \lambda^3 A_{56} + \lambda (A_{43}A_{54} - A_{41}A_{56}) \\ \lambda^4 - \lambda^2 (A_{41} + A_{52} + A_{45}A_{54}) + A_{41}A_{52} \\ \lambda [\lambda^2 (A_{45}A_{56} + A_{43}) - A_{43}A_{52}] \\ \lambda [\lambda^3 A_{56} + \lambda (A_{43}A_{54} - A_{41}A_{56})] \\ \lambda [\lambda^4 - \lambda^2 (A_{41} + A_{52} + A_{45}A_{54}) + A_{41}A_{52}] \end{bmatrix} \quad (24)$$

From Eq. (24), the Eigen vector \mathbf{X} corresponding to the Eigen value $\lambda = \lambda_i$ can easily be obtained.

We use the following notations

$$X_1 = [\mathbf{X}]_{\lambda=\lambda_1}, X_2 = [\mathbf{X}]_{\lambda=-\lambda_1}, X_3 = [\mathbf{X}]_{\lambda=\lambda_2}, X_4 = [\mathbf{X}]_{\lambda=-\lambda_2}, X_5 = [\mathbf{X}]_{\lambda=\lambda_3}, X_6 = [\mathbf{X}]_{\lambda=-\lambda_3} \quad (25)$$

The left Eigen vector $\vec{Y} = [Y_1, Y_2, Y_3, Y_4, Y_5, Y_6]$ corresponding to the Eigen value λ can be calculated as

$$\mathbf{Y} = \begin{bmatrix} \lambda^3 A_{61} + \lambda [A_{41}A_{54}A_{65} - A_{61}(A_{52} + A_{45}A_{54})] \\ A_{52} [\lambda^2 A_{65} + A_{45}A_{61} - A_{41}A_{65}] \\ \lambda^5 - \lambda^3 (A_{41} + A_{52} + A_{45}A_{54} + A_{56}A_{65}) + \lambda [A_{41}(A_{52} + A_{56}A_{65}) - A_{45}A_{56}A_{61}] \\ \lambda^2 (A_{61} + A_{54}A_{65}) - A_{52}A_{61} \\ \lambda^3 A_{65} + \lambda (A_{45}A_{61} - A_{41}A_{65}) \\ \lambda^4 - \lambda^2 (A_{41} + A_{52} + A_{45}A_{54} + A_{56}A_{65}) + A_{41}A_{52} \end{bmatrix}$$

We denote these results by

$$Y_1 = [\mathbf{Y}]_{\lambda=\lambda_1}, Y_2 = [\mathbf{Y}]_{\lambda=-\lambda_1}, Y_3 = [\mathbf{Y}]_{\lambda=\lambda_2}, Y_4 = [\mathbf{Y}]_{\lambda=-\lambda_2}, Y_5 = [\mathbf{Y}]_{\lambda=\lambda_3}, Y_6 = [\mathbf{Y}]_{\lambda=-\lambda_3} \quad (26)$$

Assuming the regularity condition at infinity (in other words: $\bar{u}, \bar{w}, \bar{\phi}, \frac{d\bar{u}}{dz}, \frac{d\bar{w}}{dz}, \frac{d\bar{\phi}}{dz} \rightarrow 0$ as $z \rightarrow \infty$), the solution of Eq. (21) can be expressed as follows:

$$\mathbf{V} = A_1 X_2 \exp(-\lambda_1 z) + A_2 X_4 \exp(-\lambda_2 z) + A_3 X_6 \exp(-\lambda_3 z) \quad (27)$$

Thus the required field functions can be expressed as follows,

$$\bar{u} = \sum_{i=1}^3 A_i [\lambda_i^2 (A_{45}A_{56} + A_{43}) - A_{43}A_{52}] \exp(-\lambda_i z) \quad (28)$$

$$\bar{w} = \sum_{i=1}^3 A_i [-\lambda_i^3 A_{56} - \lambda_i (A_{43} A_{54} - A_{41} A_{56})] \exp(-\lambda_i z) \quad (29)$$

$$\bar{\phi} = \sum_{i=1}^3 A_i [\lambda_i^4 - \lambda_i^2 (A_{41} + A_{52} + A_{45} A_{54}) + A_{41} A_{52}] \exp(-\lambda_i z) \quad (30)$$

and

$$T = \sum_{i=1}^3 (1 + a_1 k^2 - a_3 \lambda_i^2) d_i A_i \exp[-\lambda_i z + ik(x - ct)] \quad (31)$$

where, $d_i = [\lambda_i^4 - \lambda_i^2 (A_{41} + A_{52} + A_{45} A_{54}) + A_{41} A_{52}]$

The stress components can be obtained as

$$\begin{aligned} \tau_{xx} = \sum_{i=1}^3 \{ & ikc_{11} [\lambda_i^2 (A_{45} A_{56} + A_{43}) - A_{43} A_{52}] + c_{13} \lambda_i [\lambda_i^3 A_{56} + \lambda_i (A_{43} A_{54} - A_{41} A_{56})] \\ & - \beta_1 (1 + a_1 k^2 - a_3 \lambda_i^2) d_i \} A_i \exp[-\lambda_i z + ik(x - ct)] \end{aligned} \quad (32)$$

$$\begin{aligned} \tau_{zz} = \sum_{i=1}^3 \{ & c_{13} ik [\lambda_i^2 (A_{45} A_{56} + A_{43}) - A_{43} A_{52}] + c_{33} \lambda_i [\lambda_i^3 A_{56} + \lambda_i (A_{43} A_{54} - A_{41} A_{56})] \\ & - \beta_3 (1 + a_1 k^2 - a_3 \lambda_i^2) d_i \} A_i \exp[-\lambda_i z + ik(x - ct)] \end{aligned} \quad (33)$$

$$\begin{aligned} \tau_{xz} = \sum_{i=1}^3 \{ & -c_{44} \lambda_i [\lambda_i^2 (A_{45} A_{56} + A_{43}) - A_{43} A_{52}] - ikc_{44} [\lambda_i^3 A_{56} + \lambda_i (A_{43} A_{54} \\ & - A_{41} A_{56})] \} A_i \exp[-\lambda_i z + ik(x - ct)] \end{aligned} \quad (34)$$

6. Boundary conditions:

The thermo-mechanical boundary conditions on the stress free surface $z=0$ are as follows:

(a) Vanishing of the normal stress component

$$\tau_{zz} = 0 \quad (35)$$

(b) Vanishing of the tangential stress component

$$\tau_{xz} = 0 \quad (36)$$

(c) Thermal conditions

$$q_z + mT = 0 \quad (37)$$

where, $m \rightarrow 0$ corresponds to the thermally insulated surface and $m \rightarrow \infty$ corresponds to the isothermal surface.

7. Derivation of frequency equation of Rayleigh wave in magneto-orthotropic medium:

The normal component of heat flux vector q_z is associated to the temperature gradient $\phi_{,z}$ by the subsequent relation:

$$q_z = \left[\frac{-K_3 D'(1 + \tau_T D') - K_3^*(1 + \tau_V D')}{D'(1 + \tau_q D' + \frac{\tau_q^2}{2} D'^2)} \right] \phi_{,z}$$

where, $D' \equiv \frac{\partial}{\partial t}$.

Invoking the considered boundary conditions (35) – (37), one can obtain a set of three following homogeneous equations:

$$\sum_{i=1}^3 g_i A_i = 0 \quad (38)$$

$$\sum_{i=1}^3 h_i A_i = 0 \quad (39)$$

$$\sum_{i=1}^3 d_i (m - \alpha \lambda_i) = 0 \quad (40)$$

where, $\alpha = (K_3^* \tau_4 - ikc K_3 \tau_3) \tau_6$ (neglecting terms of order higher than τ_q^2) and

$$\tau_6 = \frac{(1 + ikc \tau_q - \frac{k^2 c^2}{2} \tau_q^2)}{ikc},$$

$$g_i = ikc_{13} [\lambda_i^2 (A_{45} A_{56} + A_{43}) - A_{43} A_{52}] + c_{33} \lambda_i [\lambda_i^3 A_{56} + \lambda_i (A_{43} A_{54} - A_{41} A_{56})] - \beta_3 (1 + a_1 k^2 - a_3 \lambda_i^2) d_i,$$

$$h_i = -c_{55} \lambda_i [\lambda_i^2 (A_{45} A_{56} + A_{43}) - A_{43} A_{52}] - c_{55} ik [\lambda_i^3 A_{56} + \lambda_i (A_{43} A_{54} - A_{41} A_{56})]$$

The non-trivial solutions of equations (38)-(40) exists if

$$g_1 [h_2 d_3 (m - \alpha \lambda_3) - h_3 d_2 (m - \alpha \lambda_2)] + g_2 [h_1 d_3 (m - \alpha \lambda_3) - h_3 d_1 (m - \alpha \lambda_1)] \\ + g_3 [h_1 d_2 (m - \alpha \lambda_2) - h_2 d_1 (m - \alpha \lambda_1)] = 0 \quad (41)$$

This is the frequency equation of Rayleigh surface wave in orthotropic magneto-thermoelastic half-space with two temperature theory with three-phase-lags model.

8. Particular cases:

Here we have illustrated the Rayleigh wave frequency equations for two-different thermoelastic boundary conditions:

(1) Thermally insulated surface:

For thermally insulated surface, the boundary condition is $q_z = 0$ on $z = 0$. In this case,

Eq. (41) reduces to

$$g_1(h_2d_3\lambda_3 - h_3d_2\lambda_2) + g_2(h_1d_3\lambda_3 - h_3d_1\lambda_1) + g_3(h_1d_2\lambda_2 - h_2d_1\lambda_1) = 0 \quad (42)$$

(2) Isothermal surface:

For isothermal surface, the boundary condition is $T = 0$ on $z = 0$. In this case, Eq. (36) reduces to

$$g_1(h_2d_3 - h_3d_2) + g_2(h_1d_3 - h_3d_1) + g_3(h_1d_2 - h_2d_1) = 0 \quad (43)$$

(3) If we take $H_0 = 0$ then the above problem will reduce to the problem of without magnetic effect.

(4) If we take $a_1 = a_3 = 0$ then, the problem will reduce to the problem for without two-temperature theory.

9. Discussion of secular equation:

From Eq. (41), bearing in mind the various specific values of the parameters, one can obtain the following dissimilar results in orthotropic media:

(a) If we substitute $\tau_v = \tau_q = \tau_T = 0$ and $K_i^* (i = 1, 3) = 0$ in the Eq. (41), consequently the secular Eq. (41) reduces to the frequency equation of Rayleigh wave for classical coupled thermoelasticity (CCT) theory [17].

(b) At $\tau_v = \tau_T = 0, \tau_q^2 = 0, K_i^* = 0 (i = 1, 3), \tau_q \neq 0$ in Eq. (41), the revised equation gives the frequency equation corresponding to Lord-Shulman model .

(c) The frequency equation reduces in the case of GN model type-III when we put $\tau_v = \tau_q = \tau_T = 0$ in Eq. (41).

(d) If we consider $K_i^* = 0 (i = 1, 3)$ then Eq. (41) yields the frequency equation for dual-phase-lags theory of thermoelasticity developed by Singh et al. [17].

10. Solution of the secular equation:

In the propagation of Rayleigh wave, the corresponding wave number (k) and the phase velocity (c) are mostly complex quantities.

For convenient, we consider,

$$c^{-1} = V^{-1} + i\omega^{-1}Q \quad (44)$$

Thus, the wave number of the wave propagation can be expressed as follows,

$$k = R + iQ \text{ where } R = \frac{\omega}{V} \text{ in which } V \text{ and } Q \text{ are real.}$$

The exponent in the surface wave solution (16) becomes $iR(x - Vt) - Qx$. This shows that V is the propagation speed, Q is the attenuation coefficient and ω is the angular frequency of the waves.

11. Path attenuation:

The signal path loss is fundamentally the reduction in power density of an electromagnetic wave as it propagates through the medium in which it is travelling. The ratio of energy dissipated (ΔE) to the elastic energy stored (E) in a specific cycle, during the wave propagation, is termed as path attenuation or specific loss. To define the internal friction for a material, specific loss is the commonest factor (for details see Ref. Puri and Cowin [22]). For the seismic wave propagation with comparatively small amplitudes, Kolsky [23] has shown that the path attenuation factor $\frac{\Delta W}{W}$ equals to 4π times the absolute value of the ratio of imaginary part of k to the real part of k , that is,

$$SL = \frac{\Delta W}{W} = 4\pi \left| \frac{\text{Im}(k)}{\text{Re}(k)} \right| = 4\pi \left| \frac{VQ}{\omega} \right| \quad (45)$$

12. Special cases:

We know, transversely isotropic medium is a special case of orthotropic media, consequently, $c_{11} = c_{33}$, $2c_{55} = c_{11} - c_{13}$ and $\beta_1 = \beta_3$. Further considering $\beta_1 = \beta_3 = \beta$, $H_0 = 0$ we discuss the following special cases:

Case-(1): If we take $\lambda_1 = \sqrt{k^2 - \xi_1^2}$, $\lambda_2 = \sqrt{k^2 - \xi_2^2}$, $\lambda_3 = \sqrt{k^2 - \zeta^2}$, then frequency, the equation for transversely isotropic thermally insulated half space under three-phase-lag model with two temperatures can be obtained as

$$\left[2 - \frac{2\rho c^2}{(c_{11} - c_{13})} \right]^2 [\gamma_1^2 + \gamma_1\gamma_2 + \gamma_2^2 - 1 + \frac{\rho c^2}{c_{11}}] - 4\gamma_1\gamma_2\gamma_3(\gamma_1 + \gamma_2) = 0 \quad (46)$$

The frequency equation in transversely isotropic isothermal half space under three-phase-lag model with two temperatures is obtained as

$$\left[2 - \frac{2\rho c^2}{(c_{11} - c_{13})} \right]^2 (\gamma_1 + \gamma_2) - 4\gamma_3 \left[\gamma_1\gamma_2 + 1 - \frac{\rho k^2 c^2}{c_{11}} \right] = 0 \quad (47)$$

where, $\gamma_1^2 = 1 - \frac{\xi_1^2}{k^2}$, $\gamma_2^2 = 1 - \frac{\xi_2^2}{k^2}$, $\gamma_3^2 = 1 - \frac{\zeta^2}{k^2}$, $\zeta^2 = \frac{2\rho k^2 c^2}{(c_{11} - c_{13})}$, ξ_1^2 and ξ_2^2 are the

roots of the biquadratic equation

$$\xi^4 - \left[k^2 + \frac{\{ik^3cK_1\tau_1 - k^2\tau_2K_1^* + \rho C_e k^2 c^2(1+a_1k^2)\}c_{11} + T_0\beta^2 k^2 c^2}{(K_3^*\tau_2 - ikc\tau_1K_3 - a_3\rho C_e k^2 c^2)c_{11}} + \frac{\rho k^2 c^2}{c_{11}} \right] \xi^2 + \left[\frac{ik^3cK_1\tau_1 - k^2\tau_2K_1^* + (1+a_1k^2)\rho C_e k^2 c^2}{(K_3^*\tau_2 - ikc\tau_1K_3 - a_3\rho C_e k^2 c^2)} + k^2 \right] \frac{\rho k^2 c^2}{c_{11}} = 0 \quad (48)$$

One can obtain the frequency equation for transversely isotropic half space with three-phase-lag model discarding the two temperatures by taking $a_1 = a_3 = 0$.

Case-(2): In transversely isotropic half-space, the frequency equation in classical coupled thermoelasticity discarding two-temperature model is obtained by taking

$$a_1 = a_3 = 0, \quad K_i^* (i = 1, 3) = 0, \quad \tau_q = \tau_T = \tau_v = 0$$

$$\left[2 - \frac{2\rho c^2}{(c_{11} - c_{13})} \right]^2 [\gamma_1^2 + \gamma_1\gamma_2 + \gamma_2^2 - 1 + \frac{\rho c^2}{c_{11}}] - 4\gamma_1\gamma_2\gamma_3(\gamma_1 + \gamma_2) - \frac{m}{k} \left[\left\{ 2 - \frac{2\rho c^2}{(c_{11} - c_{13})} \right\}^2 (\gamma_1 + \gamma_2) - 4\gamma_3(\gamma_1\gamma_2 + 1 - \frac{\rho k^2 c^2}{c_{11}}) \right] = 0 \quad (49)$$

where, $m \rightarrow 0$ corresponds to the thermally insulated surface and $m \rightarrow \infty$ corresponds to the isothermal surface.

Here $\gamma_1^2 = 1 - \frac{\xi_1^2}{k^2}$, $\gamma_2^2 = 1 - \frac{\xi_2^2}{k^2}$, $\gamma_3^2 = 1 - \frac{\zeta^2}{k^2}$, $\zeta^2 = \frac{2\rho k^2 c^2}{(c_{11} - c_{13})}$, ξ_1^2 and ξ_2^2 are the roots

of the biquadratic equation

$$\xi^4 - \left[\left(k^2 - \frac{K_1 k^2}{K_3} \right) + \frac{\rho k^2 c^2}{c_{11}} + (1 + \kappa) \frac{ikc\rho C_e}{K_3} \right] \xi^2 + \left[\frac{\rho k^2 c^2}{c_{11}} - \frac{K_1 \rho k^2 c^2}{K_3 c_{11}} \right] k^2 + \frac{ik^3 c^3 \rho C_e}{c_{11} K_3} = 0 \quad (50)$$

in which, $\kappa = \frac{T_0 \beta^2}{\rho C_e c_{11}}$.

Now if we consider $c_{11} = \lambda + 2\mu$, $c_{13} = \lambda$, $K_1 = K_3 = K$, the frequency equation of the Rayleigh waves for isotropic half space can be obtained in classical coupled thermoelasticity without two temperatures model as follows:

$$\left(2 - \frac{c^2}{c_2^2} \right)^2 [\gamma_1^2 + \gamma_1\gamma_2 + \gamma_2^2 - 1 + \frac{c^2}{c_1^2}] - 4\gamma_1\gamma_2\gamma_3(\gamma_1 + \gamma_2) - \frac{m}{k} \left[\left(2 - \frac{c^2}{c_2^2} \right)^2 (\gamma_1 + \gamma_2) - 4\gamma_3(\gamma_1\gamma_2 + 1 - \frac{k^2 c^2}{c_1^2}) \right] = 0 \quad (51)$$

Equation (51) is similar as the result obtained in Nowinski [24],

where, $\gamma_1^2 = 1 - \frac{\xi_1^2}{k^2}$, $\gamma_2^2 = 1 - \frac{\xi_2^2}{k^2}$, $\gamma_3^2 = 1 - \frac{\zeta^2}{k^2}$, $\zeta^2 = \frac{k^2 c^2}{c_2^2}$, ξ_1^2 and ξ_2^2 are the roots of

the biquadratic equation

$$\xi^4 - \left[\frac{k^2 c^2}{c_1^2} + (1 + \kappa) \frac{ikc \rho C_e}{K} \right] \xi^2 + \frac{ik^3 c^3 \rho C_e}{K c_1^2} = 0 \quad (52)$$

in which $\kappa = \frac{T_0 \beta^2}{\rho^2 c_1^2 C_e}$ and $c_1^2 = \frac{\lambda + 2\mu}{\rho}$, $c_2^2 = \frac{\mu}{\rho}$.

Case-(3): Discarding thermal parameters i.e. when there is no coupling between temperature and strain field, the frequency equation of orthotropic elastic half space yields

$$2(c_{33} - c_{13}) \left[\frac{(\rho c^2 - c_{11})(\rho c^2 - c_{55})}{c_{13} + 2c_{55} \quad c_{33} - c_{55} - c_{13}} \right]^{\frac{1}{2}} = \frac{(\rho c^2 - c_{55}) - 1}{c_{33} - c_{55} - c_{13}} \left[\frac{c_{33}(\rho c^2 - c_{11})}{c_{13} + 2c_{55}} + c_{13} \right] \quad (53)$$

This agrees with the result of Abd-Alla et al. [16].

Putting $c_{11} = c_{33} = \lambda + 2\mu$, $c_{13} = \lambda$, $c_{55} = \mu$ in Eq. (53), frequency equation of Rayleigh waves in isotropic elastic half space is obtained as

$$\left(2 - \frac{c^2}{c_2^2} \right)^2 = 4 \left(1 - \frac{c^2}{c_1^2} \right)^{\frac{1}{2}} \left(1 - \frac{c^2}{c_2^2} \right)^{\frac{1}{2}} \quad (54)$$

where, $c_1^2 = \frac{\lambda + 2\mu}{\rho}$, $c_2^2 = \frac{\mu}{\rho}$.

13. Expressions of the field functions:

Here, we shall derive the expressions for displacements and the change in temperatures on the surface ($z = 0$) for isothermal half space during Rayleigh wave propagation.

For the isothermal surface, we obtain on $z = 0$

$$u = UA_1 \exp(-Qx + ip) \quad (55)$$

$$w = WA_1 \exp(-Qx + ip) \quad (56)$$

$$\phi = \chi A_1 \exp(-Qx + ip) \quad (57)$$

where

$$m_i = \lambda_i^2 (A_{45} A_{56} + A_{43}) - A_{43} A_{52}, \quad n_i = -\lambda_i^3 A_{56} - \lambda_i (A_{43} A_{54} - A_{41} A_{56}),$$

$$U = m_1 + \frac{(g_3 d_1 - g_1 d_3)}{(g_2 d_3 - g_3 d_2)} m_2 + \frac{[d_1 (g_3 d_2 - g_2 d_3) + d_2 (g_1 d_3 - g_3 d_1)]}{d_3 (g_2 d_3 - g_3 d_2)} m_3,$$

$$W = n_1 + \frac{(g_3 d_1 - g_1 d_3)}{(g_2 d_3 - g_3 d_2)} n_2 + \frac{[d_1(g_3 d_2 - g_2 d_3) + d_2(g_1 d_3 - g_3 d_1)]}{d_3(g_2 d_3 - g_3 d_2)} n_3,$$

$$\chi = d_1 + \frac{(g_3 d_1 - g_1 d_3)}{(g_2 d_3 - g_3 d_2)} d_2 + \frac{[d_1(g_3 d_2 - g_2 d_3) + d_2(g_1 d_3 - g_3 d_1)]}{d_3(g_2 d_3 - g_3 d_2)} d_3, \quad p = R(x - Vt).$$

14. Path of surface particles:

Path traced out by the surface particles during Rayleigh wave propagation:

In this section, we investigate the path followed by the surface particles in an orthotropic thermoelastic half-space during the transmission of the Rayleigh wave influenced by magnetic field. It is revealed that due to thermal coupling, collaboration with magnetic field and linear approximation theory, the amplitude and the devasting factor that is slowness of the Rayleigh wave are became complex quantities (i.e. hypothetical). This is indicating the damping nature of the wave and phase differences observed in the displacement quantities.

Therefore on the surface $z = 0$, the Eqs. (55) and (56) on retaining real parts lead to

$$u = |U| H \cos(p + \alpha_1), \quad w = |W| H \cos(p + \alpha_2) \quad (58)$$

where, $H = A_1 \exp(-Qx)$, $(\alpha_1, \alpha_2) = (\arg(U), \arg(W))$

On eliminating p from above equations, we get

$$\left(\frac{u}{|U|}\right)^2 - 2\left(\frac{u}{|U|}\right)\left(\frac{w}{|W|}\right)\cos(\alpha_1 - \alpha_2) + \left(\frac{w}{|W|}\right)^2 = H^2 \sin^2(\alpha_1 - \alpha_2) \quad (59)$$

$$\text{Here } \frac{4 \cos^2(\alpha_1 - \alpha_2)}{U^2 W^2} - \frac{4}{U^2 W^2} = -\frac{4}{U^2 W^2} \sin^2(\alpha_1 - \alpha_2) < 0$$

Therefore, Eq. (59) represents an ellipse in the $u-w$ plane.

The specifications of the traced out elliptical path i.e., the length of major axis ($2X$), length of minor axis ($2Y$) and the eccentricities (e) of the elliptical paths are given by

$$X^2, Y^2 = \frac{H^2}{2} \left[|U|^2 + |W|^2 \pm \left[(|U|^2 - |W|^2)^2 + 4|U|^2 |W|^2 \cos^2(\alpha_1 - \alpha_2) \right]^{\frac{1}{2}} \right]$$

$$e^2 = \frac{2\{(|U|^2 - |W|^2)^2 + 4|U|^2 |W|^2 \cos^2(\alpha_1 - \alpha_2)\}^{\frac{1}{2}}}{|U|^2 + |W|^2 + (|U|^2 - |W|^2)^2 + 4|U|^2 |W|^2 \cos^2(\alpha_1 - \alpha_2)^{\frac{1}{2}}} \quad (60)$$

Thus, in the presence of the applied magnetic field, when a Rayleigh wave propagates into the

thermoelastic orthotropic medium, surface particles are moving in an elliptical manner and the lengths of its major as well as minor axes are depend on the term H , therefore, they increase or decrease exponentially. The decay of the amplitudes of the path of the surface particles depends on the attenuation coefficient as well as the propagation speed of the wave. Moreover, in presence of magnetic field, for a particular value of the propagation speed, the eccentricity of the elliptical path is decreased. Thus, application of magnetic field can change the shape of the surface particles' movement during Rayleigh wave propagation.

Let δ is the inclination of the major axis to the wave normal then

$$\tan(2\delta) = \frac{2\{(\tan^2 \theta - 1)|U||W| \cos(\alpha_1 - \alpha_2) - (|U|^2 - |W|^2) \tan \theta\}}{(\tan^2 \theta - 1)(|U|^2 - |W|^2) + 4|U||W| \cos(\alpha_1 - \alpha_2) \tan \theta}$$

where, θ is the angle of incidence of the wave.

It is notable also that long wavelength components of the Rayleigh surface wave penetrate more deeply in the surface layer than the shorter wavelength and thus see higher velocities. Longer wavelength means a lower frequency as,

Frequency = Seismic velocity \times Wavelength. In the thermoelastic medium, Rayleigh wave occurs as a set of dispersed wave trains with low velocity, low frequency, and high amplitudes. Consequently, an increment in the values of thermal time delay helped the ground roll (Rayleigh wave) to enhance its penetration power in the medium.

15. Numerical results and discussion:

For numerical computations, we have considered the following data values of the relevant parameters for cobalt type material as follows:

$$c_{11} = 3.071 \times 10^{11} Nm^{-2}, c_{13} = 1.027 \times 10^{11} Nm^{-2}, c_{33} = 3.581 \times 10^{11} Nm^{-2}, c_{55} = 1.510 \times 10^{11} Nm^{-2},$$

$$\beta_1 = 7.04 \times 10^6 Nm^{-2} deg^{-1}, \beta_3 = 6.90 \times 10^6 Nm^{-2} deg^{-1}, K_1 = 69 Wm^{-1} deg^{-1},$$

$$K_3 = 69 Wm^{-1} deg^{-1},$$

$$K_1^* = 13.1 Wm^{-1} deg^{-1} s^{-1}, \quad K_3^* = 15.4 Wm^{-1} deg^{-1} s^{-1}, \quad \rho = 7.14 \times 10^3 Kgm^{-3},$$

$$C_e = 381.4 JKg^{-1} deg^{-1}, \quad T_0 = 296k, \quad H_0 = 10 Am^{-1}, \quad \mu_e = 1.2 Hm^{-1}, \quad a_1 = 0.02, \quad a_3 = 0.04.$$

Phase velocity, attenuation coefficient and specific loss factor for different values of the thermal time delays in the context of three-phase-lag (TPL), dual-phase-lag (DPL),

Green-Naghdi (GN) type-III and Lord-Shulman (LS) models of generalized thermo-elasticity have been computed for various values of frequency for stress free thermally insulated as well as isothermal boundaries.

In general, we know $c = \frac{\omega}{k}$, where $k = R + iQ$, $R = \frac{\omega}{V}$ in which V and Q are real.

Therefore, for a fixed value of ω , Eqs. (42) and (43) reduce to a function of k say $G(k)$. To obtain the solution of $G(k) = 0$ we apply a fixed point iteration method up to a desired level of accuracy. The computer simulated results are presented graphically for thermally insulated and isothermal boundary conditions as a function of frequency. Figs. 1-2 display a comparison study of phase velocity and attenuation coefficients in presence of a magnetic field as well as for several generalized thermoelastic models. A separate set of velocity profiles is observed for thermally insulated and isothermal boundary conditions as a function of wave number. It is observed, from Fig. 1 that in isothermal boundary condition velocity of Rayleigh wave decreases with increasing values of wave number. As energy dissipated more in isothermal boundaries, it is obvious that from Figs. 1-2 that the Rayleigh wave velocities are decreased with wave number in isothermal boundary condition and a reverse nature is shown in the insulated boundary condition. It is also observed that Rayleigh wave velocity starts from zero initially and increases with an increasing value of wave number as well as a magnetic field (H_0) under the consideration of the surface is thermally insulated. In contrary to the results in the insulated surface condition, a vice versa nature of the velocity profile is observed in the isothermal boundary condition. As evident from the phase-velocity spectrum (i.e., the considered dispersion curve) reported in Fig. 1, in this present study, the use of two distinct temperatures (not very common in surface-wave acquisition) would produce velocity spectra easily interpretable. Also, it is shown that the attenuation coefficient decreases with the increasing value of the wave number and the intensity of the applied magnetic field. From Fig. 2, it is seen that the phase velocity of Rayleigh wave and attenuation coefficients are significantly lesser in GN as well as TPL models of generalized thermoelasticity in comparison with the LS model with respect to wave number.

Figs. 3, 4 represent variations of phase velocities with frequency (ω) when a Rayleigh surface wave propagates through a thermoelastic and orthotropic half-space. Fig. 3 gives a comparison study in TPL model thermoelasticity for different values of τ_q with respect to frequency. It has been observed that the phase-lags due to heat fluxes into the medium has no such significant impact on phase velocity. Fig. 4 gives a comparison among phase velocities for different thermoelastic models. It is seen that the Rayleigh wave velocities are almost identical in the context of various generalized thermoelasticity theories.

Figs. 5, 6 represent the comparison of attenuation coefficients in the context of the TPL model with respect to wave number (k) and frequency (ω) respectively. It has been observed that the thermal time delay due to heat fluxes has a significant impact on attenuation coefficient of Rayleigh wave. Increase amount of thermal time delay (τ_q) can influence to hike the attenuation of Rayleigh surface wave.

Figs. 7, 8 represent the comparisons of attenuation coefficients for different thermoelastic models. It has been detected from Fig. 7 that, in the context of LS as well as GN models Rayleigh wave realizes more attenuation in an orthotropic medium. Moreover, in comparison with phase-lags models LS and GN theories felt more attenuation, among them LS model gives maximum attenuation. Whereas, the TPL and DPL models are contributing almost identical attenuation in the Rayleigh wave propagation. Hence, the thermal time delay due to thermal displacement gradient (τ_v) has no such noteworthy influence on Rayleigh wave attenuation. Fig. 9 represents the variation of attenuation coefficient for different values of thermal time delay τ_v . As we have mentioned earlier, it is seen that the attenuation profiles are identical with the variation of the thermal time delay due to thermal displacement gradient (τ_v). Fig. 10 gives the comparison of attenuation of Rayleigh wave propagation for isothermal as well as insulated boundaries. It has been clearly observed that in isothermal surface condition, attenuations are much lesser than that of insulated surfaces in TPL model.

Figs. 11, 12 represent variations of specific losses for different values of phase lags due to heat fluxes and for various thermoelastic models respectively. It has been observed that an increase amount of thermal time delay due to heat fluxes helped to raise the quantity

of specific losses in Rayleigh wave propagation. Moreover, in the context of GN model Rayleigh wave realize larger amount of specific losses than TPL and LS models.

16. Conclusion:

The propagation of Rayleigh surface wave propagation in orthotropic thermoelastic solids under three-phase-lag model is investigated in the context of two-temperature generalized thermoelasticity model. Frequency equations of Rayleigh waves for insulated and isothermal boundary conditions are derived. Developed result has been validated by comparing it with the other existing results reported in the literature. Path of surface particles during Rayleigh wave propagation is found elliptical.

After analytical developments and numerical observations, we can conclude the following phenomena:

1. Rayleigh wave velocity is increased slowly with the increasing wave number for the insulated boundary condition, but a reversible nature is shown in isothermal condition.
2. The presence of magnetic field has a significant impact on the propagation of Rayleigh wave. The intensity of magnetic field facilitated to increase the attenuation in the wave.
3. The Rayleigh wave maintained a very close profile picture for several generalized thermoelastic models.
4. In Rayleigh surface wave propagation in the framework of generalized theory of thermoelasticity, the attenuation coefficients are much higher in the Lord-Shulman thermoelastic model than that of other thermoelastic models including phase-lags.
5. Increasing values of in the thermal time delays can help the ground roll (Rayleigh wave) to enhance its penetration power into the surface-layer.
6. Influence of phase-lag due to heat flux vector is more dominating in comparison with other phase lags.

In this article we have attempted a theoretical development on Rayleigh wave propagation and its several aspects. Though it is a theoretical advance, but it can provide useful information for experimental researchers working in the field of geophysics, earthquake engineering and seismologist working in the field of mining tremors and drilling into the crust of the earth.

Acknowledgments The authors are thankful to the reviewers for their valuable comments and suggestions which have helped to improve the quality of the paper.

References:

- [1] M. Biot, Thermoelasticity and irreversible thermodynamics. *J. Appl. Phys.*, vol. 27, pp. 240-253, 1956.
- [2] C. Cattaneo, Sur une forme de l'équation de la chaleur éliminant le paradoxe d'une propagation instantanée. *Comptes. Rendus. Acad. Sci.*, vol. 2(47), pp. 431-433, 1958.
- [3] H.W. Lord and Y. Shulman, A generalized dynamical theory of thermoelasticity, *J. Mech. Phys. Solid*, vol. 15, pp. 299-309, 1967.
- [4] A.E. Green and K.A. Lindsay, Thermoelasticity, *J. Elast.*, vol. 2, pp. 1-7, 1972.
- [5] A.E. Green and P.M. Naghdi, A unified procedure for construction of theories of deformable media. I. Classical continuum physics, II. Generalized continua, III. Mixture of interacting continua, *Proc. Roy. Soc. London A.*, vol. 448, pp. 335-388, 1995.
- [6] S.K. Roychoudhuri, On a thermoelastic three phase lag model, *J. Thermal Stress.*, vol. 30, pp. 231-238, 2007.
- [7] M.E. Gurtin and W.O. Williams, On the clausius-Duhem inequality, *Zeitschrift für Angewandte Mathematik und Physik ZAMP*, vol. 17(5), pp. 626-633, 1966.
- [8] M.E. Gurtin and W.O. Williams, An axiomatic foundation for continuum thermodynamics, *Arch. Rat. Mech. Anal.*, vol. 26(2), pp. 83-117, 1967.
- [9] P.J. Chen and M.E. Gurtin, On a theory of heat conduction involving two temperatures, *Zeitschrift für Angewandte Mathematik und Physik ZAMP*, vol. 19(4), pp. 614-627, 1968.
- [10] S. Shaw and B. Mukhopadhyay, Moving heat source response in micropolar half-space with two-temperature theory, *Continuum. Mech. Thermodyn.*, vol. 25, pp. 523-535, 2013.
- [11] C.P. Yu and S. Tang, Magneto-elastic waves in initially stressed conductors, *Zeitschrift für Angewandte Mathematik und Physik (ZAMP)*, vol. 17, pp. 766-775, 1966.
- [12] S.N. De and P.R. Sengupta, Surface waves in magneto-elastic initially stressed conducting media, *Pure and Applied Geophysics*, vol. 88, pp. 44-52, 1971.
- [13] S.N. De and P.R. Sengupta, Magneto-elastic waves and disturbances in initially stressed conducting media, *Pure and Applied Geophysics*, vol. 93, pp. 41-54, 1972.
- [14] A.M. Abd-Alla, S.M. Abo-Dahab and F.S. Bayones, Propagation of Rayleigh waves in magneto-thermoelastic half-space of a homogeneous orthotropic material under the effect of rotation, initial stress and gravity field, *J. Vib. Cont.*, vol. 19(9), pp. 1395-1420, 2013.

- [15] S. Shaw and B. Mukhopadhyay, Electromagnetic effects on Rayleigh surface wave propagation in a homogeneous isotropic thermo-microstretch elastic half-space, *J. Eng. Phys. Thermophys.*, vol. 85(1), pp. 229-238, 2012.
- [16] A.M. Abd-Alla, S.M. Abo-Dahab and H.A.H. Hammad, Propagation of Rayleigh waves in generalized magneto-thermoelastic orthotropic material under initial stress and gravity field, *Appl. Math. Model.*, vol. 35, pp. 2981-3000, 2011.
- [17] B. Singh, S. Kumari and J. Singh, Propagation of the Rayleigh wave in an initially stressed transversely isotropic dual phase lag magneto-thermoelastic half space, *J. Eng. Phys. Thermophys.*, vol. 87(6), pp. 1539-1547, 2014.
- [18] H. Parkus, *Magneto-Thermo-Elasticity*, Springer, New York, 1972.
- [19] J.L. Nowinski, *Theory of Thermoelasticity with Applications*, Sijthoff & Noordhoff International Publishers, The Netherlands, 1978.
- [20] K.F. Graff, *Wave Motion in Elastic Solids*, Dover Publications Inc., New York, 1991.
- [21] S. Biswas and B. Mukhopadhyay, Eigenfunction expansion method to characterize Rayleigh wave propagation in orthotropic medium with phase lags, *Waves in Random and Complex Media*. DOI: 10.1080/17455030.2018.1470355
- [22] P. Puri and S.C. Cowin, Plane waves in linear elastic materials with voids, *J. Elast.*, vol. 15, pp. 167-183, 1985.
- [23] H. Kolsky, *Stress waves in solids*, Dover press, New York, 1963.
- [24] J.L. Nowinski, *Theory of thermoelasticity with applications*, *Mech. Surf. Struct.*, 1978.

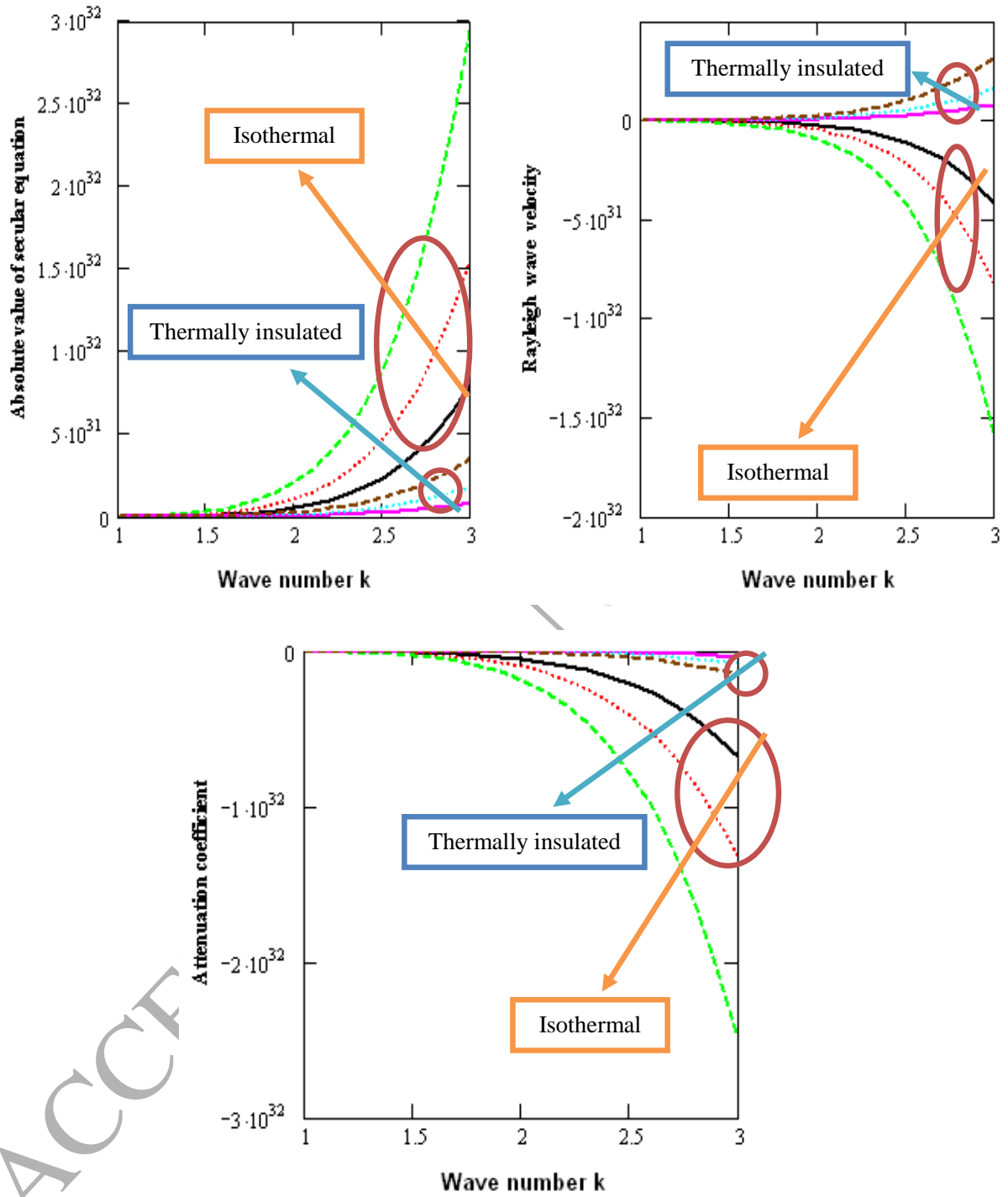


Fig. 1: Comparison between thermally insulated and isothermal surfaces in presence of magnetic field

(— $H_0 = 10$, $H_0 = 11$, --- $H_0 = 12$) with respect to wave number.

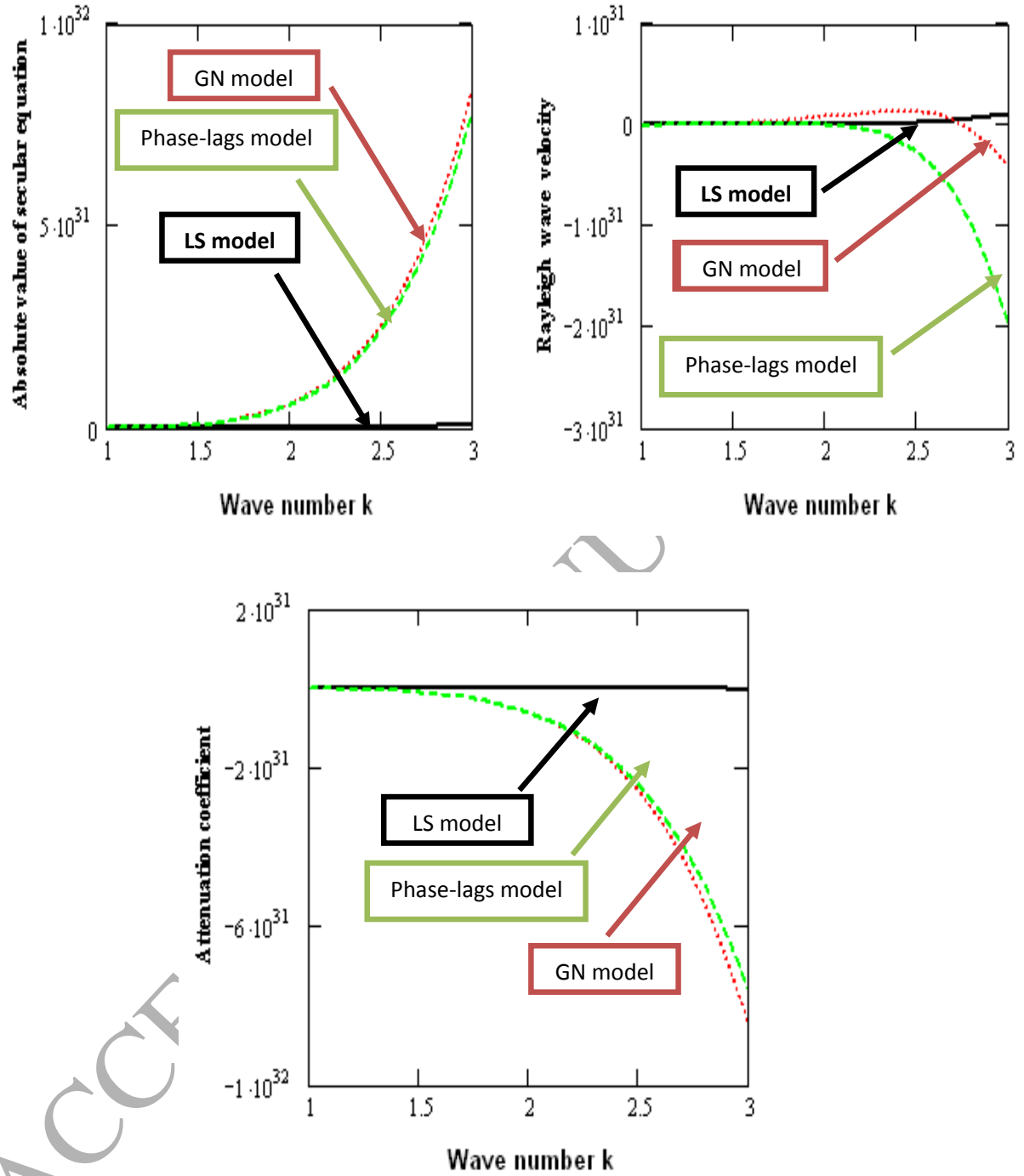


Fig. 2: Comparison among the three generalized thermoelastic models in the context of Rayleigh wave propagation (— *LS Model*, *GN Model*, ---- *TPL Model*) with respect to wave number.

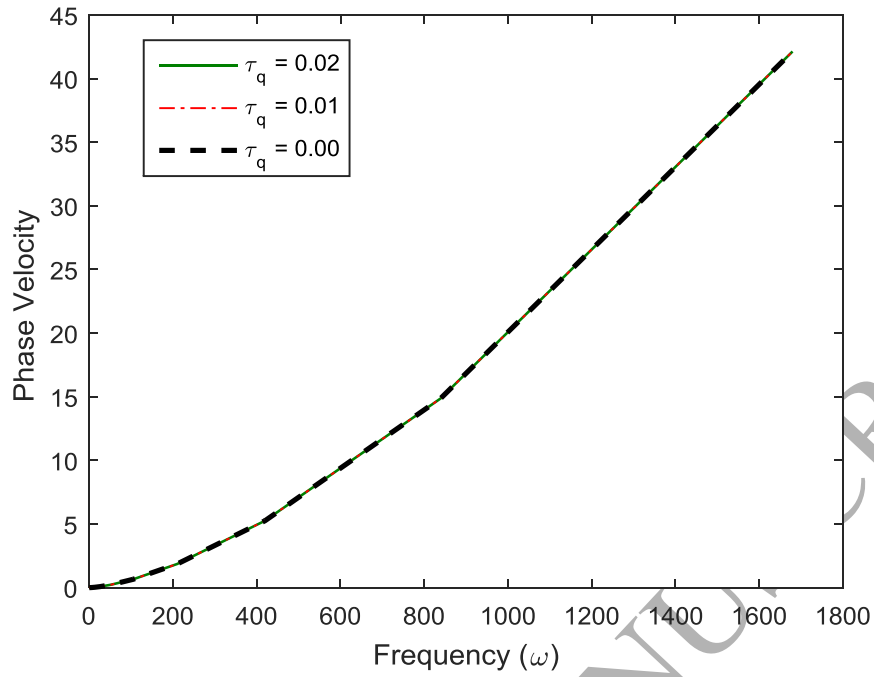


Fig. 3: Variation of phase velocity for different values of τ_q with respect to frequency.

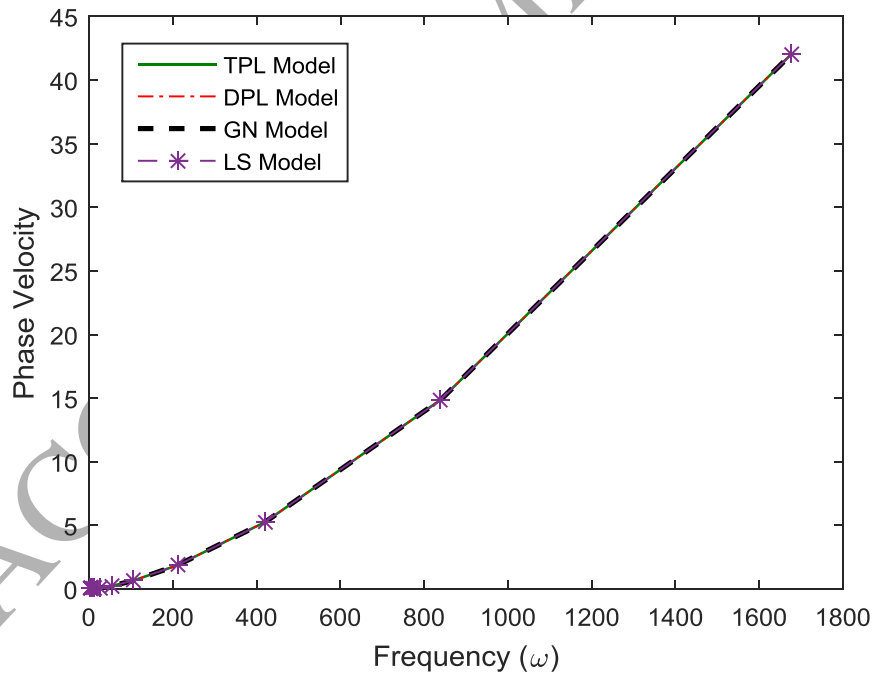


Fig.4: Variation of phase velocity for different thermoelastic models with respect to frequency.

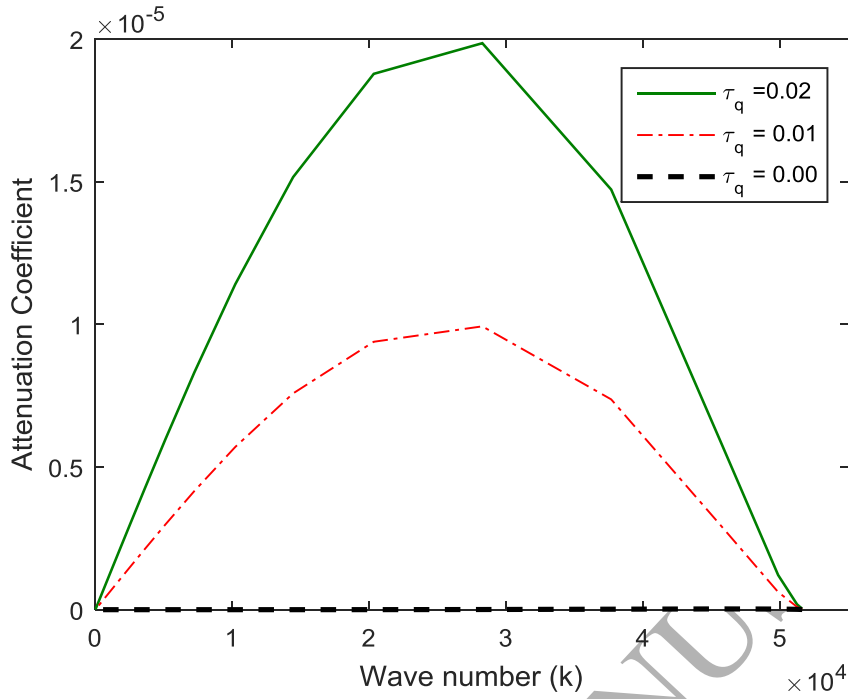


Fig.5: Variation of attenuation coefficient for different values of τ_q with respect to wave number.

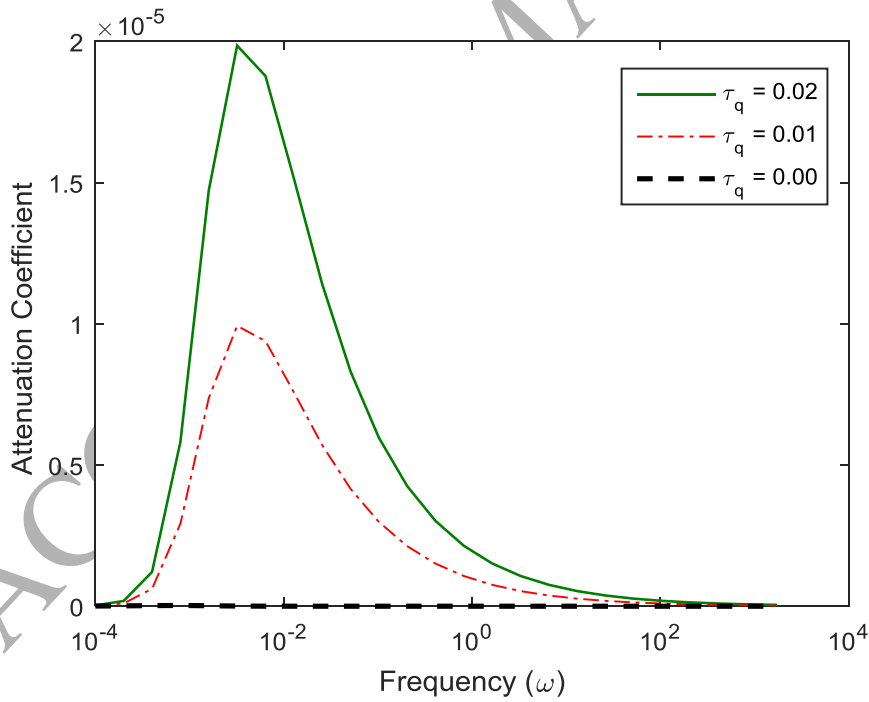


Fig.6: Variation of attenuation coefficient for different values of τ_q with respect to frequency.

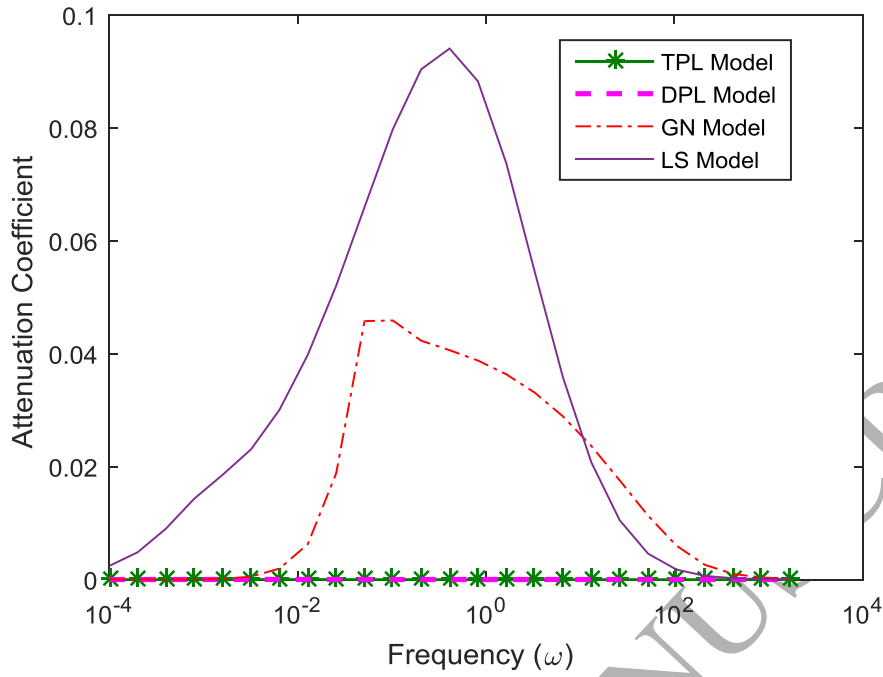


Fig.7: Variation of attenuation coefficient for different thermoelastic models with respect to frequency.

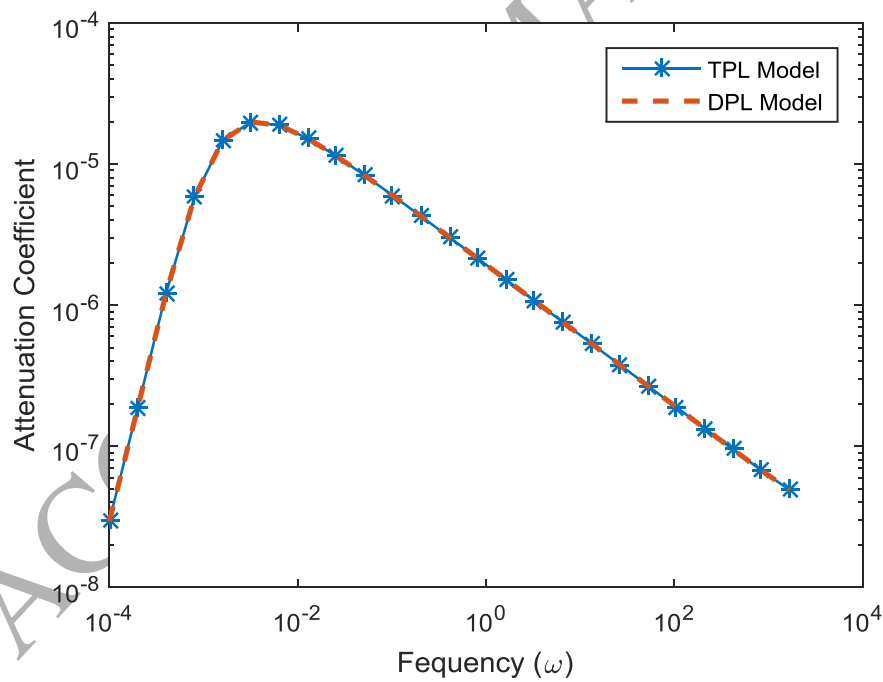


Fig.8: Variation of attenuation coefficient for TPL and DPL models with respect to frequency.

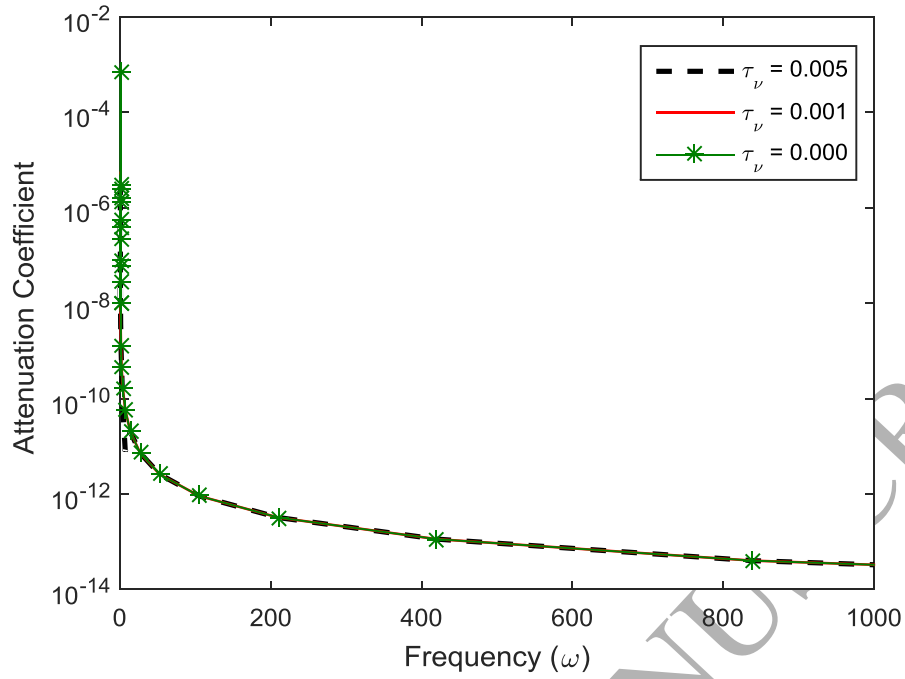


Fig.9: Variation of attenuation coefficient for different values of τ_ν with respect to frequency.

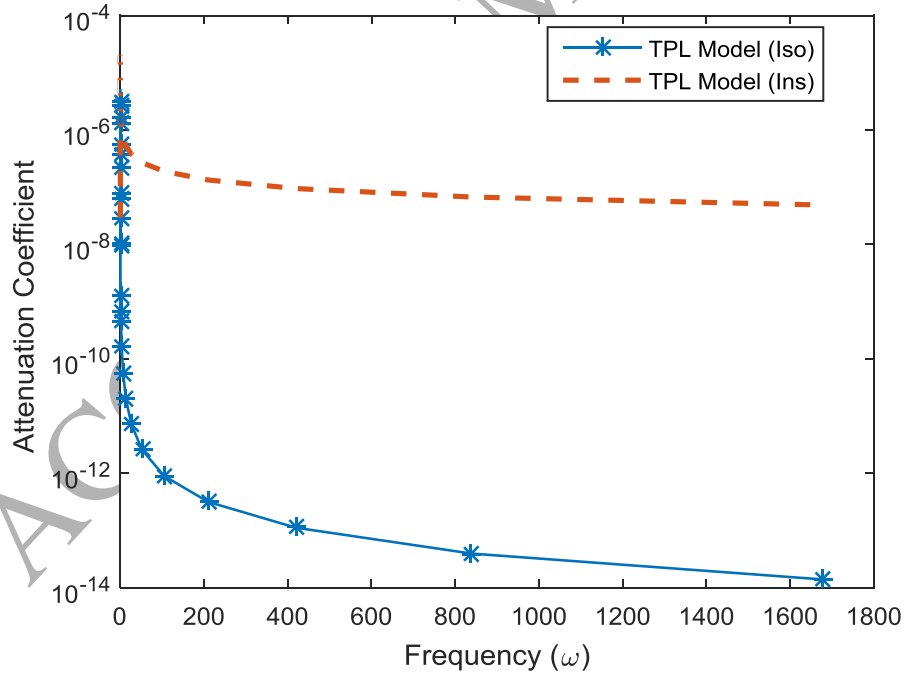


Fig.10: Variation of attenuation coefficient for isothermal and insulated boundaries with respect to frequency.

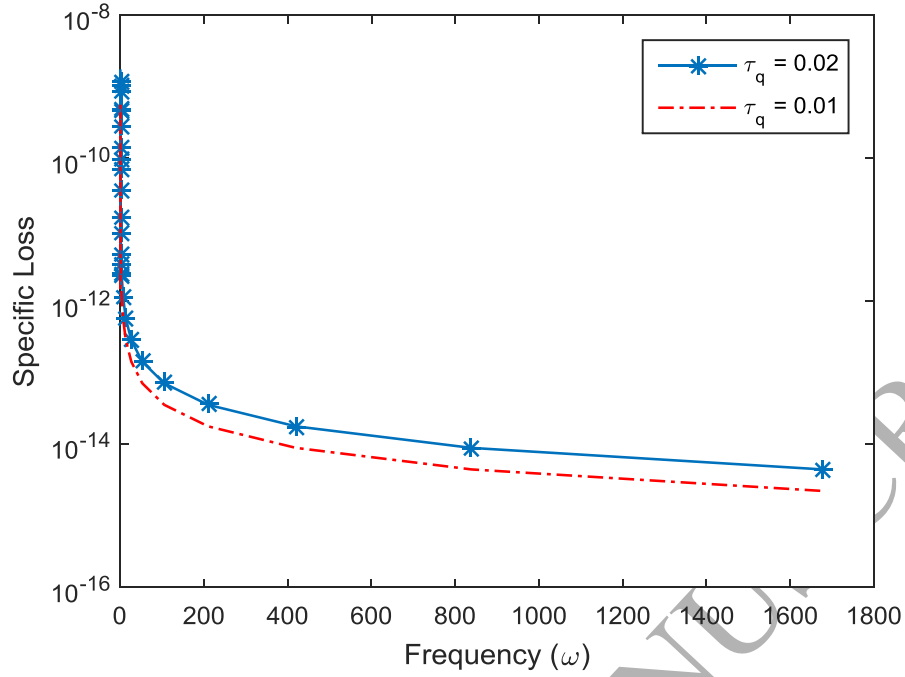


Fig.11: Variation of specific loss for different values of τ_q with respect to frequency.

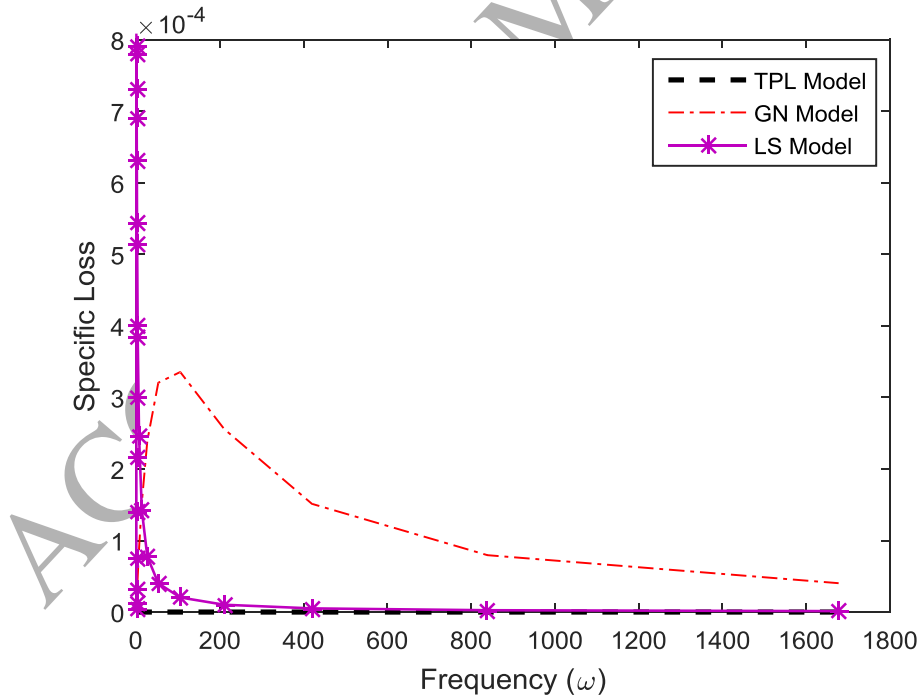


Fig.12: Variation of specific loss for different thermoelastic models with respect to frequency.

ACCEPTED MANUSCRIPT



Source details

[Feedback >](#) [Compare sources >](#)

Applied Mathematical Modelling

Scopus coverage years: from 1976 to Present

Publisher: Elsevier

ISSN: 0307-904X

Subject area: [Mathematics: Applied Mathematics](#) [Mathematics: Modeling and Simulation](#)

Source type: Journal

[View all documents >](#)

[Set document alert](#)

[Save to source list](#)

CiteScore 2022
9.4 ⓘ

SJR 2022
1.080 ⓘ

SNIP 2022
1.743 ⓘ

CiteScore

[CiteScore rank & trend](#)

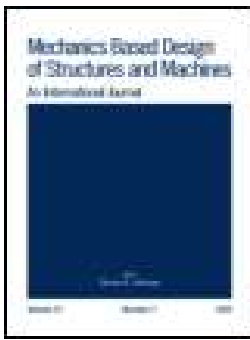
[Scopus content coverage](#)



Improved CiteScore methodology



CiteScore 2022 counts the citations received in 2019-2022 to articles, reviews, conference papers, book chapters and data papers published in 2019-2022, and divides this by the number of publications published in 2019-2022. [Learn more >](#)



Mechanics Based Design of Structures and Machines

An International Journal

ISSN: 1539-7734 (Print) 1539-7742 (Online) Journal homepage: <http://www.tandfonline.com/loi/lmbd20>

Effect of rotation in magneto-thermoelastic transversely isotropic hollow cylinder with three-phase-lag model

Siddhartha Biswas, Basudeb Mukhopadhyay & Soumen Shaw

To cite this article: Siddhartha Biswas, Basudeb Mukhopadhyay & Soumen Shaw (2019): Effect of rotation in magneto-thermoelastic transversely isotropic hollow cylinder with three-phase-lag model, Mechanics Based Design of Structures and Machines

To link to this article: <https://doi.org/10.1080/15397734.2018.1545587>



Published online: 11 Jan 2019.



Submit your article to this journal [↗](#)



View Crossmark data [↗](#)



Effect of rotation in magneto-thermoelastic transversely isotropic hollow cylinder with three-phase-lag model

Siddhartha Biswas , Basudeb Mukhopadhyay, and Soumen Shaw

Department of Mathematics, Indian Institute of Engineering Science and Technology, Shibpur, India

ABSTRACT

This article deals with the various heat source responses in a transversely isotropic hollow cylinder under the purview of three-phase-lag (TPL) generalized thermoelasticity theory. In presence of magnetic field and due to the rotating behavior of the cylinder, the governing equations are redefined for generalized thermoelasticity with thermal time delay. In order to obtain the stress, displacement and temperature field, the field functions are expressed in terms of modified Bessel functions in Laplace transformed domain. When the outer radius of hollow cylinder tends to infinity, the corresponding results are discussed. Finally an appropriate Laplace transform inversion technique is adopted.

ARTICLE HISTORY

Received 5 April 2018

Accepted 5 November 2018

KEYWORDS

Magnetic effect; rotation; transversely isotropic medium; hollow cylinder; three-phase-lag model; heat source

1. Introduction

A considerable attention has been made since last few decades due to numerous applications of thermoelasticity in various disciplines of science and technology. It is well known that the theory of coupled thermoelasticity suffers from physical drawbacks that the thermal signal propagates with the infinite speed. Biot (1956) introduced the theory of classical thermoelasticity based on the thermodynamic principles of irreversible processes. In this theory, the equation of motion is hyperbolic in nature and the heat conduction equation is parabolic. It still experiences defect of uncoupled theory due to the presence of parabolic type heat conduction equation. For the elimination of this drawback in classical thermoelasticity theory, the generalized thermoelasticity theories are developed in which the heat conduction equation is of hyperbolic type.

Cattaneo (1958) replaces the Fourier law of heat conduction by introducing a single parameter that acts as a relaxation time, thus a wave type equation is formulated by postulating a new law of heat conduction instead of classical Fourier law. The first generalization is done by Lord and Shulman (1967) and is referred to as L–S model. The L–S model is developed by a system of partial differential equations (PDE) in which in comparison to a system of classical thermoelasticity, the Fourier law of heat conduction is replaced by the Maxwell–Cattaneo law that generalizes the Fourier law and introduces a single relaxation time into consideration. The second generalization is due to Green and Lindsay (1972) which is known as G–L model. The G–L model is characterized by a system of PDE in which, in comparison to the classical system, the constitutive relations for the stress tensor and the entropy are generalized by introducing two different relaxation times into considerations. The third generalization is done by Hetnarski and Ignaczak (1993, 1996) and is known as a H–I model. The H–I model has been introduced in an attempt to describe low-temperature soliton-like thermoelastic waves. The fourth generalization to the coupled theory of

thermoelasticity is introduced by Green and Naghdi (1993) and this theory is concerned with the thermoelasticity theory without energy dissipation, referred to as G–N theory of type-II in which the classical Fourier law is replaced by a heat flux-rate temperature gradient relation. The heat transport equation does not involve a temperature rate term and as such this model admits undamped thermoelastic waves in thermoelastic material. Detailed information regarding the generalized heat conduction model can be found in the monographs of Chandrasekharaiah (1986, 1998) and Ignaczak and Hetnarski (2014).

The generalized thermoelasticity theory with the dual phase lag effect has been developed by Tzou (1995). Tzou introduced two different time lags, one for the heat flux vector and the other for the temperature gradient. The delay time τ_T is supposed to be caused by the microstructural interactions (small effects of heat transport in space, such as phonon-electron interaction or phonon scattering) and is called the phase lag of the temperature gradient. The other delay time τ_q is interpreted as the relaxation time due to fast transient effects of the thermal inertia (or small effects of heat transport in time) and is called the phase lag of the heat flux. The most recent development in thermoelasticity theory is the thermoelasticity with three-phase-lags (TPL) by Choudhuri (2007). In this model, a phase lag (τ_ν) for the thermal displacement gradient is introduced. The stability of TPL model is discussed by Quintanilla and Racke (2008). TPL model includes TPL in the heat flux vector, the temperature gradient, and in the thermal displacement gradient. To study some heat transfer problems involving very short time intervals and the problems of very high heat fluxes, the hyperbolic equation gives significantly different results than the parabolic equation. TPL is very much effective in the problems of nuclear boiling, exothermic catalytic reactions, phonon-electron interactions, phonon-scattering, etc.

Since nineteenth century the coupling phenomenon between thermo-mechanical behavior of the materials and the electromagnetic response has been started. The electromagnetic interaction with piezoelectric materials has been discovered in the early part of the twentieth century. The continued development of electromagnetic interaction of piezoelectric materials has led to huge market of products ranging from those for everyday use to most specialized devices. Since last two decades, the electromagnetic interaction with composite materials has been developed. Such composites can exhibit the field coupling which has not been seen in any of the monolithic constituent materials. These electromagnetic composite materials have been used in many devices like ultrasonic imaging devices, sensors, actuators, and transducers. Electromagnetic elastic materials have the ability that they can convert the energy from one kind to another (among mechanical, electrical, and magnetic). Due to these special characteristics, these types of materials have been used in high tech areas such as lasers, supersonic devices and in many information technological applications.

Anisotropy creates qualitatively new properties of elastic waves and acoustic phenomena that have not got close analogous in isotropic media. Some of them have already found their practical applications in real devices. A theoretical description of elastic waves in anisotropic material is a very nontrivial problem. The study of wave propagation in anisotropic materials has been a subject of extensive investigation in the literature. It is of great importance in a variety of applications ranging from seismology to nondestructive testing of composite structures used in aircraft, spacecraft, or other engineering industries.

Thermal stresses are the main cause of structural failures in industrial applications and for this reason, the exact and general solutions are required for the thermoelastic problems. Due to the presence of coupling between the energy equation and the equation of motion, the governing equations of thermoelasticity are of complexity. For this complexity, some reasonable simplifications are made on these equations, such as dropping the coupling term in the energy equation, which yields the uncoupled dynamical theory of thermoelasticity. As a general rule, the effect of coupling term in the energy equation is small and the distinction between coupled and uncoupled theories is negligible. Cylinders have many applications in engineering and it is interesting to have a general solution for the thermoelastic problem.

Chandrasekharaiah and Keshavan (1992) examined axisymmetric thermoelastic interactions in an unbounded body with cylindrical cavity. Kar and Kanoria (2007) studied thermoelastic Interaction with energy dissipation in an unbounded body with a spherical hole. Youssef (2006) considered a problem of generalized thermoelastic infinite cylindrical cavity subjected to a ramp-type heating and loading. Roychoudhury and Bandyopadhyay (2005) studied thermoelastic wave propagation in rotating elastic medium without energy dissipation. Mukhopadhyay and Kumar (2008a, 2008b) studied generalized thermoelastic interactions with a spherical cavity as well as with a cylindrical hole. Abd-Alla and Mahmoud (2010) discussed magneto-thermoelastic problem in rotating nonhomogeneous orthotropic hollow cylinder under the hyperbolic heat conduction model. Abouelregal (2013) studied generalized thermoelastic infinite transversely isotropic body with cylindrical cavity due to moving heat source and harmonically varying heat source. Recently Sherief and Raslan (2016) examined thermoelastic interactions without energy dissipation in an unbounded body with a cylindrical cavity. Kumar and Mukhopadhyay (2009) studied the effect of three phase lags on generalized thermoelasticity for an infinite medium with a cylindrical cavity. Kar and Kanoria (2009) considered generalized thermoelastic functionally graded orthotropic hollow sphere under thermal shock with TPL effect. Das, Kar, and Kanoria (2013) analyzed magneto-thermoelastic response in a transversely isotropic hollow cylinder under thermal shock with three phase lag effect. Banik and Kanoria (2012) discussed the effect of TPL on a two-temperature generalized thermoelasticity for infinite medium with spherical cavity. Abbas and Othman (2012) considered generalized thermoelasticity of thermal shock problem in an isotropic hollow cylinder and temperature dependent elastic moduli. Othman and Abbas (2012) studied generalized thermoelasticity of thermal shock problem in a nonhomogeneous isotropic hollow cylinder with energy dissipation. Othman and Abbas (2015) examined the effect of rotation on a magneto-thermoelastic hollow cylinder with energy dissipation using finite element method. Othman, Elmaklizi, and Mansour (2017) considered the effect of temperature-dependent properties on generalized magneto-thermoelastic with two-temperature under TPL model. Said (2016a) investigated the influence of gravity on generalized magneto-thermoelastic medium for TPL model. Said (2015) studied deformation of a rotating two-temperature generalized magneto-thermoelastic medium with internal heat source due to hydrostatic initial stress. Said (2017) considered fiber-reinforced thermoelastic medium with an internal heat source due to hydrostatic initial stress and gravity for the TPL model. Said (2016b) investigated wave propagation in a magneto-micropolar thermoelastic medium with two temperatures for TPL model. Yang and Lin (2018) proposed a theoretical study of the mechanism with variable compression ratio and expansion ratio. Huang (2018) discussed simulation of friction and stiction in multibody dynamics model problems. Sun, Yan, and Gao (2018) analyzed frequency-domain vibration response of thin plate attached with viscoelastic free layer damping. Bhattacharya, Ananthasuresh, and Ghoshal (2018) proposed design of a one-dimensional flexible structure for desired load-bearing capability and axial displacement.

In this study, our aim is to present magneto-thermoelastic interaction with thermal delay in transversely isotropic rotating hollow cylinder in presence of various heat sources. To solve the problem, Laplace transform technique is employed over field variables and the field functions are expressed in terms of modified Bessel functions. A complete and comprehensive analysis of the results has been presented for TPL model in presence of a magnetic field as well as rotation. Applying inverse Laplace transform technique (see [Appendix](#)), effect of magnetic field and rotation on radial stress and displacement are illustrated graphically.

2. Formulation of the problem

We consider a homogeneous transversely isotropic thermoelastic solid occupying the region of an infinitely long hollow circular cylinder of internal radius ' a ' and external radius ' b '. We shall use a cylindrical system of coordinates (r, θ, z) with the z -axis coinciding with the axis of cylinder.

We shall also assume the initial state of the medium is quiescent. The outer of this cylinder is assumed to be traction free and subjected to various heat sources that depend only on the time t , while the inner surface is assumed to be in contact with a rigid surface and is thermally insulated. We also consider the hollow cylinder is rotating in the presence of a magnetic field.

Due to radial symmetry of the problem, all functions considered are functions of the radial distance from the axis of the cylinder r and the time t only.

Thus the displacement components are

$$u_r = u(r, t), u_\theta = u_z = 0. \quad (1)$$

The strain components are as follows:

$$e_{rr} = \frac{\partial u}{\partial r}, e_{\theta\theta} = \frac{u}{r}, e_{zz} = e_{r\theta} = e_{rz} = e_{\theta z} = 0. \quad (2)$$

The cubic dilatation e is thus given by

$$e = e_{rr} + e_{\theta\theta} + e_{zz} = \frac{\partial u}{\partial r} + \frac{u}{r} = \frac{1}{r} \frac{\partial(ru)}{\partial r}. \quad (3)$$

The stress-displacement-temperature relations are given by

$$\begin{aligned} \sigma_{rr} &= c_{11} \frac{\partial u}{\partial r} + c_{12} \frac{u}{r} - \beta T \\ \sigma_{\theta\theta} &= c_{12} \frac{\partial u}{\partial r} + c_{11} \frac{u}{r} - \beta T \end{aligned}, \quad (4)$$

where T is the temperature above reference temperature, T_0 is the reference uniform temperature of the body chosen such that $|\frac{T}{T_0}| \ll 1$, c_{11}, c_{12} are elastic constants, β is the thermal moduli, σ_{rr} is the radial stress, and $\sigma_{\theta\theta}$ is the tangential stress.

The equation of motion in presence of magnetic field and rotation can be taken as

$$\sigma_{rr,r} + \frac{\sigma_{rr} - \sigma_{\theta\theta}}{r} + F_r = \rho \frac{\partial^2 u}{\partial t^2} + R_r, \quad (5)$$

where ρ is the mass density, F_r is the component of Lorentz force, and R_r is the component of body force due to rotation.

We consider that the homogeneous transversely isotropic thermoelastic hollow cylinder is rotating uniformly with angular velocity $\vec{\Omega} = \Omega \vec{n}$ where \vec{n} is a unit vector representing the direction of the axis of rotation. The displacement equation in the rotating frame has two additional terms (Schoenberg and Censor 1973):

- i. Centripetal acceleration $\vec{\Omega} \times (\vec{\Omega} \times \vec{u})$ due to time-varying motion only and
- ii. Coriolis acceleration $2\vec{\Omega} \times \dot{\vec{u}}$.

These terms do not appear in nonrotating media. The term Coriolis acceleration is neglected here as this term appears only in case of moving frame.

If $\vec{\Omega} = (0, 0, \Omega)$ represents the rotation vector, the component of rotation is given by

$$R_r = -\rho \Omega^2 u. \quad (6)$$

Let us consider that the cylinder is placed in a magnetic field with constant intensity $\vec{H}_0 = (0, 0, H_0)$ acting parallel to the direction of the z -axis.

The Lorentz force \vec{F} is given by

$$\vec{F} = \mu_0 (\vec{J} \times \vec{H}), \quad (7)$$

where \vec{J} is the current density vector.

For a perfectly electrically and magnetically conducting elastic body, the electromagnetic field is governed by Maxwell's equations:

$$\vec{\nabla} \times \vec{h} = \vec{J} + \varepsilon_0 \dot{\vec{E}}, \quad (8)$$

$$\vec{\nabla} \times \vec{E} = -\mu_0 \dot{\vec{h}}, \quad (9)$$

$$\vec{\nabla} \cdot \vec{h} = 0, \quad (10)$$

$$\vec{\nabla} \cdot \vec{E} = 0, \quad (11)$$

where μ_0 and ε_0 are the electric permeability and magnetic permittivity respectively, $\vec{\nabla}$ is the Hamiltonian's operator, \vec{H}_0 is initial magnetic field, \vec{h} is perturbed magnetic field, and \vec{E} is an induced electric field.

For perfectly conducting medium from generalized Ohm's law, we obtain

$$\vec{E} = -\mu_0 (\dot{\vec{u}} \times \vec{H}). \quad (12)$$

As the magnitude of the perturbed magnetic field (\vec{h}) is very small, in the discussion of linear theory of elasticity we may neglect the product term involving h and its higher degrees.

From Eqs. (9) and (12) the induced field components in the cylinder are found to be

$$\vec{E} = (0, E, 0) = \left(0, \mu_0 H_0 \frac{\partial u}{\partial t}, 0\right), \vec{h} = (0, 0, h) = (0, 0, -H_0 e). \quad (13)$$

From Eqs. (8) and (13), the components of current density vector have the following form:

$$\vec{J} = \left(0, H_0 \frac{\partial e}{\partial r} - \varepsilon_0 \mu_0 H_0 \frac{\partial^2 u}{\partial t^2}, 0\right). \quad (14)$$

The components of Lorentz force can be obtained from Eqs. (7) and (14) as

$$\vec{F} = \left[\mu_0 H_0^2 \left(\frac{\partial e}{\partial r} - \varepsilon_0 \mu_0 \frac{\partial^2 u}{\partial t^2}\right), 0, 0\right]. \quad (15)$$

Maxwell's electromagnetic stress tensor σ_{ij}^* is given by

$$\sigma_{ij}^* = \mu_0 [H_i h_j + H_j h_i - (\vec{H} \cdot \vec{h}) \delta_{ij}]; i, j = r, \theta, z$$

Radial Maxwell stress $\sigma_{rr}^* = \mu_0 H_0^2 e$

We take $\sigma_r = \sigma_{rr} + \sigma_{rr}^*$

TPL model in transversely isotropic cylindrical medium can be taken as

$$\left[K^* + (K + \tau_\nu K^*) \frac{\partial}{\partial t} + K \tau_T \frac{\partial^2}{\partial t^2} \right] \nabla^2 T = \left(1 + \tau_q \frac{\partial}{\partial t} + \frac{\tau_q^2}{2} \frac{\partial^2}{\partial t^2} \right) \left(\rho C_e \frac{\partial^2 T}{\partial t^2} + \beta T_0 \frac{\partial^2 e}{\partial t^2} \right). \quad (16)$$

where K is the classical thermal conductivity, K^* is the material constant characteristic of the theory, C_e is the specific heat at the constant strain, τ_q, τ_T , and τ_ν are the phase lags of heat flux, temperature gradient, and thermal displacement gradient, respectively where $0 \leq \tau_T \leq \tau_q$, t denotes time and $\nabla^2 = \frac{\partial^2}{\partial r^2} + \frac{1}{r} \frac{\partial}{\partial r}$.

Using Eqs. (4), (6), and (15) in the Eq. (5), we get

$$(c_{11} + \mu_0 H_0^2) \frac{\partial e}{\partial r} - \beta \frac{\partial T}{\partial r} = (\rho + \varepsilon_0 \mu_0^2 H_0^2) \frac{\partial^2 u}{\partial t^2} - \rho \Omega^2 u \quad (17)$$

Multiplying both sides by r and then using the operator $\frac{1}{r} \frac{\partial}{\partial r}$ to both sides of Eq. (17), we obtain

$$(c_{11} + \mu_0 H_0^2) \nabla^2 e - \beta \nabla^2 T = (\rho + \varepsilon_0 \mu_0^2 H_0^2) \frac{\partial^2 e}{\partial t^2} - \rho \Omega^2 e. \quad (18)$$

We now consider the following initial conditions Eq. (19) and various boundary conditions.

3. Initial conditions

We assume following initial conditions to solve the problem:

$$u = \frac{\partial u}{\partial t} = T = \frac{\partial T}{\partial t} = 0 \text{ at } t = 0 \quad (19)$$

4. Boundary conditions

The boundary conditions can be written in the following form:

1. The thermal boundary conditions:

$$T(b, t) = F(t) \quad (20)$$

$$\frac{\partial T}{\partial r}(a, t) = 0 \quad (21)$$

2. Mechanical boundary condition:

$$\sigma_r(b, t) = 0 \quad (22)$$

$$u(a, t) = 0. \quad (23)$$

5. Solution in the Laplace transformed domain

Introducing the Laplace transform domain defined by the following formula:

$$\bar{f}(x, s) = L[f(x, t)] = \int_0^\infty f(x, t) e^{-st} dt, \operatorname{Re}(s) > 0 \quad (24)$$

in Eqs. (18) and (16) and using homogeneous initial conditions, we obtain

$$(c_{11} + \mu_0 H_0^2) \nabla^2 \bar{e} - \beta \nabla^2 \bar{T} = [(\rho + \varepsilon_0 \mu_0^2 H_0^2) s^2 - \rho \Omega^2] \bar{e} \quad (25)$$

$$\nabla^2 \bar{T} = \tau s^2 (\rho C_e \bar{T} + \beta T_0 \bar{e}) \quad (26)$$

where $\tau_1 = 1 + s\tau_\nu$, $\tau_2 = 1 + s\tau_T$, $\tau_3 = 1 + s\tau_q + \frac{s^2 \tau_a^2}{2}$, $\tau = \frac{\tau_3}{K^* \tau_1 + sK\tau_2}$.

Eliminating \bar{e} from Eqs. (25) and (26), we get

$$(\nabla^4 - A\nabla^2 + B)(\bar{T}, \bar{e}) = 0 \quad (27)$$

which can be written as

$$(\nabla^2 - k_1^2)(\nabla^2 - k_2^2)(\bar{T}, \bar{e}) = 0 \quad (28)$$

where $k_i (i = 1, 2)$ is the square root of the positive real part of the roots k_i^2 of the following characteristic equation:

$$k^4 - Ak^2 + B = 0 \quad (29)$$

where $A = \frac{a_6 \beta + a_2 s^2 - a_3}{a_1}$, $B = \frac{(a_2 s^2 - a_1 - a_3) a_5}{a_1}$, $a_1 = c_{11} + \mu_0 H_0^2$, $a_2 = \rho + \varepsilon_0 \mu_0^2 H_0^2$,

$$a_3 = \rho\Omega^2, a_4 = \tau s^2, a_5 = a_4\rho C_e, a_6 = a_4\beta T_0.$$

The solutions of Eq. (28) have the following form:

$$\bar{T} = \sum_{i=1}^2 [A_i I_0(k_i r) + B_i K_0(k_i r)] \quad (30)$$

$$\bar{e} = \sum_{i=1}^2 [A'_i I_0(k_i r) + B'_i K_0(k_i r)] \quad (31)$$

where A_i, A'_i, B_i, B'_i are parameters depending on s and $I_n(\cdot), K_n(\cdot)$ denote the modified Bessel functions of order n of the first, and second kind, respectively.

Substituting the values of \bar{T} and \bar{e} in Eq. (25), we obtain

$$A'_i = \frac{\beta k_i^2}{[a_1 k_i^2 - (a_2 s^2 - a_3)]} A_i, B'_i = \frac{\beta k_i^2}{[a_1 k_i^2 - (a_2 s^2 - a_3)]} B_i \quad (32)$$

Now using the above relations in Eq. (31), we get

$$\bar{e} = \sum_{i=1}^2 \frac{\beta k_i^2}{[a_1 k_i^2 - (a_2 s^2 - a_3)]} [A_i I_0(k_i r) + B_i K_0(k_i r)] \quad (33)$$

Integrating Eq. (33) with respect to r , we obtain

$$\bar{u} = \sum_{i=1}^2 m_i [A_i I_1(k_i r) - B_i K_1(k_i r)] \quad (34)$$

where $m_i = \frac{\beta k_i}{[a_1 k_i^2 - (a_2 s^2 - a_3)]}, i = 1, 2$

In obtaining Eq. (34), we have used the following integral relations of the modified Bessel functions:

$$\int x I_0(x) dx = x I_1(x), \int x K_0(x) dx = -x K_1(x)$$

Thus we obtain

$$\begin{aligned} \bar{\sigma}_{rr} = & c_{11} \left[\sum_{i=1}^2 m_i \left(\left(k_i I_0(k_i r) - \frac{I_1(k_i r)}{r} \right) A_i + \left(k_i K_0(k_i r) + \frac{K_1(k_i r)}{r} \right) B_i \right) \right] \\ & + c_{12} \left[\sum_{i=1}^2 \frac{m_i}{r} \{ A_i I_1(k_i r) - B_i K_1(k_i r) \} \right] - \beta \left[\sum_{i=1}^2 \{ A_i I_0(k_i r) - B_i K_0(k_i r) \} \right] \end{aligned} \quad (35)$$

6. Applications

In this section, we discuss the effect of various heat sources on the transversely isotropic hollow cylinder.

Case 1: (Constant heat source)

For constant heat source, we take the boundary conditions as

$$T(b, t) = T_0 H(t) \quad (36)$$

$$\frac{\partial T(a, t)}{\partial r} = 0 \quad (37)$$

$$\sigma_r(b, t) = 0 \quad (38)$$

$$u(a, t) = 0 \quad (39)$$

where $H(t)$ denotes Heaviside function.

Now the transformed boundary conditions become

$$\bar{T}(b, s) = \frac{T_0}{s} \tag{40}$$

$$\frac{\partial \bar{T}(a, s)}{\partial r} = 0 \tag{41}$$

$$\bar{\sigma}_r(b, s) = 0 \tag{42}$$

$$\bar{u}(a, s) = 0 \tag{43}$$

Thus from the boundary conditions Eqs. (40)–(43), we obtain the following system of linear equations in A_1, A_2, B_1 and B_2 as

$$A_1 W_{11} + A_2 W_{12} + B_1 W_{13} + B_2 W_{14} = \frac{T_0}{s}, \tag{44}$$

$$A_1 W_{21} + A_2 W_{22} + B_1 W_{23} + B_2 W_{24} = 0, \tag{45}$$

$$A_1 W_{31} + A_2 W_{32} + B_1 W_{33} + B_2 W_{34} = 0, \tag{46}$$

$$A_1 W_{41} + A_2 W_{42} + B_1 W_{43} + B_2 W_{44} = 0, \tag{47}$$

where

$$(W_{1i}, W_{1j}) = \{I_0(k_i b), K_0(k_{j-2} b)\}$$

$$(W_{2i}, W_{2j}) = \{k_i I_1(k_i a), -k_{j-2} K_1(k_{j-2} a)\}. \tag{48}$$

$$(W_{3i}, W_{3j}) = \left[I_0(k_i b)(c_{11} m_i k_i - \beta) + \frac{m_i}{b} I_1(k_i b)(c_{12} - 1) + \mu_o H_0^2 m_i k_i I_0(k_i b), K_0(k_{j-2} b)(c_{11} k_{j-2} m_{j-2} + \beta) \right. \\ \left. + \frac{m_{j-2}}{b} K_1(k_{j-2} b)(1 - c_{12}) + \mu_o H_0^2 m_{j-2} k_{j-2} K_0(k_{j-2} b) \right]$$

$$(W_{4i}, W_{4j}) = \{m_i I_1(k_i a), -m_{j-2} K_1(k_{j-2} a)\}$$

and $i = 1, 2, j = 3, 4$.

From Eqs. (44)–(47), the values of A_1, A_2, B_1 , and B_2 are obtained as

$$\begin{pmatrix} A_1 \\ A_2 \\ B_1 \\ B_2 \end{pmatrix} = M^{-1} \begin{pmatrix} \frac{T_0}{s} \\ 0 \\ 0 \\ 0 \end{pmatrix}. \tag{49}$$

The Matrix M is given by

$$M = \begin{pmatrix} W_{11} & W_{12} & W_{13} & W_{14} \\ W_{21} & W_{22} & W_{23} & W_{24} \\ W_{31} & W_{32} & W_{33} & W_{34} \\ W_{41} & W_{42} & W_{43} & W_{44} \end{pmatrix}. \tag{50}$$

The elements of Matrix M are given by Eq. (48).

Case 2: (Periodically varying heat source)

For periodically varying heat source the boundary Eq. (36) will be replaced by Eq. (51) and other Eqs. (37), (38), and (39) will remain same.

$$T(b, t) = \begin{cases} T_0 \sin \frac{\pi t}{\gamma}; & 0 \leq t \leq \gamma. \\ 0; & t > \gamma \end{cases} \tag{51}$$

Equation (40) will be replaced by the Eq. (52) and other Eqs. (41–43) will remain same.

$$\bar{T}(b, s) = \frac{T_0 \pi \gamma (1 + e^{-s\gamma})}{(\pi^2 + s^2 \gamma^2)}. \quad (52)$$

The values of A_1, A_2, B_1 , and B_2 are obtained as

$$\begin{pmatrix} A_1 \\ A_2 \\ B_1 \\ B_2 \end{pmatrix} = M^{-1} \begin{pmatrix} \frac{T_0 \pi \gamma (1 + e^{-s\gamma})}{(\pi^2 + s^2 \gamma^2)} \\ 0 \\ 0 \\ 0 \end{pmatrix}. \quad (53)$$

The elements of Matrix M are given by Eq. (48).

Case 3: (Instantaneous heat source)

For instantaneous heat source, the boundary Eq. (36) will be replaced by Eq. (54) and other Eqs. (37), (38), and (39) will remain same.

$$T(b, t) = T_0 \delta(t). \quad (54)$$

Equation (40) will be replaced by Eq. (55) and other Eqs. (41), (42), and (43) will remain same.

$$\bar{T}(b, s) = T_0. \quad (55)$$

The values of A_1, A_2, B_1 , and B_2 are obtained as

$$\begin{pmatrix} A_1 \\ A_2 \\ B_1 \\ B_2 \end{pmatrix} = M^{-1} \begin{pmatrix} T_0 \\ 0 \\ 0 \\ 0 \end{pmatrix}. \quad (56)$$

The elements of Matrix M are given by Eq. (48).

7. Limiting cases

- If we put $K^* = \tau_\nu = \tau_T = \tau_q^2 = 0$, $\tau_q \neq 0$ then Eq. (16) converts to Lord–Shulman model.
- If we put $\tau_q = \tau_\nu = \tau_T = 0$ then Eq. (16) reduces to Green–Naghdi model type-III.
- If we put $K^* = 0$ then Eq. (16) reduces to dual-phase-lag model.

8. Particular cases

- If we put $c_{11} = \lambda + 2\mu$, $c_{12} = \lambda$ then the above analysis reduces for isotropic material.
- If we put $\Omega = 0$, then the above study reduces for transversely isotropic hollow cylinder without rotation.
- If we put $H_0 = 0$, then the above study converts for transversely isotropic hollow cylinder without magnetic field.

9. Special case (cylindrical hole in infinite transversely isotropic medium)

When outer radius b approaches to infinity, we obtain an infinite transversely isotropic medium with a cylindrical hole.

We write

$$\bar{\sigma}_{rr} = \bar{\sigma}_{rr}(I) + \bar{\sigma}_{rr}(K), \quad (57)$$

$$\bar{\sigma}_{\theta\theta} = \bar{\sigma}_{\theta\theta}(I) + \bar{\sigma}_{\theta\theta}(K), \quad (58)$$

where

$$\bar{\sigma}_{rr}(I) = \sum_{i=1}^2 \left[(c_{11}m_i k_i - \beta)I_0(k_i r) - \frac{m_i}{r}(c_{11} - c_{12})I_1(k_i r) \right] A_i, \tag{59}$$

$$\bar{\sigma}_{rr}(K) = \sum_{i=1}^2 \left[(c_{11}m_i k_i + \beta)K_0(k_i r) + \frac{m_i}{r}(c_{11} - c_{12})K_1(k_i r) \right] B_i, \tag{60}$$

$$\bar{\sigma}_{\theta\theta}(I) = \sum_{i=1}^2 \left[(c_{12}m_i k_i - \beta)I_0(k_i r) - \frac{m_i}{r}(c_{12} - c_{11})I_1(k_i r) \right] A_i, \tag{61}$$

$$\bar{\sigma}_{\theta\theta}(K) = \sum_{i=1}^2 \left[(c_{12}m_i k_i + \beta)K_0(k_i r) + \frac{m_i}{r}(c_{12} - c_{11})K_1(k_i r) \right] B_i. \tag{62}$$

The asymptotic expression of $I_\alpha(m), K_\alpha(m)$ are given as

$$I_\alpha(m) \approx \frac{e^m}{\sqrt{2\pi m}} \left(1 - \frac{4\alpha^2 - 1}{8m} + \frac{(4\alpha^2 - 1)(4\alpha^2 - 9)}{2!(8m)^2} - \frac{(4\alpha^2 - 1)(4\alpha^2 - 9)(4\alpha^2 - 25)}{3!(8m)^3} + \dots \right), \tag{63}$$

$$K_\alpha(m) \approx \frac{e^{-m}}{\sqrt{2\pi m}} \left(1 + \frac{4\alpha^2 - 1}{8m} + \frac{(4\alpha^2 - 1)(4\alpha^2 - 9)}{2!(8m)^2} + \frac{(4\alpha^2 - 1)(4\alpha^2 - 9)(4\alpha^2 - 25)}{3!(8m)^3} + \dots \right), \tag{64}$$

where $\alpha = 0, 1$.

For large values of b , $K_0(k_i b)$ and $K_1(k_i b)$ tend to zero.

As at a large distance the effect of stress vanishes, we must have $A_1 = A_2 = 0$.

Therefore, as $b \rightarrow \infty$ we get

$$\bar{\sigma}_{rr} = \sum_{i=1}^2 \left[(c_{11}m_i k_i + \beta)K_0(k_i r) + \frac{m_i}{r}(c_{11} - c_{12})K_1(k_i r) \right] B_i, \tag{65}$$

$$\bar{\sigma}_{\theta\theta} = \sum_{i=1}^2 \left[(c_{12}m_i k_i + \beta)K_0(k_i r) + \frac{m_i}{r}(c_{12} - c_{11})K_1(k_i r) \right] B_i, \tag{66}$$

where B_i ($i = 1, 2$) are given as

$$B_1 = \frac{-m_2 \bar{F}(s) K_1(k_2 a)}{[m_1 K_0(k_2 b) K_1(k_1 a) - m_2 K_0(k_1 b) K_1(k_2 a)]},$$

$$B_2 = \frac{m_1 \bar{F}(s) K_1(k_1 a)}{[m_1 K_0(k_2 b) K_1(k_1 a) - m_2 K_0(k_1 b) K_1(k_2 a)]}.$$

10. Numerical discussion

For numerical computation, we take the following values of transversely isotropic material:

$$c_{11} = 128\text{MPa}, c_{12} = 6\text{MPa}, T_0 = 298\text{K}, C_e = 2 \times 10^{-4}\text{J/KgK}, \beta = 0.04/\text{m}^2\text{K}, \rho = 8.836 \times 10^3\text{Kg/m}^3, K = 100\text{W/mK}, K^* = 17\text{W/mKs}, \tau_q = 2 \times 10^{-7}\text{s}, \tau_T = 1.5 \times 10^{-7}\text{s}, \tau_\nu = 1 \times 10^{-8}\text{s}, \Omega = 100\text{rps}, t = 0.2\text{s}.$$

Further for numerical purpose, we take $\mu_0 = 1.2\text{Hm}^{-1}$, $\varepsilon_0 = 1.2\text{Fm}^{-1}$, $H_0 = 10\text{Am}^{-1}$.

Figures 1–5 represent the graphs for constant heat source. In Fig. 1, it is observed that the radial stress $\sigma_{rr}(r, t)$ decreases with respect to distance. The graph representation for different

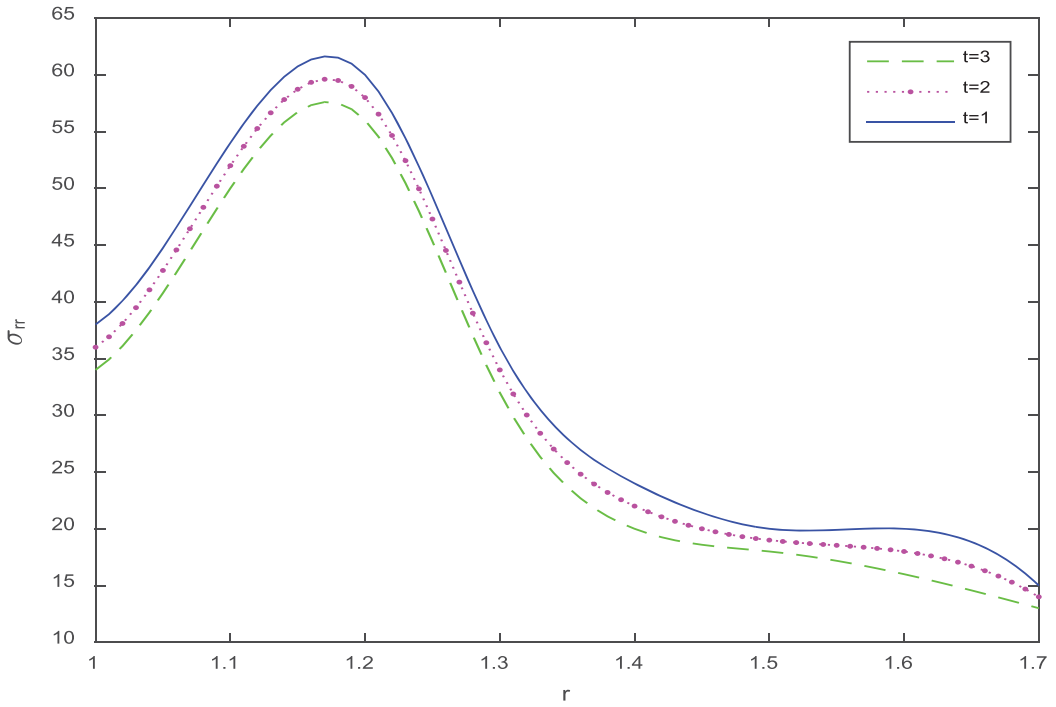


Figure 1. Distribution of radial stress with respect to r for different values of t (for constant heat source).

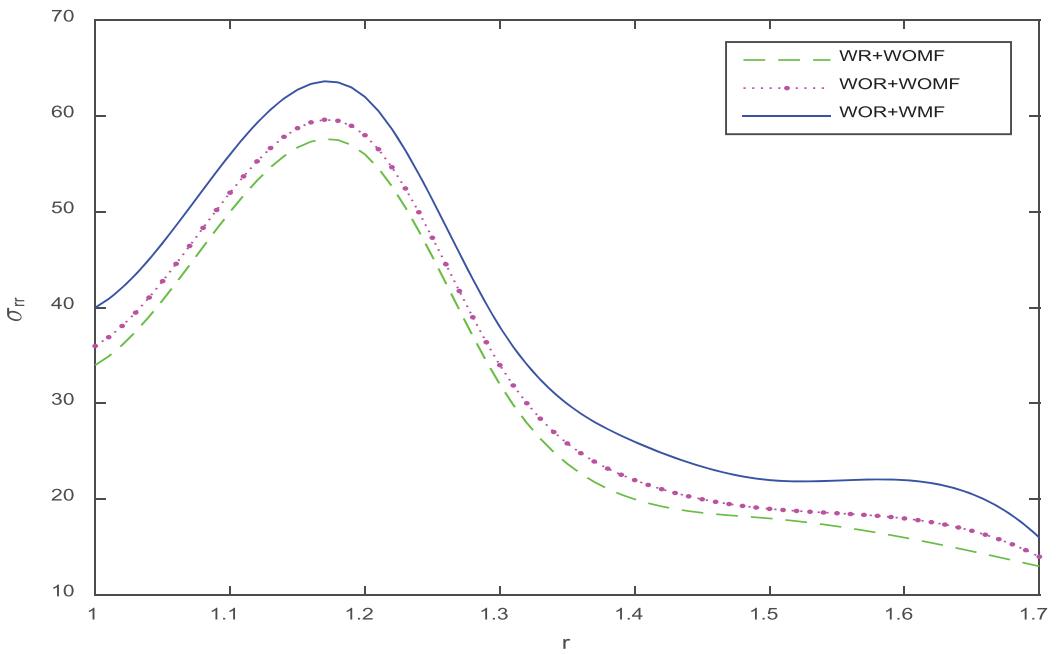


Figure 2. Distribution of radial stress with respect to r (for constant heat source).

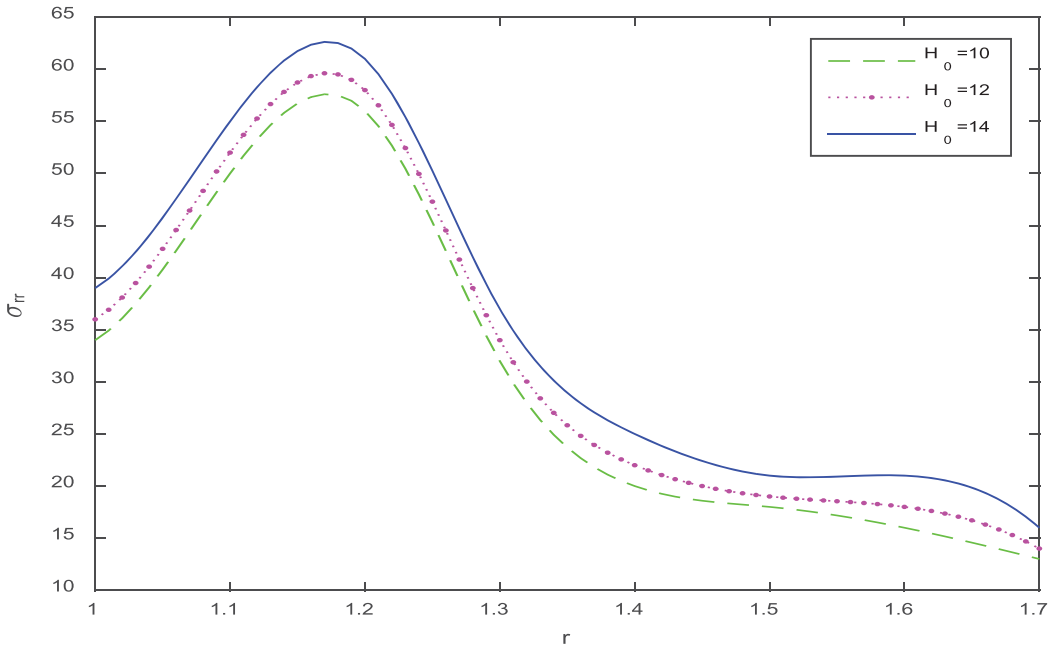


Figure 3. Distribution of radial stress with respect to r for magnetic effect.

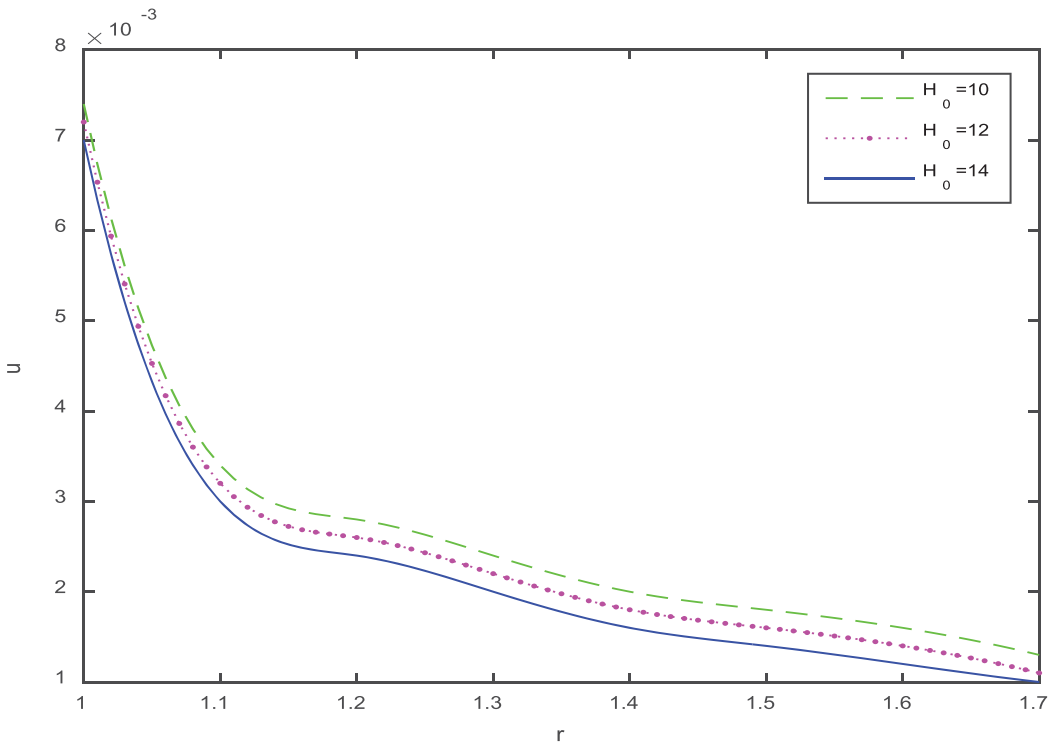


Figure 4. Distribution of displacement with respect to r for magnetic effect.

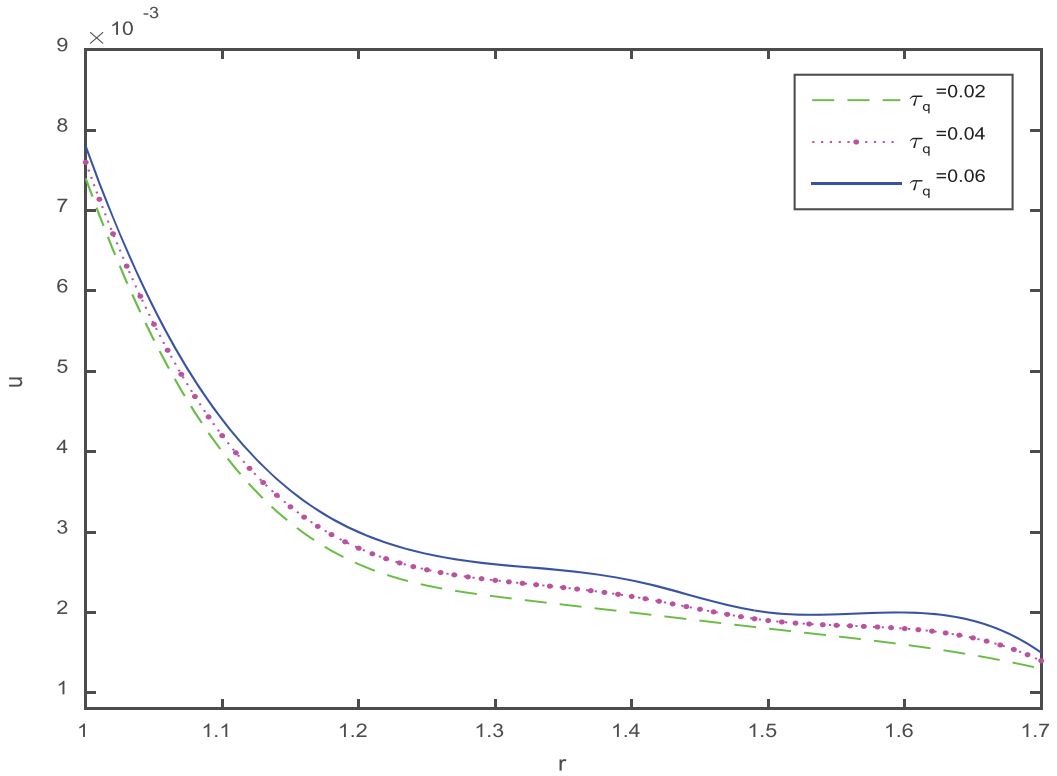


Figure 5. Distribution of displacement with respect to r for different phase lag.
Case 2: (Periodically varying heat source)

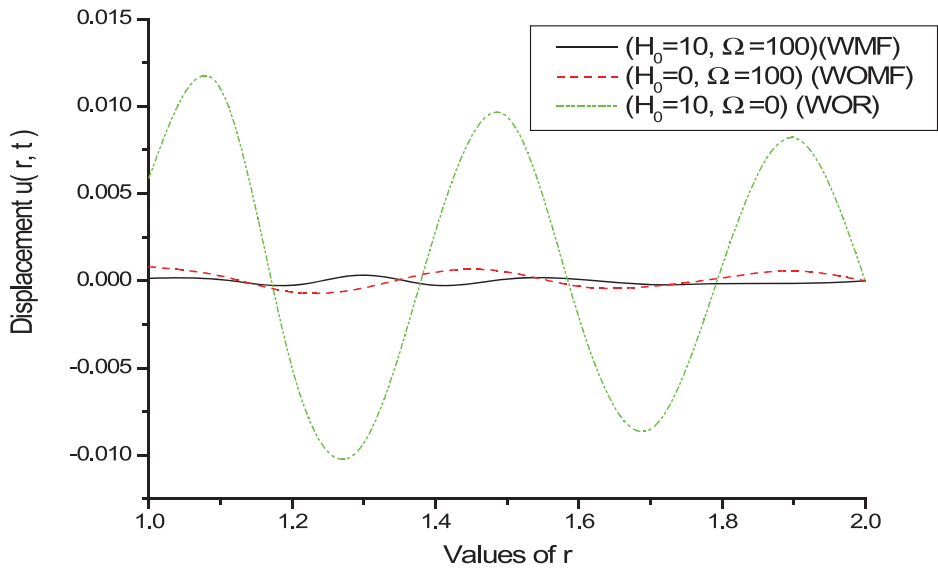


Figure 6. Distribution of displacement with respect to r (for periodically varying heat source).

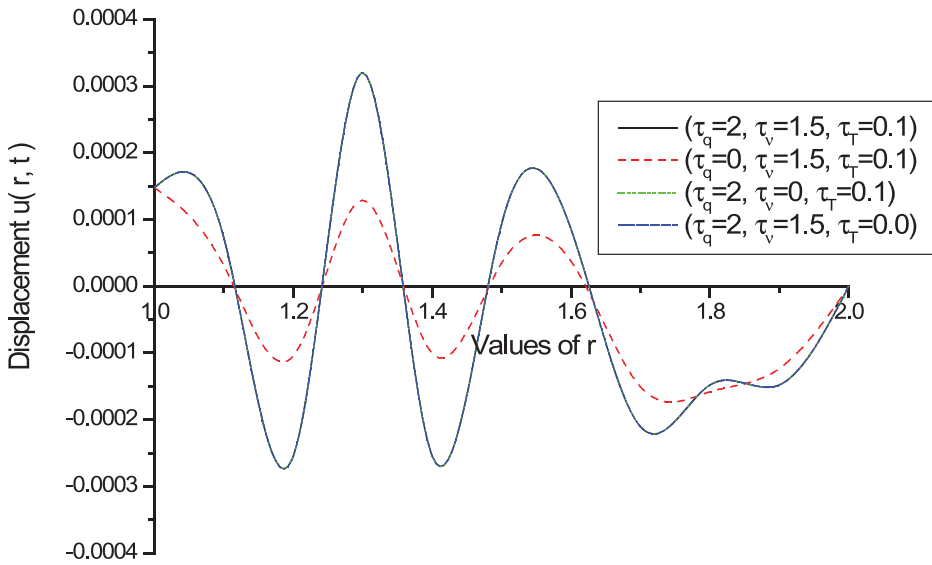


Figure 7. Distribution of displacement with respect to r for various phase lags (for periodically varying heat source).

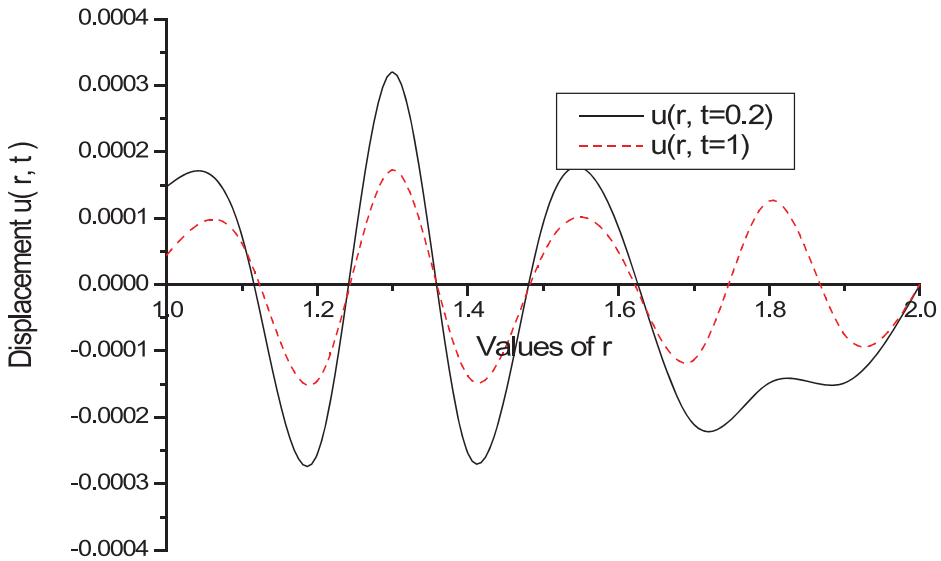


Figure 8. Distribution of displacement with respect to r for different values of t (for periodically varying).

time revealed that stress decreases with the increase of time. In Fig. 2, the effect of rotation and magnetic field on radial stress is shown where it is noticed that the effect of magnetic field is dominating. In Fig. 3, distribution of radial stress with respect to distance for different values of magnetic field is shown. Radial stress increases with the increase of magnetic field. In Fig. 4, distribution of displacement $u(r, t)$ with respect to distance is presented for different values of magnetic field. It is observed that displacement decreases with the increase of magnetic field. In Fig. 5, distribution of radial stress with respect to distance for different values of phase lag is presented and displacement increases with the increase of phase lag.

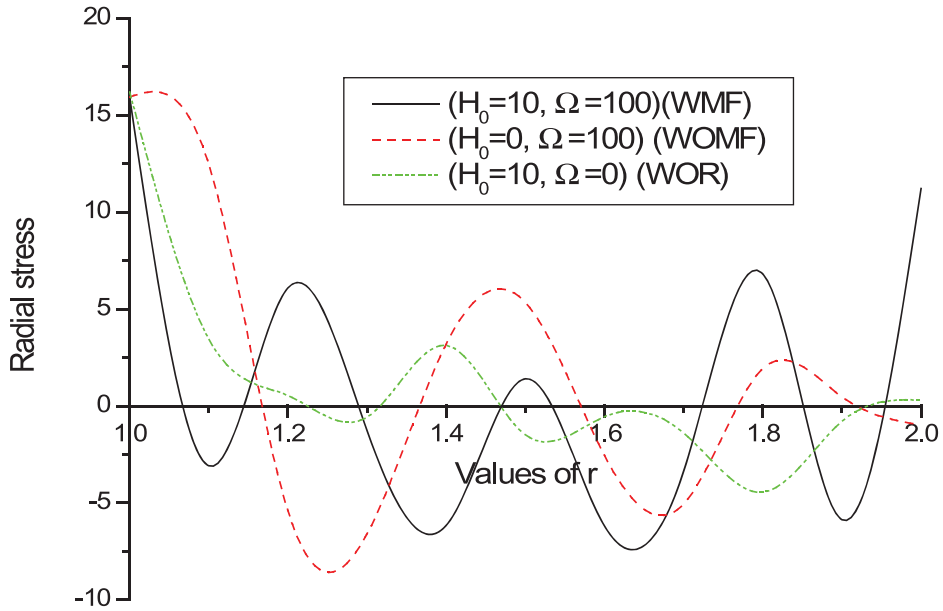


Figure 9. Distribution of radial stress with respect to r (for periodically varying heat source).

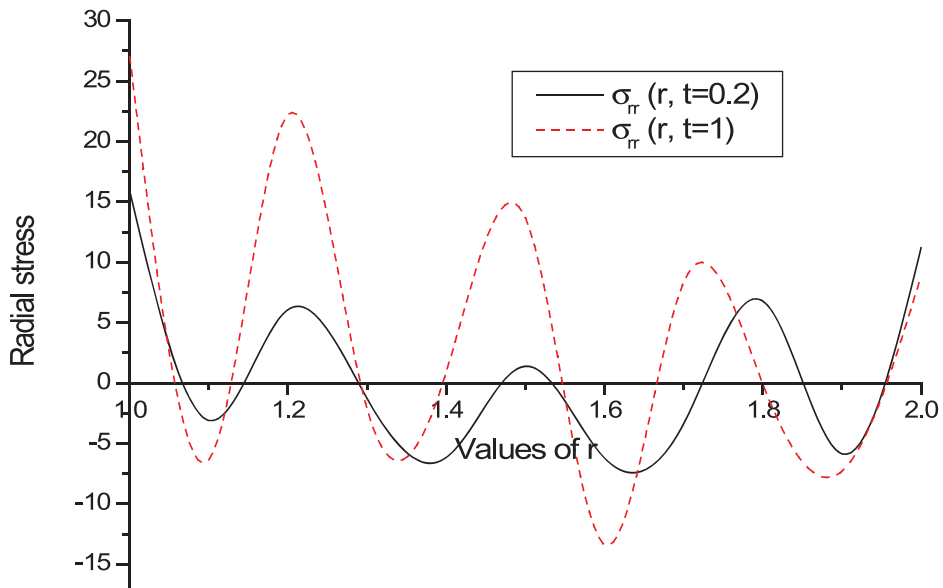


Figure 10. Distribution of radial stress with respect to r for different values of t (for periodically varying heat source).
Case 3: (Instantaneous heat source)

Figures 6–10 represent the graphs for the periodically varying heat source. In Fig. 6, the displacement is showing oscillatory behavior with respect to distance. The graph representing without the effect of rotation is dominating here. In Fig. 7, the effect of various phase lags on displacement is shown where it is noticed that the effect of phase lag for heat flux is dominating here. In Fig. 8, distribution of displacement with respect to radius for different values of time is shown. The graph representing time 0.2 sec is more dominating than the graph representing time

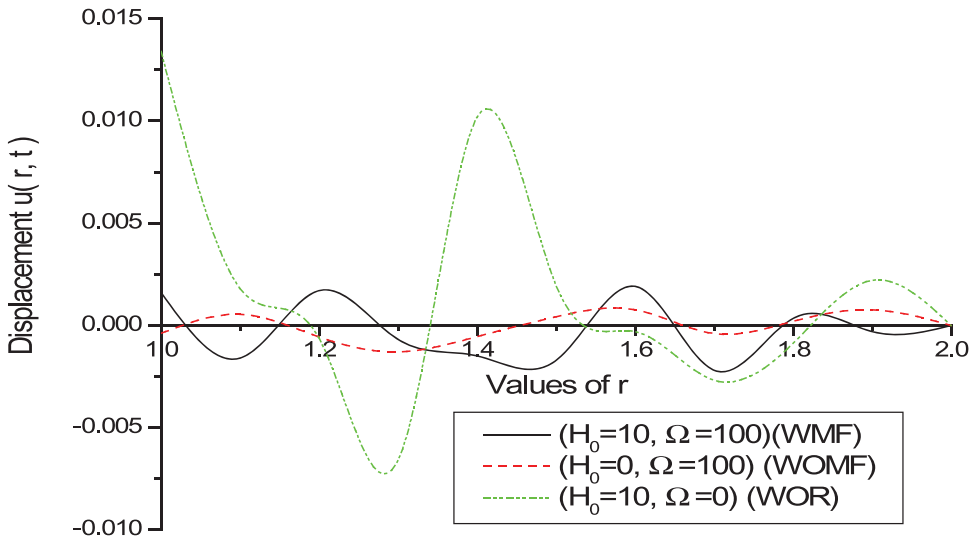


Figure 11. Distribution of displacement with respect to r (for instantaneous heat source).

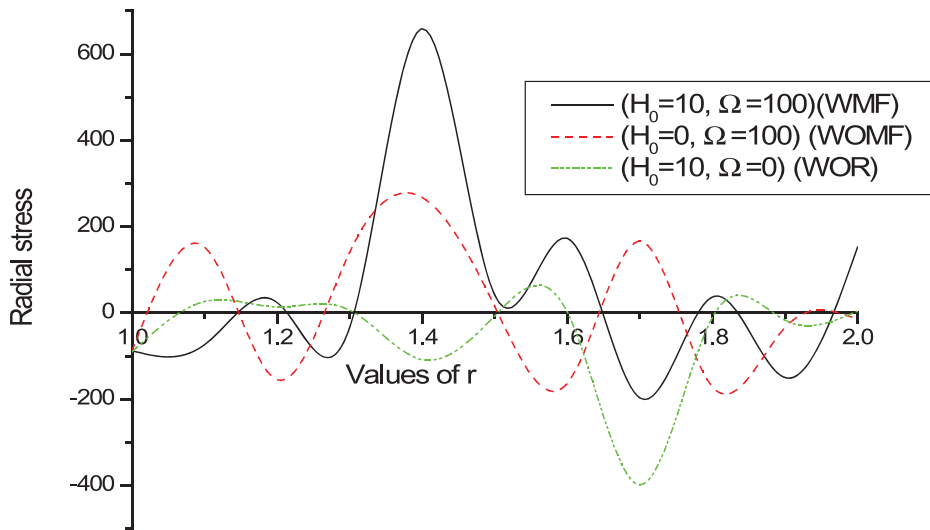


Figure 12. Distribution of radial stress with respect to r (for instantaneous heat source).

1 sec. In Fig. 9, distribution of radial stress with respect to distance is presented where all the graphs are showing oscillatory behavior i.e., wave type propagation is observed. In Fig. 10, distribution of displacement with respect to distance for different values of time is shown. The graph representing time 1 sec is more dominating than the graph representing time 0.2 sec.

Figures 11–13 represent the graphs for instantaneous heat source. In Fig. 11, the displacement is showing oscillatory behavior with respect to distance. The graph representing without the effect of rotation is dominating here. In Fig. 12, radial stress is showing oscillatory behavior with respect to distance. The effect of magnetic field and rotation is clearly observed here. In Fig. 13,

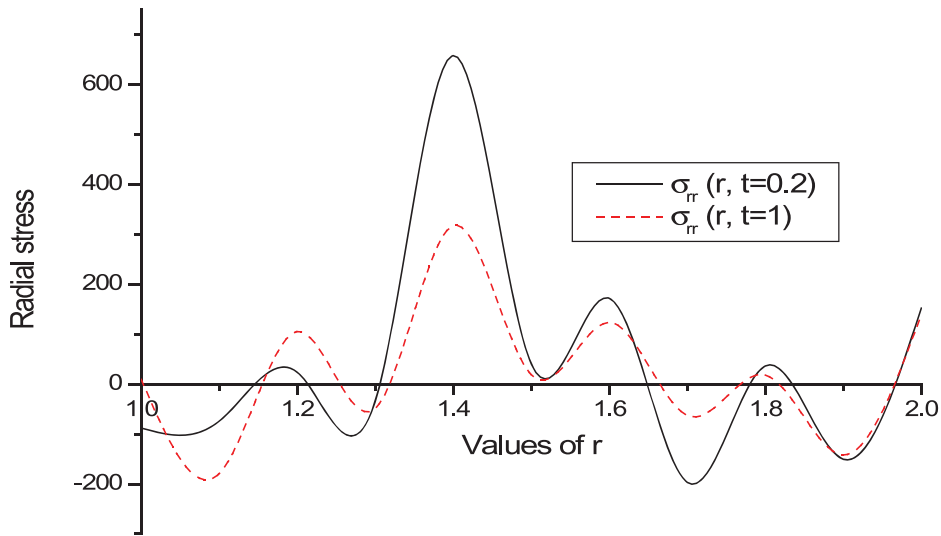


Figure 13. Distribution of radial stress with respect to r for different values of t (for instantaneous heat source).

distribution of radial stress with respect to distance for different values of time is shown. The graph representing time 1 sec is more dominating than the graph representing time 0.2 sec.

11. Conclusion

In this work, the effect of magnetic field on the thermoelastic interaction in a transversely isotropic rotating hollow cylinder has been investigated in the context of nonclassical theory of thermoelasticity. In presence of various heat sources at the external surface of the cylinder, the displacement and radial stress are derived and discussed.

The analysis of graphs permits some concluding remarks:

- i. Phase lag due to heat flux is much dominating factor in comparison with other phase lags.
- ii. For constant heat source, radial stress decreases when time increases.
- iii. For periodically varying heat source displacement and radial stress are harmonic in nature. Displacement decreases when time increases.
- iv. For instantaneous heat source displacement is converging to zero. Radial stress decreases when time increases.
- v. For all types of heat sources, displacement increases due to rotation and decreases due to magnetic effect whereas radial stress decreases due to rotation and increases due to magnetic effect.

The results presented in this article should prove useful for researchers in material science, designers of new materials, physicists as well as for those working on the development of magneto-thermoelasticity and in practical situations as in geophysics, optics, acoustics, geomagnetic, etc. The used method in this article is applicable to a wide range of problems in thermodynamics and thermoelasticity. This study may be useful for determining the strength and load carrying ability and engineering structures, including buildings, bridges, cars, planes and thousands of machine parts that most of us never see. It is especially important in the fields of mechanical, civil, aeronautical, and materials engineering.

Disclosure statement

There is no conflict of interests.

ORCID

Siddhartha Biswas  <http://orcid.org/0000-0002-3599-3431>

References

- Abbas, I. A., and M. I. A. Othman. 2012. Generalized thermoelasticity of thermal shock problem in an isotropic hollow cylinder and temperature dependent elastic moduli. *Chinese Physics B* 21 (1):14601–14606. doi:10.1088/1674-1056/21/1/014601.
- Abd-Alla, A. M., and S. R. Mahmoud. 2010. Magneto-thermoelastic problem in rotating non-homogeneous orthotropic hollow cylinder under the hyperbolic heat conduction model. *Meccanica* 45 (4):451–462. doi:10.1007/s11012-009-9261-8.
- Abouelregal, A. E. 2013. Generalized thermoelastic infinite transversely isotropic body with cylindrical cavity due to moving heat source and harmonically varying heat. *Meccanica* 48:1731–1745. doi:10.1007/s11012-013-9705-z.
- Banik, S., and M. Kanoria. 2012. Effect of three-phase-lag on two-temperature generalized thermoelasticity for infinite medium with spherical cavity. *Applied Mathematics and Mechanics* 33 (4):483–498. doi:10.1007/s10483-012-1565-8.
- Bhattacharya, S., G. K. Ananthasuresh, and A. Ghosal. 2018. Design of a one-dimensional flexible structure for desired load-bearing capability and axial displacement. *Mechanics Based Design of Structures and Machines* 46 (3):376–399. doi:10.1080/15397734.2018.1439755.
- Biot, M. A. 1956. Thermoelasticity and irreversible thermodynamics. *Journal of Applied Physics* 27 (3):240–253. doi:10.1063/1.1722351.
- Brack, L. 1999. Programs for fast numerical inversion of Laplace transforms in MATLAB language environment. *Proceedings of the 7th conference MATLAB'99, Czech Republic Prague*. 27–39. Prague: Czech Republic.
- Cattaneo, C. 1958. A form of heat equation which eliminates the paradox of instantaneous propagation. *Campptes Rendus de l'Academie Des Sciences Serie Ila: Sciences de la Terre et Des Planets* 247:431–433.
- Chandrasekharaiah, D. S. 1986. Thermoelasticity with second sound: A review. *Applied Mechanics Reviews* 39: 355–376. doi:10.1115/1.3143705.
- Chandrasekharaiah, D. S. 1998. Hyperbolic thermoelasticity: A review of recent literature. *Applied Mechanics Reviews* 51 (12):705–729. doi:10.1115/1.3098984.
- Chandrasekharaiah, D. S., and H. R. Keshavan. 1992. Axisymmetric thermoelastic interactions in an unbounded body with cylindrical cavity. *Acta Mechanica* 92 (1–4):61–76. doi:10.1007/BF01174167.
- Choudhuri, S. K. R. 2007. On thermoelastic three phase lag model. *Journal of Thermal Stresses* 30 (3):231–238. doi:10.1080/01495730601130919.
- Das, P., A. Kar, and M. Kanoria. 2013. Analysis of magneto-thermoelastic response in a transversely isotropic hollow cylinder under thermal shock with three phase lag effect. *Journal of Thermal Stresses* 36 (3):239–258. doi:10.1080/01495739.2013.765180.
- Green, A. E., and K. A. Lindsay. 1972. Thermoelasticity. *Journal of Elasticity* 2 (1):1–7. doi:10.1007/BF00045689.
- Green, A. E., and P. M. Naghdi. 1993. Thermoelasticity without energy dissipation. *Journal of Elasticity* 31 (3): 189–208. doi:10.1007/BF00044969.
- Hetnarski, R. B., and J. Ignaczak. 1993. Generalized thermoelasticity: Closed form solutions. *Journal of Thermal Stresses* 16 (4):473–498. doi:10.1080/014957399280832.
- Hetnarski, R. B., and J. Ignaczak. 1996. Soliton like waves in a low temperature non-linear thermoelastic solid. *International Journal of Engineering Science* 34 (15):1767–1787. doi:10.1016/S0020-7225(96)00046-8.
- Huang, E. 2018. Simulation of friction and stiction in multibody dynamics model problems. *Mechanics Based Design of Structures and Machines* 46 (3):296–317. doi:10.1080/15397734.2017.1341840.
- Ignaczak, J., and R. B. Hetnarski. 2014. Generalized thermoelasticity: Mathematical formulation. In *Encyclopedia of thermal stresses*, ed. R. B. Hetnarski, 1974–1986. Dordrecht, Netherlands: Springer.
- Kar, A., and M. Kanoria. 2007. Thermoelastic interaction with energy dissipation in an unbounded body with a spherical hole. *International Journal of Solids and Structures* 44 (9):2961–2971. doi:10.1016/j.ijsolstr.2006.08.030.
- Kar, A., and M. Kanoria. 2009. Generalized thermoelastic functionally graded orthotropic hollow sphere under thermal shock with three-phase-lag effect. *European Journal of Mechanics A/Solids* 39:757–767. doi:10.1016/j.euromechsol.2009.01.003.

- Kumar, R., and S. Mukhopadhyay. 2009. Effect of three phase lags on generalized thermoelasticity for an infinite medium with a cylindrical cavity. *Journal of Thermal Stresses* 32 (11):1149–1165. doi:10.1080/01495730903249185.
- Lord, H. W., and Y. Shulman. 1967. A generalized dynamical theory of thermoelasticity. *Journal of the Mechanics and Physics of Solids* 15 (5):299–309. doi:10.1016/0022-5096(67)90024-5.
- Mukhopadhyay, S., and R. Kumar. 2008a. A study of generalized thermoelastic interactions in an unbounded body with a spherical cavity. *Computers and Mathematics with Applications* 56 (9):2329–2339. doi:10.1016/j.camwa.2008.05.031.
- Mukhopadhyay, S., and R. Kumar. 2008b. A problem on thermoelastic interactions in an infinite medium with a cylindrical hole in generalized thermoelasticity. *Journal of Thermal Stresses* 31 (5):455–475. doi:10.1080/01495730801912561.
- Othman, M. I. A., and I. A. Abbas. 2012. Generalized thermoelasticity of thermal shock problem in a non-homogeneous isotropic hollow cylinder with energy dissipation. *International Journal of Thermophysics* 33 (5):913–923. doi:10.1007/s10765-012-1202-4.
- Othman, M. I. A., and I. A. Abbas. 2015. Effect of rotation on a magneto-thermoelastic hollow cylinder with energy dissipation using finite element method. *Journal of Computational and Theoretical Nanoscience* 12 (9):2399–2404. doi:10.1166/jctn.2015.4039.
- Othman, M. I. A., Y. D. Elmaklizi, and N. T. Mansour. 2017. The effect of temperature dependent properties on generalized magneto-thermoelastic with two-temperature under three-phase-lag model. *Multidiscipline Modeling in Materials and Structures* 13 (1):122–134. doi:10.1108/MMMS-08-2017-0086.
- Quintanilla, R., and R. Racke. 2008. A note on stability in three phase lag heat conduction. *International Journal of Heat and Mass Transfer* 51 (1–2):24–29. doi:10.1016/j.ijheatmasstransfer.2007.04.045.
- Roychoudhury, S. K., and N. Bandyopadhyay. 2005. Thermoelastic wave propagation in rotating elastic medium without energy dissipation. *International Journal of Mathematics and Mathematical Sciences* 2005 (1):99–107. doi:10.1155/IJMMS.2005.99.
- Said, S. M. 2015. Deformation of a rotating two-temperature generalized magneto-thermoelastic medium with internal heat source due to hydrostatic initial stress. *Meccanica* 50 (8):2077–2091. doi:10.1007/s11012-015-0136-x.
- Said, S. M. 2016a. Influence of gravity on generalized magneto-thermoelastic medium for three-phase-lag model. *Journal of Computational and Applied Mathematics* 291:142–151. doi:10.1016/j.cam.2014.12.016. [Mismatch] DOI: 10.1016/j.cam.2014.12.016.
- Said, S. M. 2016b. Wave propagation in a Magneto-Micropolar thermoelastic medium with two temperatures for three-phase-lag model. *Computers, Materials and Continua* 52 (1):1–24. doi:10.3970/cm.2016.052.001.
- Said, S. M. 2017. A fiber-reinforced thermoelastic medium with an internal heat source due to hydrostatic initial stress and gravity for the three-phase-lag model. *Multidiscipline Modeling in Materials and Structures* 13 (1):83–99. doi:10.1108/MMMS-08-2016-0040.
- Schoenberg, M., and D. Censor. 1973. Elastic waves in rotating media. *Quarterly of Applied Mathematics* 31:115–125. doi:10.1090/qam/99708.
- Sherief, H. H., and W. E. Raslan. 2016. Thermoelastic interactions without energy dissipation in an unbounded body with a cylindrical cavity. *Journal of Thermal Stresses* 39 (3):326–332. doi:10.1080/01495739.2015.1125651.
- Sun, W., X. Yan, and F. Gao. 2018. Analysis of frequency-domain vibration response of thin plate attached with viscoelastic free layer damping. *Mechanics Based Design of Structures and Machines* 46 (2):209–224. doi:10.1080/15397734.2017.1327359.
- Tzou, D. Y. 1995. A unique field approach for heat conduction from macro to micro scales. *Journal of Heat Transfer* 117 (1):8–16. doi:10.1115/1.2822329.
- Yang, S., and J. Lin. 2018. A theoretical study of the mechanism with variable compression ratio and expansion ratio. *Mechanics Based Design of Structures and Machines* 46 (3):267–284. doi:10.1080/15397734.2017.1332526.
- Youssef, H. M. 2006. Problem of generalized thermoelastic infinite cylindrical cavity subjected to a ramp-type heating and loading. *Archive of Applied Mechanics* 75 (8–9):553–565. doi:10.1007/s00419-005-0440-3.

Appendix

We now outline the numerical inversion method (Branck 1999) used to find the solutions in the physical domain.

An n dimensional Laplace Transform of a real function $f(t)$, with $t = (t_1, t_2, \dots, t_n)$ as a row vector of n real variables, is defined as

$$F(s) = \int_0^{\infty} \dots \int_0^{\infty} (n\text{-fold}) \int_0^{\infty} f(t) \exp(-st^{tr}) \prod_{i=1}^n dt_i, \quad (A1)$$

where $s = (s_1, s_2, \dots, s_n)$ and tr means transposition.

Under an assumption $|\bar{f}(t)| < \chi \exp(\alpha t^r)$, with χ real positive and $\alpha = (\alpha_1, \dots, \alpha_n)$ being a minimal abscissa of convergence, and the nD Laplace Transform $F(s)$ defined on a region $\{s \in c^n : \text{Re}[s] > \alpha\}$ with $c = (c_1, c_2, \dots, c_n)$ as an abscissa of convergence and the inequality taken component wise, the original function is given by an n -fold Bromwich integral

$$f(t) = \frac{1}{(2\pi j)^n} \int_{c_1 - j\infty}^{c_1 + j\infty} \dots \int_{c_n - j\infty}^{c_n + j\infty} F(s) \exp(st^r) \prod_{i=1}^n dt_i. \tag{A2}$$

Substituting $s_i = c_i + j\omega_i$ into Eq. (A2) and using a rectangular rule of the integration, namely $\omega_i = m_i \Omega_i$ and $\Omega_i = \frac{2\pi}{\bar{\tau}_i}$ as generalized frequency steps, with τ_i forming a region of the solution, $t \in [0, \bar{\tau}_1) \times \dots \times [0, \bar{\tau}_n)$ an approximate formula is

$$\tilde{f}(t) = \exp(ct^r) \left(\prod_{i=1}^n \bar{\tau}_i^{-1} \right) \sum_{m_1=-\infty}^{\infty} \dots \sum_{m_n=-\infty}^{\infty} F(s) \exp\left(j \sum_{m=1}^n m_i \Omega_i t_i\right), \tag{A3}$$

with $s_i = c_i + jm_i \Omega_i$, for all i .

A limiting relative error δ_M of Eq. (A3) can be controlled by setting $c = (c_1, c_2, \dots, c_n)$, defining paths of the integration in Eq. (A2) namely

$$c_i = \alpha_i - \frac{1}{\bar{\tau}_i} \ln \left(1 - \frac{1}{\sqrt{1 + \delta_M n}} \right) \approx \alpha_i - \frac{1}{\bar{\tau}_i} \ln \frac{\delta_M}{n}, \tag{A4}$$

for $i = 1, 2, \dots, n$ and while keeping the equalities $\bar{\tau}_1(c_1 - \alpha_1) = \bar{\tau}_2(c_2 - \alpha_2) = \dots = \bar{\tau}_n(c_n - \alpha_n)$.

The simplification in Eq. (A4) is enabled due to small values δ_M considered in practice. The last equation is used for setting up parameters of the nD NILT method relating them to a limiting relative error δ_M required for practical computations.

The technique of practical evaluation of the n -fold infinite sum Eq. (A3) follows from the properties of the n -fold Bromwich integral Eq. (A2), namely, we can arrange it into the form

$$f(t_1, t_2, \dots, t_n) = \frac{1}{2\pi j} \int_{c_1 - j\infty}^{c_1 + j\infty} \left(\frac{1}{2\pi j} \int_{c_2 - j\infty}^{c_2 + j\infty} \left(\dots \frac{1}{2\pi j} \int_{c_n - j\infty}^{c_n + j\infty} F(s_1, s_2, \dots, s_n) e^{s_n t_n} ds_n \dots \right) e^{s_2 t_2} ds_2 \right) e^{s_1 t_1} ds_1, \tag{A5}$$

or shortly

$$f(t_1, t_2, \dots, t_n) = L_1^{-1} \left[L_2^{-1} \left[\dots L_n^{-1} F[(s_1, s_2, \dots, s_n)] \dots \right] \right]. \tag{A6}$$

Although the order of the integration may be arbitrary on principle, here the above one will be used for an explanation. Similarly Eq. (A3) can be rewritten as

$$\tilde{f}(t_1, t_2, \dots, t_n) = \frac{e^{c_1 t_1}}{\bar{\tau}_1} \sum_{m_1=-\infty}^{\infty} \left(\frac{e^{c_2 t_2}}{\bar{\tau}_2} \sum_{m_2=-\infty}^{\infty} \left(\dots \frac{e^{c_n t_n}}{\bar{\tau}_n} \sum_{m_n=-\infty}^{\infty} F(s_1, s_2, \dots, s_n) e^{jm_n \Omega_n t_n} \dots \right) e^{jm_2 \Omega_2 t_2} \right) e^{jm_1 \Omega_1 t_1}, \tag{A7}$$

with $s_i = c_i + jm_i \Omega_i$. If we define $F_n \equiv F(s_1, s_2, \dots, s_n), \dots$ and $F_0 \equiv f(t_1, \dots, t_n)$, then n consequential partial inversions are performed as

$$\begin{aligned} L_n^{-1}(F_n) &= F_{n-1}(s_1, \dots, s_{n-1}, t_n), \\ L_{n-1}^{-1}(F_{n-1}) &= F_{n-2}(s_1, \dots, t_{n-1}, t_n), \end{aligned} \tag{A8}$$

.....

$$L_1^{-1}(F_1) = f(t_1, \dots, t_{n-1}, t_n)$$

As is obvious we need to use a procedure able to make the inversion of Laplace Transform dependent on other $(n-1)$ parameters, complex in general. Let us denote arguments in Eq. (A8) by $p_i = (p_1, \dots, p_{n-1}, p_n)$.

Then the ILT of the type

$$F_{i-1}(p_{i-1}) = L_i^{-1}(F_i(p_i)) = \frac{1}{2\pi j} \int_{c_i - j\infty}^{c_i + j\infty} F_i(p_i) e^{s_i t_i} ds_i, \tag{A9}$$

can be used n times, $i = n, n-1, \dots, 1$ to evaluate Eq. (A8) with $p_n = (s_1, \dots, s_{n-1}, s_n), p_{n-1} = (s_1, s_2, \dots, s_{n-1}, t_n), \dots, p_1 = (s_1, \dots, t_{n-1}, t_n)$ and $p_0 = (t_1, \dots, t_{n-1}, t_n)$, while $p_j = s_j$ for $j \leq i$ and $p_j = t_j$ otherwise.

A further technique is based on demand to find the solution on a whole region of discrete points. Then, taking into account $t_{ik} = kT_i$ in Eq. (A9) with T_i as the sampling periods in the original domain, we can write the approximate formula

$$\tilde{F}_{i-1}(p_{i-1}) = \frac{e^{c_i k T_i}}{\bar{\tau}_i} \sum_{n=-\infty}^{\infty} \tilde{F}_i(p_i) e^{j2\pi n k T_i / \bar{\tau}_i}, \quad (\text{A10})$$

$i = n, n-1, \dots, 1$ and with $\Omega_i = \frac{2\pi}{\bar{\tau}_i}$ substituted. As follows from the error analysis a relative error is predictable on the region $O_{err} = [0, \bar{\tau}_1] \times \dots \times [0, \bar{\tau}_n]$. For $k = 0, 1, 2, \dots, M_i - 1$, $i = 1, \dots, n$, a maximum reachable region is $O_{max} = [0, (M_1 - 1)T_1] \times \dots \times [0, (M_n - 1)T_n]$. Thus, to meet the necessity condition $O_{max} \subset O_{err}$ we can set up fittingly $\bar{\tau}_i = M_i T_i$, $i = 1, 2, \dots, n$. In practice, a region of the calculation is chosen to be $O_{cal} = [O, t_{1cal}] \times \dots \times [O, t_{ncal}]$ with $t_{ical} = (M_i/2 - 1)T_i$, $i = 1, \dots, n$ to provide certain margins.



Source details

[Feedback](#) > [Compare sources](#) >

Mechanics Based Design of Structures and Machines

Formerly known as: [Mechanics of Structures and Machines](#)

Scopus coverage years: from 2003 to Present

Publisher: Taylor & Francis

ISSN: 1539-7734 E-ISSN: 1539-7742

Subject area: [Mathematics: General Mathematics](#) [Engineering: Ocean Engineering](#) [Engineering: Aerospace Engineering](#) [Engineering: Mechanical Engineering](#) [Engineering: Civil and Structural Engineering](#) [Engineering: Automotive Engineering](#) [Engineering: Mechanics of Materials](#) [View all](#) v

Source type: Journal

[View all documents](#) >

[Set document alert](#)

[Save to source list](#)

CiteScore 2022 **9.4** [i](#)

SJR 2022 **0.646** [i](#)

SNIP 2022 **1.433** [i](#)

[CiteScore](#) [CiteScore rank & trend](#) [Scopus content coverage](#)



Improved CiteScore methodology



CiteScore 2022 counts the citations received in 2019-2022 to articles, reviews, conference papers, book chapters and data papers published in 2019-2022, and divides this by the number of publications published in 2019-2022. [Learn more](#) >

Theory of Generalized Thermoelasticity with Memory-Dependent Derivatives

Soumen Shaw¹

Abstract: This paper theoretically demonstrates two aspects of a generalized heat conduction model with memory-dependent derivatives. The characteristics of transient effects in an isotropic, thermoelastic medium were analyzed in terms of memory-dependent thermoelasticity theory. The Lord–Shulman (LS) model gives an upper bound of thermal disturbances in a memory-dependent generalized thermoelasticity model. For numerical implementation, a one-dimensional semi-infinite medium with one end subjected to a transient load was considered. An integral transform method and, while in inverse transformation, an efficient and pragmatic numerical inverse Laplace transform (NILT) were adopted. Parameter studies were performed to evaluate the effect of the kernel function and time delay. An appropriate Lyapunov function, which is a significant scheme to study numerous qualitative properties, is proposed. DOI: 10.1061/(ASCE)EM.1943-7889.0001569. © 2019 American Society of Civil Engineers.

Author keywords: Memory-dependent derivative; Nonlocal thermoelasticity theory; Transient load; Lyapunov function.

Introduction

Nonlocal continuum field theories are concerned with the physics of material bodies whose behavior at a material point is influenced by the state of all points of the body. The nonlocal theory generalizes the classical field theory in two respects: (1) the energy balance law is considered valid globally; and (2) the state of the body at a material point is described by the response functional. In this description, nonlocality in time is known as memory dependence. The theory of heat conduction in continuous media with memory has drawn the attention of many researchers. Initially, the motivation was to avoid the unpleasant feature of the classical coupled heat conduction model in which the thermal disturbance produced at some point in the body is felt instantaneously at all other points. This contradicts the fact that energy cannot propagate at a speed exceeding the velocity of light.

Various physical interpretations and consequences of the classical coupled dynamic thermoelasticity theories, which were formed by the mixed parabolic-hyperbolic governing equations of Biot (1956), produced infinite speed of thermal signals. To overcome this technical issue, by incorporating the thermal time delay (i.e., thermal relaxation times) factor into the heat flux model, several researchers have attempt to modify the coupled dynamic thermoelasticity theory. These studies were based on several modifications of Fourier's law of heat conduction. The aim of enhancement was to derive hyperbolic-type partial differential equations to govern the heat conduction properties to simultaneously satisfy the following conditions: (1) finiteness of heat signal propagation speed, (2) spatial propagation of thermoelastic waves without attenuation, and (3) existence of distortionless waveforms akin to the classical d'Alembert-type waves. Cattaneo (1958) proposed a wave-type heat equation by postulating a new law of heat

conduction to replace the classical Fourier's law. Lord and Shulman (1967), Green and Lindsay (1972), and Green and Naghdi (1991) proposed three different generalized heat conduction equations which are the most discussed hyperbolic-type heat equations in the literature.

Memory-dependent derivatives (MDDs) were first incorporated in Fourier's law of heat conduction, a new hyperbolic-type heat conduction equation by Wang and Li (2011). This new generalization of hyperbolic-type heat conduction models is accepted as the modified heat conduction law with measuring memory. The present paper derives a generalized heat conduction equation with memory-dependent derivatives in the form of a Fredholm integral equation with a memory-dependent kernel. In addition, a one-dimensional thermal shock problem and a punch problem are investigated using the new memory-dependent heat conduction equation. Some parametric studies are performed to evaluate the effect of time delay and kernel function on the thermoelastic response.

Memory in Material Modeling

Scott Blair's model (Mainardi 2010), which is basically a material model, includes a formula for memory phenomena in various disciplines. The model takes the form

$${}_0D_t^\alpha \varepsilon(t) = \chi \sigma(t) \quad (1)$$

where ${}_0D_t^\alpha \varepsilon(t)$ = fractional (fractional-order) derivative which depends on the strain history from 0 to t , where ${}_0D_t^\alpha \varepsilon(t) = D^n \varepsilon(t) = d^n/dt^n \varepsilon(t)$ if α is an integer n ; and χ = positive constant.

A fractional-order derivative is a generalization of an integer-order derivative and integral. It originated from a letter of L'Hôpital to Leibnitz in 1695 regarding the meaning of the half-order derivative. It is a promising tool for describing memory phenomena (Rossikhin and Shitikova 2011; Stiasnie 1979). The kernel function of a fractional derivative is termed the memory function, but it does not replicate any physical process. Imprecise physical meaning has been a big obstacle that keeps fractional derivatives lagging far behind the integer-order calculus.

There are several definitions of a fractional derivative. The Riemann–Liouville derivative is one of most standard definitions

¹Research Associate, Dept. of Mathematics, Indian Institute of Engineering Science and Technology, Shibpur, Howrah, West Bengal 711103, India. Email: shaw_soumen@rediffmail.com

Note. This manuscript was submitted on April 24, 2018; approved on August 22, 2018; published online on January 3, 2019. Discussion period open until June 3, 2019; separate discussions must be submitted for individual papers. This paper is part of the *Journal of Engineering Mechanics*, © ASCE, ISSN 0733-9399.

$${}_0D_t^\alpha \varepsilon(t) = \frac{1}{\Gamma(m-\alpha)} \frac{d^m}{dt^m} \int_0^t \frac{\varepsilon(\tau)}{(t-\tau)^{\alpha+1-m}} d\tau \quad (2)$$

where Γ = Euler's gamma function; and m = integer satisfying $m-1 \leq \alpha < m$. A memory process generally consists of two stages. The first is short, with permanent retention at the beginning, and it cannot be neglected in general; the second is governed by the fractional model Eq. (1). The critical point between the fresh stage and the working stage is usually not the origin. This is quite different from the traditional fractional models of one stage.

The key point is that the order of a fractional derivative is an index of memory. The dimensionless form of the solution of Eq. (1) is

$$E = \tau^\alpha - (\tau - 1)^\alpha \quad (3)$$

where $\tau = t/t_M$; and $E(\tau) = \varepsilon(t)/\varepsilon_M$, where ε_M = strain at the end of time of creeping $t = t_M$. The dimensionless relation E increases with an increase of α . The higher the value of the index α , the slower is the forgetting during the process. In particular, at $\alpha = 0$, $E = 0$ (nothing is memorized), and $E = 1$ (nothing is forgotten) if $\alpha = 1$. Therefore, the fractional order α is defined as the index of memory.

For a standard creep and recovery process, the specimen is usually loaded under a constant stress $\sigma(t) = \sigma_0$ from 0 to t_M , and the load is removed at the instant $t = t_M$; then $\sigma(t) = 0$ for $t \geq t_M$. If $H(t)$ is the Heaviside function, Eq. (1) takes the following form:

$${}_0D_t^\alpha \varepsilon(t) = \chi \sigma_0 (H(t) - H(t - t_M)) \quad (4)$$

where ${}_0D_t^\alpha \varepsilon(t)$ = Riemann–Liouville fractional-order derivative with zero initial condition. The superposition method gives the solution of Eq. (4) as follows:

$$\varepsilon(t) = \frac{\chi \sigma_0}{\Gamma(\alpha + 1)} (t^\alpha H(t) - (t - t_M)^\alpha H(t - t_M)) \quad (5)$$

This is in agreement with the early observation of the behavior of some viscoelastic materials.

Eq. (1) works not only in modeling viscoelastic materials, but also in modeling biological kinetics with memory. For example, for protein adsorption kinetics, if the symbols σ and ε are replaced with the concentration c and the surface density Γ of fibronectin therein, respectively, then

$$\sigma(t) = \sigma_0 [H(t) - H(t - t_M) + H(t - t_N)] \quad (6)$$

where $\sigma_0 = 50 \mu\text{g/ml}$; $t_M = 240 \text{ s}$; and $t_N = 1,150 \text{ s}$. The absorbed density is found to be

$$\varepsilon(t) = \frac{\chi \sigma_0}{\Gamma(\alpha + 1)} (t^\alpha H(t) - (t - t_M)^\alpha H(t - t_M) + (t - t_N)^\alpha H(t - t_N)) \quad (7)$$

Memory-Dependent Derivatives

In the last decade, non-integral (fractional)-order derivatives and fractional differential equations have gained considerably more attention in the fields of applied sciences and various engineering disciplines (e.g., Ezzat 2010; Shaw and Mukhopadhyay 2011, 2016). Sabatier et al. (2007), Hilfer (2000), and Atanacković et al. (2014) provided diverse theoretical advances and recent applications of fractional calculus. One hindrance to the wider use of fractional-order methods by engineers is the absence of a simple geometric picture for the fractional-order integral. There are several definitions of fractional derivatives (e.g., Riemann–Liouville,

Caputo, Reisz, and Grunwald–Letnikov), each of which has specific advantages and limitations, particularly when used to define a distribution of fluxes into a control volume or the effects of fading memory on the forces applied in a free body diagram. Diethelm (2010) incorporated a kernel function and modified a Caputo-type fractional-order derivative as

$$D_a^\alpha f(t) = \int_a^t k_\alpha(t-\xi) f^{(m)}(\xi) d\xi \quad (8)$$

where $k_\alpha(t-\xi)$ = kernel function; and $f^{(m)}$ = m th order derivative. In applications, $k_\alpha(t-\xi)$ takes some specific form

$$k_\alpha(t-\xi) = \frac{(t-\xi)^{m-\alpha-1}}{\Gamma(m-\alpha)} \quad (9)$$

Wang and Li (2011) proposed another form of the fractional derivative with arbitrary kernel over a slipping interval as follows:

$$D_\omega^{(1)} f(x, t) = \frac{1}{\omega} \int_{t-\omega}^t k(t-\xi) f'(x, \xi) d\xi \quad (10)$$

where ω = time delay; and $k(t-\xi)$ = kernel function. Both can be chosen freely.

The preceding modifications of fractional-ordered derivatives are termed memory-dependent derivatives.

This paper uses the following definition of memory dependent derivative:

Definition: For a differentiable function $f(t)$, the m th order memory-dependent derivative of the function $f(t)$ relative to the time delay $a > 0$ is defined as

$$D_a^{(m)} f(t) = \frac{1}{a} \int_{t-a}^t k(t, p) f^{(m)}(p) dp \quad (11)$$

where the time delay a denotes the memory scale; and the kernel function $k(t, p)$ must be a differentiable function with respect to its arguments. The kernel function and the memory scales must be chosen in such a way that they are compatible with the physical problem, so this type of derivative provides more possibilities to capture the material response. In this process, a nonlocality effect comes into play in the theory of thermodynamics (Shaw and Mukhopadhyay 2017; Banerjee et al. 2018).

Thermoelasticity Model Based on Memory-Dependent Derivatives

From the Maxwell–Cattaneo theory to Green–Naghdi generalized thermoelasticity models, it is well established that thermal memory has a significant role in the theory of thermoelasticity (Shaw 2017). In the 21st century, memory components have been introduced in terms of fractional-order derivatives in numerous forms, as follows:

1. Sherief et al. (2010) introduced fractional derivatives in the heat flux laws and modified Fourier's law in the following manner:

$$q_i + \tau^\alpha \frac{\partial^\alpha}{\partial t^\alpha} q_i = -K\theta_{,i}, \quad 0 < \alpha \leq 1 \quad (12)$$

2. Youssef (2010) introduced a fractional integral into the heat flow relation

$$q_i + \tau q_i = -KI^{\alpha-1} \theta_{,i}, \quad 0 < \alpha \leq 2 \quad (13)$$

3. Ezzat and Fayik (2011) adopted the generalized fractional-order Taylor series expansion

$$q_i + \frac{\tau^\alpha}{\alpha!} \frac{\partial^\alpha}{\partial t^\alpha} q_i = -K\theta_{,i}, \quad 0 < \alpha \leq 1 \quad (14)$$

In these fractional models of modified heat flux laws, the memory response is described by the fractional index parameter.

Yu et al. (2014) introduced memory-dependent derivatives in the heat conduction law in the following way:

$$q_i + \tau D_a q_i = -K\theta_{,i} \quad (15)$$

where

$$D_a q_i = D_a^{(1)} q_i = \frac{1}{a} \int_{t-a}^t k(t, p) q_i^{(1)}(p) dp \quad (16)$$

where the kernel $k(t, p)$ and the time delay a may be chosen arbitrarily, which provides more possibilities to capture the material's physical characteristics.

Eq. (15) provides the following advantages compared with the aforementioned amendments of Fourier's law by using fractional derivatives: (1) the influence of memory dependency claims its superiority in terms of memory scale parameter; (2) in a limiting sense, this simplification develops the Lord-Shulman model of generalized thermoelasticity; and (3) because the kernel function and the memory scale parameters may be chosen subjectively, it is more malleable in many practical applications.

In general, the kernel function takes the following form:

$$k(t, p) = \left(\frac{p-t}{a} + 1 \right)^b \quad (17)$$

For $b = 0, 1$, and 2 , the kernel is called constant, linear, or parabolic, respectively, and accordingly Eq. (15) takes the respective forms

$$q(x, t) + \frac{\tau}{a} [q(x, t) - q(x, t-a)] = -K \frac{\partial \theta(x, t)}{\partial x} \quad (18a)$$

$$\left(1 + \frac{\tau}{a} \right) q(x, t) - \frac{\tau}{a^2} \int_{t-a}^t q(x, p) dp = -K \frac{\partial \theta(x, t)}{\partial x} \quad (18b)$$

$$\left(1 + \frac{\tau}{a} \right) q(x, t) - \frac{2\tau}{a^2} \left[\left(\frac{p-t}{a} + 1 \right) \int_{p=t-a}^t q(x, p) dp \right]^t - \int_{p=t-a}^t \left[\frac{2\tau}{a^3} \int q(x, p) dp \right] dp = -K \frac{\partial \theta(x, t)}{\partial x} \quad (18c)$$

In this respect, Shaw (2017), who studied generalized thermoelasticity with memory-dependent derivatives, showed how MDDs have a significant impact in thermoelasticity theory.

Applications

With a new memory-dependent generalized thermoelasticity model based upon memory-dependent derivatives established, this section provides an alternative approach to describe memory dependence, which has been commonly depicted by the fractional generalized thermoelasticity model. Transient wave propagation in an isotropic thermoelastic half-space with the memory-dependent generalized thermoelasticity model and some parametric studies are performed to determine the effect of memory and kernel function on the thermoelasticity response.

Governing Equations

In the absence of heat sources, the equation for energy conservation may be expressed as follows:

$$q_{i,i} = -\rho T_0 \dot{\eta} \quad (19)$$

where ρ , T_0 , and η = mass density, reference temperature, and entropy density, respectively.

The equation of motion may be written

$$\sigma_{ij,j} + f_i = \rho \ddot{u}_i \quad (20)$$

where σ_{ij} = stress tensor; u_i = displacement vector; and f_i = component of body forces.

The constitutive equation for linear isotropic thermoelastic medium may be described as

$$\begin{aligned} \sigma_{ij} &= \lambda \varepsilon_{kk} \delta_{ij} + 2\mu \varepsilon_{ij} - \gamma \theta \delta_{ij} \\ \rho \eta &= \gamma \varepsilon_{kk} + \frac{\rho C_e}{T_0} \theta \end{aligned} \quad (21)$$

where λ and μ = Lamé constants, where $\gamma = (3\lambda + 2\mu)\alpha_t$, where α_t = coefficient of linear thermal expansion; C_e = specific heat at constant strain; and

$$\varepsilon_{ij} = \frac{1}{2} (u_{i,j} + u_{j,i}) \quad (22)$$

represents the strain measures.

Appropriate boundary conditions associated with the preceding governing equations must be adopted for a well-posed problem. The displacement and temperature are prescribed on the two subregions of the surface, A_u and A_θ , respectively, as

$$\begin{aligned} u_i &= \bar{u}_i \text{ on } A_u \\ \text{and } \theta_i &= \bar{\theta}_i \text{ on } A_\theta \end{aligned}$$

where \bar{u}_i and $\bar{\theta}_i$ = prescribed values.

On the other hand, if surface traction and surface flux are applied to the corresponding surfaces A_σ and A_q , then

$$\begin{aligned} \sigma_{ij} n_j &= \bar{T}_i \text{ on } A_\sigma \\ \text{and } q_i n_i &= \bar{Q} \text{ on } A_q \end{aligned}$$

where \bar{T}_i and \bar{Q} = given surface traction and flux, respectively.

Memory Response in Solution of Thermoelastic Problems

Thermal Shock Problem

This section considers a slim strip problem of a thermoelastic medium which is assumed to be unstrained and unstressed initially. The dimension in one direction (the x -direction) is much greater than that in the other direction, so the problem may be simplified as a one-dimensional problem. The boundary at one end is traction-free while subjected to the instantaneous thermal shock $T_0 \delta(t)$, and it is further assumed that neither elastic waves nor heat reach the other end during the analysis. Therefore the problem can ultimately be viewed as a one-dimensional semi-infinite traction-free medium with instantaneous thermal loading $T_0 \delta(t)$ at one end, which is mathematically expressed as the following initial boundary conditions:

$$\begin{aligned}
u(x, t) = \dot{u}(x, t) = 0, \quad \theta(x, t) = \dot{\theta}(x, t) = 0 \quad \text{at } t = 0 \\
\sigma(x, t) = 0, \quad \theta(x, t) = T_0 \delta(t) \quad \text{at } x = 0 \\
u(x, t) \rightarrow 0, \quad \theta(x, t) \rightarrow 0 \quad \text{as } x \rightarrow \infty, \quad t > 0
\end{aligned} \tag{23}$$

In terms of memory-dependent generalized thermoelasticity, to solve the problem, one may obtain the governing equations from the Eqs. (18)–(20) in terms of the displacement component u and temperature θ as follows:

$$(\lambda + 2\mu) \frac{\partial^2 u(x, t)}{\partial x^2} - \gamma \frac{\partial \theta(x, t)}{\partial x} = \rho \frac{\partial^2 u(x, t)}{\partial t^2} \tag{24}$$

$$\begin{aligned}
\left(1 + \frac{\tau}{a}\right) \left[\gamma T_0 \frac{\partial^2 u(x, t)}{\partial x \partial t} + \rho C_e \frac{\partial \theta(x, t)}{\partial t} \right] \\
- \frac{\tau}{a} \left[\gamma T_0 \frac{\partial^2 u(x, t-a)}{\partial x \partial t} + \rho C_e \frac{\partial \theta(x, t-a)}{\partial t} \right] = K \frac{\partial^2 \theta(x, t)}{\partial x^2}
\end{aligned} \tag{25}$$

For convenience, the following dimensionless quantities are introduced:

$$\begin{aligned}
(\bar{x}, \bar{u}) &= n_1 n_2(x, u) \\
(\bar{t}, \bar{\tau}, \bar{a}) &= n_1^2 n_2(t, \tau, a) \\
\bar{\sigma}_{ij} &= \frac{\sigma_{ij}}{\mu}, \quad \bar{\theta} = \frac{\theta}{T_0}, \quad \text{where } n_1 = \sqrt{\frac{\lambda + 2\mu}{\rho}}, \quad n_2 = \frac{\rho C_e}{K}
\end{aligned}$$

Eqs. (24) and (25) may be recast in the following manner (the bars of dimensionless quantities have been left out for brevity):

$$\beta_1 \left(\frac{\partial^2 u(x, t)}{\partial x^2} - \frac{\partial^2 u(x, t)}{\partial t^2} \right) = \beta_2 \frac{\partial \theta(x, t)}{\partial x} \tag{26}$$

$$\begin{aligned}
\frac{\partial^2 \theta(x, t)}{\partial x^2} &= \left(1 + \frac{\tau}{a}\right) \frac{\partial \theta(x, t)}{\partial t} - \frac{\tau}{a} \frac{\partial \theta(x, t-a)}{\partial t} \\
&+ g \left[\left(1 + \frac{\tau}{a}\right) \frac{\partial^2 u(x, t)}{\partial x \partial t} - \frac{\tau}{a} \frac{\partial^2 u(x, t-a)}{\partial x \partial t} \right]
\end{aligned} \tag{27}$$

where

$$\beta_1 = \lambda + 2\mu, \quad \beta_2 = \gamma T_0, \quad g = \frac{\gamma}{\rho C_e}$$

To solve the preceding system of coupled partial differential equations with the prescribed boundary conditions Eq. (23), the integral transformation technique is applied, and for inverse transformation, an efficient numerical inverse Laplace transform (NILT) algorithm is adopted (Appendix II).

Taking the Laplace transform with respect to the variable t and denoting $L[f(x, t); t \rightarrow s] = \hat{f}(x, s)$, from Eqs. (26) and (27) as well as considering the Laplace transforms of the corresponding initial, obtains

$$\beta_1 \left(\frac{d^2}{dx^2} - s^2 \right) \hat{u}(x, s) = \beta_2 \frac{\partial \hat{\theta}(x, s)}{\partial x} \tag{28}$$

$$\frac{d^2 \hat{\theta}}{dx^2} = h \left[\hat{\theta} + g \frac{d\hat{u}}{dx} \right], \quad \text{where } h = s - \frac{\tau}{a} s (e^{-sa} - 1) \tag{29}$$

Eliminating $\hat{\theta}(x, s)$ from Eqs. (28) and (29) obtains the following fourth-order differential equation:

$$\left(A \frac{d^4}{dx^4} + B \frac{d^2}{dx^2} + C \right) \hat{u}(x, s) = 0 \tag{30}$$

where $A = \beta_1$; $B = -\beta_1(h^2 + s^2) - \beta_2 g h$; and $C = h \beta_1 s^2$. Eq. (30) can be factorized as

$$\left(\frac{d^2}{dx^2} - k_1^2 \right) \left(\frac{d^2}{dx^2} - k_2^2 \right) \hat{u}(x, s) = 0 \tag{31}$$

where $k_i^2 (i = 1, 2)$ = root of the following characteristic equation:

$$A k^4 + B k^2 + C = 0 \tag{32}$$

Therefore the solution of Eq. (31) may of the form

$$\hat{u}(x, s) = \sum_{i=1}^2 \hat{u}_i(x, s) \tag{33}$$

where \hat{u}_i is the solution of

$$\left(\frac{d^2}{dx^2} - k_i^2 \right) \hat{u}_i(x, s) = 0, \quad i = 1, 2 \tag{34}$$

Considering the boundary condition $\hat{u}(x, s) \rightarrow 0$ as $x \rightarrow \infty$, Eq. (33) may be expressed as

$$\hat{u}(x, s) = \sum_{i=1}^2 \hat{u}_i(s) e^{-k_i x} \tag{35}$$

where k_i = root of $k^2 - k_i^2 = 0$, ($i = 1, 2$), where $\text{Re}(k_i) > 0$ (Appendix I).

Accordingly, one may express the solution of the temperature as

$$\hat{\theta}(x, s) = \sum_{i=1}^2 \hat{\theta}_i(s) e^{-k_i x} \tag{36}$$

where $\hat{u}_i(s)$ and $\hat{\theta}_i(s)$ ($i = 1, 2$) depend on the parameter s and can be determined by the prescribed boundary conditions.

Substituting Eqs. (35) and (38) into Eq. (28) obtains

$$\hat{\theta}_i(s) = -\frac{\beta_1 (k_i^2 - s^2)}{k_i \beta_2} \hat{u}_i(s) \tag{37}$$

Therefore, only two of the parameters $\hat{u}_i(s)$ or $\hat{\theta}_i(s)$ ($i = 1, 2$) need to be clarified with the help of boundary conditions in Laplace domain

$$\hat{\sigma}(x, s) = 0, \quad \hat{\theta}(x, s) = T_0 \quad \text{at } x = 0 \tag{38}$$

Introducing the solutions of the displacement and temperature into the nondimensional constitutive equation

$$\hat{\sigma}(x, s) = \beta_1 \frac{d\hat{u}(x, s)}{dx} - \beta_2 \hat{\theta}(x, s)$$

$$\text{yields } \hat{\sigma}(x, s) = \sum_{i=1}^2 \hat{\sigma}_i(s) e^{-k_i x} \tag{39}$$

where $\hat{\sigma}_i(s) = -\beta_1 k_i \hat{u}_i(s) - \beta_2 \hat{\theta}_i(s)$.

Combining Eqs. (38) and (39) with Eq. (36) obtains

$$\hat{\theta}(x=0, s) = \sum_{i=1}^2 \hat{\theta}_i(s) = T_0 \quad \text{and} \quad \hat{\sigma}(x=0, s) = \sum_{i=1}^2 \hat{\sigma}_i(s) = 0 \tag{40}$$

from which

$$\begin{aligned}\hat{\theta}_1(s) &= \frac{k_1^2 - s^2}{k_1^2 - k_2^2} T_0, & \hat{\theta}_2(s) &= -\frac{k_2^2 - s^2}{k_1^2 - k_2^2} T_0 \quad \text{and} \\ \hat{u}_1(s) &= \frac{-k_1 \beta_2}{\beta_1 (k_1^2 - k_2^2)} T_0, & \hat{u}_2(s) &= \frac{k_2 \beta_2}{\beta_1 (k_1^2 - k_2^2)} T_0\end{aligned}\quad (41)$$

Punch Problem

For a one-dimensional punch problem, the corresponding mathematical formulation can be expressed in the following form:

$$\begin{aligned}u(x, t) = \dot{u}(x, t) = 0, & \quad \theta(x, t) = \dot{\theta}(x, t) = 0 \quad \text{at } t = 0 \\ \sigma(x, t) = \sigma_0 \delta(x, t), & \quad \theta(x, t) = T_0 \quad \text{at } x = 0 \\ u(x, t) \rightarrow 0, & \quad \theta(x, t) \rightarrow 0 \quad \text{as } x \rightarrow \infty, \quad t > 0\end{aligned}\quad (42)$$

As in previous problem, the solution of the problem may be expressed in the Laplace transform domain as follows:

$$\hat{u}(x, s) = \sum_{i=1}^2 \hat{u}_i(s) e^{-k_i x}, \quad \hat{\theta}(x, s) = \sum_{i=1}^2 \hat{\theta}_i(s) e^{-k_i x} \quad (43)$$

where k_i = root of $k^2 - k_i^2 = 0$, ($i = 1, 2$), where $\text{Re}(k_i) > 0$ (Appendix I).

Satisfying the boundary conditions

$$\hat{\theta}(x=0, s) = \sum_{i=1}^2 \hat{\theta}_i(s) = \frac{T_0}{s}, \quad \hat{\sigma}(x=0, s) = \sum_{i=1}^2 \hat{\sigma}_i(s) = \sigma_0 \quad (44)$$

obtains

$$\begin{aligned}\hat{\theta}_1(s) &= \frac{k_1^2 - s^2}{s(k_1^2 - k_2^2)} \left[T_0 - \frac{\sigma_0 k_2^2 - s^2}{\beta_2 s} \right], \\ \hat{\theta}_2(s) &= -\frac{k_2^2 - s^2}{s(k_1^2 - k_2^2)} \left[T_0 + \frac{\sigma_0 k_1^2 - s^2}{\beta_2 s} \right] \quad \text{and} \\ \hat{u}_1(s) &= \frac{-k_1 \beta_2}{\beta_1 s (k_1^2 - k_2^2)} \left[T_0 - \frac{\sigma_0 k_2^2 - s^2}{\beta_2 s} \right], \\ \hat{u}_2(s) &= \frac{k_2 \beta_2}{\beta_1 s (k_1^2 - k_2^2)} \left[T_0 + \frac{\sigma_0 k_1^2 - s^2}{\beta_2 s} \right]\end{aligned}\quad (45)$$

Generalization of Memory-Dependent Heat Conduction Equations

For $b = 1$, in the expression of the kernel given by Eq. (17), the generalized heat conduction equation takes the identical form as in Eq. (29) with

$$h = \left(1 + \frac{\tau}{a} \right) s - \frac{\tau}{a^2} (1 - e^{-as}) \quad (46)$$

Therefore, in the Laplace transform domain, the displacement component satisfies the same equation

$$\left(A \frac{d^4}{dx^4} + B \frac{d^2}{dx^2} + C \right) \hat{u}(x, s) = 0$$

Similarly, for $b = 2$, the heat conduction Eq. (29) takes the modified form:

$$h = s \left(1 + \frac{\tau}{a} \right) + \frac{2\tau}{a^2} (1 - e^{-as}) \quad (47)$$

During the investigation of memory response, Ezzat (2014, 2016), Ezzat et al. (2017), and Karamany et al. (2018) proposed the expression of the kernel function in an alternative way

$$D_\omega f(t) = \frac{1}{\omega} \int_{t-\omega}^t k(t-\xi) f'(\xi) d\xi$$

where

$$k(t-\xi) = 1 - \frac{2b}{\omega} (t-\xi) + \frac{a^2 (t-\xi)^2}{\omega^2} \quad (48)$$

$$= \begin{cases} 1, & \text{if } a = b = 0 \\ 1 - \frac{t-\xi}{\omega}, & \text{if } a = 0, b = \frac{1}{2} \\ 1 - (t-\xi), & \text{if } a = 0, b = \frac{\omega}{2} \\ \left(1 - \frac{t-\xi}{\omega} \right)^2, & \text{if } a = b = 1 \end{cases} \quad (49)$$

They discussed different aspects of thermal memory for different values of the parameters a and b . To compare the results of Ezzat et al. (2017) in the framework of the present analysis, substitute $\tau_\theta = 0$, $\tau_q = \tau$, and $\tau_q^2 = 0$.

Consequently, $\hat{u}(x, s)$ satisfies the equation

$$\left(A \frac{d^4}{dx^4} + B \frac{d^2}{dx^2} + C \right) \hat{u}(x, s) = 0$$

where $A = 1$; $B = -[s^2 + s\alpha(1 + \varepsilon)]$; and $C = \alpha$

where $\alpha(s) = 1 + \frac{\tau}{\omega} G(s)$ and

$$G(s) = 1 - \frac{2b}{\omega s} + \frac{2a^2}{\omega^2 s^2} - e^{-\omega s} \left(1 - 2b + a^2 + \frac{2(a^2 - b)}{\omega s} + \frac{2a^2}{\omega^2 s^2} \right) \quad (50)$$

Numerical Computation

Nonlocality responses have developed in the expressions of displacements, temperature, and stresses. This section is confined to locating the discontinuity and the magnitudes of the increase in thermal deformation and the temperature distribution for different values of the parameters of memory kernel. Because the roots k_1^2 and k_2^2 of Eq. (32) are functions of s implicitly, analytical inversion of the Laplace transformation of the field functions is a formidable task for all values of s . To obtain the physical nature of the field functions, this paper adopts an efficient numerical technique for inversion of the Laplace transform (Appendix II).

The numerical simulation considers a copper-like material with the following physical data values: $\lambda = 77.6$ GPa, $\mu = 38.6$ GPa, $\alpha_t = 1.78 \times 10^{-5}$ m/K, $\rho = 8,945$ kg/m³, $C_e = 381$ J/(kg · K), $K = 400$ W · m⁻¹ · K⁻¹, and $T_0 = 293$ K.

Figs. 1 and 2 show that with the increasing values of the parameters of the memory-dependent kernel, the response of the heat flux into the medium is decreased, and consequently the thermal displacements are also decreased. Therefore the heat flux response into the medium can be predicted more accurately by choosing an appropriate form of the kernel function.

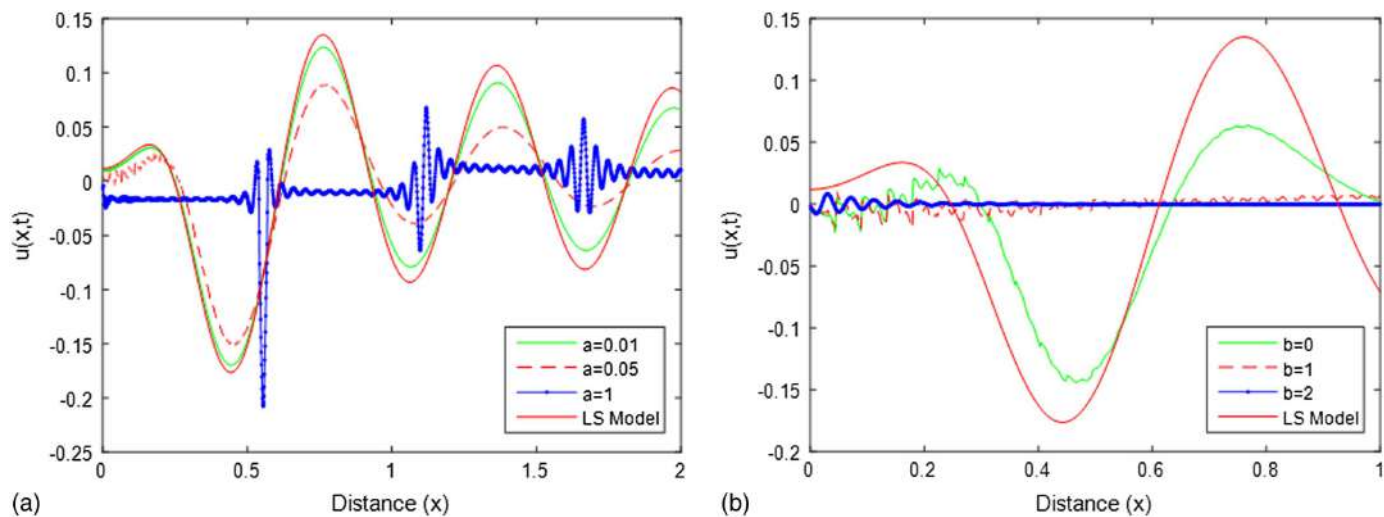


Fig. 1. Thermal displacement at $t = 0.2$ with different values of (a) a ; and (b) b .

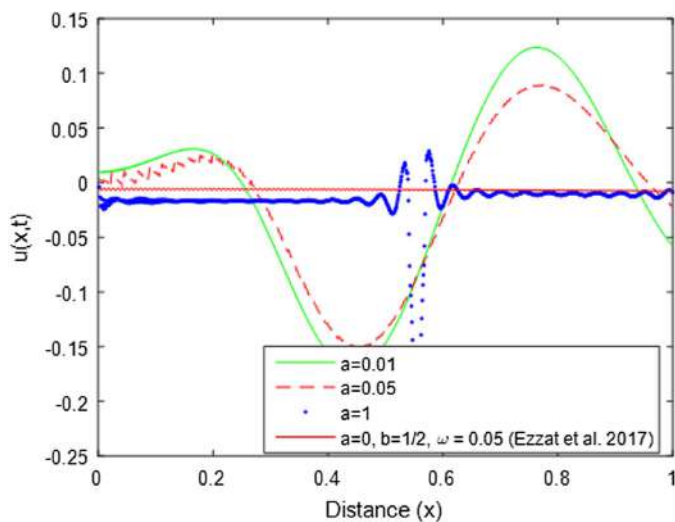


Fig. 2. Comparison of thermal displacement at $t = 0.2$ with the results of Ezzat et al. (2017).

Because some additional phenomena of heat fluxes into the medium can be captured through the memory-dependent generalized law of heat conduction, and the thermal disturbances decrease with the higher-order of the kernel functions, according to the linear theory of thermoelasticity, the rate of heat flux decreases with increasing values of the memory parameters. The temperature distribution profiles also decrease from linear to nonlinear forms of the memory kernel (Fig. 3). In comparison with Ezzat et al. (2017), the temperature profile is flat and high if some approximate (Taylor series expansion) form of the kernel function is considered (Figs. 2 and 4).

The thermal stresses generated into the medium decrease with the increasing values of the parameter, and the stress generated by the LS model gives an upper bound of the memory-dependent linear thermoelasticity models (Figs. 5 and 6).

Systematic overlapping of the thermal waves sometimes generates few peaks in the thermal disturbances, which are seen in the displacement versus distance figures. Generally, these peaks are comparatively higher near the heat source and decrease with distance. For smaller values of a (e.g., $a = 0.01$ and 0.05) the length of memory is shorter, so the displacement profiles look like a waveform. However, for $a = 1$, the length of the memory scale is long

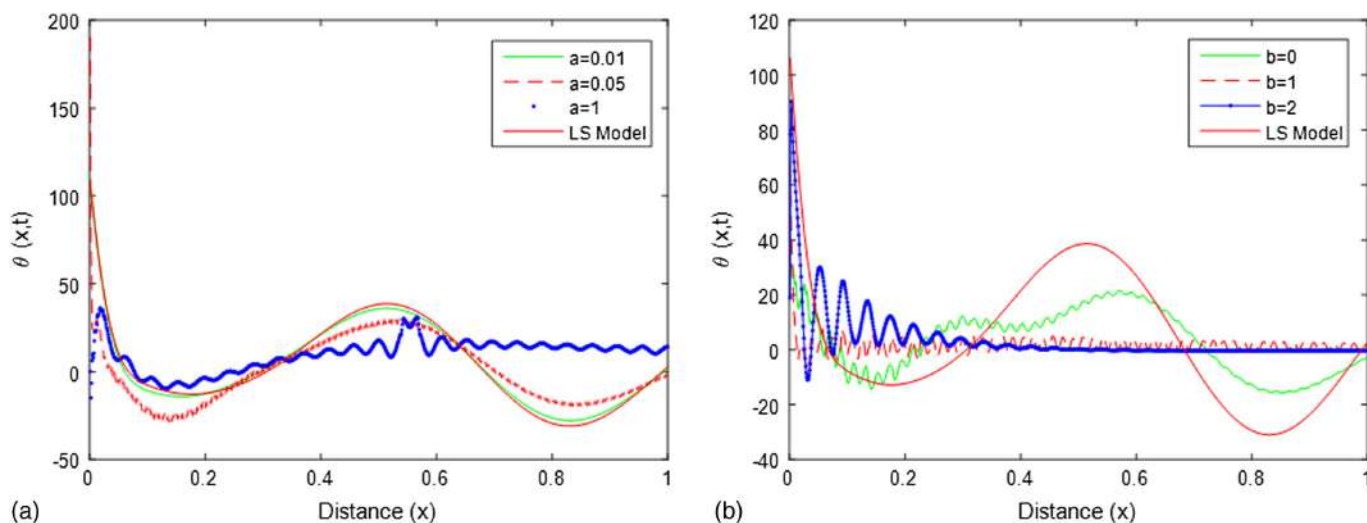


Fig. 3. Temperature versus displacement at $t = 0.2$ with different values of (a) a ; and (b) b .

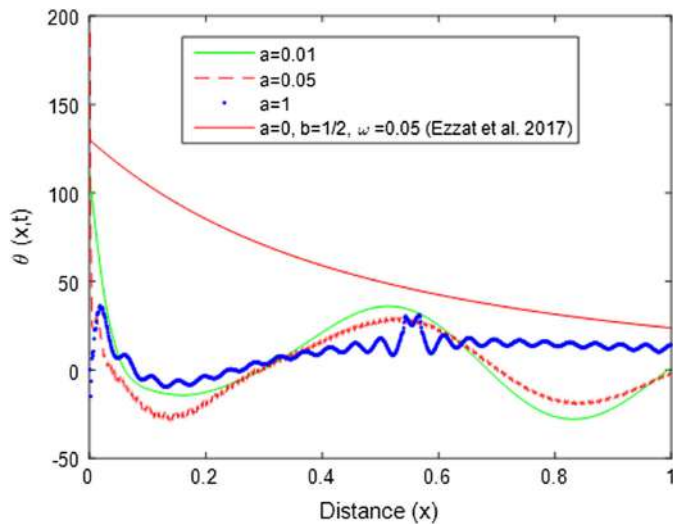


Fig. 4. Comparison of temperature distribution at $t = 0.2$ with the results of Ezzat et al. (2017).

and consequently the displacement profile has some dissimilar nature. In response to an instantaneous heat source at $x = 0$, displacement profiles have reasonably higher peaks near the origin and decrease with distance from the heat source. The memory response in the punch problem is nearly identical in nature to the values of the parameters such as thermal shock (Figs. 7–9).

The displacement is continuous for all values of x (Figs. 1, 2 and 7). A discontinuity in the displacement means formation of a crack in the medium or that one portion of matter penetrates into another, which violates the hypothesis of continuum mechanics, but this thermo-elastic process does not allow those inconsistencies.

The temperature distribution which is revealed by the memory-dependent generalized thermoelasticity theory in the medium is presumed to be continuous. If any fracture arises, then the entire temperature field remains continuous, although at the crack surfaces the observed temperatures may be dissimilar [Fig. 10(a)]. In that case, the temperature field demonstrates a finite gradient over the thickness of the fracture, i.e., across the fracture domain [Fig. 10(b)]. The temperature sharing in the material domain is piecewise continuous [Fig. 10(c)].

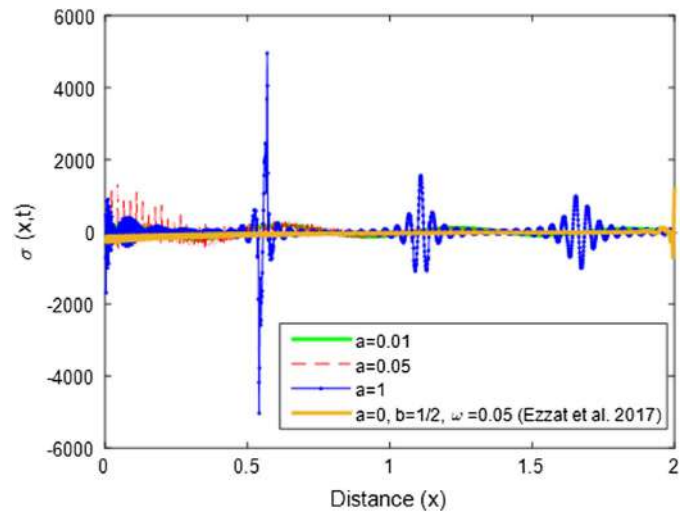


Fig. 6. Comparison of stress distribution at $t = 0.2$ with the results of Ezzat et al. (2017).

Stability Analysis

This section considers the problem defined in a smooth bounded domain B with the following initial-boundary conditions:

$$\begin{aligned} \theta(x, 0) = T_0(x), \quad \dot{\theta}(x, 0) = \vartheta_0(x), \quad \ddot{\theta}(x, 0) = \eta_0(x), \\ x \in B, \quad \text{and} \quad \theta(x, t) = 0, \quad x \in \partial B \end{aligned}$$

Define the following energy functional, which is a useful tool for this study:

$$F(t) = \frac{1}{2} \int_B (\rho C_e (\dot{\theta} + \tau D_a \dot{\theta})^2 + K \tau |\nabla \dot{\theta}|^2) dv$$

Therefore

$$\begin{aligned} F'(t) &= - \int_B \nabla (\dot{\theta} + \tau D_a \dot{\theta}) \cdot (K \nabla \dot{\theta}) dv + K \tau \int_B (\nabla \dot{\theta}) (\nabla \ddot{\theta}) dv \\ &= - \int_B (K |\nabla \dot{\theta}|^2) dv - K \tau \int_B \nabla (D_a \dot{\theta} - \ddot{\theta}) \cdot (\nabla \dot{\theta}) dv \leq 0 \end{aligned}$$

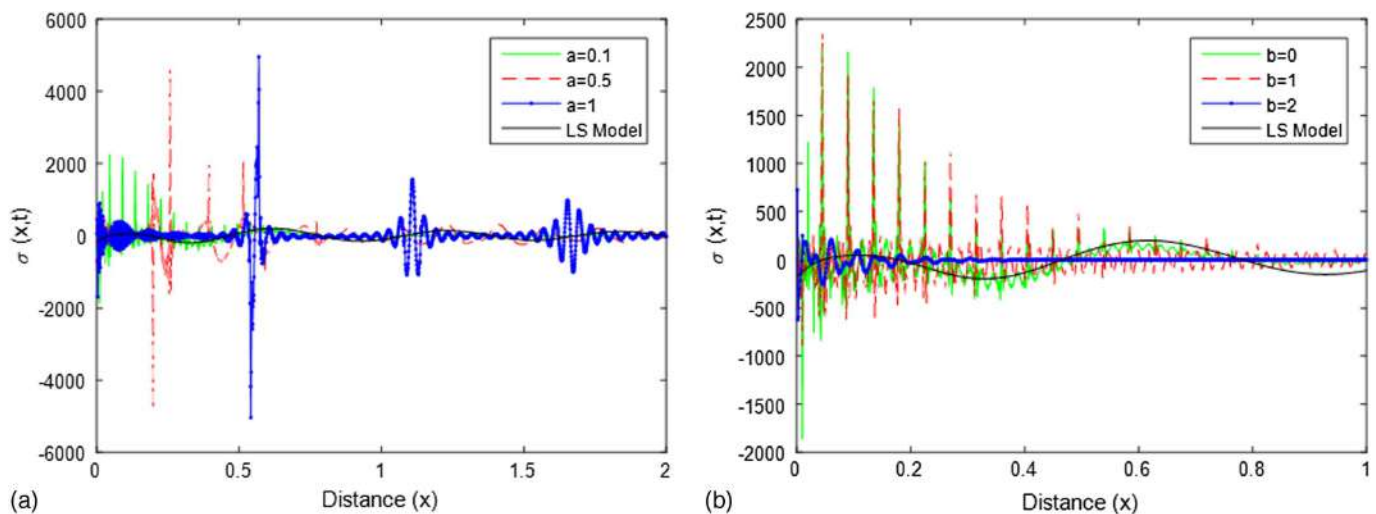


Fig. 5. Stress distribution at $t = 0.2$ with different values of (a) a ; and (b) b .

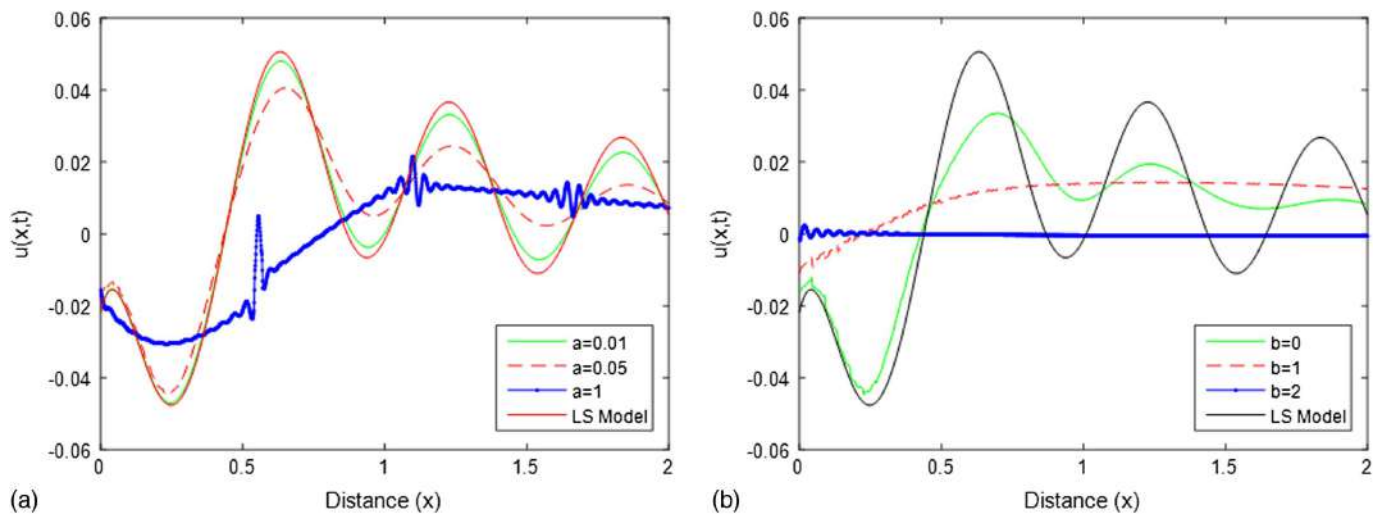


Fig. 7. Variation of displacement with different values of (a) a ; and (b) b .

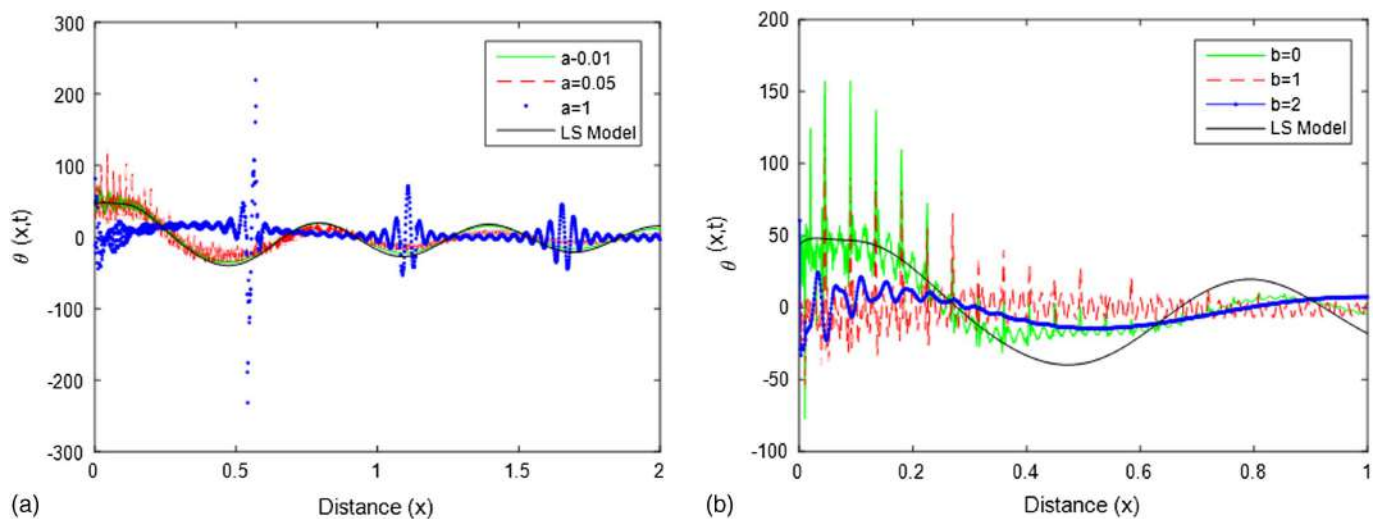


Fig. 8. Variation of temperature with different values of (a) a ; and (b) b .

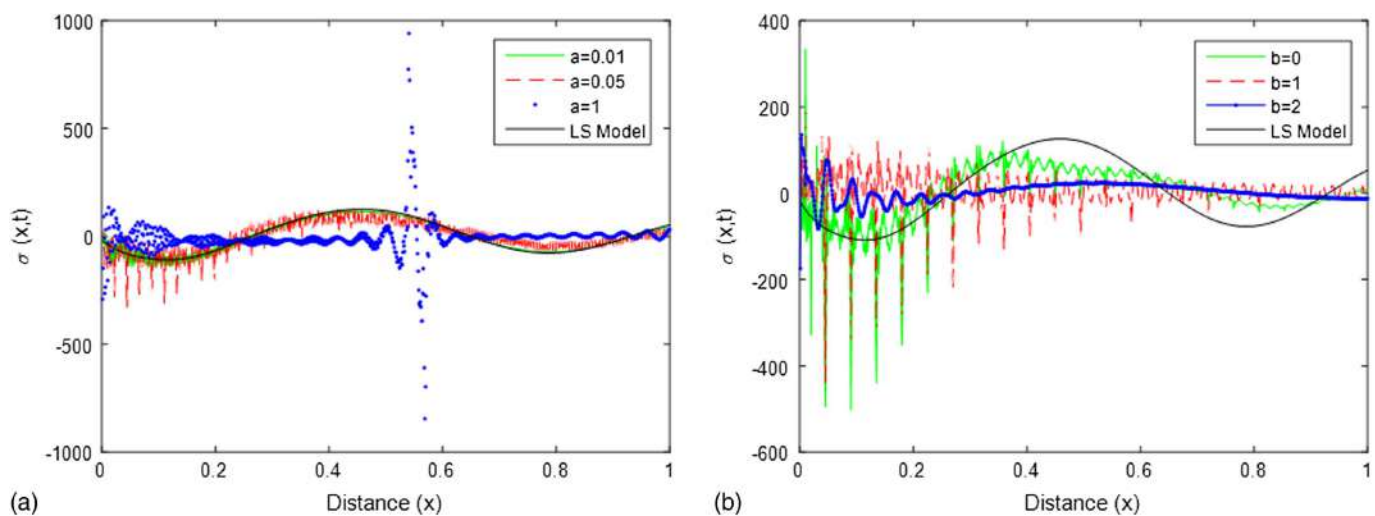


Fig. 9. Stress distribution at $t = 0.2$ with different values of (a) a ; and (b) b .

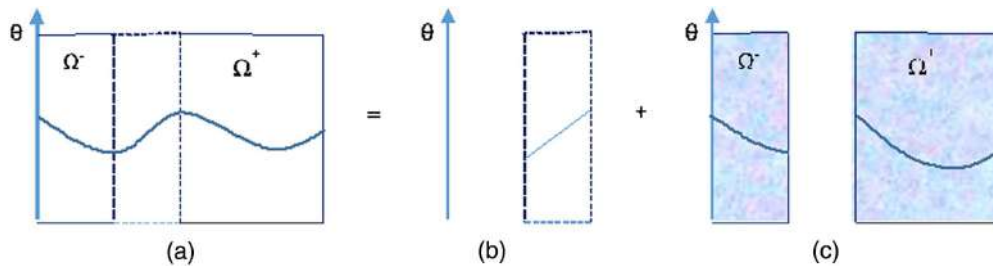


Fig. 10. Temperature distribution in a fractured medium: (a) fractured medium; (b) fracture domain; and (c) material domain.

This inequality shows that the solutions of the considered problem are stable whenever the memory dependent derivatives are assumed to satisfy the condition $D_a \dot{\theta} \geq \ddot{\theta}$.

However, in order to perceive stronger results our aim to prove that the solution decaying in an exponential way, first define another function

$$G(t) = \int_B \left(\frac{K}{2} |\nabla \theta|^2 + \rho C_e \theta \dot{\theta} + \rho C_e \theta D_a \theta \right) dv$$

$$\text{So that } G'(t) = \int_B (\rho C_e \dot{\theta}^2 + \rho C_e \theta D_a \theta) dv$$

It is clear that $F'(t) + \varepsilon G'(t)$ defines an equivalent norm to $F(t)$, where ε is a small quantity, such that

$$F'(t) + \varepsilon G'(t) = - \int_B (K |\nabla \dot{\theta}|^2 + K \tau \nabla (D_a \dot{\theta} - \ddot{\theta}) \cdot (\nabla \dot{\theta})) dv + \varepsilon \int_B (\rho C_e \dot{\theta}^2 + \rho C_e \theta D_a \theta) dv$$

is equivalent to an energy type of the form

$$\int_B (|\nabla \dot{\theta}|^2 + |\nabla \ddot{\theta}|^2) dv$$

Thus

$$F'(t) + \varepsilon G'(t) \leq -K(F(t) + \varepsilon G(t))$$

which shows that the solutions decay in an exponential way.

Conclusion

This paper analyzed the theory of memory-dependent generalized thermoelasticity and its applications in the mechanics of solids. In terms of theoretical developments and numerical computations, the following conclusions are reached:

1. The higher the value of the memory parameters, the slower is the rate of heat flux into the medium;
2. The appropriate form of the kernel function can be chosen to predict the response of the heat flux rate into the medium accurately;
3. The Lord–Shulman model of thermoelasticity gives an upper bound of thermal displacement and stresses for memory-dependent generalized thermoelasticity theory;
4. It is encouraging that MDD also makes sense compared with other generalized thermoelasticity theories; and
5. The stability of the solutions was proved and it was found that the solutions are always (exponentially) stable only if the memory derivative satisfies $D_a \dot{\theta} \geq \ddot{\theta}$.

The theoretical developments investigated in this paper may be useful for researchers who are concentrating on material science, mathematical physics, thermodynamics at low temperatures, and the development of hyperbolic thermoelasticity theory.

Appendix I. Solution of Biquadratic Eq. (32)

Eq. (32) is exactly in the following form:

$$A(s)k^4 + B(s)k^2 + C(s) = 0, \quad s \in C$$

Substituting $k^2 = \lambda$ obtains

$$A(s)\lambda^2 + B(s)\lambda + C(s) = 0$$

Therefore, $\lambda_{1,2} = (-B \pm \sqrt{B^2 - 4AC})/2A = x + iy$

Therefore $\sqrt{x + iy} = \pm \left(\left[\left(\sqrt{x^2 + y^2} + x \right) / \sqrt{2} \right] + i \left\{ [Sgn(y)] / \sqrt{2} \right\} \sqrt{\sqrt{x^2 + y^2} - x} \right)$.

Special Case: $c, d \in R, d > 0$

$$\sqrt{c + id} = \pm \left(\frac{\sqrt{\sqrt{c^2 + d^2} + c}}{\sqrt{2}} + i \frac{d}{\sqrt{2}} \sqrt{\sqrt{c^2 + d^2} - c} \right)$$

Appendix II. Numerical Inversion of Laplace Transform

Computation of the Laplace inversion numerically for the values of $t > 0$ is a formidable task. Quite a few research articles have been reported in the literature in this regard, and it remains a challenge to the scientific computing community. Several methodologies for the computation of this inversion technique are found, but most of the problems are ill-posed (Davies and Martin 1979; Honig and Hirdes 1984; Epstein and Schotland 2008; Gzyl et al. 2013 and references therein). To reduce the propagation of errors, the regularization method is one of the common approaches to overcome these ill-posedness of the problems.

This paper adopts a very simple methodology to compute the inverse Laplace transform numerically over a real axis without considering the regularization approaches. First, discretize the transform function

$$\tilde{f}(s) = L[f(t); t \rightarrow s] = \int_0^\infty f(t) e^{-st} dt \quad (51)$$

as follows:

$$\int_0^{\infty} e^{-st} f(t) dt \approx \frac{\pi^2}{4N} \sum_{k=1}^N (2k-1) e^{-s\{\frac{\pi^2(2k-1)^2}{16N}\}} f(t_k),$$

$$\text{Re}(s) > 0 \quad (52)$$

Next evaluate the preceding quadrature at some points $0 < s_1 < s_2 < \dots < s_M$, which yields a linear system of equations. To obtain the inverse Laplace transformation, these equations must be solved. Instead of using regularization methods, the instability can be controlled by choosing the number of nodes s_k ($k = 1, 2, \dots, M$) as well as the values of N .

Let $0 < s_1 < s_2 < \dots < s_M$ be $M < N$ nodes chosen from the s -plane. Then Eq. (51) takes the matrix form

$$\bar{f}(s_j) = \sum_{k=1}^N \mathbf{L}_{jk} f(t_k), \quad j = 1, 2, \dots, M \quad (53)$$

where \mathbf{L} denotes a matrix of order $M \times N$ where

$$\mathbf{L}_{jk} = \frac{\pi^2}{4N} (2k-1) e^{-s_j\{\frac{\pi^2(2k-1)^2}{16N}\}}$$

$$j = 1, 2, \dots, M; \quad k = 1, 2, \dots, N$$

Thus

$$(\mathbf{L}\mathbf{L}^T)_{jk} = \frac{2\pi}{\sqrt{N}} \sum_{l=1}^N x_l e^{-(s_j+s_k)x_l} \Delta\sigma(x_l), \quad \text{where } \Delta\sigma(x_l) \approx \frac{\pi}{2\sqrt{N}}$$

Therefore, if $s_j \neq s_k$, $\mathbf{L}\mathbf{L}^T$ is nonsingular and $\text{rank}(\mathbf{L}) = M$. This indicates that the linear system Eq. (53) can be written in the simple form $\mathbf{L}f = \bar{f}$, which has a solution which can be found by using the right inverse $\mathbf{L}^T(\mathbf{L}\mathbf{L}^T)^{-1}$, which yields

$$f = \mathbf{L}^T(\mathbf{L}\mathbf{L}^T)^{-1}\bar{f} \quad (54)$$

This is the form by which the approximate numerical values of the inverse Laplace transform can be obtained.

References

- Atanacković, T. M., S. Pilipović, B. Stanković, and D. Zorica. 2014. *Fractional calculus with application in mechanics*. London: Wiley.
- Banerjee, S., S. Shaw, and B. Mukhopadhyay. 2018. "Memory response on thermal wave propagation emanating from a cavity in an unbounded elastic solid." *J. Therm. Stress*. 41 (8): 970–988. <https://doi.org/10.1080/01495739.2018.1461041>.
- Biot, M. 1956. "Thermoelasticity and irreversible thermodynamics." *J. Appl. Phys.* 27 (3): 240–253. <https://doi.org/10.1063/1.1722351>.
- Cattaneo, C. 1958. "Sur une forme de l'équation de la chaleur éliminant le paradoxe d'une propagation instantanée [On a form of the heat equation eliminating the paradox of the instantaneous spread]." [In French.] *Comptes. Rendus. Acad. Sci.* 2 (47): 431–433.
- Davies, B., and B. Martin. 1979. "Numerical inversion of the Laplace transform: A survey and comparison of methods." *J. Comput. Phys.* 33 (1): 1–32. [https://doi.org/10.1016/0021-9991\(79\)90025-1](https://doi.org/10.1016/0021-9991(79)90025-1).
- Diethelm, K. 2010. *Analysis of fractional differential equation: An application oriented exposition using differential operators of Caputo type*. Berlin: Springer.
- Epstein, C. L., and J. Schotland. 2008. "The bad truth about Laplace's transform." *SIAM Rev.* 50 (3): 504–520. <https://doi.org/10.1137/060657273>.
- Ezzat, M. A. 2010. "Thermoelastic MHD non-Newtonian fluid with fractional derivative heat transfer." *Physica B* 405 (19): 4188–4194. <https://doi.org/10.1016/j.physb.2010.07.009>.
- Ezzat, M. A. 2014. "Generalized thermo-viscoelasticity with memory-dependent derivatives." *Int. J. Mech. Sci.* 89: 470–475. <https://doi.org/10.1016/j.jmeosci.2014.10.006>.
- Ezzat, M. A. 2016. "Modelling of memory-dependent derivative in generalized thermoelasticity." *Euro. Phys. J. Plus*. 131 (10): 372. <https://doi.org/10.1140/epjp/i2016-16372-3>.
- Ezzat, M. A., and M. A. Fayik. 2011. "Fractional order theory of thermoelastic diffusion." *J. Therm. Stresses* 34 (8): 851–872. <https://doi.org/10.1080/01495739.2011.586274>.
- Ezzat, M. A., A. S. Karamany, and A. A. El-Bary. 2017. "On dual-phase lag thermoelasticity theory with memory dependent derivative." *Mech. Adv. Mat. Struct.* 24 (11): 908–916. <https://doi.org/10.1080/15376494.2016.1196793>.
- Green, A. E., and K. A. Lindsay. 1972. "Thermoelasticity." *J. Elast.* 2 (1): 1–7. <https://doi.org/10.1007/BF00045689>.
- Green, A. E., and P. M. Naghdi. 1991. "A re-examination of the basic postulates of thermomechanics." *Proc. Roy. Soc. London Ser.* 432 (1885): 171–194. <https://doi.org/10.1098/rspa.1991.0012>.
- Gzyl, H., A. Tagliani, and M. Milev. 2013. "Laplace transform inversion on the real line is truly ill-conditioned." *Appl. Math. Comput.* 219 (18): 9805–9809. <https://doi.org/10.1016/j.amc.2013.03.112>.
- Hilfer, R. 2000. *Application of fractional calculus to physics*. Singapore: World Scientific.
- Honig, G., and U. Hirdes. 1984. "A method for the numerical inversion of Laplace transforms." *J. Comput. Appl. Math.* 10 (1): 113–132. [https://doi.org/10.1016/0377-0427\(84\)90075-X](https://doi.org/10.1016/0377-0427(84)90075-X).
- Karamany, A. S., M. A. Ezzat, and A. A. El-Bary. 2018. "Thermodiffusion with two time delays and kernel functions." *Math. Mech. Solids* 23 (2): 195–208. <https://doi.org/10.1177/1081286516676870>.
- Lord, H., and Y. Shulman. 1967. "A generalized dynamic theory of thermoelasticity." *J. Mech. Phys. Solids* 15 (5): 299–309. [https://doi.org/10.1016/0022-5096\(67\)90024-5](https://doi.org/10.1016/0022-5096(67)90024-5).
- Mainardi, F. 2010. *Fractional calculus and waves in linear viscoelasticity*. London: Imperial College Press.
- Rossikhin, Y. A., and M. V. Shitikova. 2011. "Application of fractional calculus for dynamic problems of solid mechanics: Novel trends and recent results." *Appl. Mech. Rev.* 63 (1): 1562–1567. <https://doi.org/10.1115/1.4000563>.
- Sabatier, J., O. P. Agrawal, and M. Tenreiro. 2007. "Advances in fractional calculus." In *Theoretical developments and applications in physics and engineering*. Dordrecht, Netherlands: Springer.
- Shaw, S. 2017. "A note on generalized thermoelasticity with memory dependent derivatives." *J. Heat Transf.* 139 (9): 092005. <https://doi.org/10.1115/1.4036461>.
- Shaw, S., and B. Mukhopadhyay. 2011. "Generalized theory of micropolar fractional ordered thermoelasticity with two-temperature." *Int. J. Appl. Math. Mech.* 7 (19): 32–48.
- Shaw, S., and B. Mukhopadhyay. 2016. "Theory of fractional ordered thermoelastic diffusion." *Eur. Phys. J. Plus* 131 (6): 1–10. <https://doi.org/10.1140/epjp/i2016-16183-6>.
- Shaw, S., and B. Mukhopadhyay. 2017. "A discontinuity analysis of generalized thermoelasticity theory with memory-dependent derivatives." *Acta Mech.* 228 (7): 2675–2689. <https://doi.org/10.1007/s00707-017-1853-0>.
- Sherief, H. H., A. M. A. El-Sayed, and A. M. A. El-Latif. 2010. "Fractional order generalized thermoelasticity." *Int. J. Solids Struct.* 47 (2): 269–275. <https://doi.org/10.1016/j.ijsolstr.2009.09.034>.
- Stiassnie, M. 1979. "On the application of fractional calculus for formulation of viscoelastic model." *Appl. Math. Model.* 3 (4): 300–302. [https://doi.org/10.1016/S0307-904X\(79\)80063-3](https://doi.org/10.1016/S0307-904X(79)80063-3).
- Wang, J. L., and H. F. Li. 2011. "Surpassing the fractional derivative: Concept of the memory-dependent derivative." *Comput. Math. Appl.* 62 (3): 1562–1567. <https://doi.org/10.1016/j.camwa.2011.04.028>.
- Youssef, H. H. 2010. "Theory of fractional order generalized thermoelasticity." *J. Heat Transf.* 132 (6): 061301. <https://doi.org/10.1115/1.4000705>.
- Yu, Y., W. Hu, and X. Tian. 2014. "A novel generalized thermoelasticity model based on memory dependent-derivatives." *Int. J. Eng. Sci.* 81: 123–134. <https://doi.org/10.1016/j.jengsci.2014.04.014>.



Source details

[Feedback >](#) [Compare sources >](#)

Journal of Engineering Mechanics - ASCE

Formerly known as: [Journal of the Engineering Mechanics Division](#)

Scopus coverage years: from 1981 to Present

Publisher: American Society of Civil Engineers

ISSN: 0733-9399

Subject area: [Engineering: Mechanical Engineering](#) [Engineering: Mechanics of Materials](#)

Source type: Journal

[View all documents >](#)

[Set document alert](#)

[Save to source list](#)

CiteScore 2022

5.7



SJR 2022

0.920



SNIP 2022

1.368



[CiteScore](#)

[CiteScore rank & trend](#)

[Scopus content coverage](#)



Improved CiteScore methodology



CiteScore 2022 counts the citations received in 2019-2022 to articles, reviews, conference papers, book chapters and data papers published in 2019-2022, and divides this by the number of publications published in 2019-2022. [Learn more >](#)



Bending of a Thin Rectangular Isotropic Micropolar Plate

Soumen Shaw*

To cite this article: Soumen Shaw* (2019): Bending of a Thin Rectangular Isotropic Micropolar Plate, International Journal for Computational Methods in Engineering Science and Mechanics, DOI: [10.1080/15502287.2019.1568616](https://doi.org/10.1080/15502287.2019.1568616)

To link to this article: <https://doi.org/10.1080/15502287.2019.1568616>



Published online: 14 Feb 2019.



Submit your article to this journal [↗](#)



View Crossmark data [↗](#)

Bending of a Thin Rectangular Isotropic Micropolar Plate

Soumen Shaw*

Department of Mathematics, IEST, Shibpur, India

ABSTRACT

In this note, deflection of a thin rectangular isotropic micropolar plate is observed under the influence of transverse loading. From the properties of asymptotic solution, a set of hypotheses is considered and the corresponding governing equations of bending are derived. The solutions are validated by comparing the numerical results and with their counterparts reported in literature for classical Timoshenko plate theory and the Kirchhoff's theory of plate deformation.

KEYWORDS

Micropolar plate, Transverse loading, Theory of deflection, Asymptotic solution

1. Introduction

The development of continuum mechanics is closely related to the construction of generalized mathematical models taking into account asymmetric elastic theory. Owing to new problems in modern micro-mechanics and nanotechnology, recently, asymmetric micropolar moment theory gained an enormous interest. It has been established that asymmetric theory of elasticity offers a rigorous mathematical approach, based on field equations, to describe the deformations of solids with internal structure or continuously distributed defects. Despite that fact, since last one decade, micropolar theory of elasticity is rapidly developing in both theoretical and applied directions [1–5].

Thin rectangular plate is a significant structural component uses in numerous engineering applications such as rigid pavements of highways and airports, house and bridge decks etc. Because of its enormous applications in several fields, in the last one or two decades thin elastic plates with various boundary conditions have been studied by several authors, among them, we can mention, Ciarlet [6, 7], Timoshenko and Woinowsky-Krieger [8], Goldenveizer [9], Neff and Jeong [10], Naghdi [11], etc.

After the pioneering work of Kirchhoff, classical plate theory explored with various aspects. Later on, a number of research articles have been published to give the foundations and methods of presumption of Kirchhoff-Love theory and its possible improvements. Mainly there are two methods to determine the deflection of thin plate: (a) method of hypothesis (see,

Timoshenko and Woinowsky-Krieger [8]) and (b) method of asymptotic expansion (see Goldenveizer [9], Friedrichs and Dressler [12], Ciarlet and Destuynder [13]).

There is another important classical theory that takes into account the shear effect that is ignored in the Kirchhoff-Love theory, which is known as the Reissner-Mindlin Plate theory.

In the year 1986, the Cosserat brothers, Eugen and Francois, published a monograph [14], where they presented a new variant of continuum mechanics as well as the mechanics of rods and shells. They have attempted to unify the field theories of mechanics, optics, and electrodynamics through a common principle of least action. They postulated that the invariance of energy under Euclidean transformation was able to derive the balance of force and balance of momentum. However, they never wrote down the constitutive relations. Later on, this continuum theory of elasticity is named as Cosserat or micropolar continuum solid. The Cosserat theory of elasticity is one of the most prominent extended continuum models that feature three additional degrees of freedom which are related to the rotation of particles and they need not coincide with the macroscopic rotation of continuum.

The Cosserat model can be posed in a variational format as a two-field minimization problem for usual displacement (\vec{u}) and microrotation ($\vec{\phi}$). Application of such approach in the development of plate theory was discussed by Neff and Jeong [10] and Altenbach and Eremeyev [15].

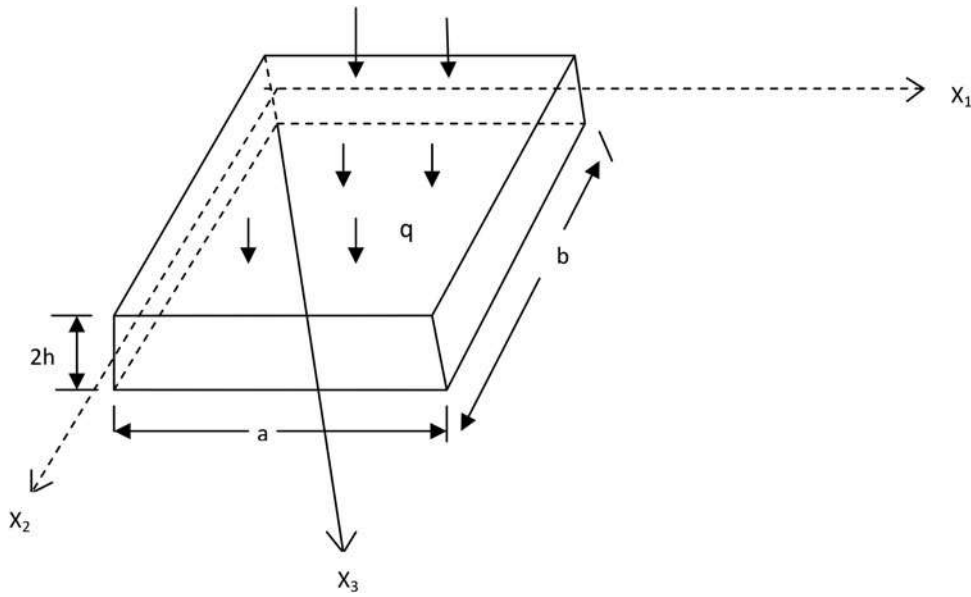


Figure 1. Deflection of a thin micropolar plate.

Like Kirchhoff-Love classical plate theory, taking the following assumptions over the variation of unknowns across the plate thickness, a linear theory of micropolar plates has been formulated by Eringen [16].

- (i) The transverse displacement component is independent of transverse coordinate. The in-plane displacement components are not only function of the in-plane coordinates but they are also linear function of transverse coordinate.
- (ii) Both transverse and in-plane components of microrotation are independent of transverse coordinate.

The two-dimensional equations of this theory are deduced with the help of independent integration over the plate thickness. Later on Green and Naghdi [17] derived a different set of governing equations of micropolar plate by using asymptotic expression method. They concluded that the method used by Eringen [16] does not provide a consistent approximate theory of plates based on three dimensional equations of micropolar elasticity. More information and various aspects of micropolar plate theories of Eringen can be found in the work of and Wang [18]. Recently, boundary value problems of the asymmetric theory of thin elastic plate and high frequency vibrations have been discussed by respectively, Sargsyan [19] and Shaw [20].

In this article, classical Kirchhoff-Love plate theory is developed in the context of micropolar theory of elasticity. Adopting the method of hypothesis, owing to Timoshenko and Woinowsky-Krieger, a set of hypotheses which are compatible with micropolar theory of elasticity, is established. As an application, two

special cases (S-S and C-C modes) are considered. Finally, a comparison study is being made on the plate deflection as well as bending stresses over classical plate (including transverse shear strain).

2. Formulation of the problem

We consider a rectangular isotropic micropolar thin plate in the Cartesian system (x_1, x_2, x_3) , as shown in Fig. 1. The length, width, and thickness of the plate are a, b , and $2h$, respectively. The coordinate plane Ox_1x_2 is attached to the middle plane of the plate with a static mechanical load q in x_3 direction.

We use the following basic equations (in the Cartesian coordinate of x_n , where $n = 1, 2, 3$) of the spatial static problem of linear micropolar theory of elasticity with independent fields of displacements and rotations [1]:

Equilibrium equations:

$$\sigma_{mn,m} = 0, \mu_{mn,m} + \varepsilon_{nlk}\sigma_{lk} = 0 \quad (1)$$

Constitutive relations:

$$\sigma_{mn} = (\mu + \alpha)\gamma_{mn} + (\mu - \alpha)\gamma_{nm} + \lambda\chi_{kk}\delta_{nm} \quad (2)$$

$$\mu_{mn} = (\gamma + \varepsilon)\chi_{mn} + (\gamma - \varepsilon)\chi_{nm} + \beta\chi_{kk}\delta_{nm} \quad (3)$$

Geometrical relations:

$$\gamma_{nm} = u_{m,n} - \varepsilon_{knm}\phi_k, \chi_{nm} = \phi_{m,n} \quad (4)$$

Here σ_{nm} and μ_{nm} are the components of force and couple stress tensors, γ_{nm} and χ_{nm} are the components of bending strain and torsion tensors. u_n and ϕ_n are

the components of the displacements vector and the independent rotation of the body points. α, β, γ , and are the elastic constants of the micropolar material,

$$\lambda = \frac{E\nu}{(1+\nu)(1-2\nu)}, \quad \mu = \frac{E}{2(1+\nu)}$$

where E and ν , respectively, denotes Young's modulus and Poisson's ratio of the material, subscripts n after the comma denotes differentiation with respect to x_n coordinate, $-h \leq x_3 \leq h$, ε_{kmn} is the Levi-Civita tensor, δ_{mn} is the Kronecker delta and each subscripts l, m, n , and k takes the values 1, 2, 3.

At $\alpha = 0$, system of Eqs. (1)–(3) is divided into the classical elasticity theory equations and the pure bending theory equations.

The solution of the problem (1)–(3) is the sum of the solutions for the problems that are symmetric and anti-symmetric with regard to x_3 . In the symmetric problem (plane stress state of the plate) $\sigma_{ii}, \sigma_{ij}, \sigma_{33}, \mu_{i3}, \mu_{3i}, u_i, \phi_3$ are even functions with respect to x_3 and $\sigma_{i3}, \sigma_{3i}, \mu_{ii}, \mu_{ij}, \mu_{33}, u_3, \phi_i$ are odd functions. In the anti-symmetric problem (bending of the plate) $\sigma_{ii}, \sigma_{ij}, \sigma_{33}, \mu_{i3}, \mu_{3i}, u_i, \phi_3$ are odd function with regard to x_3 , and $\sigma_{i3}, \sigma_{3i}, \mu_{ii}, \mu_{ij}, \mu_{33}, u_3, \phi_i$ are even functions. Henceforth, in this paper, the subscripts i and j ($i \neq j$) take the values 1 and 2.

Now we construct a model of a micropolar thin elastic plate based on the method of hypotheses. These hypotheses are formulated on the basis of the results of the asymptotic analysis of the BVP (1)–(4) in areas such as plates [19].

Determination of the internal (and boundary) stress–strain state is highly dependent on the material moduli of the plate. We consider the case where the following assumptions are valid for the dimensionless physical parameters of the plate:

$$\frac{\mu}{\alpha} \sim 1, \frac{a^2 \mu}{\beta} \sim 1, \frac{a^2 \mu}{\gamma} \sim 1, \frac{a^2 \mu}{\varepsilon} \sim 1 \quad (5)$$

In the construction of two-dimensional model of micropolar thin plates with independent fields of displacements and rotations in this case, the qualitative results of the asymptotic solution (see Ref. [19]) of the BVP (1)–(4) allow us to accept the following hypotheses:

- (i) The element originally perpendicular to the mid plane of the plate remains straight after deformation but may not be perpendicular to the deformed mid plane, and it freely rotates by a certain angle, while its length does not change.

Consequently, there is a linear relationship of changes of displacements and free rotations:

$$\begin{aligned} u_i &= x_3 \Psi_i(x_1, x_2), \quad u_3 = w(x_1, x_2), \quad \phi_i = \Omega_i(x_1, x_2), \\ \phi_3 &= x_3 \Gamma(x_1, x_2), \end{aligned} \quad (6)$$

where Ψ_i are the total angles of rotations, Ω_i are the free angles of rotations of the initially normal element with respect to x_i axes, w is the distance over which the middle plane points are displaced in the direction of x_3 axis and Γ is the intensity of the free rotation ϕ_3 with respect to x_3 axis.

- (ii) In the constitutive relation (2), the stress σ_{33} is negligibly small compared with the stresses σ_{ii} ($i = 1, 2$).
- (iii) From the asymptotic expansion of stress, displacement and independent rotation, we know that [19],

$$Q = \sum_{s=0}^s \delta^{s-q} Q^{(s)}$$

where s is the number of the asymptotic approximation, Q is any of the stresses, displacements and independent rotations, q is a natural number, which is different for different quantities and is determined from the condition of self-consistency. $\delta = h/a \ll 1$ is the perturbation parameter.

For bending of the micropolar plate:

$$\begin{aligned} q &= 1 \text{ for } \sigma_{i3}, \sigma_{3i}, \mu_{ij}, \mu_{ii}, \mu_{33}, u_3, \phi_i \\ q &= 0 \text{ for } \sigma_{ii}, \sigma_{ij}, \sigma_{33}, \mu_{i3}, \mu_{3i}, u_i, \phi_3 \end{aligned}$$

So in determining the strains (bending and torsion), the force stress σ_{3i} and couple stress μ_{33} are taken in the form:

$$\sigma_{3i} = \sigma_{3i}^{(0)}(x_1, x_2), \quad \mu_{33} = \mu_{33}^{(0)}(x_1, x_2) \quad (7)$$

Introducing these quantities, σ_{3i} and μ_{33} are defined as the sum of the values in Eq. (7) and the result of integrating first two equations or sixth equation of Eq. (1), respectively. These stresses should satisfy the condition that their values averaged over the plate thickness are vanishes.

3. Construction of governing equations

Equilibrium Eq. (1) can be rewritten in the following form:

$$\frac{\partial \sigma_{1i}}{\partial x_1} + \frac{\partial \sigma_{2i}}{\partial x_2} + \frac{\partial \sigma_{3i}}{\partial x_3} = 0 \quad (8a)$$

$$\frac{\partial \sigma_{13}}{\partial x_1} + \frac{\partial \sigma_{23}}{\partial x_2} + \frac{\partial \sigma_{33}}{\partial x_3} = 0 \quad (8b)$$

$$\frac{\partial \mu_{1i}}{\partial x_1} + \frac{\partial \mu_{2i}}{\partial x_2} + \frac{\partial \mu_{3i}}{\partial x_3} + (-1)^j (\sigma_{j3} - \sigma_{3j}) = 0 \quad (8c)$$

$$\frac{\partial \mu_{13}}{\partial x_1} + \frac{\partial \mu_{23}}{\partial x_2} + \frac{\partial \mu_{33}}{\partial x_3} + \sigma_{12} - \sigma_{21} = 0 \quad (8d)$$

and the constitutive relations:

$$\frac{\partial u_i}{\partial x_i} = \frac{\sigma_{ii} - \nu(\sigma_{jj} + \sigma_{33})}{E} \quad (9a)$$

$$\frac{\partial u_3}{\partial x_3} = \frac{\sigma_{33} - \nu(\sigma_{11} + \sigma_{22})}{E} \quad (9b)$$

$$\frac{\partial u_j}{\partial x_i} - (-1)^j \phi_3 = \sigma_{ij} \frac{\mu + \alpha}{4\mu\alpha} - \sigma_{ji} \frac{\mu - \alpha}{4\mu\alpha} \quad (9c)$$

$$\frac{\partial u_3}{\partial x_i} + (-1)^j \phi_j = \sigma_{i3} \frac{\mu + \alpha}{4\mu\alpha} - \sigma_{3i} \frac{\mu - \alpha}{4\mu\alpha} \quad (9d)$$

$$\frac{\partial u_i}{\partial x_3} - (-1)^j \phi_j = \sigma_{3i} \frac{\mu + \alpha}{4\mu\alpha} - \sigma_{i3} \frac{\mu - \alpha}{4\mu\alpha} \quad (9e)$$

$$\frac{\partial \phi_i}{\partial x_i} = \frac{\beta + \gamma}{\gamma(3\beta + 2\gamma)} \left[\mu_{ii} - \frac{\beta}{2(\beta + \gamma)} (\mu_{jj} + \mu_{33}) \right] \quad (9f)$$

$$\frac{\partial \phi_3}{\partial x_3} = \frac{\beta + \gamma}{\gamma(3\beta + 2\gamma)} \left[\mu_{33} - \frac{\beta}{2(\beta + \gamma)} (\mu_{11} + \mu_{22}) \right] \quad (9g)$$

$$\frac{\partial \phi_i}{\partial x_j} = \frac{(\gamma + \varepsilon)\mu_{ji} - (\gamma - \varepsilon)\mu_{ij}}{4\gamma\varepsilon} \quad (9h)$$

$$\frac{\partial \phi_3}{\partial x_i} = \frac{(\gamma + \varepsilon)\mu_{i3} - (\gamma - \varepsilon)\mu_{3i}}{4\gamma\varepsilon} \quad (9i)$$

$$\frac{\partial \phi_i}{\partial x_3} = \frac{(\gamma + \varepsilon)\mu_{3i} - (\gamma - \varepsilon)\mu_{i3}}{4\gamma\varepsilon} \quad (9j)$$

We consider the force stresses and couple stresses, on the plate faces $x_3 = \pm h$, are prescribed as:

$$\sigma_{3i} = \frac{p_i}{2}, \sigma_{33} = \pm \frac{p_3}{2}, \mu_{3i} = \pm \frac{m_i}{2}, \mu_{33} = \frac{m_3}{2} \quad (10)$$

Depending on the ways of application of external load and plate fixation, the boundary conditions on the lateral surface are written in terms of stresses, couple stresses, displacements, and rotations or in mixed form.

It is convenient to rewrite Eqs. (9c)–(9e);

$$\frac{\partial u_2}{\partial x_1} + \frac{\partial u_1}{\partial x_2} = \frac{\sigma_{12} + \sigma_{21}}{2\mu} \quad (11)$$

$$\frac{\partial u_3}{\partial x_i} + \frac{\partial u_i}{\partial x_3} = \frac{\sigma_{i3} + \sigma_{3i}}{2\mu} \quad (12)$$

$$\phi_i = (-1)^{j+1} \frac{1}{2} \left(\frac{\partial u_j}{\partial x_3} - \frac{\partial u_3}{\partial x_j} \right) + (-1)^j \frac{\sigma_{3j} - \sigma_{j3}}{4\alpha} \quad (13)$$

$$\phi_3 = -\frac{1}{2} \left(\frac{\partial u_1}{\partial x_2} - \frac{\partial u_2}{\partial x_1} \right) + \frac{\sigma_{21} - \sigma_{12}}{4\alpha} \quad (14)$$

Now solving Eq. (9f) and using Eq. (6) we get,

$$\mu_{ii} = \frac{4\gamma(\beta + \gamma)}{\beta + 2\gamma} \frac{\partial \Omega_i}{\partial x_i} + \frac{2\beta\gamma}{\beta + 2\gamma} \frac{\partial \Omega_j}{\partial x_j} + \frac{\beta}{\beta + 2\gamma} \mu_{33} \quad (15)$$

and from Eq. (9h) we get,

$$\mu_{ij} = (\gamma - \varepsilon) \frac{\partial \Omega_i}{\partial x_j} + (\gamma + \varepsilon) \frac{\partial \Omega_j}{\partial x_i} \quad (16)$$

which are independent of x_3 coordinate.

Again, using Eqs. (6), (7), and (15), from Eq. (9g) we obtain

$$\Gamma(x_1, x_2) = -\frac{1}{\beta + 2\gamma} \left[\beta(\Omega_{1,1} + \Omega_{2,2}) - \mu_{33}^{(0)} \right] \quad (17)$$

Using Eq. (7), from Eq. (9d) we get

$$\sigma_{i3} = \frac{4\mu\alpha}{\mu + \alpha} \left[\frac{\partial w}{\partial x_i} + (-1)^j \Omega_j \right] + \frac{\mu - \alpha}{\mu + \alpha} \sigma_{3i}^{(0)} \quad (18)$$

Now integrating Eq. (9e) with respect to x_3 and using Eq. (18) we get,

$$u_i = \frac{x_3}{\mu + \alpha} \left\{ \sigma_{3i}^{(0)} - (\mu - \alpha) \frac{\partial w}{\partial x_i} + (-1)^j 2\alpha \Omega_j \right\} \quad (19)$$

Integrating Eq. (8b) with respect to x_3 we get,

$$\sigma_{33} = -x_3 \left[\frac{\partial \sigma_{13}}{\partial x_1} + \frac{\partial \sigma_{23}}{\partial x_2} \right] \quad (20)$$

Upon using the boundary condition (10) yields,

$$\sigma_{33} = -x_3 \frac{p_3}{2h} \quad (21)$$

Substituting the value of σ_{33} from Eq. (21) in Eq. (9a) and using Eq. (6) we get,

$$\sigma_{ii} = x_3 \frac{E}{1 - \nu^2} \left[\frac{\partial \Psi_i}{\partial x_i} + \nu \frac{\partial \Psi_j}{\partial x_j} \right] - \frac{\nu}{1 - \nu} \frac{x_3 p_3}{2h} \quad (22)$$

The stresses σ_{12} and σ_{21} can be determined by solving the system of Eq. (9c) with the help of Eq. (6);

$$\sigma_{ij} = (\mu + \alpha) \frac{\partial u_j}{\partial x_i} + (\mu - \alpha) \frac{\partial u_i}{\partial x_j} - (-1)^j 2\alpha x_3 \Gamma(x_1, x_2) \quad (23)$$

Now we consider the equilibrium Eq. (8c). In view of the third assumption and with regard for the fact that the couple stresses μ_{ii} and μ_{ij} are independent of x_3 . Integrating Eq. (8c) with respect to x_3 we get,

$$\mu_{3i} = -x_3 \left\{ \frac{\partial \mu_{1i}}{\partial x_1} + \frac{\partial \mu_{2i}}{\partial x_2} + (-1)^j (\sigma_{j3} - \sigma_{3j}^{(0)}) \right\}$$

Upon using the boundary condition (10) we get,

$$\mu_{3i} = x_3 \frac{m_i}{2h} \quad (24)$$

Again, using Eqs. (9f), (6), and (24) we get,

$$\mu_{i3} = -x_3 \left[\frac{\gamma - \varepsilon}{\gamma + \varepsilon} \frac{m_i}{2h} - \frac{4\gamma\varepsilon}{\gamma + \varepsilon} \frac{\partial \Gamma}{\partial x_i} \right] \quad (25)$$

Integrating the equilibrium Eq. (8a) and using Eqs. (22) and (23) we obtain

$$\begin{aligned} \sigma_{3i}(x_1, x_2, x_3) = & -x_3^2 \frac{\partial}{\partial x_i} \left[\frac{E}{1-\nu^2} \left\{ \frac{\partial \Psi_i}{\partial x_i} + \nu \frac{\partial \Psi_j}{\partial x_j} \right\} - \frac{\nu}{1-\nu} \frac{p_3}{2h} \right] \\ & - x_3^2 \frac{\partial}{\partial x_i} \left[(\mu + \alpha) \frac{\partial \Psi_i}{\partial x_j} + (\mu - \alpha) \frac{\partial \Psi_j}{\partial x_i} - (-1)^j 2\alpha \Gamma \right] + \bar{\sigma}(x_1, x_2) \end{aligned} \quad (26)$$

Now from the 3rd assumption, $\sigma_{3i}(x_1, x_2, x_3)$ must satisfy

$$\int_{-h}^h \sigma_{3i}(x_1, x_2, x_3) dx_3 = 0 \quad (27)$$

Hence, one can determine the expression of $\bar{\sigma}(x_1, x_2)$ from the condition (27). Then finally we obtain,

$$\begin{aligned} \sigma_{3i}(x_1, x_2, x_3) = & \sigma_{3i}^{(0)}(x_1, x_2) - \left(x_3^2 - \frac{h^2}{3} \right) \frac{\partial}{\partial x_i} \\ & \left[\frac{E}{1-\nu^2} \left(\frac{\partial \Psi_i}{\partial x_i} + \nu \frac{\partial \Psi_j}{\partial x_j} \right) - \frac{\nu}{1-\nu} \frac{p_3}{2h} \right] - \left(x_3^2 - \frac{h^2}{3} \right) \\ & \frac{\partial}{\partial x_j} \left[(\mu + \alpha) \frac{\partial \Psi_i}{\partial x_j} + (\mu - \alpha) \frac{\partial \Psi_j}{\partial x_i} - (-1)^j 2\alpha \Gamma \right] \end{aligned} \quad (28)$$

Again integrating the equilibrium Eq. (8d) and using Eq. (25) we get,

$$\begin{aligned} \mu_{33}(x_1, x_2, x_3) = & \bar{\mu}(x_1, x_2) - x_3^2 \left[\frac{2\gamma\varepsilon}{\gamma + \varepsilon} \left(\frac{\partial^2 \Gamma}{\partial x_1^2} + \frac{\partial^2 \Gamma}{\partial x_2^2} \right) \right. \\ & \left. + \alpha \left(\frac{\partial \Psi_2}{\partial x_1} + \frac{\partial \Psi_1}{\partial x_2} \right) + (\mu - \alpha) \Gamma(x_1, x_2) \right] \end{aligned} \quad (29)$$

From the 3rd assumption we know,

$$\int_{-h}^h \mu_{33}(x_1, x_2, x_3) dx_3 = 0 \quad (30)$$

Hence,

$$\begin{aligned} \mu_{33}(x_1, x_2, x_3) = & \mu_{33}^{(0)}(x_1, x_2) + \left(\frac{h^2}{3} - x_3^2 \right) \\ & \left[\frac{2\gamma\varepsilon}{\gamma + \varepsilon} \left(\frac{\partial^2 \Gamma}{\partial x_1^2} + \frac{\partial^2 \Gamma}{\partial x_2^2} \right) + \alpha \left(\frac{\partial \Psi_2}{\partial x_1} + \frac{\partial \Psi_1}{\partial x_2} \right) + (\mu - \alpha) \Gamma(x_1, x_2) \right] \end{aligned} \quad (31)$$

With the complete formulas for the tangential stress σ_{3i} and couple stress μ_{33} , one can satisfy the boundary condition (10) for these quantities. As a result, we obtain the following two equations:

$$\begin{aligned} p_i = & \sigma_{3i}^{(0)}(x_1, x_2) - \frac{2h^2}{3} \left\{ \frac{\partial}{\partial x_i} \left[\frac{E}{1-\nu^2} \left(\frac{\partial \Psi_i}{\partial x_i} + \nu \frac{\partial \Psi_j}{\partial x_j} \right) - \frac{\nu}{1-\nu} \frac{p_3}{2h} \right] \right. \\ & \left. + \frac{\partial}{\partial x_j} \left[(\mu + \alpha) \frac{\partial \Psi_i}{\partial x_j} + (\mu - \alpha) \frac{\partial \Psi_j}{\partial x_i} - (-1)^j 2\alpha \Gamma \right] \right\} \end{aligned} \quad (32)$$

$$\begin{aligned} m_3 = & \mu_{33}^{(0)}(x_1, x_2) - \frac{2h^3}{3} \left[\frac{2\gamma\varepsilon}{\gamma + \varepsilon} \left(\frac{\partial^2 \Gamma}{\partial x_1^2} + \frac{\partial^2 \Gamma}{\partial x_2^2} \right) \right. \\ & \left. + \alpha \left(\frac{\partial \Psi_2}{\partial x_1} + \frac{\partial \Psi_1}{\partial x_2} \right) + (\mu - \alpha) \Gamma(x_1, x_2) \right] \end{aligned} \quad (33)$$

For the bending problem, from the equivalence condition one obtain the following formulas for the internal transverse forces averaged across the plate thickness ($N_{13}, N_{23}, N_{31}, N_{32}$), bending and torsional moments of the stresses ($M_{11}, M_{12}, M_{21}, M_{22}$), bending and torsional moments of the couple stresses ($L_{11}, L_{12}, L_{21}, L_{22}$) and hypermoments ($\Lambda_{13}, \Lambda_{23}$):

$$\begin{aligned} N_{i3} = & \int_{-h}^h \sigma_{i3} dx_3, N_{3i} = \int_{-h}^h \sigma_{3i} dx_3, M_{ii} = \int_{-h}^h x_3 \sigma_{ii} dx_3, M_{ij} = \int_{-h}^h x_3 \sigma_{ij} dx_3 \\ L_{ii} = & \int_{-h}^h \mu_{ii} dx_3, L_{ij} = \int_{-h}^h \mu_{ij} dx_3, L_{33} = \int_{-h}^h \mu_{33} dx_3, \Lambda_{i3} = \int_{-h}^h x_3 \mu_{i3} dx_3 \end{aligned} \quad (34)$$

Thus the system of governing equations of bending theory are given by,

$$\begin{aligned} N_{3i} - \frac{\partial M_{ii}}{\partial x_i} - \frac{\partial M_{ji}}{\partial x_j} &= hp_i \\ \frac{\partial N_{13}}{\partial x_1} + \frac{\partial N_{23}}{\partial x_2} &= -p_3 \\ \frac{\partial L_{ii}}{\partial x_i} + \frac{\partial L_{ji}}{\partial x_j} + (-1)^j (N_{j3} - N_{3j}) &= -m_i \\ L_{33} - \left(\frac{\partial \Lambda_{13}}{\partial x_1} + \frac{\partial \Lambda_{23}}{\partial x_2} + M_{12} - M_{21} \right) &= hm_3 \end{aligned} \quad (35)$$

where

$$N_{3i} = 2h[(\mu + \alpha)\gamma_{3i} + (\mu - \alpha)\gamma_{i3}], N_{i3} = 2h \frac{4\mu\alpha}{\mu + \alpha} \gamma_{i3} + \frac{\mu - \alpha}{\mu + \alpha} N_{3i}$$

$$\begin{aligned} M_{ii} = & \frac{2h^3}{3} \frac{E}{1-\nu^2} \left[\frac{\partial \Psi_i}{\partial x_i} + \nu \frac{\partial \Psi_j}{\partial x_j} \right] - \frac{\nu}{1-\nu} \frac{h^2 p_3}{3} \\ M_{ij} = & \frac{2h^3}{3} \left[(\mu + \alpha) \frac{\partial \Psi_j}{\partial x_i} + (\mu - \alpha) \frac{\partial \Psi_i}{\partial x_j} \right] - (-1)^j \frac{4\alpha h^3}{3} \Gamma(x_1, x_2) \end{aligned}$$

$$L_{ii} = 2h \left[\frac{4\gamma(\beta + \gamma)}{\beta + 2\gamma} \chi_{ii} + \frac{4\beta\gamma}{\beta + 2\gamma} \chi_{jj} \right] + \frac{\beta}{\beta + 2\gamma} L_{33}$$

$$L_{ij} = 2h [(\gamma + \varepsilon)\chi_{ji} + (\gamma - \varepsilon)\chi_{ij}]$$

$$L_{33} = 2h [\beta(\chi_{11} + \chi_{22}) + (\beta + 2\gamma)\Gamma(x_1, x_2)]$$

$$\Lambda_{i3} = \frac{2h^3}{3} \left[\frac{4\gamma\varepsilon}{\gamma + \varepsilon} \frac{\partial\Gamma}{\partial x_i} + \frac{m_i}{2h} \frac{\gamma - \varepsilon}{\gamma + \varepsilon} \right]$$

At $\alpha = 0$, the system of Eq. (35) and boundary conditions (10) are reduced to the Timoshenko theory of elastic plates [8]. This system (Eqs. (35) and (10)) is slightly different from the equations of the classical theory of Timoshenko of elastic plates due to the use of static hypothesis (iii).

If we neglect the transverse shear strains in the system i.e., if we assume that

$$\gamma_{i3} + \gamma_{3i} = 0, \text{ or, } \Psi_i = -\frac{\partial w}{\partial x_i} \quad (36)$$

we obtain a model of micropolar elastic plates with independent fields of displacements and rotations, which is based on the Kirchhoff 's hypothesis generalized to the micropolar elastic plate.

4. Applications

The equations in the study of elasticity are elliptic and conditions on the boundary are necessary. For a system with a single coordinate, it becomes the boundary conditions at two ends. This is the so-called two-point boundary value problem in mathematics. It is reasonable or otherwise there will be numerical instability due to the presence of exponents. For instance, the boundary conditions of Timoshenko beam usually are:

4.1. Simply supported edges

In this case the boundary conditions are (taking into account the transverse shear strains);

$$w = 0, M_{ii} = 0, L_{ij} = 0 \text{ at } x_i = 0, a \quad (37)$$

and (without transverse shear strains)

$$w = 0, \frac{\partial^2 w}{\partial x_i^2} = 0, L_{ij} = 0 \text{ at } x_i = 0, a \quad (38)$$

Here we consider the problem of bending of a rectangular micropolar thin plate under the action of a transverse load normal to the middle plane with the intensity

$$q = q_0 \sin\left(\frac{\pi x_1}{a}\right) \sin\left(\frac{\pi x_2}{b}\right), 0 \leq x_1 \leq a, 0 \leq x_2 \leq b$$

In action of this external loading, the solution of the system of Eq. (35) satisfying the boundary conditions (37) or (38) is found in the following form:

$$w = A_1 \sin\left(\frac{\pi x_1}{a}\right) \sin\left(\frac{\pi x_2}{b}\right), \Omega_1 = A_2 \sin\left(\frac{\pi x_1}{a}\right) \cos\left(\frac{\pi x_2}{b}\right),$$

$$\Omega_2 = A_3 \cos\left(\frac{\pi x_1}{a}\right) \sin\left(\frac{\pi x_2}{b}\right)$$

$$\Psi_1 = A_4 \cos\left(\frac{\pi x_1}{a}\right) \sin\left(\frac{\pi x_2}{b}\right), \Psi_2 = A_5 \sin\left(\frac{\pi x_1}{a}\right) \cos\left(\frac{\pi x_2}{b}\right),$$

$$\Gamma = A_6 \cos\left(\frac{\pi x_1}{a}\right) \cos\left(\frac{\pi x_2}{b}\right)$$

$$\tilde{\sigma}_{11} = (\sigma_{11}^{Max})_{micropolar} / (\sigma_{11}^{Max})_{classical},$$

$$\tilde{w} = (w^{Max})_{micropolar} / (w^{Max})_{classical}$$

4.2. Clamped Edges

The boundary conditions are (taking into account the transverse shear strains);

$$w = 0, \Omega_i = 0, \Psi_j = 0, \Lambda_{i3} = 0 \text{ at } x_i = 0, a \quad (39)$$

and (without transverse shear strains)

$$w = 0, \Omega_i = 0, \frac{\partial w}{\partial x_j} = 0, \Lambda_{i3} = 0 \text{ at } x_i = 0, a \quad (40)$$

In this situation, we consider the transverse load normal to the middle plane with the intensity

$$q = q_0 \sin^2\left(\frac{\pi x_1}{a}\right) \sin^2\left(\frac{\pi x_2}{b}\right), 0 \leq x_1 \leq a, 0 \leq x_2 \leq b$$

Solution of the system of Eq. (35) satisfying the boundary conditions (39) or (40) is can be taken in the following form:

$$w = B_1 \sin^2\left(\frac{\pi x_1}{a}\right) \sin^2\left(\frac{\pi x_2}{b}\right), \Omega_1 = B_2 \sin^2\left(\frac{\pi x_1}{a}\right) \sin\left(\frac{2\pi x_2}{b}\right),$$

$$\Omega_2 = B_3 \sin\left(\frac{2\pi x_1}{a}\right) \sin^2\left(\frac{\pi x_2}{b}\right), \Psi_1 = B_4 \sin\left(\frac{2\pi x_1}{a}\right) \sin^2\left(\frac{\pi x_2}{b}\right),$$

$$\Psi_2 = B_5 \sin^2\left(\frac{\pi x_1}{a}\right) \sin\left(\frac{2\pi x_2}{b}\right), \Gamma = B_6 \sin\left(\frac{2\pi x_1}{a}\right) \sin\left(\frac{2\pi x_2}{b}\right)$$

5. Discussion on numerical results

With the view of theoretical consequences derived in the preceding sections, in order to illustrate the analytical developments, in the application section we present two special situations of the said plate such as (i) all four edges are simply supported and (ii) edges are clamped. To study the specific cases, we considered aluminum-epoxy composite material whose physical data (see, Gauthier [21]) are given as follows:

$$\lambda = 7.59 \times 10^9 \text{ Nm}^{-2}, \mu = 1.89745 \times 10^9 \text{ Nm}^{-2},$$

$$\alpha = 0.00745 \times 10^9 \text{ Nm}^{-2}, \beta = 2.26 \times 10^3 \text{ N}$$

Table 1. Numerical results for simply supported plate.

δ	a (mm)	h (mm)	Timoshenko generalized hypothesis		Kirchhoff's generalized hypothesis		
			$\tilde{\sigma}_{11}$	\tilde{w}	$\tilde{\sigma}_{11}$	\tilde{w}	
$\frac{1}{50}$	10	0.2	0.4501	0.4534	0.6216	0.6216	
	30	0.6	0.5562	0.5588	0.7088	0.7088	
	50	1	0.6797	0.6816	0.8007	0.8007	
	70	1.4	0.7740	0.7753	0.8648	0.8648	
	90	1.8	0.8377	0.8386	0.9053	0.9053	
	110	2.2	0.8799	0.8806	0.9311	0.9311	
	130	2.6	0.9085	0.9090	0.9481	0.9481	
	150	3	0.9284	0.9288	0.9597	0.9597	
	170	3.4	0.9426	0.9430	0.9679	0.9679	
	190	3.8	0.9531	0.9534	0.9739	0.9739	
	$\frac{1}{100}$	10	0.1	0.1705	0.1717	0.2911	0.2911
		30	0.3	0.2394	0.2405	0.3783	0.3783
		50	0.5	0.3476	0.3486	0.5012	0.5012
		70	0.7	0.4623	0.4631	0.6152	0.6152
90		0.9	0.5644	0.5650	0.7051	0.7051	
110		1.1	0.6479	0.6484	0.7717	0.7717	
130		1.3	0.7137	0.7141	0.8204	0.8204	
150		1.5	0.7650	0.7653	0.8562	0.8562	
170		1.7	0.8049	0.8052	0.8829	0.8829	
190		1.9	0.8362	0.8364	0.9031	0.9031	

Table 2. Numerical results for clamped edges plate.

δ	a (mm)	h (mm)	Timoshenko generalized hypothesis		Kirchhoff's generalized hypothesis		
			$\tilde{\sigma}_{11}$	\tilde{w}	$\tilde{\sigma}_{11}$	\tilde{w}	
$\frac{1}{50}$	10	0.2	0.6774	0.6825	0.8103	0.8103	
	30	0.6	0.7141	0.7187	0.8299	0.8299	
	50	1	0.7657	0.7696	0.8578	0.8578	
	70	1.4	0.8093	0.8131	0.8841	0.8841	
	90	1.8	0.9373	0.9331	0.9051	0.9051	
	110	2.2	0.9026	0.9034	0.9208	0.9208	
	130	2.6	0.9205	0.9214	0.9323	0.9323	
	150	3	0.9355	0.9362	0.9408	0.9408	
	170	3.4	0.9470	0.9477	0.9472	0.9472	
	190	3.8	0.9560	0.9565	0.9521	0.9521	
	$\frac{1}{100}$	10	0.1	0.3470	0.3496	0.5163	0.5163
		30	0.3	0.3874	0.3899	0.5488	0.5488
		50	0.5	0.4529	0.4553	0.5997	0.5997
		70	0.7	0.5191	0.5216	0.6531	0.6531
90		0.9	0.7750	0.7715	0.7003	0.7003	
110		1.1	0.6992	0.6999	0.7386	0.7386	
130		1.3	0.7445	0.7453	0.7686	0.7686	
150		1.5	0.7850	0.7857	0.7919	0.7919	
170		1.7	0.8184	0.8190	0.8099	0.8099	
190		1.9	0.8455	0.8460	0.8240	0.8240	

$$\gamma = 2.445 \times 10^3 N, \varepsilon = 0.185 \times 10^3 N,$$

$$\rho = 2.19 \times 10^3 Kgm^{-3}, j = 0.00196 \times 10^{-4} m^2$$

Here we considered rectangular micropolar thin plate, with various lateral dimensions shown in tables, in which the values of 'a' and 'h' are vary simultaneously such that $\delta = \frac{h}{a}$ is fixed and the dimension of 'b' is three forth that of the dimension of 'a'. Using mathematical simulation technique with the help of Matlab-9.1 software, the maximum values of the deflection (w) as well as longitudinal stress (σ_{11}) are obtained for the cases of Timoshenko generalized

hypothesis and Kirchhoff's generalized hypothesis (Taking $q_0 = 1N/m^2$). A comparison has been made with the classical results.

From Table 1, it is observed that deflection and longitudinal stress is proportional with plate length as well as thickness. For a fixed value of 'a', when 'h' is decreased both the deflection of the plate and longitudinal stress are increased. Again, for the case of micropolar thin plate deflection is much smaller than that of classical plate. Since the longitudinal stress is smaller than the classical plate, thus bending moment of the micropolar plate is also much laser than the classical plate. But if we neglect the transverse shear

strains (i.e., in the case of Kirchhoff's generalized hypothesis), the deflection is not that much smaller than that of Timoshenko generalized hypothesis and the longitudinal stress is higher than the classical plate.

From Table 2 (i.e., in the case of clamped plate), it is seen that when thickness of the plate is much smaller than the length of the plate (100 times) deflection and longitudinal stress are smaller. But, for the other cases deflection of the plate is almost identical with the classical plate. Although for Kirchhoff's generalized hypothesis deflection as well as the longitudinal stress both are larger than that of for the Timoshenko hypothesis, in the clamped edges plate both deflection and longitudinal stress follows same nature.

6. Conclusion

In this article, we have studied theory of deflection of a thin rectangular isotropic micropolar plate under transverse loading. On the basis of hypothesis a set of governing equations are formulated for thin micropolar plate. In the case of thin isotropic rectangular micropolar plate deflection and bending moment are smaller than that of classical plate. Thus, we may establish the following phenomena:

1. Since the deflection as well as bending moment of a thin micropolar plate are smaller than classical plate, hence as per the deflection is concern, micropolar plate is more useful than classical plate.
2. Stiffness of the thin micropolar plate is higher than that of classical plate.

Nomenclature

Symbol	Name of the representing quantity
σ_{nm}	stress tensor
μ_{nm}	couple stress tensor
γ_{nm}	bending strain tensor
χ_{nm}	torsional tensor
u_n	component of displacement vector
ϕ_n	component of rotation
$\alpha, \beta, \gamma, \varepsilon$	micropolar material moduli
E	Young's modulus
ν	Poisson's ratio
ε_{kmn}	Levi-Civita tensor
δ_{mn}	Kronecker delta
x_n	coordinate system
a	length of the plate
b	width of the plate
h	half of the thickness of the plate
q	mechanical load

References

- [1] A. C. Eringen. Microcontinuum Field Theories. Vol. 1: Foundation and Solids, Springer, New York, 1999.
- [2] M. Godio, I. Stefanou, K. Sab, and J. Sulem, Multisurface plasticity for Cosserat materials: plate element implementation and validation, *Int. J. Numer. Meth. Engng.*, vol. 108, pp. 456 - 484, 2016. .
- [3] R. D. Gauthier, and W. E. Jahsman, A Quest for Micropolar Elastic Constants. Part II, *Arch. Mech.*, vol. 33, pp. 717-737, 1981.
- [4] R. Lakes, Experimental Methods for Study of Cosserat Elastic Solids and Other Generalized Elastic Continua, in H. Muhlhaus (ed.), *Continuum Models for Materials with Micro-Structure*. Wiley, New York, No. 1, pp. 122, 1995.
- [5] A. E. Green, and P. M. Naghdi, The Linear Elastic Cosserat Surface and Shell Theory, *Int. J. Solids Struct.*, vol. 4, no. 6, pp. 585-592, 1968.
- [6] P. Ciarlet, *Theory of Plates, Mathematical Elasticity II*. Elsevier, Amsterdam, 1997.
- [7] P. Ciarlet, *Theory of Plates, Mathematical Elasticity III*, Elsevier, Amsterdam, 2000.
- [8] S. P. Timoshenko, and S. Woinowsky-Krieger, *Theory of Plates and Shells*, McGraw Hill, New York, 1985.
- [9] A. L. Goldenveizer, Derivation of Asymptotic Theory of Bending of a Plate by the Method of Asymptotic Integration of the Equations of the Theory of Elasticity, *J. Appl. Math. Mech. (PPM)*, vol. 26, pp. 1000-1025, 1964.
- [10] P. Neff, and J. A. Jeong, New Paradigm: The Linear Isotropic Cosserat Model With Conformally Invariant Curvature Energy, *ZAMM*, vol. 89, no. 2, pp. 107-122, 2009.
- [11] P. Naghdi, On the Formulation of Contact Problems of Shells and Plates, *J. Elast.*, vol. 39, pp. 133-163, 1995.
- [12] K. O. Friedrichs, and R. F. Dressler, A Boundary-Layer Theory of Elastic Plates, *Comm. Pure Appl. Math.*, vol. 14, pp. 1-33, 1961.
- [13] P. Ciarlet, and P. Destuynder, A Justification of Two-Dimensional Linear Plate Model, *J. Mecanique*, vol. 18, pp. 315-344, 1979.
- [14] E. Cosserat, and F. Cosserat, Sur la theorie de l'elastocite, *Ann. Toulouse*, vol. 10, no. 3-4, pp. 1-116, 1896.
- [15] H. Altenbach, and V. A. Eremeyev, On the Linear Theory of Micropolar Plates, *Z. Angew. Math. Mech.*, vol. 89, no. 4, pp. 242-246, 2009.
- [16] A. C. Eringen, Theory of Micropolar Plate, *ZAMP*, vol. 18, pp. 12-30, 1967.
- [17] A. E. Green, and P. M. Naghdi, Micropolar and Director Theories of Plates, *Quart. J. Mech. Appl. Math.*, vol. 20, no. 2, pp. 183-199, 1967.
- [18] F. Y. Wang, On the Solutions of Eringen's Micropolar Plate Equations and of Other Approximation Equations, *Int. J. Eng. Sci.*, vol. 28, no. 9, pp. 919-925, 1990.
- [19] S. O. Sarkisyan, Boundary Value Problems of Thin Plates in the Asymmetric Theory of Elasticity, *Prikl. Mat. Mekh.*, vol. 72, pp. 129-147, 2008.
- [20] S. Shaw, High Frequency Vibration of a Rectangular Micropolar Beam: A Dynamical Analysis, *Int. J. Mech. Sci.*, vol. 108, pp. 83-89, 2016.
- [21] R. D. Gauthier, Experimental Investigations on Micropolar Media, in E.D. Brulin and R.K.T. Hsieh (eds.), *Mechanics of Micropolar Media*, World Scientific, Singapore, 1982.



Source details

[Feedback >](#) [Compare sources >](#)

International Journal for Computational Methods in Engineering Science and Mechanics

Formerly known as: [International Journal of Computational Engineering Science](#)

Scopus coverage years: from 2005 to Present

Publisher: Taylor & Francis

ISSN: 1550-2287 E-ISSN: 1550-2295

Subject area: [Engineering: Computational Mechanics](#) [Mathematics: Computational Mathematics](#)

Source type: Journal

[View all documents >](#)

[Set document alert](#)

[Save to source list](#)

CiteScore 2022 ?
2.1

SJR 2022 ?
0.215

SNIP 2022 ?
0.383

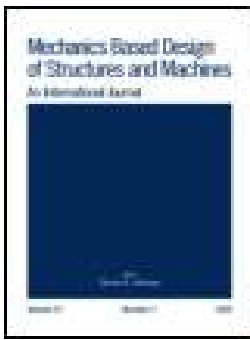
[CiteScore](#) [CiteScore rank & trend](#) [Scopus content coverage](#)



Improved CiteScore methodology

CiteScore 2022 counts the citations received in 2019-2022 to articles, reviews, conference papers, book chapters and data papers published in 2019-2022, and divides this by the number of publications published in 2019-2022. [Learn more >](#)





Mechanics Based Design of Structures and Machines

An International Journal

ISSN: 1539-7734 (Print) 1539-7742 (Online) Journal homepage: <http://www.tandfonline.com/loi/lmbd20>

Effect of rotation in magneto-thermoelastic transversely isotropic hollow cylinder with three-phase-lag model

Siddhartha Biswas, Basudeb Mukhopadhyay & Soumen Shaw

To cite this article: Siddhartha Biswas, Basudeb Mukhopadhyay & Soumen Shaw (2019): Effect of rotation in magneto-thermoelastic transversely isotropic hollow cylinder with three-phase-lag model, Mechanics Based Design of Structures and Machines

To link to this article: <https://doi.org/10.1080/15397734.2018.1545587>



Published online: 11 Jan 2019.



Submit your article to this journal [↗](#)



View Crossmark data [↗](#)



Effect of rotation in magneto-thermoelastic transversely isotropic hollow cylinder with three-phase-lag model

Siddhartha Biswas , Basudeb Mukhopadhyay, and Soumen Shaw

Department of Mathematics, Indian Institute of Engineering Science and Technology, Shibpur, India

ABSTRACT

This article deals with the various heat source responses in a transversely isotropic hollow cylinder under the purview of three-phase-lag (TPL) generalized thermoelasticity theory. In presence of magnetic field and due to the rotating behavior of the cylinder, the governing equations are redefined for generalized thermoelasticity with thermal time delay. In order to obtain the stress, displacement and temperature field, the field functions are expressed in terms of modified Bessel functions in Laplace transformed domain. When the outer radius of hollow cylinder tends to infinity, the corresponding results are discussed. Finally an appropriate Laplace transform inversion technique is adopted.

ARTICLE HISTORY

Received 5 April 2018

Accepted 5 November 2018

KEYWORDS

Magnetic effect; rotation; transversely isotropic medium; hollow cylinder; three-phase-lag model; heat source

1. Introduction

A considerable attention has been made since last few decades due to numerous applications of thermoelasticity in various disciplines of science and technology. It is well known that the theory of coupled thermoelasticity suffers from physical drawbacks that the thermal signal propagates with the infinite speed. Biot (1956) introduced the theory of classical thermoelasticity based on the thermodynamic principles of irreversible processes. In this theory, the equation of motion is hyperbolic in nature and the heat conduction equation is parabolic. It still experiences defect of uncoupled theory due to the presence of parabolic type heat conduction equation. For the elimination of this drawback in classical thermoelasticity theory, the generalized thermoelasticity theories are developed in which the heat conduction equation is of hyperbolic type.

Cattaneo (1958) replaces the Fourier law of heat conduction by introducing a single parameter that acts as a relaxation time, thus a wave type equation is formulated by postulating a new law of heat conduction instead of classical Fourier law. The first generalization is done by Lord and Shulman (1967) and is referred to as L–S model. The L–S model is developed by a system of partial differential equations (PDE) in which in comparison to a system of classical thermoelasticity, the Fourier law of heat conduction is replaced by the Maxwell–Cattaneo law that generalizes the Fourier law and introduces a single relaxation time into consideration. The second generalization is due to Green and Lindsay (1972) which is known as G–L model. The G–L model is characterized by a system of PDE in which, in comparison to the classical system, the constitutive relations for the stress tensor and the entropy are generalized by introducing two different relaxation times into considerations. The third generalization is done by Hetnarski and Ignaczak (1993, 1996) and is known as a H–I model. The H–I model has been introduced in an attempt to describe low-temperature soliton-like thermoelastic waves. The fourth generalization to the coupled theory of

thermoelasticity is introduced by Green and Naghdi (1993) and this theory is concerned with the thermoelasticity theory without energy dissipation, referred to as G–N theory of type-II in which the classical Fourier law is replaced by a heat flux-rate temperature gradient relation. The heat transport equation does not involve a temperature rate term and as such this model admits undamped thermoelastic waves in thermoelastic material. Detailed information regarding the generalized heat conduction model can be found in the monographs of Chandrasekharaiah (1986, 1998) and Ignaczak and Hetnarski (2014).

The generalized thermoelasticity theory with the dual phase lag effect has been developed by Tzou (1995). Tzou introduced two different time lags, one for the heat flux vector and the other for the temperature gradient. The delay time τ_T is supposed to be caused by the microstructural interactions (small effects of heat transport in space, such as phonon-electron interaction or phonon scattering) and is called the phase lag of the temperature gradient. The other delay time τ_q is interpreted as the relaxation time due to fast transient effects of the thermal inertia (or small effects of heat transport in time) and is called the phase lag of the heat flux. The most recent development in thermoelasticity theory is the thermoelasticity with three-phase-lags (TPL) by Choudhuri (2007). In this model, a phase lag (τ_ν) for the thermal displacement gradient is introduced. The stability of TPL model is discussed by Quintanilla and Racke (2008). TPL model includes TPL in the heat flux vector, the temperature gradient, and in the thermal displacement gradient. To study some heat transfer problems involving very short time intervals and the problems of very high heat fluxes, the hyperbolic equation gives significantly different results than the parabolic equation. TPL is very much effective in the problems of nuclear boiling, exothermic catalytic reactions, phonon-electron interactions, phonon-scattering, etc.

Since nineteenth century the coupling phenomenon between thermo-mechanical behavior of the materials and the electromagnetic response has been started. The electromagnetic interaction with piezoelectric materials has been discovered in the early part of the twentieth century. The continued development of electromagnetic interaction of piezoelectric materials has led to huge market of products ranging from those for everyday use to most specialized devices. Since last two decades, the electromagnetic interaction with composite materials has been developed. Such composites can exhibit the field coupling which has not been seen in any of the monolithic constituent materials. These electromagnetic composite materials have been used in many devices like ultrasonic imaging devices, sensors, actuators, and transducers. Electromagnetic elastic materials have the ability that they can convert the energy from one kind to another (among mechanical, electrical, and magnetic). Due to these special characteristics, these types of materials have been used in high tech areas such as lasers, supersonic devices and in many information technological applications.

Anisotropy creates qualitatively new properties of elastic waves and acoustic phenomena that have not got close analogous in isotropic media. Some of them have already found their practical applications in real devices. A theoretical description of elastic waves in anisotropic material is a very nontrivial problem. The study of wave propagation in anisotropic materials has been a subject of extensive investigation in the literature. It is of great importance in a variety of applications ranging from seismology to nondestructive testing of composite structures used in aircraft, spacecraft, or other engineering industries.

Thermal stresses are the main cause of structural failures in industrial applications and for this reason, the exact and general solutions are required for the thermoelastic problems. Due to the presence of coupling between the energy equation and the equation of motion, the governing equations of thermoelasticity are of complexity. For this complexity, some reasonable simplifications are made on these equations, such as dropping the coupling term in the energy equation, which yields the uncoupled dynamical theory of thermoelasticity. As a general rule, the effect of coupling term in the energy equation is small and the distinction between coupled and uncoupled theories is negligible. Cylinders have many applications in engineering and it is interesting to have a general solution for the thermoelastic problem.

Chandrasekharaiah and Keshavan (1992) examined axisymmetric thermoelastic interactions in an unbounded body with cylindrical cavity. Kar and Kanoria (2007) studied thermoelastic Interaction with energy dissipation in an unbounded body with a spherical hole. Youssef (2006) considered a problem of generalized thermoelastic infinite cylindrical cavity subjected to a ramp-type heating and loading. Roychoudhury and Bandyopadhyay (2005) studied thermoelastic wave propagation in rotating elastic medium without energy dissipation. Mukhopadhyay and Kumar (2008a, 2008b) studied generalized thermoelastic interactions with a spherical cavity as well as with a cylindrical hole. Abd-Alla and Mahmoud (2010) discussed magneto-thermoelastic problem in rotating nonhomogeneous orthotropic hollow cylinder under the hyperbolic heat conduction model. Abouelregal (2013) studied generalized thermoelastic infinite transversely isotropic body with cylindrical cavity due to moving heat source and harmonically varying heat source. Recently Sherief and Raslan (2016) examined thermoelastic interactions without energy dissipation in an unbounded body with a cylindrical cavity. Kumar and Mukhopadhyay (2009) studied the effect of three phase lags on generalized thermoelasticity for an infinite medium with a cylindrical cavity. Kar and Kanoria (2009) considered generalized thermoelastic functionally graded orthotropic hollow sphere under thermal shock with TPL effect. Das, Kar, and Kanoria (2013) analyzed magneto-thermoelastic response in a transversely isotropic hollow cylinder under thermal shock with three phase lag effect. Banik and Kanoria (2012) discussed the effect of TPL on a two-temperature generalized thermoelasticity for infinite medium with spherical cavity. Abbas and Othman (2012) considered generalized thermoelasticity of thermal shock problem in an isotropic hollow cylinder and temperature dependent elastic moduli. Othman and Abbas (2012) studied generalized thermoelasticity of thermal shock problem in a nonhomogeneous isotropic hollow cylinder with energy dissipation. Othman and Abbas (2015) examined the effect of rotation on a magneto-thermoelastic hollow cylinder with energy dissipation using finite element method. Othman, Elmaklizi, and Mansour (2017) considered the effect of temperature-dependent properties on generalized magneto-thermoelastic with two-temperature under TPL model. Said (2016a) investigated the influence of gravity on generalized magneto-thermoelastic medium for TPL model. Said (2015) studied deformation of a rotating two-temperature generalized magneto-thermoelastic medium with internal heat source due to hydrostatic initial stress. Said (2017) considered fiber-reinforced thermoelastic medium with an internal heat source due to hydrostatic initial stress and gravity for the TPL model. Said (2016b) investigated wave propagation in a magneto-micropolar thermoelastic medium with two temperatures for TPL model. Yang and Lin (2018) proposed a theoretical study of the mechanism with variable compression ratio and expansion ratio. Huang (2018) discussed simulation of friction and stiction in multibody dynamics model problems. Sun, Yan, and Gao (2018) analyzed frequency-domain vibration response of thin plate attached with viscoelastic free layer damping. Bhattacharya, Ananthasuresh, and Ghoshal (2018) proposed design of a one-dimensional flexible structure for desired load-bearing capability and axial displacement.

In this study, our aim is to present magneto-thermoelastic interaction with thermal delay in transversely isotropic rotating hollow cylinder in presence of various heat sources. To solve the problem, Laplace transform technique is employed over field variables and the field functions are expressed in terms of modified Bessel functions. A complete and comprehensive analysis of the results has been presented for TPL model in presence of a magnetic field as well as rotation. Applying inverse Laplace transform technique (see [Appendix](#)), effect of magnetic field and rotation on radial stress and displacement are illustrated graphically.

2. Formulation of the problem

We consider a homogeneous transversely isotropic thermoelastic solid occupying the region of an infinitely long hollow circular cylinder of internal radius ' a ' and external radius ' b '. We shall use a cylindrical system of coordinates (r, θ, z) with the z -axis coinciding with the axis of cylinder.

We shall also assume the initial state of the medium is quiescent. The outer of this cylinder is assumed to be traction free and subjected to various heat sources that depend only on the time t , while the inner surface is assumed to be in contact with a rigid surface and is thermally insulated. We also consider the hollow cylinder is rotating in the presence of a magnetic field.

Due to radial symmetry of the problem, all functions considered are functions of the radial distance from the axis of the cylinder r and the time t only.

Thus the displacement components are

$$u_r = u(r, t), u_\theta = u_z = 0. \quad (1)$$

The strain components are as follows:

$$e_{rr} = \frac{\partial u}{\partial r}, e_{\theta\theta} = \frac{u}{r}, e_{zz} = e_{r\theta} = e_{rz} = e_{\theta z} = 0. \quad (2)$$

The cubic dilatation e is thus given by

$$e = e_{rr} + e_{\theta\theta} + e_{zz} = \frac{\partial u}{\partial r} + \frac{u}{r} = \frac{1}{r} \frac{\partial(ru)}{\partial r}. \quad (3)$$

The stress-displacement-temperature relations are given by

$$\begin{aligned} \sigma_{rr} &= c_{11} \frac{\partial u}{\partial r} + c_{12} \frac{u}{r} - \beta T \\ \sigma_{\theta\theta} &= c_{12} \frac{\partial u}{\partial r} + c_{11} \frac{u}{r} - \beta T \end{aligned}, \quad (4)$$

where T is the temperature above reference temperature, T_0 is the reference uniform temperature of the body chosen such that $|\frac{T}{T_0}| \ll 1$, c_{11}, c_{12} are elastic constants, β is the thermal moduli, σ_{rr} is the radial stress, and $\sigma_{\theta\theta}$ is the tangential stress.

The equation of motion in presence of magnetic field and rotation can be taken as

$$\sigma_{rr,r} + \frac{\sigma_{rr} - \sigma_{\theta\theta}}{r} + F_r = \rho \frac{\partial^2 u}{\partial t^2} + R_r, \quad (5)$$

where ρ is the mass density, F_r is the component of Lorentz force, and R_r is the component of body force due to rotation.

We consider that the homogeneous transversely isotropic thermoelastic hollow cylinder is rotating uniformly with angular velocity $\vec{\Omega} = \Omega \vec{n}$ where \vec{n} is a unit vector representing the direction of the axis of rotation. The displacement equation in the rotating frame has two additional terms (Schoenberg and Censor 1973):

- i. Centripetal acceleration $\vec{\Omega} \times (\vec{\Omega} \times \vec{u})$ due to time-varying motion only and
- ii. Coriolis acceleration $2\vec{\Omega} \times \dot{\vec{u}}$.

These terms do not appear in nonrotating media. The term Coriolis acceleration is neglected here as this term appears only in case of moving frame.

If $\vec{\Omega} = (0, 0, \Omega)$ represents the rotation vector, the component of rotation is given by

$$R_r = -\rho \Omega^2 u. \quad (6)$$

Let us consider that the cylinder is placed in a magnetic field with constant intensity $\vec{H}_0 = (0, 0, H_0)$ acting parallel to the direction of the z -axis.

The Lorentz force \vec{F} is given by

$$\vec{F} = \mu_0 (\vec{J} \times \vec{H}), \quad (7)$$

where \vec{J} is the current density vector.

For a perfectly electrically and magnetically conducting elastic body, the electromagnetic field is governed by Maxwell's equations:

$$\vec{\nabla} \times \vec{h} = \vec{J} + \varepsilon_0 \dot{\vec{E}}, \quad (8)$$

$$\vec{\nabla} \times \vec{E} = -\mu_0 \dot{\vec{h}}, \quad (9)$$

$$\vec{\nabla} \cdot \vec{h} = 0, \quad (10)$$

$$\vec{\nabla} \cdot \vec{E} = 0, \quad (11)$$

where μ_0 and ε_0 are the electric permeability and magnetic permittivity respectively, $\vec{\nabla}$ is the Hamiltonian's operator, \vec{H}_0 is initial magnetic field, \vec{h} is perturbed magnetic field, and \vec{E} is an induced electric field.

For perfectly conducting medium from generalized Ohm's law, we obtain

$$\vec{E} = -\mu_0 (\dot{\vec{u}} \times \vec{H}). \quad (12)$$

As the magnitude of the perturbed magnetic field (\vec{h}) is very small, in the discussion of linear theory of elasticity we may neglect the product term involving h and its higher degrees.

From Eqs. (9) and (12) the induced field components in the cylinder are found to be

$$\vec{E} = (0, E, 0) = \left(0, \mu_0 H_0 \frac{\partial u}{\partial t}, 0\right), \vec{h} = (0, 0, h) = (0, 0, -H_0 e). \quad (13)$$

From Eqs. (8) and (13), the components of current density vector have the following form:

$$\vec{J} = \left(0, H_0 \frac{\partial e}{\partial r} - \varepsilon_0 \mu_0 H_0 \frac{\partial^2 u}{\partial t^2}, 0\right). \quad (14)$$

The components of Lorentz force can be obtained from Eqs. (7) and (14) as

$$\vec{F} = \left[\mu_0 H_0^2 \left(\frac{\partial e}{\partial r} - \varepsilon_0 \mu_0 \frac{\partial^2 u}{\partial t^2}\right), 0, 0\right]. \quad (15)$$

Maxwell's electromagnetic stress tensor σ_{ij}^* is given by

$$\sigma_{ij}^* = \mu_0 [H_i h_j + H_j h_i - (\vec{H} \cdot \vec{h}) \delta_{ij}]; i, j = r, \theta, z$$

Radial Maxwell stress $\sigma_{rr}^* = \mu_0 H_0^2 e$

We take $\sigma_r = \sigma_{rr} + \sigma_{rr}^*$

TPL model in transversely isotropic cylindrical medium can be taken as

$$\left[K^* + (K + \tau_\nu K^*) \frac{\partial}{\partial t} + K \tau_T \frac{\partial^2}{\partial t^2} \right] \nabla^2 T = \left(1 + \tau_q \frac{\partial}{\partial t} + \frac{\tau_q^2}{2} \frac{\partial^2}{\partial t^2} \right) \left(\rho C_e \frac{\partial^2 T}{\partial t^2} + \beta T_0 \frac{\partial^2 e}{\partial t^2} \right). \quad (16)$$

where K is the classical thermal conductivity, K^* is the material constant characteristic of the theory, C_e is the specific heat at the constant strain, τ_q, τ_T , and τ_ν are the phase lags of heat flux, temperature gradient, and thermal displacement gradient, respectively where $0 \leq \tau_T \leq \tau_q$, t denotes time and $\nabla^2 = \frac{\partial^2}{\partial r^2} + \frac{1}{r} \frac{\partial}{\partial r}$.

Using Eqs. (4), (6), and (15) in the Eq. (5), we get

$$(c_{11} + \mu_0 H_0^2) \frac{\partial e}{\partial r} - \beta \frac{\partial T}{\partial r} = (\rho + \varepsilon_0 \mu_0^2 H_0^2) \frac{\partial^2 u}{\partial t^2} - \rho \Omega^2 u \quad (17)$$

Multiplying both sides by r and then using the operator $\frac{1}{r} \frac{\partial}{\partial r}$ to both sides of Eq. (17), we obtain

$$(c_{11} + \mu_0 H_0^2) \nabla^2 e - \beta \nabla^2 T = (\rho + \varepsilon_0 \mu_0^2 H_0^2) \frac{\partial^2 e}{\partial t^2} - \rho \Omega^2 e. \quad (18)$$

We now consider the following initial conditions Eq. (19) and various boundary conditions.

3. Initial conditions

We assume following initial conditions to solve the problem:

$$u = \frac{\partial u}{\partial t} = T = \frac{\partial T}{\partial t} = 0 \text{ at } t = 0 \quad (19)$$

4. Boundary conditions

The boundary conditions can be written in the following form:

1. The thermal boundary conditions:

$$T(b, t) = F(t) \quad (20)$$

$$\frac{\partial T}{\partial r}(a, t) = 0 \quad (21)$$

2. Mechanical boundary condition:

$$\sigma_r(b, t) = 0 \quad (22)$$

$$u(a, t) = 0. \quad (23)$$

5. Solution in the Laplace transformed domain

Introducing the Laplace transform domain defined by the following formula:

$$\bar{f}(x, s) = L[f(x, t)] = \int_0^\infty f(x, t) e^{-st} dt, \operatorname{Re}(s) > 0 \quad (24)$$

in Eqs. (18) and (16) and using homogeneous initial conditions, we obtain

$$(c_{11} + \mu_0 H_0^2) \nabla^2 \bar{e} - \beta \nabla^2 \bar{T} = [(\rho + \varepsilon_0 \mu_0^2 H_0^2) s^2 - \rho \Omega^2] \bar{e} \quad (25)$$

$$\nabla^2 \bar{T} = \tau s^2 (\rho C_e \bar{T} + \beta T_0 \bar{e}) \quad (26)$$

where $\tau_1 = 1 + s\tau_\nu$, $\tau_2 = 1 + s\tau_T$, $\tau_3 = 1 + s\tau_q + \frac{s^2 \tau_a^2}{2}$, $\tau = \frac{\tau_3}{K^* \tau_1 + sK\tau_2}$.

Eliminating \bar{e} from Eqs. (25) and (26), we get

$$(\nabla^4 - A\nabla^2 + B)(\bar{T}, \bar{e}) = 0 \quad (27)$$

which can be written as

$$(\nabla^2 - k_1^2)(\nabla^2 - k_2^2)(\bar{T}, \bar{e}) = 0 \quad (28)$$

where $k_i (i = 1, 2)$ is the square root of the positive real part of the roots k_i^2 of the following characteristic equation:

$$k^4 - Ak^2 + B = 0 \quad (29)$$

where $A = \frac{a_6 \beta + a_2 s^2 - a_3}{a_1}$, $B = \frac{(a_2 s^2 - a_1 - a_3) a_5}{a_1}$, $a_1 = c_{11} + \mu_0 H_0^2$, $a_2 = \rho + \varepsilon_0 \mu_0^2 H_0^2$,

$$a_3 = \rho\Omega^2, a_4 = \tau s^2, a_5 = a_4\rho C_e, a_6 = a_4\beta T_0.$$

The solutions of Eq. (28) have the following form:

$$\bar{T} = \sum_{i=1}^2 [A_i I_0(k_i r) + B_i K_0(k_i r)] \quad (30)$$

$$\bar{e} = \sum_{i=1}^2 [A'_i I_0(k_i r) + B'_i K_0(k_i r)] \quad (31)$$

where A_i, A'_i, B_i, B'_i are parameters depending on s and $I_n(\cdot), K_n(\cdot)$ denote the modified Bessel functions of order n of the first, and second kind, respectively.

Substituting the values of \bar{T} and \bar{e} in Eq. (25), we obtain

$$A'_i = \frac{\beta k_i^2}{[a_1 k_i^2 - (a_2 s^2 - a_3)]} A_i, B'_i = \frac{\beta k_i^2}{[a_1 k_i^2 - (a_2 s^2 - a_3)]} B_i \quad (32)$$

Now using the above relations in Eq. (31), we get

$$\bar{e} = \sum_{i=1}^2 \frac{\beta k_i^2}{[a_1 k_i^2 - (a_2 s^2 - a_3)]} [A_i I_0(k_i r) + B_i K_0(k_i r)] \quad (33)$$

Integrating Eq. (33) with respect to r , we obtain

$$\bar{u} = \sum_{i=1}^2 m_i [A_i I_1(k_i r) - B_i K_1(k_i r)] \quad (34)$$

where $m_i = \frac{\beta k_i}{[a_1 k_i^2 - (a_2 s^2 - a_3)]}, i = 1, 2$

In obtaining Eq. (34), we have used the following integral relations of the modified Bessel functions:

$$\int x I_0(x) dx = x I_1(x), \int x K_0(x) dx = -x K_1(x)$$

Thus we obtain

$$\begin{aligned} \bar{\sigma}_{rr} = & c_{11} \left[\sum_{i=1}^2 m_i \left(\left(k_i I_0(k_i r) - \frac{I_1(k_i r)}{r} \right) A_i + \left(k_i K_0(k_i r) + \frac{K_1(k_i r)}{r} \right) B_i \right) \right] \\ & + c_{12} \left[\sum_{i=1}^2 \frac{m_i}{r} \{ A_i I_1(k_i r) - B_i K_1(k_i r) \} \right] - \beta \left[\sum_{i=1}^2 \{ A_i I_0(k_i r) - B_i K_0(k_i r) \} \right] \end{aligned} \quad (35)$$

6. Applications

In this section, we discuss the effect of various heat sources on the transversely isotropic hollow cylinder.

Case 1: (Constant heat source)

For constant heat source, we take the boundary conditions as

$$T(b, t) = T_0 H(t) \quad (36)$$

$$\frac{\partial T(a, t)}{\partial r} = 0 \quad (37)$$

$$\sigma_r(b, t) = 0 \quad (38)$$

$$u(a, t) = 0 \quad (39)$$

where $H(t)$ denotes Heaviside function.

Now the transformed boundary conditions become

$$\bar{T}(b, s) = \frac{T_0}{s} \tag{40}$$

$$\frac{\partial \bar{T}(a, s)}{\partial r} = 0 \tag{41}$$

$$\bar{\sigma}_r(b, s) = 0 \tag{42}$$

$$\bar{u}(a, s) = 0 \tag{43}$$

Thus from the boundary conditions Eqs. (40)–(43), we obtain the following system of linear equations in A_1, A_2, B_1 and B_2 as

$$A_1 W_{11} + A_2 W_{12} + B_1 W_{13} + B_2 W_{14} = \frac{T_0}{s}, \tag{44}$$

$$A_1 W_{21} + A_2 W_{22} + B_1 W_{23} + B_2 W_{24} = 0, \tag{45}$$

$$A_1 W_{31} + A_2 W_{32} + B_1 W_{33} + B_2 W_{34} = 0, \tag{46}$$

$$A_1 W_{41} + A_2 W_{42} + B_1 W_{43} + B_2 W_{44} = 0, \tag{47}$$

where

$$(W_{1i}, W_{1j}) = \{I_0(k_i b), K_0(k_{j-2} b)\}$$

$$(W_{2i}, W_{2j}) = \{k_i I_1(k_i a), -k_{j-2} K_1(k_{j-2} a)\}. \tag{48}$$

$$(W_{3i}, W_{3j}) = \left[I_0(k_i b)(c_{11} m_i k_i - \beta) + \frac{m_i}{b} I_1(k_i b)(c_{12} - 1) + \mu_o H_0^2 m_i k_i I_0(k_i b), K_0(k_{j-2} b)(c_{11} k_{j-2} m_{j-2} + \beta) \right. \\ \left. + \frac{m_{j-2}}{b} K_1(k_{j-2} b)(1 - c_{12}) + \mu_o H_0^2 m_{j-2} k_{j-2} K_0(k_{j-2} b) \right]$$

$$(W_{4i}, W_{4j}) = \{m_i I_1(k_i a), -m_{j-2} K_1(k_{j-2} a)\}$$

and $i = 1, 2, j = 3, 4$.

From Eqs. (44)–(47), the values of A_1, A_2, B_1 , and B_2 are obtained as

$$\begin{pmatrix} A_1 \\ A_2 \\ B_1 \\ B_2 \end{pmatrix} = M^{-1} \begin{pmatrix} \frac{T_0}{s} \\ 0 \\ 0 \\ 0 \end{pmatrix}. \tag{49}$$

The Matrix M is given by

$$M = \begin{pmatrix} W_{11} & W_{12} & W_{13} & W_{14} \\ W_{21} & W_{22} & W_{23} & W_{24} \\ W_{31} & W_{32} & W_{33} & W_{34} \\ W_{41} & W_{42} & W_{43} & W_{44} \end{pmatrix}. \tag{50}$$

The elements of Matrix M are given by Eq. (48).

Case 2: (Periodically varying heat source)

For periodically varying heat source the boundary Eq. (36) will be replaced by Eq. (51) and other Eqs. (37), (38), and (39) will remain same.

$$T(b, t) = \begin{cases} T_0 \sin \frac{\pi t}{\gamma}; & 0 \leq t \leq \gamma. \\ 0; & t > \gamma \end{cases} \tag{51}$$

Equation (40) will be replaced by the Eq. (52) and other Eqs. (41–43) will remain same.

$$\bar{T}(b, s) = \frac{T_0 \pi \gamma (1 + e^{-s\gamma})}{(\pi^2 + s^2 \gamma^2)}. \quad (52)$$

The values of A_1, A_2, B_1 , and B_2 are obtained as

$$\begin{pmatrix} A_1 \\ A_2 \\ B_1 \\ B_2 \end{pmatrix} = M^{-1} \begin{pmatrix} \frac{T_0 \pi \gamma (1 + e^{-s\gamma})}{(\pi^2 + s^2 \gamma^2)} \\ 0 \\ 0 \\ 0 \end{pmatrix}. \quad (53)$$

The elements of Matrix M are given by Eq. (48).

Case 3: (Instantaneous heat source)

For instantaneous heat source, the boundary Eq. (36) will be replaced by Eq. (54) and other Eqs. (37), (38), and (39) will remain same.

$$T(b, t) = T_0 \delta(t). \quad (54)$$

Equation (40) will be replaced by Eq. (55) and other Eqs. (41), (42), and (43) will remain same.

$$\bar{T}(b, s) = T_0. \quad (55)$$

The values of A_1, A_2, B_1 , and B_2 are obtained as

$$\begin{pmatrix} A_1 \\ A_2 \\ B_1 \\ B_2 \end{pmatrix} = M^{-1} \begin{pmatrix} T_0 \\ 0 \\ 0 \\ 0 \end{pmatrix}. \quad (56)$$

The elements of Matrix M are given by Eq. (48).

7. Limiting cases

- If we put $K^* = \tau_\nu = \tau_T = \tau_q^2 = 0$, $\tau_q \neq 0$ then Eq. (16) converts to Lord–Shulman model.
- If we put $\tau_q = \tau_\nu = \tau_T = 0$ then Eq. (16) reduces to Green–Naghdi model type-III.
- If we put $K^* = 0$ then Eq. (16) reduces to dual-phase-lag model.

8. Particular cases

- If we put $c_{11} = \lambda + 2\mu$, $c_{12} = \lambda$ then the above analysis reduces for isotropic material.
- If we put $\Omega = 0$, then the above study reduces for transversely isotropic hollow cylinder without rotation.
- If we put $H_0 = 0$, then the above study converts for transversely isotropic hollow cylinder without magnetic field.

9. Special case (cylindrical hole in infinite transversely isotropic medium)

When outer radius b approaches to infinity, we obtain an infinite transversely isotropic medium with a cylindrical hole.

We write

$$\bar{\sigma}_{rr} = \bar{\sigma}_{rr}(I) + \bar{\sigma}_{rr}(K), \quad (57)$$

$$\bar{\sigma}_{\theta\theta} = \bar{\sigma}_{\theta\theta}(I) + \bar{\sigma}_{\theta\theta}(K), \quad (58)$$

where

$$\bar{\sigma}_{rr}(I) = \sum_{i=1}^2 \left[(c_{11}m_i k_i - \beta)I_0(k_i r) - \frac{m_i}{r}(c_{11} - c_{12})I_1(k_i r) \right] A_i, \tag{59}$$

$$\bar{\sigma}_{rr}(K) = \sum_{i=1}^2 \left[(c_{11}m_i k_i + \beta)K_0(k_i r) + \frac{m_i}{r}(c_{11} - c_{12})K_1(k_i r) \right] B_i, \tag{60}$$

$$\bar{\sigma}_{\theta\theta}(I) = \sum_{i=1}^2 \left[(c_{12}m_i k_i - \beta)I_0(k_i r) - \frac{m_i}{r}(c_{12} - c_{11})I_1(k_i r) \right] A_i, \tag{61}$$

$$\bar{\sigma}_{\theta\theta}(K) = \sum_{i=1}^2 \left[(c_{12}m_i k_i + \beta)K_0(k_i r) + \frac{m_i}{r}(c_{12} - c_{11})K_1(k_i r) \right] B_i. \tag{62}$$

The asymptotic expression of $I_\alpha(m), K_\alpha(m)$ are given as

$$I_\alpha(m) \approx \frac{e^m}{\sqrt{2\pi m}} \left(1 - \frac{4\alpha^2 - 1}{8m} + \frac{(4\alpha^2 - 1)(4\alpha^2 - 9)}{2!(8m)^2} - \frac{(4\alpha^2 - 1)(4\alpha^2 - 9)(4\alpha^2 - 25)}{3!(8m)^3} + \dots \right), \tag{63}$$

$$K_\alpha(m) \approx \frac{e^{-m}}{\sqrt{2\pi m}} \left(1 + \frac{4\alpha^2 - 1}{8m} + \frac{(4\alpha^2 - 1)(4\alpha^2 - 9)}{2!(8m)^2} + \frac{(4\alpha^2 - 1)(4\alpha^2 - 9)(4\alpha^2 - 25)}{3!(8m)^3} + \dots \right), \tag{64}$$

where $\alpha = 0, 1$.

For large values of $b, K_0(k_i b)$ and $K_1(k_i b)$ tend to zero.

As at a large distance the effect of stress vanishes, we must have $A_1 = A_2 = 0$.

Therefore, as $b \rightarrow \infty$ we get

$$\bar{\sigma}_{rr} = \sum_{i=1}^2 \left[(c_{11}m_i k_i + \beta)K_0(k_i r) + \frac{m_i}{r}(c_{11} - c_{12})K_1(k_i r) \right] B_i, \tag{65}$$

$$\bar{\sigma}_{\theta\theta} = \sum_{i=1}^2 \left[(c_{12}m_i k_i + \beta)K_0(k_i r) + \frac{m_i}{r}(c_{12} - c_{11})K_1(k_i r) \right] B_i, \tag{66}$$

where $B_i (i = 1, 2)$ are given as

$$B_1 = \frac{-m_2 \bar{F}(s) K_1(k_2 a)}{[m_1 K_0(k_2 b) K_1(k_1 a) - m_2 K_0(k_1 b) K_1(k_2 a)]},$$

$$B_2 = \frac{m_1 \bar{F}(s) K_1(k_1 a)}{[m_1 K_0(k_2 b) K_1(k_1 a) - m_2 K_0(k_1 b) K_1(k_2 a)]}.$$

10. Numerical discussion

For numerical computation, we take the following values of transversely isotropic material:

$$c_{11} = 128\text{MPa}, c_{12} = 6\text{MPa}, T_0 = 298\text{K}, C_e = 2 \times 10^{-4}\text{J/KgK}, \beta = 0.04/\text{m}^2\text{K}, \rho = 8.836 \times 10^3\text{Kg/m}^3, K = 100\text{W/mK}, K^* = 17\text{W/mKs}, \tau_q = 2 \times 10^{-7}\text{s}, \tau_T = 1.5 \times 10^{-7}\text{s}, \tau_\nu = 1 \times 10^{-8}\text{s}, \Omega = 100\text{rps}, t = 0.2\text{s}.$$

Further for numerical purpose, we take $\mu_0 = 1.2\text{Hm}^{-1}, \varepsilon_0 = 1.2\text{Fm}^{-1}, H_0 = 10\text{Am}^{-1}$.

Figures 1–5 represent the graphs for constant heat source. In Fig. 1, it is observed that the radial stress $\sigma_{rr}(r, t)$ decreases with respect to distance. The graph representation for different

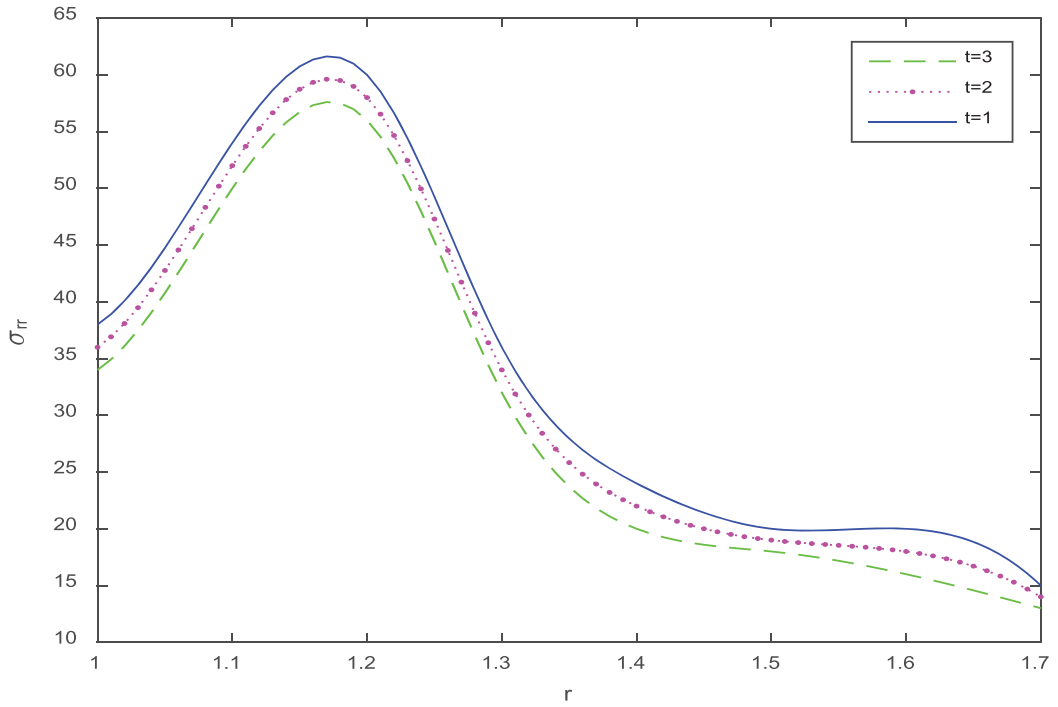


Figure 1. Distribution of radial stress with respect to r for different values of t (for constant heat source).

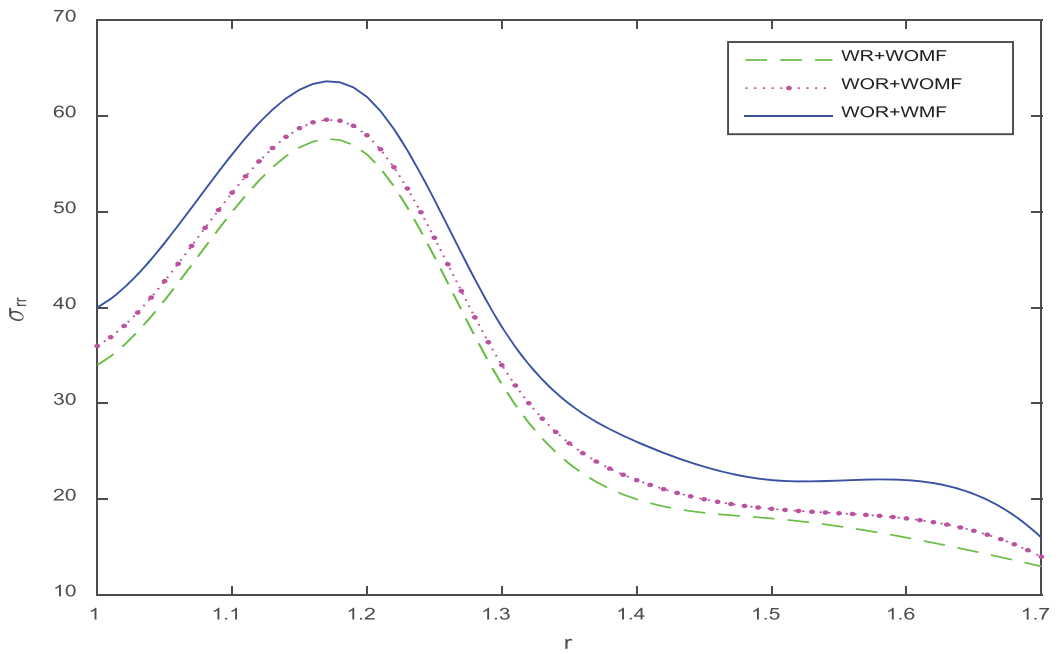


Figure 2. Distribution of radial stress with respect to r (for constant heat source).

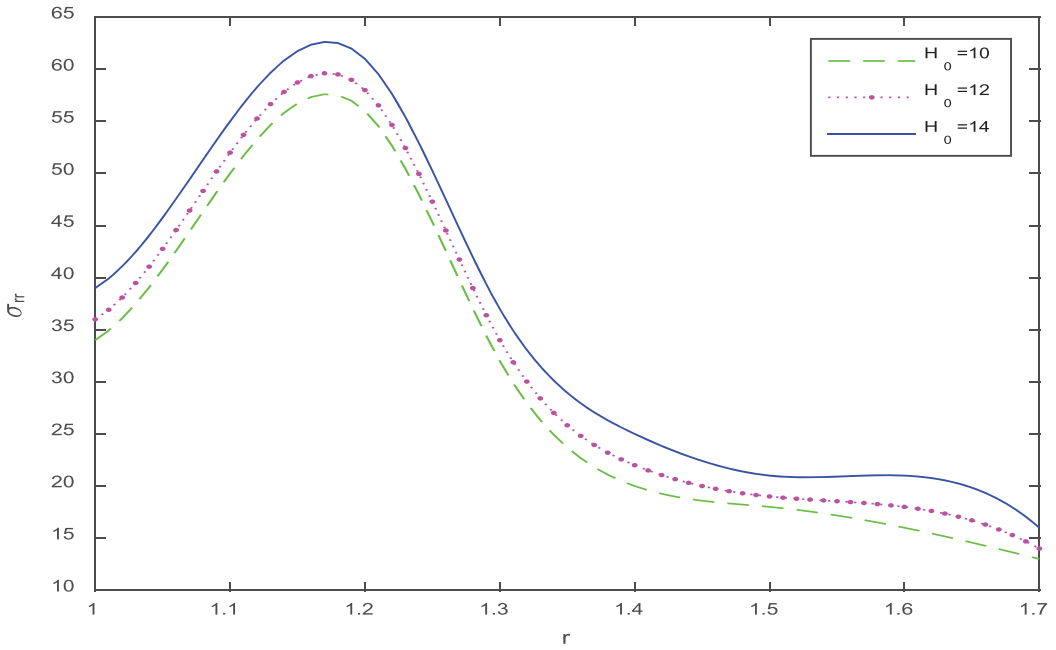


Figure 3. Distribution of radial stress with respect to r for magnetic effect.

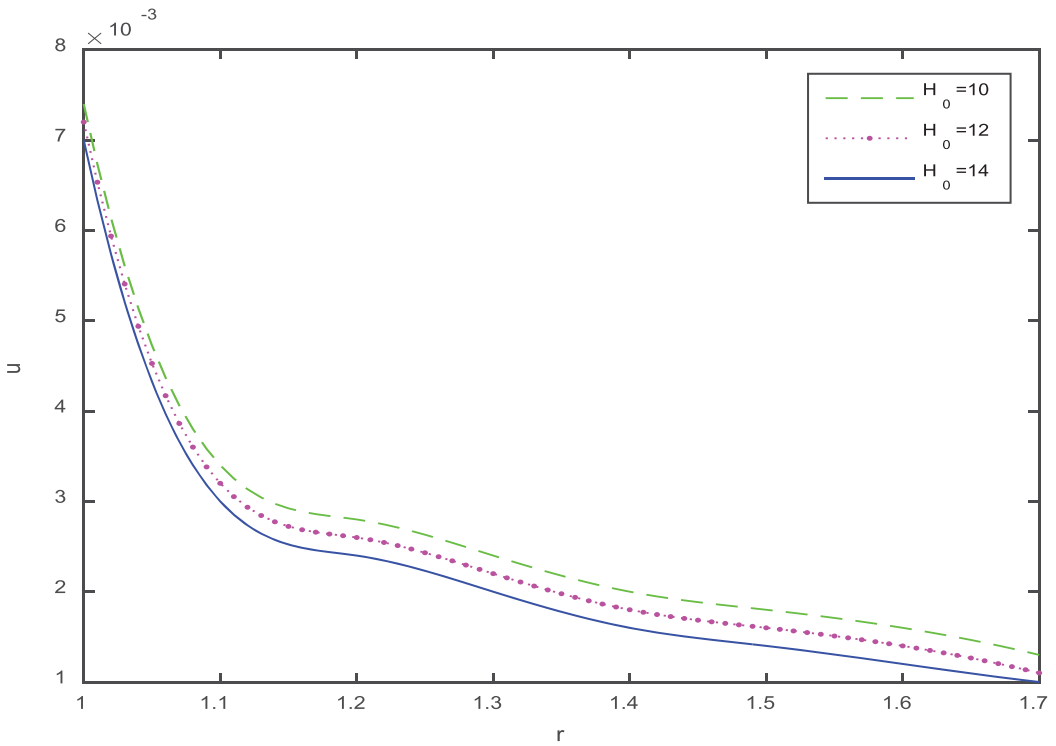


Figure 4. Distribution of displacement with respect to r for magnetic effect.

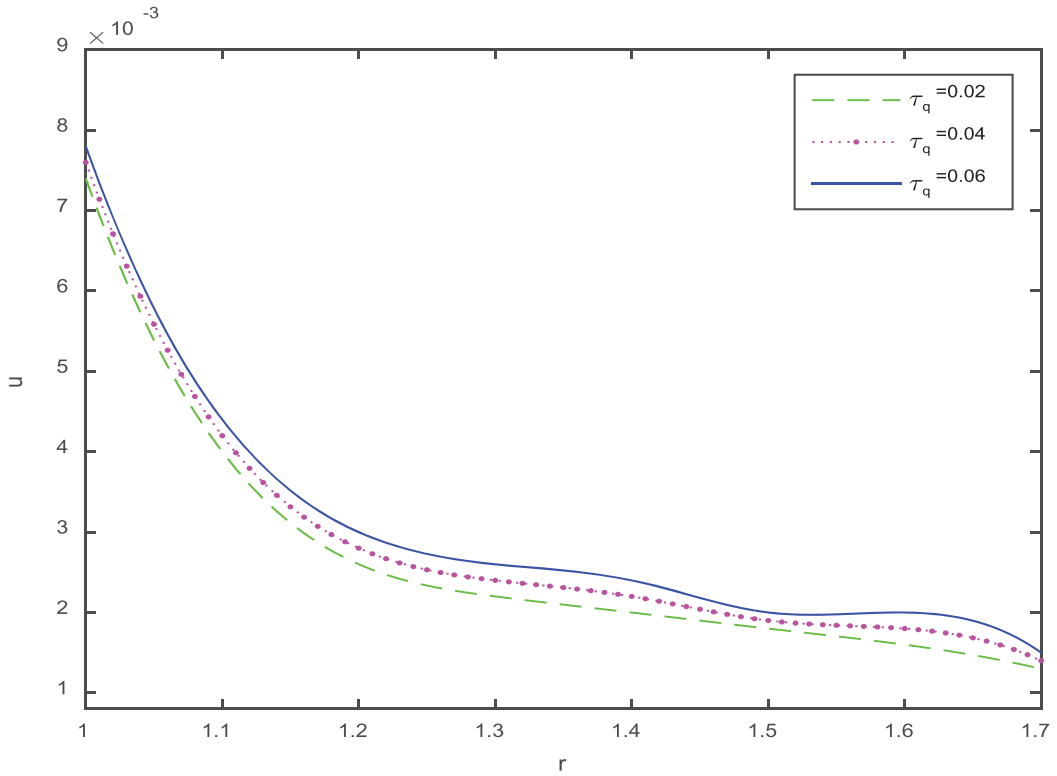


Figure 5. Distribution of displacement with respect to r for different phase lag.
Case 2: (Periodically varying heat source)

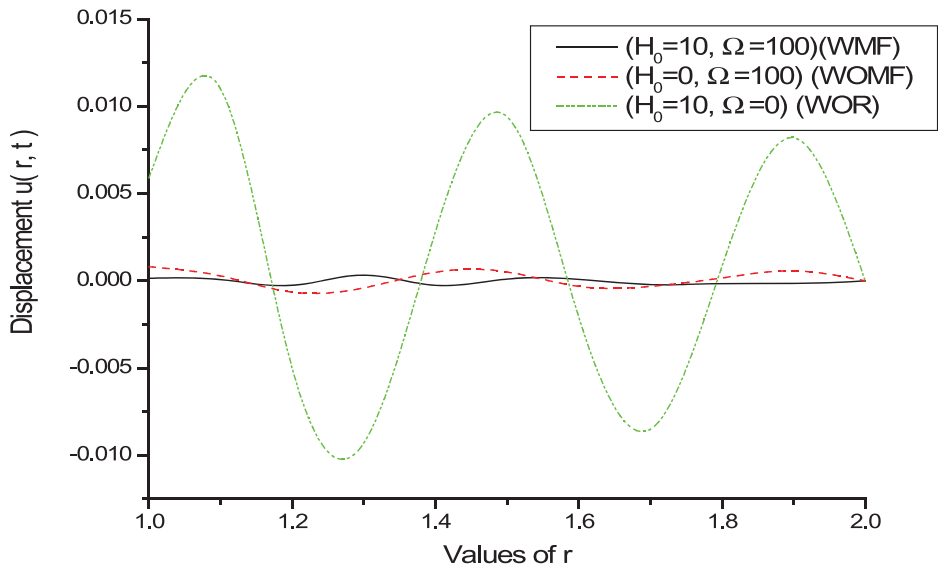


Figure 6. Distribution of displacement with respect to r (for periodically varying heat source).

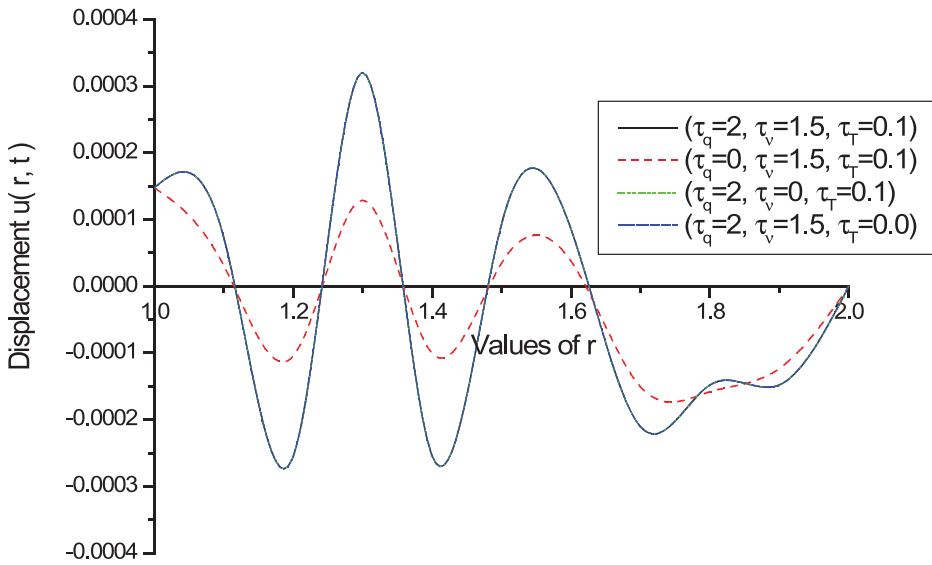


Figure 7. Distribution of displacement with respect to r for various phase lags (for periodically varying heat source).

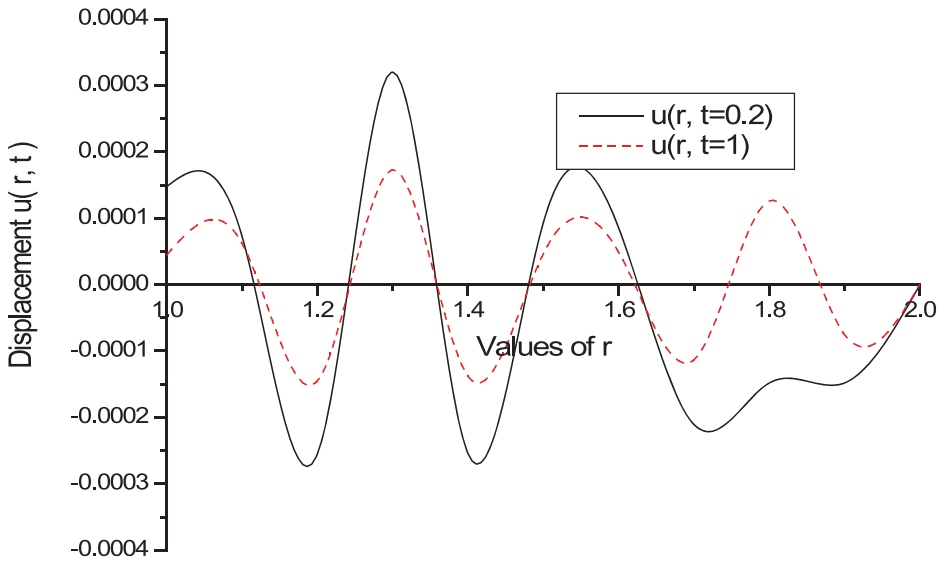


Figure 8. Distribution of displacement with respect to r for different values of t (for periodically varying).

time revealed that stress decreases with the increase of time. In Fig. 2, the effect of rotation and magnetic field on radial stress is shown where it is noticed that the effect of magnetic field is dominating. In Fig. 3, distribution of radial stress with respect to distance for different values of magnetic field is shown. Radial stress increases with the increase of magnetic field. In Fig. 4, distribution of displacement $u(r, t)$ with respect to distance is presented for different values of magnetic field. It is observed that displacement decreases with the increase of magnetic field. In Fig. 5, distribution of radial stress with respect to distance for different values of phase lag is presented and displacement increases with the increase of phase lag.

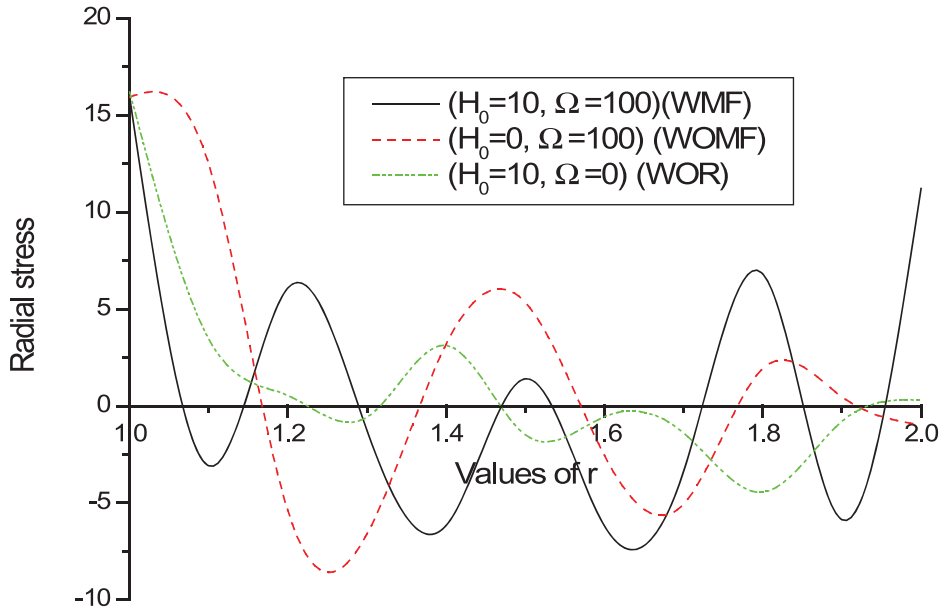


Figure 9. Distribution of radial stress with respect to r (for periodically varying heat source).

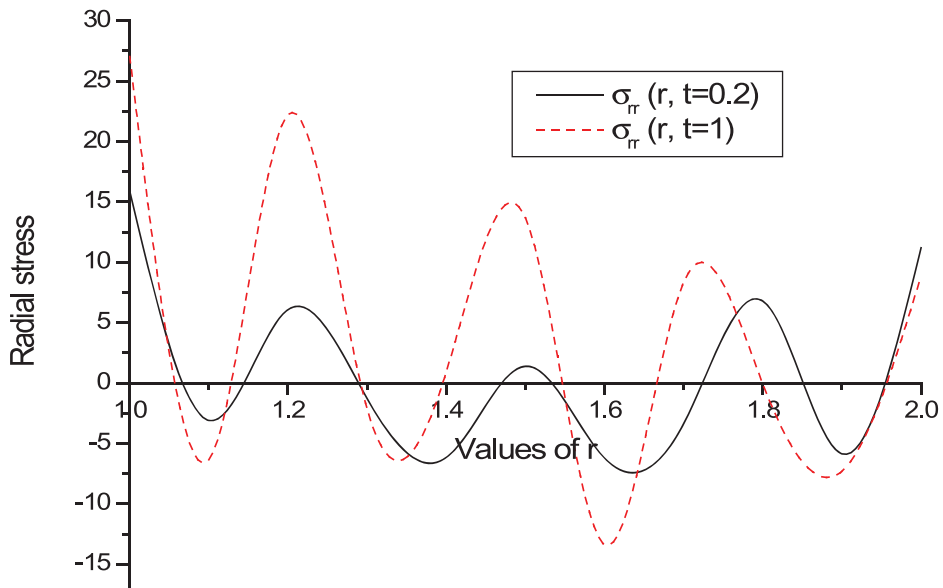


Figure 10. Distribution of radial stress with respect to r for different values of t (for periodically varying heat source).
Case 3: (Instantaneous heat source)

Figures 6–10 represent the graphs for the periodically varying heat source. In Fig. 6, the displacement is showing oscillatory behavior with respect to distance. The graph representing without the effect of rotation is dominating here. In Fig. 7, the effect of various phase lags on displacement is shown where it is noticed that the effect of phase lag for heat flux is dominating here. In Fig. 8, distribution of displacement with respect to radius for different values of time is shown. The graph representing time 0.2 sec is more dominating than the graph representing time

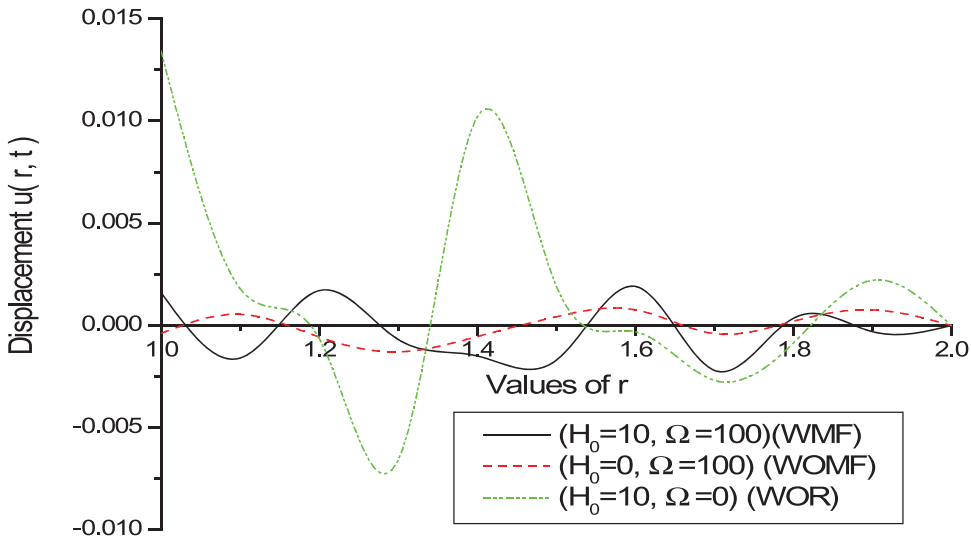


Figure 11. Distribution of displacement with respect to r (for instantaneous heat source).

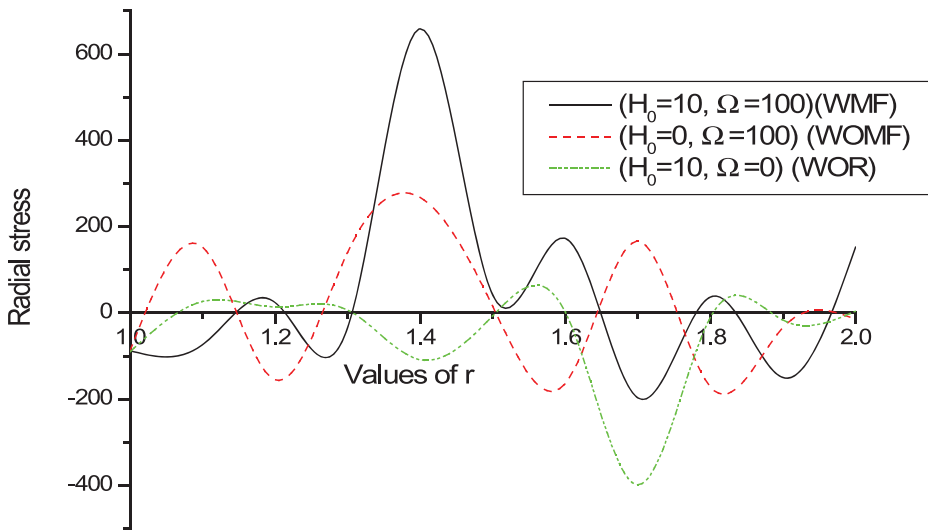


Figure 12. Distribution of radial stress with respect to r (for instantaneous heat source).

1 sec. In Fig. 9, distribution of radial stress with respect to distance is presented where all the graphs are showing oscillatory behavior i.e., wave type propagation is observed. In Fig. 10, distribution of displacement with respect to distance for different values of time is shown. The graph representing time 1 sec is more dominating than the graph representing time 0.2 sec.

Figures 11–13 represent the graphs for instantaneous heat source. In Fig. 11, the displacement is showing oscillatory behavior with respect to distance. The graph representing without the effect of rotation is dominating here. In Fig. 12, radial stress is showing oscillatory behavior with respect to distance. The effect of magnetic field and rotation is clearly observed here. In Fig. 13,

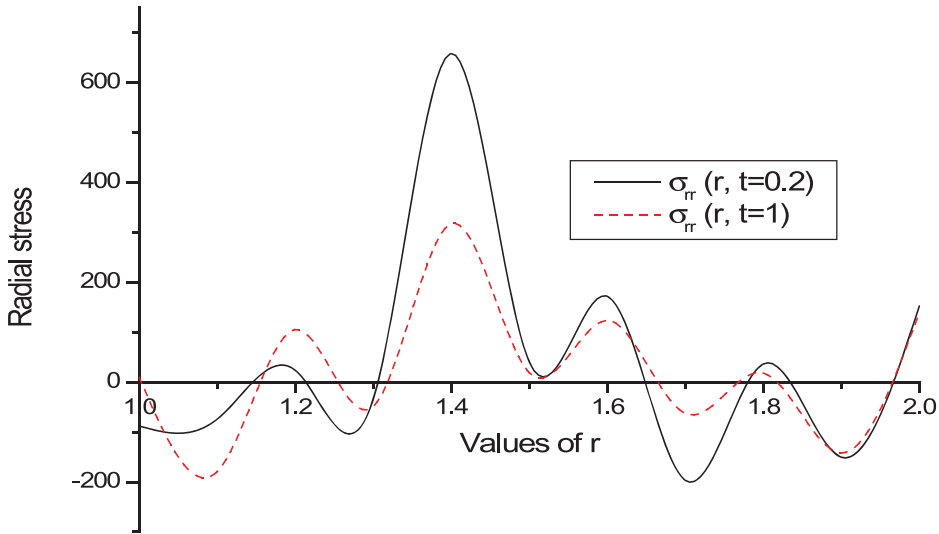


Figure 13. Distribution of radial stress with respect to r for different values of t (for instantaneous heat source).

distribution of radial stress with respect to distance for different values of time is shown. The graph representing time 1 sec is more dominating than the graph representing time 0.2 sec.

11. Conclusion

In this work, the effect of magnetic field on the thermoelastic interaction in a transversely isotropic rotating hollow cylinder has been investigated in the context of nonclassical theory of thermoelasticity. In presence of various heat sources at the external surface of the cylinder, the displacement and radial stress are derived and discussed.

The analysis of graphs permits some concluding remarks:

- i. Phase lag due to heat flux is much dominating factor in comparison with other phase lags.
- ii. For constant heat source, radial stress decreases when time increases.
- iii. For periodically varying heat source displacement and radial stress are harmonic in nature. Displacement decreases when time increases.
- iv. For instantaneous heat source displacement is converging to zero. Radial stress decreases when time increases.
- v. For all types of heat sources, displacement increases due to rotation and decreases due to magnetic effect whereas radial stress decreases due to rotation and increases due to magnetic effect.

The results presented in this article should prove useful for researchers in material science, designers of new materials, physicists as well as for those working on the development of magneto-thermoelasticity and in practical situations as in geophysics, optics, acoustics, geomagnetic, etc. The used method in this article is applicable to a wide range of problems in thermodynamics and thermoelasticity. This study may be useful for determining the strength and load carrying ability and engineering structures, including buildings, bridges, cars, planes and thousands of machine parts that most of us never see. It is especially important in the fields of mechanical, civil, aeronautical, and materials engineering.

Disclosure statement

There is no conflict of interests.

ORCID

Siddhartha Biswas  <http://orcid.org/0000-0002-3599-3431>

References

- Abbas, I. A., and M. I. A. Othman. 2012. Generalized thermoelasticity of thermal shock problem in an isotropic hollow cylinder and temperature dependent elastic moduli. *Chinese Physics B* 21 (1):14601–14606. doi:10.1088/1674-1056/21/1/014601.
- Abd-Alla, A. M., and S. R. Mahmoud. 2010. Magneto-thermoelastic problem in rotating non-homogeneous orthotropic hollow cylinder under the hyperbolic heat conduction model. *Meccanica* 45 (4):451–462. doi:10.1007/s11012-009-9261-8.
- Abouelregal, A. E. 2013. Generalized thermoelastic infinite transversely isotropic body with cylindrical cavity due to moving heat source and harmonically varying heat. *Meccanica* 48:1731–1745. doi:10.1007/s11012-013-9705-z.
- Banik, S., and M. Kanoria. 2012. Effect of three-phase-lag on two-temperature generalized thermoelasticity for infinite medium with spherical cavity. *Applied Mathematics and Mechanics* 33 (4):483–498. doi:10.1007/s10483-012-1565-8.
- Bhattacharya, S., G. K. Ananthasuresh, and A. Ghosal. 2018. Design of a one-dimensional flexible structure for desired load-bearing capability and axial displacement. *Mechanics Based Design of Structures and Machines* 46 (3):376–399. doi:10.1080/15397734.2018.1439755.
- Biot, M. A. 1956. Thermoelasticity and irreversible thermodynamics. *Journal of Applied Physics* 27 (3):240–253. doi:10.1063/1.1722351.
- Brack, L. 1999. Programs for fast numerical inversion of Laplace transforms in MATLAB language environment. *Proceedings of the 7th conference MATLAB'99, Czech Republic Prague*. 27–39. Prague: Czech Republic.
- Cattaneo, C. 1958. A form of heat equation which eliminates the paradox of instantaneous propagation. *Campptes Rendus de l'Academie Des Sciences Serie Ila: Sciences de la Terre et Des Planets* 247:431–433.
- Chandrasekharaiah, D. S. 1986. Thermoelasticity with second sound: A review. *Applied Mechanics Reviews* 39: 355–376. doi:10.1115/1.3143705.
- Chandrasekharaiah, D. S. 1998. Hyperbolic thermoelasticity: A review of recent literature. *Applied Mechanics Reviews* 51 (12):705–729. doi:10.1115/1.3098984.
- Chandrasekharaiah, D. S., and H. R. Keshavan. 1992. Axisymmetric thermoelastic interactions in an unbounded body with cylindrical cavity. *Acta Mechanica* 92 (1–4):61–76. doi:10.1007/BF01174167.
- Choudhuri, S. K. R. 2007. On thermoelastic three phase lag model. *Journal of Thermal Stresses* 30 (3):231–238. doi:10.1080/01495730601130919.
- Das, P., A. Kar, and M. Kanoria. 2013. Analysis of magneto-thermoelastic response in a transversely isotropic hollow cylinder under thermal shock with three phase lag effect. *Journal of Thermal Stresses* 36 (3):239–258. doi:10.1080/01495739.2013.765180.
- Green, A. E., and K. A. Lindsay. 1972. Thermoelasticity. *Journal of Elasticity* 2 (1):1–7. doi:10.1007/BF00045689.
- Green, A. E., and P. M. Naghdi. 1993. Thermoelasticity without energy dissipation. *Journal of Elasticity* 31 (3): 189–208. doi:10.1007/BF00044969.
- Hetnarski, R. B., and J. Ignaczak. 1993. Generalized thermoelasticity: Closed form solutions. *Journal of Thermal Stresses* 16 (4):473–498. doi:10.1080/014957399280832.
- Hetnarski, R. B., and J. Ignaczak. 1996. Soliton like waves in a low temperature non-linear thermoelastic solid. *International Journal of Engineering Science* 34 (15):1767–1787. doi:10.1016/S0020-7225(96)00046-8.
- Huang, E. 2018. Simulation of friction and stiction in multibody dynamics model problems. *Mechanics Based Design of Structures and Machines* 46 (3):296–317. doi:10.1080/15397734.2017.1341840.
- Ignaczak, J., and R. B. Hetnarski. 2014. Generalized thermoelasticity: Mathematical formulation. In *Encyclopedia of thermal stresses*, ed. R. B. Hetnarski, 1974–1986. Dordrecht, Netherlands: Springer.
- Kar, A., and M. Kanoria. 2007. Thermoelastic interaction with energy dissipation in an unbounded body with a spherical hole. *International Journal of Solids and Structures* 44 (9):2961–2971. doi:10.1016/j.ijsolstr.2006.08.030.
- Kar, A., and M. Kanoria. 2009. Generalized thermoelastic functionally graded orthotropic hollow sphere under thermal shock with three-phase-lag effect. *European Journal of Mechanics A/Solids* 39:757–767. doi:10.1016/j.euromechsol.2009.01.003.

- Kumar, R., and S. Mukhopadhyay. 2009. Effect of three phase lags on generalized thermoelasticity for an infinite medium with a cylindrical cavity. *Journal of Thermal Stresses* 32 (11):1149–1165. doi:10.1080/01495730903249185.
- Lord, H. W., and Y. Shulman. 1967. A generalized dynamical theory of thermoelasticity. *Journal of the Mechanics and Physics of Solids* 15 (5):299–309. doi:10.1016/0022-5096(67)90024-5.
- Mukhopadhyay, S., and R. Kumar. 2008a. A study of generalized thermoelastic interactions in an unbounded body with a spherical cavity. *Computers and Mathematics with Applications* 56 (9):2329–2339. doi:10.1016/j.camwa.2008.05.031.
- Mukhopadhyay, S., and R. Kumar. 2008b. A problem on thermoelastic interactions in an infinite medium with a cylindrical hole in generalized thermoelasticity. *Journal of Thermal Stresses* 31 (5):455–475. doi:10.1080/01495730801912561.
- Othman, M. I. A., and I. A. Abbas. 2012. Generalized thermoelasticity of thermal shock problem in a non-homogeneous isotropic hollow cylinder with energy dissipation. *International Journal of Thermophysics* 33 (5):913–923. doi:10.1007/s10765-012-1202-4.
- Othman, M. I. A., and I. A. Abbas. 2015. Effect of rotation on a magneto-thermoelastic hollow cylinder with energy dissipation using finite element method. *Journal of Computational and Theoretical Nanoscience* 12 (9):2399–2404. doi:10.1166/jctn.2015.4039.
- Othman, M. I. A., Y. D. Elmaklizi, and N. T. Mansour. 2017. The effect of temperature dependent properties on generalized magneto-thermoelastic with two-temperature under three-phase-lag model. *Multidiscipline Modeling in Materials and Structures* 13 (1):122–134. doi:10.1108/MMMS-08-2017-0086.
- Quintanilla, R., and R. Racke. 2008. A note on stability in three phase lag heat conduction. *International Journal of Heat and Mass Transfer* 51 (1–2):24–29. doi:10.1016/j.ijheatmasstransfer.2007.04.045.
- Roychoudhury, S. K., and N. Bandyopadhyay. 2005. Thermoelastic wave propagation in rotating elastic medium without energy dissipation. *International Journal of Mathematics and Mathematical Sciences* 2005 (1):99–107. doi:10.1155/IJMMS.2005.99.
- Said, S. M. 2015. Deformation of a rotating two-temperature generalized magneto-thermoelastic medium with internal heat source due to hydrostatic initial stress. *Meccanica* 50 (8):2077–2091. doi:10.1007/s11012-015-0136-x.
- Said, S. M. 2016a. Influence of gravity on generalized magneto-thermoelastic medium for three-phase-lag model. *Journal of Computational and Applied Mathematics* 291:142–151. doi:10.1016/j.cam.2014.12.016. [Mismatch] DOI: 10.1016/j.cam.2014.12.016.
- Said, S. M. 2016b. Wave propagation in a Magneto-Micropolar thermoelastic medium with two temperatures for three-phase-lag model. *Computers, Materials and Continua* 52 (1):1–24. doi:10.3970/cm.2016.052.001.
- Said, S. M. 2017. A fiber-reinforced thermoelastic medium with an internal heat source due to hydrostatic initial stress and gravity for the three-phase-lag model. *Multidiscipline Modeling in Materials and Structures* 13 (1):83–99. doi:10.1108/MMMS-08-2016-0040.
- Schoenberg, M., and D. Censor. 1973. Elastic waves in rotating media. *Quarterly of Applied Mathematics* 31:115–125. doi:10.1090/qam/99708.
- Sherief, H. H., and W. E. Raslan. 2016. Thermoelastic interactions without energy dissipation in an unbounded body with a cylindrical cavity. *Journal of Thermal Stresses* 39 (3):326–332. doi:10.1080/01495739.2015.1125651.
- Sun, W., X. Yan, and F. Gao. 2018. Analysis of frequency-domain vibration response of thin plate attached with viscoelastic free layer damping. *Mechanics Based Design of Structures and Machines* 46 (2):209–224. doi:10.1080/15397734.2017.1327359.
- Tzou, D. Y. 1995. A unique field approach for heat conduction from macro to micro scales. *Journal of Heat Transfer* 117 (1):8–16. doi:10.1115/1.2822329.
- Yang, S., and J. Lin. 2018. A theoretical study of the mechanism with variable compression ratio and expansion ratio. *Mechanics Based Design of Structures and Machines* 46 (3):267–284. doi:10.1080/15397734.2017.1332526.
- Youssef, H. M. 2006. Problem of generalized thermoelastic infinite cylindrical cavity subjected to a ramp-type heating and loading. *Archive of Applied Mechanics* 75 (8–9):553–565. doi:10.1007/s00419-005-0440-3.

Appendix

We now outline the numerical inversion method (Branck 1999) used to find the solutions in the physical domain.

An n dimensional Laplace Transform of a real function $f(t)$, with $t = (t_1, t_2, \dots, t_n)$ as a row vector of n real variables, is defined as

$$F(s) = \int_0^{\infty} \dots \int_0^{\infty} (n\text{-fold}) \int_0^{\infty} f(t) \exp(-st^{tr}) \prod_{i=1}^n dt_i, \quad (A1)$$

where $s = (s_1, s_2, \dots, s_n)$ and tr means transposition.

Under an assumption $|\overline{f(t)}| < \chi \exp(\alpha t^r)$, with χ real positive and $\alpha = (\alpha_1, \dots, \alpha_n)$ being a minimal abscissa of convergence, and the nD Laplace Transform $F(s)$ defined on a region $\{s \in c^n : \text{Re}[s] > \alpha\}$ with $c = (c_1, c_2, \dots, c_n)$ as an abscissa of convergence and the inequality taken component wise, the original function is given by an n -fold Bromwich integral

$$f(t) = \frac{1}{(2\pi j)^n} \int_{c_1 - j\infty}^{c_1 + j\infty} \dots \int_{c_n - j\infty}^{c_n + j\infty} F(s) \exp(st^r) \prod_{i=1}^n dt_i. \tag{A2}$$

Substituting $s_i = c_i + j\omega_i$ into Eq. (A2) and using a rectangular rule of the integration, namely $\omega_i = m_i \Omega_i$ and $\Omega_i = \frac{2\pi}{\bar{\tau}_i}$ as generalized frequency steps, with τ_i forming a region of the solution, $t \in [0, \bar{\tau}_1) \times \dots \times [0, \bar{\tau}_n)$ an approximate formula is

$$\tilde{f}(t) = \exp(ct^r) \left(\prod_{i=1}^n \bar{\tau}_i^{-1} \right) \sum_{m_1=-\infty}^{\infty} \dots \sum_{m_n=-\infty}^{\infty} F(s) \exp\left(j \sum_{m=1}^n m_i \Omega_i t_i\right), \tag{A3}$$

with $s_i = c_i + jm_i \Omega_i$, for all i .

A limiting relative error δ_M of Eq. (A3) can be controlled by setting $c = (c_1, c_2, \dots, c_n)$, defining paths of the integration in Eq. (A2) namely

$$c_i = \alpha_i - \frac{1}{\bar{\tau}_i} \ln \left(1 - \frac{1}{\sqrt{1 + \delta_M n}} \right) \approx \alpha_i - \frac{1}{\bar{\tau}_i} \ln \frac{\delta_M}{n}, \tag{A4}$$

for $i = 1, 2, \dots, n$ and while keeping the equalities $\bar{\tau}_1(c_1 - \alpha_1) = \bar{\tau}_2(c_2 - \alpha_2) = \dots = \bar{\tau}_n(c_n - \alpha_n)$.

The simplification in Eq. (A4) is enabled due to small values δ_M considered in practice. The last equation is used for setting up parameters of the nD NILT method relating them to a limiting relative error δ_M required for practical computations.

The technique of practical evaluation of the n -fold infinite sum Eq. (A3) follows from the properties of the n -fold Bromwich integral Eq. (A2), namely, we can arrange it into the form

$$f(t_1, t_2, \dots, t_n) = \frac{1}{2\pi j} \int_{c_1 - j\infty}^{c_1 + j\infty} \left(\frac{1}{2\pi j} \int_{c_2 - j\infty}^{c_2 + j\infty} \left(\dots \frac{1}{2\pi j} \int_{c_n - j\infty}^{c_n + j\infty} F(s_1, s_2, \dots, s_n) e^{s_n t_n} ds_n \dots \right) e^{s_2 t_2} ds_2 \right) e^{s_1 t_1} ds_1, \tag{A5}$$

or shortly

$$f(t_1, t_2, \dots, t_n) = L_1^{-1} \left[L_2^{-1} \left[\dots L_n^{-1} F[(s_1, s_2, \dots, s_n)] \dots \right] \right]. \tag{A6}$$

Although the order of the integration may be arbitrary on principle, here the above one will be used for an explanation. Similarly Eq. (A3) can be rewritten as

$$\tilde{f}(t_1, t_2, \dots, t_n) = \frac{e^{c_1 t_1}}{\bar{\tau}_1} \sum_{m_1=-\infty}^{\infty} \left(\frac{e^{c_2 t_2}}{\bar{\tau}_2} \sum_{m_2=-\infty}^{\infty} \left(\dots \frac{e^{c_n t_n}}{\bar{\tau}_n} \sum_{m_n=-\infty}^{\infty} F(s_1, s_2, \dots, s_n) e^{jm_n \Omega_n t_n} \dots \right) e^{jm_2 \Omega_2 t_2} \right) e^{jm_1 \Omega_1 t_1}, \tag{A7}$$

with $s_i = c_i + jm_i \Omega_i$. If we define $F_n \equiv F(s_1, s_2, \dots, s_n), \dots$ and $F_0 \equiv f(t_1, \dots, t_n)$, then n consequential partial inversions are performed as

$$\begin{aligned} L_n^{-1}(F_n) &= F_{n-1}(s_1, \dots, s_{n-1}, t_n), \\ L_{n-1}^{-1}(F_{n-1}) &= F_{n-2}(s_1, \dots, t_{n-1}, t_n), \end{aligned} \tag{A8}$$

.....

$$L_1^{-1}(F_1) = f(t_1, \dots, t_{n-1}, t_n)$$

As is obvious we need to use a procedure able to make the inversion of Laplace Transform dependent on other $(n-1)$ parameters, complex in general. Let us denote arguments in Eq. (A8) by $p_i = (p_1, \dots, p_{n-1}, p_n)$.

Then the ILT of the type

$$F_{i-1}(p_{i-1}) = L_i^{-1}(F_i(p_i)) = \frac{1}{2\pi j} \int_{c_i - j\infty}^{c_i + j\infty} F_i(p_i) e^{s_i t_i} ds_i, \tag{A9}$$

can be used n times, $i = n, n-1, \dots, 1$ to evaluate Eq. (A8) with $p_n = (s_1, \dots, s_{n-1}, s_n), p_{n-1} = (s_1, s_2, \dots, s_{n-1}, t_n), \dots, p_1 = (s_1, \dots, t_{n-1}, t_n)$ and $p_0 = (t_1, \dots, t_{n-1}, t_n)$, while $p_j = s_j$ for $j \leq i$ and $p_j = t_j$ otherwise.

A further technique is based on demand to find the solution on a whole region of discrete points. Then, taking into account $t_{ik} = kT_i$ in Eq. (A9) with T_i as the sampling periods in the original domain, we can write the approximate formula

$$\tilde{F}_{i-1}(p_{i-1}) = \frac{e^{c_i k T_i}}{\bar{\tau}_i} \sum_{n=-\infty}^{\infty} \tilde{F}_i(p_i) e^{j2\pi n k T_i / \bar{\tau}_i}, \quad (\text{A10})$$

$i = n, n-1, \dots, 1$ and with $\Omega_i = \frac{2\pi}{\bar{\tau}_i}$ substituted. As follows from the error analysis a relative error is predictable on the region $O_{err} = [0, \bar{\tau}_1] \times \dots \times [0, \bar{\tau}_n]$. For $k = 0, 1, 2, \dots, M_i - 1$, $i = 1, \dots, n$, a maximum reachable region is $O_{max} = [0, (M_1 - 1)T_1] \times \dots \times [0, (M_n - 1)T_n]$. Thus, to meet the necessity condition $O_{max} \subset O_{err}$ we can set up fittingly $\bar{\tau}_i = M_i T_i$, $i = 1, 2, \dots, n$. In practice, a region of the calculation is chosen to be $O_{cal} = [O, t_{1cal}] \times \dots \times [O, t_{ncal}]$ with $t_{ical} = (M_i/2 - 1)T_i$, $i = 1, \dots, n$ to provide certain margins.



Source details

[Feedback >](#) [Compare sources >](#)

Mechanics Based Design of Structures and Machines

Formerly known as: [Mechanics of Structures and Machines](#)

Scopus coverage years: from 2003 to Present

Publisher: Taylor & Francis

ISSN: 1539-7734 E-ISSN: 1539-7742

Subject area: [Mathematics: General Mathematics](#) [Engineering: Ocean Engineering](#) [Engineering: Aerospace Engineering](#) [Engineering: Mechanical Engineering](#)
[Engineering: Civil and Structural Engineering](#) [Engineering: Automotive Engineering](#) [Engineering: Mechanics of Materials](#) [View all](#)

Source type: Journal

[View all documents >](#) [Set document alert](#) [Save to source list](#)

CiteScore 2022
9.4

SJR 2022
0.646

SNIP 2022
1.433

CiteScore CiteScore rank & trend Scopus content coverage



Improved CiteScore methodology

CiteScore 2022 counts the citations received in 2019-2022 to articles, reviews, conference papers, book chapters and data papers published in 2019-2022, and divides this by the number of publications published in 2019-2022. [Learn more >](#)



IDENTIFICATION OF IRON OXIDES MINERALS IN WESTERN JAHAJPUR REGION, INDIA USING AVIRIS-NG HYPERSPECTRAL REMOTE SENSING

Himanshu Govil¹, Mahesh Kumar Tripathi¹*, Prabhat Diwan¹, Subhanil Guha¹, Monika¹

¹ Department of Applied Geology, National Institute of Technology Raipur, India - tripathi.mahesh1@gmail.com

Commission V, SS: Natural Resources Management

KEYWORDS: AVIRIS-NG, Iron-oxide, Limonite, Western Jahajpur belt, Hyperspectral remote sensing.

ABSTRACT:

Hyperspectral remote sensing is being considered as an advanced technique for mineral identification of surficial deposits. In this research different iron oxides minerals such as limonite, goethite has been identified using AVIRIS-NG airborne hyperspectral remote sensing covering the Omkarpura, Itwa, and Chhabadiya mines area in Jahajpur Bhilwara, Rajasthan, India. AVIRIS-NG has shown robust performance in iron oxide identification in the study area. Mineral spectral signatures of the AVIRIS-NG data were compared with spectra of USGS spectral library, and field investigated mineral spectra of iron oxides and found very promising. The results allow us to conclude that due the high signal to noise ratios of the AVIRIS-NG, it is capable to identify the different iron bearing minerals in the visible and infrared portion of the electromagnetic spectrum.

1. INTRODUCTION

"The Airborne Visible-Infrared Imaging Spectrometer - Next Generation (AVIRIS-NG) has been developed to provide continued access to high signal-to-noise ratio imaging spectroscopy measurements"(JPL NASA, 2015). Joint mission of ISRO-NASA has made an execution plan on February 04, 2016 to capture the surficial mineraldeposits in Jahajpur group belt of Bhilwara super group Rajasthan(SAC, 2016, JPL NASA, 2015). The surface mineralogy mapped and identify through characteristic absorption features which are located in the range of visible to shortwave-infrared range(Bell et al., 2010).The minerals which associated with Fe³⁺, Al- OH, Mg-OH, CO₃²⁻, and SO₄²⁻ can be mapped and discriminated by hyperspectral remote sensing data, smoothly (Clark et al., 1990, Crósta et al., 2003, Faroq and Govil, 2014, Jing et al., 2014, Clark, 1999, Eduardo et al., 2011).* According to Parashar (2015) the hydrothermally developed hydroxyl minerals such as clay group of minerals and K-micas allow for remote identification which show the diagnostic absorption in infrared region(Parashar, 2015). The presence of mineral containing iron, such as goethite, jarosite, limonite and hematite due to erosion and weathering of hydrothermally developed sulphide deposits have various different absorptions in VNIR/SWIR regions(Parashar, 2015, Dhara, 1978).There are two major spectral intervals which is used for mineral identification and mapping in range of 0.4-2.5 μm of EMR spectrum. The 0.4-1.1 μm of VNIR region are ubiquitous Fe²⁺ and Fe³⁺ have multispectral absorptions related to electronic transitions. The Fe²⁺, Fe³⁺ have shown charge-transfer absorptions are at around 0.6 μm band width. There are various distinct electronic absorption features near 0.6 μm and 0.9 μm by Limonite and Goethite (Roberto and Filho, 2000). The Fe³⁺ have shown

absorption at 0.43, 0.5 and 0.6 μm , and Fe²⁺ have shown absorption features in 0.9 -1.2 μm (Magendran and Sanjeevi, 2014, Murphy and Monteiro, 2013, Govil et al., 2018, Cloutisa et al., 2006, Bell et al., 2010, Pour and Hashim, 2015).

2. GEOLOGICAL SETTINGS OF THE STUDY AREA

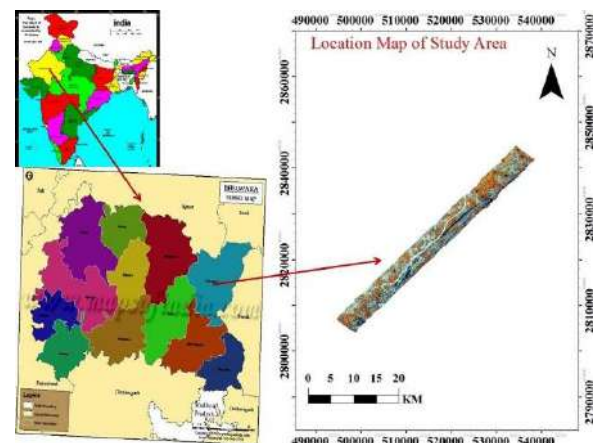


Figure 1. Location map of the study area

The basement rock of Jahajpur group of Bhilwara supergroup are archaean age. There are two parallel ridges of dolomitic limestone and quartzite striking in north east direction along and across the Banas river. The quaternary sediments are exposed in the river channels. The western part of Jahajpur group is intruded with Mangalwar complex and in east surrounded by Hindoli groups of rocks. There are four types of rocks are reported by various scientist and researchers such as dolomite, phyllite, quartzites, banded iron formation (BIF), and quaternary sediments. The identified minerals which is reported by geological society

* Corresponding author

of India are iron, clay, talc, and soapstone(Geological Survey of India-District Report., 1977, Sinha-Roy, 1984, Sinha Roy and Malhotra, 1988, Sinha-Roy, 2001, Saxena and Pandit, 2012, Heron, 1935, Srivastava, 1968, Yadav et al., 2001, Shekhawat and Sharma, 2001).

3. DATA AND METHODOLOGY

The acquired date of AVIRIS NG hyperspectral image is 04/02/2016 for Jahajpur region of Bhilwara district Rajasthan. AVIRIS-NG have 427 contiguous channels with 5nm and 8.1 spectral and spatial resolution respectively in spectrum region 0.3 -2.5 μm of EMR(Hamlin et al., 2011, JPL NASA, 2015, SAC, 2016).The concepts and instruments of AVIRIS-NG are completely free from keystone and smile error distortions.The AVIRIS-NG data have highest signal to noise ratio. The adopted approach of methodology is that preprocessing and determination of AVIRIS-NG airborne hyperspectral data, Image calibration, atmospheric correction, bad band removal, and dark subtraction method related to preprocessing of image, and extraction spectral features are related to determination process of approach. The extracted mineral spectra are correlated and compared with USGS spectral library, and field spectra(King and Clark, 2000). Minerals are identified through absorption and reflectance in a particular bandwidth for particular minerals through interpretation(Molan et al., 2014) and compared with mineral spectral library of USGS..

Sensor Altitude	4-8 km	Spectral Range	380 nm to 2510 nm
Spatial Resolution	8.1 m	Spectral Coverage	Continuous
Swath Width	4-6 km	Spectral Resolution	5nm \pm 0.5 nm
VNIR Range	400nm-1000nm	SWIR range	900nm-2500nm
IFOV (mrad)	1.0 mrad	Total number of bands	425

Table 1. The specified parameters of AVIRIS-NG (Hamlin et al., 2011, Bhattacharya, 2016, JPL NASA, 2015)

4. RESULT AND DISCUSSION

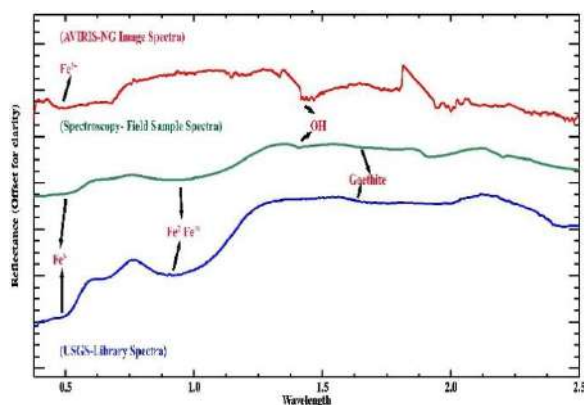


Figure 2:Spectral features of goethite minerals.

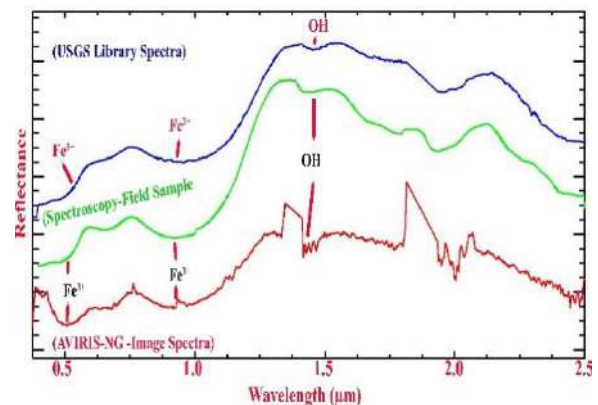


Figure 3: Spectral features of goethite/limonite minerals

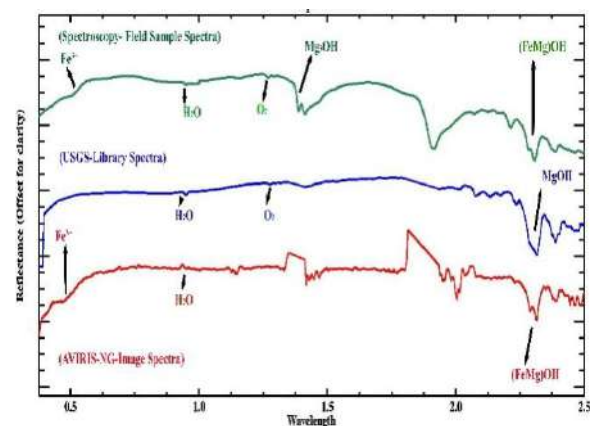


Figure 4: Spectral features talc minerals and associated goethite minerals

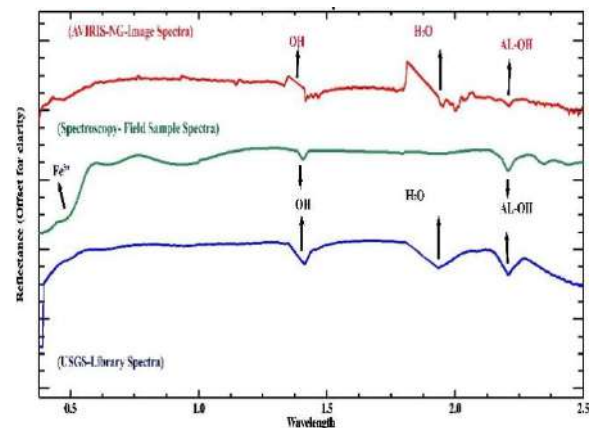


Figure 5: Spectral features of montmorillonite and goethite /limonite

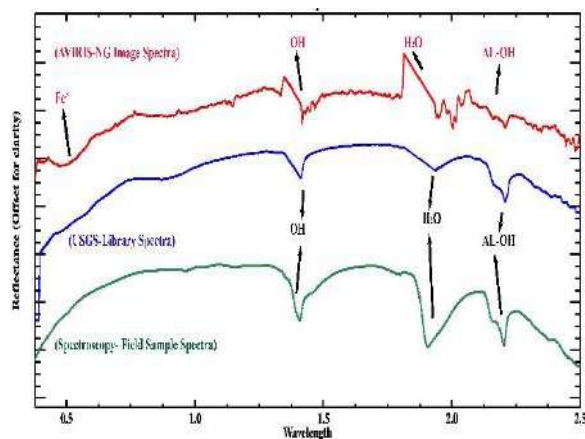


Figure 3: Spectral features of kaolinite and goethite minerals

The hydrothermal alteration product limonite ($\text{Fe}^{+3}\text{O}(\text{OH}) \cdot n\text{H}_2\text{O}$) iron oxide minerals are identified in dolomitic rocks, near Itwa/Omkarpura village (Figure 2 and 3) and near Ghevaria talc mines (Figure 4), Chhabadiya village (Figure 5), Omkarpura village (Figure 6) of Jahajpur, Bhilwara, Rajasthan. The image spectra of limonite at location Itwa and Omkarpura, showing distinct absorption features at bandwidth of image spectra such as at 0.5417, 0.9274 μm with presence of OH absorptions at 1.331-1.4182 μm and 1.8080-1.934 μm , but at location Chhabadiya and Ghevaria iron oxides are present as minor content as impurity in clay and talc minerals. There is similarity between field measured spectra of limonite, USGS mineral spectral library, and image spectra. Field measured spectra have shown absorptions at 0.5070 μm , 0.6260 μm , 0.9310 μm , 1.4132 μm , 1.8080 μm . (Magendran and Sanjeevi, 2014, Murphy and Monteiro, 2013, Mielke et al., 2016, Roberto and Filho, 2000, Govil et al., 2018, Pour and Hashim, 2014, Pour and Hashim, 2015, Zhang et al., 2016, Boesche et al., 2015).

5. CONCLUSION

The interpretation and identification of iron oxides/hydroxide (Highway, 1991) minerals Limonite/Goethite measured through field spectra using spectroradiometer, and image spectra of AVIRIS-NG and compared with USGS mineral spectral library, which have shown absorptions at 0.46, 0.54 (Grebby et al., 2014) 0.76, 0.92 (Pour and Hashim, 2014), 2.0, 2.2, 2.35 and 2.39 μm in VNIR-SWIR indicates association of oxides/hydroxides, clay, talc, and carbonate minerals. This result shows that the AVIRIS-NG data have robust performance and capability in mapping and identification of the alteration zones because association of these minerals are indicating phyllic, argillic (Lagat, 2009, Zhang et al., 2016) and supergene product of gossan (Ramakrishnan and Bharti, 1996) and alteration of oxidation and reduction, and weathering environment. The conclusion is that AVIRIS-NG have better capability to differentiate and identify the oxides minerals and facies alteration.

ACKNOWLEDGEMENTS

This work is supported by Space Application Center, Indian Space Research Organization India grant EPSA/4.2/2017.

REFERENCES

- Bell, J. H., Bowen, B. B. and Martini, B. A. (2010) 'Imaging spectroscopy of jarosite cement in the Jurassic Navajo Sandstone', *Remote Sensing of Environment*. Elsevier Inc., 114(10), pp. 2259–2270. doi: 10.1016/j.rse.2010.05.002.
- Bhattacharya, B. K. (2016) 'AVIRIS Programme and Science Plan', (February), pp. 18–22.
- Boesche, N. K. et al. (2015) 'Hyperspectral REE (rare earth element) mapping of outcrops-applications for neodymium detection', *Remote Sensing*, 7(5). doi: 10.3390/rs70505160.
- Clark, R.N. et al. (1990) 'High spectral resolution reflectance spectroscopy of minerals.', *J. Geophys. Res.*, 95, pp. 12653–12680.
- Clark, R. N. (1999) *Spectroscopy of Rocks and Minerals, and Principles of Spectroscopy*.
- Cloutis, Edward A., et al., (2006) 'Detection and discrimination of sulfate minerals using reflectance spectroscopy.', *Icarus*, 184(1), pp. 121–157.
- Crósta, A.P. et al. (2003) 'Targeting key alteration minerals in epithermal deposits in Patagonia, Argentina, using ASTER imagery and principal component analysis.', *Int. J. Remote Sens.*, 24, pp. 4233–4240.
- Dhara, M. K. (1978) Geological survey of India report on exploration of lead-zinc deposits in the Tiranga hill block, Pur banera belt, Bhilwara district, Rajasthan, (Field Season 1974-75 and 1975-76).
- Eduardo, L., Roberto, C. and Filho, D. S. (2011) 'Identification of mineral components in tropical soils using reflectance spectroscopy and advanced spaceborne thermal emission and reflection radiometer (ASTER) data', *Remote Sensing of Environment*. Elsevier Inc., 115(8), pp. 1824–1836. doi: 10.1016/j.rse.2011.02.023.
- Farooq, S. and Govil, H. (2014) 'Mapping Regolith and Gossan for Mineral Exploration in the Eastern Kumaon Himalaya, India using hyperion data and object oriented image classification', *Advances in Space Research*, 53(12). doi: 10.1016/j.asr.2013.04.002.
- Geological Survey of India-District Report. (1977) *Geology and minerals resources of Bhilwar district*.

- Govil, H. et al. (2018) 'Identification of new base metal mineralization in Kumaon Himalaya, India, using hyperspectral remote sensing and hydrothermal alteration', *Ore Geology Reviews*. Elsevier, 92(September 2017), pp. 271–283. doi: 10.1016/j.oregeorev.2017.11.023.
- Grebbly, S. et al. (2014) 'The Impact of Vegetation on Lithological Mapping Using Airborne Multispectral Data: A Case Study for the North Troodos Region, Cyprus', pp. 10860–10887. doi: 10.3390/rs61110860.
- Hamlin, L. et al. (2011) 'Imaging spectrometer science measurements for terrestrial ecology: AVIRIS and new developments', *IEEE Aerospace Conference Proceedings*, (August). doi: 10.1109/AERO.2011.5747395.
- Heron, A. (1935) 'Heron, A.M (1935) Synopsis of the pre-Vindhyan Geology of Rajputana.', *Trans. Nat. Instt. Sci. India*, I, pp. 17–33.
- Highway, F. (1991) 'Rock and Mineral Identification for Engineers', (November).
- Jing, C. et al. (2014) 'Regional-scale mineral mapping using ASTER VNIR / SWIR data and validation of reflectance and mineral map products using airborne hyperspectral CASI / SASI data', *International Journal of Applied Earth Observations and Geoinformation*. Elsevier B.V., 33, pp. 127–141. doi: 10.1016/j.jag.2014.04.014.
- JPL NASA (2015) ISRO - NASA AVIRIS – NG Airborne Flights over India Science Plan Document for Hyperspectral Remote Sensing.
- King, T. V. V. and Clark, R. N. (2000) 'Verification of remotely sensed data.', In: Kuehn, F., King, T., Hoerig, B., Pieters, D. (Eds.), *Remote Sensing for Site Characterization*. Springer, Berlin, pp. 59–61.
- Lagat, J. (2009) 'Hydrothermal alteration mineralogy in geothermal fields with case example from Olkaria domes geothermal fields, Kenya', pp. 1–24.
- Magendran, T. and Sanjeevi, S. (2014) 'Hyperion image analysis and linear spectral unmixing to evaluate the grades of iron ores in parts of Noamundi, Eastern India', *International Journal of Applied Earth Observations and Geoinformation*. Elsevier B.V., 26, pp. 413–426. doi: 10.1016/j.jag.2013.09.004.
- Mielke, C. et al. (2016) 'EnGeoMAP 2.0—Automated Hyperspectral Mineral Identification for the German EnMAP Space Mission', *Remote Sensing*. Multidisciplinary Digital Publishing Institute, 8(2), p. 127. doi: 10.3390/rs8020127.
- Molan, Y. E., Refahi, D. and Tarashti, A. H. (2014) 'Mineral mapping in the Maherabad area, eastern Iran, using the hyMap remote sensing data', *International Journal of Applied Earth Observation and Geoinformation*, 27(PARTB). doi: 10.1016/j.jag.2013.09.014.
- Murphy, R. J. and Monteiro, S. T. (2013) 'Mapping the distribution of ferric iron minerals on a vertical mine face using derivative analysis of hyperspectral imagery (430–970nm)', *ISPRS Journal of Photogrammetry and Remote Sensing*. International Society for Photogrammetry and Remote Sensing, Inc. (ISPRS), 75, pp. 29–39. doi: 10.1016/j.isprsjprs.2012.09.014.
- Parashar, C. (2015) Mapping of Alteration mineral zones by combining techniques of Remote Sensing and Spectroscopy in the parts of SE- Rajasthan. Andhra University.
- Pour, A. B. and Hashim, M. (2014) 'Exploration of gold mineralization in a tropical region using Earth Observing-1 (EO1) and JERS-1 SAR data: a case study from Bau gold field, Sarawak, Malaysia', 1, pp. 2393–2406. doi: 10.1007/s12517-013-0969-3.
- Pour, A. B. and Hashim, M. (2015) 'Hydrothermal alteration mapping from Landsat-8 data, Sar Cheshmeh copper mining district, south-eastern Islamic Republic of Iran', *Journal of Taibah University for Science*. Taibah University, 9(2), pp. 155–166. doi: 10.1016/j.jtusci.2014.11.008.
- Ramakrishnan, D. and Bharti, R. (1996) 'Hyperspectral Remote Sensing and Applications', *CURRENT SCIENCE*, 108(v. 2821), pp. 879–891. Available at: <https://books.google.co.uk/books?id=N-tOAAAAMAAJ>.
- Roberto, C. and Filho, D. E. S. (2000) 'Hyperspectral remote sensing for mineral mapping: A case study at: A case-study at Alto Paraiso de Goias, Central Brazil.', *Revista Brasileira de Geociências*, 30(3), pp. 551–554.
- SAC, I. (2016) 'Space Application Center.pdf', *SAC COURIER*, 41(3). Available at: <http://www.sac.gov.in/SACSITE/SAC Courier/July2016.pdf>.
- Saxena, A. S. H. A. and Pandit, M. K. (2012) 'Geochemistry of Hindoli Group Metasediments, SE Aravalli Craton, NW India: Implications for Palaeoweathering and Provenance', *Journal geological society of India*, 79(March), pp. 267–278. Available at: http://mecl.gov.in/Reports/EXE_SUMM_BANERA.pdf.
- Shekhawat, L. S. and Sharma, V. (2001) Basemetal exploration in Pachanpura-Chhabriya block, Umedpura-Manoharpura block, Gelaji (East) and Amargarh blocks, Jahajpur belt, Bhilwara district, Rajasthan (Final Report For The Field Seasons 1999-2000 & 2000-2001).
- Sinha-Roy, S. (1984) 'Precambrian folded unconformity in Rajasthan.pdf', *CURRENT SCIENCE*, 53(22), pp. 1205–1207.
- Sinha-Roy, S. (2001) 'Neotectonically controlled catchment capture: An example from the Banas and Chambal drainage basins, Rajasthan', *Current Science*, 80(2), pp. 293–298.

Sinha Roy, S and Malhotra, G. (1988) 'Structural relations of Proterozoic cover and its basement: An example from the Jahazpur belt, Rajasthan.', Jour. Geol. Sec. India (in press).

Srivastava, R. P. (1968) Geological survey of India- systematic geological mapping in parts of Ajmer, Bhilwara and Udaipur districts, Rajasthan included in topo-sheet nos. 45 K/1 & 5. (Progress Report for the field-season 1966-67).

Yadav, O. P. et al. (2001) 'Short communications and its significance in west Jahajpur basin, Bhilwara district, Rajasthan', Journal geological society of India, 58(DEC), pp. 0–3.

Zhang, T. et al. (2016) 'Integrating data of ASTER and Landsat-8 OLI (AO) for hydrothermal alteration mineral mapping in duolong porphyry cu-au deposit, Tibetan Plateau, China', Remote Sensing, 8(11). doi: 10.3390/rs8110890.



Source details

[Feedback >](#) [Compare sources >](#)

International Archives of the Photogrammetry, Remote Sensing and Spatial Information Sciences - ISPRS Archives

Open Access [i](#)

Scopus coverage years: 2000, from 2002 to Present

ISSN: 1682-1750

Subject area: [Social Sciences: Geography, Planning and Development](#) [Computer Science: Information Systems](#)

Source type: Conference Proceeding

[View all documents >](#)

[Set document alert](#)

[Save to source list](#)

CiteScore 2022
1.8 [i](#)

SJR 2022
0.274 [i](#)

SNIP 2022
0.427 [i](#)

CiteScore [CiteScore rank & trend](#) [Scopus content coverage](#)

[i](#) Improved CiteScore methodology

CiteScore 2022 counts the citations received in 2019-2022 to articles, reviews, conference papers, book chapters and data papers published in 2019-2022, and divides this by the number of publications published in 2019-2022. [Learn more >](#)



IDENTIFICATION AND MEASUREMENT OF DEFORMATION USING SENTINEL DATA AND PSINSAR TECHNIQUE IN COALMINES OF KORBA

Monika^{1,*}, H. Govil¹, R.S.Chatterjee², Kapil Malik³, P. Diwan¹, Mahesh Kumar Tripathi¹, Subhanil Guha¹

¹Department of Applied Geology, National Institute of Technology, Raipur, India - geniousmonika11@gmail.com

²Indian Institute of Remote Sensing, Dehradun, India

³Indian Institute of Technology, Dhanbad, India

Commission V, SS: Disaster Monitoring, Damage Assessment and Risk Reduction

KEYWORDS: PSInSAR, Korba, Sentinel-1, Deformation

ABSTRACT

Natural Resources extraction for production of goods increases the stress on land and on the environment. Coal Mines are the primary source for energy production. This process increases the continuous deformation on land by disturbing equilibrium beneath the surface. Interferometry techniques have a capability to detect the minute deformation with millimetre precision on the ground using microwave SAR data. The study area covers the largest open cast coal mines of Asia. In this study for minute deformation identification, Persistent Scatterer Interferometry Synthetic Aperture Radar (PSInSAR) technique has been used. Research focuses on the application of PSInSAR technique for terrain deformation detection using 17 SAR scene of Korba, Chhattisgarh, India acquired by the Sentinel-1 satellite of European Space Agency. This technique is capable to monitor the minute deformation in the coal mines of Korba, Chhattisgarh, India. The results predicted that the area is deformed with the velocity up to 30 mm/year in the coal mines and surroundings areas. The PSInSAR technique with the Sentinel-1 data provides the proficient tool for deformation monitoring in coal mines of Korba.

1. INTRODUCTION

Mining deformation in the form of subsidence is the biggest problem in open cast and underground mines and their surrounding areas due to mining activities. Deformation happens in the mining area due to improper extraction methods of the mineral resources or due to the rock/slope failure. The traditional deformation monitoring techniques in India were time-consuming and costly. Recently Microwave remote sensing has gained a significant success to identify the minute deformation. In the Microwave technology, the Persistent Scatterer interferometry (PSInSAR) technology gives a new turn to monitor the subsidence/deformation.

The research focused on spaceborne synthetic aperture radar (SAR) imagery for monitoring mine subsidence which provided an alternative to prediction displacement (Engineering, Informatics, and Systems 2007). The technology has improved with enhancement of different space-borne (Jiang et al. 2011) SAR sensors, which provide high-resolution imagery over a wide area with day-night capturing capability in any atmospheric conditions (Tomiyasu 1978) (Geymen 2014) (Ng et al. 2011). The SAR interferometry concept has been introduced in the last 1980s (Gabriel, Goldstein, and Zebker 1989). Interferometry SAR (InSAR) (Aydoner, Maktav, and Alparslan 2004) techniques are widely used, to measure the topographic profile and surface deformations (Ishwar and Kumar 2017) (Fulton 2000) and for subsidence monitoring (Strozzi et al. 2001). SAR is the radar antenna which synthesizes images by the principle of Doppler effect, the antenna is focused on an object/ element to generate an image in the along track and across track direction. SAR-Interferometry (InSAR) is one of the competent techniques used to understand the land surface motion and land subsidence (land surface sinking) (Ishwar and Kumar 2017) (Strozzi et al. 2001) (Sahu, Pradhan, and Jade 2016) over a large area (Boni et al. 2017) at a cost lower than the traditional techniques (Ng et al. 2011) (Ferretti, Prati, and Rocca 2001a). The common traditional techniques used for

measuring deformation at ground based on regional level are precise leveling, total station, global navigation satellite system (GNSS), etc. that monitor ground subsidence at a pin point location. Though these methods are tedious, require more time, manpower and are costlier, they can measure height information at millimeter to centimeter levels of accuracy on local area levels (Cao et al. 2007).

The mine deformation is the displacement of land due to the extraction of resources. The coal mines have basically three kinds of subsidence, crack, pit hole and sag (Sahu and Lokhande 2015) (Lokhande et al. 2005). The subsidence has been noticed and written in 1556 in the literature of Agricola's *De RE Metallica* (Singh 1992) but for subsidence engineering, the formal study was started for European coal mines in the 19th century (Ishwar and Kumar 2017). Typically subsidence occurs due to resource extraction (States 1991) (Sahu and Lokhande 2015) and less buoyancy to support the external pressure (Fulton 2000). Deformation has a certain effect of underground mining (Singh 1992) and open cast. The displacement affected area is generally larger than the extracted area of a mine. Mining at any depth can result in subsidence. The deformation, not only impacts the mines but also impacts the ecosystem (Sahu and Lokhande 2015) due to the release of pollutants like toxic gases (Jiang et al. 2011), smog, dust, etc. in the affected areas.

2. STUDY AREA

The study area is in Korba coal field of Chhattisgarh, which lies between the 22°18'N to 22°24' N 82°46'E to 22°29'E. In the research area opencast and underground coal mines are presently shown in figure 1. The underground mine (Surakchhar) was started in 1963 and the opencast Gevera mines are the largest open-pit mine in Asia. The Husdo river unequally divides the study area into two parts. The shale, coal and sandstone are present in this region

3. DATA USE AND METHODOLOGY

A stack of 17 Interferometric Wide Swath (IW) Single Look Complex (SLC) Sentinel-1 images spanning from February

* Corresponding author

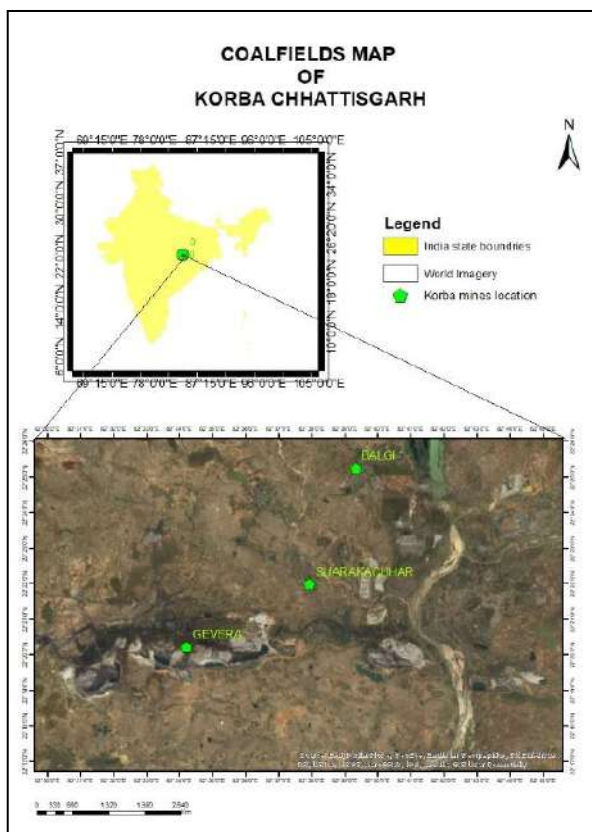


Figure 1 Coalfields of Korba, Chhattisgarh

2015 to February 2017 of Sentinel-1 data acquired freely from the European Space Agency (ESA) has been used in the present study. The acquired data specifications are given in table 1. Sentinel-1 has launched on 4th April 2014 by ESA. It acquires interferometric C-band SAR data and improved data acquisition capability as compared to previous C-band SAR sensors (ERS1/2, Radarsat). Sentinel-1A acquired images with a swath width of 250 by 180 with revisiting time 12 days in the IW data acquisition mode, it is reduced to 6 days if the images acquired by the Sentinel-1B satellite are available. These data are freely available and highly beneficial for deformation monitoring in coal mine area of Korba, Chhattisgarh.

The methodology adopted in the present study is shown in the flowchart in figure 2. The methodology is having three sections

S.No.	Data acquisition	Polarization	Temporal baseline
1	2015/02/28	VV	-323.999919
2	2015/06/28	VV	-203.999947
3	2015/07/10	VV	-191.999956
4	2015/07/22	VV	-179.999944
5	2015/12/13	VV	-35.999985
6	2015/12/25	VV	-23.999992
7	2016/01/06	VV	-11.999996
8	2016/01/18	VV	0.000000
9	2016/02/23	VV	36.000152
10	2016/05/29	VV	132.000065
11	2016/07/16	VV	180.000096
12	2016/07/28	VV	192.000103
13	2016/09/02	VV	228.000123
14	2016/09/14	VV	240.000130
15	2016/12/07	VV	324.000191
16	2017/01/12	VV	360.000164
17	2017/02/05	VV	384.000157

Table 1 Acquired Data specification

preprocessing, estimation and visualization and interpretation. Each segment is important for deformation estimation of Korba Coalfields.

From the stack of 17 images, the image acquired on 2016/01/18 has been chosen as reference or master image other 16 images are slave images. By using the reference image all the total images are analyzed for temporal baseline, perpendicular baseline, coherence, PS estimation, etc. In pre-processing, coregistration is done by cross-correlation of slave with the referenced image and interferograms has been generated by averaging the corresponding amplitude and differencing the corresponding phase at each point in the image (Ferretti et al. 2007).

In the estimation part, PS points are stable points and derived from the temporal data or single coherent pixel called permanent scatterer (Ferretti, Prati, and Rocca 2001b). PS points are calculated evaluating the amplitude dispersion index value and Atmospheric Scatter Index (ASI) which derive from backscattered of each pixel. Atmospheric phase screen (APS) is

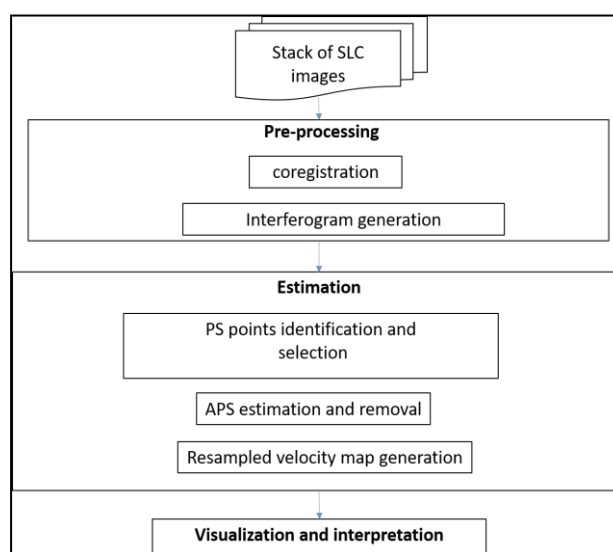


Figure 2 Methodology flow chart

responsible for phase fluctuation of the received signals in linear phase term in range and azimuth direction so it needs to be estimated and removed for better results for deformation measurement. The subsidence is monitored by the pixel by pixel estimation of the reference of PS candidates and radar parameter estimation of phase displacement or movement in the image. The images of 2 years data acquired from 28 Feb'2015 to 05 Feb'2017 were stacked to form the stacked interferogram of the 21 images. The images of 2 years data acquired from 28 Feb'2015 to 05 Feb'2017 were stacked to form the stacked interferogram of the 17 images. The PSs supports for an algorithm for linear contribution to monitor displacement measurement in coalfield of Korba. The interferometric phase (ϕ) analysis for all the k permanent point selected point in the pixel in n th flattened and topographically corrected interferogram is (Qiu, Ma, and Guo 2016)

$$\phi_{diff,n,k} = \phi_{flat,n,k} + \phi_{topo,n,k} + \phi_{aps,n,k} + \phi_{scat,n,k} + \phi_{noise,n,k} \quad (1)$$

Where, $\phi_{diff,n,k}$ is total phase difference due to all the factors along the LOS observed by two different satellite or displacement. $\phi_{flat,n,k}$ is a phase of flat terrain, $\phi_{aps,n,k}$ is the phase difference occur due to supplementary atmospheric disruption.

$\phi_{scat,n,k}$ is the phase difference occur due to echo characteristic. $\phi_{noise,n,k}$ is the noise in the phase by geometrical and temporal decorrelation. Linear displacement and velocity relation to measuring deformation by assuming that the movement is linear in time:

$$\varphi_{disp,n,k} = \frac{4\pi}{\lambda} \Delta v(k) B_{n,k} \quad (2)$$

Where,

Δv is the relative velocity

$B_{n,k}$ is temporal baseline.

Subsidence is monitor by referenced PS points and displacements along the line of sight of the satellite.

By estimating resampled velocity data visualized and interpreted on an interface of google earth for results justification.

4. RESULTS AND DISCUSSION

The PSI products derived with the help of the 17 scenes of IW SLC Sentinel-1 images, spanning the period from February 2015 to February 2017 are accumulated displacement map and the time series of the deformation derived. In figure 3, a total area which has been processed is about 450 sq.km. in which the approx. 300 sq.km area has been under observation for deformation monitoring in the present study. The points in the figures are showing PS candidates which undergo deformation in observed in the areas. The observation is done in and around coal mine area of Korba (marked as rectangles in figure 3). The total processed area map of time series has been superimposed on Google Earth is showing in figure 3 and the area under

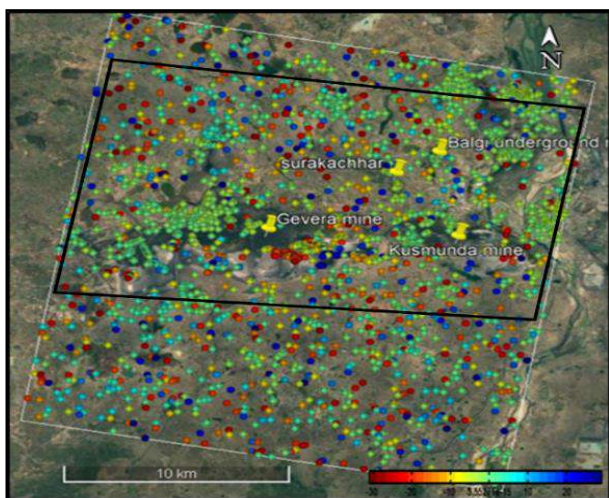


Figure 3 Resampled map of the total processed area and in black color rectangle is mine's area under observation.

investigation is shown in figure 4. Figure 4 shows the accumulated displacement map obtained with the direct integration of the consecutive interferogram. The more

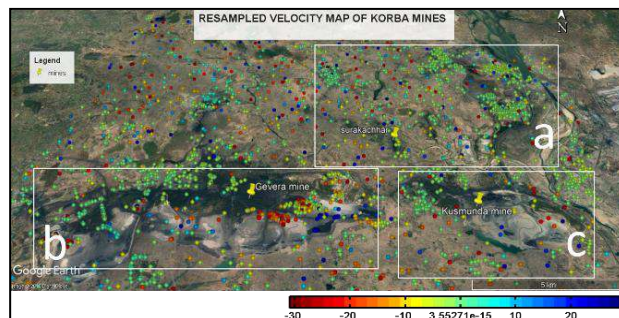


Figure 4 Resampled velocity map superimposed to Google Earth. The rectangle area are the mines (a) Surakachhar, (b) Gevera and (c) Kusmunda

deformed areas are demarcated or encircled shows the rate of deformation occurring in and around coal mine of Korba. The points in the figure3, 4 shows a good coverage of PS candidate over all the area of coal mines and its surrounding area and have a good connection between all the urban areas. Figure 4 shows accumulated displacement map over an area of Korba coalfields and its nearby areas which have been superimposed on to Google Earth for deformation estimation. Figure 4 shows the area of 4a Surakachhar, 4b Gevera, and 4c Kusmunda opencast coal mine. The zoomed view of underground coal mine of



Figure 5 Zoomed view of in and around underground mine Surakachhar

Surakachhar has been shown in figure 5, rectangles in the figures showing more deformation in the area where broadly the deformation rate varies from -3 to -27 mm/year. The Balgi underground mine and its surrounding areas show more deformation demarcated by rectangles in figure 5. Both the underground mines affect the area slowly and gradually in the form of deformation. The rate of deformation is slow but at some places, it's demarcated at a high rate (red color points in the area) which is more than -25mm/year. The area is deformed mainly active mining area and settlements which are permanent feature and having more PS points in the regions. Which provide precision for deformation monitoring. This cannot be neglected due to the presence of underground mines in the area. In the future, this adverse effect in the area can be dangerous for the property and life of the people.

In open cast mine of Gevera, and Kustumunda the deformation has been estimated very high up to -30mm/year, zoomed view shown in figure 6 and Figure7. The areas in green to red color showing that the area continuously away from the line of sight (LOS) of the satellite and rate of deformation which has been noticeable in the area upto30mm/year. Gevera mine deformation rate is more demarcated in the figure 6, green point's area showing the deformation has been started in the Gevera mines and surrounding area. The area in yellow shows the moderate rate of deformation occurs with the rate of -5 to -

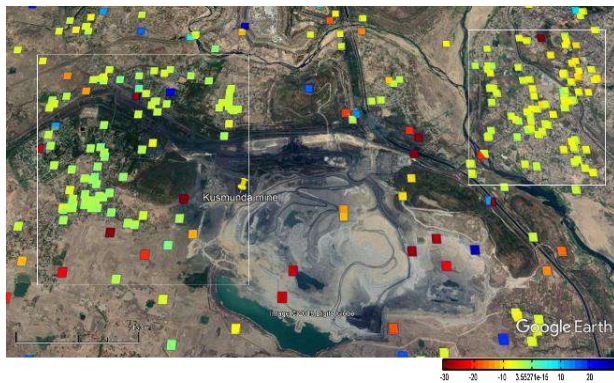


Figure 7 Zoomed view of Kustumunda opencast mine

10mm/year and red color in opencast mine is showing that moderate to the very high rate of deformation is occurring in the area. The points have been noticed in the mines are permanent features like dumping zone, working stations, coal washeries, etc. so it finds more PS point in this region which helps to improve the accuracy of deformation results. The more deformed area demarcated or encircled in figure 6 and 7. In Gevera and Kustumunda due to mining activities directly or indirectly disturbs the area of mine and its nearby areas by drilling, blasting, waterlogging, water sprinkling, slumping and heavy vehicle activities which deformed the infrastructure.

In opencast mines, waterlogging can easily identify on google earth high-resolution images which provide good information for interpretation. Figure 8 showing some zoomed view of

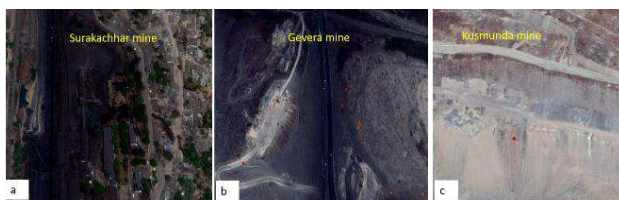


Figure 8 Coal mine areas of Korba zoomed view of deformation points (a) Surakachhar, (b) Gevera and (c) Kustumunda

deformed areas on google earth images of underground and opencast mines of Korba. In the underground mine of



Figure 4 Ground photographs of Kustumunda mine area

Surakachhar, the zoomed view of the area near the working station in which infrastructure undergo deformation up to 10 mm/year has been shown in figure 8a. Underground activities of mining disturb the areas of Surakachhar mine and surrounding residential area slowly which can be a cause of the forthcoming disaster, so it requires frequent attention and maintenance. In figure 8b opencast mine Gevera, roads, slumping areas and dumping sites which deformed highly from -15 to -30mm/year. In figure 8c and figure 9 opencast mine Kustumunda, zoomed view of slumping site near the road is showing the deformation rate is -26.5mm/year. Figure 9, showing some photograph of Kustumunda mine which indicates the deformation of the mine areas. The results in the present study showing more deformation in the opencast mine as compare to underground mines. Gevera mines, having very high deformation rate as compared to all mines present in the present study area because it is having more production as compared to other.

5. CONCLUSION

The deformation monitoring is very necessary for the areas of coal mining for prediction of change and monitoring the indicators of forthcoming hazard. In the present study, PSInSAR technique and C-band sentinel-1 data have been used for deformation monitoring in underground and opencast mines of Korba, Chhattisgarh. The PS point's estimation has been done for deformation monitoring using 17 IW SLC images. The results have been estimated in Korba mines showing that -3 to -30 mm/year deformation occur in different areas of underground and opencast mines. This study also helps to predict deformation in other coal mines of the India and world.

ACKNOWLEDGMENT

The authors express their sincere thanks to the European Space Agency for providing Interferometric datasets of Sentinel-1 C-band. We would express our gratitude to SARPROZ software team for providing software.

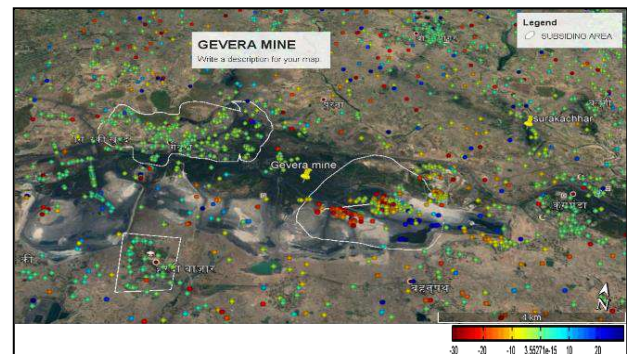


Figure6 Zoomed view of in and around opencast mine Gevera

REFERENCES

- Aydoner, C., D. Maktav, and E. Alparslan. 2004. "Ground Deformation Mapping Using InSAR." *ISPRS Congress Technical Commission I* 120–23. Retrieved July 14, 2017 (<http://www.isprs.org/proceedings/XXXV/congress/comm1/papers/23.pdf>).
- Boni, Roberta et al. 2017. "Exploitation of Satellite A-DInSAR Time Series for Detection, Characterization and Modelling of Land Subsidence." *Geosciences* 7(2):25. Retrieved August 10,

- 2017 (<http://www.mdpi.com/2076-3263/7/2/25>).
- Cao, Li et al. 2007. "Coal Mine Land Subsidence Monitoring By Using Spaceborne Insar." *Archives* (495):255–62. Retrieved September 12, 2017 (http://www.isprs.org/proceedings/XXXVII/congress/8_pdf/2_WG-VIII-2/15.pdf).
- Engineering, Environmental Information, Spatial Informatics, and Spatial Information Systems. 2007. "Differential Radar Interferometry and Its Application in Monitoring Underground Coal Mining-Induced Subsidence." *Science* (1989):227–32. Retrieved October 9, 2017 (http://www.isprs.org/proceedings/XXXVIII/7-C4/227_GSEM2009.pdf).
- Ferretti, Alessandro, Andrea Monti-guarnieri, Claudio Prati, and Fabio Rocca. 2007. *InSAR Principles: Guidelines for SAR Interferometry Processing and Interpretation (TM-19, February 2007)*.
- Ferretti, Alessandro, Claudio Prati, and Fabio Rocca. 2001a. "Permanent Scatterers in SAR Interferometry." *IEEE Transactions on Geoscience and Remote Sensing* 39(1):8–20.
- Ferretti, Alessandro, Claudio Prati, and Fabio Rocca. 2001b. "Permanent Scatterers in SAR Interferometry." *IEEE Transactions on Geoscience and Remote Sensing* 39(1):8–20.
- Fulton, Allan. 2000. "Land Subsidence: What Is It and Important Aspect of Groundwater Management." Retrieved July 6, 2017 (<http://www.water.ca.gov/groundwater/docs/WhatIsLandSubsidence.pdf>).
- Gabriel, Andrew K., Richard M. Goldstein, and Howard A. Zebker. 1989. "Mapping Small Elevation Changes over Large Areas: Differential Radar Interferometry." *Journal of Geophysical Research* 94(B7):9183. Retrieved July 14, 2017 (<http://doi.wiley.com/10.1029/JB094iB07p09183>).
- Geymen, Abdurrahman. 2014. "Digital Elevation Model (DEM) Generation Using the SAR Interferometry Technique." *Arabian Journal of Geosciences* 7(2):827–37. Retrieved July 8, 2017 (<http://link.springer.com/10.1007/s12517-012-0811-3>).
- Ishwar, S. G. and Dheeraj Kumar. 2017. "Application of DInSAR in Mine Surface Subsidence Monitoring and Prediction." *Current Science* 112(1):46–51. Retrieved June 13, 2017 (<http://www.currentscience.ac.in/Volumes/112/01/0046.pdf>).
- Jiang, Liming, Hui Lin, Jianwei Ma, Bing Kong, and Yao Wang. 2011. "Potential of Small-Baseline SAR Interferometry for Monitoring Land Subsidence Related to Underground Coal Fires: Wuda (Northern China) Case Study." *Remote Sensing of Environment* 115(2):257–68. Retrieved (<http://dx.doi.org/10.1016/j.rse.2010.08.008>).
- Lokhande, R. D., A. Prakash, K. B. Singh, and K. K. K. Singh. 2005. "Subsidence Control Measures in Coalmines: A Review." *Journal of Scientific and Industrial Research* 64(5):323–32.
- Ng, A. H. M., L. Ge, K. Zhang, and X. Li. 2011. "Application of Persistent Scatterer Interferometry for Land Subsidence Monitoring in Sydney, Australia Using ENVISAT ASAR Data." in *34th International Symposium on Remote Sensing of Environment - The GEOSS Era: Towards Operational Environmental Monitoring*. Retrieved September 13, 2017 (<http://www.isprs.org/proceedings/2011/ISRSE-34/211104015Final00415.pdf>).
- Qiu, Zhiwei, Yuxiao Ma, and Xiantao Guo. 2016. "Atmospheric Phase Screen Correction in Ground-Based SAR with PS Technique." *SpringerPlus* 5(1):1–15.
- Sahu, Poonam and Ritesh D. Lokhande. 2015. "An Investigation of Sinkhole Subsidence and Its Preventive Measures in Underground Coal Mining." *Procedia Earth and Planetary Science* 11:63–75. Retrieved (<http://linkinghub.elsevier.com/retrieve/pii/S1878522015000600>).
- Sahu, Poonam, Manoj Pradhan, and Ravi K. Jade. 2016. "Study the Variations of Sinkhole Depth with Respect to Working Height in Underground Coal Mines." (Rare):547–51.
- Singh, Madan M. 1992. "Mine Subsidence." *SME Mining Engineering Handbook* 938–971.
- States, United. 1991. "Land Subsidence in the United States." 1–6.
- Strozzi, T., U. Wegmuller, L. Tosi, G. Bitelli, and V. Spreckels. 2001. "Land Subsidence Monitoring with Differential SAR Interferometry." *Photogrammetric Engineering & Remote Sensing* 67(11):1261–70.
- Tomiyasu, Kiyoo. 1978. "Tutorial Review of Synthetic-Aperture Radar (SAR) with Applications to Imaging of the Ocean Surface." *Proceedings of the IEEE* 66(5):563–83.



Source details

[Feedback >](#) [Compare sources >](#)

International Archives of the Photogrammetry, Remote Sensing and Spatial Information Sciences - ISPRS Archives

Open Access [i](#)

Scopus coverage years: 2000, from 2002 to Present

ISSN: 1682-1750

Subject area: [Social Sciences: Geography, Planning and Development](#) [Computer Science: Information Systems](#)

Source type: Conference Proceeding

[View all documents >](#) [Set document alert](#) [Save to source list](#)

CiteScore 2022
1.8 [i](#)

SJR 2022
0.274 [i](#)

SNIP 2022
0.427 [i](#)

[CiteScore](#) [CiteScore rank & trend](#) [Scopus content coverage](#)



Improved CiteScore methodology

CiteScore 2022 counts the citations received in 2019-2022 to articles, reviews, conference papers, book chapters and data papers published in 2019-2022, and divides this by the number of publications published in 2019-2022. [Learn more >](#)



EVALUATING CROSTA TECHNIQUE FOR ALTERATION MINERAL MAPPING IN MALANJKHAND COPPER MINES, INDIA

S. Guha^{1,*}, H. Govil¹, M. Tripathi¹, M. Besoya¹

¹ Department of Applied Geology, National Institute of Technology Raipur, Raipur, India- (subhanilguha, himgeo, tripathi.mahesh1, geniousmonika11@gmail.com)

Commission V, SS: Natural Resources Management

KEY WORDS: Crosta technique, Landsat, Hydroxyl, Carbonate, Iron oxide

ABSTRACT:

Landsat-8 Operational Land Imager (OLI) data has been successfully employed in the field of mineral exploration to detect important minerals. In this study, Crosta technique was applied to identify the diagnostic features of hydroxyl minerals, carbonate minerals and iron oxides in Malanjkhand copper mines, India. The Crosta technique was applied to six [blue, green, red, near-infrared (NIR), shortwave infrared1 (SWIR1), shortwave infrared2 (SWIR2) bands and two sets of four (blue, red, NIR, SWIR1; and blue, near-infrared, SWIR1, SWIR2) bands of OLI data. Results show that the areas with alteration zones are enhanced much better by using six bands of OLI data. The alteration differences are examined with the Crosta technique using four band combinations. Crosta technique is very useful in generating the images of hydroxyl minerals, carbonate minerals, and iron oxides.

1. INTRODUCTION

Principal component analysis (PCA) technique is widely considered as an effective technique for alteration mineral mapping (Tangestani and Moore 2001, Ranjbar et al. 2002). The Crosta technique is known as a feature-based selection of principal components. It detects the principal components that contain spectra information about particular minerals using the analysis of eigenvector values. This technique presents the bright or dark pixels in the principal components according to the magnitude and sign of the eigenvectors loadings. This technique can be applied to four and six selected bands of Landsat data (Crosta and Moore 1989, Rutz-Armenta and Prol-Ledesma 1998).

The objective of this study is to evaluate the Crosta technique for alteration mineral mapping in Malanjkhand area using Landsat-8 OLI data.

2. MATERIALS AND METHODS

In this study, cloud-free imageries of Landsat-8 OLI for April 17, 2017 of the study area (path/row 143/45) were freely downloaded from the US Geological Survey (USGS) Earth Resources Observation and Science Center (<http://earthexplorer.usgs.gov>).

The Crosta technique used here mainly followed the studies of Crosta and Moore (1989), Tangestani and Moore (2000, 2001, 2002) and Torres-Vera and Prol-Ledesma (2003). The Crosta technique or Feature Oriented Principal Components Selection (FPCS) is the analysis of the eigenvector values, which allows identification of the PCs that contain spectral information about specific materials, as well as the contribution of each of the original bands of the components in relation with the spectral response of the materials of interest. This technique also

indicates whether the materials are represented by bright or dark pixels in the principal components according with the magnitude and sign of the eigenvectors. The Crosta technique was applied to six non-thermal OLI bands, and to four bands selected on the basis of the spectral characteristics of the hydrothermal minerals and the vegetation.

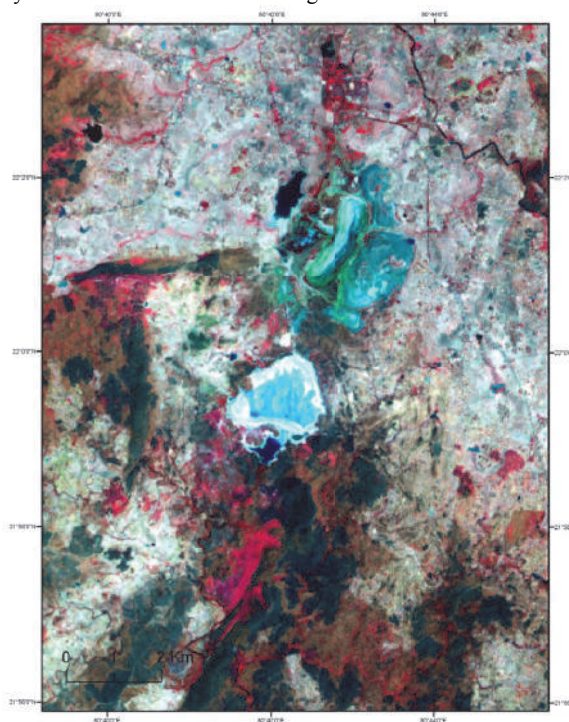


Figure 1: Location of the study area

* Corresponding author

3. RESULTS AND DISCUSSION

Relevant images mapping hydroxyls and iron oxides as bright pixels need inverting as both loadings for SWIR1 in PC5 and NIR in PC5 and PC4 are marked by a negative sign. The PC4s of two separate four-band associations (i.e. blue, red, NIR, SWIR1; and blue, NIR, SWIR1, SWIR2) using Crosta technique primarily hold the information concerning hydroxyls and iron oxides because the greatest loadings were connected to either SWIR1 and SWIR2 or NIR and blue band. Results indicated the false color composites (SWIR2 (red), NIR (green), blue (blue)) overlaid with the remote-sensing anomalies and through Crosta technique using four bands or six bands.

3.1 Crosta technique using six bands

The results of the principal component transformation (band load) was described in Table 1, using as input the six OLI bands (OLI-2, OLI-3, OLI-4, OLI-5, OLI-6, and OLI-7) from the Malanjkhanda image. It was observed from Table 1 that the first principal component did not contain spectral features relevant in the analysis, as it was a combination of all bands with a major contribution from OLI-6 (68%). This component contained 87.72% of the variance of the six bands; hence it gave mainly information about albedo and topography. In the second principal component (PC2), most of the information came from the visible and near-infrared bands. The spectral information of hydroxyls and iron oxide should be contained in PC4, PC5 or PC6; however, the dominant band loads in these components did not correspond to the spectral characteristics of those minerals. Crosta anomalies, pink, red and yellow for hydroxyls, and Cambridge blue, blue and cyan for iron oxides (Figure 2).

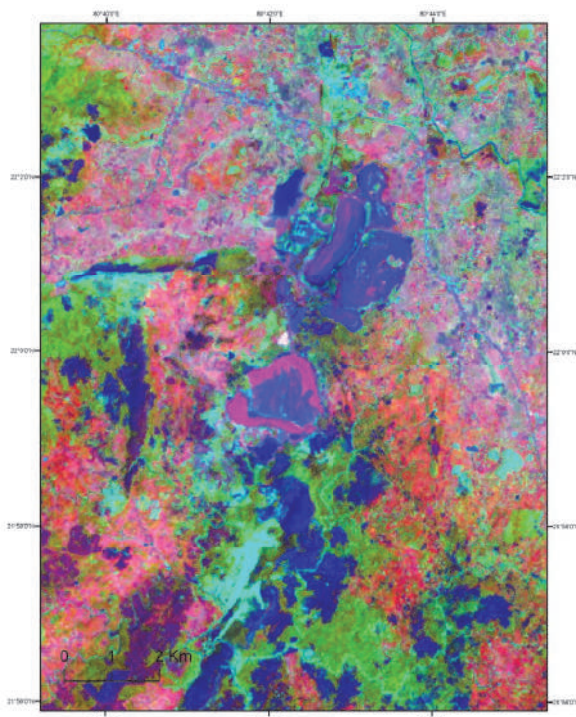


Figure 2. PCA image of six non-thermal OLI bands

Eigenvector	PC1	PC2	PC3	PC4	PC5	PC6
Band2	0.10	-0.12	0.35	0.17	0.67	0.61
Band3	0.17	-0.08	0.54	0.09	0.33	-0.74
Band4	0.28	-0.14	0.55	0.36	-0.65	0.22
Band5	0.36	0.82	0.22	-0.37	-0.02	0.09
Band6	0.68	0.06	-0.49	0.52	0.12	-0.09
Band7	0.54	-0.52	-0.05	-0.65	-0.04	0.06
% of variance	87.72	7.06	4.49	0.56	0.15	0.03

Table 1. Results of the principal component transformation (band loads) applied to the six non-thermal bands

3.2 Crosta technique using four bands for iron oxide and hydroxyl mapping

The selection of four bands as input for the PCA was based on laboratory spectra of the minerals related with hydrothermal alteration. Mapping of iron oxide was carried out using bands OLI-2, OLI-4, OLI-5, and OLI-6. The analysis for hydroxyl mapping must include bands OLI-2, OLI-5, OLI-6, and OLI-7. The PC band loads for iron oxide mapping were presented in Table 2. The magnitude and sign of the eigenvectors indicated that PC1 has positive values in all bands, it contained 88.83% of the data variance, therefore it consisted of albedo and topographic data. PC2 was the representative of the visible bands. The PC4 band loads yield a minimal contribution from OLI-5 and OLI-6 bands (3% and 6%, respectively) with respect to OLI-2 and OLI-4 bands (86% and -50%, respectively); furthermore, the eigenvalues had opposite sign in agreement with the spectral response of the oxide bearing rocks that would be represented as dark pixels. The image shown in Figure 3 was obtained as the PC4 inverse image in order to represent as bright pixels the oxide bearing rocks; however, no good discrimination of oxides was obtained.

Eigenvector	PC1	PC2	PC3	PC4
Band2	0.11	-0.12	0.48	0.86
Band4	0.32	-0.22	0.77	-0.50
Band5	0.47	0.88	0.07	0.03
Band6	0.82	-0.40	-0.41	0.06
% of variance	88.83	6.44	4.55	0.19

Table 2. Principal component band load for iron oxide mapping (analyzed bands OLI-2, OLI-4, OLI-5, and OLI-6)

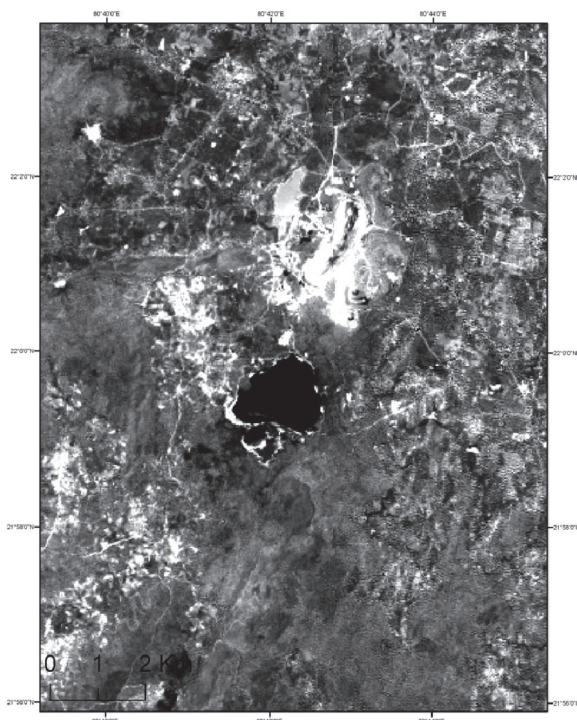


Figure 3. PC4 inverse image that resulted from the Crosta technique applied to bands OLI-2, OLI-4, OLI-5, and OLI-6, where bright pixels represent the oxide-bearing rocks.

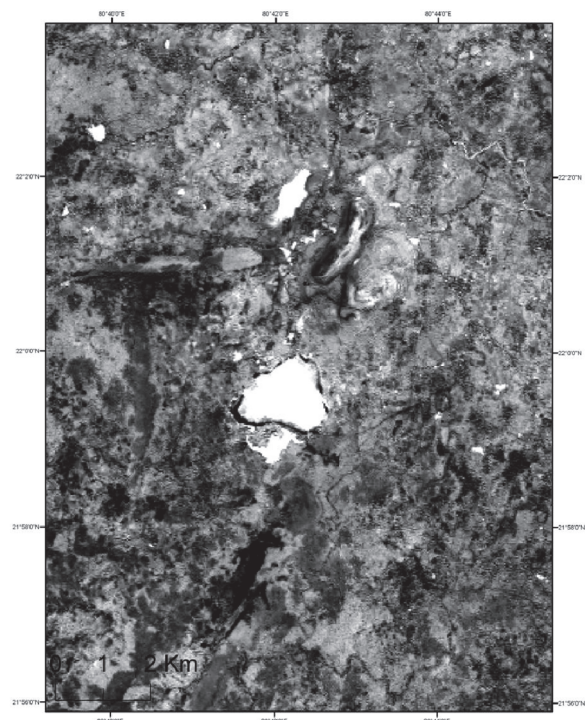


Figure 4. Results of the Crosta technique applied to bands OLI-2, OLI-5, OLI-6, and OLI-7, where PC4 is shown as bright pixels the hydroxyl-bearing rocks.

The results of the principal component analysis including OLI-2, OLI-5, OLI-6, and OLI-7 bands to map hydroxyl-bearing minerals were given in Table 3. The bands were chosen to take into account the spectral characteristics of the hydroxyl-bearing minerals, and OLI-3 and OLI-4 bands were omitted to avoid mapping iron oxide. In the similar procedure applied in the oxide analysis, the eigenvector loading for PC1, PC2, and PC3 yield analogous results. The eigenvector loading for PC4 shows a large negative value for OLI-7 (45%) and a positive value for OLI-6 (36%). These values significantly correlated with the spectral response for hydroxyl; therefore, the inverse image of PC4 should present the areas with high hydroxyl concentrations as bright pixels (Figure 4). It was observed that some areas gave a sharp response but large areas also had a high brightness value that should be taken into account.

Eigenvector	PC1	PC2	PC3	PC4
Band2	0.10	-0.08	0.60	0.79
Band5	0.38	0.83	0.33	-0.21
Band6	0.72	-0.01	0.59	0.36
Band7	0.57	-0.55	0.42	-0.45
% of variance	89.80	7.93	1.80	0.40

Table 3. Principal component band load for hydroxyl mapping (analyzed bands OLI-2, OLI-5, OLI-6, and OLI-7)

In the light of all the results, it can be concluded that the Crosta technique is effective in determining the alteration types, using six or selected four Landsat OLI bands. The analysis performed using four Landsat OLI bands were found to be a less effective differentiator than the analysis using the six Landsat OLI bands.

4. CONCLUSION

The present study focused on the effectiveness of Crosta technique in alteration mineral mapping using Landsat OLI datasets in Malanjkhand copper mines of Madhya Pradesh, India. Crosta technique is very useful in detecting hydroxyl-mineral, carbonate mineral, and iron oxides. The present study analyzed that the Crosta technique was more effective with six non-thermal Landsat-8 OLI bands combination. The results were significantly comparable to the published geological map.

The Crosta technique relies on the PC transform to map information common to all bands - overall Scene brightness or albedo - into the first principal component and specific spectral contrasts into successive components. The simple methodology for hydroxyl mapping by PCA on OLI bands 2, 5, 6, and 7 was to examine the eigenvector loadings for bands 6 and 7 to find a moderate or strong loading from both bands with opposite signs. Carrying out the PCA on unstretched bands of Malanjkhand area enhances the hydroxyl bearing area in PC4 as dark pixels. The enhancement was unique for hydroxyl without any kind of presence of vegetation. If the PCA is carried out on the stretched images, the vegetation area will also be enhanced in dark pixels. Standard principal component analysis, however, enhanced the alteration areas in one of the PCAs but was a time-consuming procedure and all the PCA images must be examined to find the alteration PC. Using the thermal band of OLI in transformation only shifts the alteration PC from PC5 to

PC6. Thus, the hydroxyl mapping technique of Crosta methodology was suggested for alteration mapping in Malanjhand copper mining area, India.

ACKNOWLEDGEMENTS

Authors are thankful to United States Geological Survey (USGS).

REFERENCES

- Crosta, A., Moore, J.McM. 1989. Enhancement of Landsat thematic mapper imagery for residual soil mapping in SW Minas Gerais State, Brazil: a prospecting case history in Greenstone belt terrain. In: Proceedings of 7th ERIM Thematic Conference: Remote sensing for exploration geology, pp. 1173–1187
- Ranjbar, H., Honarmand, M., Moezifar, Z., Ilaghi, O. 2002. Integration and analysis of remote sensing, airborne geophysics and geochemical data of Shar Cheshmeh area, using directed principal component analysis. In: 9th International Remote Sensing Conference, Agia Pelagia, Greece, 23–26 September, pp. 429–437.
- Rutz-Armenta, J.R., Prol-Ledesma, R.M. 1998. Techniques for enhancing the spectral response of hydrothermal alteration minerals in Thematic Mapper images of Central Mexico. *International Journal of Remote Sensing*, 19, pp. 1981–2000
- Tangestani, M.H., Moore, F. 2000. Iron-Oxide and Hydroxyl Enhancement Using the Crosta Method; A Case Study from the Zagros Belt, Fars Province, Iran. *ITC Journal*, in press.
- Tangestani, M.H., Moore, F. 2001. Comparison of three principal component analysis techniques to porphyry copper alteration mapping. A case study, Meiduk area, Kerman, Iran. *Canadian Journal of Remote Sensing*, 27, pp. 176–182
- Tangestani, M.H., Moore, F. 2002. Porphyry copper alteration mapping at the Meiduk area, Iran. *International Journal of Remote Sensing*, 23, pp. 4815–4825
- Torres-Vera, M.A., Prol-Ledesma, R.M. 2003. Spectral enhancement of selected pixels in Thematic Mapper images of the Guanajuato district (Mexico) to identify hydrothermally altered rocks. *International Journal of Remote Sensing*, 24, pp. 4357–4373



Source details

[Feedback >](#) [Compare sources >](#)

International Archives of the Photogrammetry, Remote Sensing and Spatial Information Sciences - ISPRS Archives

Open Access

Scopus coverage years: 2000, from 2002 to Present

ISSN: 1682-1750

Subject area: [Social Sciences: Geography, Planning and Development](#) [Computer Science: Information Systems](#)

Source type: Conference Proceeding

[View all documents >](#)

[Set document alert](#)

[Save to source list](#)

CiteScore 2022
1.8



SJR 2022
0.274



SNIP 2022
0.427



[CiteScore](#)

[CiteScore rank & trend](#)

[Scopus content coverage](#)



Improved CiteScore methodology

CiteScore 2022 counts the citations received in 2019-2022 to articles, reviews, conference papers, book chapters and data papers published in 2019-2022, and divides this by the number of publications published in 2019-2022. [Learn more >](#)



IDENTIFICATION OF ROCKS AND THEIR QUARTZ CONTENT IN AMARKANTAK, INDIA USING ASTER TIR DATA

S. Guha^{1,*}, H. Govil¹, M. Tripathi¹, M. Besoya¹

¹ Department of Applied Geology, National Institute of Technology Raipur, Raipur, India- (subhanilguha, himgeo, tripathi.mahesh1, geniusmonika11@gmail.com)

Commission V, SS: Natural Resources Management

KEY WORDS: Quartz, Principal component analysis, Thermal infrared, ASTER

ABSTRACT:

Quartz (SiO₂) abundance in rock is an important indicator of mineralization in many metal deposits and quartz detection has a great role in mineral exploration. The present study identified the quartz contained rocks in Amarkantak region, India applying thermal infrared bands (bands 10-14) of the Advanced Spaceborne Thermal Emission and Reflection Radiometer (ASTER) image. After atmospheric correction, principal component analysis technique was applied on the TIR bands and the resulting principal component images were analyzed. The three optimal principal components were selected based on the spectral interaction strength and the eigenvalues of each band of the ASTER data. The result presented that extrusive igneous rock and carbonate sedimentary rocks are quartz-poor while sedimentary rocks made up of organic particles and sandstone is quartz-rich.

1. INTRODUCTION

Hyperspectral and multispectral satellite images were frequently applied for extracting lithological and mineralogical information (vanderMeer et al. 2012; Pour and Hashim 2012). Visible-near-infrared (VNIR) and short wave infrared (SWIR) regions of electromagnetic spectrum is not so useful for detecting quartz and feldspar minerals (Lyon, 1972; Salisbury and Walter, 1989) whereas thermal infrared (TIR) region is extremely useful for the delineation of the aforesaid minerals because of the vibration of Si–O bonds (Farmer, 1974; Kahle, 1976; Lyon, 1972). Lithological mapping is an important task of geological exploration. Remote sensing techniques plays a significant role in lithological and mineralogical mapping. TIR region are less studied than VNIR or SWIR regions for mineral exploration due to the less availability of satellite sensors in TIR domain. Advanced Spaceborne Thermal Emission and Reflection Radiometer (ASTER) data is considered as one of the most effective data for lithological and mineralogical mapping due to its high sensitivity to rock mineral elements (alunite, kaolinite, calcite, dolomite, chlorite, talc, muscovite, etc.) and low-cost (Tornabean et al. 2005; Gad and Kusky 2007). ASTER data has three VNIR bands, six SWIR bands, and five TIR bands. Based on the analysis of ASTER TIR band based emissivity spectra of rocks, Ninomiya et al. (2005) have proposed few popular spectral indices for the mapping of quartz, carbonate, and mafic rocks using ASTER data. Many important geological units were also mapped using TIR bands of ASTER data using emissivity as a parameter (Bertoldi et al., 2011; Ding et al., 2014; Matar and Bamousa, 2013; Ninomiya et al., 2005; Rowan et al., 2005). However, mineralogically sensitive indices often derived significant results in terms of delineating mineralogical contrast by highlighting variations in thermal emissivity of terrain elements recorded in selected numbers of bands. The term granitoids include family of felsic igneous rocks viz. alkali granites, granites, granodiorites,

tonalities; which are essentially constituted with quartz, varied proportions of alkali feldspar and plagioclase feldspar (Bose, 1997). Alkali feldspar rich granite is characterised with high ratio of alkali feldspar to plagioclase feldspar content whereas the ratio is progressively lower in granodiorite and tonalite (Bose, 1997). Mafic mineral content (biotite, hornblende etc.) is low in granitoids in general. However, mafic mineral abundances are also progressively higher as we go from granite to tonalite in granite–granodiorite–tonalite sequence.

In this study, ASTER TIR bands (bands 10-14) were applied to quartz-rich and quartz-poor rocks mapping in Amarkantak using principal component analysis (PCA) technique.

2. MATERIALS AND METHODS

ASTER image of 23 February 2003 was used in this study (Fig. 1). Only the ASTER thermal infrared (TIR) bands were used in this study because within 8–14 μ m, quartz minerals exhibit strong vibrational absorption feature spectrally (Pour and Hashim 2012a, 2012b). Specification of ASTER thermal bands was provided in Table 1. We analyzed resampled (i.e., resampled to the bandwidth of ASTER thermal bands) laboratory derived emissivity spectra of quartz, orthoclase, and plagioclase minerals; three key minerals of granitoids. The lithologic and mineral map prepared from satellite data were widely used to for the visual validation of the rock element identification. To differentiate between vegetation area and outcrop areas, normalized difference vegetation index (NDVI) was used (Fig. 2). The vegetation and cloud affected areas were masked from the TIR bands and only the outcrop area was subjected to PCA.

* Corresponding author

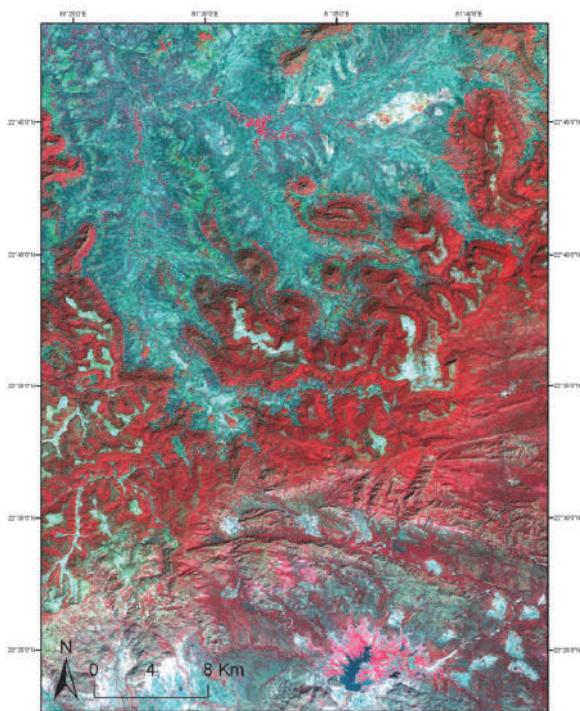


Figure 1. Location of the study area

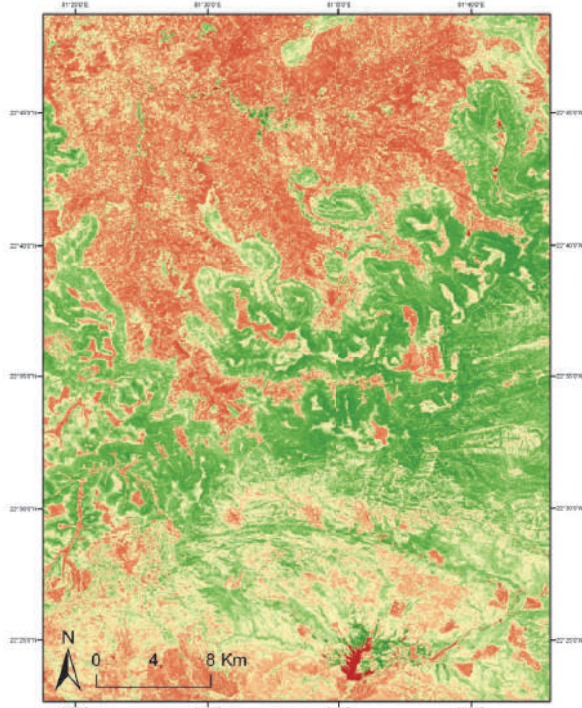


Figure 2. NDVI image

It was observed that quartz was characterized with emissivity minima at band 12 (for quartz) with the relative high in emissivity in band 10 and band 13 of ASTER bands. Feldspar is characterized with lower emissivity (for both plagioclase and orthoclase feldspar but the emissivity minima were more intense for orthoclase feldspar or K-feldspar) in band 11 than band 10 of ASTER thermal bands (Fig. 3). It is also known that mafic minerals and rocks are known for their emissivity minima in

band 13 of ASTER sensor than band 12 and band 14 (Son et al., 2014). It was observed that emissivity spectra of quartz and feldspar had a reverse trend in band 11 and band 12 (Son et al., 2014). Therefore, emissivity minima of feldspar would be nullified by the high emissivity of quartz in band 11 with respect to band 12 if quartz and feldspar are present in the same rock. Based on the above observations on emissivity spectra of constituent minerals of granitoids and their respective image spectra, the following indices were derived to delineate quartz, feldspar and mafic mineral variation in granitoids based on the processing of ASTER bands.

ASTER granule ID	Sensor type	Band number	Spectral wavelength (μm)	Spatial resolution (m)	Radiometric resolution
ASTB03 0223051 412 Date:23 Feb 2003	TIR	10	8.125-8.475	90	12 bits
	TIR	11	8.475-8.825	90	12 bits
	TIR	12	8.925-9.275	90	12 bits
	TIR	13	10.25-10.95	90	12 bits
	TIR	14	10.95-11.65	90	12 bits

Table 1. Specification of ASTER TIR bands

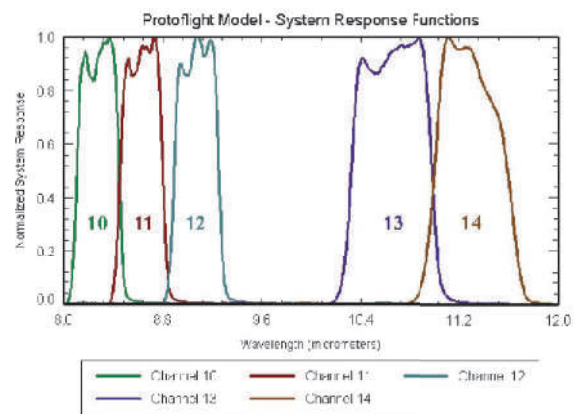


Figure 3. Spectral ASTER TIR bands in the wavelength of the electromagnetic spectrum (Source: NASA Jet Propulsion Laboratory)

Quartz has no such spectral absorption features in the visible and near infrared or shortwave infrared spectrum but have a very powerful molecular absorption features in TIR (8–10 μm) bands. We used PCA transformation of the five ASTER TIR bands (bands 10–14) to generate five different principal components (PC1, PC2, PC3, PC4, and PC5). The eigenvalues were analyzed to select the most significant three PCs components for identifying quartz richness (Pour and Hashim 2011a). The three selected PCs (PC1, PC3, and PC4) were used to generate RGB false colour composite (FCC) of the study area (Fig. 4). After visual examination of the FCC relative to the existing map, the PCs composite image was classified into four different rock types [quartz concentration (quartz-rich and quartz-poor), quartz-rich sedimentary rock, quartz-poor igneous rock, and quartz-poor limestone)] based on quartz richness using and maximum likelihood supervised classification method. Finally, the accuracy of the classified image was assessed through error matrix.

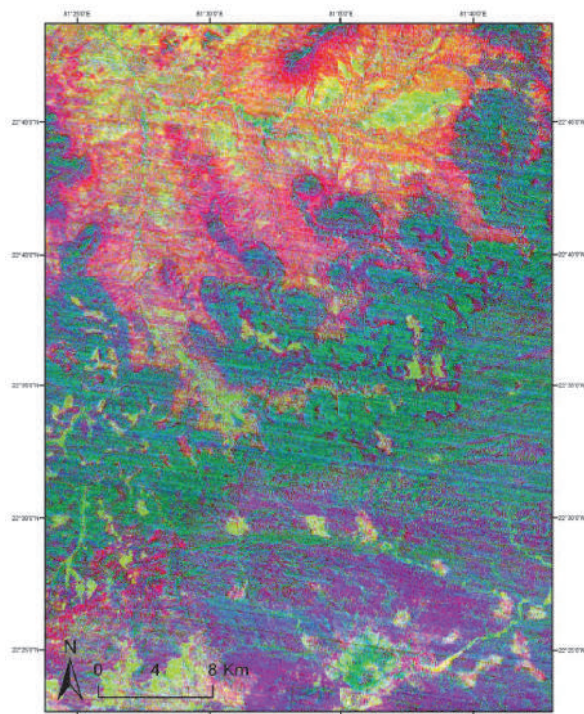


Figure 4. PCA image

3. RESULTS AND DISCUSSION

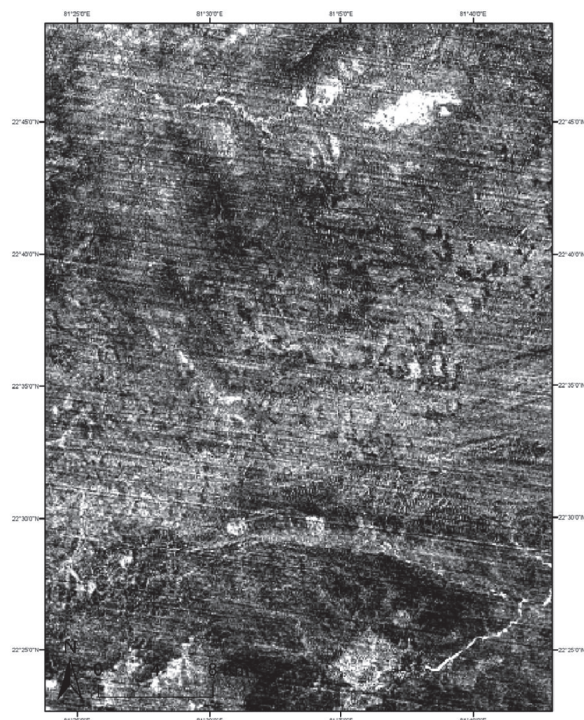


Figure 5. QRI image

ASTER TIR bands are quite effective to detect silicate and carbonate rocks, while bands 10 and 12 are particularly effective for detecting quartz absorption features and band 14 records high emissivity (Pour and Hashim 2012b; Surip et al. 2015). The positive eigenvalues reflect that the band plays a

major role in the variation of a particular component while negative eigenvalues reflect a minor role to the variation of the derived component. The quartz content is reflected by thermal bands 10 and 12 of ASTER data due to high absorption property and by thermal band 14 due to high emissivity. It means that the eigenvalues of bands 10 and 12 have positive signs while band 14 is negative (Pour and Hashim 2011b).

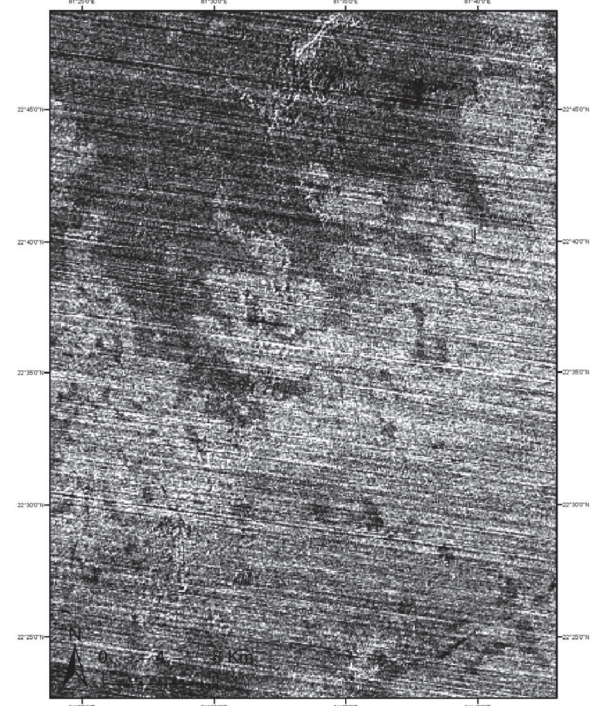


Figure 6. FRI image

Quartz rock index (QRI), feldspar rock index (FRI), and Mafic rock index (MRI), propounded by Guha and Kumar (2016) were applied in this study. It was observed that silica variation in alkali-granite and granite was enhanced in the QRI image. Quartz rich alkali granite appeared brighter in QRI image (Fig. 5). This quartz rock also appeared as bright green colour in PCA image. This is due to the fact quartz and feldspar are characterized with contrasting emissivity features in these bands. Therefore, it was difficult to indicate quartz enrichment in rocks which were rich in feldspar and quartz using band 11 and band 12. In FRI image, feldspar enriched alkali granite was brighter than darker granitic patch as alkali granite was relatively rich in alkali feldspar (Fig. 6). MRI images highlighted the mafic rocks in the study area (Fig. 7).

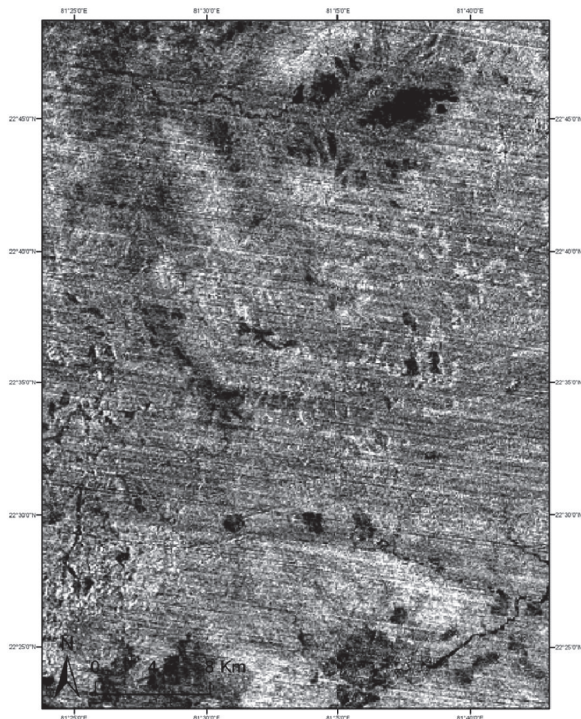


Figure 7. MRI image

Here, PC1, PC3, and PC4 satisfied the enabling conditions to identify quartz-rich and quartz-poor rocks. Results present that, ASTER TIR bands have the high capability to differentiate between different categories of rock and their quartz content using PCA spectral transformation. The results may have spatial and seasonal variations due to the presence or absence of the controlling factors of mechanical or chemical weathering.

Eigenvector	PC1	PC2	PC3	PC4	PC5
Band10	0.39	-0.31	-0.78	0.38	-0.01
Band11	0.43	-0.31	-0.06	-0.82	0.21
Band12	0.48	-0.54	0.61	0.37	-0.07
Band13	0.49	0.45	0.02	-0.16	-0.73
Band14	0.48	0.56	0.10	0.19	0.64
% of variance	99.49	0.34	0.08	0.04	0.03

Table 2. PCA for five ASTER TIR bands

4. CONCLUSION

ASTER TIR bands may be used successfully to detect different rocks and their quartz content richness. Guha's QRI image was very effective in identifying the quartz content in rocks along with the PCA image. FRI and MRI images were also supported a lot to detect the feldspar and mafic rocks, respectively which can be regarded as useful tool in signifying the quartz content of rocks. These lithological indices are important as it could delineate variation in the content of quartz, feldspar and mafic minerals in granitoids. Generally, it may be stated that quartz mineral was not uniformly presented among the different rocks. The results were significantly comparable to the published geological map.

ACKNOWLEDGEMENTS

Authors are thankful to United States Geological Survey (USGS).

REFERENCES

- Bertoldi, L., Massironi, M., Visona, D., Carosi, R., Montomoli, C., Gubert, F., et al., 2011. Mapping the Buraburi granite in the Himalaya of Western Nepal: remote sensing analysis in a collisional belt with vegetation cover and extreme variation of topography. *Remote Sens. Environ.* 115 (5), pp. 1129–1144
- Bose, M.K., 1997. *Igneous Petrology*. World Press, Kolkata.
- Ding, C., Liu, X., Liu, W., Liu, M., Li, Y., 2014. Mafic and ultramafic and quartz-rich rock indices deduced from ASTER thermal infrared data using a linear approximation to the Planck function. *Ore Geol. Rev.* 60, pp. 161–173
- Farmer, V.C. (Ed.), 1974. *The Infrared Spectra of Minerals*, 4. Mineralogical Society, London, p. 539
- Gad, S., Kusky, T. 2007. ASTER spectral ratioing for lithological mapping in the Arabian-Nubian shield, the Neoproterozoic Wadi Kid area, Sinai, Egypt. *Gondwana Research*, 11 (3), pp. 326–335
- Guha, A., Kumar, V.K., 2016. New ASTER derived thermal indices to delineate mineralogy of different granitoids of an Archaean Craton and analysis of their potentials with reference to Ninomiya's indices for delineating quartz and mafic minerals of granitoids—An analysis in Dharwar Craton, India. *Ore Geol. Rev.* 74, pp. 76–87
- Kahle, A.B., 1976. Thermal inertia imaging: a new geologic mapping tool. *Geophys. Res. Lett.* 3, pp. 419–421
- Lyon, R.J.P., 1972. Infrared spectral emittance in geological mapping: airborne spectrometer data from Pisgah Crater. *Science* 7, 983–986.
- Matar, S.S., Bamousa, A.O., 2013. Integration of the ASTER thermal infra-red bands imageries with geological map of Jabal Al Hasir area, Asir Terrane, the Arabian Shield. *J. Taibah Univ. Sci.* 7 (1), 1–7.
- Ninomiya, Y., Fu, B., Cudahy, T.J., 2005. Detecting lithology with Advanced Spaceborne Thermal Emission and Reflection Radiometer (ASTER) multispectral thermal infrared radiance-at-sensor data. *Remote Sens. Environ.* 99, 127–139.
- Pour, A.B., Hashim, M. 2011a. Application of advanced spaceborne thermal emission and reflection radiometer (ASTER) data in geological mapping. *International Journal of Physical Sciences*, 6 (33), pp. 7657–7668
- Pour, A.B., Hashim, M. 2011b. Identification of hydrothermal alteration minerals for exploring of porphyry copper deposit using ASTER data, SE Iran. *Journal of Asian Earth Sciences*, 42 (6), pp. 1309–1323
- Pour, A.B., Hashim, M. 2012a. The application of ASTER remote sensing data to porphyry copper and epithermal gold deposits. *Ore Geology Reviews*, 44, pp. 1–9

Pour, A.B., Hashim, M. 2012b. Identifying areas of high economic potential copper mineralization using ASTER data in the Urumieh-Dokhtar Volcanic Belt, Iran. *Advances in Space Research*, 49 (4), pp. 753–769

Rowan, L.C., Mars, J.C., Simpson, C.J., 2005. Lithologic mapping of the Mordor, NT, Australia ultramafic complex by using the Advanced Spaceborne Thermal Emission and Reflection Radiometer (ASTER). *Remote Sens. Environ.* 99 (1–2), 105–126.

Salisbury, J.W., Walter, L.S., 1989. Thermal infrared (2.5–13.5 μm) spectroscopic remote sensing of igneous rock types on particulate planetary surfaces. *J. Geophys. Res.* 94 (B7), 9192–9202.

Son, Y.-S., Kang, M.-K., Yoon, W.-J., 2014. Lithological and mineralogical survey of the Oyu Tolgoi region, South-eastern Gobi, Mongolia using ASTER reflectance and emissivity data. *Int. J. Appl. Earth Obs. Geoinf.* 26, 205–216.

Surip, N., Hamzah, A.H., Zakaria, M.R., Napiah, A., Talib, J.A. 2015. Mapping of gold in densely vegetated area using remote sensing and GIS techniques in Pahang, Malaysia. *Open Geosciences*, 7, pp. 149–161

Tornabene, L.L., Moersch, J.E., Osinski, G.R., Lee, P., Wright, S.P. 2005. Spaceborne visible and thermal infrared lithologic mapping of impact-exposed subsurface lithologies at the Haughton impact structure, Devon Island, Canadian High Arctic: applications to Mars. *Meteoritics and Planetary Science*, 40 (12), pp. 1835–1858

vanderMeer, F.D., vanderWerff, H.M.A., vanRuitenbeek, F.J.A., et al. 2012. Multi and hyperspectral geologic remote sensing: a review. *International Journal of Applied Earth Observation and Geoinformation*, 14 (1), pp. 112–128



Source details

[Feedback >](#) [Compare sources >](#)

International Archives of the Photogrammetry, Remote Sensing and Spatial Information Sciences - ISPRS Archives

Open Access [i](#)

Scopus coverage years: 2000, from 2002 to Present

ISSN: 1682-1750

Subject area: [Social Sciences: Geography, Planning and Development](#) [Computer Science: Information Systems](#)

Source type: Conference Proceeding

[View all documents >](#)

[Set document alert](#)

[Save to source list](#)

CiteScore 2022
1.8 [i](#)

SJR 2022
0.274 [i](#)

SNIP 2022
0.427 [i](#)

[CiteScore](#) [CiteScore rank & trend](#) [Scopus content coverage](#)



Improved CiteScore methodology

CiteScore 2022 counts the citations received in 2019-2022 to articles, reviews, conference papers, book chapters and data papers published in 2019-2022, and divides this by the number of publications published in 2019-2022. [Learn more >](#)



Journal of Applied Remote Sensing

RemoteSensing.SPIEDigitalLibrary.org

Analytical study of seasonal variability in land surface temperature with normalized difference vegetation index, normalized difference water index, normalized difference built-up index, and normalized multiband drought index

Subhanil Guha
Himanshu Govil
Prabhat Diwan

SPIE.

Subhanil Guha, Himanshu Govil, Prabhat Diwan, "Analytical study of seasonal variability in land surface temperature with normalized difference vegetation index, normalized difference water index, normalized difference built-up index, and normalized multiband drought index," *J. Appl. Remote Sens.* **13**(2), 024518 (2019), doi: 10.1117/1.JRS.13.024518.

Analytical study of seasonal variability in land surface temperature with normalized difference vegetation index, normalized difference water index, normalized difference built-up index, and normalized multiband drought index

Subhanil Guha,* Himanshu Govil, and Prabhat Diwan

National Institute of Technology Raipur, Department of Applied Geology, Chhattisgarh, India

Abstract. Remote sensing technique often analyzes the thermal characteristics of any area. Our study focuses on estimating land surface temperature (LST) of Raipur City, emphasizing the urban heat island (UHI) and non-UHI inside the city boundary and the relationships of LST with four spectral indices (normalized difference vegetation index, normalized difference water index, normalized difference built-up index, and normalized multiband drought index). Mono-window algorithm is used as LST retrieval method on Landsat 8 Operational Land Imager (OLI) and Thermal Infrared Sensor (TIRS) data, which needs spectral radiance and emissivity of TIRS bands. The entire study is performed on 11 multirate Landsat 8 OLI and TIRS images taken from four different seasons; premonsoon, monsoon, postmonsoon, and winter, in a single-year time period. The Landsat 8 data derived LST is validated significantly with Moderate Resolution Imaging Spectroradiometer (MOD11A1) data. The results show that the UHI zones are mainly developed along the northern and southern portions of the city. The common area of UHI for four different seasons is developed mainly in the northwestern parts of the city, and the value of LST in the common UHI area varies from 26.45°C to 36.51°C. Moreover, the strongest regression between LST and these spectral indices is observed in monsoon and postmonsoon seasons, whereas winter and premonsoon seasons revealed comparatively weak regression. The results also indicate that landscape heterogeneity reduces the reliability of the regression between LST with these spectral indices. © 2019 Society of Photo-Optical Instrumentation Engineers (SPIE) [DOI: [10.1117/1.JRS.13.024518](https://doi.org/10.1117/1.JRS.13.024518)]

Keywords: land surface temperature; normalized multiband drought index; normalized difference built-up index; normalized difference vegetation index; normalized difference water index; spectral indices; urban heat island.

Paper 180975 received Dec. 17, 2018; accepted for publication Apr. 17, 2019; published online May 13, 2019.

1 Introduction

Land surface temperature (LST) estimation is considered as one of the most significant tasks in thermal remote sensing study, where thermal impacts of changing land use/land cover (LULC) may regulate the generation of urban heat island (UHI) in mixed urban landscapes.¹⁻⁵ The effect of UHI on some major cities (e.g., Beijing, Columbus, Shanghai, Baltimore, and Chicago) in the world is growing at an alarming rate and is directly related to the LULC categories.⁶⁻¹¹ Various LULC indices (vegetation, impervious surface area, etc.) were applied in a UHI related remote sensing study to determine the changed pattern of LST in different types of natural and man-made landscape systems.¹²⁻¹⁶ Some recent articles discussed the statistical linear regression between LST and some selected LULC indices for separate study areas like Brisbane,¹⁷ Raipur,¹⁸ Shanghai,¹⁹ Addis Ababa,²⁰ Mexico,²¹ Philadelphia,²² Florence, and Naples.²³

A more recent direction includes the application of some sophisticated statistical techniques to estimate the seasonal variability of LST in the urban area. Cui and de Foy²⁴ showed that

*Address all correspondence to Subhanil Guha, E-mail: subhanilguha@gmail.com

vegetation cover, daytime insolation, and atmospheric stability are related to seasonal UHI variations in Mexico City, Mexico. Zhou et al.²⁵ made an attempt in Baltimore, USA, to build relationships between land cover and UHI and their seasonal variability. Haashemi et al.²⁶ presented a seasonal variability in the regression between LST and fractional vegetation cover, albedo, impervious surfaces, and elevation in Tehran, Iran.

In later studies, seasonal variation in the UHI effect was critically analyzed. Seasonal effects in urban thermal patterns were determined by spatial regression analyses in Ohio, USA.²⁷ Multiple statistical methods were integrated to show the seasonal contrast of some LULC indices for LST distribution in Shenzhen, China.²⁸ A seasonal variation in LST and selected LULC indices was investigated in Jaipur, India.²⁹ A trend and seasonal decomposition model for LST change over Beijing, China, was investigated.³⁰ A regression-based model was performed to determine the average annual and seasonal trend of LST in peninsular Spain.^{31,32} The relationship of urbanization and climate variability with urban and rural LST for 31 cities of China was critically investigated.³³ An analytical research work performed in more than 86 major cities of China presented that UHI is seasonally different and is negatively related to the cloud cover percentage in transitional seasons.³⁴ A landscape source-sink distance index was applied to relate the landscape connectivity and LST variation in Beijing, China.³⁵ A variation of LST due to elevation change in summer, winter, and monsoon season for Jaipur, India, was assessed.³⁶ In summary, recent researchers tried to make a true attempt in the seasonal variability of LST in UHI of the major cities using common statistical methods.

This paper was an analytical study based on the seasonal variability of LST distribution inside the UHI and the area outside the UHI zones in a typical Indian city. The area outside the UHI zones is described here as non-UHI.^{18,23} Basically, the term “non-UHI” is slightly different from the term “urban cool island (UCI).” Generally, the term UCI indicates that the low-temperature zones inside an urban area are characterized by urban vegetation, wetland, and water bodies, whereas the term “non-UHI” is used to present an area other than the UHI, which is actually denoted moderate-to low-temperature zones of an urban area. Hence, UCI can be considered as a part of non-UHI in an urban area. Another term “common-UHI” was used in this study to show the common area of UHI for each and every satellite image (total of 11 images) for four different seasons.^{18,23}

Landsat TIR data are often used in the identification of UHI zones.^{37–39} LST derivation using Landsat TIR data becomes popular through the introduction of some algorithms, such as mono-window algorithm,^{40,41} single-channel algorithm,^{41–45} radiative transfer algorithm,^{41,45} split-window algorithm.^{41,45–47} Landsat 8 TIRS dataset has two TIR bands (bands 10 and 11). Generally, TIR band 10 is used for LST derivation as TIR band 11 is associated with larger uncertainties and thus it is not recommended to use the split-window algorithm. In the radiative transfer equation, LST estimation requires atmospheric correction and emissivity correction, which are difficult to perform.⁴¹ Ground emissivity, atmospheric transmittance, and effective mean atmospheric temperature are the parameters needed to derive the LST using mono-window algorithm, whereas single-channel algorithm needs atmospheric transmissivity, upwelling, and downwelling atmospheric radiance. Single-channel algorithm and mono-window algorithm both present significant results in LST retrieval.^{18,23,43,48} In this study, LST derivation process was conducted using the mono-window algorithm.

The specific aims of the study were: (1) to describe the nature of LST in the UHI, non-UHI, common UHI, and the whole of Raipur City for Landsat 8 OLI and TIRS images selected from premonsoon, monsoon, postmonsoon, and winter seasons in a single-year span and (2) to examine the variation in nature and strength of regression between LST and normalized difference vegetation index (NDVI), normalized difference water index (NDWI), normalized difference built-up index (NDBI), and normalized multiband drought index (NMDI) for the UHI, non-UHI, and common UHI and for the whole of Raipur City in these four particular aforesaid images.

2 Study Area and Data

Raipur, the capital city and the largest city of Chhattisgarh State in east-central India, located along the west of Mahanadi River, was selected for the present research work. Raipur is

characterized by comparatively dry climate having no influence of coastal or maritime climatic condition. Moreover, Raipur is a rapidly growing city in India where a lot of new conversions of land have been seen in the recent time period. It has a wide variety in the population. The city has also seen exponential growth in industrial sectors and has emerged as a major business hub in central India. It is also ranked seventh in Ease of Living Index 2018 by Union Ministry of Housing and Urban Affairs.⁴⁹ Raipur is considered to be one of the modern and smart technological cities in India due to the addition of new technology to the older system, power plant retrofit, home energy retrofit, seismic retrofit, eco-friendly, and sustainable nature; and thus the city was selected as the study area of the research work. Due to the presence of various types of surface materials, the nature of LST distribution is too dynamic. The latitudinal and longitudinal extents of Raipur City are $21^{\circ}11'22''\text{N}$ - $21^{\circ}20'02''\text{N}$ and $81^{\circ}32'20''\text{E}$ - $81^{\circ}41'50''\text{E}$, respectively (Fig. 1). The mean elevation of the city is around 298 m. Raipur City is characterized by a tropical wet and dry climate. There are four seasons observed in Raipur according to the India Meteorological Department, i.e., premonsoon or summer (March to May), monsoon (June to September), postmonsoon (October to November), and winter (December to February). Generally, the summer months (March to May) remain hot and dry. The mean annual temperature of Raipur City lies between 21°C to 34°C . Amount of rainfall is moderate (average annual rainfall is 120 to 150 cm.). Rain occurs mainly in the monsoon season. At that time, vegetation was looking green and healthy, containing more chlorophyll component. In the rainy monsoon season, temperature falls at a significant rate from the summer or premonsoon season. A pleasant weather condition persists throughout the postmonsoon season. Winter season remains cool and dry. December is considered the coldest month (average temperature 12°C) of the city.

A total of eleven (three from the premonsoon, two from the monsoon, three from the postmonsoon, and three from winter season) Landsat 8 Operational Land Imager (OLI) and Thermal Infrared Sensor (TIRS) data (<10% cloud coverage) were selected to determine the UHI zones over all of Raipur City (Table 1). The Landsat 8 datasets were freely downloaded from the website of the United States Geological Survey.⁵⁰ Only Landsat TIR band 10 data were

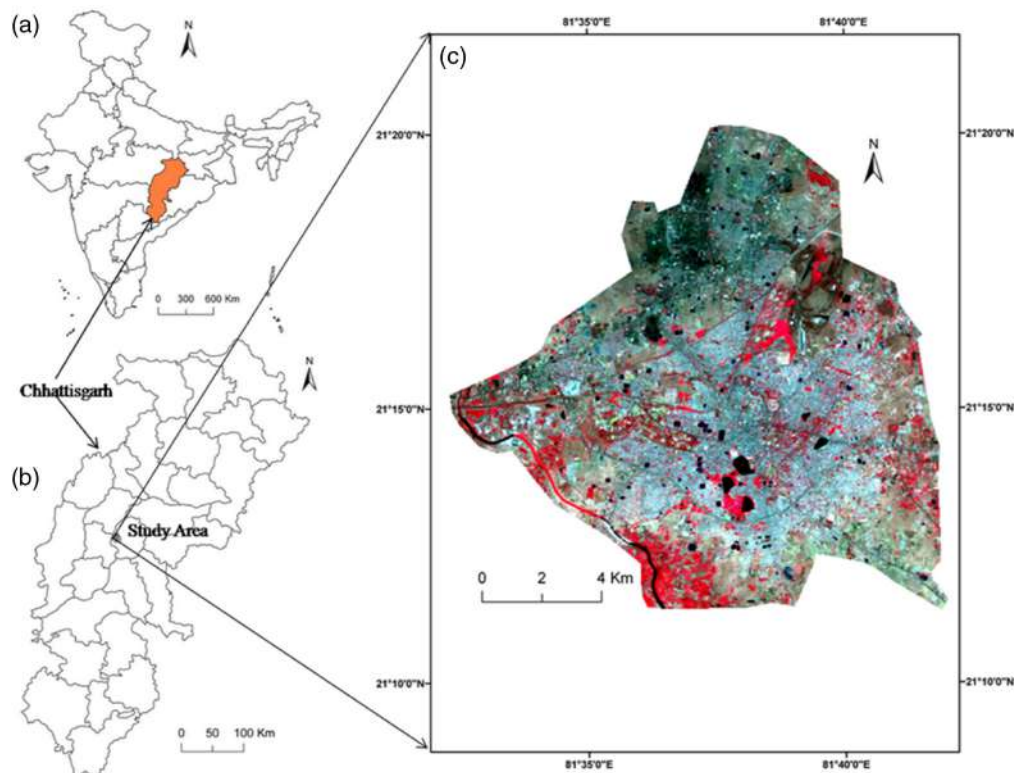


Fig. 1 The study area: (a) Chhattisgarh in India, (b) Raipur City in Chhattisgarh, and (c) Raipur City.

Table 1 Specification of multirate Landsat 8 OLI and TIRS satellite images.

Date of acquisition	Season	Time	Path/row	Sun elevation (deg)	Sun azimuth (deg)	Cloud cover (%)	Earth-Sun distance (astronomical unit)
09-Nov-2013	Postmonsoon	14:27:51	142/044	47.1003	152.5147	0.03	0.9905
25-Nov-2013	Postmonsoon	14:27:43	142/044	43.2895	153.9750	0.00	0.9871
11-Dec-2013	Winter	14:27:42	142/044	40.6309	153.5245	0.00	0.9847
27-Dec-2013	Winter	14:27:33	142/044	39.5066	151.6083	1.69	0.9835
28-Jan-2014	Winter	14:27:13	142/044	42.3669	144.8623	0.49	0.9849
17-Mar-2014	Premonsoon	14:26:36	142/044	55.9542	129.3872	0.00	0.9949
02-Apr-2014	Premonsoon	14:26:19	142/044	60.9189	121.7216	0.00	0.9995
20-May-2014	Premonsoon	14:25:38	142/044	68.5638	90.4085	5.46	1.0118
05-Jun-2014	Monsoon	14:25:45	142/044	68.3821	83.3098	0.02	1.0146
25-Sep-2014	Monsoon	14:26:11	142/044	59.2100	134.1804	0.81	1.0030
12-Nov-2014	Postmonsoon	14:26:21	142/044	46.2266	152.4664	7.59	0.9899

used for LST retrieval process because TIR band 11 data faces some calibration uncertainty. Optical bands 3, 4, 5, 6, and 7 datasets were used in developing NDVI, NDWI, NDBI, and NMDI. The entire study was performed in the environment of some sophisticated image processing and GIS software packages.

3 Methodology

3.1 Determination of NDVI, NDWI, NDBI, and NMDI

NDVI⁵¹ is considered one of the most frequently used vegetation indices in remote sensing study. It is also applied in deriving LST and normally shows a negative regression with LST. NDWI⁵² is generally used for water body extraction. NDBI⁵³ is another spectral index, which was applied in this study for built-up area extraction. NMDI⁵⁴ was also used to extract the dry soil or bare land. The formulation of these four spectral indices was presented in Table 2. Integration of suitable threshold values of these spectral indices is useful in identifying several LULC types.⁵⁵

3.2 LST Derivation Using Landsat 8 OLI and TIRS Band

For retrieving LST using mono-window algorithm, the original Landsat 8 TIR band (100-m resolution) was resampled into 30 m. The entire procedure included the following equations.⁵⁶

Table 2 Description of NDVI, NDWI, NDBI, and NMDI.

Acronym	Description	Formulation	Reference
NDVI	Normalized difference vegetation index	$\frac{NIR-Red}{NIR+Red}$	51
NDWI	Normalized difference water index	$\frac{Green-NIR}{Green+NIR}$	52
NDBI	Normalized difference built-up index	$\frac{SWIR1-NIR}{SWIR1+NIR}$	53
NMDI	Normalized multiband difference index	$\frac{NIR-(SWIR1+SWIR2)}{NIR+(SWIR1+SWIR2)}$	54

$$L_{\lambda} = 0.0003342 \times DN + 0.1, \quad (1)$$

where L_{λ} is spectral radiance ($\text{Wm}^{-2} \text{sr}^{-1} \text{mm}^{-1}$)

$$T_b = \frac{K_2}{\ln\left(\frac{K_1}{L_{\lambda}} + 1\right)}, \quad (2)$$

where T_b is the at-sensor brightness temperature (K),⁵⁷ K_2 and K_1 are the calibration constants. Here K_1 is 774.89 ($\text{Wm}^{-2} \text{sr}^{-1} \text{mm}^{-1}$) and K_2 is 1321.08 ($\text{Wm}^{-2} \text{sr}^{-1} \text{mm}^{-1}$)

$$F_v = \left(\frac{\text{NDVI} - \text{NDVI}_{\min}}{\text{NDVI}_{\max} - \text{NDVI}_{\min}} \right)^2, \quad (3)$$

where NDVI_{\min} is the minimum value (0.2) of NDVI for bare soil pixel and NDVI_{\max} is the maximum value (0.5) of NDVI for healthy vegetation pixel.⁵⁸⁻⁶⁰

$d\epsilon$ is the geometric distribution effect for the natural surface and internal reflection. The value of $d\epsilon$ may be 2% for mixed and elevated land surfaces⁵⁸

$$d\epsilon = (1 - \epsilon_s)(1 - F_v)F\epsilon_v, \quad (4)$$

where ϵ_s is the soil emissivity, F_v is the fractional vegetation, F is a shape factor (0.55),⁵⁸ and ϵ_v is the vegetation emissivity

$$\epsilon = \epsilon_v F_v + \epsilon_s (1 - F_v) + d\epsilon, \quad (5)$$

where ϵ is land surface emissivity. The value of ϵ is determined by the following equation.⁵⁸

$$\epsilon = 0.004 \times F_v + 0.986. \quad (6)$$

Water vapour content is determined by the following equation.⁶¹

$$w = 0.0981 \times \left\{ 10 \times 0.6108 \times \exp\left[\frac{17.27 \times (T_0 - 273.15)}{237.3 + (T_0 - 273.15)}\right] \times \text{RH} \right\} + 0.1697, \quad (7)$$

where w is the water vapor content (g/cm^2), T_0 is the near-surface air temperature (K), and RH is the relative humidity (%). These parameters of the atmospheric profile were the average values of 14 stations around Raipur, which were obtained from the Meteorological Centre, Raipur and the Regional Meteorological Centre, Nagpur.

$$\tau = 1.031412 - 0.11536w, \quad (8)$$

where τ is the total atmospheric transmittance.⁶²

Raipur City is located in a tropical region. Thus the following equations were applied to compute the effective mean atmospheric transmittance of Raipur:

$$T_a = 17.9769 + 0.91715T_0, \quad (9)$$

$$T_s = \frac{\{a(1 - C - D) + [b(1 - C - D) + C + D]T_b - DT_a\}}{C}, \quad (10)$$

$$C = \epsilon\tau, \quad (11)$$

$$D = (1 - \tau)[1 + (1 - \epsilon)\tau], \quad (12)$$

where T_a is the mean atmospheric temperature, T_s is the LST, $a = -67.355351$, and $b = 0.458606$.

3.3 Mapping UHI and Non-UHI Inside a City Area

UHI and non-UHI zones were demarcated using the following methods:^{18,23}

$$LST > \mu + 0.5 * \sigma, \quad (13)$$

$$0 < LST \leq \mu + 0.5 * \sigma, \quad (14)$$

where μ and σ are the mean and standard deviation values of LST for the whole area of the city.

4 Results and Discussion

4.1 Variation in the Distribution of NDVI, NDWI, NDBI, and NMDI

The descriptive statistics (Table 3) were presented the reliable nature of NDVI, NDWI, NDBI, and NMDI (Fig. 2) for the whole of Raipur City. The highest mean NDVI value (0.1468) was found in the monsoon season. Premonsoon season reflected the minimum value (−0.1466) of mean NDWI. The lowest mean value (−0.0569) of NDBI was observed in the postmonsoon season. The highest (−0.2743) mean NMDI was found in premonsoon season and the lowest (−0.2866) mean NMDI value was found in winter. In the winter season, all the four indices had the least value of standard deviation.

Table 3 Descriptive statistics of NDVI, NDWI, NDBI, and NMDI for the whole of Raipur City in four seasons.

Season	Min	Max	Mean	Standard deviation
NDVI values				
Premonsoon (mean)	−0.1082	0.4702	0.1428	0.0645
Monsoon (mean)	−0.1089	0.4664	0.1468	0.0635
Postmonsoon (mean)	−0.1025	0.4183	0.1392	0.0659
Winter (mean)	−0.1265	0.4284	0.0954	0.0561
NDWI values				
Premonsoon (mean)	−0.4112	0.1514	−0.1426	0.0576
Monsoon (mean)	−0.4102	0.1434	−0.1466	0.0564
Postmonsoon (mean)	−0.3596	0.1371	−0.1192	0.0602
Winter (mean)	−0.4006	0.1582	−0.0877	0.0398
NDBI values				
Premonsoon (mean)	−0.3195	0.1668	−0.0198	0.0474
Monsoon (mean)	−0.3219	0.2373	−0.0158	0.0477
Postmonsoon (mean)	−0.3153	0.1754	−0.0569	0.0426
Winter (mean)	−0.3508	0.1857	−0.0199	0.0374
NMDI values				
Premonsoon (mean)	−0.4635	0.0773	−0.2743	0.0518
Monsoon (mean)	−0.5483	0.0714	−0.2761	0.0511
Postmonsoon (mean)	−0.5361	0.0602	−0.2385	0.0499
Winter (mean)	−0.5946	0.0958	−0.2866	0.0398

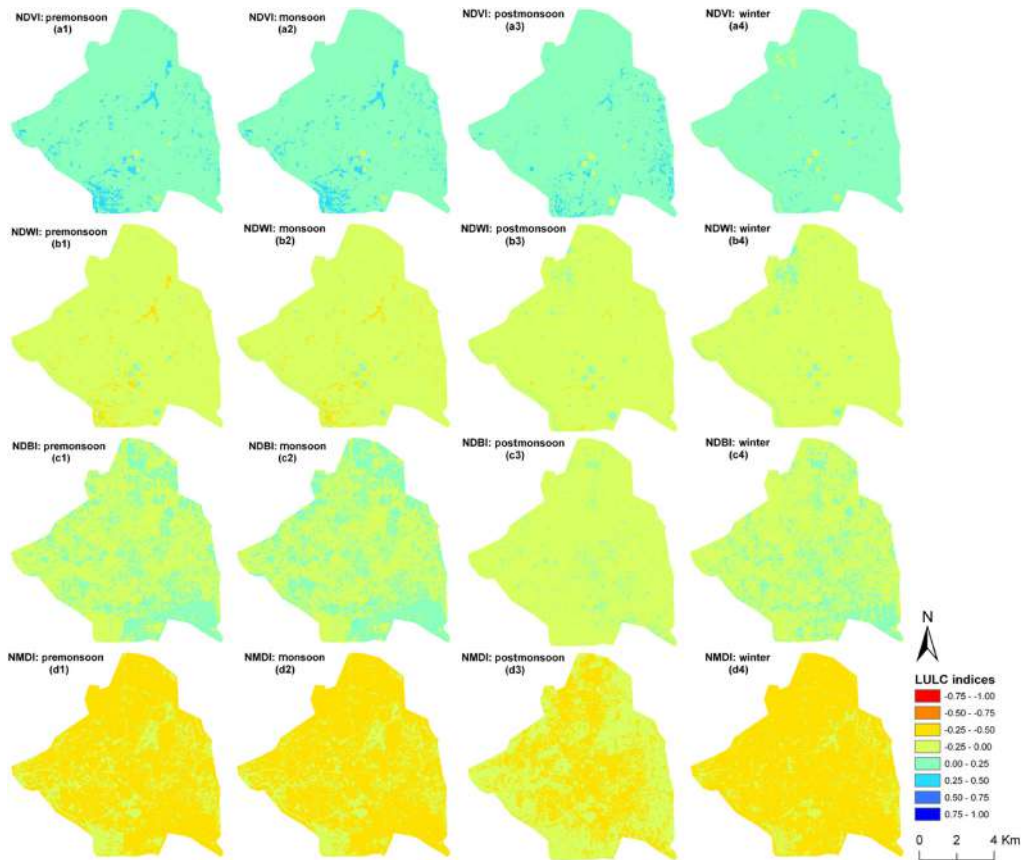


Fig. 2 Seasonal variations of NDVI, NDWI, NDBI, and NMDI values in the whole of Raipur City: (a) premonsoon, (b) monsoon, (c) postmonsoon, and (d) winter.

4.2 Variation of LST Distribution

The LST maps retrieved from satellite image were shown in Fig. 3. Seasonal variation in the LST distribution showed a specific thermal pattern. The mean LST values in the premonsoon, monsoon, postmonsoon, and winter seasons were 34.40°C, 31.70°C, 25.22°C, and 24.71°C, respectively. The ranges of temperature (maximum temperature–minimum temperature) were found as 12.71°C in premonsoon image, 10.20°C in monsoon image, 8.81°C in the postmonsoon image, and 10.03°C in the winter image, respectively. For UHI zones of the study area, the highest threshold LST (35.23°C) was observed in the premonsoon season. Postmonsoon season reflected the least standard deviation value (1.06°C) of LST (Table 4). Basically, this type of LST variation was noticed due to the change in vegetation abundance and soil moisture content. Monsoon and postmonsoon seasons were characterized by healthy vegetation and wet soil.

4.3 LST Validation with Respect to MODIS Satellite Sensor

A validation of retrieved LST using Landsat 8 data with *in situ* measurement or with any other satellite data is mandatory to conduct any kind of further analysis. Due to the unavailability of *in situ* measurement, Moderate Resolution Imaging Spectroradiometer (MODIS) satellite data were applied as a reference image for the validation of LST retrieved from Landsat 8 data. The MODIS LST daily product is derived from bands 31 and 32 by the emissivity of land cover types, atmospheric column water vapor, and lower boundary air surface temperature.^{63,64}

Landsat and MODIS sensors could not provide images of the same study area for any particular date. Thus the acquisition dates of MODIS data were either one day before or one day after the acquisition dates of Landsat 8 data. A total of eleven (three from the premonsoon season, two from the monsoon season, three from the postmonsoon season, and three from winter season) MOD11A1 data were taken for the validation of estimated LST using Landsat 8 data.

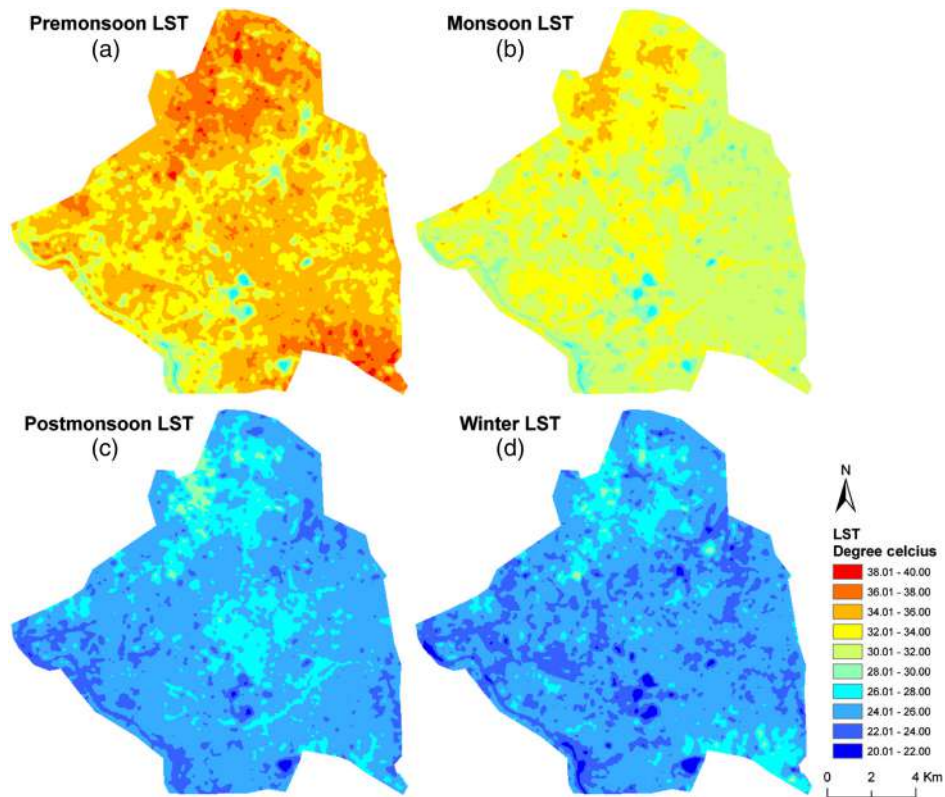


Fig. 3 Seasonal variations in LST maps of Raipur City: (a) premonsoon, (b) monsoon, (c) postmonsoon, and (d) winter.

Table 4 Seasonal variations in spatial distribution of LST (°C) for the whole of Raipur City.

Season	LST (minimum)	LST (maximum)	LST (mean)	LST (standard deviation)	Threshold LST for UHI
Premonsoon (mean)	26.97	39.68	34.40	1.65	35.23
Monsoon (mean)	26.43	36.63	31.70	1.16	32.28
Postmonsoon (mean)	21.53	30.34	25.22	1.06	25.75
Winter (mean)	20.12	30.15	24.71	1.15	25.29

No such atmospheric disturbances were noticed in the acquisition dates of the selected satellite images for both the sensors. For MOD11A1 and Landsat 8 data, the spatial resolution of retrieved LST was 1000 and 100 m, respectively. Therefore, before integrating the data, 1000-m pixel size was resampled into 100-m pixel size (Fig. 4). There was found a small difference between Landsat derived mean LST and the corresponding MODIS derived mean LST values due to (a) 30 min intervals between the Landsat 8 and MODIS sensors (b) water vapor content, and (c) scale effect in resampling method.⁶³ Figure 4 compared four Landsat 8 data derived LST images with the four corresponding MODIS LST images for four different seasons.

For the validation of the results, the pixel-wise regression analysis method was applied between Landsat 8 retrieved LST values and the corresponding MODIS retrieved LST values. Significant positive correlation coefficients (0.70 for the premonsoon, 0.75 for the monsoon, 0.69 for the postmonsoon, and 0.59 for winter) were found between Landsat 8 data derived LST and MODIS data derived LST (Table 5). Hence, it can be said that the results were reliable and consistent in spite of lacking some LST retrieval parameters.

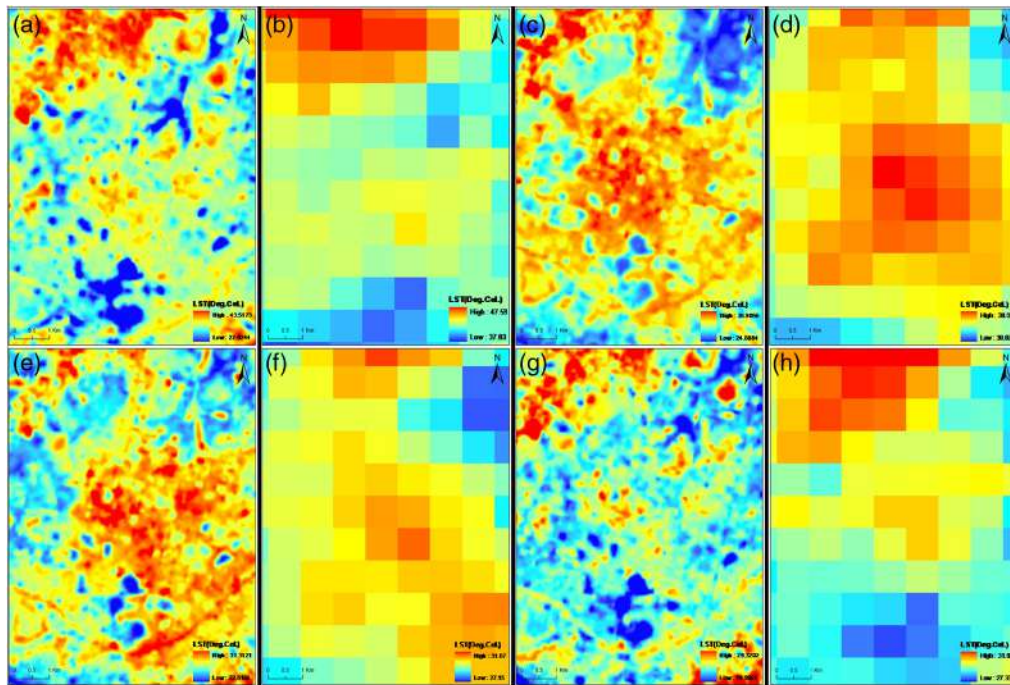


Fig. 4 Retrieved LST from Landsat 8 data and MODIS data: (a) 02-Apr-2014 (Landsat 8), (b) 03-Apr-2014 (MODIS), (c) 25-Sep-2014 (Landsat 8), (d) 24-Sep-2014 (MODIS), (e) 09-Nov-2013 (Landsat 8), (f) 08-Nov-2013 (MODIS), (g) 27-Dec-2013 (Landsat 8), and (h) 28-Dec-2013 (MODIS).

Table 5 Validation of LST retrieved from Landsat 8 data with MODIS data in different dates of acquisition.

Landsat 8 data	MODIS data	Correlation coefficient
09-Nov-2013	08-Nov-2013	0.69
25-Nov-2013	26-Nov-2013	0.66
11-Dec-2013	12-Dec-2013	0.61
27-Dec-2013	28-Dec-2013	0.68
28-Jan-2014	27-Jan-2014	0.45
17-Mar-2014	18-Mar-2014	0.74
02-Apr-2014	03-Apr-2014	0.68
20-May-2014	21-May-2014	0.68
05-Jun-2014	04-Jun-2014	0.73
25-Sep-2014	24-Sep-2014	0.77
12-Nov-2014	13-Nov-2014	0.71
Premonsoon (mean)		0.70
Monsoon (mean)		0.75
Postmonsoon (mean)		0.69
Winter (mean)		0.59

Table 6 Seasonal variations in LST (°C) of UHI, non-UHI, and common UHI in Raipur City.

Season	LST (minimum)			LST (maximum)			LST (mean)			LST (standard deviation)		
	UHI	Non-UHI	Common UHI	UHI	Non-UHI	Common UHI	UHI	Non-UHI	Common UHI	UHI	Non-UHI	Common UHI
Premonsoon (mean)	35.23	26.97	35.23	39.68	35.23	39.68	36.23	33.69	36.51	0.78	1.32	0.78
Monsoon (mean)	32.28	26.43	32.28	36.63	32.28	36.63	33.07	31.20	33.57	0.76	0.83	0.81
Postmonsoon (mean)	25.75	21.53	25.75	30.34	25.75	30.34	26.49	24.73	26.99	0.71	0.70	0.79
Winter (mean)	25.29	20.12	25.29	30.15	25.29	30.15	26.17	24.21	26.45	0.76	0.78	0.78

4.4 UHI, Non-UHI, and Common UHI of the Study Area

The UHI intensity (difference between the mean LST of UHI and the mean LST of non-UHI) of the study area was determined in Table 6. In premonsoon and winter seasons, the UHI zones were mainly generated in the north, west, and south-east periphery (Fig. 5). But in monsoon and postmonsoon seasons, the northern and central parts (the main built-up areas and bare lands of the city) were considered as the UHI zones. The UHI intensity for the whole of Raipur City was 2.54°C, 1.87°C, 1.76°C, and 1.96°C in the premonsoon, monsoon, postmonsoon, and winter seasons, respectively. The mean LST values of the common UHI of the city in all four seasons

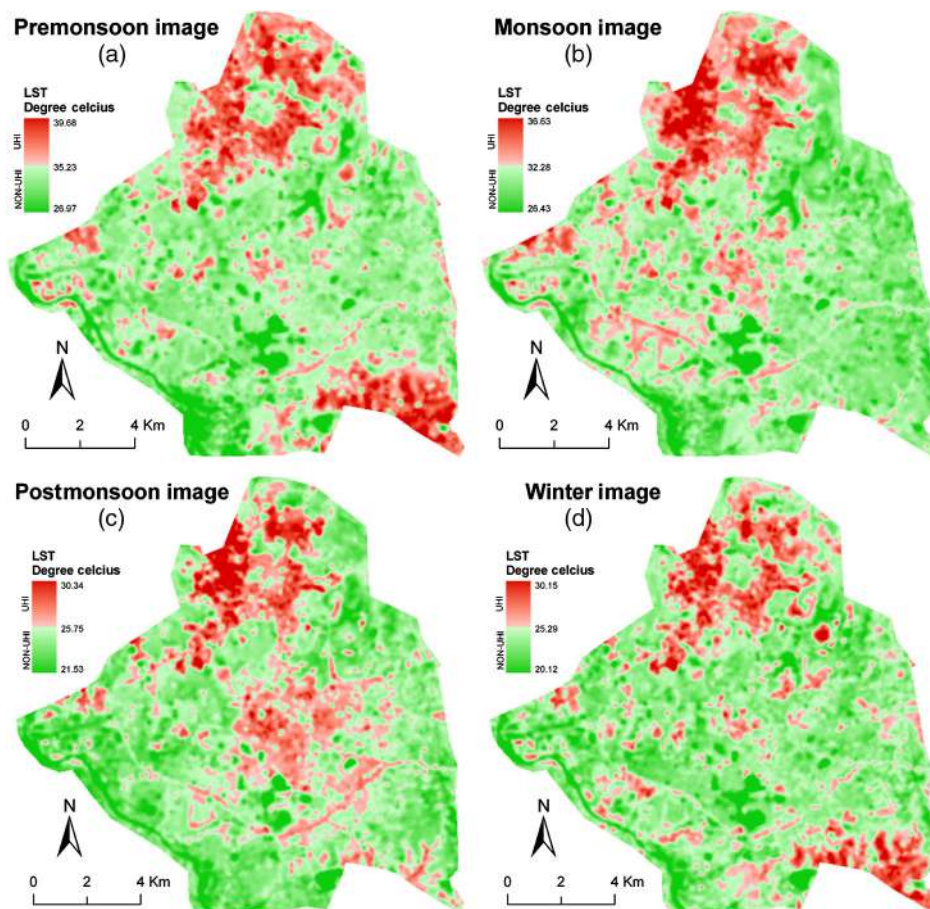


Fig. 5 Seasonal variations in UHI and non-UHI of Raipur City: (a) premonsoon, (b) monsoon, (c) postmonsoon, and (d) winter.

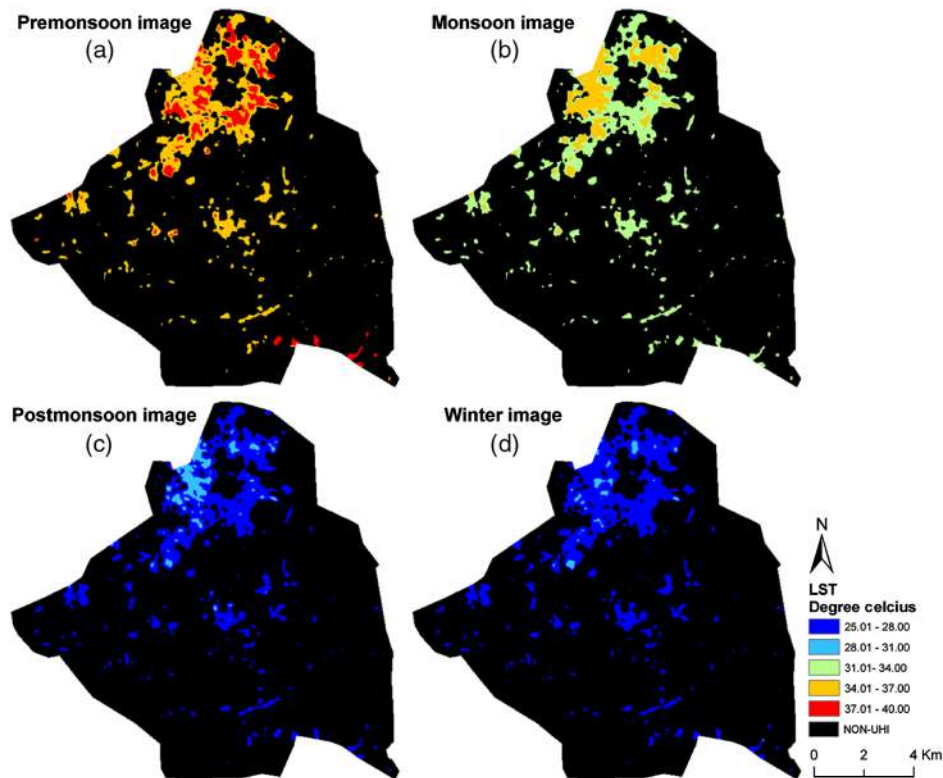


Fig. 6 Seasonal variations in common UHI of Raipur City: (a) premonsoon, (b) monsoon, (c) postmonsoon, and (d) winter.

were ranged between 26.45°C (winter image) and 36.51°C (premonsoon or summer image). Regardless of any particular season, the common UHI zones were developed mainly in the northwest portion (bare lands and built-up areas) of the city (Fig. 6).

4.5 Relationship of LST with NDVI, NDWI, NDBI, and NMDI for the Whole Area, UHI, non-UHI, and Common UHI of Raipur City

Generally, LST built negative relationships with NDVI and NMDI, whereas it built positive relationships with NDWI and NDBI. This particular pattern was seen in the whole of Raipur City, irrespective of dates (Table 7). NDBI and NMDI equally built strong regression with LST for four seasons. Their relationships became stronger in the premonsoon, monsoon, and postmonsoon seasons compared to winter. NDVI and NDWI showed weak relationships with LST compared to NDBI and NMDI. NDVI presented a slightly better relationship than NDWI. Winter season was the least reliable season for the relationships between LST and the four LULC indices. LST-NDWI relationship remained almost neutral in winter. This is partially due to the presence of high amount of dust particles in the air in winter.

But these relationships tend to be changed within the UHI of the city where NDVI and NDWI reflected a stronger regression with LST for all the four seasons (Table 7). Again, the scenario became different within the non-UHI portions of the city where NDBI and NMDI presented a stronger regression with LST compare to the other two spectral indices. In the common UHI region, NDVI and NDWI had a much better regression with LST, but these relationships became gradually weak with the increase of the heterogeneous surface features. Monsoon and postmonsoon images revealed a better regression of LST with NDVI and NDWI due to the higher percentage of water and vegetation.

In the UHI and common UHI, high LST values were found in such areas where NDVI values were low but NDWI values were high. NDWI showed the strongest positive regression with LST, whereas NDVI showed the strongest negative regression. The monsoon and postmonsoon season revealed the most consistent relationship. In the non-UHI, the high LST values were

Table 7 Correlation coefficients for LST-NDVI, LST-NDWI, LST-NDBI, and LST-NMDI relationships.

Season	LST-NDVI	LST-NDWI	LST-NDBI	LST-NMDI
(Whole of Raipur City)				
Premonsoon (mean)	-0.4235	0.2937	0.6984	-0.6988
Monsoon (mean)	-0.4978	0.4123	0.4528	-0.5291
Postmonsoon (mean)	-0.5124	0.4272	0.6239	-0.6647
Winter (mean)	-0.1748	0.0414	0.5676	-0.5509
(UHI of Raipur City)				
Premonsoon (mean)	-0.3298	0.2609	0.2883	-0.1622
Monsoon (mean)	-0.4998	0.5755	-0.0850	-0.0876
Postmonsoon (mean)	-0.4866	0.5144	0.0905	-0.2367
Winter (mean)	-0.3104	0.2572	0.2213	-0.3657
(Non-UHI of Raipur City)				
Premonsoon (mean)	-0.2834	0.1234	0.6877	-0.6553
Monsoon (mean)	-0.2608	0.0859	0.5437	-0.5509
Postmonsoon (mean)	-0.2032	0.0822	0.5827	-0.5637
Winter (mean)	0.0141	-0.1633	0.5497	-0.4782
(Common UHI of Raipur City)				
Premonsoon (mean)	-0.3591	0.3267	0.1759	-0.2477
Monsoon (mean)	-0.5170	0.5908	-0.1992	0.0183
Postmonsoon (mean)	-0.5607	0.5452	0.1579	-0.3367
Winter (mean)	-0.3314	0.2726	0.0696	-0.1892

corresponding to high NDBI and low NMDI values. Due to the presence of more moisture content in soil and air, the relationships between LST and these spectral indices became more consistent in the monsoon and postmonsoon images. NDBI showed the strongest positive regression with LST, whereas NMDI showed the strongest negative regression. The premonsoon season reflected the most significant relationship.

The best regression between LST and the four spectral indices was found for the whole of Raipur City, irrespective of any date. This relationship became weaker with the increase in heterogeneity in an urban landscape. Common UHI of all seasons simply indicated the built-up area and semibare lands, which were more heterogeneous. Thus the least regression was found in the common UHI of the city area. UHI and non-UHI of the city reflected the moderate range of the correlation coefficient values.

5 Conclusion

In this paper, eleven Landsat 8 data of four different seasons in a single-year span were selected for analyzing the effect of UHI intensity in Raipur City of India and to interpret the seasonal variations for the relationships of NDVI, NDWI, NDBI, and NMDI with LST. The above relationships were examined for the whole area, UHI, non-UHI, and common UHI of the Raipur City. UHIs were identified through the spatial distribution of LST, which mainly existed in the northern and southern parts of the city. Generally, high LST values were generated in the bare

land and built-up area. LST level was reduced significantly in the vegetal covered areas and water bodies.

Moreover, the relationships of LST to NDVI, NDWI, NDBI, and NMDI were analyzed using linear regression per-pixel level. In whole Raipur City, LST showed a strong positive regression with NDBI and a moderate to strong negative regression with NMDI, irrespective of any season. Inside the UHI, NDVI and NDWI showed a stronger regression (NDVI-negative and NDWI-positive) with LST in comparison with the other indices. Conversely, inside the non-UHI zone, NDBI and NMDI presented a stronger regression (NDBI-positive and NMDI-negative). Again, NDVI-LST and NDWI-LST regression became stronger within the common UHI in all seasons.

Another objective of the research was to estimate the variations in the regression analysis for the satellite images of four different seasons. Monsoon and postmonsoon seasons were more prominent in showing the regression between LST and spectral indices due to the higher percentage of healthy green vegetation and soil moisture. The premonsoon season was less dominant compared to the monsoon and postmonsoon seasons while this regression became weakest in the winter image.

Acknowledgments

The authors were indebted to the United States Geological Survey.³⁶ The authors also thank the anonymous reviewers whose feedback improved this manuscript significantly.

References

1. J. Arnfield, "Two decades of urban climate research: a review of turbulence, exchanges of energy and water, and the urban heat island," *Int. J. Climatol.* **23**(1), 1–26 (2003).
2. P. A. Mirzaei, "Recent challenges in modeling of urban heat island," *Sustain. Cities Soc.* **19**, 200–206 (2015).
3. A. M. Rizwan et al., "A review on the generation, determination and mitigation of the urban heat island," *J. Environ. Sci.* **20**(1), 120–128 (2008).
4. C. Rinner and M. Hussain, "Toronto's urban heat island exploring the relationship between land use and surface temperature," *Remote Sens.* **3**, 1251–1265 (2011).
5. M. Zhao et al., "Influence of urban expansion on the urban heat island effect in Shanghai," *Int. J. Geogr. Inf. Sci.* **30**(12), 2421–2441 (2016).
6. B. Chun and J.-M. Guldmann, "Spatial statistical analysis and simulation of the urban heat island in high-density central cities," *Landsc. Urban Plann.* **125**, 76–88 (2014).
7. Z. Dai et al., "Spatial regression models of park and land-use impacts on the urban heat island in central Beijing," *Sci. Total Environ.* **626**, 1136–1147 (2018).
8. J.-P. Kim and J.-M. Guldmann, "Land-use planning and the urban heat island," *Environ. Plann. B* **41**, 1077–1099 (2014).
9. H. Zhang et al., "Analysis of land use/ land cover change, population shift, and their effects on spatiotemporal patterns of urban heat islands in metropolitan Shanghai, China," *Appl. Geogr.* **44**, 121–133 (2013).
10. W. Q. Zhou et al., "Does spatial configuration matter? Understanding the effects of land cover pattern on land surface temperature in urban landscapes," *Landsc. Urban Plann.* **102**(1), 54–63 (2011).
11. P. Coseo and L. Larsen, "How factors of land use/land cover, building configuration, and adjacent heat sources and sinks explain Urban Heat Islands in Chicago," *Landsc. Urban Plann.* **125**, 117–129 (2014).
12. J. Li et al., "Impacts of landscape structure on surface urban heat islands: a case study of Shanghai, China," *Remote Sens. Environ.* **115**, 3249–3263 (2011).
13. J. Peng et al., "Urban thermal environment dynamics and associated landscape pattern factors: a case study in the Beijing metropolitan region," *Remote Sens. Environ.* **173**, 145–155 (2016).
14. R. Amiri et al., "Spatial-temporal dynamics of land surface temperature in relation to fractional vegetation cover and land use/ cover in the Tabriz urban area, Iran," *Remote Sens. Environ.* **113**, 2606–2617 (2009).

15. J. Song et al., "The relationships between landscape compositions and land surface temperature: quantifying their resolution sensitivity with spatial regression models," *Landsc. Urban Plann.* **123**, 145–157 (2014).
16. W. Kuang et al., "What are hot and what are not in an urban landscape: quantifying and explaining the land surface temperature pattern in Beijing, China," *Landsc. Ecol.* **30**, 357–373 (2015).
17. K. Deilami and M. Kamruzzaman, "Modelling the urban heat island effect of smart growth policy scenarios in Brisbane," *Land Use Policy* **64**, 38–55 (2017).
18. S. Guha et al., "Dynamic analysis and ecological evaluation of urban heat islands in Raipur City, India," *J. Appl. Remote Sens.* **11**(3), 036020 (2017).
19. Q. Nie et al., "Spatiotemporal impact of urban impervious surface on land surface temperature in Shanghai, China," *Can. J. Remote Sens.* **42**(6), 680–689 (2016).
20. G. L. Feyisa et al., "Locally optimized separability enhancement indices for urban land cover mapping: exploring thermal environmental consequences of rapid urbanization in Addis Ababa, Ethiopia," *Remote Sens. Environ.* **175**, 14–31. (2016).
21. J. M. R. Lopez et al., "Frontiers of urbanization: identifying and explaining urbanization hot spots in the south of Mexico City using human and remote sensing," *Appl. Geogr.* **79**, 1–10 (2017).
22. H. Pearsall, "Staying cool in the compact city: vacant land and urban heating in Philadelphia, Pennsylvania," *Appl. Geogr.* **79**, 84–92 (2017).
23. S. Guha et al., "Analytical study of land surface temperature with NDVI and NDBI using Landsat 8 OLI and TIRS data in Florence and Naples city, Italy," *Eur. J. Remote Sens.* **51**(1), 667–678 (2018).
24. Y. Y. Cui and B. de Foy, "Seasonal variations of the urban heat island at the surface and the near-surface and reductions due to urban vegetation in Mexico City," *J. Appl. Meteorol. Clim.* **51**, 855–868 (2012).
25. W. Zhou et al., "Relationships between land cover and the surface urban heat island: seasonal variability and effects of spatial and thematic resolution of land cover data on predicting land surface temperatures," *Landsc. Ecol.* **29**, 153–167 (2014).
26. S. Haashemi et al., "Seasonal variations of the surface urban heat island in a semi-arid city," *Remote Sens.* **8**, 352 (2016).
27. B. Chun and J. M. Guldmann, "Impact of greening on the urban heat island: seasonal variations and mitigation strategies," *Comput. Environ. Urban Syst.* **71**, 165–176 (2018).
28. J. Peng et al., "Seasonal contrast of the dominant factors for spatial distribution of land surface temperature in urban areas," *Remote Sens. Environ.* **215**, 255–267 (2018).
29. A. Mathew et al., "Investigating spatial and seasonal variations of urban heat island effect over Jaipur city and its relationship with vegetation, urbanization and elevation parameters," *Sustain. Cities Soc.* **35**, 157–177 (2017).
30. J. Quan et al., "Time series decomposition of remotely sensed land surface temperature and investigation of trends and seasonal variations in surface urban heat islands," *J. Geophys. Res-Atmos.* **121**(6), 2638–2657 (2016).
31. M. Khorchani et al., "Trends in LST over the peninsular Spain as derived from the AVHRR imagery data," *Global. Planet. Change* **166**, 75–93 (2018).
32. M. Khorchani et al., "Average annual and seasonal land surface temperature, Spanish Peninsular," *J. Maps.* **14**(2), 465–475 (2018).
33. R. Yao et al., "Interannual variations in surface urban heat island intensity and associated drivers in China," *J. Environ. Manage.* **222**, 86–94 (2018).
34. J. Lai et al., "Does quality control matter? Surface urban heat island intensity variations estimated by satellite-derived land surface temperature products," *ISPRS J. Photogramm. Remote Sens.* **139**, 212–227 (2018).
35. R. Sun et al., "A landscape connectivity model to quantify contributions of heat sources and sinks in urban regions," *Landsc. Urban Plann.* **178**, 43–50 (2018).
36. S. Khandelwal et al., "Assessment of land surface temperature variation due to change in elevation of area surrounding Jaipur, India," *Egypt. J. Remote Sens. Space Sci.* **21**(1), 87–94 (2018).

37. Q. Weng, "A remote sensing-GIS evaluation of urban expansion and its impact on surface temperature in Zhujiang Delta, China," *Int. J. Remote Sens.* **22**(10), 1999–2014 (2001).
38. Q. Weng and S. Yang, "Managing the adverse thermal effects of urban development in a densely populated Chinese city," *J. Environ. Manage.* **70**(2), 145–156 (2004).
39. Z. Zhang et al., "Towards an operational method for land surface temperature retrieval from Landsat 8 data," *Remote Sens. Lett.* **7**(3), 279–288 (2016).
40. Z. Qin et al., "A mono-window algorithm for retrieving land surface temperature from Landsat TM data and its application to the Israel–Egypt border region," *Int. J. Remote Sens.* **22**(18), 3719–3746 (2001).
41. Z.-L. Li et al., "Satellite-derived land surface temperature: current status and perspectives," *Remote Sens. Environ.* **131**, 14–37 (2013).
42. J. C. Munoz and J. A. Sobrino, "A generalized single channel method for retrieving land surface temperature from remote sensing data," *J. Geophys. Res.* **108**(D22), 4688 (2003).
43. J. C. Munoz et al., "Revision of the single-channel algorithm for land surface temperature retrieval from Landsat thermal-infrared data," *IEEE Trans. Geosci. Remote Sens.* **47**(1), 339–349 (2009).
44. J. C. Munoz and J. A. Sobrino, "A single-channel algorithm for land-surface temperature retrieval from ASTER data," *IEEE Geosci. Remote Sens. Lett.* **7**(1), 176–179 (2010).
45. X. Yu et al., "Land surface temperature retrieval from Landsat 8 TIRS—comparison between radiative transfer equation-based method, split window algorithm and single channel method," *Remote Sens.* **6**, 9829–9852 (2014).
46. O. Rozenstein et al., "Derivation of Land Surface Temperature for Landsat-8 TIRS Using a Split Window Algorithm," *Sensors* **14**(4), 5768–5780 (2014).
47. Z. Qin et al., "Derivation of split window algorithm and its sensitivity analysis for retrieving land surface temperature from NOAA-advanced very high resolution radiometer data," *J. Geophys. Res.* **106**(D19), 22655–22670 (2001).
48. A. Bendib et al., "Contribution of Landsat 8 data for the estimation of land surface temperature in Batna city, Eastern Algeria," *Geocarto Int.* **32**(5), 503–513 (2016).
49. Staff Reporter, RAIPUR, "Raipur beats Indore, Bhopal in ease of living index," <https://www.dailypioneer.com/2018/state-editions/raipur-beats-indore-bhopal-in-ease-of-living-index.html> (accessed 14 August 2018).
50. EarthExplorer, "Home-United States Geological Survey," <http://earthexplorer.USGS.gov>.
51. T. S. Purevdorj et al., "Relationships between percent vegetation cover and vegetation indices," *Int. J. Remote Sens.* **19** (18), 3519–3535 (1998).
52. C. Gao, "NDWI—a normalized difference water index for remote sensing of vegetation liquid water from space," *Remote Sens. Environ.* **58**(3), 257–266 (1996).
53. Y. Zha et al., "Use of normalized difference built-up index in automatically mapping urban areas from TM imagery," *Int. J. Remote Sens.* **24**(3), 583–594 (2003).
54. L. Wang and J. J. Qu, "NMDI: a normalized multi-band drought index for monitoring soil-land vegetation moisture with satellite remote sensing," *Geophys. Res. Lett.* **34**(20), L20405 (2007).
55. X. C. Chen et al., "Remote sensing image-based analysis of the relationship between urban heat island and land use/cover changes," *Remote Sens. Environ.* **104**(2), 133–146 (2006).
56. B. L. Markham and J. K. Barker, "Spectral characteristics of the LANDSAT thematic mapper sensors," *Int. J. Remote Sens.* **6**(5), 697–716 (1985).
57. G. E. Wukelic et al., "Radiometric calibration of Landsat thematic mapper thermal band," *Remote Sens. Environ.* **28**, 339–347 (1989).
58. J. A. Sobrino et al., "Land surface temperature retrieval from Landsat TM 5," *Remote Sens. Environ.* **90**, 434–440 (2004).
59. J. A. Sobrino et al., "A comparative study of land surface emissivity retrieval from NOAA data," *Remote Sens. Environ.* **75**(2), 256–266 (2001).
60. T. N. Carlson and D. A. Ripley, "On the relation between NDVI, fractional vegetation cover, and leaf area index," *Remote Sens. Environ.* **62**, 241–252 (1997).
61. J. Li, "Estimating land surface temperature from Landsat-5 TM," *Remote Sens. Technol. Appl.* **21**(4), 322–326 (2006).

62. Q. Sun et al., "An ERDAS image processing method for retrieving LST and describing urban heat evolution: a case study in the Pearl River Delta Region in South China," *Environ. Earth Sci.* **59**, 1047–1055 (2010).
63. Z. Wan and Z. L. Li, "MODIS land surface temperature and emissivity," in *Land Remote Sensing and Global Environmental Change NASA's Earth Observing System and the Science of ASTER and MODIS*, B. Ramachandran, C. O. Justice, and M. J. Abrams, Eds., Springer-Verlag, Heidelberg, New York, p. 567 (2011).
64. L. Yang et al., "Land surface temperature retrieval for arid regions based on Landsat-8 TIRS data: a case study in Shihezi, Northwest China," *J. Arid Land.* **6**, 704–716 (2014).

Subhanil Guha received his MSc degree in geography from the University of Calcutta, India, and his postgraduate diploma degree in geoinformatics from the International Institute for Geo-Information Science and Earth Observation (ITC), Enschede, The Netherlands, and IIRS, Dehradun, India. He is pursuing his PhD in the Department of Applied Geology, National Institute of Technology (NIT), Raipur, India. His research interests include applications of thermal infrared remote sensing in geography, environment, and geology.

Himanshu Govil received his MSc and PhD degrees in geology from Aligarh Muslim University, Aligarh, India, and his postgraduate diploma degree in geoinformatics from the ITC, Enschede, The Netherlands, and IIRS, Dehradun, India. Currently, he is an assistant professor in the Department of Applied Geology, NIT, Raipur, India. His research interests include application of hyperspectral remote sensing in mineral exploration and geological mapping.

Prabhat Diwan received his MTech and PhD degrees in geology from Dr. Harisingh Gour University, Sagar, India. Currently, he is an associate professor and a head of the Department of Applied Geology, NIT, Raipur, India. His research interests include structural geology, economic geology, and remote sensing.



Source details

[Feedback >](#) [Compare sources >](#)

Journal of Applied Remote Sensing

Scopus coverage years: from 2007 to 2023

Publisher: SPIE

ISSN: 1931-3195

Subject area: Earth and Planetary Sciences: General Earth and Planetary Sciences

Source type: Journal

[View all documents >](#)

[Set document alert](#)

[Save to source list](#)

CiteScore 2022

3.4



SJR 2022

0.388



SNIP 2022

0.564



[CiteScore](#) [CiteScore rank & trend](#) [Scopus content coverage](#)



Improved CiteScore methodology

CiteScore 2022 counts the citations received in 2019-2022 to articles, reviews, conference papers, book chapters and data papers published in 2019-2022, and divides this by the number of publications published in 2019-2022. [Learn more >](#)



A GREEN APPROACH FOR THE SYNTHESIS OF ANTIMICROBIAL BIO-SURFACTANT SILVER NANOPARTICLES BY USING A FERN

A. CHATTERJEE^a, S. KHATUA^{c,d}, K. ACHARYA^{c,e}, J. SARKAR^{b,c,*}

^aDepartment of Botany, University of Kalyani, Kalyani, Nadia, West Bengal, India, Pin—741235.

^bDepartment of Botany, Dinabandhu Andrews College, Garia, Kolkata, West Bengal, India, Pin—700084.

^cMolecular and Applied Mycology and Plant Pathology Laboratory, Centre of Advanced Study, Department of Botany, University of Calcutta, Kolkata, West Bengal, India, Pin—700019.

^dDepartment of Botany, Krishnagar Govt. College, Krishnagar, Nadia, West Bengal, India, Pin-741101.

^eCenter for Research in Nanoscience & Nanotechnology, Technology Campus, University of Calcutta, Kolkata, West Bengal, India, Pin—700098.

Advancement of an environment-friendly, trustworthy, and speedy route for the generation of Ag-NP using natural system is an essential urge in nanotechnology. This study accounts for the efficacy of liquid extract of *Adiantum lunulatum* Burm. f. for the synthesis of Ag-NP. This is the first attempt of introducing the biosynthesis mechanism of Ag-NP using the extract of this plant along with the antimicrobial evaluation of the Ag-NP. All the detailed features of the fabricated nanoparticles were well documented by UV-Vis, DLS, Zeta Potential, FTIR, EDX, XRD, and TEM. The mean diameter of Ag-NP was about 28±2 nm. Antibacterial proficiency of Ag-NP was also determined against various gram natured pathogenic bacteria.

(Received April 4, 2019; Accepted June 14, 2019)

Keywords: *Adiantum lunulatum*, Biosynthesis, Silver Nanoparticles, Antimicrobial

1. Introduction

Nanotechnology is an imperative tool for the expansion of science in the present era. It is the competence to produce and design structure at nano-metric range [1] and a stimulus for the expansion of several other fields like physiochemical [2], optical [3], electrical [4], sensing [5], catalysis [6], photochemical [7], etc. due their exclusive feature of sizeable surface area to volume ratio.

Silver is one of the safe inorganic elements which is projected as “next-gen” antimicrobial agent [8]. As consequences metallic silver made an incredible response in the form of Ag-NP. This has unfolded novel strategies to use metallic silver. Ag-NP has extensive angles of application concerning bio-labeling [9], [10], antibiotics [11], antibacterial [12], [13], antifouling & anti-parasitic [14] properties, drug delivery mechanisms [15] etc. They are also highly effectual in triggering of inflammation & apoptosis than bulk silver material. It also acts as a catalyst for the reduction of dye like methylene blue [16], enhances radiation therapy [17], used in ESR dosimetry [18], glyconano sensors for diseases diagnosis [19]. But still, there are many lacunas regarding the appliance of Ag-NP on the evaluation of the risk of human health and environment and human health [20].

Various protocols are known to date for developing metallic nanoparticles. They are mainly parted into two approaches- (i) top-down and (ii) bottom up [21]. The former one defines to be a reduction in the size of bulk material by means of mechanical methods, and later one is a

*Corresponding author: jsarkar80@gmail.com

process of assembling smaller particle into a larger entity. Production of nanoparticles by chemical means is one such example [22]. However, the nanoparticles synthesized via chemical means are hazardous as for the utilization of various toxic and corrosive chemicals during the production process [23]. Moreover, the process is not so cost-effective [11]. Therefore, an urge to develop an eco-friendly and a non-hazardous route to manufacture nanoparticles which can meet both cost & energy demands [24] has become an urgent need.

Consequently, the biological performances are considered as an alternative and advancement over former approaches as it involves natural compounds such as sugars, biodegradable polymers, plants extracts [3], [25]–[28]. Metallic nanoparticles manufactured by fungi [11], [29], [30], bacteria [31], algae [27] and plants [26], [32] are well known. Furthermore, the rate of plant synthesized nanoparticles is much faster [26], [32], stable [24] and are highly mono-dispersive [33] in relation to supplementary biological methods.

Among cryptograms, the use of algae [24] & bryophytes [34] to fabricate nanoparticles are quite popular. Unlike that of pteridophytes (fern & fern allies) for forging of nanoparticles are less investigated. Till date only few of the pteridophytes like *Adiantum capillus-veneris* [35], *Adiantum caudatum* [36], *Adiantum philippense* [37], [38], *Azolla microphylla* [39], [40], *Pteris tripartita* [41], *Asplenium scolopendrium* [42], *Actinopteris radiata* [43], *Christella dentata*, *Cyclosorus interruptus*, *Nephrolepis cordifolia* [44] have been used so far.

Adiantum lunulatum Burm. f. is recognized for its antioxidant [45], antimicrobial [46] & medicinal properties like anti-hyperglycemic action [47] against influenza and tuberculosis [48]. The plant is enriched with carbohydrates, terpenoids, phenols, and flavonoids [45], [49], [50]. These versatile features of this plant made it our choice in the first place to fulfill our goals. Thus, this current study was designed with an intention of synthesis of Ag-NP by a greener route by using the fern *Adiantum lunulatum* and assessment of the antibacterial nature of these Ag-NP against various pathogenic microorganisms.

2. Experimental

2.1. Chemicals

The chemical silver nitrate (AgNO_3) was procured from Sigma, St. Louis, MO, USA.

2.2. Plant material

The plant was collected from different areas of West Bengal like Kalyani (22.9751° N, 88.4345° E) of the district Nadia, West Bengal, Kalingpong district (27.066668° N, 88.466667° E) and Rajpur-Sonarpur Municipality area (22.4491° N, 88.3915° E) of the district South 24 Parganas, West Bengal, India. The respective plant specimen was self-identified and binomially jointly by Pteridology & Paleobotany Lab, Department of Botany, University of Kalyani, Kalyani, Nadia, West Bengal, India, Pin-741235 and Department of Botany, Dinabandhu Andrews College, Garia, Kolkata, West Bengal, India, Pin-700084. Voucher specimens were made from the collected specimen and further deposited both at the Herbarium of the Botany Department, University of Kalyani as well as Herbarium of the Botany Department, Dinabandhu Andrews College.

2.3. Preparation of plant extract

At first, the whole plant was washed entirely by tap water and distilled water respectively. The superficial water was dried from the plant body by proper desiccation. Then, 5 gm of that desiccated plant material was crushed in mortar & pestle into a paste. After that hundred ml of distilled water was mixed to that paste [37]. Filtration of the crude solution was done thrice by Whatman filter paper no.1. Finally, the filtrate was collected all together for future reference.

2.4. Synthesis of Ag-NP

Hundred ml of 1mM AgNO_3 solution was mixed to the liquid extract (1:5v/v) and stirred constantly for 1 hour [11], [13]. Both, positive (plant extract) and negative control (AgNO_3 solution only) were conserved under similar environments.

Centrifugation was followed to separate out the Ag-NP (at 12000 g for 15 min), and the settled nanoparticles were washed (three times) in deionized water. The purified Ag-NP were re-suspended in deionized water and ultra-sonicated by Piezo-u-sonic ultrasonic cleaner (Pus-60w) and kept at normal room temperature (37°C) [30].

2.5. UV–Vis absorption spectroscopy analysis

Adiantum lunulatum mediated biosynthesized nanoparticles had been observed under Hitachi 330 Spectrophotometer with plasmon peaks at varied regions of the spectral range 300 to 700 nm which resembled different signature marks for the production of different nanoparticles respectively [51], [52]. Deionized water was selected for reference.

2.6. Particle size measurement by DLS experiment

Particle size was found out by using Zen 1600 Malvern nanosize particle analyzer ranging between 0.6 nm and 6.0 μm under such conditions particle having an absorption coefficient of 0.01, particle refractive index 1.590, water refractive index 1.33, viscosity –cP, Temperature-25°C and a broad calculation model for irregular particles. About 10–15 measurement cycles of 10 s each was taken in account. The acquired data were averaged by the preloaded software (DTS, version 5.00 from Malvern) of the respective instrument [53].

2.7. Zeta potential measurement

Using Beckman Coulter Delsa™ Nano Particle Analyser (USA) zeta potential (Charge distribution) of the nanoparticles was investigated by revealing the solution with He–Ne laser in a sample cell (658 nm). Using Phase Analysis Light Scattering mode measurements were taken with an Ag electrode [54].

2.8. EDS analysis

A small amount of sample was taken in glass slide creating a reedy layer of the sample. An additional sample was blotted off and then the sample was permitted to dry for overnight [55]. Hitachi S 3400N instrument was the automatic choice for us to carry out the analysis of the samples. The spectra were recorded for future analysis.

2.9. XRD- measurement

The crystallinity of forged Ag-NP was confirmed and determined by XRD analysis. The XRD sample was all set on a microscopic glass slide by depositing the centrifuged sample and thereafter dried at 45°C in a vacuum drying oven overnight. The vacuum dried Ag-NP were then used for powder X-ray diffraction analysis.

The diffractogram was documented from PANalytical, XPERTPRO diffractometer using Cuk (Cu K α radiation, λ 1.54443) as X-ray source running at 45 kV and 30 mA [56]. The diffracted intensities were noted from 35° to 99° 2 θ angles [53], [57], [58].

2.10. FTIR analysis

The vacuum dried inorganic metal nanoparticles were mixed up individually with KBr, alkali halide at a ratio of 1:100 (weight/weight). The two materials were then grounded to a fine powder in a mortar and pestle separately. Then the mixture was converted into a pellet press consisting of two pistons in a smooth cylindrical chamber. The pressure of up to 25000 psi was then applied for different measures of time in a vacuum. After that, the pistons were removed and the clear pellet was placed in a holder of the spectrophotometer. Since the KBr did not absorb infrared radiation in the region 4,000 and 400 cm^{-1} a complete spectrum of the solid was obtained [59]. The spectra were viewed by Shimadzu 8400S FTIR spectrophotometer. The spectral domain was set down in between four thousand and four hundred cm^{-1} [56].

2.11. TEM inspection of nanoparticles

Morphological and topographical characterization of the nanoparticles had been well established by the TEM studies [21]. On a carbon-coated copper grid thin films of the synthesized Ag-NP were prepared (30 μm \times 30 μm mesh size) and a droplet of the Ag-NP suspension was

spotted on the grid. With the help of blotting paper, the excess sample was blotted off and then it was kept for drying off under a mercury lamp for five minutes. The synthesized particles were examined and visualized by TEM using a Tecnai G2 spirit Biotwin instrument (FP 5018/40), operating at around 80 kV accelerating voltage [60].

2.12. Estimation of antibacterial potentiality

Bacillus subtilis MTCC Code 736, *Listeria monocytogenes* MTCC Code 657, *Staphylococcus aureus* MTCC Code 96, *Escherichia coli* MTCC Code 68, *Klebsiella pneumoniae* MTCC Code 109 and *Salmonella typhimurium* MTCC Code 98 were obtained from MTCC, Institute of Microbial Technology, Chandigarh, India. Antibacterial nature was estimated by determining minimum inhibitory concentration (MIC) values according to the microdilution method [61], [62]. The six investigating bacteria were freshly cultured and 1×10^5 CFU/ml concentrated dilutions were constructed separately. Reactions were performed in ninety-six well plate consisting of 200 μ l of NB, 20 μ l of inoculum and different dilutions of polymers. Following incubation for one day at 37°C, 40 μ l of INT dye (0.2 milligrams/milliliter) was mixed and incubated for the next round of thirty min. The concentration that inhibited 50% progression of bacteria growth as compared with positive control was calculated as MIC value. Streptomycin was cast-off as a standard drug.

3. Results and discussion

3.1. Characterization and identification of the plant specimen

The plant is rhizomatous, sub-erect to erect in posture, Entire body appears to be shiny and glabrous. Plant body ranges between 9–18 inches and are non-articulate (Fig. 1A). The mature stem appears to be brownish to dark in colour. Lamina is simply pinnate, lanceolate. Pinnae is finely leathery which is deep green or pale in colour, glabrous above and below, up to 10 pairs, stalked, alternate, fan-shaped (Fig. 1C) [63]–[65]. Venation pattern of the pinnae is dichotomous (Fig. 1D)[63]. Sporophylls are not grouped in strobili, whereas sporangia are enclosed in sporocarps. Sori is not dorsal and have false indusium, sporangia formed in definite groups [66]. T.S of the stem shows sclerenchymatous ground tissue and are 3–4 layered followed by parenchymatous cells. The xylem appears to be V-shaped with two arms that are turned inwards (Fig. 1B). Xylems are also both exarch and diarch [63], [67], [68]. The outer wall of spore appears to be rugulate under SEM which is an enlisted characteristic of the species [69] (Fig. E-G). Hence, the observation made from the above evidence identifies the specimen to be *Adiantum lunulatum* Burm.f. (*A. Philippense* Linn.) of the family Pteridaceae.

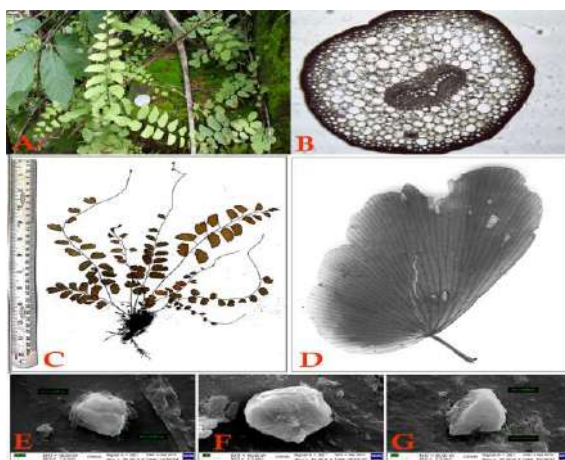


Fig. 1. (A) Digital photograph of the sporophyte of *Adiantum lunulatum* Burm. f. used in the biosynthesis of Ag-NP, (B) Transverse Section of the stem of *Adiantum lunulatum*, (C) Photograph of the Herbarium Specimen of *Adiantum lunulatum* Burm. f., (D) Venation pattern of the leaf of *Adiantum lunulatum*, (E–G) Scanning Electron Microscopic images of the spores of *Adiantum lunulatum*.

3.2. Production and characterization of Ag-NP

Ag-NP exhibits dark brown colour in liquid solution due to excitation of SPR in Ag-NP. Reduction of the Ag ions to Ag-NP at the time of contact to the liquid extract of *Adiantum lunulatum* could be followed by colour change. The liquid extract mediated synthesis of Ag-NP was validated by visually monitoring three flasks containing the AgNO₃ solution, a liquid extract of *Adiantum lunulatum* and the reaction mixture of the liquid plant extract with AgNO₃ solution respectively. An instantaneous and immediate turn over in the colour of the reaction mixture from colourless solution to brown colour signified the formation of Ag-NP (Fig. 2B) [70], whereas the liquid plant extract (Fig. 2A) and the AgNO₃ solution (Fig. 2C) were observed to retain their original colour. The colour of the control samples showed no change with cumulative incubation time. The appearance of a prominent brown colour designated the occurrence of the reaction and the development of the Ag-NP [53].



Fig. 2. Three flasks containing (A) only the liquid plant extract, (B) reaction mixture of liquid plant extract and AgNO₃ solution and (C) Only AgNO₃ solution, respectively.

3.3. UV–Visible spectroscopic analysis of Ag-NP

The evolution of silver from Ag⁺ ions to Ag⁰ state was categorized for spectral analysis. A broad and strong SPR band of the reaction solution was obtained in the visible spectrum at 420 nm, which was specific for Ag-NP (Fig. 3). Furthermore, this spectral analysis advocated that the Ag-NP were not in aggregated form. They scattered very well in the suspension [43], [53].

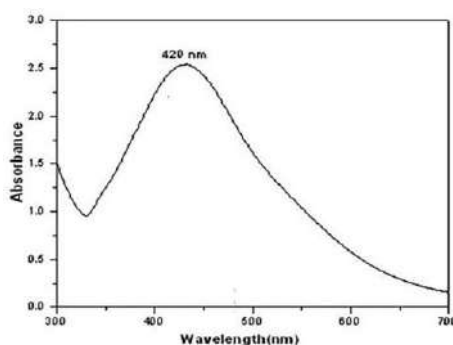


Fig. 3. UV–VIS spectrum of the synthesized silver nanoparticles.

3.4. Particle size measurement of Ag-NP

The DLS measurement was performed to get the knowledge of the size of the Ag-NP. Laser diffraction had shown that particle size found in the between 30–98 nm range (Fig. 4) The average diameter of these AgNO₃ nanoparticles was calculated to be 65±2 nm [71].

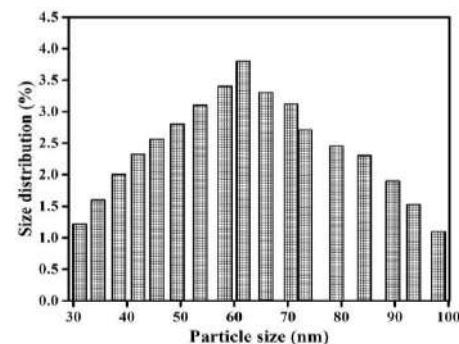


Fig. 4. The particle size distribution of bioreduced silver nanoparticles.

3.5. Zeta potential of Ag-NP

As displayed in Fig. 5, the zeta potential obtained from the Ag-NP showed a surface charge with a value of -84.11 mv [72]. The particles repel each other in suspension either having a negative or a positive zeta potential and also there shall be a very less tendency for the particles to come along. The slightly negative charge on the nanoparticles was probably resulting in the high stability of the Ag-NP without forming any aggregates when kept for an extended episode of time of more than a month [73]. Even the samples were retained their characteristic nature for more than a year (data not shown).

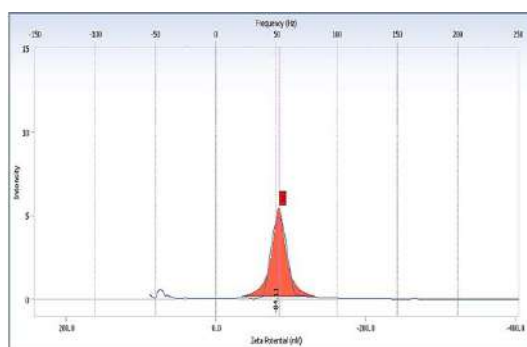


Fig. 5. Zeta potential of the biosynthesized silver nanoparticles.

3.6. EDX observation of Ag-NP

Fig. 6 illustrates the spot-profile mode of the EDX spectrum recorded from one of the densely-populated Ag-NP areas. In EDX spectra of Ag-NP, a sharp wide peak was detected in between 3–4 keV spectral region. The peak around 3–4 keV spectral region associated with the binding energies of silver [74]. The incident of that sturdy signal from Ag atoms (87.76%) itemized that the nanoparticles were solely made by silver. Therefore, EDX spectra of the Ag-NP established the presence of silver in the nanoparticles without any impurity of peaks [34]. However, there were other peaks of EDX for Cl and P, signifying that they were mixed precipitates from the plant extracts.

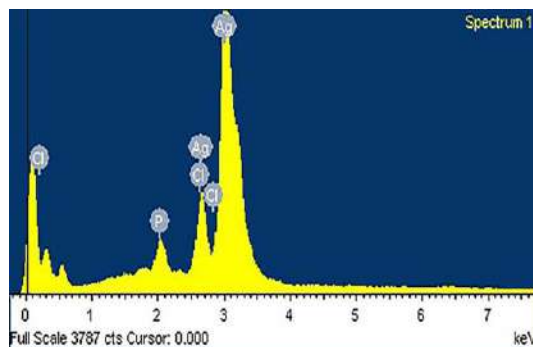


Fig. 6. EDX spectrum of silver nanoparticles.

3.7. Analyses of the crystallinity of Ag-NP by XRD

XRD measurement often proves to be a useful analytical gizmo for the identification of the crystalline nature of the newly formed compounds and their respective phases. XRD patterns of the dried Ag-NP revealed the subsistence of sharp diffraction lines at low angles (2° to 99°). The Ag-NP pointed out four sharp peaks of Ag at $2\theta = 38^\circ$, 44° , 64° and 78° that could be indexed to the (111), (200), (220) and (311) facets of Ag, respectively (JCPDS card file no. 04-0783) [Fig. 7] [75]–[79]. Thus, the XRD-spectrum measurement, answered in four strong peaks agreed to the Bragg's reflection of silver nanocrystals, finalized the crystalline nature of the Ag-NP [80]. The unambiguous background noise was undoubtedly due to the shell of protein around the nanoparticles [56].

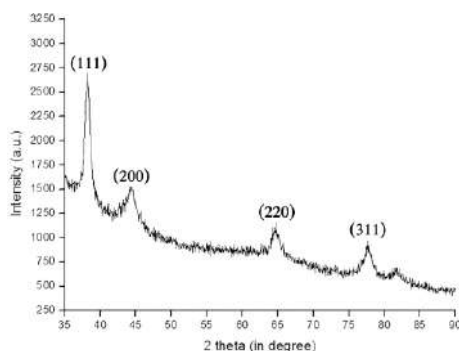


Fig. 7. XRD pattern of silver nanoparticles.

3.8. FTIR analysis of Ag-NP

FTIR absorption spectra of biosynthesized vacuum-dried Ag-NP have presented in Fig. 8. The spectra exhibited an extensive and strong absorption band corresponding to the O–H stretching vibration at around $\sim 3,066\text{ cm}^{-1}$. Symmetric and anti-symmetric modes of C–H stretching vibration were observed in the spectral region around $\sim 2,889\text{ cm}^{-1}$ and $\sim 2,820\text{ cm}^{-1}$ respectively [81]–[83]. Taraschewski et al. [84] reported earlier that the peak at around $\sim 2,360\text{ cm}^{-1}$ was observed due to CO_2 vibration that might not be necessarily from the sample. Peaks at around $\sim 1,567$, $\sim 1,380$, and $\sim 1,070\text{ cm}^{-1}$ were attributed to C=C stretching, $-\text{NH}_2$ symmetric stretch, and CO vibrations, respectively [34], [82], [85]–[87]. The band at around $\sim 1,567\text{ cm}^{-1}$, which commensurate to bending vibration movements in amides II, was earlier reported during the synthesis of Ag-NP [34]. The bands are visible in between the range of 500 to 750 cm^{-1} which confirmed the presence of R-CH group which might come from the liquid plant extract [88]. From this result, it could be stated that the soluble polypeptides present in the liquid plant extract may have acted as a capping agent to prevent the aggregation of Ag-NP in solution, and thus playing a

relevant role in their extracellular synthesis and shaping of the quasi-spherical Ag-NP [11], [30], [89].

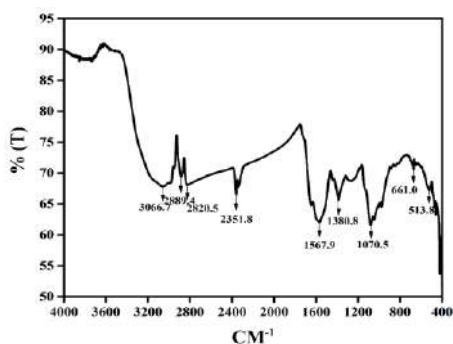


Fig. 8. FTIR absorption spectra of biosynthesized Ag-NP.

3.9. TEM of Ag-NP

TEM image, shown in Fig. 9, recorded dissimilar dimensions of Ag-NP which arose from the bio-reduction of the silver solution by liquid plant extract at room temperature (30°C). The particles were found to be hexagonal, quasi-spherical as well as monodisperse in nature (Fig. 9 A-C) [11]. The measured diameter of these Ag-NP was in the domain of about 10–60 nm [90]. The average diameter of these Ag-NP was calculated to be 28 ± 2 nm. The SAED pattern showed bright circular spots which further confirmed the single crystalline property of the Ag-NP (Figure 8D) [71]. It was thought-provoking to note that most of the Ag-NP in the TEM images were not in physical contact but were separated by a fairly undeviating inter-particle distance. Due to the developmental course of the sample preparation, the observed diameter of the Ag-NP during TEM analysis was quite unlike from that of the results obtained from DLS measurement as because Ag-NP were in a dry state in TEM whereas in the hydrated state in DLS experiment [91].

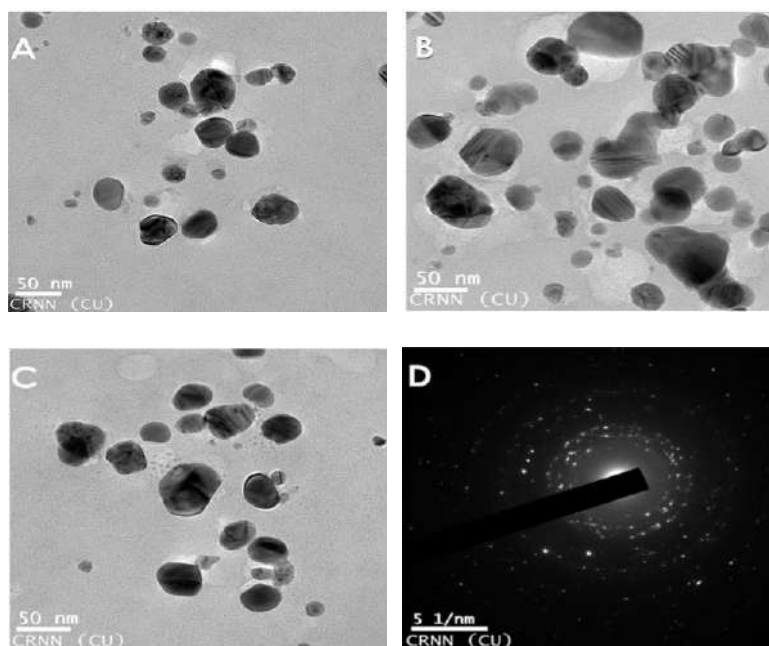


Fig. 9. (A–C) TEM images of Ag-NP (D) Selected area electron diffraction (SAED) patterns of crystalline Ag-NP.

3.10. Analysis of the effect of synthesized Ag-NP on some pathogenic bacteria

The biosynthesized Ag-NP was studied in 96 well plates for determining its antibacterial activity against both Gram-positive and Gram-negative bacteria. As presented in Table 1, the growth of all experimental strains was found to be subdued by the treatment of the Ag-NP as compared to Gram-negative control. In the case of *Listeria monocytogenes*, a Gram-positive bacterium, introduction of 25 µg/ml of Ag-NP caused 72.64±4.58% of reduction of bacterial density. Interestingly, growth of all examined Gram-negative bacteria were also noticed to be affected in the presence of a similar dose of the nanomaterials. Treatment of 25 µg/milliliter of synthesized Ag-NP showed maximum inhibition 48.45±2.87 and 88.7±5.62% with reference to *S. typhimurium* and *E. coli* respectively. These findings recommended strong antibacterial potentiality of synthesized Ag-nano.

Table 1. Antibacterial activity of synthesized silver nanoparticles as determined by the minimum inhibitory concentration value (µg/ml) (mean ± standard deviation; n = 3).

Type of bacteria	Name of bacteria	Nanoparticles	Streptomycin
Gram positive	<i>Listeria monocytogenes</i>	17.55 ± 3.57	4.68 ± 0.17
	<i>Staphylococcus aureus</i>	17.85 ± 1.71	6.29 ± 0.16
	<i>Bacillus subtilis</i>	105.41 ± 14.23	5.61 ± 0.01
Gram negative	<i>Escherichia coli</i>	12.36 ± 2.68	5.41 ± 0.11
	<i>Salmonella typhimurium</i>	28.77 ± 1.47	5.09 ± 0.03
	<i>Klebsiella pneumoniae</i>	17.84 ± 0.58	5.29 ± 0.14

4. Conclusions

The current work described biosynthesis of stable Ag-NP using liquid plant extract of *Adiantum lunulatum*. The production of biosynthesized nanomaterial was established by UV-Vis, DLS, EDX, XRD, FTIR and TEM analysis. The green synthesized Ag-NP presented strong antibacterial potentiality against pathogenic Gram-positive (*Listeria monocytogenes*, *Staphylococcus aureus*, and *Bacillus subtilis*) and Gram-negative (*Escherichia coli*, *Salmonella typhimurium* and *Klebsiella pneumoniae*) bacteria. Thus, the green synthesis of antimicrobial Ag-NP using liquid plant extract was an environment-friendly method as compared to the conventional physical and chemical synthesis techniques.

Acknowledgements

The authors thank Dr. Sudha Gupta, Assistant Professor, Pteridology & Paleobotany Lab, Department of Botany, University of Kalyani, Kalyani, Nadia, West Bengal, India, Pin-741235 for her entire effort in plant specimen identification and encouragement regarding this work. We also acknowledge Sinha Institute of Medical Science and Technology for providing us with the centrifugation and -20°C refrigeration facility.

Conflict of interest

On behalf of all listed authors, the corresponding author declares that there is not any sort of financial and non-financial conflict of interests in the subject materials mentioned in this manuscript.

References

- [1] V. Filipe, A. Hawe, W. Jiskoot, *Pharm. Res.* **27**(5), 796 (2010).
- [2] S. Galindo-Rodriguez, E. Allémann, H. Fessi, E. Doelker, *Pharm. Res.* **21**(8), 1428 (2004).
- [3] A. Vilchis-Nestor, V. Sánchez-Mendieta, *Mater. Lett.* **62**(17–18), 3103 (2008).
- [4] P. Magudapathy, P. Gangopadhyay, *Phys. B Condens.* **299**(1–2), 142 (2001).
- [5] F. Frederix, J. Friedt, K. Choi, W. Laureyn, *Anal. Chem.* **75**(24), 6894 (2003).
- [6] N. Jana, T. Sau, T. Pal, *J. Phys. Chem. B* **103**(1), 115 (1999).
- [7] N. Chandrasekharan, P. Kamat, *J. Phys.* **104**(46), 10851 (2000).
- [8] A. Gade, A. Ingle, C. Whiteley, M. Rai, *Biotechnology Letters* **32**(5), 593 (2010).
- [9] M. Hayat, *Colloidal gold: principles, methods, and applications*. Academic Press INC, 2012.
- [10] V. Filipe, A. Hawe, W. Jiskoot, *Pharm. Res.* **27**(5), 796 (2010).
- [11] J. Sarkar et al., *Dig. J. Nanomater. Biostructures* **6**(2), 563 (2011).
- [12] D. Maity et al., *J. Appl. Polym. Sci.* **122**, 2189 (2011).
- [13] M. M. R. Mollick et al., *Int. J. Green Nanotechnol.* **4**(3), 230 (2012).
- [14] S. K. Srikar, D. D. Giri, D. B. Pal, P. K. Mishra, S. N. Upadhyay, *Green Sustain. Chem.* **6**(1), 34 (2016).
- [15] S. Mann, G. A. Ozin, *Nature* **382**(6589), 318 (1996).
- [16] T. J. I. Edison, M. G. Sethuraman, *Process Biochem.* **47**(9), (2012).
- [17] R. Lu, D. Yang, D. Cui, Z. Wang, L. Guo, *Int. J. Nanomedicine* **7**, 2101 (2012).
- [18] E. J. Guidelli, A. P. Ramos, M. E. D. Zaniquelli, P. Nicolucci, O. Baffa, *Radiat. Phys. Chem.* **81**(3), 301 (2012).
- [19] C. L. Schofield, A. H. Haines, R. A. Field, D. A. Russell, *Langmuir* **22**(15), 6707 (2006).
- [20] V. Colvin, *Nat. Biotechnol.* **21**(10), 1166 (2003).
- [21] G. Cao, *Nanostructures and nanomaterials: synthesis, properties and applications*. 2004.
- [22] V. Rotello, *Nanoparticles: building blocks for nanotechnology*. Springer, Boston, MA, 2004.
- [23] W. De Jong, P. Borm, *Int. J. Nanomedicine*, 2008.
- [24] S. Saif, A. Tahir, Y. Chen, *Nanomaterials* **6**(11), 209 (2016).
- [25] K. Mukunthan, S. Balaji, *Int. J. Green* **4**(1), 54 (2012).
- [26] V. V. Makarov et al., *Acta Naturae* **6**(1), 35 (2014).
- [27] S. Iravani, “Green synthesis of metal nanoparticles using plants,” *Green Chem.*, 2011.
- [28] S. S. Shankar, A. Rai, A. Ahmad, M. Sastry, *J. Colloid Interface Sci.* **275**(2), 496 (2004).
- [29] J. Sarkar, M. Ghosh, A. Mukherjee, D. Chattopadhyay, K. Acharya, *Bioprocess Biosyst. Eng.* **37**(2), 165 (2014).
- [30] J. Sarkar, S. Ray, D. Chattopadhyay, A. Laskar, K. Acharya, *Bioprocess Biosyst. Eng.* **35**(4), 637 (2012).
- [31] N. Friis, P. Myers- Keith, *Biotechnol. Bioeng.* **28**(1), 21 (1986).
- [32] S. Ahmed, M. Ahmad, B. L. Swami, S. Ikram, *Journal of Advanced Research* **7**(1), 17 (2016).
- [33] G. Dhillon, S. Brar, S. Kaur, *Crit. Rev.* **32**(1), 49 (2012).
- [34] K. Acharya, J. Sarkar, *Int. J. Pharm. Sci. Rev. Res.* **29**(1), 82 (2014).
- [35] S. Santhoshkumar, K. Arts, T. Nadu, “No Title,” **5**(12), 5511 (2014).
- [36] A. J. De Britto, D. H. S. Gracelin, P. B. Jeya, R. Kumar, P. Molecular, T. Nadu, *Int. J. Univers. Pharm. Life Sci.* **2**(4), 92 (2012).
- [37] D. G. Sant et al., *J. Nanoparticles* **2013**, 1 (2013).
- [38] S. Kalita, R. Kandimalla, K. K. Sharma, A. C. Katagi, M. Deka, J. Kotoky, *Mater. Sci. Eng. C* **61**, 720 (2016).
- [39] A. K. Jha, K. Prasad, *Int. J. Nanosci.* **15**(1–2), 1 (2016).
- [40] B. Ch, S. Kunjiappan, C. Bhattacharjee, R. Chowdhury, *Nanomed. J.* **2**(1), 88 (2015).
- [41] X. Baskaran, A. V. G. Vigila, T. Parimelazhagan, D. Muralidhara-Rao, S. Zhang, *Int. J. Nanomedicine* **11**, 5789 (2016).
- [42] N. A. Şuţan, I. Fierăscu, R. C. Fierăscu, D. Ş. Manolescu, L. C. Soare, *Ind. Crops Prod.* **83**, 379 (2016).
- [43] B. Koteswaramma, J. Kamakshamma, S. Varalakshmi, *Int. J. Pharma Bio Sci.* **8**(1), 121 (2017).
- [44] N. John, “of the ferns Cyclosorous,” **9**(2), 125 (2016).

- [45] M. S. Ali, M. R. Amin, C. M. I. Kamal, M. A. Hossain, *Asian Pac. J. Trop. Biomed.* **3**(6), 464 (2013).
- [46] M. Johnson, *J. Microbiol. Exp.* **4**, (41), (2017).
- [47] T. Paul, B. Das, K. G. Apte, S. Banerjee, R. C. Saxena, *J. Diabetes Metab.* **3**(9), (2012).
- [48] R. Sikarwar, B. Pathak, A. Jaiswal, *Int. J. Tradit. Knowl.* **7**(4), 613 (2008).
- [49] C. Pan, Y. G. Chen, X. Y. Ma, J. H. Jiang, F. He, Y. Zhang, *Tropical Journal of Pharmaceutical Research* **10**(5), 681 (2011).
- [50] M. Mithraja, J. Marimuthu, M. Mahesh, Z. Paul, *Trop. Biomed.* **2**(1), S40 (2012).
- [51] A. Henglein, *J. Phys. Chem.* **97**(21), 5457 (1993).
- [52] M. Sastry et al., *Curr. Sci.* **85**(2), 162 (2003).
- [53] S. Saha, J. Sarkar, D. Chattopadhyay, S. Patra, A. Chakraborty, K. Acharya, *Dig. J. Nanomater. Biostruc.* **5**(4), 887 (2010).
- [54] M. Behera, G. Giri, *Mater. Sci.* **32**(4), 702 (2014).
- [55] S. M. Mukhopadhyay, *Sample Preparation for Microscopic and Spectroscopic Characterization of Solid Surfaces and Films.* 2003.
- [56] N. Vigneshwaran, A. A. Kathe, P. V. Varadarajan, R. P. Nachane, R. H. Balasubramanya, *Langmuir* **23**(13), 7113 (2007).
- [57] Y. Sun, Y. Xia, *Science* (80-.). **298**(5601), 2176 (2002).
- [58] S. Pal, Y. Tak, J. Song, *Appl Env. Microbiol.* **73**, 1712 (2007).
- [59] T. Bonnal, G. Foray, E. Prud, S. Tadier, *European Journal of Environmental and Civil Engineering 1* (2017).
- [60] B. Schaffer, U. Hohenester, A. Trugler, F. Hofer, *Phys. Rev. B - Condens. Matter Mater. Phys.* **79**(4), (2009).
- [61] D. Stojković et al., *Food Res. Int.* **53**(1), 56 (2013).
- [62] D. Stojković, J. Petrović, M. Soković, J. Glamočlija, J. Kukić-Marković, S. Petrović, *J. Sci. Food Agric.* **93**(13), 3205 (2013).
- [63] V. G. K. L. C. V. A. Pallavi, *Int J Pharm. Biol. Arch.* **2**(6), 1668 (2011).
- [64] D. M. Hillis, *Annu. Rev. Ecol. Syst.* **18**(1), 23 (1987).
- [65] B. Verdcourt, "Flora of Tropical East Africa," 2002.
- [66] K. U. Kramer, P. S. (Peter S. Green, and E. Götz, *Pteridophytes and gymnosperms.* Springer-Verlag, 1990.
- [67] S. Resmi, T. Vp, S. Vk, in *Kerala* **2**(1), 115 (2016).
- [68] *A. B. Hungarica* **58**(1909), 199 (2016).
- [69] A. F. Tryon, B. Lugardon, *Spores of the Pteridophyta*, New York, NY: Springer New York, 1991, pp. 1–26.
- [70] G. Singhal, R. Bhavesh, K. Kasariya, A. R. Sharma, R. P. Singh, *J. Nanoparticle Res.* **13**(7), 2981 (2011).
- [71] M. M. R. Mollick et al., *Microfluid. Nanofluidics* **16**(3), 541 (2014).
- [72] M. Gohel, T. Soni, L. Hingorani, A. Patel, N. Patel, *Curr. Res. Drug Discov.* **1**(2), 29 (2014).
- [73] J. Sarkar, P. Dey, S. Saha, K. Acharya, *Micro Nano Lett.* **6**(8), 599 (2011).
- [74] S. Kunjiappan, R. Chowdhury, C. Bhattacharjee, *Front. Mater. Sci.* **8**(2), 123 (2014).
- [75] G. Li et al., *Int. J. Mol. Sci.* **13**(1), 466 (2012).
- [76] K. Selvi, T. Sivakumar, *Int. J. Curr. Microbiol. App. Sci.* **1**(1), 56 (2012).
- [77] D. R. Patil, *Int. J. Res. Stud. Biosci.* **3**(10), 146(2015).
- [78] B. V. Bhimba, S. Gurung, S. U. Nandhini, *Int. J. ChemTech Res.* **7**(1), 68 (2015).
- [79] K. Jyoti, M. Baunthiyal, A. Singh, *J. Radiat. Res. Appl. Sci.* **9**(3), 1 (2016).
- [80] H. W. Lu, S. H. Liu, X. L. Wang, X. F. Qian, J. Yin, Z. K. Zhu, *Mater. Chem. Phys.* **81**, 104, (2003).
- [81] N. Sundaramurthy, C. Parthiban, *Int. Res. J. Eng. Technol.* **2**(6), 332 (2015).
- [82] S. Chandra, N. Chakraborty, A. Dasgupta, J. Sarkar, K. Panda, K. Acharya, *Sci. Rep.* **5**, 15195 (2015).
- [83] R. Sanghi, P. Verma, *Bioresour Technol.* **100**(1), 501 (2009).
- [84] M. Taraschewski, H. K. Cammenga, R. Tuckermann, S. Bauerecker, *J. Phys. Chem. A* **109**(15), 3337 (2005).
- [85] R. M. Silverstein, F. X. Webster, D. J. Kiemle, *Microchemical Journal* **21**, 496 (2005).

- [86] C. Y. Kim, T. Sekino, K. Niihara, *J. Am. Ceram. Soc.* **86**(9), 1464 (2003).
- [87] Y. F. Zhang, J. X. Zhang, Q. M. Lu, Q. Y. Zhang, *Mater. Lett.* **60**(20), 2443 (2006).
- [88] A. K. Singh, M. Talat, D. P. Singh, O. N. Srivastava, *J. Nanoparticle Res.* **12**, 1667 (2010).
- [89] J. Sarkar, K. Acharya, *Synth. React. Inorganic, Met. Nano-Metal Chem.* **47**(3), 365 (2017).
- [90] K. P. Bankura et al., *Carbohydr. Polym.* **89**(4), 1159 (2012).
- [91] R. M. M. Mollick et al., *RSC Adv.* **4**(71), 37838 (2014).



Source details

[Feedback >](#) [Compare sources >](#)

Digest Journal of Nanomaterials and Biostructures

Open Access

Scopus coverage years: from 2009 to Present

Publisher: S.C. Virtual Company of Physics S.R.L

ISSN: 1842-3582

Subject area: [Materials Science: General Materials Science](#) [Physics and Astronomy: Condensed Matter Physics](#) [Chemistry: Physical and Theoretical Chemistry](#)

[Physics and Astronomy: Atomic and Molecular Physics, and Optics](#) [Engineering: Biomedical Engineering](#) [View all](#)

Source type: Journal

[View all documents >](#)[Set document alert](#)[Save to source list](#)

CiteScore 2022

1.4

SJR 2022

0.188

SNIP 2022

0.341

[CiteScore](#)[CiteScore rank & trend](#)[Scopus content coverage](#)



OPEN ACCESS

Edited by:

Brice Rotureau,
Institut Pasteur, France

Reviewed by:

Joel Barratt,
University of Technology Sydney,
Australia

Carlos Robello,
Institut Pasteur de Montevideo,
Uruguay

***Correspondence:**

Nahid Ali
nali@iicb.res.in

†Present Address:

Mohammad Shadab,
Department of Dermatology, School of
Medicine, University of Alabama,
Birmingham, AL, United States

Roma Sinha,
Infection, Immunity and Metabolism
Group, Translational Research
Institute, Mater Research Institute and
The University of Queensland,
Brisbane, QLD, Australia

Mohammad Asad,
Department of Dermatology, School of
Medicine, University of Alabama,
Birmingham, AL, United States

Baijayanti Jha,
Department of Biochemistry,
University of Lausanne, Epalinges,
Switzerland

Specialty section:

This article was submitted to
Parasite and Host,
a section of the journal
Frontiers in Cellular and Infection
Microbiology

Received: 23 August 2018

Accepted: 17 January 2019

Published: 05 February 2019

Citation:

Shadab M, Das S, Banerjee A,
Sinha R, Asad M, Kamran M, Maji M,
Jha B, Deepthi M, Kumar M,
Tripathi A, Kumar B, Chakrabarti S
and Ali N (2019) RNA-Seq Revealed
Expression of Many Novel Genes
Associated With *Leishmania donovani*
Persistence and Clearance in the Host
Macrophage.
Front. Cell. Infect. Microbiol. 9:17.
doi: 10.3389/fcimb.2019.00017

RNA-Seq Revealed Expression of Many Novel Genes Associated With *Leishmania donovani* Persistence and Clearance in the Host Macrophage

Mohammad Shadab^{1†}, Sonali Das¹, Anindyajit Banerjee², Roma Sinha^{1†}, Mohammad Asad^{1†}, Mohd Kamran¹, Mithun Maji¹, Baijayanti Jha^{1†}, Makaraju Deepthi¹, Manoharan Kumar³, Abhishek Tripathi³, Bipin Kumar³, Saikat Chakrabarti² and Nahid Ali^{1*}

¹ Infectious Diseases and Immunology Division, Indian Institute of Chemical Biology, Kolkata, India, ² Structural Biology and Bio-Informatics Division, Indian Institute of Chemical Biology, Kolkata, India, ³ Nucleome Informatics Pvt. Ltd., Hyderabad, India

Host- as well as parasite-specific factors are equally crucial in allowing either the *Leishmania* parasites to dominate, or host macrophages to resist infection. To identify such factors, we infected murine peritoneal macrophages with either the virulent (vAG83) or the non-virulent (nvAG83) parasites of *L. donovani*. Then, through dual RNA-seq, we simultaneously elucidated the transcriptomic changes occurring both in the host and the parasites. Through Kyoto Encyclopedia of Genes and Genomes (KEGG) pathway analysis of the differentially expressed (DE) genes, we showed that the vAG83-infected macrophages exhibit biased anti-inflammatory responses compared to the macrophages infected with the nvAG83. Moreover, the vAG83-infected macrophages displayed suppression of many important cellular processes, including protein synthesis. Further, through protein-protein interaction study, we showed significant downregulation in the expression of many hubs and hub-bottleneck genes in macrophages infected with vAG83 as compared to nvAG83. Cell signaling study showed that these two parasites activated the MAPK and PI3K-AKT signaling pathways differentially in the host cells. Through gene ontology analyses of the parasite-specific genes, we discovered that the genes for virulent factors and parasite survival were significantly upregulated in the intracellular amastigotes of vAG83. In contrast, genes involved in the immune stimulations, and those involved in negative regulation of the cell cycle and transcriptional regulation, were upregulated in the nvAG83. Collectively, these results depicted a differential regulation in the host and the parasite-specific molecules during *in vitro* persistence and clearance of the parasites.

Keywords: transcriptome, RNA seq, macrophage, signaling/signaling pathways, *Leishmania donovani*

INTRODUCTION

Macrophages are known to have microbicidal functions and are considered as the sentinels of the immune system (Franken et al., 2016). However, their interaction with pathogens (of high and low virulence) varies significantly. Virulent pathogens avert the antimicrobial functions of the macrophages to survive and persist, while the less virulent ones are unable to exhibit the same

and thus get eliminated (Chakrabarty et al., 1996; Olivier et al., 2005). During this host-pathogen interaction, global changes in the gene expression pattern occur, both in the host (macrophages) as well as the infecting pathogens. If we could identify those genes, they could serve as tools to develop potent antimicrobial interventions. In this study, we attempted to identify the host as well as the parasite-specific genes, which were modulated when the host macrophages interacted with the virulent and the non-virulent *L. donovani* parasites (vAG83 and nvAG83, respectively) (Sinha et al., 2018). To obtain nvAG83 parasites, we first cultured the vAG83 for several passages in medium, and then performed genomic and transcriptomic studies on both the early passaged vAG83 and the late passaged nvAG83 parasites (Sinha et al., 2018). With these two parasites, we infected the non-elicited murine peritoneal macrophages (Ghosn et al., 2010), and measured the transcriptome of both the host as well as the infecting parasites with high-throughput deep sequencing (RNA-Seq) technology. RNA-Seq ensures a highly sensitive technique with high accuracy and provides a far more precise measurement of the level of transcripts than most other methods (Wang et al., 2009).

Numerous other studies have elucidated the host cell gene expression in response to *Leishmania* infection using microarray analysis (Probst et al., 2012; Ovalle-Bracho et al., 2015). One such study compared the gene expression in macrophages infected by two different *Leishmania* parasites (*L. donovani* and *L. major*) (Gregory et al., 2008). Another study compared the effect of a single strain of the *Leishmania* parasite (*L. amazonensis*) on the gene expression of two different macrophages that were isolated from the peritoneal cavity of C57BL/6 and CBA mice (Probst et al., 2012). Reports on the gene expression study, in the context of both the host as well as the infecting *Leishmania* parasites, are limited. There is a study using serial analysis of gene expression (SAGE), which has simultaneously analyzed gene expression patterns in human macrophages and the infecting *L. major* parasites (Guerfali et al., 2008). However, due to the limitations associated with this tag-based sequencing technique, it is difficult to achieve a comprehensive gene expression profiling (transcriptome) of both the interacting subjects in question (the host and the parasites). However, with the newly-developed RNA-Seq technology, these limitations have been overcome quite convincingly (Wang et al., 2009). Recently, with RNA-Seq, simultaneous transcriptional profiling of *L. major* and its host macrophages was done to understand how virulent parasites could evade host responses in order to survive in the mammalian environment (Dillon et al., 2015). These studies, however, did not address changes in gene expression, when the host cells kill non-virulent parasites.

Simultaneous gene expression studies in macrophages infected with *L. donovani* parasites have not been done so far. Moreover, though the gene expression analysis in macrophages infected with vAG83 (a virulent strain) has been reported through microarray analysis (Buates and Matlashewski, 2001), such studies in macrophages infected with nvAG83 (a non-virulent strain) have also not been evaluated so far. Therefore, the focus of our study was to unravel host as well as

parasite-specific genes that were modulated when vAG83 persists and nvAG83 gets eliminated in the host macrophages.

Through KEGG pathway and gene ontology analyses, we discovered a significant difference in the host responses evoked by the vAG83 and the nvAG83 parasites. It was found that vAG83 induces an immunosuppressive condition, whereas nvAG83 induced an immune-stimulatory environment within the host cells. In these two parasite-infected macrophages, we also found that the protein-protein interactome was altered differentially. While vAG83 downregulated, nvAG83 upregulated the expression of many hub and hub-bottleneck genes in the host macrophages. Further, the mitogen-activated protein kinase (MAPK) and Phosphatidylinositol 3-kinase (PI3K) signaling pathways were also modulated differentially. It was noted that vAG83 induced higher activation of ERK1/2 and AKT (ser437) in the host macrophages as compared to nvAG83. Conversely, nvAG83 induced higher activation of P38 in the host macrophages as compared to vAG83. A differential gene expression pattern was also observed in the two infecting parasites. Gene expression analyses showed that the genes related to virulence and survival were significantly overexpressed in vAG83 as compared to nvAG83. In contrast, the immunostimulatory genes and negative regulators of cell survival machinery were significantly overexpressed in nvAG83 as compared to vAG83. Thus, this work provided valuable insights into how the host responses could become modulated upon infection with a virulent and a non-virulent AG83 parasite. Moreover, it also provides good insights into the responses generated in these two infecting parasites. Overall, this study deciphered various important factors of the host as well as the parasites, which are significantly associated with either the parasite's survival or clearance in the host macrophages.

MATERIALS AND METHODS

Animals and Parasites

BALB/c mice, bred in the animal house facility of the Indian Institute of Chemical Biology (Calcutta, India), were used for the experiments. *L. donovani* strain AG83 (MHOM/IN/1983/AG83), originally isolated from an Indian kala azar patient, was maintained by serial passage in 4- to 6-week-old Syrian golden hamsters (*Mesocricetus auratus*) reared in a pathogen-free animal care facility of the Indian Institute of Chemical Biology. Animal monitoring was done as per the Animal Ethics Committee approved protocol. Animals were not sedated for any procedures. The animals were euthanized for isolating *L. donovani* amastigotes periodically as per the approved animal ethics of our institute (147/1999/CPSCEA). These amastigotes were then transformed into promastigotes in Schneider's medium supplemented with 20% heat-inactivated FCS and penicillin G (100 U/ml) and streptomycin sulfate (100 µg/ml), and then the culture was maintained in M199 supplemented with 10% FCS, 2 mM glutamine, penicillin G (100 U/ml) and streptomycin sulfate (100 µg/ml) at 22°C by weekly passaging up to the 25th passage. The early passaged parasites (2nd) were considered as virulent and the late passaged (25th) were considered as non-virulent based on infection study.

Preparation of Peritoneal Macrophages and Infection

BALB/c mice, bred in the animal house facility of the Indian Institute of Chemical Biology (Calcutta, India), 8–10 weeks old were used for the experiments. By cervical dislocation mice were sacrificed. Their peritoneal macrophages were then collected by infusing the peritoneal cavity with ice-cold sterile RPMI supplemented with 3% FCS. Cells (1×10^6) were then dispensed into 6-well plates and allowed to adhere overnight at 37°C in 5% CO₂. Non-adherent cells were washed off, and wells were replenished with RPMI 1640 containing 10% FCS. Cells were infected at a parasite-to-macrophage ratio of 10:1 for 3 h at 37°C in a humidified atmosphere of 5% CO₂, after which non-ingested promastigotes were washed off with warm RPMI and incubated for the indicated time point. The cells were then lysed in trizol for RNA isolation. RNA samples from two independent experiments were pooled together for poly (A)-enriched cDNA preparation.

In vitro Infection

For *in vitro* infection, 2×10^5 peritoneal macrophages were cultured on cover slips and incubated overnight. The next day coverslips were washed with warm RPMI medium to remove the unattached cells and then infected at a 1:10 ratio with the parasites. After 3 h of incubation, the uningested parasites were removed by washing three times with the RPMI medium. The infected cells were then incubated for various time points post-infection. The coverslips were then washed twice with PBS and air-dried. After methanol fixation, the cells were Giemsa-stained and the number of amastigotes in 100 macrophage cells was counted under a light microscope using oil emersion lenses.

Infection to Animals and Determination of Splenic and Hepatic Parasite Burden

BALB/c mice (4–5 weeks) were infected by injecting 2×10^7 stationary phase promastigotes as described above. Mice were sacrificed at 12 weeks post-infection for determination of parasite burden.

Leishman-Donovan Units (LDU)

Spleen and liver were removed at specified times, and multiple impression smears were prepared and stained with Giemsa (Banerjee et al., 2008). Organ parasite burdens, expressed as LDU, were calculated as the number of parasites per 1,000 nucleated cells \times organ weight (in mg).

Limiting Dilution Assay (LDA)

To further evaluate whether the spleen and liver contained live parasites, the parasite burden was quantified in these tissues by serial dilution assay (Banerjee et al., 2008). Briefly, a weighed piece of spleen or liver from experimental mice was first homogenized in Schneider's medium supplemented with 10% FCS, and then diluted with the same medium to a final concentration of 1 mg/ml. Five-fold serial dilutions of the homogenized tissue suspensions were then plated in 96-well plates and incubated at 22°C for 21 days. Wells were examined

for viable and motile promastigotes at 7-day intervals, and the reciprocal of the highest dilution that was positive for parasites was considered to be the parasite concentration per mg of tissue. The total organ parasite burden was calculated using the weight of the respective organs.

RNA Isolation and cDNA Library Preparation

Total RNA was isolated using the Trizol[®] reagent (Invitrogen, CA), treated with DNase and purified using the Qiagen RNeasy mini kit. Quality checks of the RNA samples were performed with Qubit (picogreen) to assess sample concentration. Subsequent steps were followed according to the protocols prescribed by Illumina (Cat# RS-930-1001). Poly (A)-enriched cDNA library preparation involved purifying the poly-A-containing mRNA molecules from total RNA using oligo-dT-attached magnetic beads. Following purification, the mRNA is fragmented into small pieces using divalent cations under elevated temperature. The cleaved RNA fragments are copied into first-strand cDNA using reverse transcriptase and random primers. Second-strand cDNA synthesis followed, using DNA Polymerase I and RNase H. The cDNA fragments then went through an end repair process, the addition of a single "A" base, and then ligation of the adapters. The products were then purified and enriched with PCR to create the final cDNA library.

Sequencing

Sequencing of both QC passed libraries was performed on the Illumina HiSeq2500 system. The HiSeq 2500 system is a powerful and efficient ultra-high-throughput sequencing system that supports the broadest range of applications and study sizes (Reuter et al., 2015). Unrivaled data quality using Illumina's proven SBS Chemistry (Ambardar et al., 2016) have made the HiSeq2500 the instrument of choice for Molecular Biologists (Table 1).

RNA-Seq Data Generation, Pre-processing and Quality Trimming

The next-generation sequencing run for whole transcriptome sequencing was performed using the paired-end (PE) 2×150 bp library on the Illumina HiSeq 2500. Raw data were generated for each of the libraries from the three samples (Supplementary Table 1). Trimmomatic version-0.33 was used for pre-processing of raw reads generated for the samples. Parameters considered for filtration were as follows: ADAPTER TRIMMING: 2:30:10. SLIDINGWINDOW: 4:20. MINLENGTH: 50. For paired-end data, two input files were specified to Trimmomatic, and Trimmomatic produced 4 output files, 2 for the "paired/PE" output where both reads survived the processing, and 2 for corresponding "unpaired/single-end/SE" output where a read survived, but the partner read did not. Thus, the total clean reads obtained for each sample was calculated as PEx2+SE. Sequence quality metrics were assessed using FastQC (version: 0.11.3) (<http://www.bioinformatics.babraham.ac.uk/projects/fastqc/>).

TABLE 1 | Sequencing summary.

INSTRUMENT	
Manufacturer	Illumina
Version	HiSeq 2500
Slot used	A
Basecalling pipeline	-HiSeq Control Software 2.2.38 -RTA 1.18.61.0 -CASAVA-1.8.2
RUN	
Mode	HiSeq high output (HO) version 4
Number of cycles	2 × 150 + 7
Number of lanes	1
Flow cell ID	HL7FHCCXX
Flow cell version	HiSeq Flow Cell v4
Kit version	HiSeq SBS Kit v4
Indexing	Single-Indexing
Data output C	5.18 Gb
Data output (nvAG83 infected macrophage)	4.36 Gb
Data output (vAG83 infected macrophage)	4.36 Gb
SEQUENCING SPECIFICATION	
Service	Full lane
Error rate	1.5%
Q30	80%

Mapping cDNA Fragments to the Reference Genome, Read Count and Data Normalization

Clean reads from each sample were aligned independently to the *Mus Musculus* (UCSC mm10) reference genome and *L. donovani* (LdBPK282A1) reference genome using TopHat 2 (parameter: -g 1 and default) (Trapnell et al., 2009). TopHat is a fast splice junction mapper for RNA-Seq reads. It aligns RNA-Seq reads to mammalian-sized genomes using the ultra-high-throughput short read aligner Bowtie, and then analyzes the mapping results to identify splice junctions between exons. The HTSeq tool was used to count the number of reads aligned to protein coding genes. HTSeq is a Python package that provides infrastructure to process data from high-throughput sequencing assays.

Differential Expression Analysis

The DESeq tool was used for differential gene expression analysis between samples in protein coding genes. The DESeq is an R package to estimate variance-mean dependence in count data from high-throughput sequencing assays and testing for differential expression based on a model using the negative binomial distribution. Differentially expressed (DE) genes were defined as genes with a Benjamini-Hochberg multiple testing *p* value of <0.05.

KEGG Pathway Analysis

ConsensusPathDB-mouse was done to identify signaling and metabolic pathways that were over-represented in the mouse DE gene lists. KOBAS was used to find the enrichment analysis in KEGG and Gene Ontology. Both *p* < 0.05 and *paj*/FDR

value < 0.05 genes were used for KEGG enrichment analysis. KOBAS can identify statistically significantly enriched pathways, human diseases, and functional terms for an input set of genes using biological knowledge from well-known pathway databases, disease databases, and gene ontology. The Hypergeometric test and Fisher's exact test were used for statistical testing in enrichment analysis and Benjamini-Hochberg was used for the FDR correction method. For each KEGG pathway, a *P*-value was calculated using a hypergeometric test, and a cutoff of 0.01 was applied to identify enriched KEGG pathways. Genes that were DE more than 2-fold in *L. donovani*-infected cells relative to uninfected controls were used as input, with up- and down-regulated genes considered separately. For generating heat maps of these genes, in-house script software was used.

Gene Ontology (GO) Analysis

GO categories enriched in the *L. donovani* DE gene lists were identified using the Goseq package in R. It detects gene ontology and/or other user-defined categories that are over/under-represented in RNA-Seq data. Gene ontology analysis was used for RNA-Seq and other length-biased data. For each comparison, upregulated and downregulated gene sets (no fold change cut-off) were input separately into Goseq. A *p*-value cut-off of 0.05 was used. The hypergeometric method was used for enrichment analysis.

Isolation of Total RNA, cDNA Synthesis and Real-Time PCR

Total RNA from macrophage cells (uninfected and infected with both parasites) was isolated using Trizol reagent (Invitrogen), according to the manufacturer's instructions. A total of 2 µg of RNA from each sample was reverse-transcribed to cDNA using the iScript cDNA synthesis kit (Bio-rad), according to the manufacturer's protocol. Using LightCycler 96 (Roche), real-time PCR was performed according to the SYBER GREEN method (KAPA BIOSYSTEMS). The PCR thermocycling parameters were kept as 95°C for 10 min, 45 cycles of 95°C for 15 s, 55°C for 30 s and 72°C for 25 s. GAPDH was used as an internal control. Samples were run in duplicates. The fold induction was determined by the $2^{-\Delta\Delta CT}$ method (Schmittgen and Livak, 2008). Fold induction of duplicate samples were averaged.

Construction of Protein-Protein Interaction of the Deregulated Genes

Protein-protein interactions (PPI) of the virulent and non-virulent specific macrophage genes were searched in the STRING database (von Mering et al., 2003). Interactions with the highest confidence values [experimental evidences score ≥ 0.9] were collected to construct the network, which was further used for network topology analysis for identifying important interactive nodes of the network. The Hub Objects Analyzer (Hubba) (Lin et al., 2008) is a web-based plug-in incorporated in Cytoscape (Shannon et al., 2003) was used to determine the important network nodes—i.e., the hub (He and Zhang, 2006) and bottleneck (Yu et al., 2007; McDermott et al., 2009).

Preparation of Bone Marrow-Derived Macrophages (BMM)

To generate bone marrow-derived macrophages (BMM), uninfected BALB/C mouse femurs were aseptically harvested and sterilized in 70% (vol/vol) ethanol for 1 min and then washed thrice in Dulbecco's phosphate-buffered saline (PBS). The contents of the femurs were flushed out with complete DMEM using a 25-gauge needle. Bone marrow cells were then cultured and differentiated in 35 mm cell culture dishes containing DMEM supplemented with 100 U/ml penicillin-streptomycin, 10% fetal bovine serum, and 10 ng/ml MCSF for 7 days at 37°C in a humidified atmosphere of 5% CO₂.

Western Blotting

Macrophages ($1-2 \times 10^6$) cultured in 35 mm cell culture dishes were infected with promastigotes of *L. donovani* at a 1:10 ratio for different time points. Cells were then washed with PBS and lysed in cell lysis buffer containing protease and phosphatase inhibitor cocktail, and the protein concentrations in the cleared supernatants were estimated using Lowry's method. The cell lysates were resolved by 10% SDS-PAGE and then transferred to Nitrocellulose membranes (BioRad). The membranes were blocked with 5% BSA in Tris-buffered saline (TBS) for 1 h at room temperature and probed with primary Ab for 2 h at a dilution recommended by the manufacturers. Membranes were then washed three times with wash buffer (TBS containing 0.5% tween) and then incubated with HRP-conjugated secondary Ab and detected by an ECL detection system according to the manufacturer's instructions.

Statistical Calculations

All data comparisons were tested for significance with the two-tailed Student's *t*-test using GraphPad software; *P*-values < 0.05 were considered significant.

RESULTS AND DISCUSSION

Infection Dynamics and the Global Transcriptional Changes in Macrophages Infected With vAG83 and nvAG83 Parasites

We first determined a time-dependent infection pattern in the murine peritoneal macrophages, co-cultured with the promastigotes of vAG83 (2nd passaged) and nvAG83 (25th passaged). Parasite load was estimated after 3, 24, 48, and 72 h post-infection (p.i.). It was observed that the initial parasite count at 3 h p.i. was comparable for both the parasites, although it was slightly lower for nvAG83. However, vAG83 exhibited a progressive increase in the parasite burden with time. nvAG83, in contrast, showed a time-dependent decrease in parasite load (Figure 1). To validate these *in vitro* results in an *in vivo* set-up, BALB/c mice were infected with promastigotes derived from different passages, and the parasite burden was determined in both the liver and the spleen, using methods like Leishman Donovan Units (LDU) and Limiting Dilution Assay (LDA). The *in vivo* infectivity of the parasites also declined when they were cultured in the medium repeatedly.

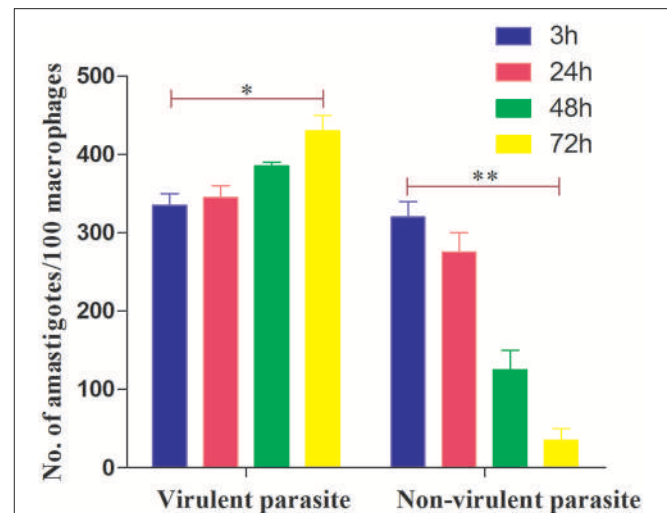


FIGURE 1 | Dynamics of murine macrophage infection with virulent and non-virulent *L. donovani* promastigotes. Murine macrophages were infected with either virulent (2nd passage) or non-virulent (25th passage) *L. donovani* promastigotes for 3 h, washed, and further incubated until 24, 48, and 72 h p.i. The number of internalized parasites in 100 macrophages was determined microscopically by Giemsa staining. The results are expressed as mean S.E (*n* = 3). **P* < 0.01, ***P* < 0.001.

The results of the LDU and the LDA revealed that, with an increasing number of parasite passage, there was a progressive suppression in liver as well as splenic parasite burden (Table 2). Thus, these results confirmed that early passaged parasites were potent enough to establish successful infection, but the late passaged ones were weak and unable to do so, both *in vitro* (in macrophages) as well as *in vivo* (in mice model). Previously, we have shown differences in the *in vivo* parasite burden in the spleen and liver of hamsters infected with the early and the late passage promastigotes (Sinha et al., 2018). We found that these differences were attributed to a differential expression of several virulence factors and cytoskeletal proteins in the parasites. At the genomic level, we observed subtle changes, mostly in defense-related, nutrient acquisition and signal transduction-related genes between the two passages. We also observed SNPs in ABC transporter and calpain-like cysteine protease genes, which are emerging as patho-adaptive factors in clinical isolates of *Leishmania* (Sinha et al., 2018).

Subsequently, to determine the global gene expression pattern in both the host and the parasites, we infected murine peritoneal macrophages with vAG83 and nvAG83 for 12 h and generated the transcriptomic data using RNA-Seq. This time point of infection was chosen based on our study on the *in vitro* macrophage infectivity, where we found that after this time point, the infection is directed toward progression for vAG83 and reduction for nvAG83. Progressive clearance of nvAG83 with time hinders the effort of getting an ample amount of *Leishmania*-specific RNA that could be analyzed for their change. A total of 12 h of infection allowed us to compare the transcriptomic changes between the vAG83 and

TABLE 2 | *In vivo* parasite burden in mice.

Passage number	LDU ± S.E. (n = 3–5/group)		log ₁₀ parasite burden ± S.E. (n = 3–5/group)	
	Liver	Spleen	Liver	Spleen
2nd	1056 ± 117.9	602.1 ± 109.3	16.34 ± 2.4	12 ± 1.18
5th	945.1 ± 94.87	514.5 ± 74.51	14.23 ± 3.15	11.52 ± 2.08
15th	302.9 ± 54.30	78.78 ± 15.10	7.94 ± 1.54	5.17 ± 1.88
25th	54.83 ± 11.04	7.96 ± 3.069	3.28 ± 2.11	2.29 ± 1.76

BALB/c mice were infected with 2×10^7 *L. donovani* promastigotes of different passages as indicated in the table. At 12 weeks, *p.i.* mice were sacrificed and parasite burden of the liver and spleen were determined by LDU and LDA. Data represent mean ± S.E.M of 3–5 animals per group.

the nvAG83 infective stages of the parasites. The bioinformatics analysis workflow is represented in **Supplementary Figure 1**. Raw data (reads) were generated for the three samples (uninfected macrophages, and macrophages infected with vAG83 and nvAG83) (**Supplementary Table 1**), which were further processed to give clean reads. Reads (paired end/PE plus unpaired/single-end/SE) with a sequence of 150 nucleotides were generated (see Material and Methods), which yielded a total of 89.19 million high-quality reads from the three samples (**Supplementary Table 2**). The infected samples consisted of a pool of mixed RNAs from the mouse macrophages and the *Leishmania* parasites. However, the reads generated for the whole sample can be mapped to the genome of the mouse and the parasite RNAs, respectively. But the possibilities of error in mapping the reads across the two species cannot be denied as well. This is mainly because mapping of reads to both the species genome from the same sample depends on several factors, including the use of random hexamer for reverse transcription of poly (A) RNA, which may not retain information contained on the DNA strand that is actually expressed (Mortazavi et al., 2008). Secondly, the size of the final fragment to be sequenced is crucial for proper sequencing and subsequent analysis. Longer reads improve mappable data and transcript identification, whereas short SE reads are normally sufficient for studies of gene expression levels in well-annotated organisms (Garber et al., 2011). Depth of sequencing is also crucial in detection and quantification of the transcript in a precise manner (Mortazavi et al., 2008). For example, 70 and 90% of regular RNA-Seq reads are expected to map to the mouse genome depending on the read mapper used (Dobin et al., 2013). Thus, we can say that the fraction of reads mapping to the mouse vs. parasite reference genomes depicted the proportion of RNA molecules from each source but without denying all these factors. The percentage of PE and SE reads mapping to the mouse genome was found to be 82.6 and 84%, respectively, for the uninfected macrophages (**Supplementary Table 3**). Likewise, the percentage of PE and SE reads mapping to the mouse genome was found to be 67 and 66%, respectively, in the macrophages infected with vAG83, and 65.2 and 66.4%, respectively, in the macrophages infected with nvAG83. Similarly, the proportion of parasite-specific PE and SE reads in vAG83-infected macrophages corresponded to 14.5 and 16.3%, respectively, and in nvAG83-infected

macrophages, parasite-specific PE and SE reads corresponded to 16.6 and 18.3%, respectively (**Supplementary Table 4**). Similar observations for mouse and parasite reads were reported earlier (Dillon et al., 2015). The reason for not getting 100% reads mapping to mouse and parasite genomes in these studies is not well understood. It may be that due to the dynamicity of the transcriptional activity, probing the whole transcriptome at a particular time is not feasible to obtain reads that can map to 100% to the reference genome.

From the sequencing data set, we next identified differentially expressed (DE) genes in the infected macrophages as compared to the uninfected control. Thus, we prepared two gene lists, one for the macrophages infected with vAG83 (**Supplementary Data Sheet 1A** vAG83) and the other for the macrophages infected with nvAG83 (**Supplementary Data Sheet 1B** nvAG83). Moreover, we considered only those genes in the gene list, which were DE > 2-fold, with upregulated and downregulated genes, considered separately. We found that in the host macrophages, vAG83 and nvAG83 induced 456 and 473 DE genes, respectively, that were differentially expressed at a *p*-value cutoff of < 0.05 compared to the uninfected control. Intriguingly, out of these various DE genes, only 20.3% were found to be upregulated by vAG83 and 52.2% by nvAG83. Conversely, 79.6% of the DE genes were downregulated by vAG83, and 47.7% by nvAG83 (**Figure 2A**). Moreover, when we compared the overlap in these DE genes (Venn diagram, **Figure 3**), we found that although 245 genes were modulated by both the parasites, 211 and 228 genes were uniquely modulated by vAG83 and nvAG83, respectively. Further, of the 245 commonly modulated genes, it was found that ~66.0% were downregulated, and 34.0% were upregulated. But of the unique 211 genes modulated by the vAG83, ~95.0% were found to be downregulated and only 5.0% were upregulated. In contrast, of the unique 228 genes modulated by the nvAG83, only ~30.0% were observed to be downregulated and ~70.0% were upregulated. This clearly shows that, in addition to the common genes, vAG83 downregulated many unique genes compared to nvAG83. On the contrary, nvAG83, in addition to the common genes, upregulated many unique genes compared to vAG83. Modulation of these common genes could be explained by the fact that the same parasite, when it loses its virulence upon several passages, may still possess some factors that modulate the host cells in a similar fashion. Overall, there was a significant difference in the host cell gene expression induced by the virulent and the non-virulent parasites. vAG83 employs strategic suppression of macrophage genes at a large scale that may allow them to establish themselves in the host cells (Buates and Matlashewski, 2001). In contrast, the upregulation of many DE genes by nvAG83 parasites might be responsible for their clearance within the host cells (Bhattacharya et al., 2015).

Validation of the DE Genes by Real-Time PCR

Since RNA-Seq of a single sample was done for each condition, so as to avoid artifacts and erroneous results, we validated

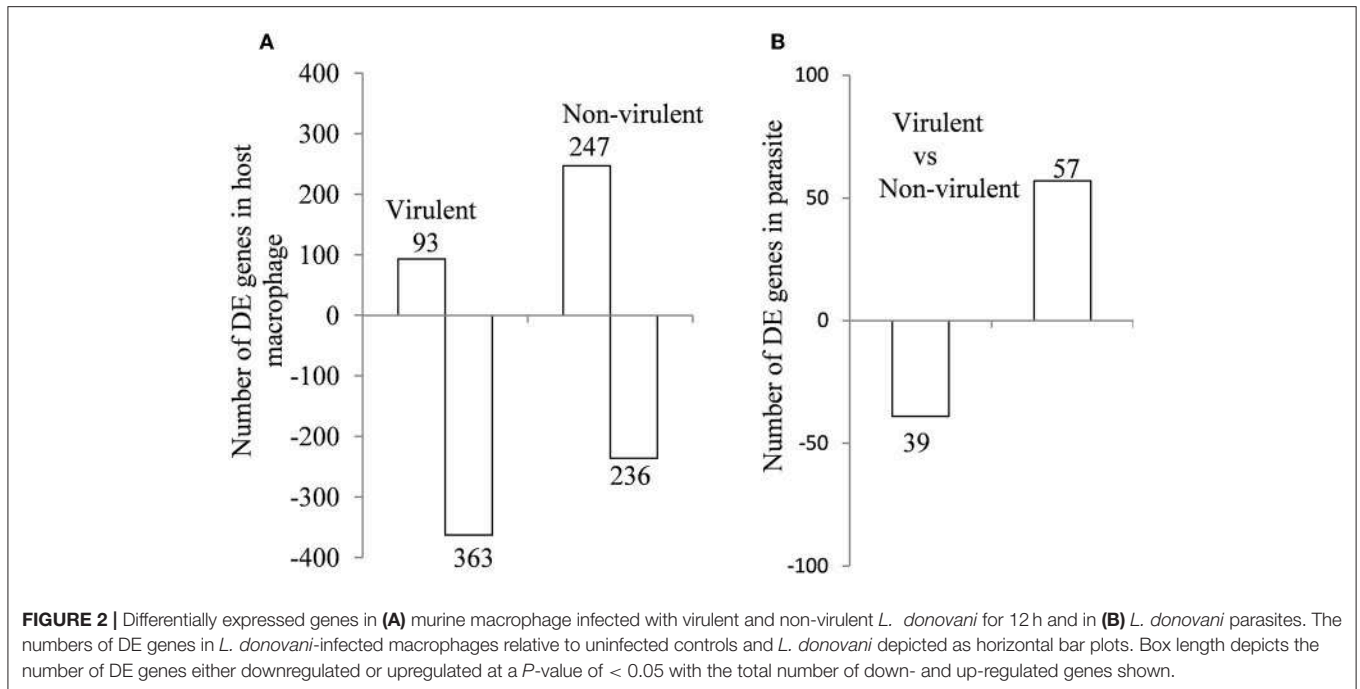


FIGURE 2 | Differentially expressed genes in **(A)** murine macrophage infected with virulent and non-virulent *L. donovani* for 12 h and in **(B)** *L. donovani* parasites. The numbers of DE genes in *L. donovani*-infected macrophages relative to uninfected controls and *L. donovani* depicted as horizontal bar plots. Box length depicts the number of DE genes either downregulated or upregulated at a *P*-value of < 0.05 with the total number of down- and up-regulated genes shown.

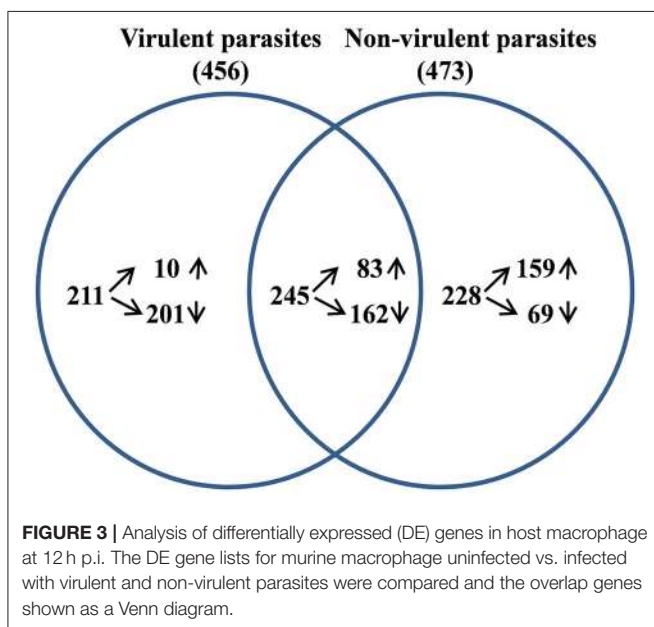
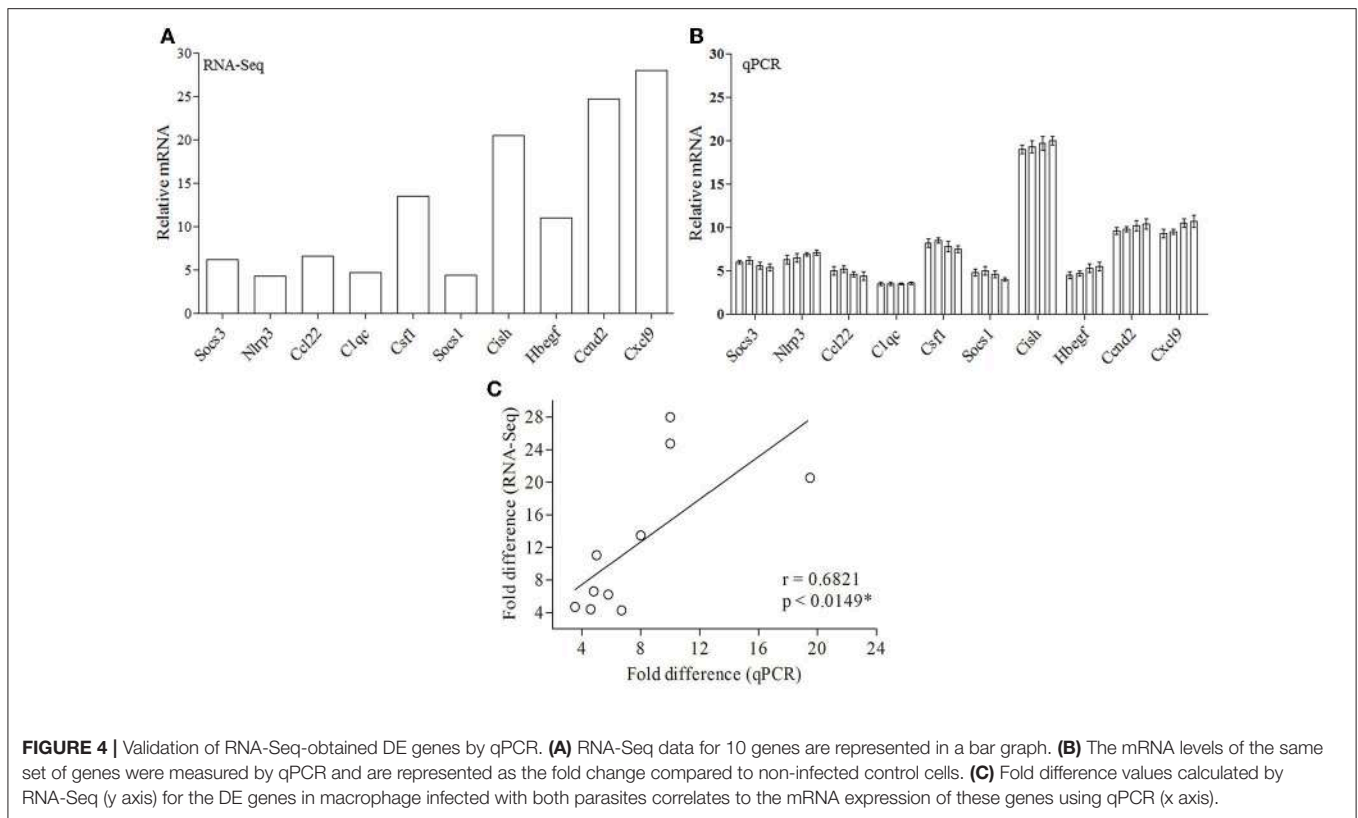


FIGURE 3 | Analysis of differentially expressed (DE) genes in host macrophage at 12 h p.i. The DE gene lists for murine macrophage uninfected vs. infected with virulent and non-virulent parasites were compared and the overlap genes shown as a Venn diagram.

Pathway-Based Enrichment Analyses Depicted a Differential Host Macrophage Response to Infection With vAG83 and nvAG83 Parasites

We next used KEGG pathway enrichment analysis of the DE genes to decipher how the cellular responses evoked against infection by vAG83 and nvAG83 may differ. First, we compared the total number of KEGG pathways, upregulated by both the parasites. We found that vAG83 upregulated only three KEGG pathways, mainly related to immune response and signal transduction, including cytokine-cytokine receptor interaction (Table 3). In contrast, nvAG83 upregulated 34 pathways, of which most are related to immune response and signaling such as cytokine signaling in the immune system, signaling by GPCR, Toll-like receptor signaling and NF-kappa B signaling (Table 4). Similarly, a comparison of the total number of KEGG pathways, downregulated by both the parasites, showed that vAG83 downregulated 13 KEGG pathways, including immune system, signal transduction, gene expression, endocytosis, and phagosome (Table 3). Conversely, nvAG83 downregulated only eight KEGG pathways, including the immune system, signal transduction and transmembrane transport of small molecules (Table 4). This shows that there is a vast difference in the number of KEGG pathways regulated in the host by the two parasites, indicating a huge disparity in the host responses generated against infection by vAG83 and nvAG83. Moreover, this suggests that the macrophages infected with the two parasites may respond to their immediate environment differently. For instance, the nvAG83-infected macrophages (where many pathways of macrophage activation including inflammation are upregulated), seem to become more sensitive

the data obtained from RNA-Seq (Figure 4A) by performing real-time PCR of 10 genes from four biological replicates (Figure 4B). Ten DE genes from macrophages infected with both the parasites, were randomly selected for real-time RT-PCR analysis. The primers of selected genes are listed in Supplementary Table 5. The qRT-PCR results showed a strong correlation with the RNA-Seq-generated data (Pearson correlation coefficients $r = 0.6973$; Figure 4C), thus validating the RNA-Seq results.



to inflammatory signals. Previous reports showed that several inflammatory signaling pathways, including the IL-2 signaling pathway, TNF signaling pathway, Jak-STAT signaling pathway, NF-kappa B signaling pathway, and Toll-like receptor signaling pathway, trigger potent anti-leishmanial immune responses in the host macrophages (Shadab and Ali, 2011). Thus, owing to the immunosuppressive nature of the disease caused by the virulent strain of *L. donovani*, the induction of these pathways by the non-virulent ones highlights the importance of the immune responses against the parasites. Hence, the pathways which were totally shut down by vAG83 seem to have been upregulated in case of nvAG83 infection, which could possibly activate the macrophages to kill the nvAG83 parasites.

It was noted that some of the pathways were both upregulated and downregulated by each of the parasites. For example, pathways like the immune system and signal transduction were both up- and down-regulated by vAG83. Similarly, pathways like the immune system, homeostasis, metabolism, signal transduction and the PI3K-Akt signaling pathway, were both up- and down-regulated by nvAG83. This can be explained by the fact that the genes enriched in the up- and the down-regulated pathways are different that may ensue different infection outcomes, based on their functions including positive or negative regulators of infection. For example, in contrast to the genes including Nr4a1, Il1b, Cma1, Socs3, and Dtx1 etc. that were enriched in the upregulated pathways (immune system and signal transduction), the genes of the same pathways when downregulated include Ifi204, Ptprc, Hsp90b1, Actr2,

Itga4, Tlr7, Cybb, Trip12, Tax1bp1, Prkcb, Cltc, Hsp90aa1. Apart from these, we also found that some of the pathways downregulated by vAG83 were upregulated by nvAG83—for example, innate immune system, adaptive immune system and disease. Moreover, there were some pathways specifically downregulated by vAG83. These include the adaptive immune system, innate immune system, endocytosis, phagosome, mRNA processing, gene expression and pathways in cancer. The genes enriched in these pathways include Ptprc, Itga4, Trip12, Cybb, Cltc, Prkcb Cav2, Cav1, Met, Csde1, Sf3b1, Eif2ak2, Ddx3x, Pum2, Cpeb4, etc. Previous studies have shown that virulent *Leishmania* parasites hijack the host machinery by employing multiple strategies, including dampening of host immune responses (Gupta et al., 2013), manipulation of endocytosis processes (Verma et al., 2017), inhibition of phagosome biogenesis (Desjardins and Descoteaux, 1997), etc. Altogether, suppression of many key pathways in the host is directly associated with the survival of the virulent parasites. Conversely, their activation is associated with the clearance of the non-virulent parasites.

Heat Maps Revealed Differential Expression Pattern in the KEGG Pathway-Associated DE Genes Modulated by Virulent and Non-virulent Parasites

Heat maps were generated to visualize the level of gene expression induced in the host macrophages by vAG83 and nvAG83. A color code was used to represent high and low levels

TABLE 3 | KEGG pathways enriched in DE genes in murine macrophages infected with vAG83.

Direction of regulation and KEGG pathway	Number of DE genes	Pathway size
KEGG PATHWAY, UPREGULATED		
Cytokine-cytokine receptor interaction	7	256
Immune system	6	877
Signal transduction	8	1,855
KEGG PATHWAY, DOWNREGULATED		
Adaptive Immune System	7	446
Disease	6	605
Endocytosis	6	216
Gene expression	7	703
Hemostasis	7	411
Immune system	14	877
Innate immune system	7	475
mRNA processing	6	451
Pathways in cancer	6	323
Phagosome	7	171
PI3K-Akt signaling pathway	6	348
Signal Transduction	8	1,855
XPodNet—protein-protein interactions in the podocyte expanded by STRING	13	827

KEGG pathway analysis was carried out to identify pathways related to immune response, signaling and metabolism etc., overrepresented in genes that constitute the mammalian response to vAG83 infection (P -value < 0.01) relative to uninfected controls. Genes that were differentially expressed (DE) by more than 2-fold were used as input with up- and down-regulated genes considered separately. Moreover, pathways filtered based count of DE genes expressed was considered for more than 5 genes. For each enriched KEGG pathway, the number of DE genes assigned to that pathway and the total number of genes in the pathway, are reported.

of expression of the individual genes. These maps were generated from only those genes which constituted the KEGG pathways. This allowed us to achieve a clear picture of how these parasites could produce a different host response, by inducing different levels of gene expression. It was found that vAG83 (Figure 5A) downregulated many genes with significant suppression in their level of expression. In contrast, genes downregulated by nvAG83 (Figure 5B) were smaller in number, with lower suppression compared to that shown by vAG83. Interestingly, a reversed phenomenon was observed for the upregulated genes induced by both the parasites. It was found that vAG83 (Figure 5C) upregulated a smaller number of genes and with a low level of expression. In contrast, nvAG83 (Figure 5D) upregulated many genes with a higher level of expression. Altogether, the heat map reveals that vAG83 and nvAG83 exhibit a differential impact on the number, as well as on the level, of host cell gene expression, which may underlie the differential outcome of the infection.

Differential Host Macrophage Response to Infection With vAG83 and nvAG83 Involved Biased Inflammatory and Anti-inflammatory Immune Response

Next, the biological functions of the KEGG pathway genes were analyzed, to understand how they could have modulated host

TABLE 4 | KEGG pathways enriched in DE genes in murine macrophages infected with nvAG83.

Direction of regulation and KEGG pathway	Number of DE genes	Pathway size
KEGG PATHWAY, UPREGULATED		
Adaptive immune system	13	446
Adipogenesis	7	133
B Cell receptor signaling pathway	8	156
Chagas disease (American trypanosomiasis)	6	103
Chemokine receptors bind chemokines	6	50
Chemokine signaling pathway	8	183
Class A/1 (Rhodopsin-like receptors)	9	282
Cytokine-cytokine receptor interaction	19	256
Cytokine signaling in immune system	7	192
Disease	7	605
Downstream signaling events of B cell receptor (BCR)	6	107
Extracellular matrix organization	6	226
Fc epsilon receptor (FCER1) signaling	6	154
GPCR ligand binding	10	391
Hematopoietic cell lineage	6	85
Hemostasis	10	411
HTLV-I infection	10	272
IL-2 signaling pathway	7	76
Immune system	20	877
Innate immune system	9	475
Jak-STAT signaling pathway	8	154
Malaria	6	46
Metabolism	7	1,368
NF-kappa B signaling pathway	8	97
Peptide ligand-binding receptors	8	180
PI3K-Akt signaling pathway	9	348
Rheumatoid arthritis	8	82
Signaling by GPCR	11	1,149
Signaling by SCF-KIT	7	124
Signaling by the B Cell Receptor (BCR)	8	133
Signal Transduction	23	1,855
TNF signaling pathway	6	109
Toll-like receptor signaling pathway	8	96
XPodNet—protein-protein interactions in the podocyte expanded by STRING	13	827
KEGG pathway, downregulated		
Focal adhesion	6	182
Hemostasis	8	411
Immune system	9	877
Metabolism	9	1,368
PI3K-Akt signaling pathway	8	348
Signal transduction	7	1,855
Transmembrane transport of small molecules	6	496
XPodNet—protein-protein interactions in the podocyte expanded by STRING	12	827

KEGG pathway analysis was carried out to identify pathways related to immune response, signaling and metabolism, etc., overrepresented in genes that constitute the mammalian response to nvAG83 infection (P -value < 0.01) relative to uninfected controls. Genes that were differentially expressed (DE) by more than 2-fold were used as input with up- and down-regulated genes considered separately. Moreover, pathways filtered based count of DE genes expressed was considered for more than 5 genes. For each enriched KEGG pathway, the number of DE genes assigned to that pathway and the total number of genes in the pathway are reported.

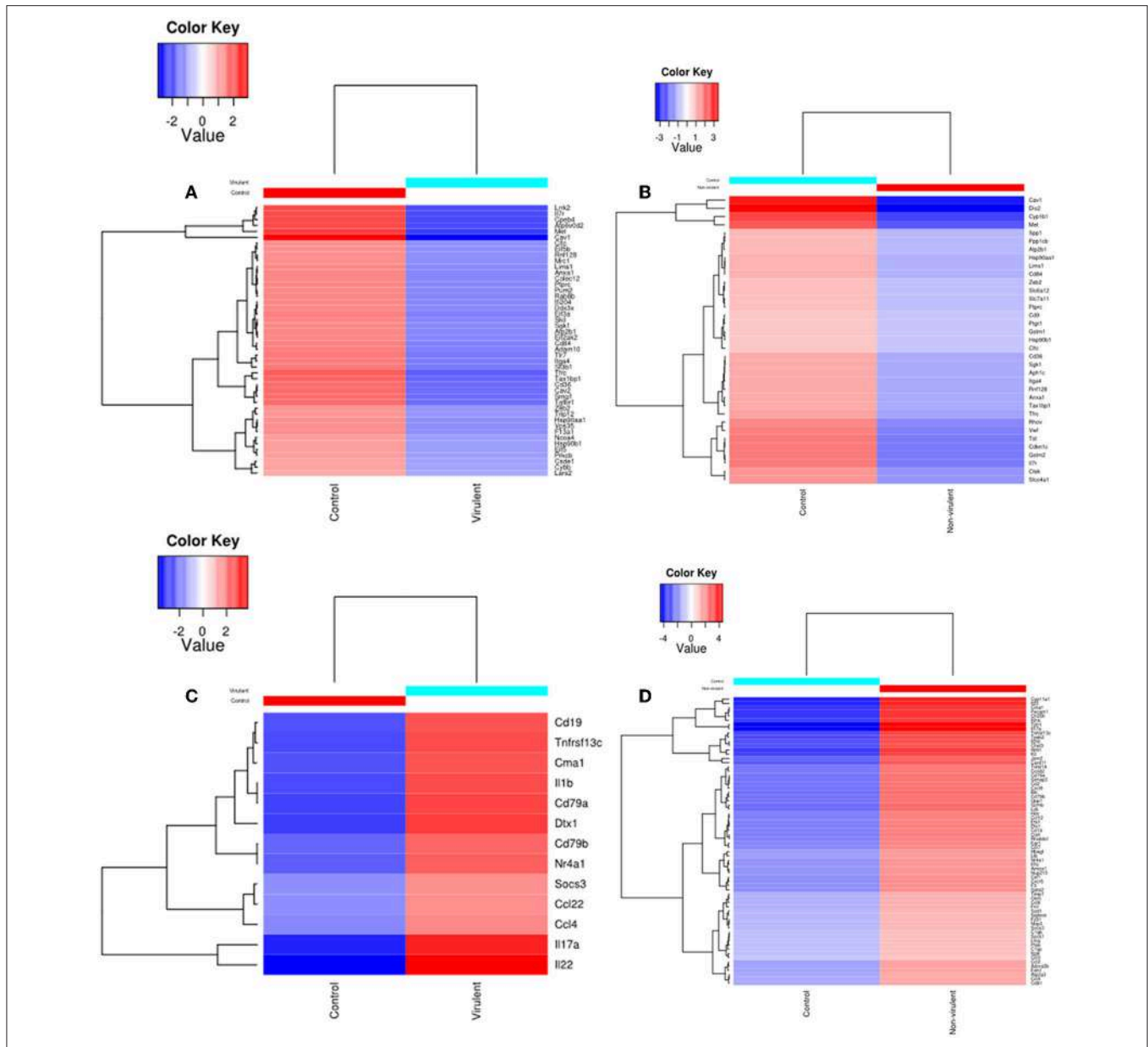


FIGURE 5 | Heat Map of DE genes in infected macrophage compared to control macrophage. The DE genes involved in KEGG pathways downregulated by (A) virulent and (B) non-virulent parasites are represented as heat maps. Similarly, the DE genes involved in KEGG pathways upregulated by (C) virulent and (D) Non-virulent parasites are represented.

cell responses that lead to parasite persistence or clearance (Supplementary Data Sheet 2). We first analyzed the functions of the upregulated genes and found that the host responses evoked by vAG83 and nvAG83 were paradoxical, with clearly biased anti-inflammatory and inflammatory immune responses, respectively. This is because the products of the encoded genes are those which are involved in either enhancing or suppressing the antimicrobial immune responses. For instance, vAG83, which upregulated few inflammatory genes including Il1b, Il17a, and Il22 (Faleiro et al., 2014), also upregulated genes with anti-inflammatory characters, including Ccl22, ccl12,

Socs3, and dtx1 (Teixeira et al., 2006). Similarly, nvAG83, in addition to upregulating many inflammatory genes, including Il1b, Il17a, Il22, Ccl2, Ccl3, Ccl4, Ccl12, Cxcl9, Il2ra, Il2rb, and Nlrp3 (Murray et al., 1993; Faleiro et al., 2014), also upregulated genes with anti-inflammatory properties, including Socs1, Socs3, Osm, and Hbegf (Bertholet et al., 2003). Thus, when we analyzed the functions of the downregulated genes, we found that vAG83 suppressed many genes, including Ifi204, Tlr7, Il7r, Nox-2, Eif2ak2, and Prkcb, which are known to be involved in inflammation, macrophage activation and respiratory burst (Nilsson et al., 2006; Shadab and Ali, 2011). However,

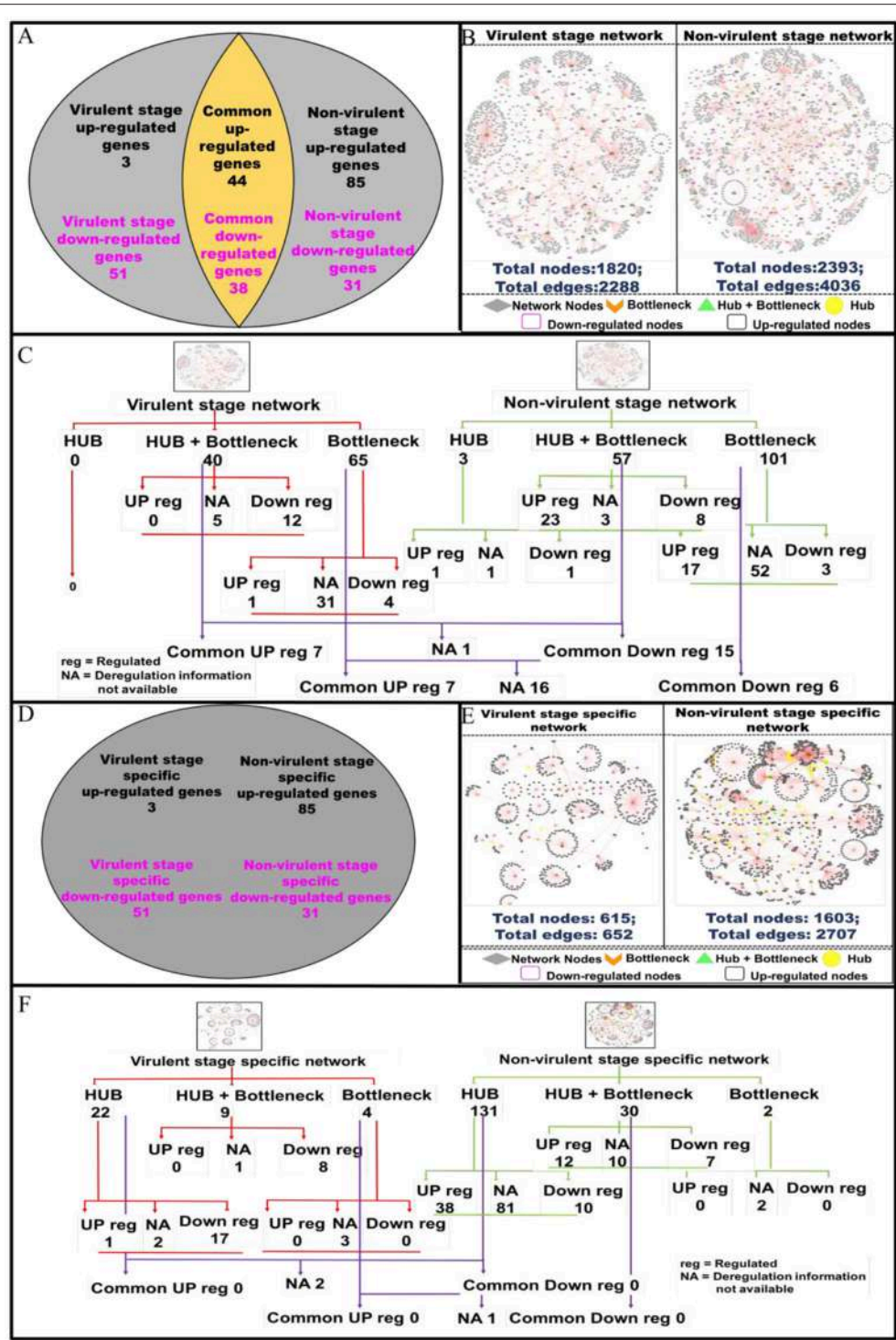


FIGURE 6 | Pictorial representation of the constructed protein-protein interaction network of the deregulated macrophage genes in virulent and non-virulent stages of *L. donovani* infection and analyzing the important nodes of the network. **(A)** Shows the expression status of macrophage genes during virulent and non-virulent stages of *L. donovani* infection, where 54 (3 up-regulated and 51 down-regulated) and 116 (85 up-regulated and 31 down-regulated) genes were found to be expressed during the virulent and non-virulent stages of infection and 82 genes were expressed commonly in both stages. **(B)** Depicts the representation of the constructed virulent and non-virulent protein-protein interaction network. **(C)** Shows the schematic representation of the important nodes of the network. **(D)** Provides the number stage specific deregulated murine macrophage genes at virulent and non-virulent *L. donovani* infection stages. **(E)** Represents the constructed protein-protein interaction network of stage-specific (virulent and non-virulent) deregulated genes. **(F)** Shows the schematic representation of the important network nodes from the stage-specific networks.

nvAG83 did not lead to downregulation of too many genes as was observed with vAG83. All these findings are consistent to previous reports, which showed that *Leishmania* parasites could exhibit a differential regulation of macrophage gene expression with mixed immune responses (Gregory et al., 2008). Moreover, they impart a potent and general suppression of macrophage gene expression to establish themselves in the host cells. However, in addition to these, we made an interesting observation that vAG83 downregulated some genes known to be negative regulators of anti-inflammation, like Adam10 (van der Vorst et al., 2015) and Skil (Massagué, 2012). Altogether, these findings indicated that vAG83 tries to maintain an anti-inflammatory environment in the host cells. However, nvAG83 induces an inflammatory environment. This may be the reason that vAG83 persists and nvAG83 gets eliminated in the host cells.

Modulations in Network Nodes Highlight Their Importance in Parasite Persistence and Clearance in the Host Macrophages

Protein-protein interactions (PPI) are essential to almost every process in a cell to maintain its homeostasis (Kuzmanov and Emili, 2013). The proteins involved in such interactions could be of diverse nature, based on their functions viz. enzymes, transcriptional regulators, etc. The complete map of protein interactions occurring in a living organism is called an interactome (De Las Rivas and Prieto, 2012). If the interactome is in any way perturbed, it could lead to alterations in the normal functioning of the cell. Thus, we evaluated how infection with vAG83 and nvAG83 affects host cell interactome by analyzing the macrophage genes that were expressed at $p < 0.01$ (Supplementary Data Sheet 3). These genes were modulated differently by the two parasites. It was found that 3 and 51 macrophage genes ($p < 0.01$) were up- and down-regulated by vAG83, respectively. However, 85 and 31 genes were up- and down-regulated by nvAG83 infection (Figure 6A), respectively. In addition, 44 and 38 common genes were up- and down-regulated respectively, by both parasites. To begin our analysis, we first constructed PPI networks from the total genes, modulated by each of the parasites. We found that the virulent-stage PPI network (VS_PPIN), derived from STRING database, consisted of 2288 interactions with 1820 proteins nodes, whereas the non-virulent-stage PPI network (NVS_PPIN) consisted of 4036 interactions with 2,393 protein nodes (Figure 6B). Based on the graph theory approach, using a topology-based scoring method, important network nodes like hubs and bottlenecks were identified (Figure 6C). “Hubs” are sets of interactive nodes of the network that have a significantly higher amount of connectivity within the network compared to other network nodes (Pang et al., 2016). “Bottlenecks” are network nodes with high betweenness centrality and are key connectors of the sub-networks, thus maintaining the network architecture (McDermott et al., 2009). “Hub-bottlenecks” are the bottlenecks that tend to have high connectivity (Yu et al., 2007). Hub analysis showed that while no hub was found in the virulent-stage network, 3 were found in the non-virulent-stage network. Out of the 3 non-virulent-stage hubs, 1 was downregulated

and 1 was upregulated. Interestingly, 40 hub-bottlenecks for the virulent and 57 for the non-virulent stages were found. Overlap of the hub, hub-bottlenecks and bottleneck proteins, identified for virulent and non-virulent stages, are shown in Figure 6C. Overall, the downregulation of many hub-bottlenecks and bottlenecks in macrophages infected with vAG83, indicates a huge collapse in the protein interaction network, restoration of which could otherwise have activated these cells to fight against infection. Meanwhile, in nvAG83-infected macrophages, the upregulation of many hub-bottlenecks and bottlenecks indicates that the overall interactome gets facilitated significantly. This may have activated the host cells to clear off the parasites. Previous study on the responses of macrophages to virulent and attenuated *Mycobacterium bovis* also showed that these two parasites differentially modulate hub and bottleneck genes in the host cells (Killick et al., 2014). We therefore constructed networks based on unique genes, modulated by each of the parasites (Figure 6D). The virulent-stage-specific PPI network (VSP_PPIN) was found to contain 652 interactions comprised of 615 nodes, whereas the non-virulent-stage-specific PPI network (NVSP_PPIN) contained 2,707 interactions, formed by 1,603 nodes (Figure 6E). Figure 6F shows the overlap of the hub, hub-bottlenecks, and bottleneck proteins identified for virulent- and non-virulent-stage-specific networks. Here also, we observed a relatively higher number of downregulated hubs and hub-bottlenecks in the virulent stage network, with upregulation of many hubs and hub-bottlenecks in the non-virulent stage specific network.

Functional and pathway information regarding the deregulated important network proteins are also provided in (Supplementary Data Sheet 4). Molecular function annotation of the virulent-stage-specific important proteins indicates their probable involvement in cytoskeleton structural activity, transcription factor binding, regulation of the RIG-I signaling pathway, membrane trafficking, etc. Further, non-virulent-stage-specific proteins are known to be involved in Wnt-protein binding activity, response to interferon-gamma, inflammatory response, cytokine activity, CXCR3 chemokine receptor binding, CD4 and CD8 receptor binding and CARD domain binding activities. (Supplementary Data Sheet 5). Previous studies have shown that *Leishmania* parasites manipulate actin cytoskeleton (Roy et al., 2014), membrane trafficking (Matte and Descoteaux, 2016), and pathogen-associated molecular pattern signaling, including RIG-I-like receptor signaling (Fernandes et al., 2016), to establish infection in the host cells. However, activation of the inflammatory signals like interferon-gamma (Kima and Soong, 2013), Wnt5a (Chakraborty et al., 2017), and CXCR3 chemokine receptor signaling (Murray et al., 2017), were shown to resist *Leishmania* infection. Altogether, vAG83 significantly downregulated the network nodes, which may help the parasites to evade the host cell’s anti-leishmanial immune responses. On the contrary, nvAG83 significantly upregulated the network nodes, which may have activated the host macrophages to kill the parasites.

We next evaluated the modulation in the protein network nodes, which have the highest degree of connectivity (DOC). For this, we analyzed the expression of the top 30 network nodes regulated by vAG83 and nvAG83 (Supplementary Figure 2).

Interestingly, vAG83 downregulated many such nodes (25 of 30) compared to nvAG83 (16 of 30). In contrast, nvAG83 upregulated many of the nodes (14 of 30) compared to vAG83 (5 of 30). Together, this suggests that vAG83 not only hampered the physiological expression, but also decreased the number of interactions by downregulating many network proteins, including hub and bottlenecks (Anax1, Hsp90aa1, Psme4, Sf3b1, Smg1, Cav1, Cd36, Hsp90b1, Cybb, Adam10, etc.), leading to the deactivation of the host cells. Conversely, nvAG83 not only upregulated the expression, but also increased the number of interactions by upregulating many network proteins, including hub and bottlenecks (Ccl6, Cxcr5, Edn1, Timp, Kit, etc.), resulting in activation of the host cells.

vAG83 and nvAG83 Differentially Activated MAPK and PI3K Signaling in the Host Macrophages

It is well known that the activation of a specific signaling pathway triggers specific sets of gene expression in the cells (Sweeney et al., 2001). In the context of *L. donovani* infection, previous studies have reported that the host cell's signaling is activated in such a way that it allows parasite survival in the host macrophages (Shadab and Ali, 2011). In this study, since we found that vAG83 and nvAG83 induced differential gene expression, we evaluated how these parasites could have manipulated signaling in the host cells. We studied mainly the MAPK and PI3K signaling pathways, whose role in *Leishmania* infection has been reported earlier (Junghae and Raynes, 2002). Through western blot analysis using a specific Ab for phosphorylated form of P38, we showed that vAG83 induced a mild activation of p38 MAPK in the host macrophages as compared to the uninfected control (Figures 7A,A1). In contrast, nvAG83 induced a sustained activation up to 60 min post-infection (p.i.) (Figures 7B,B1). As a positive control, macrophages were stimulated with LPS for 30 min. Studying ERK1/2 MAPK showed that the vAG83 induced ERK1/2 activation in the host macrophages at 30 min p.i., which was enhanced further at 60 min of infection, compared to the uninfected control (Figures 7C,C1). In contrast, nvAG83 induced mild activation of ERK1/2, which remained so until 60 min p.i. (Figures 7D,D1). When we measured the phosphorylation of AKT at Ser473, we found that vAG83 initially induced low activation of AKT (ser 437) as early as 15 min p.i., which increased further at 60 min of infection as compared to the uninfected control (Figures 7E,E1). In contrast, nvAG83 induced AKT (ser 437) activation, which peaked at 30 min p.i. but diminished later on at 60 min of infection (Figures 7F,F1). Similar to murine peritoneal macrophages, BMM were infected with vAG83 and nvAG83 to check if a similar phenomenon was occurring in both the macrophage systems. We found that vAG83 induced P38 activation in the host macrophages until 60 min p.i., which diminished later at 180 min p.i. compared to the uninfected control. However, nvAG83 maintained P38 activation even at 180 min p.i. (Figures 7G,G1). A marked difference in the activation of ERK1/2 MAPK and AKT was observed. vAG83 induced ERK1/2 activation in the host macrophages, which progressively increased, peaking at 180 min p.i. compared

to the uninfected cell. In contrast, nvAG83 induced mild activation of ERK1/2 that remained active until 180 min p.i. (Figures 7G,G2). Similarly, vAG83 induced AKT activation as early as 30 min p.i. that remained active until 180 min of infection. In contrast, nvAG83, though inducing AKT activation at 30 min p.i., diminished progressively until 180 min of infection (Figures 7H,H1). Taken together, these results suggest that the two parasites differentially activated MAPK (P38 and ERK1/2) and PI3K signaling both in peritoneal macrophages and BMM, with a similar trend of activation. Interestingly, this differential activation is not linked to an opposite phenomenon of activation and deactivation by the two parasites, but it entails a temporal regulation of the same repertoire of signaling proteins. It has been reported earlier that spatiotemporal activation profiles of the same repertoire of signaling proteins exhibit different gene expression patterns and diverse physiological responses in a cell (Kholodenko, 2006). Hence, the additional time for which a particular kinase remained active before its dephosphorylation seems to produce significant difference in the host cell's gene expression.

The role of ERK1/2 and P38 MAPK in differentially regulating gene expression has been documented previously. It has been shown that ERK1/2 negatively regulates, whereas P38 MAPK positively regulates gene expression (Carter and Hunninghake, 2000). Our finding that vAG83 rather than nvAG83 induced higher activation of ERK1/2 over P38 MAPK indicates a probable strategy employed by the virulent parasite to negatively regulate gene expression and dampen host immune response. Activation of AKT by the virulent *L. donovani* parasite has been shown to inhibit host cell apoptosis (Gupta et al., 2016). Our observation that vAG83 rather than nvAG83 induced higher and sustained activation of AKT in the host cells indicates additional ways of evading host immune responses by the virulent parasites. Why the two parasites impart a differential activation of MAPK and PI3K signaling is not yet clear. There have been reports that the difference in the virulence factors, including cell surface molecules, leads to difference in infectivity of the *Leishmania* parasites (Descoteaux and Turco, 1999). With long-term culture, modifications in nvAG83 (Sinha et al., 2018) which could have triggered different signaling patterns in the host macrophages. Overall, the manipulation of host cell gene expression through specific modulation of MAPK and PI3K signaling by vAG83 and nvAG83 seems to play an important role in the survival or clearance of these parasites in the host cell.

The observation that BMM, as compared to peritoneal macrophages, manifested longer MAPK, and PI3K activation profiles, is not well understood. The peritoneal resident macrophages are un-manipulated cells (Zhang et al., 2008), whereas the bone marrow-derived macrophages are differentiated mature macrophages, which are achieved after differentiating the progenitor cells by adding macrophage colony-stimulating factor (M-CSF) (Austin et al., 1971). Hence, a small disparity in these two macrophage systems can occur which may lead to such difference. Future study can unveil the importance of such difference in *Leishmania* infection, as many

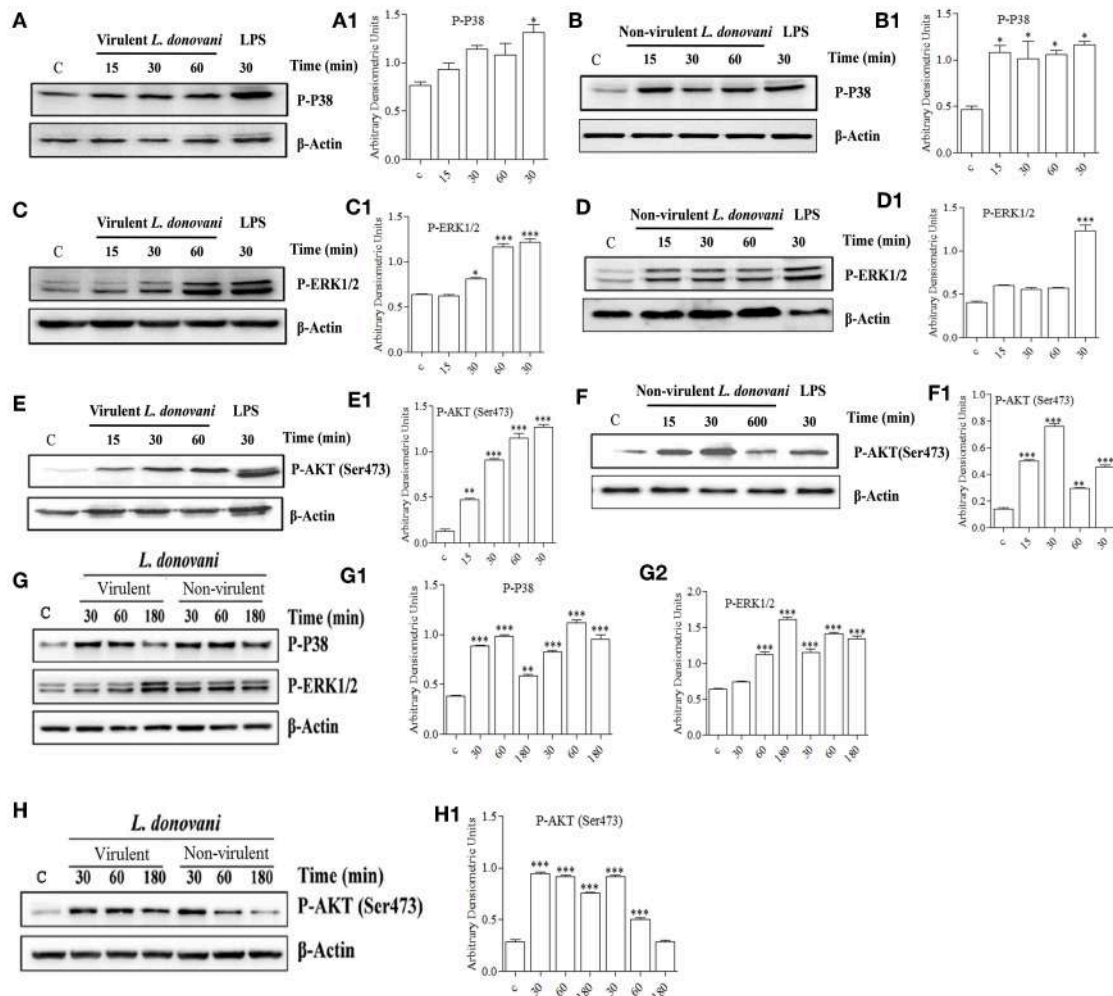


FIGURE 7 | Effect of *L. donovani* infection on MAPK and PI3K activation. Peritoneal macrophages were exposed to virulent and non-virulent *L. donovani* promastigotes for various times as indicated. LPS-treated macrophages were taken as a positive control and non-treated macrophages were taken as a negative control. Whole-cell lysates were prepared and subjected to western blotting using antibodies specific for **(A,A1,B,B1)** phospho-P38 MAPK, **(C,C1,D,D1)** phospho-ERK1/2 MAPK, and **(E,E1,F,F1)** phospho-AKT (ser473). Similarly, cell lysates of BMM exposed to virulent and non-virulent *L. donovani* promastigotes for various times as indicated were probed for **(G,G1,G2)** phospho-P38 MAPK and phospho-ERK1/2 MAPK, **(H)** phospho-AKT (ser473). β -actin was used as loading control for all the blots as described in materials and methods. The figures are representative of 2 independent experiments. Bands were analyzed densitometrically and bar graphs expressing arbitrary units are presented adjacent to corresponding western blots. Error bar represent mean \pm S.D., $n = 2$. * $P < 0.01$, ** $P < 0.001$, *** $P < 0.0001$.

sites including bone marrow, liver and spleen, have been shown to be infected with the parasites (Sinha et al., 2015).

Differentially Expressed *L. donovani* Genes and Gene Ontology-Based Enrichment Analyses for vAG83 and nvAG83 When They Are in the Host Cells

Differential gene expression analyses were carried out for the parasite-specific genes to determine how the expression of the same genes is regulated in the two parasites. It was found that 96 genes were DE between the intracellular amastigotes of vAG83 and nvAG83 at a p value cutoff of <0.05 , which reflected a differential modulation, occurring in these parasites, as they

enter the host cells (**Supplementary Data Sheet 6**). Reasons for not getting a large number of the DE genes could be due to factors including the number of reads, generated for the samples (Mortazavi et al., 2008), the expression level of the genes at this time point of infection, etc. Since these 96 genes were enriched at a lower cutoff value, the functional importance of the genes that showed up beyond this cutoff (data not shown) cannot be denied, and it could modulate parasite responses. Of the DE genes mentioned here, we found $\sim 60\%$ were upregulated and $\sim 40\%$ were downregulated in the amastigotes of vAG83 compared to the nvAG83 (**Figure 2B**). Moreover, we found that out of all these genes, $\sim 49\%$ (47 of 96) are with uncharacterized function. These hypothetical genes thus constitute a significant portion of the transcriptomic signature of the intracellular amastigotes

of *L. donovani* parasites. Future study toward unveiling their function could allow better understanding of their role in the parasites. Moreover, this could boost further the effort in identification of key drug targets, with the possibility that these DE genes might be an integral part of various machineries, operating in the parasites, which are required for their survival.

Next, to evaluate the probable effects of the DE genes on the intracellular amastigotes of the parasites, we performed gene ontology (GO) analysis of these DE genes (Supplementary Data Sheet 7). GO analysis of the up- and down-regulated genes revealed a total of 27 enriched GO categories (Table 5). Of these, 16 GO categories were found to be upregulated in the amastigotes of vAG83 compared to nvAG83. In vAG83, the enriched GO terms (for the upregulated genes) were primarily those that relate to virulence and the survival factors of the parasites. The genes, for example receptor-adenylate cyclases, calpain-like cysteine peptidase, protein kinase, protein kinase-like protein, serine/threonine-protein kinase and mitogen-activated protein kinase, contributed strongly to the GO enrichment results for these parasites (Supplementary Data Sheet 8). Interestingly, these genes were found to be downregulated significantly in nvAG83. The role of receptor-adenylate cyclase in the intracellular amastigotes of *Leishmania* parasites is not known. But in other parasites like *Trypanosoma brucei*, adenylate cyclase is known to inhibit innate immune response of the host (Salmon et al., 2012). Though cysteine peptidase—with higher activity in the intracellular amastigotes compared to the promastigotes of *Leishmania* (Mottram et al., 2004)—is reported, the role of cysteine peptidase with calpain domains is yet to be determined. But in higher eukaryotes, calpains play important roles in calcium-regulated functions such as signal transduction and cell differentiation (Besteiro et al., 2007), indicating that they may have some key roles in the *Leishmania* parasites. Several protein kinases, like CRK3 of the CMGC family and MAPK, have been shown to have essential roles in the proliferation and/or the viability of the *Leishmania* parasites (Naula et al., 2005). Hence, pharmacological inhibition and gene disruption of CRK3 and MAPK, respectively, showed inhibition in the growth and replication of *L. donovani* amastigotes in infected macrophages (Wiese, 1998). Altogether, it indicates that the higher expression of these genes in vAG83 is likely to play a key role in the survival of the parasites in the host cells.

Some other genes that were upregulated in the intracellular amastigotes of vAG83 are those that relate to translation machinery, including RNA-binding protein, polyadenylate-binding protein (PABP), ATP-dependent RNA helicase, etc., and protein folding, including Chaperonin HSP60, mitochondrial. This indicates that the protein synthesis in the amastigotes of the virulent parasites is regulated in such a way that may help them to survive and multiply in the host macrophages. Conversely, their downregulation in the non-virulent parasites appears to hamper the production of survival factors that may lead to their clearance.

We found that some of the upregulated GO categories enriched in the intracellular amastigotes of vAG83, as compared to nvAG83, were those that relate to metabolic processes and activities, such as NAD biosynthetic

TABLE 5 | Gene ontology (GO) categories enriched across virulent to non-virulent *L. donovani* intracellular stages.

GO ID	Go term	P-value
UPREGULATED GO TERM IN VIRULENT PARASITE COMPARED TO NON-VIRULENT PARASITE		
GO:0005524	MF ATP binding	0.003015992
GO:0004514	MF nicotinate-nucleotide diphosphorylase (carboxylating) activity	0.008264463
GO:0004516	MF nicotinate phosphoribosyltransferase activity	0.008264463
GO:0004657	MF proline dehydrogenase activity	0.008264463
GO:0006562	BP proline catabolic process	0.008264463
GO:0009678	MF hydrogen-translocating pyrophosphatase activity	0.008264463
GO:0019357	BP nicotinate nucleotide biosynthetic process	0.008264463
GO:0004198	MF calcium-dependent cysteine-type endopeptidase activity	0.011468442
GO:0005215	MF transporter activity	0.013800439
GO:0015992	BP proton transport	0.016462677
GO:0004427	MF inorganic diphosphatase activity	0.024595158
GO:0009435	BP NAD biosynthetic process	0.024595158
GO:0004672	MF protein kinase activity	0.030803132
GO:0042026	BP protein refolding	0.032662417
GO:0000166	MF nucleotide binding	0.041422298
GO:0004674	MF protein serine/threonine kinase activity	0.048451125
DOWNREGULATED GO TERM IN VIRULENT PARASITE COMPARED TO NON-VIRULENT PARASITE		
GO:0051920	MF peroxiredoxin activity	0.000103507
GO:0004601	MF peroxidase activity	0.000342495
GO:0017061	MF S-methyl-5-thioadenosine phosphorylase activity	0.006010518
GO:0004140	MF dephospho-CoA kinase activity	0.011986407
GO:0015937	BP coenzyme A biosynthetic process	0.017927857
GO:0050708	BP regulation of protein secretion	0.017927857
GO:0004402	MF histone acetyltransferase activity	0.023835058
GO:0006414	BP translational elongation	0.023835058
GO:0009116	BP nucleoside metabolic process	0.029708199
GO:0005643	CC nuclear pore	0.035547467
GO:0019843	MF rRNA binding	0.041353051

GOseq was used to identify enriched GO categories between the virulent and non-virulent intracellular amastigotes at a p-value cutoff of <0.05. For the difference between both the parasites, up- and down-regulated genes were considered separately. The category for each enriched GO term is indicated (BP, biological process; MF, molecular function; CC, cellular component).

process, nicotinate nucleotide biosynthetic process, nicotinate phosphoribosyltransferase activity, nicotinate-nucleotide diphosphorylase (carboxylating) activity, proline catabolic process and proline dehydrogenase activity. The genes involved in these processes, including nicotinate phosphoribosyltransferase and proline oxidase, were found to be significantly upregulated. Though the role of these genes in *Leishmania* is not yet known, previous studies have highlighted a major role for NAD⁺ metabolism in the interactions between different pathogens and their host by directly affecting intracellular replication (Kim et al., 2004),

virulence expression (Domergue et al., 2005), or pathogen dissemination (Ma et al., 2007). Similarly, proline oxidase, which catalyzes L-proline oxidation to glutamate (Paes et al., 2013) in addition to contributing to the cellular energy supply, plays an important role in the intracellular redox homeostasis and in defense mechanisms against various abiotic and biotic stresses, thus benefiting a broad range of organisms (Ayliffe et al., 2005). Altogether, it thus appears that the host-pathogen interaction, in addition to potentiating metabolic processes in the virulent parasites, also seems to bestow upon them strategies to resist oxidative stress. This, in turn, may allow them to survive and proliferate unrestrictedly in the host cells.

The genes, whose encoded products are known to be involved in transporter activity, proton transport and hydrogen-translocating pyrophosphatase activity, were also upregulated in vAG83. These include ABC1, ABC3, and PPase1. The ABC transporters related to the ABCA, ABCB, ABCC, and ABCG subfamilies have been described in *Leishmania* (Castanys-Muñoz et al., 2008). In fact, ABCC family transporters including MRPA were previously shown to be involved in antimony resistance (Moreira et al., 2013). Moreover, the resistance mechanisms involving increased MRPA expression in the clinical isolates of kala azar were previously implicated (Mukherjee et al., 2007). However, the role of H⁺-PPases in *Leishmania* parasites is not yet known and could be explored in future. Altogether, it appears that the significant upregulation of these genes in the virulent amastigotes is associated with the defense mechanism in the parasites, against the host.

GO terms that were enriched among downregulated genes in virulent amastigotes but upregulated in the non-virulent ones, were mainly related to translation, transcriptional regulation, metabolism and oxidative stress. The product of the DE genes associated with these processes includes 60S acidic ribosomal protein P2, Histone acetyltransferase, Methylthioadenosine phosphorylase, Tryparedoxin peroxidase, etc. Acidic ribosomal protein P2 has been described as a prominent antigen in leishmaniasis. The ribosomal protein P2 from *Leishmania* spp. has in fact been shown to be immunostimulatory (Soto et al., 1995). We also found ribosomal protein S4, a component of the 40S subunit of ribosome, to be significantly upregulated in the amastigotes of nvAG83. Though its role in *Leishmania* parasites is not well understood, yeast Asc1p and mammalian RACK1, which are functionally orthologous core 40S ribosomal proteins, are known to repress gene expression (Gerbasi et al., 2004). A similar function was reported for some other proteins, such as two MYST proteins—Sas2 and Sas3 (Histone Acetyltransferase)—that exhibit transcriptional silencing in *S. cerevisiae* (Sterner and Berger, 2000). Intriguingly, the expression of the putative MOZ/SAS family acetyltransferase was significantly upregulated in the intracellular amastigotes of nvAG83 compared to vAG83. Thus, it reveals that the host-parasite interaction-dependent modulation of the transcriptional regulators in the parasites is vital to the survival of these pathogens in the host cells.

In order to metabolize exogenous and endogenous peroxides, distinct cytosolic and mitochondrial tryparedoxin peroxidases (TXNPx) are present in *Leishmania* as well as *Trypanosomes*. However, some other antioxidant systems, including superoxide

dismutases and low-molecular weight thiols, are also present in these organisms (Van Assche et al., 2011). We found that the expression of tryparedoxin peroxidases was upregulated in nvAG83 compared to vAG83. This reflects the fact that despite its higher expression, due to the other factors including loss of virulence, nvAG83 parasites get eliminated by the host cells. Moreover, though earlier studies have shown tryparedoxin peroxidases to overcome oxidative stress when virulent promastigotes enter macrophages (Dillon et al., 2015), the role of other antioxidant systems—including low-molecular weight thiols—should not be denied, which may help virulent parasites to persist within the host cells (Mitra, 2015). Besides tryparedoxin peroxidases, we found that the expression of S-methyl-5'-thioadenosine phosphorylase, MTAP, was also significantly upregulated in the amastigotes of nvAG83 compared to vAG83. MTAP catalyzes the breakdown of S-methyl-5'-thioadenosine (MTA), a major byproduct of polyamine biosynthesis, to adenine and 5-methylthioribose-1-phosphate. Though the role of this gene in *Leishmania* infection is not known, in human cancers including osteosarcoma, malignant melanoma and gastric cancer, MTAP activity acts as a negative regulator of cancer (Miyazaki et al., 2007). Thus, it could be that the upregulated expression of MTA in nvAG83 is a negative feedback mechanism to restrict survival and multiplication of the parasites in the host cells, a supposition that can be explored in future study.

CONCLUSION

This study provided a global gene expression pattern of both the host and the parasite, depicting a broad and clear picture of how the changes occurring in these interacting organisms are crucial in determining the final fate of either parasite persistence or clearance. Moreover, this study unraveled many unknown molecules that are associated with these two conditions. This work thus provided valuable information that could serve as a public resource for future efforts toward developing effective anti-leishmanial interventions.

ETHICS STATEMENT

The study was approved by and carried out under the guidelines of the Ethical Committee of the Indian Institute of Chemical Biology, Kolkata. All subjects who participated in this study provided informed consent in writing according to the Indian Institute of Chemical Biology guidelines and approval. The animal experiments were approved by the Animal Ethical Committee (147/1999/CPSCEA) of the institute, according to the National Regulatory Guidelines issued by the Committee for the Purpose of Control and Supervision on Experimental Animals (CPCSEA), under the Division of Animal Welfare, Ministry of Environment and Forest, Government of India.

AUTHOR CONTRIBUTIONS

MS, SD, RS, NA, and SC conceived and designed the experiments. MS, RS, SD, MD, and BJ performed the experiments. MS, RS, AB,

SC, NA, SD, MA, MM, MK, AT, MKu, and BK analyzed the data. MS, RS, AB, BJ, SK, and NA wrote the paper.

FUNDING

This work was funded by Council of Scientific and Industrial Research (CSIR) Government of India network project BSC0114. MS, AB, RS, MM, and SD received the fellowships from CSIR. MK and MA received the fellowships from ICMR.

ACKNOWLEDGMENTS

We gratefully acknowledge the help of Mohd. Shameel Iqbal and Richa Shrivastav for the real-time PCR study. We are also grateful to Dr. Sucheta Tripathy, Subhadeep Das, Abdus Sabur, and Manjarika De for discussion on the manuscript. We are thankful to Amy Jasani for improving manuscript writing. We thank Dr. Samit Chattopadhyay, Director IICB, for supporting this work.

SUPPLEMENTARY MATERIAL

The Supplementary Material for this article can be found online at: <https://www.frontiersin.org/articles/10.3389/fcimb.2019.00017/full#supplementary-material>

Supplementary Figure 1 | Bioinformatics Analysis Workflow. Step-by-step bioinformatics analysis was done for the reads generated for each of the three samples.

Supplementary Figure 2 | Top gene nodes that displayed the highest DOC with their expression pattern. **(A)** Top 30 gene nodes modulated by virulent parasite with highest DOC and their level of expression represented as log₂ fold change. **(B)** Top 30 gene nodes modulated by non-virulent parasite with highest DOC and their level of expression represented as log₂ fold change.

Supplementary Table 1 | Raw data statistics.

Supplementary Table 2 | Clean data statistics.

Supplementary Table 3 | Alignment Statistics. Read alignment to *Mus musculus* genome.

Supplementary Table 4 | Alignment Statistics. Read alignment to *Leishmania donovani* genome.

REFERENCES

- Ambardar, S., Gupta, R., Trakroo, D., Lal, R., and Vakhlu, J. (2016). High throughput sequencing: an overview of sequencing chemistry. *Indian J Microbiol.* 56, 394–404. doi: 10.1007/s12088-016-0606-4
- Austin, P. E., McCulloch, E. A., and Till, J. E. (1971). Characterization of the factor in L-cell conditioned medium capable of stimulating colony formation by mouse marrow cells in culture. *J. Cell Physiol.* 77, 121–134. doi: 10.1002/jcp.1040770202
- Ayliffe, M. A., Mitchell, H. J., Deuschle, K., and Pryor, A. J. (2005). Comparative analysis in cereals of a key proline catabolism gene. *Mol. Genet. Genomics* 274, 494–505. doi: 10.1007/s00438-005-0048-x
- Banerjee, A., De, M., and Ali, N. (2008). Complete cure of experimental visceral leishmaniasis with amphotericin B in stearylamine-bearing cationic liposomes

Supplementary Table 5 | Primer sequences used for real-time PCR. Primers for the respective genes were designed using Input3 primer design software and validated using IdT oligoanalyser software and blast software.

Supplementary Data Sheet 1 | Gene list for the DE genes in murine macrophage infected with **(A)** virulent and **(B)** non-virulent *L. donovani* parasites. In infected macrophages compared to uninfected control, genes that were differentially expressed (DE) at a *P*-value < 0.05 were used as input with up- and down-regulated genes considered separately.

Supplementary Data Sheet 2 | List of DE genes constituting the KEGG pathways enriched in murine macrophages infected with **(A)** virulent and **(B)** non-virulent *L. donovani*. In infected macrophages compared to uninfected control, genes that were differentially expressed (DE) by more than 2-fold at a *P*-value < 0.01 were used as input with up- and down-regulated genes considered separately.

Supplementary Data Sheet 3 | List of DE genes in murine macrophage infected with virulent and non-virulent *L. donovani* parasites. In infected macrophage compared to uninfected control, genes that were differentially expressed (DE) at a *P*-value < 0.01, were used as input with up- and down-regulated genes considered separately. The unique genes modulated by **(A)** virulent and **(B)** Non-virulent and **(C)** common downregulated, **(D)** common upregulated genes were listed separately.

Supplementary Data Sheet 4 | Pathways, molecular functions and cellular functions of important protein network nodes modulated by each of the parasites. List of Hub and Bottleneck, Bottleneck constructed from Virulent and Non-virulent *L. donovani* infected macrophage genes with their involvement in different pathways, having specific molecular functions and their impact on cellular function including pathogenesis.

Supplementary Data Sheet 5 | Pathways, molecular functions and cellular functions of important protein network nodes modulated by each of the parasites. List of Hub-Bottleneck, Hub constructed from Virulent and Non-virulent *L. donovani* infected macrophage genes with their involvement in different pathways, having specific molecular functions and their impact on cellular function including pathogenesis.

Supplementary Data Sheet 6 | Gene list for the DE genes in *L. donovani* parasites. In virulent parasite compared to the non-virulent ones, genes that were differentially expressed (DE) at a *P*-value < 0.05, were used as input with up- and down-regulated genes considered separately.

Supplementary Data Sheet 7 | Gene ontology for the DE genes in *L. donovani* parasites. In virulent parasite compared to the non-virulent ones, gene ontology analysis of the DE genes at a *P*-value < 0.05, was done to elucidate their probable functions in host macrophage.

Supplementary Data Sheet 8 | The DE genes enriched for each GO term in *L. donovani* parasites. In virulent parasites compared to the non-virulent ones, genes that were differentially expressed at a *P*-value < 0.05, were searched for their enrichment in the GO terms to elucidate their probable functions in host macrophage.

- involves down-regulation of IL-10 and favorable T cell responses. *J. Immunol.* 181, 1386–1398. doi: 10.4049/jimmunol.181.2.1386
- Bertholet, S., Dickensheets, H. L., Sheikh, F., Gam, A. A., Donnelly, R. P., and Kenney, R. T. (2003). *Leishmania donovani*-induced expression of suppressor of cytokine signaling 3 in human macrophages: a novel mechanism for intracellular parasite suppression of activation. *Infect. Immun.* 71, 2095–2101. doi: 10.1128/IAI.71.4.2095-2101.2003
- Besteiro, S., Williams, R. A., Coombs, G. H., and Mottram, J. C. (2007). Protein turnover and differentiation in *Leishmania*. *Int. J. Parasitol.* 37, 1063–1075. doi: 10.1016/j.ijpara.2007.03.008
- Bhattacharya, P., Dey, R., Dagur, P. K., Kruhlak, M., Ismail, N., Debrabant, A., et al. (2015). Genetically modified live attenuated *Leishmania donovani* parasites induce innate immunity through classical activation of macrophages that direct the th1 response in mice. *Infect. Immun.* 83, 3800–3815. doi: 10.1128/IAI.00184-15

- Buates, S., and Matlashewski, G. (2001). General suppression of macrophage gene expression during *Leishmania donovani* infection. *J. Immunol.* 166, 3416–3422. doi: 10.4049/jimmunol.166.5.3416
- Carter, A. B., and Hunninghake, G. W. (2000). A constitutive active MEK → ERK pathway negatively regulates NF- κ B-dependent gene expression by modulating TATA-binding protein phosphorylation. *J. Biol. Chem.* 275, 27858–27864. doi: 10.1074/jbc.M003599200
- Castanys-Muñoz, E., Pérez-Victoria, J. M., Gamarro, F., and Castanys, S. (2008). Characterization of an ABCG-like transporter from the protozoan parasite *Leishmania* with a role in drug resistance and transbilayer lipid movement. *Antimicrob. Agents Chemother.* 52, 3573–3579. doi: 10.1128/AAC.00587-08
- Chakrabarty, R., Mukherjee, S., Lu, H. G., McGwire, B. S., Chang, K. P., and Basu, M. K. (1996). Kinetics of entry of virulent and avirulent strains of *Leishmania donovani* into macrophages: a possible role of virulence molecules (gp63 and LPG). *J. Parasitol.* 82, 632–635. doi: 10.2307/3283790
- Chakraborty, A., Kurati, S. P., Mahata, S. K., Sundar, S., Roy, S., and Sen, M. (2017). Wnt5a signaling promotes host defense against *Leishmania donovani* infection. *J. Immunol.* 199, 992–1002. doi: 10.4049/jimmunol.1601927
- De Las Rivas, J., and Prieto, C. (2012). Protein interactions: mapping interactome networks to support drug target discovery and selection. *Methods Mol. Biol.* 910, 279–296. doi: 10.1007/978-1-61779-965-5_12
- Descoteaux, A., and Turco, S. J. (1999). Glycoconjugates in *Leishmania* infectivity. *Biochim. Biophys. Acta Mol. Basis Dis.* 1455, 341–352. doi: 10.1016/S0925-4439(99)00065-4
- Desjardins, M., and Descoteaux, A. (1997). Inhibition of phagolysosomal biogenesis by the *Leishmania lipophosphoglycan*. *J. Exp. Med.* 185, 2061–2068. doi: 10.1084/jem.185.12.2061
- Dillon, L. A., Suresh, R., Okrah, K., Corrada Bravo, H., Mosser, D. M., and El-Sayed, N. M. (2015). Simultaneous transcriptional profiling of *Leishmania* major and its murine macrophage host cell reveals insights into host-pathogen interactions. *BMC Genomics* 16:1108. doi: 10.1186/s12864-015-2237-2
- Dobin, A., Davis, C. A., Schlesinger, F., Drenkow, J., Zaleski, C., Jha, S., et al. (2013). STAR: ultrafast universal RNA-seq aligner. *Bioinformatics* 29, 15–21. doi: 10.1093/bioinformatics/bts635
- Domergue, R., Castaño, I., De Las Peñas, A., Zupancic, M., Lockatell, V., Hebel, J. R., et al. (2005). Nicotinic acid limitation regulates silencing of *Candida* adhesins during UTI. *Science* 308, 866–870. doi: 10.1126/science.1108640
- Faleiro, R. J., Kumar, R., Hafner, L. M., and Engwerda, C. R. (2014). Immune regulation during chronic visceral leishmaniasis. *PLoS Negl. Trop. Dis.* 8:e2914. doi: 10.1371/journal.pntd.0002914
- Fernandes, M. C., Dillon, L. A., Belew, A. T., Bravo, H. C., Mosser, D. M., and El-Sayed, N. M. (2016). Dual transcriptome profiling of leishmania-infected human macrophages reveals distinct reprogramming signatures. *MBio* 7:e00027-16. doi: 10.1128/mBio.00027-16
- Franken, L., Schiwon, M., and Kurts, C. (2016). Macrophages: sentinels and regulators of the immune system. *Cell Microbiol.* 18, 475–487. doi: 10.1111/cmi.12580
- Garber, M., Grabherr, M. G., Guttman, M., and Trapnell, C. (2011). Computational methods for transcriptome annotation and quantification using RNA-seq. *Nat. Methods* 8, 469–477. doi: 10.1038/nmeth.1613
- Gerbasi, V. R., Weaver, C. M., Hill, S., Friedman, D. B., and Link, A. J. (2004). Yeast Asc1p and mammalian RACK1 are functionally orthologous core 40S ribosomal proteins that repress gene expression. *Mol. Cell Biol.* 24, 8276–8287. doi: 10.1128/MCB.24.18.8276-8287.2004
- Ghosh, E. E., Cassado, A. A., Govoni, G. R., Fukuhara, T., Yang, Y., Monack, D. M., et al. (2010). Two physically, functionally, and developmentally distinct peritoneal macrophage subsets. *Proc. Natl. Acad. Sci. U.S.A.* 107, 2568–2573. doi: 10.1073/pnas.0915000107
- Gregory, D. J., Sladek, R., Olivier, M., and Matlashewski, G. (2008). Comparison of the effects of *Leishmania major* or *Leishmania donovani* infection on macrophage gene expression. *Infect. Immun.* 76, 1186–1192. doi: 10.1128/IAI.01320-07
- Guerfali, F. Z., Laouini, D., Guizani-Tabbane, L., Ottones, F., Ben-Aissa, K., Benkahl, A., et al. (2008). Simultaneous gene expression profiling in human macrophages infected with *Leishmania major* parasites using SAGE. *BMC Genom.* 9:238. doi: 10.1186/1471-2164-9-238
- Gupta, G., Oghumu, S., and Satoskar, A. R. (2013). Mechanisms of immune evasion in leishmaniasis. *Adv. Appl. Microbiol.* 82, 155–184. doi: 10.1016/B978-0-12-407679-2.00005-3
- Gupta, P., Srivastav, S., Saha, S., Das, P. K., and Ukil, A. (2016). *Leishmania donovani* inhibits macrophage apoptosis and pro-inflammatory response through AKT-mediated regulation of beta-catenin and FOXO-1. *Cell Death Differ.* 23, 1815–1826. doi: 10.1038/cdd.2016.101
- He, X., and Zhang, J. (2006). Why do hubs tend to be essential in protein networks? *PLoS Genet.* 2:e88. doi: 10.1371/journal.pgen.0020088
- Junghae, M., and Raynes, J. G. (2002). Activation of p38 mitogen-activated protein kinase attenuates *Leishmania donovani* infection in macrophages. *Infect. Immun.* 70, 5026–5035. doi: 10.1128/IAI.70.9.5026-5035.2002
- Kholodenko, B. N. (2006). Cell-signalling dynamics in time and space. *Nat. Rev. Mol. Cell Biol.* 7, 165–176. doi: 10.1038/nrm1838
- Killick, K. E., Magee, D. A., Park, S. D., Taraktoglou, M., Browne, J. A., Conlon, K. M. et al. (2014). Key hub and bottleneck genes differentiate the macrophage response to virulent and attenuated *Mycobacterium bovis*. *Front. Immunol.* 5:422. doi: 10.3389/fimmu.2014.00422
- Kim, S., Kurokawa, D., Watanabe, K., Makino, S., Shirahata, T., and Watarai, M. (2004). *Brucella abortus* nicotinamidase (PncA) contributes to its intracellular replication and infectivity in mice. *FEMS Microbiol. Lett.* 234, 289–295. doi: 10.1111/j.1574-6968.2004.tb09546.x
- Kima, P. E., and Soong, L. (2013). Interferon gamma in leishmaniasis. *Front. Immunol.* 4:156. doi: 10.3389/fimmu.2013.00156
- Kuzmanov, U., and Emili, A. (2013). Protein-protein interaction networks: probing disease mechanisms using model systems. *Genome Med.* 5:37. doi: 10.1186/gm441
- Lin, C. Y., Chin, C. H., Wu, H. H., Chen, S. H., Ho, C. W., Ko, M. T. (2008). Hubba: hub objects analyzer—a framework of interactome hubs identification for network biology. *Nucleic Acids Res.* 36, W438–W443. doi: 10.1093/nar/gkn257
- Ma, B., Pan, S. J., Zupancic, M. L., and Cormack, B. P. (2007). Assimilation of NAD(+) precursors in *Candida glabrata*. *Mol. Microbiol.* 66, 14–25. doi: 10.1111/j.1365-2958.2007.05886.x
- Massagué, J. (2012). TGFbeta signalling in context. *Nat. Rev. Mol. Cell Biol.* 13, 616–630. doi: 10.1038/nrm3434
- Matte, C., and Descoteaux, A. (2016). Exploitation of the Host cell membrane fusion machinery by leishmania is part of the infection process. *PLoS Pathog.* 12:e1005962. doi: 10.1371/journal.ppat.1005962
- McDermott, J. E., Taylor, R. C., Yoon, H., and Heffron, F. (2009). Bottlenecks and hubs in inferred networks are important for virulence in *Salmonella typhimurium*. *J. Comput. Biol.* 16, 169–180. doi: 10.1089/cmb.2008.04TT
- Mitra, P. (2015). Pathogenicity of *Leishmania donovani* is associated with the high expression of a group low molecular weight proteins. *Trop. Parasitol.* 5:106. doi: 10.4103/2229-5070.162521
- Miyazaki, S., Nishioka, J., Shiraishi, T., Matsumine, A., Uchida, A., Nobori, T. (2007). Methylthioadenosine phosphorylase deficiency in Japanese osteosarcoma patients. *Int. J. Oncol.* 31, 1069–1076. doi: 10.3892/ijo.31.5.1069
- Moreira, D. S., Monte Neto, R. L., Andrade, J. M., Santi, A. M., Reis, P. G., Frézard, F., et al. (2013). Molecular characterization of the MRPA transporter and antimony uptake in four New World *Leishmania* spp. susceptible and resistant to antimony. *Int. J. Parasitol. Drugs Drug Resist.* 3, 143–153. doi: 10.1016/j.ijpddr.2013.08.001
- Mortazavi, A., Williams, B. A., McCue, K., Schaeffer, L., and Wold, B. (2008). Mapping and quantifying mammalian transcriptomes by RNA-Seq. *Nat. Methods* 5, 621–628. doi: 10.1038/nmeth.1226
- Mottram, J. C., Coombs, G. H., and Alexander, J. (2004). Cysteine peptidases as virulence factors of *Leishmania*. *Curr. Opin. Microbiol.* 7, 375–381. doi: 10.1016/j.mib.2004.06.010
- Mukherjee, A., Padmanabhan, P. K., Singh, S., Roy, G., Girard, I., Chatterjee, M., et al. (2007). Role of ABC transporter MRPA, gamma-glutamylcysteine synthetase and ornithine decarboxylase in natural antimony-resistant isolates of *Leishmania donovani*. *J. Antimicrob. Chemother.* 59, 204–211. doi: 10.1093/jac/dkl494
- Murray, H. W., Luster, A. D., Zheng, H., and Ma, X. (2017). Gamma interferon-regulated chemokines in *Leishmania donovani* infection in the liver. *Infect. Immun.* 85:e00824-16. doi: 10.1128/IAI.00824-16

- Murray, H. W., Miralles, G. D., Stoeckle, M. Y., and McDermott, D. F. (1993). Role and effect of IL-2 in experimental visceral leishmaniasis. *J. Immunol.* 151, 929–938.
- Naula, C., Parsons, M., and Mottram, J. C. (2005). Protein kinases as drug targets in trypanosomes and Leishmania. *Biochim. Biophys. Acta* 1754, 151–159. doi: 10.1016/j.bbapap.2005.08.018
- Nilsson, R., Bajic, V. B., Suzuki, H., di Bernardo, D., Björkegren, J., Katayama, S., et al. (2006). Transcriptional network dynamics in macrophage activation. *Genomics* 88, 133–142. doi: 10.1016/j.ygeno.2006.03.022
- Olivier, M., Gregory, D. J., and Forget, G. (2005). Subversion mechanisms by which Leishmania parasites can escape the host immune response: a signaling point of view. *Clin. Microbiol. Rev.* 18, 293–305. doi: 10.1128/CMR.18.2.293-305.2005
- Ovalle-Bracho, C., Franco-Muñoz, C., Londoño-Barbosa, D., Restrepo-Montoya, D., and Clavijo-Ramirez, C. (2015). Changes in macrophage gene expression associated with *Leishmania (Viannia) braziliensis* infection. *PLoS ONE* 10:e0128934. doi: 10.1371/journal.pone.0128934
- Paes, L. S., Suárez Mantilla, B., Zimbres, F. M., Pral, E. M., Diogo de Melo, P., Tahara, E. B., et al. (2013). Proline dehydrogenase regulates redox state and respiratory metabolism in *Trypanosoma cruzi*. *PLoS ONE* 8:e69419. doi: 10.1371/journal.pone.0069419
- Pang, E., Hao, Y., Sun, Y., and Lin, K. (2016). Differential variation patterns between hubs and bottlenecks in human protein-protein interaction networks. *BMC Evol. Biol.* 16:260. doi: 10.1186/s12862-016-0840-8
- Probst, C. M., Silva, R. A., Menezes, J. P., Almeida, T. E., Gomes, I. N., Dallabona, A. C., Ozaki, L. S., Buck, G. A., Pavoni, D. P., Krieger, M. A., Veras, P. S. et al. (2012). A comparison of two distinct murine macrophage gene expression profiles in response to *Leishmania amazonensis* infection. *BMC Microbiol.* 12:22. doi: 10.1186/1471-2180-12-22
- Reuter, J. A., Spacek, D. V., and Snyder, M. P. (2015). High-throughput sequencing technologies. *Mol. Cell* 58:586–597. doi: 10.1016/j.molcel.2015.05.004
- Roy, S., Kumar, G. A., Jafurulla, M., Mandal, C., and Chattopadhyay, A. (2014). Integrity of the actin cytoskeleton of host macrophages is essential for *Leishmania donovani* infection. *Biochim. Biophys. Acta* 1838, 2011–2018. doi: 10.1016/j.bbamem.2014.04.017
- Salmon, D., Vanwallegem, G., Morias, Y., Denoed, J., Krumbholz, C., Lhommé, F., et al. (2012). Adenylate cyclases of *Trypanosoma brucei* inhibit the innate immune response of the host. *Science* 337, 463–466. doi: 10.1126/science.1222753
- Schmittgen, T. D., and Livak, K. J. (2008). Analyzing real-time PCR data by the comparative C_T method. *Nat. Protoc.* 3, 1101–1108. doi: 10.1038/nprot.2008.73
- Shadab, M., and Ali, N. (2011). Evasion of host defence by *Leishmania donovani*: subversion of signaling pathways. *Mol. Biol. Int.* 2011:343961. doi: 10.4061/2011/343961
- Shannon, P., Markiel, A., Ozier, O., Baliga, N. S., Wang, J. T., Ramage, D., et al. (2003). Cytoscape: a software environment for integrated models of biomolecular interaction networks. *Genome Res.* 13, 2498–2504. doi: 10.1101/gr.1239303
- Sinha, R., Roychoudhury, J., Palit, P., and Ali, N. (2015). Cationic liposomal sodium stibogluconate (SSG), a potent therapeutic tool for treatment of infection by SSG-sensitive and -resistant *Leishmania donovani*. *Antimicrob. Agents Chemother.* 59, 344–355. doi: 10.1128/AAC.03305-14
- Sinha, R. C., Raghwan, M. M., Das, S., Shadab, M., Chowdhury, R., Tripathy, S., et al. (2018). Genome plasticity in cultured *Leishmania donovani*: comparison of early and late passages. *Front. Microbiol.* 9:1279. doi: 10.3389/fmicb.2018.01279
- Soto, M., Requena, J., Quijada, L., Angel, S., Gomez, L., Guzman, F., et al. (1995). During active viscerocutaneous leishmaniasis the anti-P2 humoral response is specifically triggered by the parasite P proteins. *Clin. Exp. Immunol.* 100, 246–252. doi: 10.1111/j.1365-2249.1995.tb03661.x
- Sterner, D. E., and Berger, S. L. (2000). Acetylation of histones and transcription-related factors. *Microbiol. Mol. Biol. Rev.* 64, 435–459. doi: 10.1128/MMBR.64.2.435-459.2000
- Sweeney, C., Fambrough, D., Huard, C., Diamonti, A. J., Lander, E. S., Cantley, L. C., et al. (2001). Growth factor-specific signaling pathway stimulation and gene expression mediated by ErbB receptors. *J. Biol. Chem.* 276, 22685–22698. doi: 10.1074/jbc.M100602200
- Teixeira, M. J., Teixeira, C. R., Andrade, B. B., Barral-Netto, M., and Barral, A. (2006). Chemokines in host-parasite interactions in leishmaniasis. *Trends Parasitol.* 22, 32–40. doi: 10.1016/j.pt.2005.11.010
- Trapnell, C., Pachter, L., and Salzberg, S. L. (2009). TopHat: discovering splice junctions with RNA-Seq. *Bioinformatics* 25, 1105–1111. doi: 10.1093/bioinformatics/btp120
- Van Assche, T., Deschacht, M., da Luz, R. A. I., Maes, L., and Cos, P. (2011). Leishmania-macrophage interactions: insights into the redox biology. *Free Radical Biol. Med.* 51, 337–351. doi: 10.1016/j.freeradbiomed.2011.05.011
- van der Vorst, E. P., Jeurissen, M., Wolfs, I. M., Keijbeck, A., Theodorou, K., Wijnands, E., et al. (2015). Myeloid A disintegrin and metalloproteinase domain 10 deficiency modulates atherosclerotic plaque composition by shifting the balance from inflammation toward fibrosis. *Am. J. Pathol.* 185, 1145–1155. doi: 10.1016/j.ajpath.2014.11.028
- Verma, J. K., Rastogi, R., and Mukhopadhyay, A. (2017). *Leishmania donovani* resides in modified early endosomes by upregulating Rab5a expression via the downregulation of miR-494. *PLoS Pathog.* 13:e1006459. doi: 10.1371/journal.ppat.1006459
- von Mering, C., Huynen, M., Jaeggi, D., Schmidt, S., Bork, P., and Snel, B. (2003). STRING: a database of predicted functional associations between proteins. *Nucleic Acids Res.* 31, 258–261. doi: 10.1093/nar/gkg034
- Wang, Z., Gerstein, M., and Snyder, M. (2009). RNA-Seq: a revolutionary tool for transcriptomics. *Nat. Rev. Genet.* 10, 57–63. doi: 10.1038/nrg2484
- Wiese, M. (1998). A mitogen-activated protein (MAP) kinase homologue of *Leishmania mexicana* is essential for parasite survival in the infected host. *EMBO J.* 17, 2619–2628. doi: 10.1093/emboj/17.9.2619
- Yu, H., Kim, P. M., Sprecher, E., Trifonov, V., and Gerstein, M. (2007). The importance of bottlenecks in protein networks: correlation with gene essentiality and expression dynamics. *PLoS Comput. Biol.* 3:e59. doi: 10.1371/journal.pcbi.0030059
- Zhang, X., Goncalves, R., and Mosser, D. M. (2008). The isolation and characterization of murine macrophages. *Curr. Protoc. Immunol.* 14:11. doi: 10.1002/0471142735.im1401s83

Conflict of Interest Statement: The authors declare that the research was conducted in the absence of any commercial or financial relationships that could be construed as a potential conflict of interest.

Copyright © 2019 Shadab, Das, Banerjee, Sinha, Asad, Kamran, Maji, Jha, Deepthi, Kumar, Tripathi, Kumar, Chakrabarti and Ali. This is an open-access article distributed under the terms of the Creative Commons Attribution License (CC BY). The use, distribution or reproduction in other forums is permitted, provided the original author(s) and the copyright owner(s) are credited and that the original publication in this journal is cited, in accordance with accepted academic practice. No use, distribution or reproduction is permitted which does not comply with these terms.



Source details

[Feedback >](#) [Compare sources >](#)

Frontiers in Cellular and Infection Microbiology

Open Access [i](#)

Scopus coverage years: from 2011 to Present

Publisher: Frontiers Media SA

ISSN: 2235-2988

Subject area: [Medicine: Infectious Diseases](#) [Medicine: Microbiology \(medical\)](#) [Immunology and Microbiology: Microbiology](#)
[Immunology and Microbiology: Immunology](#)

Source type: Journal

[View all documents >](#)[Set document alert](#)[Save to source list](#)

CiteScore 2022

6.4



SJR 2022

1.308



SNIP 2022

1.198



Earth and Space Science

RESEARCH ARTICLE

10.1029/2018EA000468

Key Points:

- The solar wind-magnetosphere coupling has been analyzed using a cellular automata model based on the concept of self-organized criticality
- A new coupling function is introduced to determine the cusp width
- A threshold value of B_z , the z th component of the interplanetary magnetic field related to the yearly mean total number of sunspots, is introduced

Supporting Information:

- Supporting Information S1
- Data Set S1
- Data Set S2
- Data Set S3
- Data Set S4

Correspondence to:

A. Bej,
 amaresh_bej@yahoo.com

Citation:

Banerjee, A., Bej, A., Chatterjee, T. N., & Majumdar, A. (2019). An SOC approach to study the solar wind-magnetosphere energy coupling. *Earth and Space Science*, 6, 565–576. <https://doi.org/10.1029/2018EA000468>

Received 5 SEP 2018

Accepted 3 FEB 2019

Accepted article online 6 FEB 2019

Published online 8 APR 2019

©2019. The Authors.

This is an open access article under the terms of the Creative Commons Attribution-NonCommercial-NoDerivs License, which permits use and distribution in any medium, provided the original work is properly cited, the use is non-commercial and no modifications or adaptations are made.

An SOC Approach to Study the Solar Wind-Magnetosphere Energy Coupling

Adrija Banerjee¹, Amaresh Bej¹ , T. N. Chatterjee², and Abhijit Majumdar¹

¹Department of Physics, Indian Institute of Engineering Science and Technology, Howrah, India, ²Department of Electronics, Dinabandhu Andrews College, Kolkata, India

Abstract Solar wind-magnetosphere interaction and the injection of large quantity of plasma particles into the Earth's magnetosphere are the primary reasons behind geomagnetic storm, auroral effects, and, in general, all the fluctuations observed in the terrestrial magnetic field. In this paper, we analyzed the perturbed magnetosphere as a sandpile-like cellular automata model based on the concept of self-organized criticality and many-body interactive system and proposed a solar wind-magnetosphere energy coupling function in terms of interplanetary magnetic field B_z , the z th component of interplanetary magnetic field. The function determines the cusp width W depending on the intensity of $(-B_z - B_{Th})$ where B_{Th} is the threshold value. The model generates two output series, which are the numerical representation of the real-time Dst index and AE index series, respectively. For our study, the range of years 1997–2007 of the 23rd solar cycle had been considered here. The threshold value B_{Th} plays a significant role in the analysis and exhibits a proportional relationship with the yearly mean total number of sunspots for each year of the range 1997–2007 of the 23rd solar cycle. For each year, the two resultant output time series of the model display high-correlation coefficients with the real-time Dst and AE indexes, respectively, which denotes the acceptability of the proposed energy coupling function and its relation with the solar activities.

1. Introduction

The solar wind-magnetosphere interaction and the energy coupling can be considered as the key factor to understand the various dynamical properties of the terrestrial magnetosphere. The solar wind, a stream of highly energized plasma particles, emitted from the Sun's outer atmosphere, is coming toward the Earth with an average speed of 400 km/s. These huge amounts of particles are injected into the Earth's magnetosphere through the cusps controlled by the z th component of the interplanetary magnetic field (IMF), B_z . The direction and magnitude of IMF B_z is the primary controller of the solar wind-magnetosphere reconnection along with the dynamic pressure of the solar wind. A detailed knowledge of the energy coupling mechanism is important to estimate the total amount of injected solar wind energy in the geospace as this energy drives all the geomagnetic fluctuations in the terrestrial magnetosphere, causing intense geomagnetic storm or auroral activities (Russell, 2000, 2013).

Extreme geomagnetic activity is considered to be a serious threat to the Earth's technological and electrical systems. In the time of severe geomagnetic storm, solar wind injects a large amount of ionized particles into the Earth's magnetosphere, rapidly changing the intensity of the magnetic field which in turn induces an electric field on the surface of the Earth. This induced electric field then drives a current through any electrical network by forming a potential difference between the ground points of that network. This current is known as geomagnetically induced current (GIC). The intensity of GIC has been noted as large as over 100 A, though a few amperes is sufficient to unexpectedly collapse any electrical infrastructure causing a huge loss of money and related hazards (Kappenman et al., 1997). The 13 March 1989 geomagnetic storm and the complete collapse of Hydro Quebec power grid resulting in 9 hr blackout for 6 million customers [Hydro-Québec, Understanding Electricity, 1989; Kappenman et al., 1997], the 30-hr blackout of the Wide Area Augmentation System managed by the Federal Aviation Administration, and the damage of Japanese ADEOS-2 satellite due to the Halloween solar storm in 2003 are some of the most prominent examples [CENTRA Technology Inc. report 2011; NOAA Technical Memorandum 2003; Workshop report of National Research Council of the National Academics 2008]. Also, past records of GIC-triggered hazards include complete disruption of power grids and transformers; malfunction of railway equipment and satellite hardware; severe collapsing of telecommunication, navigation, and computer systems; and increase of

steel corrosion in pipeline networks, particularly in countries like the United States and Canada or northern Europe, located in the upper latitudes and affected most by the auroral electrojet current [CENTRA Technology Inc. report 2011; Kappenman et al., 1997; NOAA Technical Memorandum 2003]. So a comprehensive knowledge of the solar wind-magnetosphere interaction and the underlying physical process of geomagnetic activity is crucial to save human society from its severe negative effects.

The solar wind-magnetosphere energy coupling mechanism became a subject of keen interest and curiosity in the past decades. The complex dynamics of the energy coupling process, the rate of energy transfer into the magnetosphere, and the distribution of the injected energy in the magnetosphere-ionosphere system as well as the role of the various solar wind parameters controlling the overall process had been rigorously studied, analyzed, and characterized in numerous works. A number of solar wind energy coupling functions had been presented (Akasofu, 1981; Finch & Lockwood, 2007; Gonzalez, 1990; Gonzalez et al., 1989; Kan & Lee, 1979; Newell et al., 2007; Perreault & Akasofu, 1978), while the nature of solar wind-magnetosphere interaction had been extensively studied in relation with the other solar wind parameters like velocity, ion density, and dynamic pressure [Crooker et al., 1977; Crooker & Gringauz, 1993; Dungey, 1961; Mawad et al., 2016; Newell et al., 2007; Papitashvili et al., 2000; Temerin & Li, 2006; Wygant et al., 1983; Youssef et al., 2011]. Global magnetohydrodynamic simulations [Palmroth et al., 2003, 2005, 2006, 2010, 2012; Papadopoulos et al., 1999. Pulkkinen et al., 2002, 2008, 2010; Wang et al., 2014] along with various other methods (Bargatze et al., 1986; Murayama, 1982; Stamper et al., 1999) were also taken into account. The estimation of the percentage of solar wind energy injected into the geospace, how much of this energy is dissipating in the magnetosphere or in the ionosphere, and in general the entire energy transfer and dissipation process long became the focus point of detailed investigations [Lu et al., 1998, 2013; Scurry & Russell, 1991; Stern, 1984; Tanskanen et al., 2002; Tenfjord & Ostgaard, 2013; Turner et al., 2001; Østgaard et al., 2002; Vasyliunas et al., 1982]. Though all these serious efforts produced significant results, solar wind-magnetosphere-ionosphere interaction still demands further attention to understand the complex nature of geomagnetic disturbances.

In our previous work, we came to realize that geomagnetic disturbances on the Earth is an essentially complex natural phenomenon having a number of underlying dynamics and quite impossible to predict accurately, whereas *Dst* index, the measurement of geomagnetic activity, is a positively correlated fractional Brownian motion having long-range correlation (Banerjee et al., 2011). Enlightened by this outcome, we aimed to develop a sandpile-like cellular automata model, analogous to the Earth's magnetosphere to investigate the dynamical characteristics of the geomagnetic storm (Banerjee et al., 2015). Now sandpile model was selected as the first example displaying the concept of self-organized criticality, introduced by Bak et al. in their 1987, 1988 pioneering papers. Since then, this algorithm had been extensively used to study and analysis the physical process of geomagnetic fluctuations (Chang, 1992, 1999; Chapman et al., 1998; Consolini, 1997; Consolini & Lui, 1999; Klimas et al., 2000; Takalo et al., 1999; Uritsky, 1996; Uritsky & Pudovkin, 1998a, 1998b; Uritsky & Semenov, 2000). Our proposed 2015 model was a dissipative dynamical system with both spatial and temporal degrees of freedom, based on the concept of self-organized criticality and a refined version of the model presented by Uritsky et al. (2001). Though it was a first-order model with basic considerations, the resultant time series exhibited similar statistical characteristics of the real-time *Dst* index. The acceptability of the model and its curious outcome made us realize the significance of the solar wind-magnetosphere interaction and motivated us to further investigate the true nature of the energy coupling mechanism.

In the present paper, we continued our analysis based on the sandpile-like cellular automata model of the terrestrial magnetosphere, presented in our 2015 paper (Banerjee et al., 2015). We proposed a definite solar wind-magnetosphere energy coupling function in terms of IMF B_z and a threshold value, B_{Th} . The function is a hyperbolic tangent one which determines the cusp width W at any time t . The model produces two output series which are the numerical representations of the real-time *Dst* index and *AE* index series, respectively. To examine the validity of the proposed energy coupling function, the correlation coefficients between the simulated output series, the real-time *Dst*, and *AE* index series had been estimated respectively. The entire 23rd solar cycle had been studied, and the real-time data of solar ion density, flow speed, and IMF B_z had been considered here. The result shows significant values of correlation coefficients between the simulated and real-time series for a specific value of the B_{Th} for each year. The parameter B_{Th} plays a key

role here as it varies exactly proportionally to the variation of the yearly mean total number of sunspots for each year of the range 1997–2007 of the 23rd solar cycle, revealing the direct influence of solar activities on the solar wind-magnetosphere reconnection phenomena.

2. Method

The cellular automata-based sandpile model presented here is a refinement of the model proposed in our previous paper (Banerjee et al., 2015). In summary, the model, a numerical representation of the Earth's magnetosphere, is a finite matrix of $n \times n$ elements, characterized by energy E , which is a function of time and space. With analogy to the Earth, open boundary condition had been considered, denoting upper ($i = 1, j = 1$ to n) and lower ($i = n, j = 1$ to n) boundary regions of the system. Solar wind emitted from the Sun is coming toward the Earth. It interacts with the terrestrial magnetosphere, a reconnection occurs, and a significant amount of ionized particle penetrates into the geospace through the cusp, altering its energy. The energy unit dE at any time t is calculated using the real-time ion density and flow speed data obeying the equation

$$dE(t) = \text{norm}^{1/2} \times \text{ion density} \times (\text{flow speed})^2 \quad (1)$$

For initialization, each of the cells of the matrix is credited with a small amount of solar wind energy following the equations

$$E_{t+1}(i,j) = E_t(i,j) + K_r \times dE(t) \text{ for } i = 2 \text{ to } n+1, j = 1 \text{ to } n \quad (2)$$

and

$$E_{t+1}(i,j) = E_t(i,j) + K_a \times dE(t) \text{ for } i = 1, j = 1 \text{ to } n \quad (3)$$

where K_r and K_a are constants.

Both the direction and the intensity of the z th component of the IMF, B_Z determines the cusp width W , thus controlling the amount of energy injected into the system. For the cellular automata model of $n \times n$ matrix presented here, the cusp width W is a square of cells surrounding the cell ($i = n/2, j = n/2$), that is, the cell in the center of the matrix. For a large northward B_Z , the cusp width W is minimum 0, whereas for a large southward B_Z , the cusp width W has a maximum value, $W_m = (n - 1)^2$. W_m has a constant value for a constant n .

The functional relationship of W and B_Z proposed here is

$$W(t) = W_m * ((\tanh((-B_Z - B_{Th})/\lambda) + 1)/2) \quad (4)$$

where B_{Th} is the threshold value of IMF B_Z to open up the cusp and λ is a constant. The parameter B_{Th} is the most significant factor in the entire analysis as it controls the net amount of solar wind-magnetosphere energy coupling area. At any time t , the hyperbolic tangent term in equation (4) generates a value in the range of 0 to 1. For a large southward B_Z , the hyperbolic tangent term is 1 and $W = W_m$, whereas for a large northward B_Z the term is 0 and $W = 0$. In between the extrema, W has an intermediate value depending on the value of $(-B_Z - B_{Th})$. W has a numeric value.

The input energy $dE(t)$ is injected into the model through W number of cells following the equation

$$E_{t+1}(i,j) = E_t(i,j) + dE(t) \text{ for } i = n/2 \pm p, j = n/2 \pm p \quad (5)$$

where $p = \text{round}((\sqrt{W} - 1)/2)$.

Now if the altered energy of the cell (i,j) crosses the threshold value E_{Th} of the system, the excess energy is distributed among the adjacent neighbors obeying the equations

$$E_{t+1}(i,j) = E_t(i,j) - 4 \quad (6)$$

and

$$E_{t+1}(i\pm 1, j\pm 1) = E_t(i\pm 1, j\pm 1) + (1 - E_d/4) \quad (7)$$

where E_d is the dissipation factor and $(i \pm 1) \geq 1$ or 2 according to the case.

The total energy of the system at any time t can be calculated as

$$E_1(t) = \sum E(i,j) \text{ for } i = 2 \text{ to } n + 1, j = 1 \text{ to } n \quad (8)$$

The differential value of the energy stored in the system at any time t is then estimated by

$$E_2(t) = \Delta E_1(t) \quad (9)$$

For further refinement, the above time series is then processed by a moving-average filter of span 72 to get the final output series as

$$E_r(t) = -\text{MA}(E_2) \quad (10)$$

$E_r(t)$ is an estimation of the differential value of the energy stored in the system and can be considered as a numerical equivalent to the *Dst* index. Now a high correlation coefficient between the simulated series $E_r(t)$ and the real-time *Dst* index can establish the validity of the proposed coupling function.

The real-time hourly averaged *Dst* index data set has been obtained from OMNIWeb. To remove the noise and fine-scale structure, the data set is further processed by a moving-average filter of span 72 to get a series, namely, $E_{Dst}(t + T)$ where T denotes the time shift or time lag. Now cross correlation is considered as a standard technique to measure the degree of similarity between two time series, and this method had been applied here to determine the correlation between the series $E_r(t)$ and $E_{Dst}(t + T)$. To estimate the optimum cross-correlation coefficient between these two series, the series $E_r(t)$ had been compared to the time-shifted real-time *Dst* index, $E_{Dst}(t + T)$ where T is varied in the range of values 0 to 720 hr, and for each value of T , the correlation coefficients between the two series had been noted down along with the exact value of T . Here T is the lag value of duration 1 hr associated with the cross-correlation method.

As open boundary condition has been considered, the excess energy transmits outside the grid after reaching the upper ($i = 1, j = 1$ to n) and lower ($i = n + 2, j = 1$ to n) boundary regions of the system. With analogy to the Earth, these upper and lower boundaries can be considered as the northern and southern polar cusps of the Earth, while this energy transfer process is similar to the transmission of the excess energy of the Earth's magnetosphere to the ionosphere through the polar cusps. Thus, the amount of excess energy dissipated through the upper boundary or northern polar cusp can be estimated as

$$E_3(t) = \sum E(i,j) \text{ for } i = 1, j = 1 \text{ to } n \quad (11)$$

and the differential energy value as

$$E_4(t) = \Delta E_3(t) \quad (12)$$

Similarly, as equation (10) the moving-average technique has been applied to equation (12) to get the following one

$$E_a(t) = \text{MA}(E_4) \quad (13)$$

Equation (13) is the measurement of the excess energy dissipated in the ionosphere from the magnetosphere through the polar cusps and can be considered as a numerical representation of the auroral electrojet (*AE*) index. Similar as before, the real-time *AE* index data series has been obtained from OMNIWeb and further processed by a moving-average filter of span 72 to get the series $E_{AE}(t + T)$, where T is the time shift or time lag. Again, the method of cross correlation had been applied here to determine the amount of correlation

between the two series $E_a(t)$ and $E_{AE}(t + T)$, considering T as the associated lag value of duration 1 hr. The correlation coefficients between the simulated series $E_a(t)$ of equation (13) and the real-time $E_{AE}(t + T)$ had been estimated to further strengthen the validity of the proposed coupling function. Here also, the series $E_a(t)$ had been compared with the time-shifted AE index, $E_{AE}(t + T)$ where T is varied in the range of values 0 to 720 hr to achieve the optimum correlation coefficient between the two series. For each value of T , the associated correlation coefficients had been recorded.

As mentioned before, the threshold value B_{Th} of equation (4) is playing the key role in the entire analysis as the term $(-B_Z - B_{Th})$ controls the widening or narrowing of the cusp width and the amount of solar wind energy injected into the magnetosphere at any time t . In this work, we had studied the variation of the magnitude of the solar wind-magnetosphere coupling with variation of B_{Th} and its subsequent effect on the overall dynamics of the system.

3. Data source

Here we used the hourly averaged Dst index, AE index, solar wind ion density, flow speed, and B_Z component of the IMF data from the year 1997 to the year 2007 as extracted from NASA/GSFC's (Goddard Space Flight Center) OMNI data set through OMNIWeb (King & Papitashvili, 2005). The OMNI data were obtained from the GSFC/SPDF (Space Physics Data Facility) OMNIWeb interface at the OMNIWeb website (<http://omniweb.gsfc.nasa.gov>). We used the Dst index and AE index data obtained from OMNIWeb to compare with the estimated series $E_r(t)$ and $E_a(t)$, respectively.

For the yearly mean total number of sunspots, the source credit is the sunspot data from the World Data Center SILSO (Sunspot Index and Long-term Solar Observations; Sunspot Number and Long-term Solar Observations, Royal Observatory of Belgium, on-line Sunspot Number catalogue: <http://www.sidc.be/SILSO/>, '1997–2007').

4. Result and Discussions

To study the dynamics of the system depending on the solar wind-magnetosphere coupling, we had considered the range of years 1997 to 2007 of the 23rd solar cycle. The input energy dE had been calculated using equation (1) and using the real-time value of flow speed and ion density. The cellular automata model is a matrix having a dimension of $n \times n$. Here it is taken as $n = 50$, that is, the matrix contains 50×50 cells. The input energy $dE(t)$, calculated from OMNIWeb data is an one-dimensional time series. At any time t , the total cusp area W is determined using equation (4). The cusp area is a square having the cells $i = 25 \pm p, j = 25 \pm p$ where $p = \text{round}((\sqrt{W} - 1)/2)$. The input energy $dE(t)$ is injected into all these cells of $i = 25 \pm p, j = 25 \pm p$ according to equation (5) stated in the section 2. The values of the different parameters are taken as $E_{Th} = 5, E_d = 0.001, K_r = 0.001, K_a = 0.1, \lambda = 0.5$. All these values are constants for each of the year in the range of 1997–2007. As referred in the section 2, our sandpile model is a refined version of the model presented in our 2015 paper which was based on the model proposed by Uritsky et al. (2001). Uritsky et al. set the threshold of excitation as $E_{Th} = 5$ and suggested the value of the dissipation term $E_d < = 0.01$ to study the wide-range scale-invariant behavior of the system. Following their work, we also set $E_{Th} = 5$ and $E_d = 0.001$ for our model. We studied the model for different values of $K_r, K_a,$ and λ and observed that the model output series matches best with the real-time series for values $K_r = 0.001, K_a = 0.1,$ and $\lambda = 0.5$. So we considered these values of $K_r, K_a,$ and λ constants for our entire analysis.

For each year, the value of parameter B_{Th} had been varied in the range of -10.00 to 10.00 nT, and for each value of B_{Th} within this range, the correlation coefficients between the simulated series $E_r(t)$ of equation (10) and the time-shifted real-time Dst index series $E_{Dst}(t + T)$ as well as the series $E_a(t)$ of equation (13) and the time-shifted real-time AE index series $E_{AE}(t + T)$ had been estimated respectively. While calculating the correlation coefficients for the above two cases, the value of time lag T had been varied from $T = 0$ to 720 hr to achieve the optimum value of the coefficients. Thus, the best correlation coefficient for each set is found annually. The exact value of B_{Th} and the particular value of T associated with the optimum coefficients had been noted down along with the value of the coefficients. Table 1 displays the optimum values of the correlation coefficients for each year in the range of 1997 to 2007 with the corresponding values of the

Table 1

The First Three Columns of the Table Shows the Yearly Mean Total Number of Sunspots and the Values of the Threshold B_Z , B_{Th} for All the Years in the Range of 1997–2007

Year	Yearly mean total number of sunspots	B_{Th} (nT)	Comparison between $E_r(t)$ and $E_{Dst}(t + T)$		Comparison between $E_a(t)$ and $E_{AE}(t + T)$	
			Optimum correlation coefficient (%)	Time lag T (hr)	Optimum correlation coefficient (%)	Time lag T (hr)
1997	28.90	1.25	70.27	24	74.53	2
1998	88.30	1.76	60.47	32	77.05	4
1999	136.30	2.18	64.23	24	66.06	5
2000	173.90	2.50	76.06	25	69.02	2
2001	170.40	2.47	72.64	21	72.28	0
2002	163.60	2.41	75.83	31	75.42	8
2003	99.30	1.86	62.99	25	59.47	10
2004	65.30	1.56	75.26	16	76.37	3
2005	45.80	1.40	60.64	35	75.96	11
2006	24.70	1.21	52.83	30	74.63	6
2007	12.60	1.10	62.79	43	81.18	12

Note. For this entire range of years, the optimum correlation coefficients between the simulated series $E_r(t)$ and the time-shifted real-time Dst index series $E_{Dst}(t + T)$ and the associated values of time lag T are displayed in the fourth and fifth columns, respectively, while in a similar fashion, the sixth and seventh columns show the optimum correlation coefficients between the simulated series $E_a(t)$ and the time-shifted real-time AE index series $E_{AE}(t + T)$ and the corresponding values of time lag T , respectively.

parameter B_{Th} and also the values of T for both the cases. The correlation coefficient R between two series A and B is calculated using the equation

$$R = \frac{\sum_m \sum_n (A_{mn} - \bar{A})(B_{mn} - \bar{B})}{\sqrt{(\sum_m \sum_n (A_{mn} - \bar{A})^2)(\sum_m \sum_n (B_{mn} - \bar{B})^2)}} \quad (14)$$

Figure 1 represents a comparison between the actual waveforms of the simulated series $E_r(t)$ and the real-time Dst index series $E_{Dst}(t + T)$ where $T = 31$ for the year of 2002. The optimum correlation coefficient between these two series is 75.83% for $B_{Th} = 2.41$ and $T = 31$ in this year. The top half of Figure 1 shows the waveform of simulated output series $E_r(t)$, while the bottom half shows the waveform of the time-shifted Dst index series, $E_{Dst}(t + T)$ for the year 2002. Both the series are 1-hourly time series having 8,578 data each. The time in hour is plotted in the x axis. Here 8,000 means $t = 8,000$, that is, the point of 8,000th hour. Each of the year in the range of 1997–2007 contains 8,000–9,000 data.

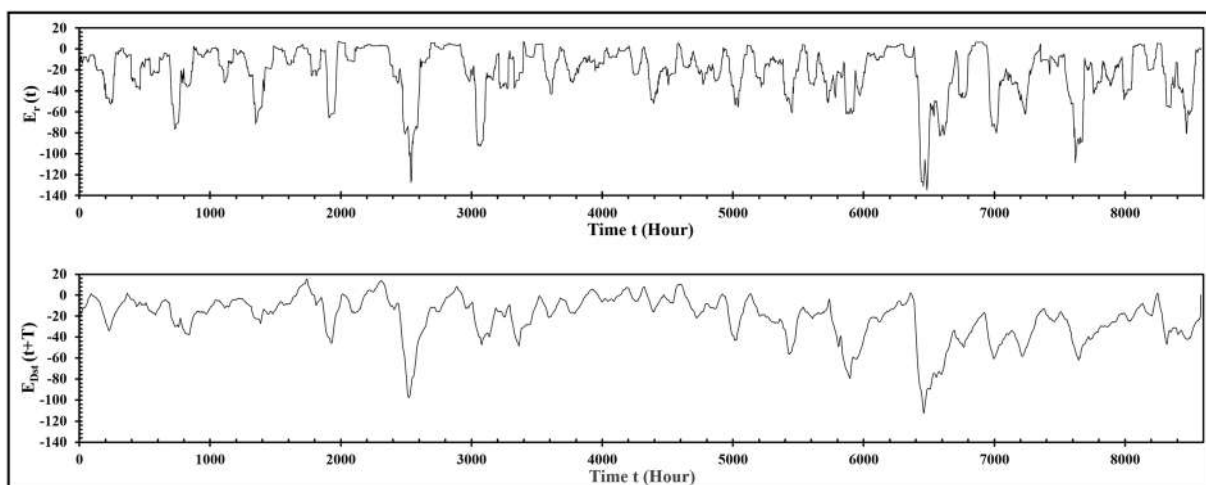


Figure 1. (top) The plot of simulated output series $E_r(t)$ and (bottom) the plot of the time-shifted Dst index series, $E_{Dst}(t + T)$ where $T = 31$ for the year 2002. Both the series are plotted with respect to time (hours). The value of $B_{Th} = 2.41$ for this year and the optimum correlation coefficient between the two series is 75.83%. The correlation coefficient between the two series is estimated using equation (14).

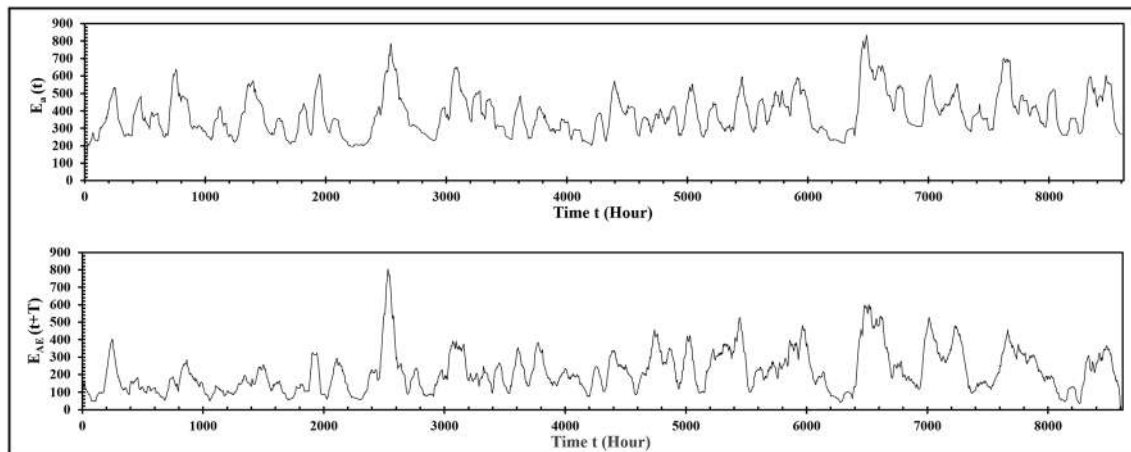


Figure 2. (top) The plot of simulated output series $E_a(t)$ and (bottom) the plot of the time-shifted AE index series, $E_{AE}(t + T)$ where $T = 8$ for the year 2002. Both the series are plotted with respect to time (hours). The value of $B_{Th} = 2.41$ for this year and the optimum correlation coefficient between the two series is 75.42%. The correlation coefficient between the two series is estimated using equation (14).

Figure 2 displays the graphs of the simulated series $E_a(t)$ and the real-time AE index $E_{AE}(t + T)$ where $T = 8$, also for the year of 2002. Here the optimum correlation coefficient between these two series is 75.42% for $B_{Th} = 2.41$ and $T = 8$. The top half of Figure 2 shows the waveform of simulated output series $E_a(t)$, while the bottom half shows the waveform of the time-shifted AE index series, $E_{AE}(t + T)$ for the year 2002. Both the series are 1-hourly time series having 8,601 data each. The time in hour is plotted in the x axis.

The current work is focused to propose a solar wind-magnetosphere energy coupling function and to study the subsequent energy transfer process using a cellular automata model of Earth's magnetosphere. To establish the validity of the model and the coupling function, the model had been simulated numerously for different set of values of the controlling parameters. For every simulation, the model output series had been compared with the real-time series. Finally, it is observed that for the set of values $K_r = 0.001$, $K_a = 0.1$, and $\lambda = 0.5$ the model output series matches best with the real-time series. So we have considered these set of values constant for the entire range of the years 1997–2007. Now T denotes the time gap between

the injection of the plasma particles into the magnetosphere and its subsequent effect on the intensity of the horizontal magnetic field of the Earth. As the amount of injected energy into the magnetosphere is not same for every year, the value of T cannot be assumed as a constant for every year beforehand; rather its value for each year had been obtained from the result.

Figure 3 shows the plot of optimum correlation coefficient for each of the years in the range of 1997–2007 for both sets of data, as obtained from Table 1.

The above result exhibits a striking connection of the solar wind-magnetosphere reconnection with solar activities. Table 1 also shows the yearly mean total number of sunspots for each year in the range of 1997–2007 of the 23rd solar cycle. As shown in Figure 4, for the entire range of years, the parameter B_{Th} varies proportionally with the yearly mean total number of sunspots. The value of B_{Th} is maximum 2.5 in the year 2000 which is also the year of solar maxima having 173.9 yearly mean total number of sunspots, while B_{Th} reaches its minimum value 1.1 in the year where the yearly mean total number of sunspots is only 12.6.

Studying the above observations thoroughly, we came to realize some significant and meaningful points about the solar wind-magnetosphere coupling and the resultant geomagnetic disturbances which can be discussed

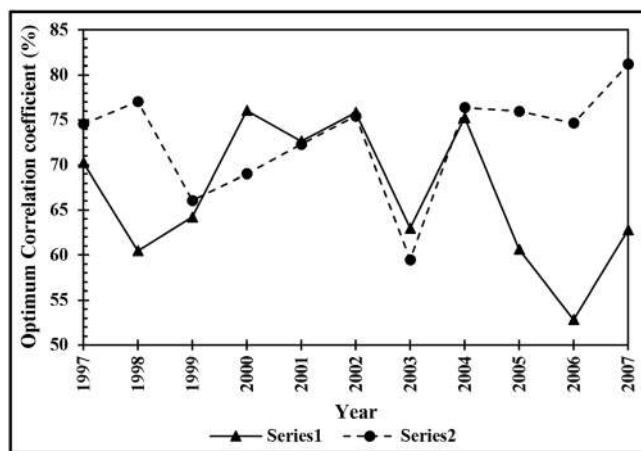


Figure 3. Series 1 is the yearly plot of the optimum correlation coefficients between the simulated series $E_r(t)$ and the time-shifted real-time Dst index series $E_{Dst}(t + T)$. Series 2 is the yearly plot of the optimum correlation coefficients between the simulated series $E_a(t)$ and the time-shifted real-time AE index series $E_{AE}(t + T)$. Year, in the range of 1997–2007 is plotted in the x axis.

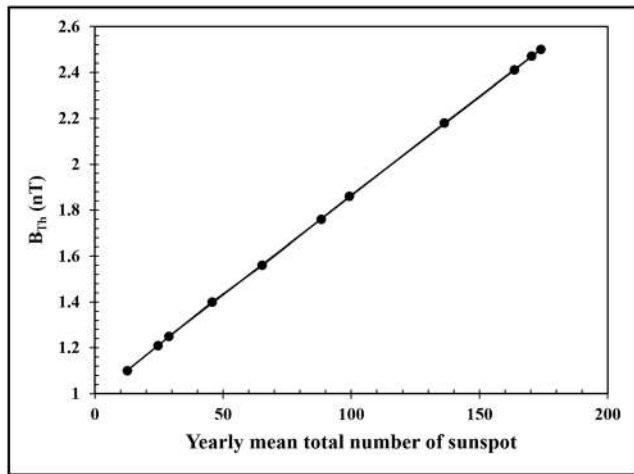


Figure 4. The threshold value, B_{Th} , is plotted with respect to the yearly mean total number of sunspots for the range of years 1997–2007 of the 23rd solar cycle. The graph shows a proportional relationship between these two parameters.

the rightness of the proposed coupling function in two ways, first in connection with the stored energy in the magnetosphere and Dst index and second in connection with the excess energy dissipated into the ionosphere and AE index. The correlation coefficients are associated to a particular value of the parameter B_{Th} for each year. Most significantly, the parameter B_{Th} displays a proportional relationship with the yearly mean total number of sunspots for the entire solar cycle, revealing an influence of solar activities on the threshold value, B_{Th} . Higher number of solar spots indicates higher solar activity which increases solar wind and also the coronal mass ejections, resulting in an injection of huge amount of plasma particles into the terrestrial magnetosphere. The magnetic fields associated with coronal mass ejections also play a significant role in magnetic reconnection. In this case, the cusp opens up for a comparatively higher value of northward B_Z . Now the threshold value of B_Z to open up the cusp and enable the energy injection process into the magnetosphere is denoted by B_{Th} , and it is observed from the result that the value of B_{Th} is the highest at 2.5 nT of northward B_Z in the year 2000, the year of solar maxima of the 23rd cycle having 119.6 number of solar spots. On the other hand, a lower value of B_{Th} is observed in the years with lower number of solar spots. The year 2007 observed only 7.6 number of sun spots and the threshold value of B_{Th} is 1.1 nT of northward B_Z for that particular year.

Finally, some meaningful insights can be extracted from the number of shifts associated with the value of the correlation coefficients for both sets of data series for each year. To estimate the optimum value of correlation between the simulated series and the real-time series, the simulated series had been compared to the real-time series shifted by T hours. The value of T is different for different years. For the year 2002, the optimum correlation coefficient between the simulated series $E_r(t)$ and $E_{Dst}(t + T)$ is 75.83% where $T = 31$. The injected plasma particles into the terrestrial magnetosphere generates the ring current which in turn deviates the intensity of the Earth's horizontal magnetic field from its average value. This deviation is measured and termed as Dst index. Here in this work, the output time series $E_r(t)$ is an estimation of the total amount of energy in the system after injection and its subsequent distribution of the input energy at any time t , and it is considered a simulated representation of this solar wind energy trapped in the magnetosphere responsible for generating the Dst index. The observation that the series $E_r(t)$ matches best with the real-time series $E_{Dst}(t + T)$ where $T = 31$ for the year of 2002 implies that the injected input energy at any time t affects the Earth's horizontal magnetic field at $(t + 31)$ hours in that very year. Similarly as the year 2002, such a time interval of 16–43 hr between the energy injection into the magnetosphere and the effective depression of horizontal magnetic field from its average value is present for all the years of the range 1997 to 2007 of the 23rd solar cycle as can be seen from Table 1.

The same observation had been noted down in the case of estimating the correlation between the simulated series $E_a(t)$ and the real-time AE index, $E_{AE}(t + T)$ also. The extra solar wind energy injected into the

here now. First of all, the cusp width W due to the magnetic reconnection is not a linear function of IMF B_Z but a hyperbolic tangent one which takes into account both the direction and magnitude of IMF B_Z and also the threshold value, B_{Th} . For large northward B_Z , the value of the function is close to 0, and the cusp is almost closed; the amount of injected particles into the magnetosphere is negligible. As the magnitude of the northward B_Z reduces below the threshold value, B_{Th} , the cusp width W starts to widen out resulting in a substantial amount of injection into the magnetosphere. As the IMF B_Z changes direction and becomes southward, the cusp width widens out further and continues to do so as long as the magnitude of the southward B_Z increases. The amount of injected particles into the magnetosphere increases rapidly with the increasing cusp width. Numerically, the cusp width can be a minimum zero value or completely closed for an extreme northward B_Z or can obtain a maximum value or completely open for an extreme southward B_Z . Between these extrema, it varies proportionally with the variation of the magnitude of $(-B_Z - B_{Th})$.

Second, the correlation coefficients between the simulated and output series, shown in Table 1, exhibit moderate to high values and support

magnetosphere is released into the ionosphere generating the westward and eastward electrojet currents in the auroral regions. *AE* index is calculated as the average value of *AU* and *AL* indexes, which in turn are the measurements of the highest and lowest depressions of the auroral magnetic field from its average value due to these westward and eastward electrojet currents, respectively. In our model the simulated output series $E_a(t)$ is equivalent to the excess energy released into the ionosphere, responsible for forming the *AE* index. For the year of 2002, the optimum value of correlation coefficient between the two series is $E_a(t)$, and $E_{AE}(t + T)$ is 75.42% for $T = 8$, which denotes a time interval of 8 hr between the energy release into the ionosphere and the depression of auroral magnetic field. All the years of 23rd solar cycle exhibit a time interval of 0 to 12 hours between the magnetosphere-ionosphere interaction and the resultant disturbances in the auroral magnetic field for similar reasons and are displayed in Table 1.

In summary, it can be realized from the above study's observations and discussions that the geomagnetic fluctuation is not an instantaneous phenomenon; rather it takes some hourly time or in some cases near about 2 days to build up the interlaying dynamics. Moreover, the proposed coupling function and the threshold value of IMF B_Z , namely, B_{Th} , plays a crucial role in the entire analysis, controlling the area of the cusp width and effectively the amount of input injection, while B_{Th} maintains a direct relationship with the yearly mean total number of sunspots and solar activities for a particular year.

5. Conclusion

Solar wind-magnetosphere coupling is the most significant physical process determining the interlaying dynamical structure of the geomagnetic storm. The energized stream of particles, known as solar wind, interacts with the terrestrial magnetosphere depending on the magnitude and direction of the z th component of the IMF, IMF B_Z . The exact dynamics of solar wind-magnetosphere reconnection process and the subsequent geomagnetic disturbances is a topic of rigorous study for the last decades. In the present paper, we investigated the nature, characteristics, and the effect of this phenomenon on the Earth's magnetosphere based on the concept of self-organized criticality and many-body interactive system. A sandpile-like cellular automata model having a dimension of $n \times n$ and characterized with energy E had been taken as a numerical representation of the terrestrial magnetosphere. The input solar wind energy at any time t can be calculated from the value of real-time ion density and flow speed data. During the reconnection process, an amount of solar wind energy is injected into the magnetosphere through the cusp and alters the energy of the cells of the system. If the total energy of any cell crosses the predetermined threshold value, the excess energy is distributed among its four adjacent neighbors though a small amount of energy is lost during this distribution process. The excess energy reaching the marginal grids dissipates from the system representing the magnetosphere-ionosphere energy transfer process. The model generates two output series. The first one is the series $E_T(t)$, which is an estimation of the total energy trapped in the system at any time t and can be considered as an equivalent to the energy responsible for generation of ring current and the depression of the Earth's horizontal magnetic field from its average value. The second output series $E_a(t)$ is the estimation of excess energy dissipated from the system at any time t and can be taken as a simulated representation of the excess energy released in the ionosphere during magnetosphere-ionosphere interaction which in turn forms the electrojet currents resulting the deviation of auroral magnetic field from its average value.

From our previous study, we came to realize the extreme importance of the solar wind-magnetosphere reconnection regarding the overall geomagnetic disturbances in the Earth and its dependency on the IMF B_Z which motivated us to opt for a deep and involving study of the nature and dynamics of the coupling. In the present paper, we proposed a coupling function to determine the cusp width in terms of IMF B_Z . The cusp width W obeys a hyperbolic tangent function of B_Z , which determines the coupling area depending on the direction and magnitude of B_Z . For extreme northward B_Z , the cusp is almost close whereas it starts to widen out as the magnitude of the northward B_Z reduces below a threshold value B_{Th} . As the B_Z becomes southward, the cusp width further increases proportionally with the increasing magnitude of B_Z and obtains a maximum value for an extremely large southward B_Z . The hyperbolic tangent term in the function numerically varies from 0 to 1 where the value 0 indicates the absolute closing of the cusp and the value 1 indicates absolute opening of the cusp respectively. For the intermediated values, the cusp width is determined according the hyperbolic tangent value of $(-B_Z - B_{Th})$.

To investigate the of the proposed coupling function, the two simulated output series $E_r(t)$ and $E_a(t)$ of the model had been compared with the real-time output of the geomagnetic phenomena, that is, with the real-time Dst index series, $E_{Dst}(t + T)$, which is a result of solar wind-magnetosphere interaction and the AE index series, $E_{AE}(t + T)$, the result of magnetosphere-ionosphere interaction. To obtain the optimum correlation between the simulated series and the real-time series, in both cases the real-time series had been time shifted by T hours and correlation coefficients had been calculated by varying the value of T . The result shows moderate to high values of correlation coefficients in both the above cases for a specific value of the threshold parameter B_{Th} for each year. Further investigation reveals that the variation of the parameter B_{Th} for the entire solar cycle of the year 1997 to the year 2007 obeys a proportional relationship with the variation of yearly mean total number of sunspots in that solar cycle. This striking outcome indicates direct influence of solar activities on the solar wind-magnetosphere reconnection process. Moreover, for the entire solar cycle, it is observed that a 16- to 43-hr time interval is present between the injection of solar wind energy into the magnetosphere during the magnetic reconnection process, and its subsequent effect on the geomagnetic weather and the depression of terrestrial horizontal magnetic field from its average value. Similarly, in the polar region, the disturbances recorded in the auroral magnetic field at any time t is due to the excess energy released in the ionosphere some 0 to 12 hr before. All these detailed studies and methodical analysis led us to the conclusion that solar wind-magnetosphere energy coupling is controlled by a hyperbolic tangent function of $(-B_z - B_{Th})$ where the threshold value, B_{Th} , plays the most significant role under the direct influence of solar activities, and the consequent geomagnetic disturbances, far from being an instantaneous phenomenon, possess an intricate underlying structure which needs some hours to nearly a couple of days' time to build up the dynamics and to change the geomagnetic weather in response to the injection of large amount of solar wind energy into the magnetosphere.

The solar wind-magnetosphere coupling is the primary controller of all the geomagnetic fluctuations on Earth. The true nature and actual dynamics of this coupling can reveal important information about all those widely discussed geomagnetic phenomena like geomagnetic storm or auroral disturbances. It is vital to know the exact amount of injected solar wind energy to understand the energy distribution in the magnetosphere along with the magnetosphere-ionosphere energy transfer. A standard coupling function can estimate the total input energy at any time t as well as the nature of the reconnection which enables us to better understand a number of complex mechanisms in the geospace, like the energy distribution process, the transfer of excess energy dissipated into the ionosphere to maintain the equilibrium, the effect of the injected energy on the Earth's magnetic field, and also the time taken for this effect, the occurrence and duration of geomagnetic storm, and many such other fluctuations related to geomagnetic weather. Moreover, the direct relation of the threshold value B_{Th} with the solar activities throws a new light on the overall analysis. The analysis is a first-order trial to investigate the complex natural process for further knowledge, and it did find out some significant points, but simultaneously also indicates the complex and intricate underlying structure possessed by the geomagnetic disturbances. Future work can be directed to acquire detailed knowledge of this structure by developing the model to a higher degree incorporating the other controlling parameters and physical effects in the algorithm.

Acknowledgments

We acknowledge use of NASA/GSFC's Space Physics Data Facility's OMNIWeb (or CDAWeb or ftp) service, OMNI data, and SIDC, RWC Belgium, World Data Centre. Data sets corresponding to Figures and Table are available as supporting information. We are also thankful to Somnath Mukherjee, Principal of Dinabandhu Andrews College, Kolkata, India, for his cordial support and constant encouragement. Finally, we would like to sincerely thank the anonymous reviewer for his most valuable comments and suggestions to improve the quality of this paper.

References

- Akasofu, S. I. (1981). Energy coupling between the solar wind and the magnetosphere. *Space Science Reviews*, 28, 121. <https://doi.org/10.1007/BF00218810>
- Bak, P., Tang, C., & Wiesenfeld, K. (1987). Self-organized criticality: An explanation of $1/f$ noise. *Physical Review Letters*, 59, 381–384.
- Bak, P., Tang, C., & Wiesenfeld, K. (1988). Self-organized criticality. *Physical Review A*, 38, 364–372.
- Banerjee, A., Bej, A., & Chatterjee, T. N. (2011). On the existence of a long range correlation in the geomagnetic disturbance storm time (Dst) index. *Astrophysics and Space Science*, 337(1), 23–32. <https://doi.org/10.1007/s10509-011-0836-1>
- Banerjee, A., Bej, A., & Chatterjee, T. N. (2015). A cellular automata-based model of Earth's magnetosphere in relation with Dst index. *Space Weather*, 13, 259–270. <https://doi.org/10.1002/2014SW001138>
- Bargatze, L. F., McPherron, R. L., & Baker, D. N. (1986). Solar wind-magnetosphere energy input functions. In Y. Kamide & J. A. Slavin (Eds.), *Solar wind-magnetosphere coupling* (pp. 93–100). Tokyo, Japan: Terrapub/Reidel.
- CENTRA Technology, Inc. report (2011). 'Geomagnetic storms,' prepared for the Office of Risk Management and Analysis, United States Department of Homeland Security.
- Chang, T. S. (1992). Low-dimensional behavior and symmetry breaking of stochastic systems near criticality—Can these effects be observed in space and in the laboratory? *IEEE Transactions of Plasma Science*, 20(6), 691–694.
- Chang, T. S. (1999). Self-organized criticality, multi-fractal spectra, sporadic localized reconnections and intermittent turbulence in the magnetotail. *Physics of Plasmas*, 6(11), 4137–4145.
- Chapman, S. C., Watkins, N. W., Dendy, R. O., Helander, P., & Rowlands, G. (1998). A simple avalanche model as an analogue for magnetospheric activity. *Geophysical Research Letters*, 25(13), 2397–2400.

- Consolini, G. (1997). Sandpile cellular automata and magnetospheric dynamics. In S. Aiello et al. (Eds.), *Conference Proceedings "Cosmic Physics in the Year 2000"* (Vol. 58, pp. 123–126). SIF, Bologna, Italy.
- Consolini, G., & Lui, A. T. Y. (1999). Sign-singularity analysis of current disruption. *Geophysical Research Letters*, 26(12), 1673–1676.
- Crooker, N. U., Feynman, J., & Gosling, J. T. (1977). High correlation between long-term averages of solar-wind speed and geomagnetic activity. *Journal of Geophysical Research*, 82(13), 1933–1937. <https://doi.org/10.1029/JA082i013p01933>
- Crooker, N. U., & Gringauz, K. I. (1993). On the low correlation between long-term averages of solar-wind speed and geomagnetic-activity after 1976. *Journal of Geophysical Research*, 98(A1), 59–62. <https://doi.org/10.1029/92JA01978>
- Dungey, J. W. (1961). Interplanetary magnetic field and auroral zones. *Physical Review Letters*, 6(2), 47–48. <https://doi.org/10.1103/PhysRevLett.6.47>
- Finch, I., & Lockwood, M. (2007). Solar wind-magnetosphere coupling functions on timescales of 1 day to 1 year. *Annales de Geophysique*, 25(2), 495–506.
- Gonzalez, W. D. (1990). A unified view of solar-wind magnetosphere coupling functions. *Planetary and Space Science*, 38(5), 627–632. [https://doi.org/10.1016/0032-0633\(90\)90068-2](https://doi.org/10.1016/0032-0633(90)90068-2)
- Gonzalez, W. D., Tsurutani, B. T., Gonzalez, A. L. C., Smith, E. J., Tang, F., & Akasofu, S.-I. (1989). Solar wind-magnetosphere coupling during intense magnetic storms (1978–1979). *Journal of Geophysical Research*, 94(A7), 8835–8851. <https://doi.org/10.1029/JA094iA07p08835>
- Hydro-Québec, Understanding electricity (1989).—Hydro-Québec. Retrieved 2010-10-2.
- Kan, J. R., & Lee, L. C. (1979). Energy coupling function and solar wind-magnetosphere dynamo. *Geophysical Research Letters*, 6, 577–580. <https://doi.org/10.1029/GL006i007p00577>
- Kappenman, J. G., Zanetti, L. J., & Radasky, W. A. (1997). *Geomagnetic storms can threaten electric power grid*, *Earth in space* (Vol. 9, pp. 9–11). Washington, DC: American Geophysical Union.
- King, J. H., & Papitashvili, N. E. (2005). Solar wind spatial scales in and comparisons of hourly Wind and ACE plasma and magnetic field data. *Journal of Geophysical Research*, 110, A02209. <https://doi.org/10.1029/2004JA010649>
- Klimas, A. J., Valdivia, J. A., Vassiliadis, D., Baker, D. N., & Hesse, M. (2000). The role of self-organized criticality in the substorm phenomenon and its relation to localized reconnection in the magnetospheric plasma sheet. *Journal of Geophysical Research*.
- Lu, G., Baker, D. N., McPherron, R. L., Farrugia, C. J., Lummerzheim, D., Ruohoniemi, J. M., Rich, F. J., et al. (1998). Global energy deposition during the January 1997 magnetic cloud event. *Journal of Geophysical Research*, 103(A6), 11,685–11,694. <https://doi.org/10.1029/98JA00897>
- Lu, J. Y., Jing, H., Liu, Z. Q., Kabin, K., & Jiang, Y. (2013). Energy transfer across the magnetopause for northward and southward interplanetary magnetic fields. *Journal of Geophysical Research: Space Physics*, 118, 2021–2033. <https://doi.org/10.1002/jgra.50093>
- Mawad, R., Kandoul, M., Yousef, S., & Abdel-sattar, W. (2016). Quantized variability of Earth's magnetopause distance. The 5th International Conference on Modern Trends in Physics Research WSP MTPR-014, Volume 9914, 77–83, 2016 ADS:2016mtrp.conf...77 M.
- Murayama, T. (1982). Coupling function between solar-wind parameters and geomagnetic indexes. *Reviews of Geophysics*, 20(3), 623–629. <https://doi.org/10.1029/RG020i003p00623>
- Newell, P. T., Sotirelis, T., Liou, K., Meng, C.-I., & Rich, F. J. (2007). A nearly universal solar wind-magnetosphere coupling function inferred from 10 magnetospheric state variables. *Journal of Geophysical Research*, 112, A01206. <https://doi.org/10.1029/2006JA012015>
- NOAA technical memorandum OAR SEC-88 (2003). Halloween space weather storms of 2003, Space Environment Center, Boulder, Colorado, June 2004
- Østgaard, N., Germany, G., Stadsnes, J., & Vondrak, R. R. (2002). Energy analysis of substorms based on remote sensing techniques, solar wind measurements, and geomagnetic indices. *Journal of Geophysical Research*, 107(A9), 1233. <https://doi.org/10.1029/2001JA002002>
- Palmroth, M., Fear, R. C., & Honkonen, I. (2012). Magnetopause energy transfer dependence on the interplanetary magnetic field and the Earth's magnetic dipole axis orientation. *Annales de Geophysique*, 30(3), 515–526. <https://doi.org/10.5194/angeo-30-515-2012>
- Palmroth, M., Janhunen, P., Pulkkinen, T. I., Aksnes, A., Lu, G., Østgaard, N., et al. (2005). Assessment of ionospheric joule heating by GUMICS-4 MHD simulation, AMIE, and satellite-based statistics: Towards a synthesis. *Annales de Geophysique*, 23(6), 2051–2068.
- Palmroth, M., Koskinen, H. E. J., Pulkkinen, T. I., Toivanen, P. K., Janhunen, P., Milan, S. E., & Lester, M. (2010). Magnetospheric feedback in solar wind energy transfer. *Journal of Geophysical Research*, 115, A00I10. <https://doi.org/10.1029/2010JA015746>
- Palmroth, M., Laitinen, T. V., & Pulkkinen, T. I. (2006). Magnetopause energy and mass transfer: Results from a global MHD simulation. *Annales de Geophysique*, 24(12), 3467–3480.
- Palmroth, M., Pulkkinen, T. I., Janhunen, P., & Wu, C. C. (2003). Stormtime energy transfer in global MHD simulation. *Journal of Geophysical Research*, 108(A1), 1048. <https://doi.org/10.1029/2002JA009446>
- Papadopoulos, K., Goodrich, C., Wiltberger, M., Lopez, R., & Lyon, J. G. (1999). The physics of substorms as revealed by the ISTP. *Physics and Chemistry of the Earth - Part C*, 24(1–3), 189–202. [https://doi.org/10.1016/S1464-1917\(98\)00028-2](https://doi.org/10.1016/S1464-1917(98)00028-2)
- Papitashvili, V. O., Papitashvili, N. E., & King, J. H. (2000). Solar cycle effects in planetary geomagnetic activity: Analysis of 36-year long OMNI dataset. *Geophysical Research Letters*, 27(17), 2797–2800. <https://doi.org/10.1029/2000GL000064>
- Perreault, P., & Akasofu, S. I. (1978). Study of geomagnetic storms. *Geophysical Journal of the Royal Astronomical Society*, 54(3), 547–573. <https://doi.org/10.1111/j.1365-246X.1978.tb05494.x>
- Pulkkinen, T. I., Ganushkina, N. Y., Kallio, E. I., Lu, G., Baker, D. N., Turner, N. E., et al. (2002). Energy dissipation during a geomagnetic storm: May 1998. *Advances in Space Research*, 30(10), 2231–2240. [https://doi.org/10.1016/S0273-1177\(02\)80232-0](https://doi.org/10.1016/S0273-1177(02)80232-0)
- Pulkkinen, T. I., Palmroth, M., Janhunen, P., Koskinen, H. E. J., McComas, D. J., & Smith, C. W. (2010). Timing of changes in the solar wind energy input in relation to ionospheric response. *Journal of Geophysical Research*, 115, A00I09. <https://doi.org/10.1029/2010JA015764>
- Pulkkinen, T. I., Palmroth, M., & Laitinen, T. (2008). Energy as a tracer of magnetospheric processes: GUMICS-4 global MHD results and observations compared. *Journal of Atmospheric and Solar - Terrestrial Physics*, 70(5), 687–707. <https://doi.org/10.1016/j.jastp.2007.10.011>
- Russell, C. T. (2000). The solar wind interaction with the Earth's magnetosphere: A tutorial. *IEEE Transactions on Plasma Science*, 28, 1818.
- Russell, C. T. (2013). Solar Wind and Interplanetary Magnetic Field: A Tutorial. In P. Song, H. J. Singer, & G. L. Siscoe (Eds.), *Space Weather*. <https://doi.org/10.1029/GM125p0073>
- Scurry, L., & Russell, C. T. (1991). Proxy studies of energy-transfer to the magnetosphere. *Journal of Geophysical Research*, 96(A6), 9541–9548. <https://doi.org/10.1029/91JA00569>
- Stamper, R., Lockwood, M., Wild, M. N., & Clark, T. D. G. (1999). Solar causes of the long-term increase in geomagnetic activity. *Journal of Geophysical Research*, 104(A12), 28,325–28,342. <https://doi.org/10.1029/1999JA900311>
- Stern, D. P. (1984). Energetics of the magnetosphere. *Space Science Reviews*, 39(1–2), 193–213.
- Takalo, J., Timonen, J., Klimas, A., Valdivia, J., & Vassiliadis, D. (1999). Nonlinear energy dissipation in a cellular automaton magnetotail field model. *Geophysical Research Letters*, 26, 1813–1816.

- Tanskanen, E., Pulkkinen, T. I., Koskinen, H. E. J., & Slavin, J. A. (2002). Substorm energy budget during low and high solar activity: 1997 and 1999 compared. *Journal of Geophysical Research*, *107*(A6), 1086. <https://doi.org/10.1029/2001JA900153>
- Temerin, M., & Li, X. (2006). *Dst* model for 1995–2002. *Journal of Geophysical Research*, *111*, A04221. <https://doi.org/10.1029/2005JA011257>
- Tenfjord, P., & Ostgaard, N. (2013). Energy transfer and flow in the solar wind-magnetosphere-ionosphere system: A new coupling function. *Journal of Geophysical Research: Space Physics*, *118*, 5659–5672. <https://doi.org/10.1002/jgra.50545>
- Turner, N. E., Baker, D. N., Pulkkinen, T. I., Roeder, J. L., Fennell, J. F., & Jordanova, V. K. (2001). Energy content in the storm time ring current. *Journal of Geophysical Research*, *106*(A9), 19,149–19,156. <https://doi.org/10.1029/2000JA003025>
- Uritsky, V. M. (1996). $1/f$ -like spectra of geomagnetic fluctuations: Expression of self-organized criticality? In Book of abstracts of the International Conference on Problems of Geocosmos, June 17–23, (p. 110). St. Petersburg, Russia.
- Uritsky, V. M., & Pudovkin, M. I. (1998a). Fractal dynamics of *AE*-index of geomagnetic activity as a marker of the self-organized criticality in the magnetosphere (in Russian). *Geomagnetizm i Aeronomia*, *38*(3), 17–28.
- Uritsky, V. M., & Pudovkin, M. I. (1998b). Low frequency $1/f$ -like fluctuations of the *AE*-index as a possible manifestation of self-organized criticality in the magnetosphere. *Annales Geophysicae*, *16*(12), 1580–1588.
- Uritsky, V. M., Pudovkin, M. I., & Steen, A. (2001). Geomagnetic substorms as perturbed self-organized critical dynamics of the magnetosphere. *Journal of Atmospheric and Solar-Terrestrial Physics*, *63*(13), 1415–1424. [https://doi.org/10.1016/S1364-6826\(00\)00243-1](https://doi.org/10.1016/S1364-6826(00)00243-1)
- Uritsky, V. M., & Semenov, V. S. (2000). A sandpile model for global statistics of reconnection events in the magnetotail. In H. K. Biernat, C. J. Farrugia, & D. F. Vogl (Eds.), *The Solar Wind - Magnetosphere System 3* (pp. 299–308). Osterreichische Akademie der Wissenschaften, Wien.
- R.A.M. Van der Linden and the SIDC team (n.d.), online catalogue of the sunspot index, <http://sidc.oma.be/html/sunspot.html>.
- Vasyliunas, V. M., Kan, J. R., Siscoe, G. L., & Akasofu, S. I. (1982). Scaling relations governing magnetospheric energy-transfer. *Planetary and Space Science*, *30*(4), 359–365. [https://doi.org/10.1016/0032-0633\(82\)90041-1](https://doi.org/10.1016/0032-0633(82)90041-1)
- Wang, C., Han, J. P., Li, H., Peng, Z., & Richardson, J. D. (2014). Solar wind-magnetosphere energy coupling function fitting: Results from a global MHD simulation. *Journal of Geophysical Research: Space Physics*, *119*, 6199–6212. <https://doi.org/10.1002/2014JA019834>
- Workshop report, National Research Council of the National Academies (2008). *Severe space weather events—Understanding societal and economic impacts—*. Washington, DC: The National Academies Press.
- Wygant, J. R., Torbert, R. B., & Mozer, F. S. (1983). Comparison of S3-3 polar-cap potential drops with the interplanetary magnetic-field and models of magnetopause reconnection. *Journal of Geophysical Research*, *88*(A7), 5727–5735. <https://doi.org/10.1029/JA088iA07p05727>
- Youssef, M., Mahrous, A., Mawad, R., Ghamry, E., Shaltout, M., El-Nawawy, M., & Fahim, A. (2011). The effects of the solar magnetic polarity and the solar wind velocity on *Bz*-component of the interplanetary magnetic field. *Advances in Space Research*, *49*(7), 1198–1202. <https://doi.org/10.1016/j.asr.2011.07.023>



Source details

[Feedback >](#) [Compare sources >](#)

Earth and Space Science

Open Access [i](#)

Scopus coverage years: from 2014 to Present

Publisher: Wiley-Blackwell

E-ISSN: 2333-5084

Subject area: [Earth and Planetary Sciences: General Earth and Planetary Sciences](#) [Environmental Science: Environmental Science \(miscellaneous\)](#)

Source type: Journal

[View all documents >](#)

[Set document alert](#)

[Save to source list](#)

CiteScore 2022

5.4



SJR 2022

0.958



SNIP 2022

1.244



Earth and Space Science

RESEARCH ARTICLE

10.1029/2018EA000468

Key Points:

- The solar wind-magnetosphere coupling has been analyzed using a cellular automata model based on the concept of self-organized criticality
- A new coupling function is introduced to determine the cusp width
- A threshold value of B_z , the z th component of the interplanetary magnetic field related to the yearly mean total number of sunspots, is introduced

Supporting Information:

- Supporting Information S1
- Data Set S1
- Data Set S2
- Data Set S3
- Data Set S4

Correspondence to:

A. Bej,
amaresh_bej@yahoo.com

Citation:

Banerjee, A., Bej, A., Chatterjee, T. N., & Majumdar, A. (2019). An SOC approach to study the solar wind-magnetosphere energy coupling. *Earth and Space Science*, 6, 565–576. <https://doi.org/10.1029/2018EA000468>

Received 5 SEP 2018

Accepted 3 FEB 2019

Accepted article online 6 FEB 2019

Published online 8 APR 2019

©2019. The Authors.

This is an open access article under the terms of the Creative Commons Attribution-NonCommercial-NoDerivs License, which permits use and distribution in any medium, provided the original work is properly cited, the use is non-commercial and no modifications or adaptations are made.

An SOC Approach to Study the Solar Wind-Magnetosphere Energy Coupling

Adrija Banerjee¹, Amaresh Bej¹ , T. N. Chatterjee², and Abhijit Majumdar¹

¹Department of Physics, Indian Institute of Engineering Science and Technology, Howrah, India, ²Department of Electronics, Dinabandhu Andrews College, Kolkata, India

Abstract Solar wind-magnetosphere interaction and the injection of large quantity of plasma particles into the Earth's magnetosphere are the primary reasons behind geomagnetic storm, auroral effects, and, in general, all the fluctuations observed in the terrestrial magnetic field. In this paper, we analyzed the perturbed magnetosphere as a sandpile-like cellular automata model based on the concept of self-organized criticality and many-body interactive system and proposed a solar wind-magnetosphere energy coupling function in terms of interplanetary magnetic field B_z , the z th component of interplanetary magnetic field. The function determines the cusp width W depending on the intensity of $(-B_z - B_{Th})$ where B_{Th} is the threshold value. The model generates two output series, which are the numerical representation of the real-time Dst index and AE index series, respectively. For our study, the range of years 1997–2007 of the 23rd solar cycle had been considered here. The threshold value B_{Th} plays a significant role in the analysis and exhibits a proportional relationship with the yearly mean total number of sunspots for each year of the range 1997–2007 of the 23rd solar cycle. For each year, the two resultant output time series of the model display high-correlation coefficients with the real-time Dst and AE indexes, respectively, which denotes the acceptability of the proposed energy coupling function and its relation with the solar activities.

1. Introduction

The solar wind-magnetosphere interaction and the energy coupling can be considered as the key factor to understand the various dynamical properties of the terrestrial magnetosphere. The solar wind, a stream of highly energized plasma particles, emitted from the Sun's outer atmosphere, is coming toward the Earth with an average speed of 400 km/s. These huge amounts of particles are injected into the Earth's magnetosphere through the cusps controlled by the z th component of the interplanetary magnetic field (IMF), B_z . The direction and magnitude of IMF B_z is the primary controller of the solar wind-magnetosphere reconnection along with the dynamic pressure of the solar wind. A detailed knowledge of the energy coupling mechanism is important to estimate the total amount of injected solar wind energy in the geospace as this energy drives all the geomagnetic fluctuations in the terrestrial magnetosphere, causing intense geomagnetic storm or auroral activities (Russell, 2000, 2013).

Extreme geomagnetic activity is considered to be a serious threat to the Earth's technological and electrical systems. In the time of severe geomagnetic storm, solar wind injects a large amount of ionized particles into the Earth's magnetosphere, rapidly changing the intensity of the magnetic field which in turn induces an electric field on the surface of the Earth. This induced electric field then drives a current through any electrical network by forming a potential difference between the ground points of that network. This current is known as geomagnetically induced current (GIC). The intensity of GIC has been noted as large as over 100 A, though a few amperes is sufficient to unexpectedly collapse any electrical infrastructure causing a huge loss of money and related hazards (Kappenman et al., 1997). The 13 March 1989 geomagnetic storm and the complete collapse of Hydro Quebec power grid resulting in 9 hr blackout for 6 million customers [Hydro-Québec, Understanding Electricity, 1989; Kappenman et al., 1997], the 30-hr blackout of the Wide Area Augmentation System managed by the Federal Aviation Administration, and the damage of Japanese ADEOS-2 satellite due to the Halloween solar storm in 2003 are some of the most prominent examples [CENTRA Technology Inc. report 2011; NOAA Technical Memorandum 2003; Workshop report of National Research Council of the National Academics 2008]. Also, past records of GIC-triggered hazards include complete disruption of power grids and transformers; malfunction of railway equipment and satellite hardware; severe collapsing of telecommunication, navigation, and computer systems; and increase of

steel corrosion in pipeline networks, particularly in countries like the United States and Canada or northern Europe, located in the upper latitudes and affected most by the auroral electrojet current [CENTRA Technology Inc. report 2011; Kappenman et al., 1997; NOAA Technical Memorandum 2003]. So a comprehensive knowledge of the solar wind-magnetosphere interaction and the underlying physical process of geomagnetic activity is crucial to save human society from its severe negative effects.

The solar wind-magnetosphere energy coupling mechanism became a subject of keen interest and curiosity in the past decades. The complex dynamics of the energy coupling process, the rate of energy transfer into the magnetosphere, and the distribution of the injected energy in the magnetosphere-ionosphere system as well as the role of the various solar wind parameters controlling the overall process had been rigorously studied, analyzed, and characterized in numerous works. A number of solar wind energy coupling functions had been presented (Akasofu, 1981; Finch & Lockwood, 2007; Gonzalez, 1990; Gonzalez et al., 1989; Kan & Lee, 1979; Newell et al., 2007; Perreault & Akasofu, 1978), while the nature of solar wind-magnetosphere interaction had been extensively studied in relation with the other solar wind parameters like velocity, ion density, and dynamic pressure [Crooker et al., 1977; Crooker & Gringauz, 1993; Dungey, 1961; Mawad et al., 2016; Newell et al., 2007; Papitashvili et al., 2000; Temerin & Li, 2006; Wygant et al., 1983; Youssef et al., 2011]. Global magnetohydrodynamic simulations [Palmroth et al., 2003, 2005, 2006, 2010, 2012; Papadopoulos et al., 1999. Pulkkinen et al., 2002, 2008, 2010; Wang et al., 2014] along with various other methods (Bargatze et al., 1986; Murayama, 1982; Stamper et al., 1999) were also taken into account. The estimation of the percentage of solar wind energy injected into the geospace, how much of this energy is dissipating in the magnetosphere or in the ionosphere, and in general the entire energy transfer and dissipation process long became the focus point of detailed investigations [Lu et al., 1998, 2013; Scurry & Russell, 1991; Stern, 1984; Tanskanen et al., 2002; Tenfjord & Ostgaard, 2013; Turner et al., 2001; Østgaard et al., 2002; Vasyliunas et al., 1982]. Though all these serious efforts produced significant results, solar wind-magnetosphere-ionosphere interaction still demands further attention to understand the complex nature of geomagnetic disturbances.

In our previous work, we came to realize that geomagnetic disturbances on the Earth is an essentially complex natural phenomenon having a number of underlying dynamics and quite impossible to predict accurately, whereas *Dst* index, the measurement of geomagnetic activity, is a positively correlated fractional Brownian motion having long-range correlation (Banerjee et al., 2011). Enlightened by this outcome, we aimed to develop a sandpile-like cellular automata model, analogous to the Earth's magnetosphere to investigate the dynamical characteristics of the geomagnetic storm (Banerjee et al., 2015). Now sandpile model was selected as the first example displaying the concept of self-organized criticality, introduced by Bak et al. in their 1987, 1988 pioneering papers. Since then, this algorithm had been extensively used to study and analysis the physical process of geomagnetic fluctuations (Chang, 1992, 1999; Chapman et al., 1998; Consolini, 1997; Consolini & Lui, 1999; Klimas et al., 2000; Takalo et al., 1999; Uritsky, 1996; Uritsky & Pudovkin, 1998a, 1998b; Uritsky & Semenov, 2000). Our proposed 2015 model was a dissipative dynamical system with both spatial and temporal degrees of freedom, based on the concept of self-organized criticality and a refined version of the model presented by Uritsky et al. (2001). Though it was a first-order model with basic considerations, the resultant time series exhibited similar statistical characteristics of the real-time *Dst* index. The acceptability of the model and its curious outcome made us realize the significance of the solar wind-magnetosphere interaction and motivated us to further investigate the true nature of the energy coupling mechanism.

In the present paper, we continued our analysis based on the sandpile-like cellular automata model of the terrestrial magnetosphere, presented in our 2015 paper (Banerjee et al., 2015). We proposed a definite solar wind-magnetosphere energy coupling function in terms of IMF B_z and a threshold value, B_{Th} . The function is a hyperbolic tangent one which determines the cusp width W at any time t . The model produces two output series which are the numerical representations of the real-time *Dst* index and *AE* index series, respectively. To examine the validity of the proposed energy coupling function, the correlation coefficients between the simulated output series, the real-time *Dst*, and *AE* index series had been estimated respectively. The entire 23rd solar cycle had been studied, and the real-time data of solar ion density, flow speed, and IMF B_z had been considered here. The result shows significant values of correlation coefficients between the simulated and real-time series for a specific value of the B_{Th} for each year. The parameter B_{Th} plays a key

role here as it varies exactly proportionally to the variation of the yearly mean total number of sunspots for each year of the range 1997–2007 of the 23rd solar cycle, revealing the direct influence of solar activities on the solar wind-magnetosphere reconnection phenomena.

2. Method

The cellular automata-based sandpile model presented here is a refinement of the model proposed in our previous paper (Banerjee et al., 2015). In summary, the model, a numerical representation of the Earth's magnetosphere, is a finite matrix of $n \times n$ elements, characterized by energy E , which is a function of time and space. With analogy to the Earth, open boundary condition had been considered, denoting upper ($i = 1, j = 1$ to n) and lower ($i = n, j = 1$ to n) boundary regions of the system. Solar wind emitted from the Sun is coming toward the Earth. It interacts with the terrestrial magnetosphere, a reconnection occurs, and a significant amount of ionized particle penetrates into the geospace through the cusp, altering its energy. The energy unit dE at any time t is calculated using the real-time ion density and flow speed data obeying the equation

$$dE(t) = \text{norm}^{1/2} \times \text{ion density} \times (\text{flow speed})^2 \quad (1)$$

For initialization, each of the cells of the matrix is credited with a small amount of solar wind energy following the equations

$$E_{t+1}(i,j) = E_t(i,j) + K_r \times dE(t) \text{ for } i = 2 \text{ to } n+1, j = 1 \text{ to } n \quad (2)$$

and

$$E_{t+1}(i,j) = E_t(i,j) + K_a \times dE(t) \text{ for } i = 1, j = 1 \text{ to } n \quad (3)$$

where K_r and K_a are constants.

Both the direction and the intensity of the z th component of the IMF, B_z determines the cusp width W , thus controlling the amount of energy injected into the system. For the cellular automata model of $n \times n$ matrix presented here, the cusp width W is a square of cells surrounding the cell ($i = n/2, j = n/2$), that is, the cell in the center of the matrix. For a large northward B_z , the cusp width W is minimum 0, whereas for a large southward B_z , the cusp width W has a maximum value, $W_m = (n - 1)^2$. W_m has a constant value for a constant n .

The functional relationship of W and B_z proposed here is

$$W(t) = W_m * ((\tanh((-B_z - B_{Th})/\lambda) + 1)/2) \quad (4)$$

where B_{Th} is the threshold value of IMF B_z to open up the cusp and λ is a constant. The parameter B_{Th} is the most significant factor in the entire analysis as it controls the net amount of solar wind-magnetosphere energy coupling area. At any time t , the hyperbolic tangent term in equation (4) generates a value in the range of 0 to 1. For a large southward B_z , the hyperbolic tangent term is 1 and $W = W_m$, whereas for a large northward B_z the term is 0 and $W = 0$. In between the extrema, W has an intermediate value depending on the value of $(-B_z - B_{Th})$. W has a numeric value.

The input energy $dE(t)$ is injected into the model through W number of cells following the equation

$$E_{t+1}(i,j) = E_t(i,j) + dE(t) \text{ for } i = n/2 \pm p, j = n/2 \pm p \quad (5)$$

where $p = \text{round}((\sqrt{W} - 1)/2)$.

Now if the altered energy of the cell (i,j) crosses the threshold value E_{Th} of the system, the excess energy is distributed among the adjacent neighbors obeying the equations

$$E_{t+1}(i,j) = E_t(i,j) - 4 \quad (6)$$

and

$$E_{t+1}(i\pm 1, j\pm 1) = E_t(i\pm 1, j\pm 1) + (1 - E_d/4) \quad (7)$$

where E_d is the dissipation factor and $(i \pm 1) \geq 1$ or 2 according to the case.

The total energy of the system at any time t can be calculated as

$$E_1(t) = \sum E(i,j) \text{ for } i = 2 \text{ to } n + 1, j = 1 \text{ to } n \quad (8)$$

The differential value of the energy stored in the system at any time t is then estimated by

$$E_2(t) = \Delta E_1(t) \quad (9)$$

For further refinement, the above time series is then processed by a moving-average filter of span 72 to get the final output series as

$$E_r(t) = -\text{MA}(E_2) \quad (10)$$

$E_r(t)$ is an estimation of the differential value of the energy stored in the system and can be considered as a numerical equivalent to the Dst index. Now a high correlation coefficient between the simulated series $E_r(t)$ and the real-time Dst index can establish the validity of the proposed coupling function.

The real-time hourly averaged Dst index data set has been obtained from OMNIWeb. To remove the noise and fine-scale structure, the data set is further processed by a moving-average filter of span 72 to get a series, namely, $E_{Dst}(t + T)$ where T denotes the time shift or time lag. Now cross correlation is considered as a standard technique to measure the degree of similarity between two time series, and this method had been applied here to determine the correlation between the series $E_r(t)$ and $E_{Dst}(t + T)$. To estimate the optimum cross-correlation coefficient between these two series, the series $E_r(t)$ had been compared to the time-shifted real-time Dst index, $E_{Dst}(t + T)$ where T is varied in the range of values 0 to 720 hr, and for each value of T , the correlation coefficients between the two series had been noted down along with the exact value of T . Here T is the lag value of duration 1 hr associated with the cross-correlation method.

As open boundary condition has been considered, the excess energy transmits outside the grid after reaching the upper ($i = 1, j = 1$ to n) and lower ($i = n + 2, j = 1$ to n) boundary regions of the system. With analogy to the Earth, these upper and lower boundaries can be considered as the northern and southern polar cusps of the Earth, while this energy transfer process is similar to the transmission of the excess energy of the Earth's magnetosphere to the ionosphere through the polar cusps. Thus, the amount of excess energy dissipated through the upper boundary or northern polar cusp can be estimated as

$$E_3(t) = \sum E(i,j) \text{ for } i = 1, j = 1 \text{ to } n \quad (11)$$

and the differential energy value as

$$E_4(t) = \Delta E_3(t) \quad (12)$$

Similarly, as equation (10) the moving-average technique has been applied to equation (12) to get the following one

$$E_a(t) = \text{MA}(E_4) \quad (13)$$

Equation (13) is the measurement of the excess energy dissipated in the ionosphere from the magnetosphere through the polar cusps and can be considered as a numerical representation of the auroral electrojet (AE) index. Similar as before, the real-time AE index data series has been obtained from OMNIWeb and further processed by a moving-average filter of span 72 to get the series $E_{AE}(t + T)$, where T is the time shift or time lag. Again, the method of cross correlation had been applied here to determine the amount of correlation

between the two series $E_a(t)$ and $E_{AE}(t + T)$, considering T as the associated lag value of duration 1 hr. The correlation coefficients between the simulated series $E_a(t)$ of equation (13) and the real-time $E_{AE}(t + T)$ had been estimated to further strengthen the validity of the proposed coupling function. Here also, the series $E_a(t)$ had been compared with the time-shifted AE index, $E_{AE}(t + T)$ where T is varied in the range of values 0 to 720 hr to achieve the optimum correlation coefficient between the two series. For each value of T , the associated correlation coefficients had been recorded.

As mentioned before, the threshold value B_{Th} of equation (4) is playing the key role in the entire analysis as the term $(-B_Z - B_{Th})$ controls the widening or narrowing of the cusp width and the amount of solar wind energy injected into the magnetosphere at any time t . In this work, we had studied the variation of the magnitude of the solar wind-magnetosphere coupling with variation of B_{Th} and its subsequent effect on the overall dynamics of the system.

3. Data source

Here we used the hourly averaged Dst index, AE index, solar wind ion density, flow speed, and B_Z component of the IMF data from the year 1997 to the year 2007 as extracted from NASA/GSFC's (Goddard Space Flight Center) OMNI data set through OMNIWeb (King & Papitashvili, 2005). The OMNI data were obtained from the GSFC/SPDF (Space Physics Data Facility) OMNIWeb interface at the OMNIWeb website (<http://omniweb.gsfc.nasa.gov>). We used the Dst index and AE index data obtained from OMNIWeb to compare with the estimated series $E_r(t)$ and $E_a(t)$, respectively.

For the yearly mean total number of sunspots, the source credit is the sunspot data from the World Data Center SILSO (Sunspot Index and Long-term Solar Observations; Sunspot Number and Long-term Solar Observations, Royal Observatory of Belgium, on-line Sunspot Number catalogue: <http://www.sidc.be/SILSO/>, '1997–2007').

4. Result and Discussions

To study the dynamics of the system depending on the solar wind-magnetosphere coupling, we had considered the range of years 1997 to 2007 of the 23rd solar cycle. The input energy dE had been calculated using equation (1) and using the real-time value of flow speed and ion density. The cellular automata model is a matrix having a dimension of $n \times n$. Here it is taken as $n = 50$, that is, the matrix contains 50×50 cells. The input energy $dE(t)$, calculated from OMNIWeb data is an one-dimensional time series. At any time t , the total cusp area W is determined using equation (4). The cusp area is a square having the cells $i = 25 \pm p, j = 25 \pm p$ where $p = \text{round}((\sqrt{W} - 1)/2)$. The input energy $dE(t)$ is injected into all these cells of $i = 25 \pm p, j = 25 \pm p$ according to equation (5) stated in the section 2. The values of the different parameters are taken as $E_{Th} = 5, E_d = 0.001, K_r = 0.001, K_a = 0.1, \lambda = 0.5$. All these values are constants for each of the year in the range of 1997–2007. As referred in the section 2, our sandpile model is a refined version of the model presented in our 2015 paper which was based on the model proposed by Uritsky et al. (2001). Uritsky et al. set the threshold of excitation as $E_{Th} = 5$ and suggested the value of the dissipation term $E_d < = 0.01$ to study the wide-range scale-invariant behavior of the system. Following their work, we also set $E_{Th} = 5$ and $E_d = 0.001$ for our model. We studied the model for different values of $K_r, K_a,$ and λ and observed that the model output series matches best with the real-time series for values $K_r = 0.001, K_a = 0.1,$ and $\lambda = 0.5$. So we considered these values of $K_r, K_a,$ and λ constants for our entire analysis.

For each year, the value of parameter B_{Th} had been varied in the range of -10.00 to 10.00 nT, and for each value of B_{Th} within this range, the correlation coefficients between the simulated series $E_r(t)$ of equation (10) and the time-shifted real-time Dst index series $E_{Dst}(t + T)$ as well as the series $E_a(t)$ of equation (13) and the time-shifted real-time AE index series $E_{AE}(t + T)$ had been estimated respectively. While calculating the correlation coefficients for the above two cases, the value of time lag T had been varied from $T = 0$ to 720 hr to achieve the optimum value of the coefficients. Thus, the best correlation coefficient for each set is found annually. The exact value of B_{Th} and the particular value of T associated with the optimum coefficients had been noted down along with the value of the coefficients. Table 1 displays the optimum values of the correlation coefficients for each year in the range of 1997 to 2007 with the corresponding values of the

Table 1

The First Three Columns of the Table Shows the Yearly Mean Total Number of Sunspots and the Values of the Threshold B_Z , B_{Th} for All the Years in the Range of 1997–2007

Year	Yearly mean total number of sunspots	B_{Th} (nT)	Comparison between $E_r(t)$ and $E_{Dst}(t + T)$		Comparison between $E_a(t)$ and $E_{AE}(t + T)$	
			Optimum correlation coefficient (%)	Time lag T (hr)	Optimum correlation coefficient (%)	Time lag T (hr)
1997	28.90	1.25	70.27	24	74.53	2
1998	88.30	1.76	60.47	32	77.05	4
1999	136.30	2.18	64.23	24	66.06	5
2000	173.90	2.50	76.06	25	69.02	2
2001	170.40	2.47	72.64	21	72.28	0
2002	163.60	2.41	75.83	31	75.42	8
2003	99.30	1.86	62.99	25	59.47	10
2004	65.30	1.56	75.26	16	76.37	3
2005	45.80	1.40	60.64	35	75.96	11
2006	24.70	1.21	52.83	30	74.63	6
2007	12.60	1.10	62.79	43	81.18	12

Note. For this entire range of years, the optimum correlation coefficients between the simulated series $E_r(t)$ and the time-shifted real-time Dst index series $E_{Dst}(t + T)$ and the associated values of time lag T are displayed in the fourth and fifth columns, respectively, while in a similar fashion, the sixth and seventh columns show the optimum correlation coefficients between the simulated series $E_a(t)$ and the time-shifted real-time AE index series $E_{AE}(t + T)$ and the corresponding values of time lag T , respectively.

parameter B_{Th} and also the values of T for both the cases. The correlation coefficient R between two series A and B is calculated using the equation

$$R = \frac{\sum_m \sum_n (A_{mn} - \bar{A})(B_{mn} - \bar{B})}{\sqrt{(\sum_m \sum_n (A_{mn} - \bar{A})^2)(\sum_m \sum_n (B_{mn} - \bar{B})^2)}} \quad (14)$$

Figure 1 represents a comparison between the actual waveforms of the simulated series $E_r(t)$ and the real-time Dst index series $E_{Dst}(t + T)$ where $T = 31$ for the year of 2002. The optimum correlation coefficient between these two series is 75.83% for $B_{Th} = 2.41$ and $T = 31$ in this year. The top half of Figure 1 shows the waveform of simulated output series $E_r(t)$, while the bottom half shows the waveform of the time-shifted Dst index series, $E_{Dst}(t + T)$ for the year 2002. Both the series are 1-hourly time series having 8,578 data each. The time in hour is plotted in the x axis. Here 8,000 means $t = 8,000$, that is, the point of 8,000th hour. Each of the year in the range of 1997–2007 contains 8,000–9,000 data.

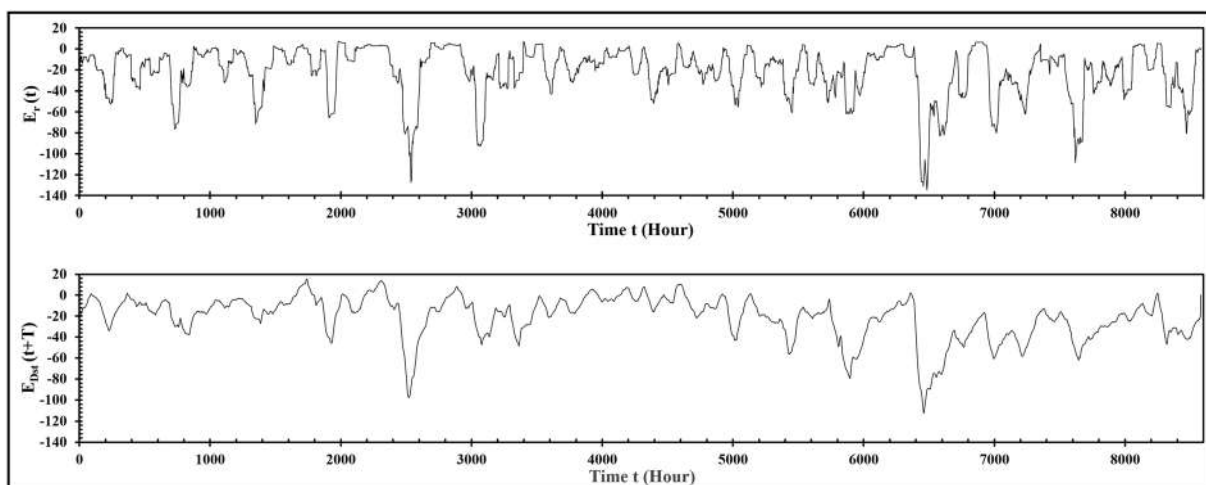


Figure 1. (top) The plot of simulated output series $E_r(t)$ and (bottom) the plot of the time-shifted Dst index series, $E_{Dst}(t + T)$ where $T = 31$ for the year 2002. Both the series are plotted with respect to time (hours). The value of $B_{Th} = 2.41$ for this year and the optimum correlation coefficient between the two series is 75.83%. The correlation coefficient between the two series is estimated using equation (14).

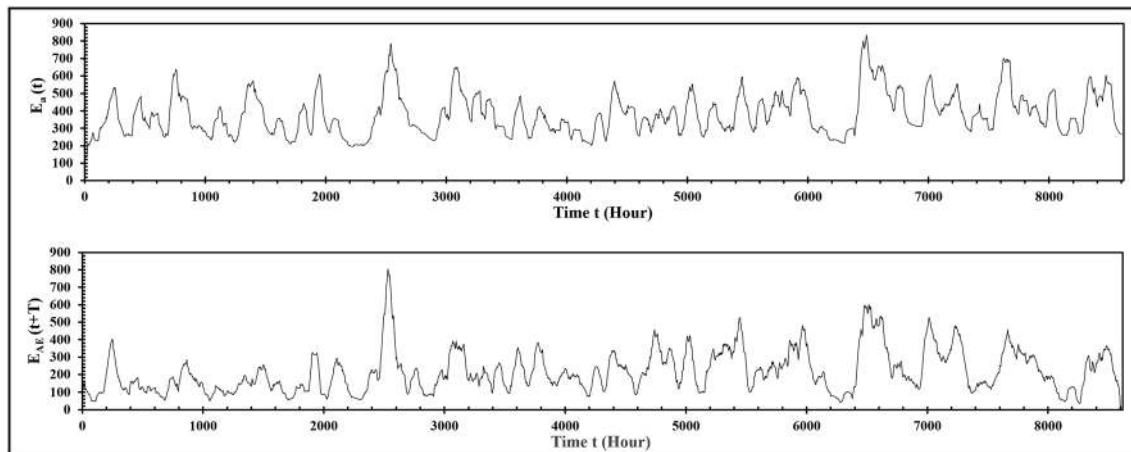


Figure 2. (top) The plot of simulated output series $E_a(t)$ and (bottom) the plot of the time-shifted AE index series, $E_{AE}(t + T)$ where $T = 8$ for the year 2002. Both the series are plotted with respect to time (hours). The value of $B_{Th} = 2.41$ for this year and the optimum correlation coefficient between the two series is 75.42%. The correlation coefficient between the two series is estimated using equation (14).

Figure 2 displays the graphs of the simulated series $E_a(t)$ and the real-time AE index $E_{AE}(t + T)$ where $T = 8$, also for the year of 2002. Here the optimum correlation coefficient between these two series is 75.42% for $B_{Th} = 2.41$ and $T = 8$. The top half of Figure 2 shows the waveform of simulated output series $E_a(t)$, while the bottom half shows the waveform of the time-shifted AE index series, $E_{AE}(t + T)$ for the year 2002. Both the series are 1-hourly time series having 8,601 data each. The time in hour is plotted in the x axis.

The current work is focused to propose a solar wind-magnetosphere energy coupling function and to study the subsequent energy transfer process using a cellular automata model of Earth's magnetosphere. To establish the validity of the model and the coupling function, the model had been simulated numerously for different set of values of the controlling parameters. For every simulation, the model output series had been compared with the real-time series. Finally, it is observed that for the set of values $K_r = 0.001$, $K_a = 0.1$, and $\lambda = 0.5$ the model output series matches best with the real-time series. So we have considered these set of values constant for the entire range of the years 1997–2007. Now T denotes the time gap between

the injection of the plasma particles into the magnetosphere and its subsequent effect on the intensity of the horizontal magnetic field of the Earth. As the amount of injected energy into the magnetosphere is not same for every year, the value of T cannot be assumed as a constant for every year beforehand; rather its value for each year had been obtained from the result.

Figure 3 shows the plot of optimum correlation coefficient for each of the years in the range of 1997–2007 for both sets of data, as obtained from Table 1.

The above result exhibits a striking connection of the solar wind-magnetosphere reconnection with solar activities. Table 1 also shows the yearly mean total number of sunspots for each year in the range of 1997–2007 of the 23rd solar cycle. As shown in Figure 4, for the entire range of years, the parameter B_{Th} varies proportionally with the yearly mean total number of sunspots. The value of B_{Th} is maximum 2.5 in the year 2000 which is also the year of solar maxima having 173.9 yearly mean total number of sunspots, while B_{Th} reaches its minimum value 1.1 in the year where the yearly mean total number of sunspots is only 12.6.

Studying the above observations thoroughly, we came to realize some significant and meaningful points about the solar wind-magnetosphere coupling and the resultant geomagnetic disturbances which can be discussed

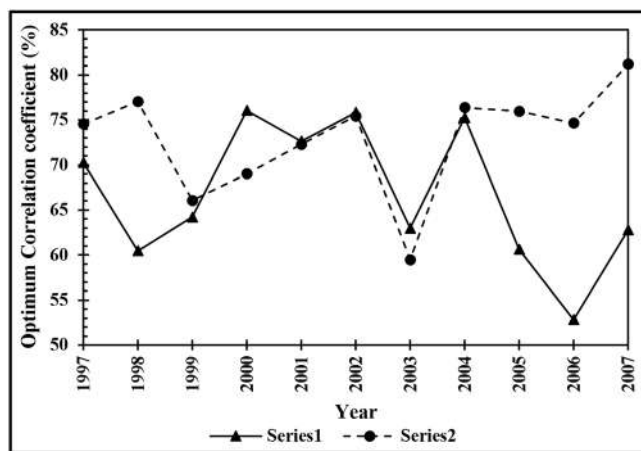


Figure 3. Series 1 is the yearly plot of the optimum correlation coefficients between the simulated series $E_r(t)$ and the time-shifted real-time Dst index series $E_{Dst}(t + T)$. Series 2 is the yearly plot of the optimum correlation coefficients between the simulated series $E_a(t)$ and the time-shifted real-time AE index series $E_{AE}(t + T)$. Year, in the range of 1997–2007 is plotted in the x axis.

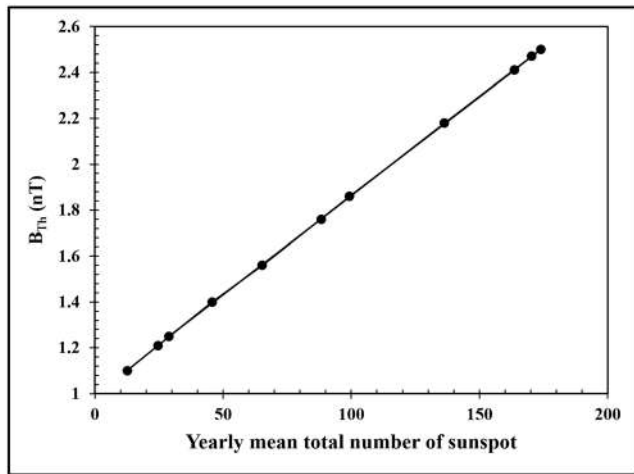


Figure 4. The threshold value, B_{Th} , is plotted with respect to the yearly mean total number of sunspots for the range of years 1997–2007 of the 23rd solar cycle. The graph shows a proportional relationship between these two parameters.

the rightness of the proposed coupling function in two ways, first in connection with the stored energy in the magnetosphere and Dst index and second in connection with the excess energy dissipated into the ionosphere and AE index. The correlation coefficients are associated to a particular value of the parameter B_{Th} for each year. Most significantly, the parameter B_{Th} displays a proportional relationship with the yearly mean total number of sunspots for the entire solar cycle, revealing an influence of solar activities on the threshold value, B_{Th} . Higher number of solar spots indicates higher solar activity which increases solar wind and also the coronal mass ejections, resulting in an injection of huge amount of plasma particles into the terrestrial magnetosphere. The magnetic fields associated with coronal mass ejections also play a significant role in magnetic reconnection. In this case, the cusp opens up for a comparatively higher value of northward B_Z . Now the threshold value of B_Z to open up the cusp and enable the energy injection process into the magnetosphere is denoted by B_{Th} , and it is observed from the result that the value of B_{Th} is the highest at 2.5 nT of northward B_Z in the year 2000, the year of solar maxima of the 23rd cycle having 119.6 number of solar spots. On the other hand, a lower value of B_{Th} is observed in the years with lower number of solar spots. The year 2007 observed only 7.6 number of sun spots and the threshold value of B_{Th} is 1.1 nT of northward B_Z for that particular year.

Finally, some meaningful insights can be extracted from the number of shifts associated with the value of the correlation coefficients for both sets of data series for each year. To estimate the optimum value of correlation between the simulated series and the real-time series, the simulated series had been compared to the real-time series shifted by T hours. The value of T is different for different years. For the year 2002, the optimum correlation coefficient between the simulated series $E_r(t)$ and $E_{Dst}(t + T)$ is 75.83% where $T = 31$. The injected plasma particles into the terrestrial magnetosphere generates the ring current which in turn deviates the intensity of the Earth's horizontal magnetic field from its average value. This deviation is measured and termed as Dst index. Here in this work, the output time series $E_r(t)$ is an estimation of the total amount of energy in the system after injection and its subsequent distribution of the input energy at any time t , and it is considered a simulated representation of this solar wind energy trapped in the magnetosphere responsible for generating the Dst index. The observation that the series $E_r(t)$ matches best with the real-time series $E_{Dst}(t + T)$ where $T = 31$ for the year of 2002 implies that the injected input energy at any time t affects the Earth's horizontal magnetic field at $(t + 31)$ hours in that very year. Similarly as the year 2002, such a time interval of 16–43 hr between the energy injection into the magnetosphere and the effective depression of horizontal magnetic field from its average value is present for all the years of the range 1997 to 2007 of the 23rd solar cycle as can be seen from Table 1.

The same observation had been noted down in the case of estimating the correlation between the simulated series $E_a(t)$ and the real-time AE index, $E_{AE}(t + T)$ also. The extra solar wind energy injected into the

here now. First of all, the cusp width W due to the magnetic reconnection is not a linear function of IMF B_Z but a hyperbolic tangent one which takes into account both the direction and magnitude of IMF B_Z and also the threshold value, B_{Th} . For large northward B_Z , the value of the function is close to 0, and the cusp is almost closed; the amount of injected particles into the magnetosphere is negligible. As the magnitude of the northward B_Z reduces below the threshold value, B_{Th} , the cusp width W starts to widen out resulting in a substantial amount of injection into the magnetosphere. As the IMF B_Z changes direction and becomes southward, the cusp width widens out further and continues to do so as long as the magnitude of the southward B_Z increases. The amount of injected particles into the magnetosphere increases rapidly with the increasing cusp width. Numerically, the cusp width can be a minimum zero value or completely closed for an extreme northward B_Z or can obtain a maximum value or completely open for an extreme southward B_Z . Between these extrema, it varies proportionally with the variation of the magnitude of $(-B_Z - B_{Th})$.

Second, the correlation coefficients between the simulated and output series, shown in Table 1, exhibit moderate to high values and support

magnetosphere is released into the ionosphere generating the westward and eastward electrojet currents in the auroral regions. *AE* index is calculated as the average value of *AU* and *AL* indexes, which in turn are the measurements of the highest and lowest depressions of the auroral magnetic field from its average value due to these westward and eastward electrojet currents, respectively. In our model the simulated output series $E_a(t)$ is equivalent to the excess energy released into the ionosphere, responsible for forming the *AE* index. For the year of 2002, the optimum value of correlation coefficient between the two series is $E_a(t)$, and $E_{AE}(t + T)$ is 75.42% for $T = 8$, which denotes a time interval of 8 hr between the energy release into the ionosphere and the depression of auroral magnetic field. All the years of 23rd solar cycle exhibit a time interval of 0 to 12 hours between the magnetosphere-ionosphere interaction and the resultant disturbances in the auroral magnetic field for similar reasons and are displayed in Table 1.

In summary, it can be realized from the above study's observations and discussions that the geomagnetic fluctuation is not an instantaneous phenomenon; rather it takes some hourly time or in some cases near about 2 days to build up the interlaying dynamics. Moreover, the proposed coupling function and the threshold value of IMF B_Z , namely, B_{Th} , plays a crucial role in the entire analysis, controlling the area of the cusp width and effectively the amount of input injection, while B_{Th} maintains a direct relationship with the yearly mean total number of sunspots and solar activities for a particular year.

5. Conclusion

Solar wind-magnetosphere coupling is the most significant physical process determining the interlaying dynamical structure of the geomagnetic storm. The energized stream of particles, known as solar wind, interacts with the terrestrial magnetosphere depending on the magnitude and direction of the z th component of the IMF, IMF B_Z . The exact dynamics of solar wind-magnetosphere reconnection process and the subsequent geomagnetic disturbances is a topic of rigorous study for the last decades. In the present paper, we investigated the nature, characteristics, and the effect of this phenomenon on the Earth's magnetosphere based on the concept of self-organized criticality and many-body interactive system. A sandpile-like cellular automata model having a dimension of $n \times n$ and characterized with energy E had been taken as a numerical representation of the terrestrial magnetosphere. The input solar wind energy at any time t can be calculated from the value of real-time ion density and flow speed data. During the reconnection process, an amount of solar wind energy is injected into the magnetosphere through the cusp and alters the energy of the cells of the system. If the total energy of any cell crosses the predetermined threshold value, the excess energy is distributed among its four adjacent neighbors though a small amount of energy is lost during this distribution process. The excess energy reaching the marginal grids dissipates from the system representing the magnetosphere-ionosphere energy transfer process. The model generates two output series. The first one is the series $E_T(t)$, which is an estimation of the total energy trapped in the system at any time t and can be considered as an equivalent to the energy responsible for generation of ring current and the depression of the Earth's horizontal magnetic field from its average value. The second output series $E_a(t)$ is the estimation of excess energy dissipated from the system at any time t and can be taken as a simulated representation of the excess energy released in the ionosphere during magnetosphere-ionosphere interaction which in turn forms the electrojet currents resulting the deviation of auroral magnetic field from its average value.

From our previous study, we came to realize the extreme importance of the solar wind-magnetosphere reconnection regarding the overall geomagnetic disturbances in the Earth and its dependency on the IMF B_Z which motivated us to opt for a deep and involving study of the nature and dynamics of the coupling. In the present paper, we proposed a coupling function to determine the cusp width in terms of IMF B_Z . The cusp width W obeys a hyperbolic tangent function of B_Z , which determines the coupling area depending on the direction and magnitude of B_Z . For extreme northward B_Z , the cusp is almost close whereas it starts to widen out as the magnitude of the northward B_Z reduces below a threshold value B_{Th} . As the B_Z becomes southward, the cusp width further increases proportionally with the increasing magnitude of B_Z and obtains a maximum value for an extremely large southward B_Z . The hyperbolic tangent term in the function numerically varies from 0 to 1 where the value 0 indicates the absolute closing of the cusp and the value 1 indicates absolute opening of the cusp respectively. For the intermediated values, the cusp width is determined according the hyperbolic tangent value of $(-B_Z - B_{Th})$.

To investigate the of the proposed coupling function, the two simulated output series $E_r(t)$ and $E_a(t)$ of the model had been compared with the real-time output of the geomagnetic phenomena, that is, with the real-time Dst index series, $E_{Dst}(t + T)$, which is a result of solar wind-magnetosphere interaction and the AE index series, $E_{AE}(t + T)$, the result of magnetosphere-ionosphere interaction. To obtain the optimum correlation between the simulated series and the real-time series, in both cases the real-time series had been time shifted by T hours and correlation coefficients had been calculated by varying the value of T . The result shows moderate to high values of correlation coefficients in both the above cases for a specific value of the threshold parameter B_{Th} for each year. Further investigation reveals that the variation of the parameter B_{Th} for the entire solar cycle of the year 1997 to the year 2007 obeys a proportional relationship with the variation of yearly mean total number of sunspots in that solar cycle. This striking outcome indicates direct influence of solar activities on the solar wind-magnetosphere reconnection process. Moreover, for the entire solar cycle, it is observed that a 16- to 43-hr time interval is present between the injection of solar wind energy into the magnetosphere during the magnetic reconnection process, and its subsequent effect on the geomagnetic weather and the depression of terrestrial horizontal magnetic field from its average value. Similarly, in the polar region, the disturbances recorded in the auroral magnetic field at any time t is due to the excess energy released in the ionosphere some 0 to 12 hr before. All these detailed studies and methodical analysis led us to the conclusion that solar wind-magnetosphere energy coupling is controlled by a hyperbolic tangent function of $(-B_z - B_{Th})$ where the threshold value, B_{Th} , plays the most significant role under the direct influence of solar activities, and the consequent geomagnetic disturbances, far from being an instantaneous phenomenon, possess an intricate underlying structure which needs some hours to nearly a couple of days' time to build up the dynamics and to change the geomagnetic weather in response to the injection of large amount of solar wind energy into the magnetosphere.

The solar wind-magnetosphere coupling is the primary controller of all the geomagnetic fluctuations on Earth. The true nature and actual dynamics of this coupling can reveal important information about all those widely discussed geomagnetic phenomena like geomagnetic storm or auroral disturbances. It is vital to know the exact amount of injected solar wind energy to understand the energy distribution in the magnetosphere along with the magnetosphere-ionosphere energy transfer. A standard coupling function can estimate the total input energy at any time t as well as the nature of the reconnection which enables us to better understand a number of complex mechanisms in the geospace, like the energy distribution process, the transfer of excess energy dissipated into the ionosphere to maintain the equilibrium, the effect of the injected energy on the Earth's magnetic field, and also the time taken for this effect, the occurrence and duration of geomagnetic storm, and many such other fluctuations related to geomagnetic weather. Moreover, the direct relation of the threshold value B_{Th} with the solar activities throws a new light on the overall analysis. The analysis is a first-order trial to investigate the complex natural process for further knowledge, and it did find out some significant points, but simultaneously also indicates the complex and intricate underlying structure possessed by the geomagnetic disturbances. Future work can be directed to acquire detailed knowledge of this structure by developing the model to a higher degree incorporating the other controlling parameters and physical effects in the algorithm.

Acknowledgments

We acknowledge use of NASA/GSFC's Space Physics Data Facility's OMNIWeb (or CDAWeb or ftp) service, OMNI data, and SIDC, RWC Belgium, World Data Centre. Data sets corresponding to Figures and and Table are available as supporting information. We are also thankful to Somnath Mukherjee, Principal of Dinabandhu Andrews College, Kolkata, India, for his cordial support and constant encouragement. Finally, we would like to sincerely thank the anonymous reviewer for his most valuable comments and suggestions to improve the quality of this paper.

References

- Akasofu, S. I. (1981). Energy coupling between the solar wind and the magnetosphere. *Space Science Reviews*, 28, 121. <https://doi.org/10.1007/BF00218810>
- Bak, P., Tang, C., & Wiesenfeld, K. (1987). Self-organized criticality: An explanation of $1/f$ noise. *Physical Review Letters*, 59, 381–384.
- Bak, P., Tang, C., & Wiesenfeld, K. (1988). Self-organized criticality. *Physical Review A*, 38, 364–372.
- Banerjee, A., Bej, A., & Chatterjee, T. N. (2011). On the existence of a long range correlation in the geomagnetic disturbance storm time (Dst) index. *Astrophysics and Space Science*, 337(1), 23–32. <https://doi.org/10.1007/s10509-011-0836-1>
- Banerjee, A., Bej, A., & Chatterjee, T. N. (2015). A cellular automata-based model of Earth's magnetosphere in relation with Dst index. *Space Weather*, 13, 259–270. <https://doi.org/10.1002/2014SW001138>
- Bargatze, L. F., McPherron, R. L., & Baker, D. N. (1986). Solar wind-magnetosphere energy input functions. In Y. Kamide & J. A. Slavin (Eds.), *Solar wind-magnetosphere coupling* (pp. 93–100). Tokyo, Japan: Terrapub/Reidel.
- CENTRA Technology, Inc. report (2011). 'Geomagnetic storms,' prepared for the Office of Risk Management and Analysis, United States Department of HomelandSecurity.
- Chang, T. S. (1992). Low-dimensional behavior and symmetry breaking of stochastic systems near criticality—Can these effects be observed in space and in the laboratory? *IEEE Transactions of Plasma Science*, 20(6), 691–694.
- Chang, T. S. (1999). Self-organized criticality, multi-fractal spectra, sporadic localized reconnections and intermittent turbulence in the magnetotail. *Physics of Plasmas*, 6(11), 4137–4145.
- Chapman, S. C., Watkins, N. W., Dendy, R. O., Helander, P., & Rowlands, G. (1998). A simple avalanche model as an analogue for magnetospheric activity. *Geophysical Research Letters*, 25(13), 2397–2400.

- Consolini, G. (1997). Sandpile cellular automata and magnetospheric dynamics. In S. Aiello et al. (Eds.), *Conference Proceedings "Cosmic Physics in the Year 2000"* (Vol. 58, pp. 123–126). SIF, Bologna, Italy.
- Consolini, G., & Lui, A. T. Y. (1999). Sign-singularity analysis of current disruption. *Geophysical Research Letters*, *26*(12), 1673–1676.
- Crooker, N. U., Feynman, J., & Gosling, J. T. (1977). High correlation between long-term averages of solar-wind speed and geomagnetic activity. *Journal of Geophysical Research*, *82*(13), 1933–1937. <https://doi.org/10.1029/JA082i013p01933>
- Crooker, N. U., & Gringauz, K. I. (1993). On the low correlation between long-term averages of solar-wind speed and geomagnetic-activity after 1976. *Journal of Geophysical Research*, *98*(A1), 59–62. <https://doi.org/10.1029/92JA01978>
- Dungey, J. W. (1961). Interplanetary magnetic field and auroral zones. *Physical Review Letters*, *6*(2), 47–48. <https://doi.org/10.1103/PhysRevLett.6.47>
- Finch, I., & Lockwood, M. (2007). Solar wind-magnetosphere coupling functions on timescales of 1 day to 1 year. *Annales de Geophysique*, *25*(2), 495–506.
- Gonzalez, W. D. (1990). A unified view of solar-wind magnetosphere coupling functions. *Planetary and Space Science*, *38*(5), 627–632. [https://doi.org/10.1016/0032-0633\(90\)90068-2](https://doi.org/10.1016/0032-0633(90)90068-2)
- Gonzalez, W. D., Tsurutani, B. T., Gonzalez, A. L. C., Smith, E. J., Tang, F., & Akasofu, S.-I. (1989). Solar wind-magnetosphere coupling during intense magnetic storms (1978–1979). *Journal of Geophysical Research*, *94*(A7), 8835–8851. <https://doi.org/10.1029/JA094iA07p08835>
- Hydro-Québec, Understanding electricity (1989).—Hydro-Québec. Retrieved 2010-10-2.
- Kan, J. R., & Lee, L. C. (1979). Energy coupling function and solar wind-magnetosphere dynamo. *Geophysical Research Letters*, *6*, 577–580. <https://doi.org/10.1029/GL006i007p00577>
- Kappenman, J. G., Zanetti, L. J., & Radasky, W. A. (1997). *Geomagnetic storms can threaten electric power grid*, *Earth in space* (Vol. 9, pp. 9–11). Washington, DC: American Geophysical Union.
- King, J. H., & Papitashvili, N. E. (2005). Solar wind spatial scales in and comparisons of hourly Wind and ACE plasma and magnetic field data. *Journal of Geophysical Research*, *110*, A02209. <https://doi.org/10.1029/2004JA010649>
- Klimas, A. J., Valdivia, J. A., Vassiliadis, D., Baker, D. N., & Hesse, M. (2000). The role of self-organized criticality in the substorm phenomenon and its relation to localized reconnection in the magnetospheric plasma sheet. *Journal of Geophysical Research*.
- Lu, G., Baker, D. N., McPherron, R. L., Farrugia, C. J., Lummerzheim, D., Ruohoniemi, J. M., Rich, F. J., et al. (1998). Global energy deposition during the January 1997 magnetic cloud event. *Journal of Geophysical Research*, *103*(A6), 11,685–11,694. <https://doi.org/10.1029/98JA00897>
- Lu, J. Y., Jing, H., Liu, Z. Q., Kabin, K., & Jiang, Y. (2013). Energy transfer across the magnetopause for northward and southward interplanetary magnetic fields. *Journal of Geophysical Research: Space Physics*, *118*, 2021–2033. <https://doi.org/10.1002/jgra.50093>
- Mawad, R., Kandoul, M., Yousef, S., & Abdel-sattar, W. (2016). Quantized variability of Earth's magnetopause distance. The 5th International Conference on Modern Trends in Physics Research WSP MTPR-014, Volume 9914, 77–83, 2016 ADS:2016mtrp.conf...77 M.
- Murayama, T. (1982). Coupling function between solar-wind parameters and geomagnetic indexes. *Reviews of Geophysics*, *20*(3), 623–629. <https://doi.org/10.1029/RG020i003p00623>
- Newell, P. T., Sotirelis, T., Liou, K., Meng, C.-I., & Rich, F. J. (2007). A nearly universal solar wind-magnetosphere coupling function inferred from 10 magnetospheric state variables. *Journal of Geophysical Research*, *112*, A01206. <https://doi.org/10.1029/2006JA012015>
- NOAA technical memorandum OAR SEC-88 (2003). Halloween space weather storms of 2003. Space Environment Center, Boulder, Colorado, June 2004
- Østgaard, N., Germany, G., Stadsnes, J., & Vondrak, R. R. (2002). Energy analysis of substorms based on remote sensing techniques, solar wind measurements, and geomagnetic indices. *Journal of Geophysical Research*, *107*(A9), 1233. <https://doi.org/10.1029/2001JA002002>
- Palmroth, M., Fear, R. C., & Honkonen, I. (2012). Magnetopause energy transfer dependence on the interplanetary magnetic field and the Earth's magnetic dipole axis orientation. *Annales de Geophysique*, *30*(3), 515–526. <https://doi.org/10.5194/angeo-30-515-2012>
- Palmroth, M., Janhunen, P., Pulkkinen, T. I., Aksnes, A., Lu, G., Østgaard, N., et al. (2005). Assessment of ionospheric joule heating by GUMICS-4 MHD simulation, AMIE, and satellite-based statistics: Towards a synthesis. *Annales de Geophysique*, *23*(6), 2051–2068.
- Palmroth, M., Koskinen, H. E. J., Pulkkinen, T. I., Toivanen, P. K., Janhunen, P., Milan, S. E., & Lester, M. (2010). Magnetospheric feedback in solar wind energy transfer. *Journal of Geophysical Research*, *115*, A00I10. <https://doi.org/10.1029/2010JA015746>
- Palmroth, M., Laitinen, T. V., & Pulkkinen, T. I. (2006). Magnetopause energy and mass transfer: Results from a global MHD simulation. *Annales de Geophysique*, *24*(12), 3467–3480.
- Palmroth, M., Pulkkinen, T. I., Janhunen, P., & Wu, C. C. (2003). Stormtime energy transfer in global MHD simulation. *Journal of Geophysical Research*, *108*(A1), 1048. <https://doi.org/10.1029/2002JA009446>
- Papadopoulos, K., Goodrich, C., Wiltberger, M., Lopez, R., & Lyon, J. G. (1999). The physics of substorms as revealed by the ISTP. *Physics and Chemistry of the Earth - Part C*, *24*(1–3), 189–202. [https://doi.org/10.1016/S1464-1917\(98\)00028-2](https://doi.org/10.1016/S1464-1917(98)00028-2)
- Papitashvili, V. O., Papitashvili, N. E., & King, J. H. (2000). Solar cycle effects in planetary geomagnetic activity: Analysis of 36-year long OMNI dataset. *Geophysical Research Letters*, *27*(17), 2797–2800. <https://doi.org/10.1029/2000GL000064>
- Perreault, P., & Akasofu, S. I. (1978). Study of geomagnetic storms. *Geophysical Journal of the Royal Astronomical Society*, *54*(3), 547–573. <https://doi.org/10.1111/j.1365-246X.1978.tb05494.x>
- Pulkkinen, T. I., Ganushkina, N. Y., Kallio, E. I., Lu, G., Baker, D. N., Turner, N. E., et al. (2002). Energy dissipation during a geomagnetic storm: May 1998. *Advances in Space Research*, *30*(10), 2231–2240. [https://doi.org/10.1016/S0273-1177\(02\)80232-0](https://doi.org/10.1016/S0273-1177(02)80232-0)
- Pulkkinen, T. I., Palmroth, M., Janhunen, P., Koskinen, H. E. J., McComas, D. J., & Smith, C. W. (2010). Timing of changes in the solar wind energy input in relation to ionospheric response. *Journal of Geophysical Research*, *115*, A00I09. <https://doi.org/10.1029/2010JA015764>
- Pulkkinen, T. I., Palmroth, M., & Laitinen, T. (2008). Energy as a tracer of magnetospheric processes: GUMICS-4 global MHD results and observations compared. *Journal of Atmospheric and Solar - Terrestrial Physics*, *70*(5), 687–707. <https://doi.org/10.1016/j.jastp.2007.10.011>
- Russell, C. T. (2000). The solar wind interaction with the Earth's magnetosphere: A tutorial. *IEEE Transactions on Plasma Science*, *28*, 1818.
- Russell, C. T. (2013). Solar Wind and Interplanetary Magnetic Field: A Tutorial. In P. Song, H. J. Singer, & G. L. Siscoe (Eds.), *Space Weather*. <https://doi.org/10.1029/GM125p0073>
- Scurry, L., & Russell, C. T. (1991). Proxy studies of energy-transfer to the magnetosphere. *Journal of Geophysical Research*, *96*(A6), 9541–9548. <https://doi.org/10.1029/91JA00569>
- Stamper, R., Lockwood, M., Wild, M. N., & Clark, T. D. G. (1999). Solar causes of the long-term increase in geomagnetic activity. *Journal of Geophysical Research*, *104*(A12), 28,325–28,342. <https://doi.org/10.1029/1999JA900311>
- Stern, D. P. (1984). Energetics of the magnetosphere. *Space Science Reviews*, *39*(1–2), 193–213.
- Takalo, J., Timonen, J., Klimas, A., Valdivia, J., & Vassiliadis, D. (1999). Nonlinear energy dissipation in a cellular automaton magnetotail field model. *Geophysical Research Letters*, *26*, 1813–1816.

- Tanskanen, E., Pulkkinen, T. I., Koskinen, H. E. J., & Slavin, J. A. (2002). Substorm energy budget during low and high solar activity: 1997 and 1999 compared. *Journal of Geophysical Research*, *107*(A6), 1086. <https://doi.org/10.1029/2001JA900153>
- Temerin, M., & Li, X. (2006). *Dst* model for 1995–2002. *Journal of Geophysical Research*, *111*, A04221. <https://doi.org/10.1029/2005JA011257>
- Tenfjord, P., & Ostgaard, N. (2013). Energy transfer and flow in the solar wind-magnetosphere-ionosphere system: A new coupling function. *Journal of Geophysical Research: Space Physics*, *118*, 5659–5672. <https://doi.org/10.1002/jgra.50545>
- Turner, N. E., Baker, D. N., Pulkkinen, T. I., Roeder, J. L., Fennell, J. F., & Jordanova, V. K. (2001). Energy content in the storm time ring current. *Journal of Geophysical Research*, *106*(A9), 19,149–19,156. <https://doi.org/10.1029/2000JA003025>
- Uritsky V. M. (1996). $1/f$ -like spectra of geomagnetic fluctuations: Expression of self-organized criticality? In Book of abstracts of the International Conference on Problems of Geocosmos, June 17–23, (p. 110). St. Petersburg, Russia.
- Uritsky, V. M., & Pudovkin, M. I. (1998a). Fractal dynamics of *AE*-index of geomagnetic activity as a marker of the self-organized criticality in the magnetosphere (in Russian). *Geomagnetizm i Aeronomia*, *38*(3), 17–28.
- Uritsky, V. M., & Pudovkin, M. I. (1998b). Low frequency $1/f$ -like fluctuations of the *AE*-index as a possible manifestation of self-organized criticality in the magnetosphere. *Annales Geophysicae*, *16*(12), 1580–1588.
- Uritsky, V. M., Pudovkin, M. I., & Steen, A. (2001). Geomagnetic substorms as perturbed self-organized critical dynamics of the magnetosphere. *Journal of Atmospheric and Solar-Terrestrial Physics*, *63*(13), 1415–1424. [https://doi.org/10.1016/S1364-6826\(00\)00243-1](https://doi.org/10.1016/S1364-6826(00)00243-1)
- Uritsky, V. M., & Semenov, V. S. (2000). A sandpile model for global statistics of reconnection events in the magnetotail. In H. K. Biernat, C. J. Farrugia, & D. F. Vogl (Eds.), *The Solar Wind - Magnetosphere System 3* (pp. 299–308). Osterreichische Akademie der Wissenschaften, Wien.
- R.A.M. Van der Linden and the SIDC team (n.d.), online catalogue of the sunspot index, <http://sidc.oma.be/html/sunspot.html>.
- Vasyliunas, V. M., Kan, J. R., Siscoe, G. L., & Akasofu, S. I. (1982). Scaling relations governing magnetospheric energy-transfer. *Planetary and Space Science*, *30*(4), 359–365. [https://doi.org/10.1016/0032-0633\(82\)90041-1](https://doi.org/10.1016/0032-0633(82)90041-1)
- Wang, C., Han, J. P., Li, H., Peng, Z., & Richardson, J. D. (2014). Solar wind-magnetosphere energy coupling function fitting: Results from a global MHD simulation. *Journal of Geophysical Research: Space Physics*, *119*, 6199–6212. <https://doi.org/10.1002/2014JA019834>
- Workshop report, National Research Council of the National Academies (2008). *Severe space weather events—Understanding societal and economic impacts—*. Washington, DC: The National Academies Press.
- Wygant, J. R., Torbert, R. B., & Mozer, F. S. (1983). Comparison of S3-3 polar-cap potential drops with the interplanetary magnetic-field and models of magnetopause reconnection. *Journal of Geophysical Research*, *88*(A7), 5727–5735. <https://doi.org/10.1029/JA088iA07p05727>
- Youssef, M., Mahrous, A., Mawad, R., Ghamry, E., Shaltout, M., El-Nawawy, M., & Fahim, A. (2011). The effects of the solar magnetic polarity and the solar wind velocity on *Bz*-component of the interplanetary magnetic field. *Advances in Space Research*, *49*(7), 1198–1202. <https://doi.org/10.1016/j.asr.2011.07.023>



Source details

[Feedback >](#) [Compare sources >](#)

Earth and Space Science

Open Access [i](#)

Scopus coverage years: from 2014 to Present

Publisher: Wiley-Blackwell

E-ISSN: 2333-5084

Subject area: [Earth and Planetary Sciences: General Earth and Planetary Sciences](#) [Environmental Science: Environmental Science \(miscellaneous\)](#)

Source type: Journal

[View all documents >](#)

[Set document alert](#)

[Save to source list](#)

CiteScore 2022

5.4



SJR 2022

0.958



SNIP 2022

1.244



Earth and Space Science

RESEARCH ARTICLE

10.1029/2018EA000468

Key Points:

- The solar wind-magnetosphere coupling has been analyzed using a cellular automata model based on the concept of self-organized criticality
- A new coupling function is introduced to determine the cusp width
- A threshold value of B_z , the z th component of the interplanetary magnetic field related to the yearly mean total number of sunspots, is introduced

Supporting Information:

- Supporting Information S1
- Data Set S1
- Data Set S2
- Data Set S3
- Data Set S4

Correspondence to:

A. Bej,
amaresh_bej@yahoo.com

Citation:

Banerjee, A., Bej, A., Chatterjee, T. N., & Majumdar, A. (2019). An SOC approach to study the solar wind-magnetosphere energy coupling. *Earth and Space Science*, 6, 565–576. <https://doi.org/10.1029/2018EA000468>

Received 5 SEP 2018

Accepted 3 FEB 2019

Accepted article online 6 FEB 2019

Published online 8 APR 2019

©2019. The Authors.

This is an open access article under the terms of the Creative Commons Attribution-NonCommercial-NoDerivs License, which permits use and distribution in any medium, provided the original work is properly cited, the use is non-commercial and no modifications or adaptations are made.

An SOC Approach to Study the Solar Wind-Magnetosphere Energy Coupling

Adrija Banerjee¹, Amaresh Bej¹ , T. N. Chatterjee², and Abhijit Majumdar¹

¹Department of Physics, Indian Institute of Engineering Science and Technology, Howrah, India, ²Department of Electronics, Dinabandhu Andrews College, Kolkata, India

Abstract Solar wind-magnetosphere interaction and the injection of large quantity of plasma particles into the Earth's magnetosphere are the primary reasons behind geomagnetic storm, auroral effects, and, in general, all the fluctuations observed in the terrestrial magnetic field. In this paper, we analyzed the perturbed magnetosphere as a sandpile-like cellular automata model based on the concept of self-organized criticality and many-body interactive system and proposed a solar wind-magnetosphere energy coupling function in terms of interplanetary magnetic field B_z , the z th component of interplanetary magnetic field. The function determines the cusp width W depending on the intensity of $(-B_z - B_{Th})$ where B_{Th} is the threshold value. The model generates two output series, which are the numerical representation of the real-time Dst index and AE index series, respectively. For our study, the range of years 1997–2007 of the 23rd solar cycle had been considered here. The threshold value B_{Th} plays a significant role in the analysis and exhibits a proportional relationship with the yearly mean total number of sunspots for each year of the range 1997–2007 of the 23rd solar cycle. For each year, the two resultant output time series of the model display high-correlation coefficients with the real-time Dst and AE indexes, respectively, which denotes the acceptability of the proposed energy coupling function and its relation with the solar activities.

1. Introduction

The solar wind-magnetosphere interaction and the energy coupling can be considered as the key factor to understand the various dynamical properties of the terrestrial magnetosphere. The solar wind, a stream of highly energized plasma particles, emitted from the Sun's outer atmosphere, is coming toward the Earth with an average speed of 400 km/s. These huge amounts of particles are injected into the Earth's magnetosphere through the cusps controlled by the z th component of the interplanetary magnetic field (IMF), B_z . The direction and magnitude of IMF B_z is the primary controller of the solar wind-magnetosphere reconnection along with the dynamic pressure of the solar wind. A detailed knowledge of the energy coupling mechanism is important to estimate the total amount of injected solar wind energy in the geospace as this energy drives all the geomagnetic fluctuations in the terrestrial magnetosphere, causing intense geomagnetic storm or auroral activities (Russell, 2000, 2013).

Extreme geomagnetic activity is considered to be a serious threat to the Earth's technological and electrical systems. In the time of severe geomagnetic storm, solar wind injects a large amount of ionized particles into the Earth's magnetosphere, rapidly changing the intensity of the magnetic field which in turn induces an electric field on the surface of the Earth. This induced electric field then drives a current through any electrical network by forming a potential difference between the ground points of that network. This current is known as geomagnetically induced current (GIC). The intensity of GIC has been noted as large as over 100 A, though a few amperes is sufficient to unexpectedly collapse any electrical infrastructure causing a huge loss of money and related hazards (Kappenman et al., 1997). The 13 March 1989 geomagnetic storm and the complete collapse of Hydro Quebec power grid resulting in 9 hr blackout for 6 million customers [Hydro-Québec, Understanding Electricity, 1989; Kappenman et al., 1997], the 30-hr blackout of the Wide Area Augmentation System managed by the Federal Aviation Administration, and the damage of Japanese ADEOS-2 satellite due to the Halloween solar storm in 2003 are some of the most prominent examples [CENTRA Technology Inc. report 2011; NOAA Technical Memorandum 2003; Workshop report of National Research Council of the National Academics 2008]. Also, past records of GIC-triggered hazards include complete disruption of power grids and transformers; malfunction of railway equipment and satellite hardware; severe collapsing of telecommunication, navigation, and computer systems; and increase of

steel corrosion in pipeline networks, particularly in countries like the United States and Canada or northern Europe, located in the upper latitudes and affected most by the auroral electrojet current [CENTRA Technology Inc. report 2011; Kappenman et al., 1997; NOAA Technical Memorandum 2003]. So a comprehensive knowledge of the solar wind-magnetosphere interaction and the underlying physical process of geomagnetic activity is crucial to save human society from its severe negative effects.

The solar wind-magnetosphere energy coupling mechanism became a subject of keen interest and curiosity in the past decades. The complex dynamics of the energy coupling process, the rate of energy transfer into the magnetosphere, and the distribution of the injected energy in the magnetosphere-ionosphere system as well as the role of the various solar wind parameters controlling the overall process had been rigorously studied, analyzed, and characterized in numerous works. A number of solar wind energy coupling functions had been presented (Akasofu, 1981; Finch & Lockwood, 2007; Gonzalez, 1990; Gonzalez et al., 1989; Kan & Lee, 1979; Newell et al., 2007; Perreault & Akasofu, 1978), while the nature of solar wind-magnetosphere interaction had been extensively studied in relation with the other solar wind parameters like velocity, ion density, and dynamic pressure [Crooker et al., 1977; Crooker & Gringauz, 1993; Dungey, 1961; Mawad et al., 2016; Newell et al., 2007; Papitashvili et al., 2000; Temerin & Li, 2006; Wygant et al., 1983; Youssef et al., 2011]. Global magnetohydrodynamic simulations [Palmroth et al., 2003, 2005, 2006, 2010, 2012; Papadopoulos et al., 1999. Pulkkinen et al., 2002, 2008, 2010; Wang et al., 2014] along with various other methods (Bargatze et al., 1986; Murayama, 1982; Stamper et al., 1999) were also taken into account. The estimation of the percentage of solar wind energy injected into the geospace, how much of this energy is dissipating in the magnetosphere or in the ionosphere, and in general the entire energy transfer and dissipation process long became the focus point of detailed investigations [Lu et al., 1998, 2013; Scurry & Russell, 1991; Stern, 1984; Tanskanen et al., 2002; Tenfjord & Ostgaard, 2013; Turner et al., 2001; Østgaard et al., 2002; Vasyliunas et al., 1982]. Though all these serious efforts produced significant results, solar wind-magnetosphere-ionosphere interaction still demands further attention to understand the complex nature of geomagnetic disturbances.

In our previous work, we came to realize that geomagnetic disturbances on the Earth is an essentially complex natural phenomenon having a number of underlying dynamics and quite impossible to predict accurately, whereas *Dst* index, the measurement of geomagnetic activity, is a positively correlated fractional Brownian motion having long-range correlation (Banerjee et al., 2011). Enlightened by this outcome, we aimed to develop a sandpile-like cellular automata model, analogous to the Earth's magnetosphere to investigate the dynamical characteristics of the geomagnetic storm (Banerjee et al., 2015). Now sandpile model was selected as the first example displaying the concept of self-organized criticality, introduced by Bak et al. in their 1987, 1988 pioneering papers. Since then, this algorithm had been extensively used to study and analysis the physical process of geomagnetic fluctuations (Chang, 1992, 1999; Chapman et al., 1998; Consolini, 1997; Consolini & Lui, 1999; Klimas et al., 2000; Takalo et al., 1999; Uritsky, 1996; Uritsky & Pudovkin, 1998a, 1998b; Uritsky & Semenov, 2000). Our proposed 2015 model was a dissipative dynamical system with both spatial and temporal degrees of freedom, based on the concept of self-organized criticality and a refined version of the model presented by Uritsky et al. (2001). Though it was a first-order model with basic considerations, the resultant time series exhibited similar statistical characteristics of the real-time *Dst* index. The acceptability of the model and its curious outcome made us realize the significance of the solar wind-magnetosphere interaction and motivated us to further investigate the true nature of the energy coupling mechanism.

In the present paper, we continued our analysis based on the sandpile-like cellular automata model of the terrestrial magnetosphere, presented in our 2015 paper (Banerjee et al., 2015). We proposed a definite solar wind-magnetosphere energy coupling function in terms of IMF B_z and a threshold value, B_{Th} . The function is a hyperbolic tangent one which determines the cusp width W at any time t . The model produces two output series which are the numerical representations of the real-time *Dst* index and *AE* index series, respectively. To examine the validity of the proposed energy coupling function, the correlation coefficients between the simulated output series, the real-time *Dst*, and *AE* index series had been estimated respectively. The entire 23rd solar cycle had been studied, and the real-time data of solar ion density, flow speed, and IMF B_z had been considered here. The result shows significant values of correlation coefficients between the simulated and real-time series for a specific value of the B_{Th} for each year. The parameter B_{Th} plays a key

role here as it varies exactly proportionally to the variation of the yearly mean total number of sunspots for each year of the range 1997–2007 of the 23rd solar cycle, revealing the direct influence of solar activities on the solar wind-magnetosphere reconnection phenomena.

2. Method

The cellular automata-based sandpile model presented here is a refinement of the model proposed in our previous paper (Banerjee et al., 2015). In summary, the model, a numerical representation of the Earth's magnetosphere, is a finite matrix of $n \times n$ elements, characterized by energy E , which is a function of time and space. With analogy to the Earth, open boundary condition had been considered, denoting upper ($i = 1, j = 1$ to n) and lower ($i = n, j = 1$ to n) boundary regions of the system. Solar wind emitted from the Sun is coming toward the Earth. It interacts with the terrestrial magnetosphere, a reconnection occurs, and a significant amount of ionized particle penetrates into the geospace through the cusp, altering its energy. The energy unit dE at any time t is calculated using the real-time ion density and flow speed data obeying the equation

$$dE(t) = \text{norm}^{1/2} \times \text{ion density} \times (\text{flow speed})^2 \quad (1)$$

For initialization, each of the cells of the matrix is credited with a small amount of solar wind energy following the equations

$$E_{t+1}(i,j) = E_t(i,j) + K_r \times dE(t) \text{ for } i = 2 \text{ to } n+1, j = 1 \text{ to } n \quad (2)$$

and

$$E_{t+1}(i,j) = E_t(i,j) + K_a \times dE(t) \text{ for } i = 1, j = 1 \text{ to } n \quad (3)$$

where K_r and K_a are constants.

Both the direction and the intensity of the z th component of the IMF, B_z determines the cusp width W , thus controlling the amount of energy injected into the system. For the cellular automata model of $n \times n$ matrix presented here, the cusp width W is a square of cells surrounding the cell ($i = n/2, j = n/2$), that is, the cell in the center of the matrix. For a large northward B_z , the cusp width W is minimum 0, whereas for a large southward B_z , the cusp width W has a maximum value, $W_m = (n - 1)^2$. W_m has a constant value for a constant n .

The functional relationship of W and B_z proposed here is

$$W(t) = W_m * ((\tanh((-B_z - B_{Th})/\lambda) + 1)/2) \quad (4)$$

where B_{Th} is the threshold value of IMF B_z to open up the cusp and λ is a constant. The parameter B_{Th} is the most significant factor in the entire analysis as it controls the net amount of solar wind-magnetosphere energy coupling area. At any time t , the hyperbolic tangent term in equation (4) generates a value in the range of 0 to 1. For a large southward B_z , the hyperbolic tangent term is 1 and $W = W_m$, whereas for a large northward B_z the term is 0 and $W = 0$. In between the extrema, W has an intermediate value depending on the value of $(-B_z - B_{Th})$. W has a numeric value.

The input energy $dE(t)$ is injected into the model through W number of cells following the equation

$$E_{t+1}(i,j) = E_t(i,j) + dE(t) \text{ for } i = n/2 \pm p, j = n/2 \pm p \quad (5)$$

where $p = \text{round}((\sqrt{W} - 1)/2)$.

Now if the altered energy of the cell (i,j) crosses the threshold value E_{Th} of the system, the excess energy is distributed among the adjacent neighbors obeying the equations

$$E_{t+1}(i, j) = E_t(i, j) - 4 \quad (6)$$

and

$$E_{t+1}(i \pm 1, j \pm 1) = E_t(i \pm 1, j \pm 1) + (1 - E_d/4) \quad (7)$$

where E_d is the dissipation factor and $(i \pm 1) \geq 1$ or 2 according to the case.

The total energy of the system at any time t can be calculated as

$$E_1(t) = \Sigma E(i, j) \text{ for } i = 2 \text{ to } n + 1, j = 1 \text{ to } n \quad (8)$$

The differential value of the energy stored in the system at any time t is then estimated by

$$E_2(t) = \Delta E_1(t) \quad (9)$$

For further refinement, the above time series is then processed by a moving-average filter of span 72 to get the final output series as

$$E_r(t) = -\text{MA}(E_2) \quad (10)$$

$E_r(t)$ is an estimation of the differential value of the energy stored in the system and can be considered as a numerical equivalent to the *Dst* index. Now a high correlation coefficient between the simulated series $E_r(t)$ and the real-time *Dst* index can establish the validity of the proposed coupling function.

The real-time hourly averaged *Dst* index data set has been obtained from OMNIWeb. To remove the noise and fine-scale structure, the data set is further processed by a moving-average filter of span 72 to get a series, namely, $E_{Dst}(t + T)$ where T denotes the time shift or time lag. Now cross correlation is considered as a standard technique to measure the degree of similarity between two time series, and this method had been applied here to determine the correlation between the series $E_r(t)$ and $E_{Dst}(t + T)$. To estimate the optimum cross-correlation coefficient between these two series, the series $E_r(t)$ had been compared to the time-shifted real-time *Dst* index, $E_{Dst}(t + T)$ where T is varied in the range of values 0 to 720 hr, and for each value of T , the correlation coefficients between the two series had been noted down along with the exact value of T . Here T is the lag value of duration 1 hr associated with the cross-correlation method.

As open boundary condition has been considered, the excess energy transmits outside the grid after reaching the upper ($i = 1, j = 1$ to n) and lower ($i = n + 2, j = 1$ to n) boundary regions of the system. With analogy to the Earth, these upper and lower boundaries can be considered as the northern and southern polar cusps of the Earth, while this energy transfer process is similar to the transmission of the excess energy of the Earth's magnetosphere to the ionosphere through the polar cusps. Thus, the amount of excess energy dissipated through the upper boundary or northern polar cusp can be estimated as

$$E_3(t) = \Sigma E(i, j) \text{ for } i = 1, j = 1 \text{ to } n \quad (11)$$

and the differential energy value as

$$E_4(t) = \Delta E_3(t) \quad (12)$$

Similarly, as equation (10) the moving-average technique has been applied to equation (12) to get the following one

$$E_a(t) = \text{MA}(E_4) \quad (13)$$

Equation (13) is the measurement of the excess energy dissipated in the ionosphere from the magnetosphere through the polar cusps and can be considered as a numerical representation of the auroral electrojet (*AE*) index. Similar as before, the real-time *AE* index data series has been obtained from OMNIWeb and further processed by a moving-average filter of span 72 to get the series $E_{AE}(t + T)$, where T is the time shift or time lag. Again, the method of cross correlation had been applied here to determine the amount of correlation

between the two series $E_a(t)$ and $E_{AE}(t + T)$, considering T as the associated lag value of duration 1 hr. The correlation coefficients between the simulated series $E_a(t)$ of equation (13) and the real-time $E_{AE}(t + T)$ had been estimated to further strengthen the validity of the proposed coupling function. Here also, the series $E_a(t)$ had been compared with the time-shifted AE index, $E_{AE}(t + T)$ where T is varied in the range of values 0 to 720 hr to achieve the optimum correlation coefficient between the two series. For each value of T , the associated correlation coefficients had been recorded.

As mentioned before, the threshold value B_{Th} of equation (4) is playing the key role in the entire analysis as the term $(-B_Z - B_{Th})$ controls the widening or narrowing of the cusp width and the amount of solar wind energy injected into the magnetosphere at any time t . In this work, we had studied the variation of the magnitude of the solar wind-magnetosphere coupling with variation of B_{Th} and its subsequent effect on the overall dynamics of the system.

3. Data source

Here we used the hourly averaged Dst index, AE index, solar wind ion density, flow speed, and B_Z component of the IMF data from the year 1997 to the year 2007 as extracted from NASA/GSFC's (Goddard Space Flight Center) OMNI data set through OMNIWeb (King & Papitashvili, 2005). The OMNI data were obtained from the GSFC/SPDF (Space Physics Data Facility) OMNIWeb interface at the OMNIWeb website (<http://omniweb.gsfc.nasa.gov>). We used the Dst index and AE index data obtained from OMNIWeb to compare with the estimated series $E_r(t)$ and $E_a(t)$, respectively.

For the yearly mean total number of sunspots, the source credit is the sunspot data from the World Data Center SILSO (Sunspot Index and Long-term Solar Observations; Sunspot Number and Long-term Solar Observations, Royal Observatory of Belgium, on-line Sunspot Number catalogue: <http://www.sidc.be/SILSO/>, '1997–2007').

4. Result and Discussions

To study the dynamics of the system depending on the solar wind-magnetosphere coupling, we had considered the range of years 1997 to 2007 of the 23rd solar cycle. The input energy dE had been calculated using equation (1) and using the real-time value of flow speed and ion density. The cellular automata model is a matrix having a dimension of $n \times n$. Here it is taken as $n = 50$, that is, the matrix contains 50×50 cells. The input energy $dE(t)$, calculated from OMNIWeb data is an one-dimensional time series. At any time t , the total cusp area W is determined using equation (4). The cusp area is a square having the cells $i = 25 \pm p, j = 25 \pm p$ where $p = \text{round}((\sqrt{W} - 1)/2)$. The input energy $dE(t)$ is injected into all these cells of $i = 25 \pm p, j = 25 \pm p$ according to equation (5) stated in the section 2. The values of the different parameters are taken as $E_{Th} = 5, E_d = 0.001, K_r = 0.001, K_a = 0.1, \lambda = 0.5$. All these values are constants for each of the year in the range of 1997–2007. As referred in the section 2, our sandpile model is a refined version of the model presented in our 2015 paper which was based on the model proposed by Uritsky et al. (2001). Uritsky et al. set the threshold of excitation as $E_{Th} = 5$ and suggested the value of the dissipation term $E_d < = 0.01$ to study the wide-range scale-invariant behavior of the system. Following their work, we also set $E_{Th} = 5$ and $E_d = 0.001$ for our model. We studied the model for different values of $K_r, K_a,$ and λ and observed that the model output series matches best with the real-time series for values $K_r = 0.001, K_a = 0.1,$ and $\lambda = 0.5$. So we considered these values of $K_r, K_a,$ and λ constants for our entire analysis.

For each year, the value of parameter B_{Th} had been varied in the range of -10.00 to 10.00 nT, and for each value of B_{Th} within this range, the correlation coefficients between the simulated series $E_r(t)$ of equation (10) and the time-shifted real-time Dst index series $E_{Dst}(t + T)$ as well as the series $E_a(t)$ of equation (13) and the time-shifted real-time AE index series $E_{AE}(t + T)$ had been estimated respectively. While calculating the correlation coefficients for the above two cases, the value of time lag T had been varied from $T = 0$ to 720 hr to achieve the optimum value of the coefficients. Thus, the best correlation coefficient for each set is found annually. The exact value of B_{Th} and the particular value of T associated with the optimum coefficients had been noted down along with the value of the coefficients. Table 1 displays the optimum values of the correlation coefficients for each year in the range of 1997 to 2007 with the corresponding values of the

Table 1

The First Three Columns of the Table Shows the Yearly Mean Total Number of Sunspots and the Values of the Threshold B_Z , B_{Th} for All the Years in the Range of 1997–2007

Year	Yearly mean total number of sunspots	B_{Th} (nT)	Comparison between $E_r(t)$ and $E_{Dst}(t + T)$		Comparison between $E_a(t)$ and $E_{AE}(t + T)$	
			Optimum correlation coefficient (%)	Time lag T (hr)	Optimum correlation coefficient (%)	Time lag T (hr)
1997	28.90	1.25	70.27	24	74.53	2
1998	88.30	1.76	60.47	32	77.05	4
1999	136.30	2.18	64.23	24	66.06	5
2000	173.90	2.50	76.06	25	69.02	2
2001	170.40	2.47	72.64	21	72.28	0
2002	163.60	2.41	75.83	31	75.42	8
2003	99.30	1.86	62.99	25	59.47	10
2004	65.30	1.56	75.26	16	76.37	3
2005	45.80	1.40	60.64	35	75.96	11
2006	24.70	1.21	52.83	30	74.63	6
2007	12.60	1.10	62.79	43	81.18	12

Note. For this entire range of years, the optimum correlation coefficients between the simulated series $E_r(t)$ and the time-shifted real-time Dst index series $E_{Dst}(t + T)$ and the associated values of time lag T are displayed in the fourth and fifth columns, respectively, while in a similar fashion, the sixth and seventh columns show the optimum correlation coefficients between the simulated series $E_a(t)$ and the time-shifted real-time AE index series $E_{AE}(t + T)$ and the corresponding values of time lag T , respectively.

parameter B_{Th} and also the values of T for both the cases. The correlation coefficient R between two series A and B is calculated using the equation

$$R = \frac{\sum_m \sum_n (A_{mn} - \bar{A})(B_{mn} - \bar{B})}{\sqrt{(\sum_m \sum_n (A_{mn} - \bar{A})^2)(\sum_m \sum_n (B_{mn} - \bar{B})^2)}} \quad (14)$$

Figure 1 represents a comparison between the actual waveforms of the simulated series $E_r(t)$ and the real-time Dst index series $E_{Dst}(t + T)$ where $T = 31$ for the year of 2002. The optimum correlation coefficient between these two series is 75.83% for $B_{Th} = 2.41$ and $T = 31$ in this year. The top half of Figure 1 shows the waveform of simulated output series $E_r(t)$, while the bottom half shows the waveform of the time-shifted Dst index series, $E_{Dst}(t + T)$ for the year 2002. Both the series are 1-hourly time series having 8,578 data each. The time in hour is plotted in the x axis. Here 8,000 means $t = 8,000$, that is, the point of 8,000th hour. Each of the year in the range of 1997–2007 contains 8,000–9,000 data.

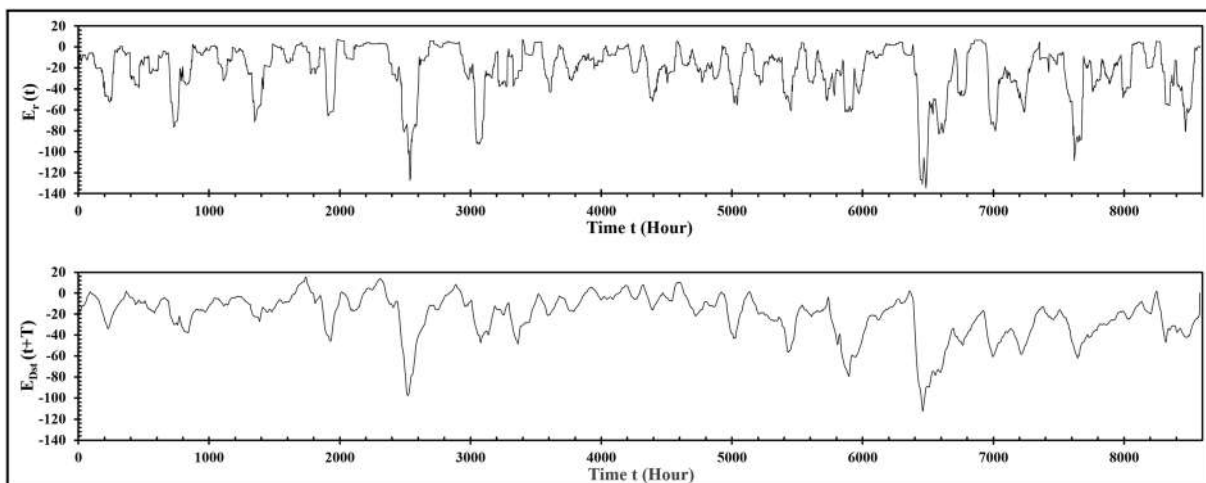


Figure 1. (top) The plot of simulated output series $E_r(t)$ and (bottom) the plot of the time-shifted Dst index series, $E_{Dst}(t + T)$ where $T = 31$ for the year 2002. Both the series are plotted with respect to time (hours). The value of $B_{Th} = 2.41$ for this year and the optimum correlation coefficient between the two series is 75.83%. The correlation coefficient between the two series is estimated using equation (14).

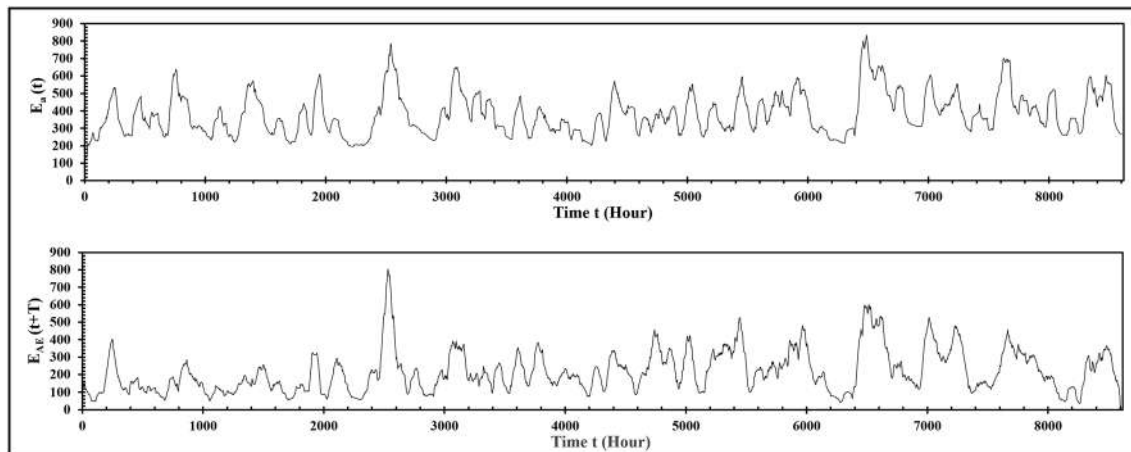


Figure 2. (top) The plot of simulated output series $E_a(t)$ and (bottom) the plot of the time-shifted AE index series, $E_{AE}(t + T)$ where $T = 8$ for the year 2002. Both the series are plotted with respect to time (hours). The value of $B_{Th} = 2.41$ for this year and the optimum correlation coefficient between the two series is 75.42%. The correlation coefficient between the two series is estimated using equation (14).

Figure 2 displays the graphs of the simulated series $E_a(t)$ and the real-time AE index $E_{AE}(t + T)$ where $T = 8$, also for the year of 2002. Here the optimum correlation coefficient between these two series is 75.42% for $B_{Th} = 2.41$ and $T = 8$. The top half of Figure 2 shows the waveform of simulated output series $E_a(t)$, while the bottom half shows the waveform of the time-shifted AE index series, $E_{AE}(t + T)$ for the year 2002. Both the series are 1-hourly time series having 8,601 data each. The time in hour is plotted in the x axis.

The current work is focused to propose a solar wind-magnetosphere energy coupling function and to study the subsequent energy transfer process using a cellular automata model of Earth's magnetosphere. To establish the validity of the model and the coupling function, the model had been simulated numerously for different set of values of the controlling parameters. For every simulation, the model output series had been compared with the real-time series. Finally, it is observed that for the set of values $K_r = 0.001$, $K_a = 0.1$, and $\lambda = 0.5$ the model output series matches best with the real-time series. So we have considered these set of values constant for the entire range of the years 1997–2007. Now T denotes the time gap between

the injection of the plasma particles into the magnetosphere and its subsequent effect on the intensity of the horizontal magnetic field of the Earth. As the amount of injected energy into the magnetosphere is not same for every year, the value of T cannot be assumed as a constant for every year beforehand; rather its value for each year had been obtained from the result.

Figure 3 shows the plot of optimum correlation coefficient for each of the years in the range of 1997–2007 for both sets of data, as obtained from Table 1.

The above result exhibits a striking connection of the solar wind-magnetosphere reconnection with solar activities. Table 1 also shows the yearly mean total number of sunspots for each year in the range of 1997–2007 of the 23rd solar cycle. As shown in Figure 4, for the entire range of years, the parameter B_{Th} varies proportionally with the yearly mean total number of sunspots. The value of B_{Th} is maximum 2.5 in the year 2000 which is also the year of solar maxima having 173.9 yearly mean total number of sunspots, while B_{Th} reaches its minimum value 1.1 in the year where the yearly mean total number of sunspots is only 12.6.

Studying the above observations thoroughly, we came to realize some significant and meaningful points about the solar wind-magnetosphere coupling and the resultant geomagnetic disturbances which can be discussed

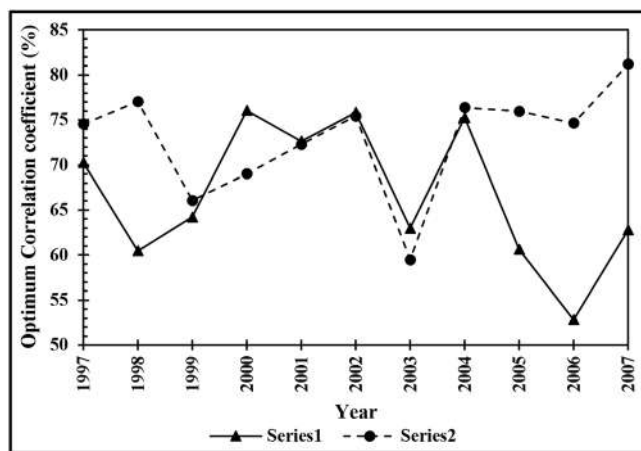


Figure 3. Series 1 is the yearly plot of the optimum correlation coefficients between the simulated series $E_r(t)$ and the time-shifted real-time Dst index series $E_{Dst}(t + T)$. Series 2 is the yearly plot of the optimum correlation coefficients between the simulated series $E_a(t)$ and the time-shifted real-time AE index series $E_{AE}(t + T)$. Year, in the range of 1997–2007 is plotted in the x axis.

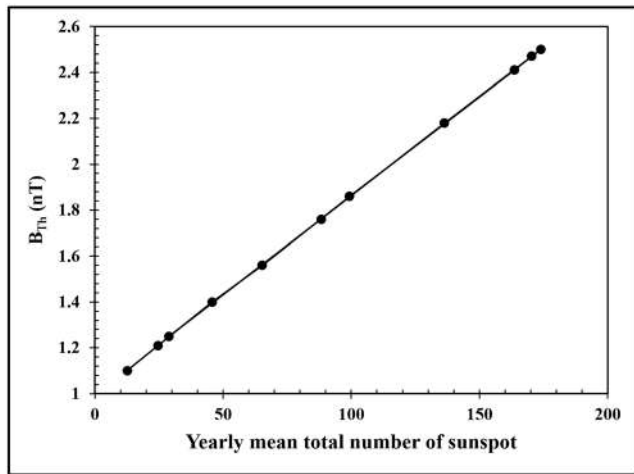


Figure 4. The threshold value, B_{Th} , is plotted with respect to the yearly mean total number of sunspots for the range of years 1997–2007 of the 23rd solar cycle. The graph shows a proportional relationship between these two parameters.

the rightness of the proposed coupling function in two ways, first in connection with the stored energy in the magnetosphere and Dst index and second in connection with the excess energy dissipated into the ionosphere and AE index. The correlation coefficients are associated to a particular value of the parameter B_{Th} for each year. Most significantly, the parameter B_{Th} displays a proportional relationship with the yearly mean total number of sunspots for the entire solar cycle, revealing an influence of solar activities on the threshold value, B_{Th} . Higher number of solar spots indicates higher solar activity which increases solar wind and also the coronal mass ejections, resulting in an injection of huge amount of plasma particles into the terrestrial magnetosphere. The magnetic fields associated with coronal mass ejections also play a significant role in magnetic reconnection. In this case, the cusp opens up for a comparatively higher value of northward B_Z . Now the threshold value of B_Z to open up the cusp and enable the energy injection process into the magnetosphere is denoted by B_{Th} , and it is observed from the result that the value of B_{Th} is the highest at 2.5 nT of northward B_Z in the year 2000, the year of solar maxima of the 23rd cycle having 119.6 number of solar spots. On the other hand, a lower value of B_{Th} is observed in the years with lower number of solar spots. The year 2007 observed only 7.6 number of sun spots and the threshold value of B_{Th} is 1.1 nT of northward B_Z for that particular year.

Finally, some meaningful insights can be extracted from the number of shifts associated with the value of the correlation coefficients for both sets of data series for each year. To estimate the optimum value of correlation between the simulated series and the real-time series, the simulated series had been compared to the real-time series shifted by T hours. The value of T is different for different years. For the year 2002, the optimum correlation coefficient between the simulated series $E_r(t)$ and $E_{Dst}(t + T)$ is 75.83% where $T = 31$. The injected plasma particles into the terrestrial magnetosphere generates the ring current which in turn deviates the intensity of the Earth's horizontal magnetic field from its average value. This deviation is measured and termed as Dst index. Here in this work, the output time series $E_r(t)$ is an estimation of the total amount of energy in the system after injection and its subsequent distribution of the input energy at any time t , and it is considered a simulated representation of this solar wind energy trapped in the magnetosphere responsible for generating the Dst index. The observation that the series $E_r(t)$ matches best with the real-time series $E_{Dst}(t + T)$ where $T = 31$ for the year of 2002 implies that the injected input energy at any time t affects the Earth's horizontal magnetic field at $(t + 31)$ hours in that very year. Similarly as the year 2002, such a time interval of 16–43 hr between the energy injection into the magnetosphere and the effective depression of horizontal magnetic field from its average value is present for all the years of the range 1997 to 2007 of the 23rd solar cycle as can be seen from Table 1.

The same observation had been noted down in the case of estimating the correlation between the simulated series $E_a(t)$ and the real-time AE index, $E_{AE}(t + T)$ also. The extra solar wind energy injected into the

here now. First of all, the cusp width W due to the magnetic reconnection is not a linear function of IMF B_Z but a hyperbolic tangent one which takes into account both the direction and magnitude of IMF B_Z and also the threshold value, B_{Th} . For large northward B_Z , the value of the function is close to 0, and the cusp is almost closed; the amount of injected particles into the magnetosphere is negligible. As the magnitude of the northward B_Z reduces below the threshold value, B_{Th} , the cusp width W starts to widen out resulting in a substantial amount of injection into the magnetosphere. As the IMF B_Z changes direction and becomes southward, the cusp width widens out further and continues to do so as long as the magnitude of the southward B_Z increases. The amount of injected particles into the magnetosphere increases rapidly with the increasing cusp width. Numerically, the cusp width can be a minimum zero value or completely closed for an extreme northward B_Z or can obtain a maximum value or completely open for an extreme southward B_Z . Between these extrema, it varies proportionally with the variation of the magnitude of $(-B_Z - B_{Th})$.

Second, the correlation coefficients between the simulated and output series, shown in Table 1, exhibit moderate to high values and support

magnetosphere is released into the ionosphere generating the westward and eastward electrojet currents in the auroral regions. *AE* index is calculated as the average value of *AU* and *AL* indexes, which in turn are the measurements of the highest and lowest depressions of the auroral magnetic field from its average value due to these westward and eastward electrojet currents, respectively. In our model the simulated output series $E_a(t)$ is equivalent to the excess energy released into the ionosphere, responsible for forming the *AE* index. For the year of 2002, the optimum value of correlation coefficient between the two series is $E_a(t)$, and $E_{AE}(t + T)$ is 75.42% for $T = 8$, which denotes a time interval of 8 hr between the energy release into the ionosphere and the depression of auroral magnetic field. All the years of 23rd solar cycle exhibit a time interval of 0 to 12 hours between the magnetosphere-ionosphere interaction and the resultant disturbances in the auroral magnetic field for similar reasons and are displayed in Table 1.

In summary, it can be realized from the above study's observations and discussions that the geomagnetic fluctuation is not an instantaneous phenomenon; rather it takes some hourly time or in some cases near about 2 days to build up the interlaying dynamics. Moreover, the proposed coupling function and the threshold value of IMF B_Z , namely, B_{Th} , plays a crucial role in the entire analysis, controlling the area of the cusp width and effectively the amount of input injection, while B_{Th} maintains a direct relationship with the yearly mean total number of sunspots and solar activities for a particular year.

5. Conclusion

Solar wind-magnetosphere coupling is the most significant physical process determining the interlaying dynamical structure of the geomagnetic storm. The energized stream of particles, known as solar wind, interacts with the terrestrial magnetosphere depending on the magnitude and direction of the z th component of the IMF, IMF B_Z . The exact dynamics of solar wind-magnetosphere reconnection process and the subsequent geomagnetic disturbances is a topic of rigorous study for the last decades. In the present paper, we investigated the nature, characteristics, and the effect of this phenomenon on the Earth's magnetosphere based on the concept of self-organized criticality and many-body interactive system. A sandpile-like cellular automata model having a dimension of $n \times n$ and characterized with energy E had been taken as a numerical representation of the terrestrial magnetosphere. The input solar wind energy at any time t can be calculated from the value of real-time ion density and flow speed data. During the reconnection process, an amount of solar wind energy is injected into the magnetosphere through the cusp and alters the energy of the cells of the system. If the total energy of any cell crosses the predetermined threshold value, the excess energy is distributed among its four adjacent neighbors though a small amount of energy is lost during this distribution process. The excess energy reaching the marginal grids dissipates from the system representing the magnetosphere-ionosphere energy transfer process. The model generates two output series. The first one is the series $E_T(t)$, which is an estimation of the total energy trapped in the system at any time t and can be considered as an equivalent to the energy responsible for generation of ring current and the depression of the Earth's horizontal magnetic field from its average value. The second output series $E_a(t)$ is the estimation of excess energy dissipated from the system at any time t and can be taken as a simulated representation of the excess energy released in the ionosphere during magnetosphere-ionosphere interaction which in turn forms the electrojet currents resulting the deviation of auroral magnetic field from its average value.

From our previous study, we came to realize the extreme importance of the solar wind-magnetosphere reconnection regarding the overall geomagnetic disturbances in the Earth and its dependency on the IMF B_Z which motivated us to opt for a deep and involving study of the nature and dynamics of the coupling. In the present paper, we proposed a coupling function to determine the cusp width in terms of IMF B_Z . The cusp width W obeys a hyperbolic tangent function of B_Z , which determines the coupling area depending on the direction and magnitude of B_Z . For extreme northward B_Z , the cusp is almost close whereas it starts to widen out as the magnitude of the northward B_Z reduces below a threshold value B_{Th} . As the B_Z becomes southward, the cusp width further increases proportionally with the increasing magnitude of B_Z and obtains a maximum value for an extremely large southward B_Z . The hyperbolic tangent term in the function numerically varies from 0 to 1 where the value 0 indicates the absolute closing of the cusp and the value 1 indicates absolute opening of the cusp respectively. For the intermediated values, the cusp width is determined according the hyperbolic tangent value of $(-B_Z - B_{Th})$.

To investigate the of the proposed coupling function, the two simulated output series $E_r(t)$ and $E_a(t)$ of the model had been compared with the real-time output of the geomagnetic phenomena, that is, with the real-time Dst index series, $E_{Dst}(t + T)$, which is a result of solar wind-magnetosphere interaction and the AE index series, $E_{AE}(t + T)$, the result of magnetosphere-ionosphere interaction. To obtain the optimum correlation between the simulated series and the real-time series, in both cases the real-time series had been time shifted by T hours and correlation coefficients had been calculated by varying the value of T . The result shows moderate to high values of correlation coefficients in both the above cases for a specific value of the threshold parameter B_{Th} for each year. Further investigation reveals that the variation of the parameter B_{Th} for the entire solar cycle of the year 1997 to the year 2007 obeys a proportional relationship with the variation of yearly mean total number of sunspots in that solar cycle. This striking outcome indicates direct influence of solar activities on the solar wind-magnetosphere reconnection process. Moreover, for the entire solar cycle, it is observed that a 16- to 43-hr time interval is present between the injection of solar wind energy into the magnetosphere during the magnetic reconnection process, and its subsequent effect on the geomagnetic weather and the depression of terrestrial horizontal magnetic field from its average value. Similarly, in the polar region, the disturbances recorded in the auroral magnetic field at any time t is due to the excess energy released in the ionosphere some 0 to 12 hr before. All these detailed studies and methodical analysis led us to the conclusion that solar wind-magnetosphere energy coupling is controlled by a hyperbolic tangent function of $(-B_z - B_{Th})$ where the threshold value, B_{Th} , plays the most significant role under the direct influence of solar activities, and the consequent geomagnetic disturbances, far from being an instantaneous phenomenon, possess an intricate underlying structure which needs some hours to nearly a couple of days' time to build up the dynamics and to change the geomagnetic weather in response to the injection of large amount of solar wind energy into the magnetosphere.

The solar wind-magnetosphere coupling is the primary controller of all the geomagnetic fluctuations on Earth. The true nature and actual dynamics of this coupling can reveal important information about all those widely discussed geomagnetic phenomena like geomagnetic storm or auroral disturbances. It is vital to know the exact amount of injected solar wind energy to understand the energy distribution in the magnetosphere along with the magnetosphere-ionosphere energy transfer. A standard coupling function can estimate the total input energy at any time t as well as the nature of the reconnection which enables us to better understand a number of complex mechanisms in the geospace, like the energy distribution process, the transfer of excess energy dissipated into the ionosphere to maintain the equilibrium, the effect of the injected energy on the Earth's magnetic field, and also the time taken for this effect, the occurrence and duration of geomagnetic storm, and many such other fluctuations related to geomagnetic weather. Moreover, the direct relation of the threshold value B_{Th} with the solar activities throws a new light on the overall analysis. The analysis is a first-order trial to investigate the complex natural process for further knowledge, and it did find out some significant points, but simultaneously also indicates the complex and intricate underlying structure possessed by the geomagnetic disturbances. Future work can be directed to acquire detailed knowledge of this structure by developing the model to a higher degree incorporating the other controlling parameters and physical effects in the algorithm.

Acknowledgments

We acknowledge use of NASA/GSFC's Space Physics Data Facility's OMNIWeb (or CDAWeb or ftp) service, OMNI data, and SIDC, RWC Belgium, World Data Centre. Data sets corresponding to Figures and Table are available as supporting information. We are also thankful to Somnath Mukherjee, Principal of Dinabandhu Andrews College, Kolkata, India, for his cordial support and constant encouragement. Finally, we would like to sincerely thank the anonymous reviewer for his most valuable comments and suggestions to improve the quality of this paper.

References

- Akasofu, S. I. (1981). Energy coupling between the solar wind and the magnetosphere. *Space Science Reviews*, 28, 121. <https://doi.org/10.1007/BF00218810>
- Bak, P., Tang, C., & Wiesenfeld, K. (1987). Self-organized criticality: An explanation of $1/f$ noise. *Physical Review Letters*, 59, 381–384.
- Bak, P., Tang, C., & Wiesenfeld, K. (1988). Self-organized criticality. *Physical Review A*, 38, 364–372.
- Banerjee, A., Bej, A., & Chatterjee, T. N. (2011). On the existence of a long range correlation in the geomagnetic disturbance storm time (Dst) index. *Astrophysics and Space Science*, 337(1), 23–32. <https://doi.org/10.1007/s10509-011-0836-1>
- Banerjee, A., Bej, A., & Chatterjee, T. N. (2015). A cellular automata-based model of Earth's magnetosphere in relation with Dst index. *Space Weather*, 13, 259–270. <https://doi.org/10.1002/2014SW001138>
- Bargatze, L. F., McPherron, R. L., & Baker, D. N. (1986). Solar wind-magnetosphere energy input functions. In Y. Kamide & J. A. Slavin (Eds.), *Solar wind-magnetosphere coupling* (pp. 93–100). Tokyo, Japan: Terrapub/Reidel.
- CENTRA Technology, Inc. report (2011). 'Geomagnetic storms,' prepared for the Office of Risk Management and Analysis, United States Department of Homeland Security.
- Chang, T. S. (1992). Low-dimensional behavior and symmetry breaking of stochastic systems near criticality—Can these effects be observed in space and in the laboratory? *IEEE Transactions of Plasma Science*, 20(6), 691–694.
- Chang, T. S. (1999). Self-organized criticality, multi-fractal spectra, sporadic localized reconnections and intermittent turbulence in the magnetotail. *Physics of Plasmas*, 6(11), 4137–4145.
- Chapman, S. C., Watkins, N. W., Dendy, R. O., Helander, P., & Rowlands, G. (1998). A simple avalanche model as an analogue for magnetospheric activity. *Geophysical Research Letters*, 25(13), 2397–2400.

- Consolini, G. (1997). Sandpile cellular automata and magnetospheric dynamics. In S. Aiello et al. (Eds.), *Conference Proceedings "Cosmic Physics in the Year 2000"* (Vol. 58, pp. 123–126). SIF, Bologna, Italy.
- Consolini, G., & Lui, A. T. Y. (1999). Sign-singularity analysis of current disruption. *Geophysical Research Letters*, 26(12), 1673–1676.
- Crooker, N. U., Feynman, J., & Gosling, J. T. (1977). High correlation between long-term averages of solar-wind speed and geomagnetic activity. *Journal of Geophysical Research*, 82(13), 1933–1937. <https://doi.org/10.1029/JA082i013p01933>
- Crooker, N. U., & Gringauz, K. I. (1993). On the low correlation between long-term averages of solar-wind speed and geomagnetic-activity after 1976. *Journal of Geophysical Research*, 98(A1), 59–62. <https://doi.org/10.1029/92JA01978>
- Dungey, J. W. (1961). Interplanetary magnetic field and auroral zones. *Physical Review Letters*, 6(2), 47–48. <https://doi.org/10.1103/PhysRevLett.6.47>
- Finch, I., & Lockwood, M. (2007). Solar wind-magnetosphere coupling functions on timescales of 1 day to 1 year. *Annales de Geophysique*, 25(2), 495–506.
- Gonzalez, W. D. (1990). A unified view of solar-wind magnetosphere coupling functions. *Planetary and Space Science*, 38(5), 627–632. [https://doi.org/10.1016/0032-0633\(90\)90068-2](https://doi.org/10.1016/0032-0633(90)90068-2)
- Gonzalez, W. D., Tsurutani, B. T., Gonzalez, A. L. C., Smith, E. J., Tang, F., & Akasofu, S.-I. (1989). Solar wind-magnetosphere coupling during intense magnetic storms (1978–1979). *Journal of Geophysical Research*, 94(A7), 8835–8851. <https://doi.org/10.1029/JA094iA07p08835>
- Hydro-Québec, Understanding electricity (1989).—Hydro-Québec. Retrieved 2010-10-2.
- Kan, J. R., & Lee, L. C. (1979). Energy coupling function and solar wind-magnetosphere dynamo. *Geophysical Research Letters*, 6, 577–580. <https://doi.org/10.1029/GL006i007p00577>
- Kappenman, J. G., Zanetti, L. J., & Radasky, W. A. (1997). *Geomagnetic storms can threaten electric power grid*, *Earth in space* (Vol. 9, pp. 9–11). Washington, DC: American Geophysical Union.
- King, J. H., & Papitashvili, N. E. (2005). Solar wind spatial scales in and comparisons of hourly Wind and ACE plasma and magnetic field data. *Journal of Geophysical Research*, 110, A02209. <https://doi.org/10.1029/2004JA010649>
- Klimas, A. J., Valdivia, J. A., Vassiliadis, D., Baker, D. N., & Hesse, M. (2000). The role of self-organized criticality in the substorm phenomenon and its relation to localized reconnection in the magnetospheric plasma sheet. *Journal of Geophysical Research*.
- Lu, G., Baker, D. N., McPherron, R. L., Farrugia, C. J., Lummerzheim, D., Ruohoniemi, J. M., Rich, F. J., et al. (1998). Global energy deposition during the January 1997 magnetic cloud event. *Journal of Geophysical Research*, 103(A6), 11,685–11,694. <https://doi.org/10.1029/98JA00897>
- Lu, J. Y., Jing, H., Liu, Z. Q., Kabin, K., & Jiang, Y. (2013). Energy transfer across the magnetopause for northward and southward interplanetary magnetic fields. *Journal of Geophysical Research: Space Physics*, 118, 2021–2033. <https://doi.org/10.1002/jgra.50093>
- Mawad, R., Kandoul, M., Yousef, S., & Abdel-sattar, W. (2016). Quantized variability of Earth's magnetopause distance. The 5th International Conference on Modern Trends in Physics Research WSP MTPR-014, Volume 9914, 77–83, 2016 ADS:2016mtrp.conf...77 M.
- Murayama, T. (1982). Coupling function between solar-wind parameters and geomagnetic indexes. *Reviews of Geophysics*, 20(3), 623–629. <https://doi.org/10.1029/RG020i003p00623>
- Newell, P. T., Sotirelis, T., Liou, K., Meng, C.-I., & Rich, F. J. (2007). A nearly universal solar wind-magnetosphere coupling function inferred from 10 magnetospheric state variables. *Journal of Geophysical Research*, 112, A01206. <https://doi.org/10.1029/2006JA012015>
- NOAA technical memorandum OAR SEC-88 (2003). Halloween space weather storms of 2003, Space Environment Center, Boulder, Colorado, June 2004
- Østgaard, N., Germany, G., Stadsnes, J., & Vondrak, R. R. (2002). Energy analysis of substorms based on remote sensing techniques, solar wind measurements, and geomagnetic indices. *Journal of Geophysical Research*, 107(A9), 1233. <https://doi.org/10.1029/2001JA002002>
- Palmroth, M., Fear, R. C., & Honkonen, I. (2012). Magnetopause energy transfer dependence on the interplanetary magnetic field and the Earth's magnetic dipole axis orientation. *Annales de Geophysique*, 30(3), 515–526. <https://doi.org/10.5194/angeo-30-515-2012>
- Palmroth, M., Janhunen, P., Pulkkinen, T. I., Aksnes, A., Lu, G., Østgaard, N., et al. (2005). Assessment of ionospheric joule heating by GUMICS-4 MHD simulation, AMIE, and satellite-based statistics: Towards a synthesis. *Annales de Geophysique*, 23(6), 2051–2068.
- Palmroth, M., Koskinen, H. E. J., Pulkkinen, T. I., Toivanen, P. K., Janhunen, P., Milan, S. E., & Lester, M. (2010). Magnetospheric feedback in solar wind energy transfer. *Journal of Geophysical Research*, 115, A00I10. <https://doi.org/10.1029/2010JA015746>
- Palmroth, M., Laitinen, T. V., & Pulkkinen, T. I. (2006). Magnetopause energy and mass transfer: Results from a global MHD simulation. *Annales de Geophysique*, 24(12), 3467–3480.
- Palmroth, M., Pulkkinen, T. I., Janhunen, P., & Wu, C. C. (2003). Stormtime energy transfer in global MHD simulation. *Journal of Geophysical Research*, 108(A1), 1048. <https://doi.org/10.1029/2002JA009446>
- Papadopoulos, K., Goodrich, C., Wiltberger, M., Lopez, R., & Lyon, J. G. (1999). The physics of substorms as revealed by the ISTP. *Physics and Chemistry of the Earth - Part C*, 24(1–3), 189–202. [https://doi.org/10.1016/S1464-1917\(98\)00028-2](https://doi.org/10.1016/S1464-1917(98)00028-2)
- Papitashvili, V. O., Papitashvili, N. E., & King, J. H. (2000). Solar cycle effects in planetary geomagnetic activity: Analysis of 36-year long OMNI dataset. *Geophysical Research Letters*, 27(17), 2797–2800. <https://doi.org/10.1029/2000GL000064>
- Perreault, P., & Akasofu, S. I. (1978). Study of geomagnetic storms. *Geophysical Journal of the Royal Astronomical Society*, 54(3), 547–573. <https://doi.org/10.1111/j.1365-246X.1978.tb05494.x>
- Pulkkinen, T. I., Ganushkina, N. Y., Kallio, E. I., Lu, G., Baker, D. N., Turner, N. E., et al. (2002). Energy dissipation during a geomagnetic storm: May 1998. *Advances in Space Research*, 30(10), 2231–2240. [https://doi.org/10.1016/S0273-1177\(02\)80232-0](https://doi.org/10.1016/S0273-1177(02)80232-0)
- Pulkkinen, T. I., Palmroth, M., Janhunen, P., Koskinen, H. E. J., McComas, D. J., & Smith, C. W. (2010). Timing of changes in the solar wind energy input in relation to ionospheric response. *Journal of Geophysical Research*, 115, A00I09. <https://doi.org/10.1029/2010JA015764>
- Pulkkinen, T. I., Palmroth, M., & Laitinen, T. (2008). Energy as a tracer of magnetospheric processes: GUMICS-4 global MHD results and observations compared. *Journal of Atmospheric and Solar - Terrestrial Physics*, 70(5), 687–707. <https://doi.org/10.1016/j.jastp.2007.10.011>
- Russell, C. T. (2000). The solar wind interaction with the Earth's magnetosphere: A tutorial. *IEEE Transactions on Plasma Science*, 28, 1818.
- Russell, C. T. (2013). Solar Wind and Interplanetary Magnetic Field: A Tutorial. In P. Song, H. J. Singer, & G. L. Siscoe (Eds.), *Space Weather*. <https://doi.org/10.1029/GM125p0073>
- Scurry, L., & Russell, C. T. (1991). Proxy studies of energy-transfer to the magnetosphere. *Journal of Geophysical Research*, 96(A6), 9541–9548. <https://doi.org/10.1029/91JA00569>
- Stamper, R., Lockwood, M., Wild, M. N., & Clark, T. D. G. (1999). Solar causes of the long-term increase in geomagnetic activity. *Journal of Geophysical Research*, 104(A12), 28,325–28,342. <https://doi.org/10.1029/1999JA900311>
- Stern, D. P. (1984). Energetics of the magnetosphere. *Space Science Reviews*, 39(1–2), 193–213.
- Takalo, J., Timonen, J., Klimas, A., Valdivia, J., & Vassiliadis, D. (1999). Nonlinear energy dissipation in a cellular automaton magnetotail field model. *Geophysical Research Letters*, 26, 1813–1816.

- Tanskanen, E., Pulkkinen, T. I., Koskinen, H. E. J., & Slavin, J. A. (2002). Substorm energy budget during low and high solar activity: 1997 and 1999 compared. *Journal of Geophysical Research*, *107*(A6), 1086. <https://doi.org/10.1029/2001JA900153>
- Temerin, M., & Li, X. (2006). *Dst* model for 1995–2002. *Journal of Geophysical Research*, *111*, A04221. <https://doi.org/10.1029/2005JA011257>
- Tenfjord, P., & Ostgaard, N. (2013). Energy transfer and flow in the solar wind-magnetosphere-ionosphere system: A new coupling function. *Journal of Geophysical Research: Space Physics*, *118*, 5659–5672. <https://doi.org/10.1002/jgra.50545>
- Turner, N. E., Baker, D. N., Pulkkinen, T. I., Roeder, J. L., Fennell, J. F., & Jordanova, V. K. (2001). Energy content in the storm time ring current. *Journal of Geophysical Research*, *106*(A9), 19,149–19,156. <https://doi.org/10.1029/2000JA003025>
- Uritsky, V. M. (1996). $1/f$ -like spectra of geomagnetic fluctuations: Expression of self-organized criticality? In Book of abstracts of the International Conference on Problems of Geocosmos, June 17–23, (p. 110). St. Petersburg, Russia.
- Uritsky, V. M., & Pudovkin, M. I. (1998a). Fractal dynamics of *AE*-index of geomagnetic activity as a marker of the self-organized criticality in the magnetosphere (in Russian). *Geomagnetizm i Aeronomia*, *38*(3), 17–28.
- Uritsky, V. M., & Pudovkin, M. I. (1998b). Low frequency $1/f$ -like fluctuations of the *AE*-index as a possible manifestation of self-organized criticality in the magnetosphere. *Annales Geophysicae*, *16*(12), 1580–1588.
- Uritsky, V. M., Pudovkin, M. I., & Steen, A. (2001). Geomagnetic substorms as perturbed self-organized critical dynamics of the magnetosphere. *Journal of Atmospheric and Solar-Terrestrial Physics*, *63*(13), 1415–1424. [https://doi.org/10.1016/S1364-6826\(00\)00243-1](https://doi.org/10.1016/S1364-6826(00)00243-1)
- Uritsky, V. M., & Semenov, V. S. (2000). A sandpile model for global statistics of reconnection events in the magnetotail. In H. K. Biernat, C. J. Farrugia, & D. F. Vogl (Eds.), *The Solar Wind - Magnetosphere System 3* (pp. 299–308). Osterreichische Akademie der Wissenschaften, Wien.
- R.A.M. Van der Linden and the SIDC team (n.d.), online catalogue of the sunspot index, <http://sidc.oma.be/html/sunspot.html>.
- Vasyliunas, V. M., Kan, J. R., Siscoe, G. L., & Akasofu, S. I. (1982). Scaling relations governing magnetospheric energy-transfer. *Planetary and Space Science*, *30*(4), 359–365. [https://doi.org/10.1016/0032-0633\(82\)90041-1](https://doi.org/10.1016/0032-0633(82)90041-1)
- Wang, C., Han, J. P., Li, H., Peng, Z., & Richardson, J. D. (2014). Solar wind-magnetosphere energy coupling function fitting: Results from a global MHD simulation. *Journal of Geophysical Research: Space Physics*, *119*, 6199–6212. <https://doi.org/10.1002/2014JA019834>
- Workshop report, National Research Council of the National Academies (2008). *Severe space weather events—Understanding societal and economic impacts—*. Washington, DC: The National Academies Press.
- Wygant, J. R., Torbert, R. B., & Mozer, F. S. (1983). Comparison of S3-3 polar-cap potential drops with the interplanetary magnetic-field and models of magnetopause reconnection. *Journal of Geophysical Research*, *88*(A7), 5727–5735. <https://doi.org/10.1029/JA088iA07p05727>
- Youssef, M., Mahrous, A., Mawad, R., Ghamry, E., Shaltout, M., El-Nawawy, M., & Fahim, A. (2011). The effects of the solar magnetic polarity and the solar wind velocity on *Bz*-component of the interplanetary magnetic field. *Advances in Space Research*, *49*(7), 1198–1202. <https://doi.org/10.1016/j.asr.2011.07.023>



Source details

[Feedback >](#) [Compare sources >](#)

Earth and Space Science

Open Access [i](#)

Scopus coverage years: from 2014 to Present

Publisher: Wiley-Blackwell

E-ISSN: 2333-5084

Subject area: [Earth and Planetary Sciences: General Earth and Planetary Sciences](#) [Environmental Science: Environmental Science \(miscellaneous\)](#)

Source type: Journal

[View all documents >](#)

[Set document alert](#)

[Save to source list](#)

CiteScore 2022

5.4



SJR 2022

0.958



SNIP 2022

1.244



Inorganic Chemistry

Ligand-Centered Radical Activity by a Zinc-Schiff-Base Complex towards Catechol Oxidation

Subrata Das,^[a] Amrita Sahu,^[b] Mayank Joshi,^[e] Suwendu Paul,^[c] Madhusudan Shit,^[d] Angshuman Roy Choudhury,^[e] and Bhaskar Biswas^{+*^[a]}

In this work, we present the synthesis and structural characterization of a new Zn(II)-Schiff base complex, [Zn(L)(H₂O)] (1), [L = *N,N'*-bis(3-methoxysalicylidene)-1,3-diamino-2-propanol]. Single crystal X-ray structural analysis reveals that 1 crystallizes in monoclinic system with *P*_{2₁}/*c* space group. The compound shows good photo-luminescence property in methanol medium. This Zn(II) complex has been evaluated as a catalytic system in the catalytic oxidation of 3,5-di-*tert*-butylcatechol (DTBC) in methanol. The Zn(II) complex displays good catecholase like activity with significant turn over, $k_{\text{cat}}(\text{h}^{-1}) = 7.99 \times 10^2$ in methanol under aerobic condition. Very interestingly, we are able to isolate the oxidation product as 3,5-di-*tert*-butylquinone (2) in association with the substrate in the form of a single

crystal. Electron paramagnetic resonance (EPR), electron spray ionization (ESI) mass and ¹H nuclear magnetic resonance (NMR) spectral analyses of the reaction mixture between Zn(II) complex and DTBC recommend that the course of catalysis proceeds through substrate-catalyst adduct formation & confirm the presence of radical pathways in favour of oxidation products. The computation studies have been executed with density functional theory and all experimental observations are well rationalised with extensive theoretical calculations. Being a redox inactive metal ion, catalytic oxidation of DTBC by Zn(II) complexes will always be a remarkable example in the scientific community.

Introduction

Coordination molecules containing Schiff base ligands have special importance for their applications in the advancement of molecular properties like catalysis, magnetism, optical properties and so on.^[1–3] In all the transition metal ions, “zinc metal ion” remains one of the most fundamental contributors in the biological system and plays significant bio-functions in living system. In this living world, nature controls elemental distribution in its own way and it is commonly observed that most of the fundamental basic processes are metal centric like Mg(II) in photosynthesis, Fe(II)/(III) in O₂ transport phenomenon, Fe–Mo metal ions in N₂ fixation etc.^[4–6] So, designing of coordination

compounds which are suitable for mimicking of active sites for different metalloenzymes has become a serious challenge to the synthetic chemists. Bio-mimicking activities will not only provide lots of important basic information about their bio-functions but also head to make a clarification of their mechanistic concern on such complex systems.^[7–9] Zn(II)-Schiff base complexes are mostly treated as potential photo-active materials.^[10] With a d¹⁰ electronic configuration, Zn(II) ion ions have a pronounced effect on their photo-physical properties. Unsaturation of coordination number at Zn(II) centre in several zinc complexes makes it stronger Lewis acids. Other characteristic features of zinc ions like Lewis acid activation, nucleophile origination, rapid ligand exchange, and stabilization of leaving group, make Zn(II) ion one of the most prevalent metal ions in material sciences.^[11,12]

Viewing of the oxidation reactions of laboratory and industrial importance, it is of paramount interest to evaluate efficient and selective oxidation catalysts.^[13] Searching of the new catalysts having ability to mimics the structural and functional aspects of catechol oxidase enzyme has created huge appeal in the modern research in bioinorganic chemistry.^[14–16] In this regards, we have synthesized a polydentate (N,O)-donor Schiff base ligand, *N,N'*-bis(3-methoxysalicylidene)-1,3-diamino-2-propanol and its mononuclear Zn(II)-Schiff base complex. The compound shows good photo-luminescence property in methanol medium. This complex has been employed as an effective catalytic system towards catechol oxidation in MeOH. EPR, ESI–Ms and ¹H NMR spectral analysis of the reaction mixture between Zn(II) complex and DTBC recommends that the course of catalysis proceeds through Substrate-Catalyst adduct formation and confirms the

[a] S. Das, Dr. B. Biswas⁺
Department of Chemistry, University of North Bengal, Darjeeling 734013, West Bengal, India
E-mail: mr.bbiswas@rediffmail.com
Homepage: www.nbu.ac.in


[b] A. Sahu
Department of Electrical Engineering, Temple University, Philadelphia 741235, USA

[c] S. Paul
Department of Chemistry, University of Kalyani, Kalyani 741235, West Bengal, India

[d] M. Shit
Department of Chemistry, Dinobandhu Andrews College, Kolkata 700084, West Bengal, India

[e] M. Joshi, Dr. A. Roy Choudhury
Department of Chemical Sciences, Indian Institute of Science Education and Research Mohali, S.A.S. Nagar, Manauli PO, Mohali 140 306, India

[⁺] On lien from Surendranath College, Kolkata 700009

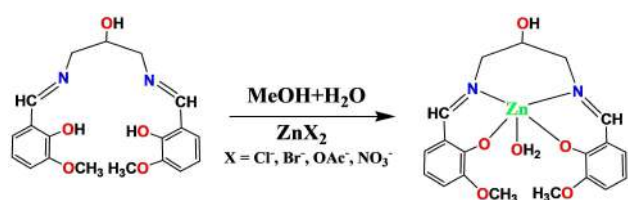
 Supporting information for this article is available on the WWW under <https://doi.org/10.1002/slct.201801084>

radical mechanistic pathways with a significant turn over number, $k_{\text{cat}}(\text{h}^{-1}) = 7.99 \times 10^2$ in methanol in favour of 3,5-di-*tert*-butylquinone. Further, all the experimental observations are well corroborated with extensive theoretical calculations.

Results and discussion

Synthesis and formulation

The Zn(II) complex was prepared in the form of single crystals by mixing of Zn(II) chloride with an (N,O)-donor Schiff base ligand in 1:1 mole ratio in an aqueous methanolic medium (Scheme 1). The structural composition of **1** was determined by



Scheme 1. Preparative method for the zinc(II) complex

different analytical techniques like IR, UV-Vis, ^1H NMR, ESI-MS, molar conductivity including single crystal X-ray diffraction study. We have tried to produce best quality crystals for this compound but we obtained best crystals with R factor ~ 10 , even at 100 K structural refinement parameters.

Description of X-ray structures with theoretical support

Single crystal X-ray structural analysis reveals that Zn(II)-Schiff base complex crystallizes in monoclinic system with $P2_1/c$ space group. An ORTEP view of the asymmetric units of **1** is shown in Figure 1. The crystallographic refinement parameters of **1** are

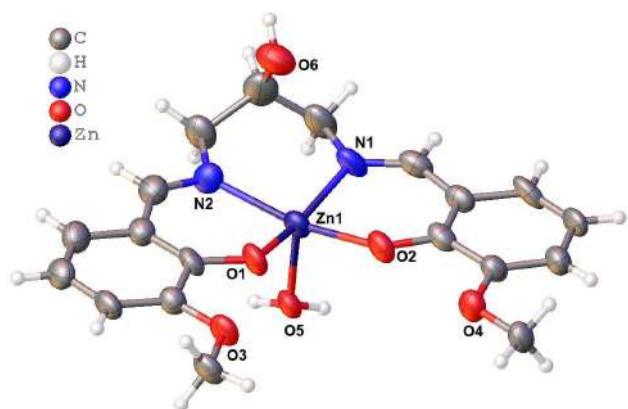


Figure 1. An ellipsoid plot (30% probability) of $[\text{Zn}(\text{L})(\text{H}_2\text{O})]$ (**1**) with atom numbering scheme.

listed in Table 1. Selected bond angles, and bond distances of **1** are presented in Table S1. The single crystal X-ray structural analysis of **1** reveals that the coordination geometry of zinc(II) centre adopts a perfect square pyramidal geometry, which is also evident from geometric index value, $\tau = 0.0$; $[\tau = |\beta - \alpha|/60]$, where $\alpha = 90.0^\circ$ and $\beta = 89.96^\circ$; τ is 1 for a perfect trigonal-bipyramidal geometry and is zero for a perfect square pyramidal geometry.^[17] The square plane in this square pyramidal structure for Zn1 consists of two nitrogen atoms and two oxygen atoms [N1,N2,O1,O2] from ligand backbone. The coordinated aqua molecule [H_2O in **1**] occupies an axial position in the square pyramid. The bond angle parameters and trigonal index value indicate about an existence of a perfect square pyramidal Zn(II)-Schiff base complex in the solid state. Though this Schiff base ligand (L) actually behaves as a polydentate ligand but all the donor centres are not employed in the formation of Zn(II) complex. Previously it was seen that this ligand acted as an important backbone for making heterometallic clusters (3d–4f) which led to important magnetic properties.^[2b,c] In this present case, this particular ligand actually displays selectivity towards Zn(II) ion and for this reason it is observed that methoxy-O (O3 & O4) and alkoxy-O (O6) remains unemployed in the structural building,

Computational study for the optimization of the molecular structure of Zn(II)-Schiff base complex in the gas phase is also performed through the DFT method in combination with B3LYP theoretical model and 6–311G basis set. The gas phase molecular structure for zinc complex is presented in Figure 2.

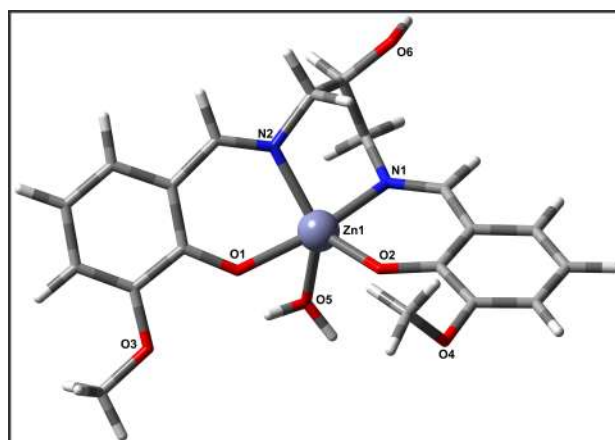


Figure 2. Gas phase molecular structure of $[\text{Zn}(\text{L})(\text{H}_2\text{O})]$ (**1**) obtained with DFT/B3LYP/6-311G theoretical method.

Gas phase structure of this Zn(II) complex also indicates the existence of a square pyramidal coordination geometry with similar coordination linkages. Phenolic-O (O1, O2) and imine-N (N1, N2) of the Schiff base ligand coordinate with Zn(II) centre in a plane through charge pair and the lone pair of electrons while water molecule (O5) sits at the axial position of the square pyramid. Gas phase structure also resembles well with the crystal structure of the zinc compound but found little bit a

Table 1. Structural refinement parameters for 1 & 2

Parameters	Compound 1	Compound 2
Empirical formula	C ₁₉ H ₂₂ N ₂ O ₆ Zn	C ₄₂ H ₆₆ O ₇
Formula weight	439.75	682.94
T (K)	293	100
Wavelength (Å)	0.71073	0.71073
Crystal system	Monoclinic	Triclinic
Space group	P2 ₁ /c	P-1
Unit cell dimensions		
a (Å)	24.014(5)	10.0551(5)
b (Å)	5.0014(12)	14.7624(7)
c (Å)	14.952(4)	15.2018(9)
α (°)	90.0	112.927(5)
β (°)	89.96(2)	92.375(4)
γ (°)	90	100.673(4)
V (Å ³)	1795.8(7)	2026.2(2)
Z	4	2
ρ (gm cm ⁻³)	1.627	1.119
Absorption coefficient (mm ⁻¹)	1.409	0.074
F(000)	912	748
Crystal size (mm ³)	0.1 × 0.2 × 0.2	0.19 × 0.2 × 0.2
Theta range for data collection	2.5 to 32.90.	2.5 to 32.80.
Index ranges (h, k, l) → -26 < h < = 26, -11 < k < = 11, -27 < l < = 27	-36,33; -7,7; -21, 21	-15,14; -21,22; -22, 22
Reflections collected	21322	45909
Independent reflections	6348	14179
R(int)	0.200	0.068
Final R indices [I > 2σ(I)]	R1 = 0.1032, wR2 = 0.2982	R1 = 0.0804, wR2 = 0.2636
Largest diff. peak and hole	1.65 and -1.29 e. Å ⁻³	1.09 and -0.67 e. Å ⁻³

distorted form. Computed bond angles, and bond distances of 1 in gas phase are also given in Table S1.

We are able to isolate the oxidation product in the form of single crystals. According to X-ray structure it is revealed that the molecules crystallise in a triclinic system with *P*-1 space group. An ORTEP view of the asymmetric units of 2 is shown in Figure S1. X-ray structural analysis of the oxidation product shows that two catechol units in different conformations in solid state form a dimeric unit through H-bonding interaction. This interaction between the dimeric catechol unit and quinone unit is also established through H bond. In this H-bonded adduct formation, it is observed that water molecule acts as a donor towards oxidation product (3,5-di-*tert*-butylquinone) and also plays an acceptor to catechol unit. The crystallographic refinement parameters of 2 are also given in Table 1. Selected bond angles and bond distances of 2 are given in Table S2. Literature survey on the crystal structure of 3,5-DTBQ indicates that Wen *et al.*^[18] isolated this compound in the form of a single crystal. Most interestingly, C–O bond distances are found in the quinone unit [C2–O1, 1.216 Å; C1–O2, 1.230 Å] while C–O distances are seen as C15–O3, 1.371 Å; C16–O4, 1.384 Å; C29–O5, 1.371 Å, C30–O6, 1.382 Å in two asymmetric catechol units. So, the crystallographic bond distances in quinone supports strongly the existence of 3,5-DTBQ unit in the solid state.

Experimental and theoretical views on the solution properties of Zn(II) complex

The structural rigidity of the mononuclear Zn(II) compound in solution state has been investigated by different analytical

methods like UV-Vis spectroscopy, steady-state fluorescence study, molar conductivity, ESI–Ms spectral analysis. The Zn(II) compound is soluble in most of the polar solvents like methanol, dichloromethane and water.

The UV-Vis spectrum for the Zn(II) compound in methanolic solution at room temperature showed high-intensity transitions up to 350 nm (Figure S2). High-intensity transitions at 246 and 311 nm are assignable to the $\pi \rightarrow \pi^*$ and $n \rightarrow \pi^*$ electronic transitions correspond to –C=N– chromophore of Schiff base ligand in methanolic solution.^[19] A broad and low-intensity transition at 337 nm indicates ligand to metal centre charge transition (LMCT) in the Zn(II)-Schiff complex. We kept the solution for 5 days in MeOH at RT and re-measured the optical spectrum for 1. The position of the spectral bands remains in the same region and supports for structural rigidity for 1.

TD-DFT is commonly used to determine the electronic properties of metal complexes in excited states. With an aim to get a better view on the nature of optical spectrum of Zn(II)-Schiff base compound, we have performed TD-DFT studies. The low energetic electronic transitions in HOMO \rightarrow LUMO/ HOMO-1 \rightarrow LUMO+1 (Figure 3) depict the electronic activity for this complex in solution. It is well known that lower the energy gap associated with HOMO & LUMO higher will be the activity and consequently lower will be the stability of a molecule. Absorption bands based on the theoretical calculation in gas phase shows the electronic transitions at ~240 and 297 nm for 1 (Figure S2). From the orbital contribution, it is clear that the absorption bands of 1 are interpreted in terms of $\rightarrow \pi^*$ and $\pi \rightarrow \pi^*$ transitions. The experimental and calculated wavelength of bands observed for 1 is reported in Table S3.

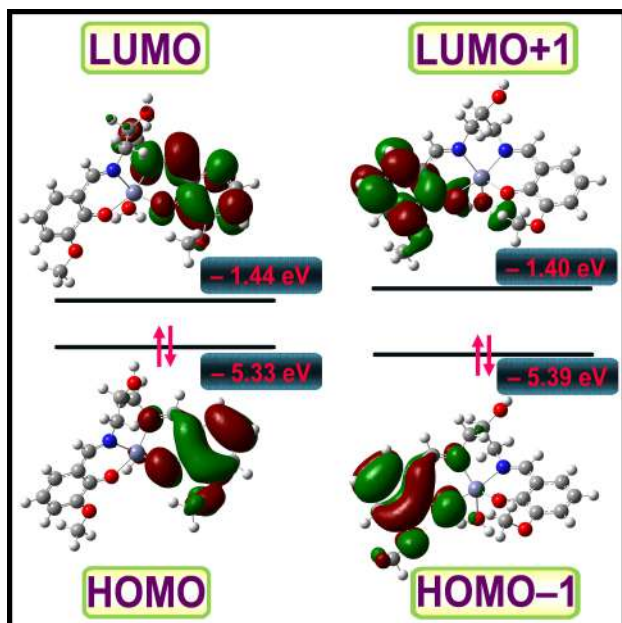


Figure 3. Images of the frontier molecular orbitals of 1 computed using B3LYP/6-311G theoretical method and methanol/IEFPCM solvent model.

The ESI-MS spectral analysis of 1 further confirms in favour of molecular integrity in solution for $[\text{Zn}(\text{L})(\text{H}_2\text{O})]$ (1). ESI mass spectrum of 1 in methanolic solution displays the base peak at m/z 360.11 for $[(\text{L}) + \text{H}^+]$ (Figure S3) while another important peak at m/z 440.87 indicates the presence of molecular ion peak in MeOH medium. The ESI-MS of methanolic solution of Zn(II) compound confirms its solution stability.

We also carried out the measurement of molar conductivity at room temperature under an aerobic condition for Zn complex. We have taken solution of 1.10×10^{-3} M concentration and found molar conductance as $5.7 \mu\text{S}/\text{cm}$. Molar conductance value of this compound strongly suggests non-electrolytic nature in methanolic solution and recommends solution stability for this Zn(II) complex.

We have also recorded ^1H NMR spectrum for the Zn(II)-Schiff base complex in CDCl_3 solvent at RT (Figure S4). From the NMR spectrum, it can also be revealed that Ph-OH and $-\text{HC}=\text{N}$ of the ligand backbone actually serve as effective donor sites towards Zn(II) ion and form an innermetallic compound of first order. While solvent aqua molecule sits at axial position to form a perfect square pyramidal structure (Figure S4).

Luminescence property with lifetime decay of the Zn(II) compound

The photoluminescence spectrum of the Zn(II) compound (λ_{ex} 246, 311 nm) in methanol at 298 K is presented in Figure 4. The emission wavelength for Zn(II) compound in methanolic solution is 355 nm (Figure 4). The excited state mean lifetime of the Zn(II)-Schiff base complex is found to have 8.19 ns. Time dependent photoluminescence decay profile for this complex is given in Figure 4. It is seen that the compound is quite stable

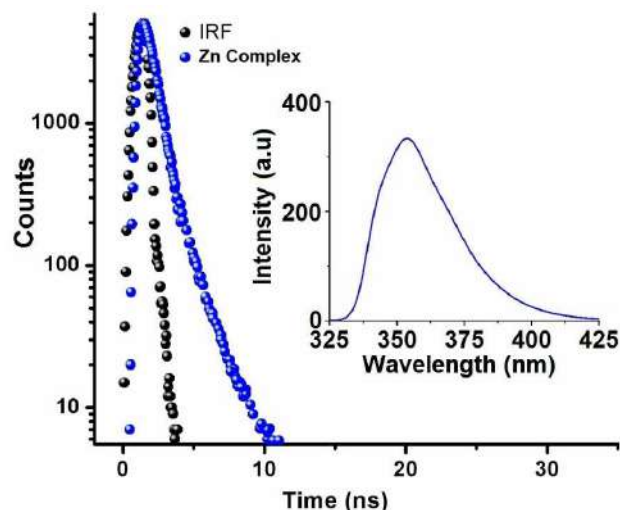
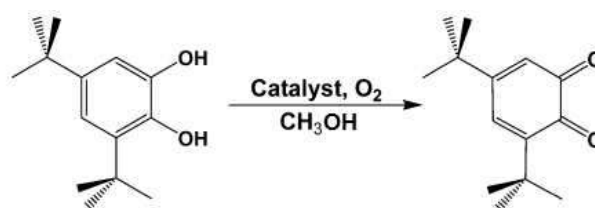


Figure 4. Time dependent photoluminescence decay profile for Zn(II) complex in MeOH [Inset: Fluorescence spectrum of 1, $\lambda_{\text{ex}} = 311$ nm].

in solution and stable in its monomeric form in solution. The nature of emission, in this case, indicates the possibility of ligand-to-metal charge transfer.^[20,21] The previous scientific literature on the Zn(II) compounds also agree with our observation [10b,c].

Catecholase activity of the Zn(II) complex and its mechanistic inferences

To study catecholase activity for Zn(II)-Schiff base complex, we have considered 3,5-di-*tert*-butyl catechol (DTBC) as a model substrate. DTBC is treated as the standard substrate for having two bulky *t*-butyl substituents to the aromatic ring and for having low quinone-catechol reduction potential. This low quinone-catechol reduction potential value actually helps to easy oxidation of catechol to the corresponding *o*-quinone, DTBQ (Scheme 2). In general, DTBQ is highly stable in solution and exhibits a maximum absorption at 401 nm in methanol.^[22]



Scheme 2. Catalytic Oxidation of 3,5-DTBC to 3,5-DTBQ in Air-Saturated methanol solvent

During the investigation of catecholase activity for this mononuclear Zn(II)-Schiff base complex in air saturated methanol solvent, a 1×10^{-4} M solution of Zn(II) complex was added

to 1×10^{-2} M (100 equiv.) of 3,5-DTBC solution in same solvent. The course of catalytic oxidation was followed by spectrophotometry at a time interval of 8 min for 2 h (Figure 5). Complex 1

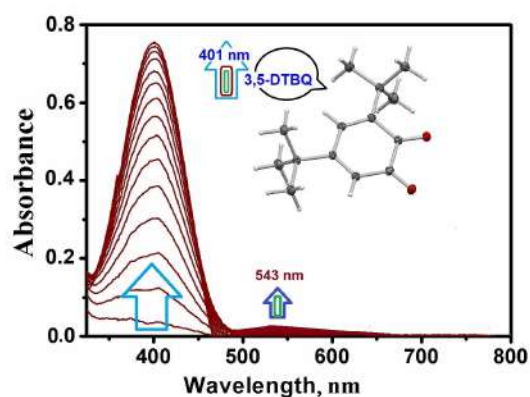


Figure 5. Increase of optical bands at 401 nm & 543 nm for semiquinone species upon addition of 100 equivalents of (3,5-DTBC to a solution containing zinc complex (1) (10^{-4} M) in methanol at 25°C. The spectra were recorded after every 8 min.

in methanol showed characteristics spectral bands at 246 and 311 nm while 3,5-DTBC exhibited a high intensity single band at 284 nm.^[23] With the progress of catalytic oxidation, it is seen that intensity of the catechol band gradually declined and concomitantly new bands correspond to the maximum at ~ 401 & 543 nm was formed (Figure 5). This observation in spectrophotometry proves the oxidation of 3,5-DTBC to 3,5-DTBQ with simultaneous production of semiquinone species in a consolidated way. The respective oxidation product, 3,5-DTBQ was extracted in isolated yield and purified by column chromatography by using hexane-ethyl acetate as an eluant mixture. The product was identified by ^1H NMR spectroscopy. ^1H NMR (CDCl_3 , 400 MHz) δ_{H} : 1.16 (s, 9H), 1.20 (s, 9H), 6.15 (d, $J = 2.4$ Hz, 1H), 6.86 (d, $J = 2.4$ Hz, 1H).

The kinetics of catalytic oxidation of 3,5-DTBC were performed by the method of initial rates. The growth of the quinone band was monitored at 401 nm as a function of time.^[24] The colour of the solution became reddish brown during the course of catalysis. This physical change is also indicative for the conversion of 3,5-DTBC to 3,5-DTBQ. The complex illustrated about a saturation kinetics where kinetic reactions followed Michaelis-Menten model. Michaelis-Menten binding constant (K_m), maximum velocity (V_{max}), and rate constant for dissociation of substrate (i.e., turnover number, k_{cat}) were determined from Lineweaver–Burk graph using the following equation, $1/V = \{K_m/V_{\text{max}}\}\{1/[S]\} + 1/V_{\text{max}}$. These kinetic parameters were obtained through the graphical plot of $1/V$ vs $1/[S]$ (Figure S5), To reveal the high catalytic activity of 1, we draw a comparison between our Zn(II)-Schiff base complex and some other Zn(II)-Schiff base complexes [Table 2]. The turnover number (k_{cat}) for the zinc complex is $7.99 \times 10^2 \text{ h}^{-1}$ in MeOH. The kinetic parameters of 1 are presented in Table 2.

Table 2. Kinetic parameters for the catalytic oxidation of DTBC by 1 in MeOH at 25°C

Complex	V_{max} (M s^{-1})	K_m (M)	k_{cat} (h^{-1})	Ref
1*	2.22×10^{-5}	9.28×10^{-4}	7.99×10^2	Present
1	3.0×10^{-3}	1.06×10^{-3}	1.33×10^3	9b
$[\text{Zn}_2 \text{L}^3\text{Cl}_3]$	8.25×10^{-4}	1.93×10^{-3}	2.97×10^3	25
$[\text{Zn}_2(\text{L}^4)_2(\text{CH}_3\text{COO})_2]$	9.78×10^{-4}	1.05×10^{-4}	3.52×10^3	25

*Std. Error for 1, V_{max} (MS^{-1}) = 9.37×10^{-7} ; Std. Error for K_m (M) = 5.95×10^{-5}

It is unprecedented that zinc complexes containing Schiff-base ligands display similar functional activities like a Cu(II) based metalloenzyme, catechol oxidase. Generally, it is seen that zinc ions are involved in the redox process with the two-electron transfer. So in order to elucidate the reason favouring catechol oxidation activity exhibited by this Zn(II)-Schiff base complex, EPR study was carried out. The X-band EPR spectra for the solutions containing Zn(II)-Schiff base complex in presence and absence of DTBC were separately recorded in CH_2Cl_2 at 298 K. The spectra are presented in Figure 6. The EPR

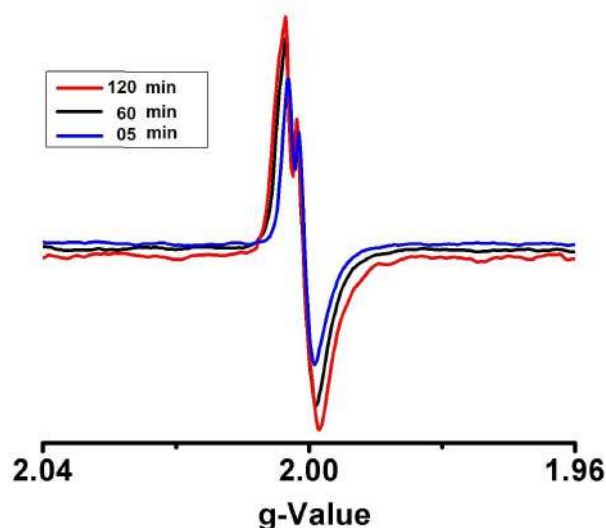


Figure 6. X-band EPR spectra of Zn-Schiff base complex in mixing with 3,5-DTBC at 5 min, 60 min & 120 min in CH_2Cl_2 solution at 298 K.

signal for this Zn(II)-Schiff base complex and DTBC at 298 K remains silent and found as EPR inactive. Mixing of different Zn(II) salts with DTBC didn't produce any signal in the EPR spectrum. The EPR study was also performed at 298 K, promptly after mixing the Zn(II) complex with 3,5-DTBC in an inert atmosphere and spectra were recorded at 5 min, 60 min and 120 min time interval. Figure 6 shows a broad, nearly isotropic EPR signal at $g \approx 2.0$. A control experiment, in identical experimental condition, shows that Zn(II) complex, as well as a mixture of different Zn(II) salts and 3,5-DTBC, found EPR silent. Thus, the EPR signal, which is a definite indication of formation of some ligand-centred radical species, is generated

only when the Zn(II) complex is mixed with 3,5-DTBC, and radical formation is most likely responsible for that oxidation as reported by our group previously.^[9b] This catalytic oxidation reaction was also performed in the presence of a radical scavenger, TEMPO (TEMPO = 2,2,6,6-tetramethylpiperidinoxy). Addition of two equivalent of TEMPO to the methanolic solution of catalyst assisted to stop the conversion from catechol to quinone. This observation provided further support that catalytic oxidation for catechol substrate based on this Zn(II) complex is proceed through generation of radical in solution. It was further observed that no catalytic oxidation reactions are occurred in an inert atmosphere and no formation of 3,5-DTBQ has been detected.^[25] However, exposure of the reaction mixture in aerobic atmosphere, formation of 3,5-DTBQ was noticed immediately. This particular observation helped us to predict that molecular oxygen remains one of the active reactants in this catalysis. In the catalytic cycle, catechol converts to the semibenzoquinone radical in the first step of catalysis and in the next step, release of quinone with subsequent regeneration of the catalyst.

In order to gain further insight of this catalytic oxidation reaction in a solution state, we have also recorded ESI-MS spectrum of a 1:100 mixture of complex 1 and 3,5-DTBC in methanol solvent. The spectrum (Figure S6) exhibits a base peak at $m/z = 243.21$ (100%) that is assignable to the quinone-sodium aggregate, $[3,5\text{-DTBQ-Na}]^+$. The peak at $m/z = 642.85$ corroborates the formation of substrate-catalyst adduct, $[Zn(L)(DTBC)]$ species as an intermediate (Figure S6).

To confirm the active participation of Schiff base, we have also recorded EPR spectrum of Schiff base in presence of 3,5-DTBC in CH_2Cl_2 at 298 K. This mixture also produced a signal at $g \approx 2.01$ and strongly recommends about the active involvement of Schiff base in the catalytic oxidation of 3,5-DTBC during the course of catalysis (Figure 7). This observation

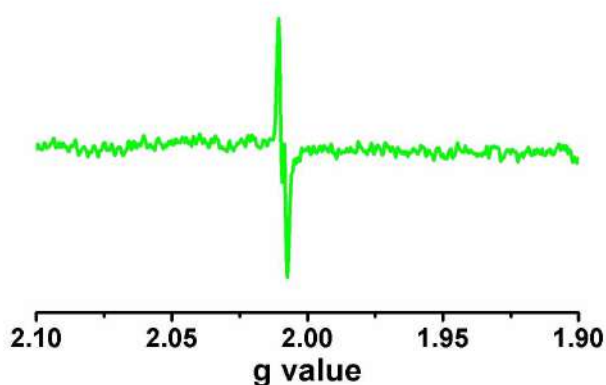
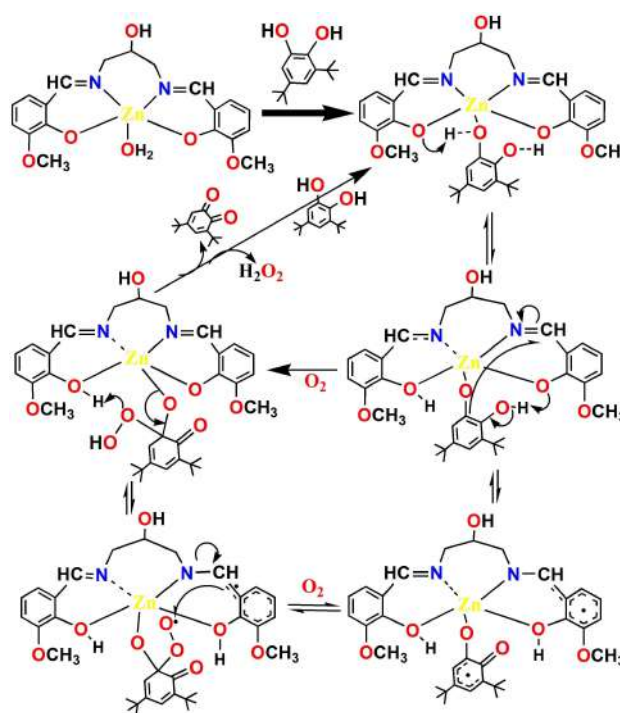


Figure 7. X-band EPR spectra of Schiff base in presence of 3,5-DTBC after 20 min in CH_2Cl_2 solution at 298 K.

helped us to conclude that Schiff base in the Zn(II) complex is the principal driving force for the generation of radical species in the catalytic oxidation of 3,5-DTBC.

In order to detect the by product, we are able to detect I_3^- through spectrophotometrically and found the development of the characteristic I_3^- band at 353 nm (Figure S7). Furthermore, to clarify the mechanistic pathway for the course of catalysis, $^1\text{H NMR}$ was recorded for our diamagnetic Zn(II)-Schiff base complex in presence of 3,5-DTBC in CDCl_3 (Figure S8). Since the course of reaction is a catalytic type, so we initially maintained the ratio of concentration, $[\text{catalyst}]: [\text{substrate}]$ as 1:100 and recorded the $^1\text{H NMR}$ of reaction mixture after 30 minutes of mixing up to 15 ppm. Under this gravity of situation, $^1\text{H NMR}$ spectrum was totally dominated by the proton signal of the substrate. In order to achieve the effective signal, the concentration ratio was reduced to 1:10 for $[\text{catalyst}]: [\text{substrate}]$ in CDCl_3 which produced characteristic proton signals for semiquinone with unreacted substrate. Some of the characteristics proton signals attached to 1° carbon and methoxy-C corresponds to ligand backbone were also appeared. However, no proton signals assignable to $\text{Ar-H} / \text{-CH=N-}$ of Schiff base were found in the spectrum. This observation further suggests that radical generation on ligand backbone during the course of catalysis made a substantial shifting of $\text{Ar-H} / \text{-CH=N-}$ in downfield and proton signals upto 15 ppm wasn't detected in the spectrum. Thus combining efforts from the EPR titration, *in situ* measurement of ESI-MS spectra, and $^1\text{H NMR}$ spectrum for the zinc complex in presence of DTBC substrate, now we are in a position to propose a mechanistic route through which the catalytic cycles are moving on (Scheme 3).



Scheme 3. Proposed mechanistic route for the ligand-centered radical activity by this Zn(II) complex

So, the course of catalysis recommends that substrate, at first, binds with catalyst (Zn(II)-Schiff base complex) and forms a Catalyst-Substrate adduct. This adduct actually generate semiquinone radical employing imine chromophore of Schiff base ligand which consequently reacts with aerobic dioxygen and produce quinone with hydrogen peroxide.

Conclusions

In summary, we have synthesized a new Zn(II)-Schiff base complex, [Zn(L)(H₂O)] (1). Single crystal X-ray analysis of this compound defines its mono-nuclearity with the square pyramidal geometry of the Zn(II) centre. The complex shows good photo-luminescence property in methanolic solution and lifetime measurement for this compound indicates its good photo-stability at transient state. Upon catalytic addition of the Zn(II) complex to the methanolic solution of DTBC under aerobic atmosphere recommends that the Zn(II) compound, (1) produces *o*-quinone species with significant turn over number, $k_{cat}(h^{-1}) = 7.99 \times 10^2$. EPR, ESI-MS and ¹H NMR spectral analyses confirm that the course of catalysis proceeds through the formation of Enzyme-Substrate adduct formation and generation of ligand-centric radical in the Zn(II) ion in Schiff base ligand backbone remains the driving force behind this significant catecholase activity. The theoretical studies through computational modelling agree very well with the experimental findings.

Supporting Information Summary:

CCDC 1835663 & 1835664 contain the supplementary crystallographic data for 1 and 2. These data can be obtained free of charge via <http://www.ccdc.cam.ac.uk/conts/retrieving.html> or from the Cambridge Crystallographic Data Centre, 12 Union Road, Cambridge CB2 1EZ, UK; fax: (+44) 1223-336-033; or e-mail: deposit@ccdc.cam.ac.uk. Experimental information such as weak interactions, Details of chemical sources, synthetic procedures, experimental and theoretical measurements, crystal structure of catechol-quinone adduct, UV-Vis, ESI-MS, IR, NMR spectra of 1, rate vs. [substrate] plot, ESI MS spectra of 1 in presence of DTBC, UV-Vis spectra of I₃⁻, ¹H NMR spectra of 1 in presence of DTBC were given here.

Acknowledgements

BB gratefully acknowledges the financial support from Science and Engineering Research Board (SERB), a Statutory body under DST, New Delhi India under the FAST TRACK SCHEME for YOUNG SCIENTIST (No. SB/FT/CS-088/2013 dtd. 21/05/2014). ARC thanks the X-ray facility of the Department of Chemical Sciences, IISER Mohali for single crystal X-ray diffraction data collection.

Conflict of Interest

The authors declare no conflict of interest.

Keywords: Bio-mimicking study · Catechol oxidase activity · Schiff base · Synthesis · X-ray structures

- [1] a) R. H. Prince, in *Comprehensive Coordination Chemistry*, ed. G. Wilkinson, Gillard, G. A. McCleverty, Pergamon, Oxford **1987**, 5, 925–1045; b) B. Biswas, N. Kole, M. Patra, S. Dutta, M. Ganguly, *J. Chem. Sci.* **2013**, *125*, 1445–1453; c) I. Majumder, P. Chakraborty, J. Adhikary, H. Kara, E. Zangrando, A. Bauza, A. Frontera, D. Das, *ChemistrySelect* **2016**, *3*, 615–625.
- [2] a) B. Biswas, M. Mitra, J. Adhikary, G. R. Krishna, P. P. Bag, C. M. Reddy, N. Aliaga-Alcalde, T. Chattopadhyay, D. Das, R. Ghosh, *Polyhedron* **2013**, *53*, 264–268; b) S. Ghosh, C. J. Gomez Garcia, J. M. Clemente-Juan, A. Ghosh, *Magnetochem* **2016**, *2*, 2; c) P. Mahapatra, S. Ghosh, S. Giri, V. Rane, R. Kadam, M. Drew, A. Ghosh, *Inorg. Chem.* **2017**, *56*, 5105–5121; d) B. Biswas, A. Pal, G. R. Krishna, C. M. Reddy, F. Tuna, R. Ghosh, *Polyhedron* **2011**, *30*, 2032–2037.
- [3] a) A. Banerje, S. Ganguly, T. Chattopadhyay, K. S. Banu, A. Patra, S. Bhattacharya, E. Zangrando, D. Das, *Inorg. Chem.* **2009**, *48*, 8695–8702; b) B. Biswas, A. Al-Hunaiti, M. T. Räisänen, S. Ansalone, M. Leskelä, T. Repo, Y.-T. Chen, H.-L. Tsai, A. D. Naik, A. P. Railliet, Y. Garcia, R. Ghosh, N. Kole, *Eur. J. Inorg. Chem.* **2012**, *2012*, 4479–4485.
- [4] a) B. L. Vallee, *Zinc Enzymes*, ed. T. G. Spiro, Wiley, New York **1983**, pp. 1–24; b) I. Bertini, C. Luchinat, M. S. Viezzoli, *Zinc Enzymes*, ed. I. Bertini, C. Luchinat, W. Maret, M. Zeppezauer, Birkhäuser, Boston **1986**, 27–47.
- [5] a) E. L. Hegg and L. Que, Jr., *Eur. J. Biochem.* **1997**, *250*, 625–629; b) D. Dey, A. De, H. R. Yadav, P. S. Guin, A. R. Choudhury, N. Kole, B. Biswas, *ChemistrySelect* **2016**, *1*, 1910–16.
- [6] W. N. Lipscomb, N. Straeter, *Chem. Rev.* **1996**, *96*, 2375–2433.
- [7] a) N. V. Kaminskaia, B. Spingler, S. J. Lippard, *J. Am. Chem. Soc.* **2000**, *122*, 6411–6422; b) P. Seth, S. Giri, A. Ghosh *Dalton Trans.* **2015**, *44*, 12863–12870.
- [8] a) G. Parkin, *Chem. Rev.* **2004**, *104*, 699–768; b) H. Vahrenkamp, *Dalton Trans.* **2007**, *0*, 4751–4759.
- [9] a) S. R. Seidel, P. J. Stang, *Acc. Chem. Res.* **2002**, *35*, 972–983; b) D. Dey, G. Kaur, A. Ranjani, L. Gyathri, P. Chakraborty, J. Adhikary, J. Pasan, D. Dhanasekaran, A. R. Choudhury, M. A. Akbarsha, N. Kole, B. Biswas, *Eur. J. Inorg. Chem.* **2014**, *2014*, 3350–3358.
- [10] a) N. Periasamy, *Fluorescence Spectroscopy and Its Applications*, Indian Academy of Science, **2007**; b) D. Dey, G. Kaur, M. Patra, A. R. Choudhury, N. Kole, B. Biswas, *Inorg. Chim. Acta.* **2014**, *421*, 335–341; c) R. Sanyal, X. Zhang, P. Kundu, T. Chattopadhyay, C. Zhao, F. A. Mautner, D. Das, *Inorg. Chem.* **2015**, *54*, 2315–2324.
- [11] J. Chen, X. Wang, Y. Zhu, J. Lin, X. Yang, Y. Li, Y. Lu, Z. Guo, *Inorg. Chem.* **2005**, *44*, 3422–3430.
- [12] a) C. Metcalfe, J. A. Thomas, *Chem. Soc. Rev.* **2003**, *32*, 215–224; b) H. Zhang, C. -S. Liu, X. -H. Bu, M. J. Yang, *Inorg. Biochem.* **2005**, *99*, 1119–1125.
- [13] a) L. Que, Jr. and R. Y. N. Ho, *Chem. Rev.* **1996**, *96*, 2607–2624; b) M. Merkel, M. Pascaly, B. Krebs, *Inorg. Chem.* **2005**, *44*, 7582–7589.
- [14] a) F. Meyer, J. Ackermann, E. Kaifer, H. Pritzkow, *Chem. Eur. J.* **2002**, *8*, 247–258; b) D. X. West, H. Gebremedhin, R. J. Butcher, J. P. Jasinski, A. E. Liberta, *Polyhedron* **1993**, *12*, 2489–2497.
- [15] a) C. Gerdemann, C. Eicken, B. Krebs, *Acc. Chem. Res.* **2002**, *35*, 183–191; b) R. K. Parashar, R. C. Sharma, A. Kumar, G. Mohan, *Inorg. Chim. Acta.* **1988**, *151*, 201–208.
- [16] a) E. I. Solomon, U. M. Sundaram, T. E. Machonkin, *Chem. Rev.* **1996**, *96*, 2563–2606; b) R. Mayilmurugan, K. Visvaganesan, E. Eringathodi Suresh, M. Palaniandavar, *Inorg. Chem.* **2009**, *48*, 8771–8783.
- [17] a) A. W. Addison, T. N. Rao, *J. Chem. Soc. Dalton Trans.* **1984**, 1349; b) D. Dey, S. Das, H. R. Yadav, A. Ranjani, L. Gyathri, S. Roy, P. S. Guin, D. Dhanasekaran, A. R. Choudhury, M. A. Akbarsha, B. Biswas, *Polyhedron* **2016**, *106*, 106–114; c) V. Chandrasekhar, A. Dey, S. Das, M. Rouzières, R. Clérac, *Inorg. Chem.* **2013**, *52*, 2588–2598.
- [18] D.-N. Horng, J.-P. Chyn, K.-J. Shieh, J.-L. Chou, Y.-S. Wen, *Acta Cryst.* **1999**, *C55*, 652–653.
- [19] J. G. Sole, L. E. Bausa, D. Jaque, *An Introduction to the Optical Spectroscopy Inorganic Solids*, John Wiley & Sons, New York, **2005**.
- [20] N. Chattopadhyay, A. Mallick, S. Sengupta, *J. Photochem. Photobiol. A* **2005**, *177*, 55–60.

- [21] P. Purkayastha, G. K. Patra, D. Datta, N. Chattopadhyay, *Indian J Chem A*. **2000**, *39*, 375.
- [22] L. -Z. Cai, W. -T. Chen, M. -S. Wang, G. -C. Guo, J. -S. Huang, *Inorg. Chem. Commun.* **2004**, *7*, 611–613.
- [23] G. Hennrich, H. Sonnenschein, U. R. Genger, *J. Am. Chem. Soc.* **1999**, *121*, 5073–5074.
- [24] S. Tsuruya, S. -I. Yanai, M. Masai, *Inorg. Chem.* **1986**, *25*, 141–146.
- [25] A. Guha, T. Chattopadhyay, N. D. Paul, M. Mukherjee, S. Goswami, T. K. Mondal, E. Zangrando, D. Das, *Inorg Chem* **2012**, *51*, 8750–8759.

Submitted: April 12, 2018

Accepted: October 1, 2018



Source details

[Feedback >](#) [Compare sources >](#)

ChemistrySelect

Scopus coverage years: from 2016 to Present

Publisher: Wiley-Blackwell

E-ISSN: 2365-6549

Subject area: [Chemistry: General Chemistry](#)

Source type: Journal

[View all documents >](#)[Set document alert](#)[Save to source list](#)

CiteScore 2022

3.6



SJR 2022

0.380



SNIP 2022

0.495



Accepted Manuscript

Synthesis and Spectroscopic Characterization of a Photo-stable Tetrazinc(II)-Schiff base Cluster: A Rare Case of Ligand Centric Phenoxazinone Synthase Activity

Mamoni Garai, Ajit Das, Mayank Joshi, Suwendu Paul, Madhusudan Shit, Angshuman Roy Choudhury, Bhaskar Biswas

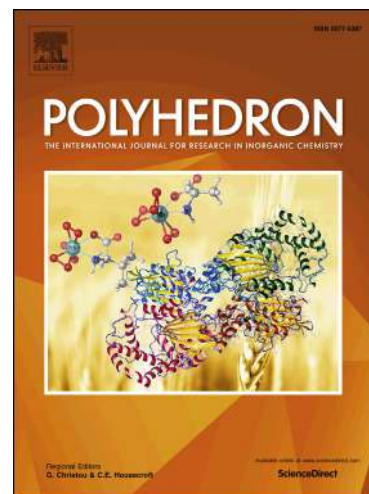
PII: S0277-5387(18)30596-5
DOI: <https://doi.org/10.1016/j.poly.2018.09.044>
Reference: POLY 13443

To appear in: *Polyhedron*

Received Date: 17 July 2018
Accepted Date: 16 September 2018

Please cite this article as: M. Garai, A. Das, M. Joshi, S. Paul, M. Shit, A.R. Choudhury, B. Biswas, Synthesis and Spectroscopic Characterization of a Photo-stable Tetrazinc(II)-Schiff base Cluster: A Rare Case of Ligand Centric Phenoxazinone Synthase Activity, *Polyhedron* (2018), doi: <https://doi.org/10.1016/j.poly.2018.09.044>

This is a PDF file of an unedited manuscript that has been accepted for publication. As a service to our customers we are providing this early version of the manuscript. The manuscript will undergo copyediting, typesetting, and review of the resulting proof before it is published in its final form. Please note that during the production process errors may be discovered which could affect the content, and all legal disclaimers that apply to the journal pertain.



Synthesis and Spectroscopic Characterization of a Photo-stable Tetrazinc(II)-Schiff base Cluster: A Rare Case of Ligand Centric Phenoxazinone Synthase Activity

Mamoni Garai,^a Ajit Das,^b Mayank Joshi,^c Suwendu Paul,^d Madhusudan Shit,^e Angshuman Roy Choudhury,^c Bhaskar Biswas^{a,§}

^aDepartment of Chemistry, University of North Bengal, Darjeeling 734013, India,

^bDepartment of Chemistry, Sidho-Kanho-Birsha University, Purulia 723104, India

^cDepartment of Chemical Sciences, Indian Institute of Science Education and Research, S.A.S. Nagar, Manauli PO, Mohali 140 306, India

^dDepartment of Chemistry, University of Kalyani, Kalyani 741235, West Bengal, India

^eDepartment of Chemistry, Dinobandhu Andrews College, Kolkata 700084, India

ABSTRACT

Herein, the synthesis and structural characterization and catalytic activity of a novel tetranuclear zinc(II)-Schiff base complex, $[Zn_4(L)_2(\mu_3-OCH_3)_2(CH_3OH)_2].2CH_3OH$ (**1**), [**L** = *N,N'*-bis(3-methoxysalicylidene)-1,3-diamino-2-propanol] was presented. Single crystal X-ray diffraction structural analysis revealed that the tetra-zinc(II) cluster crystallized in a monoclinic system with $P2_1/c$ space group. Interestingly, three different molecular bridges (methoxido-, alkoxido- and phenoxido-) simultaneously co-existed in assembling tetra-zinc(II) core, which was a very rare observation. To the best of our knowledge, this compound would be the first compound where a diverse coordination aspect was covered by a single solvent as terminal coordinator (CH_3OH), bridging(μ_3-CH_3OH) and solvent for crystallization in the existing scientific literature. The compound showed good photo-stability and excellent luminescence property with higher lifetime at transition state in ethanol. This zinc(II) complex revealed crucial role as an effective catalytic system towards oxidation of 2-aminophenol (2-AP) in ethanol. Additionally, the tetra-zinc(II) complex displayed potential phenoxazinone synthase like activity with momentous turn over number, $k_{cat}(h^{-1}) = 6.19 \times 10^2$ in ethanol under aerobic condition. ESI-MS and EPR spectral analysis of the reaction mixture between Zn(II) complex and 2-AP recommended that the course of catalysis proceeded through substrate-catalyst adduct formation and authenticated the radical mechanistic pathway in favour of oxidative coupling product. This tetranuclear zinc(II)-Schiff

base complex would be considered as the first example that catalyzed the oxidative coupling of 2-aminophenol to aminophenoxazino compound under usual aerobic condition. As complementary, detailed quantum chemical computations, performed with density functional theory (DFT) were well corroborated with the experimental results. This was the first and rarest example where a tetrazinc(II)-Schiff base cluster exhibited catalytic oxidation of 2-AP through ligand centred radical activity.

Keywords: Zinc(II); Schiff base; X-ray structure; Bio-mimicking study; Phenoxazinone synthase activity.

*Corresponding author: E-mail address: mr.bbiswas@rediffmail.com; icbbiswas@gmail.com

§On lien from: *Department of Chemistry, Surendranath College, 24/2 M.G. Road, Kolkata 700009, India,*

1. Introduction

Polymetallic cores containing atomic and/or molecular bridges based on first row transition metal ions (3d ions) with an organic backbone have drawn significant interest for their diverse applicability in modern science [1-3]. The investigation to design and construction of metallic clusters are growing on, not only for their stimulating structural aspects but also for their utility in developing the properties of electronic, optical, magnetic, and catalytic materials [4-6]. In all the transition metal ions, “zinc metal ion” remains one of the most fundamental contributors in the biological system and plays significant bio-functions in the living system. In this living world, nature controls elemental distribution in its own way and it is commonly observed that most of the fundamental basic processes are metal centric like Mg(II) in photosynthesis, Fe(II)/(III) in O₂ transport phenomenon, Fe-Mo metal ions in N₂ fixation etc. [7-9]. Therefore, designing of coordination compounds having the suitability to mimic the bio-functionalities of different metalloenzymes has become a serious challenge to the synthetic chemists. Bio-mimicking activities will not only provide lots of important basic information about their bio-functions but also lead to making a clarification of their mechanistic concern on such complex systems [10-12]. Zinc(II) Schiff base complexes are mostly treated as potential photo-active materials [13]. With a d¹⁰ electronic configuration, Zn(II) ions have a pronounced effect on their photo-physical properties. Unsaturation of coordination number at Zn(II) centre in several zinc

complexes make it stronger Lewis acids. Other characteristic features of zinc(II) ions like Lewis acid activation, nucleophile origination, rapid ligand exchange, and stabilization of leaving group, make Zn(II) ion one of the most prevalent metal ion in material sciences [14,15].

Di-, tri-, and polynuclear zinc(II) complexes have created a huge appeal for their existence in the range of important metalloenzymes [16,17] like alkaline phosphatases, zinc-dependent aminopeptidases, and metallo- β -lactamases. After surveying the importance of oxidation reactions in laboratory and industry, it is of paramount interest to evaluate efficient catalysts that enable the course of catalysis in an effective and selective way [18]. In this regards, a (N,O)-donor polydentate Schiff base ligand, *N,N'*-bis(3-methoxysalicylidene)-1,3-diamino-2-propanol and its tetranuclear zinc(II)-Schiff base complex were synthesized. The compound showed good photo-luminescence properties in ethanol medium having higher lifetime span of the transition state. The structural features provided additional appeal to the synthetic chemists since a single solvent (methanol) covered diverse coordination aspects as terminal coordinator (CH₃OH), bridging(μ_3 -CH₃OH) and solvent for crystallization and played a significant role in clustering this tetranuclear zinc(II) core. This complex was employed as an effective catalytic system towards 2-aminophenol oxidation in EtOH which revealed a significant turn over number, $k_{\text{cat}}(\text{h}^{-1}) = 6.19 \times 10^2$ in ethanol in favour of oxidative coupling of 2-aminophenol. ESI-MS and EPR spectral analysis of the reaction mixture between Zn(II) complex and 2-AP authenticated that the course of catalysis proceeded through substrate-catalyst adduct formation in combination with the generation of radical in the catalytic cycles.

2. Experimental Section

2.1. Preparation of the Schiff base ligand and complex

(a) Chemicals, solvents and starting materials

High purity *o*-vanilin (Sigma, Germany), 2-hydroxy-1,3-diaminopropane (Aldrich, USA), zinc(II) sulphate hexahydrate (Merck, India), and all other solvents were purchased from the respective concerns and used as received. 2-aminophenol (2-AP) was procured from Sigma Aldrich Corporation (St. Louis, MO, USA). All other chemicals and solvents were of analytical grade and were used without further purification.

(b) General Synthesis

The Schiff base, **L** was prepared following a reported literature [19]. To prepare the Schiff base ligand, 2-hydroxy-1,3-diaminopropane (0.0890 g, 1 mmol) was refluxed with *o*-vanilin (0.3046

g, 2 mmol) in 20 ml dehydrated alcohol for 6 hours and after 7-10 days yellowish orange coloured compound was isolated from solution, which was dried and stored *in vacuo* over CaCl_2 for subsequent use. Yield ~ 0.330 g (86%). Anal. Calc. for $\text{C}_{19}\text{H}_{22}\text{N}_2\text{O}_5$ (**L**): IR (KBr, cm^{-1}): 3365 (ν_{OH}), 1618 ($\nu_{\text{C=N}}$), 1333, 1245 (ν_{PhO}); UV-Vis (λ_{max} , nm): 255, 315, 403; ^1H NMR (δ ppm, 400 Mz, $\text{DMSO-}d^6$) δ = 13.55 (s, 1H), 9.92 (s, 1H), 9.92 (s, 1H), 7.26-6.90 (Ar-H, 6H), 5.94 (s, 1H), 3.93 (s, 3H) ppm. [**L**+ H^+] m/z 359.16.

A methanolic solution (10 mL) of **L** (0.36 g, 1 mM) was added drop-wise to a methanolic solution (15 mL) of ZnSO_4 (0.53 g, 2 mM) and was kept the reaction solution on a magnetic stirrer for 30 minutes. The bright yellow coloured solution was filtered and the supernatant liquid was kept in air for slow evaporation. Yield for **1**: 0.37 g (~69% for **1** based on metal salt).

Anal. Calc. for $\text{C}_{44}\text{H}_{60}\text{N}_4\text{O}_{16}\text{Zn}_4$ (**1**): C, 45.46; H, 5.20; N, 4.82. Found: C, 45.51; H, 5.17; N, 4.89 %. IR (KBr, cm^{-1}): 3557 (ν_{OH}), 1637, 1616 ($\nu_{\text{C=N}}$); UV-Vis (λ_{max} , Abs, nm, 10^{-4} M, EtOH): 233 (0.83), 277 (1.10), 363 (0.132). [$\text{C}_{40}\text{H}_{44}\text{N}_4\text{O}_{12}\text{Zn}_4+\text{H}^+$], m/z 1035.13

2.2. Physical measurements

Infra-red spectrum (KBr) of the complex was recorded with a FTIR-8400S SHIMADZU spectrophotometer in the range 400-3600 cm^{-1} . ^1H NMR spectrum in $\text{DMSO-}d^6$ was obtained on a Bruker Avance 300 MHz spectrometer at 25°C and was recorded at 299.948 MHz. Steady-state absorption spectral measurements were carried out with a JASCO model V-730 UV-Vis spectrophotometer. Elemental analyses were performed on a Perkin Elmer 2400 CHN microanalyser. Electrospray ionization (ESI) mass spectrum was recorded on a Q-TOF MicroTM Mass Spectrometer. Steady-state fluorescence measurements were carried out with a Hitachi F-7000 spectrofluorimeter. Molar conductivity measurement was operated using a Horiba LAQUA Benchtop DS70 conductivity meter. The X-band EPR spectra were recorded on a Magnostech GmbH MiniScope MS400 spectrometer (equipped with temperature controller TC H03), where the microwave frequency was measured with an FC400 frequency counter.

2.3. X-ray diffraction study

Single crystal X-ray diffraction data for **1** was collected using a Rigaku XtaLABmini (Fixed 2Theta and Distance) diffractometer equipped with Mercury375R (2x2 bin mode) CCD detector. The data were collected with graphite monochromated Mo- $\text{K}\alpha$ radiation ($\lambda=0.71075$ Å) at 100 K for **1** using ω scans. The data were reduced using CrysAlisPro 1.171.38.46 (Reference

Rigaku Corporation: Tokyo, Japan) and the space group determination was done using Olex2. The structure was resolved by direct method and refined by full-matrix least-squares procedures using the SHELXL-97 software package using OLEX² suite [20,21].

2.4. Catalytic oxidation of 2-AP

In order to examine the phenoxazinone synthase activity, 1×10^{-4} M solution of **1** in EtOH was treated with 100 equiv. of 2-aminophenol (2-AP) under aerobic conditions at room temperature. Absorbance vs. wavelength (wavelength scans) of the solution was recorded at a regular time interval of 11 minutes for aminophenol oxidation in the wavelength range 300-800 nm. Kinetic experiments were performed spectrophotometrically [22,23] with Zn(II) complex, **1** in presence of 2-AP in EtOH at 25°C. 0.04 mL solution of the complex, with a constant concentration of 1×10^{-4} M, was added to 2 mL of 2-AP of a particular concentration (varying its concentration from 1×10^{-3} M to 1×10^{-2} M) to achieve the ultimate concentration of the complex as 1×10^{-4} M. The conversion of 2-AP to APX was monitored with time at wavelength of 434 nm (time scan) for **1** in EtOH. To determine the dependence of rate on substrate concentration, kinetic analyses were performed in triplicate. The phenoxazinone compound was separated in pure form by column chromatography using neutral alumina as column support and benzene-ethyl acetate as an eluant mixture. The compound was isolated in high yield (85% for **1**) by slow evaporation of the eluant. The product was principally confirmed and identified by ¹H NMR spectroscopy. ¹H NMR data for 2-amino-3H-phenoxazine-3-one (APX), (CDCl₃, 400 MHz,) δ_{H} : 7.61 (m, 1H), 7.46 (m, 3H), 6.48 (s, 1H), 6.39 (s, 1H), 6.27 (s, 1H).

2.5. Detection of the presence of hydrogen peroxide in the catalytic oxidation of 2-AP

To detect the formation of hydrogen peroxide during the catalytic reaction, we followed a reported method [22b]. Reaction mixtures were prepared as in the kinetic experiments. During the course of the oxidation reaction, the solution was acidified with H₂SO₄ to pH = 2 to stop further oxidation after a certain time and an equal volume of water was added. The formed APX was extracted three times with dichloromethane. To the aqueous layer were added 1 ml of a 10% solution of KI and three drops of a 3% solution of ammonium molybdate. The formation of I₃⁻ could be monitored spectrophotometrically because of the development of the characteristic I₃⁻ band ($\lambda_{\text{max}} = 353$ nm).

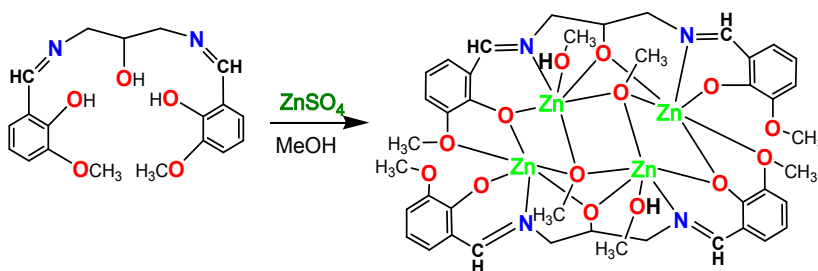
2.6. Theoretical details

To provide theoretical justification, detailed quantum chemical computations were operated using Gaussian 09W programme suite [24] without considering any symmetrical restrictions. The molecular structure of Zn(II)-Schiff base complex was optimized in vacuum utilizing B3LYP theoretical model and 6-311G basis set [25,26]. Then, the optimized structure of vacuum was again optimized in ethanol ($\epsilon = 24.852$) considering Integral Equation Formalism Polarizable Continuum Model (IEFPCM) [27] as solvent model to corroborate the theoretical outcomes with the experimental results. To ensure the optimized structures to be true minima, stability calculations were performed and the global minima was further reconfirmed with no imaginary frequency. The ground state (S_0) and first singlet excited state (S_1) calculations were accompanied with density functional theory (DFT) and with time-dependent density functional theory (TD-DFT) respectively. The theoretical UV-Vis and fluorescence spectra were calculated with Multiwfn software [28]. The details of theoretical methods could be found somewhere else [29].

3. Results and discussion

3.1. Synthesis and formulation

The tetra-zinc(II) complex was prepared in the form of single crystals by mixing of zinc(II) sulphate to the polydentate Schiff base ligand in 2:1 mole ratio in methanol medium. The structural formulation of **1** was determined by different analytical techniques including single crystal X-ray diffraction study. The unique function of methanol solvent was most significant in this synthesis. Replacement of methanol by other solvents like ethanol, acetonitrile, dichloromethane did not produce the tetra metallic core. Therefore, the exclusive selectivity of the tetra metallic core towards methanol solvent developed the novelty of this complex.



Scheme 1. Preparative procedure for zinc(II) complex

Controlled reactions exhibited that the tetra-zinc(II) Schiff base complex (**1**) could only be produced with zinc(II) sulphate with Schiff base ligand in methanol solvent. Other zinc(II) salts were not able to produce this compound in presence of Schiff base ligand.

3.2. Description of crystal structure

Single crystal X-ray structure analysis revealed that neutral tetrazinc(II)-Schiff base complex was crystallized in a monoclinic system with $P2_1/c$ space group. An ORTEP view of the asymmetric units of **1** was shown in Figure 1. The structural refinement parameters of **1** were listed in Table S1. Selected bond angles and bond distances of **1** were given in Table S2. The X-ray crystal structure of the zinc(II)-Schiff base complex (Figure 1) actually existed as a neutral tetra metallic core, $[Zn_4(\mu_3-OCH_3)_2(L)_2(CH_3OH)_2]$. Each of the Zn(II) centre in tetranuclear Zn(II)-Schiff base cluster exists in an octahedral geometry. The structural description is given by X. Liu *et al.* [30b]

The solvent methanol molecules acted a pivotal role in clustering four Zn(II) ions in association with two Schiff base ligands to a tetra metallic core through generation of methoxide ions (μ_3-O_6) in the reaction medium. Also, another two methanol molecules coordinated with Zn(II) ions and fulfilled the coordination environments around each of the Zn(II) centres. So, phenoxido-O, alkoxido-O and methoxido-O were the driving forces in organizing four Zn(II) ions in an open dicubane geometry, having Zn...Zn distances varying from 3.059 to 3.137 Å (Zn1...Zn2, 3.137 Å to Zn2...Zn1, 3.059 Å) (Figure 1). Furthermore, two $[Zn_2(L)]$ units were interlinked through two methoxide ions, in which each Zn3 triangular unit was bridged by an oxygen atom (O6, O6) from a μ_3-OCH_3 group. An extensive investigation was executed to compare structural aspects with other reported tetrazinc(II)-Schiff base complexes [30], but in reality few tetra-zinc(II)-Schiff base complexes were available in scientific literature. In comparison with one reported tetra-zinc(II)-Schiff base complex, it was found that, Zn...Zn internuclear distances in **1** vary from 3.059 to 3.137 Å while Zn...Zn distances were found within 3.12–3.23 Å reported by Y.-X. Sun *et al.* [30a]. An identical tetrazinc structure is previously reported by X. Liu *et al.* [30b].

Quantum mechanical calculations of the molecular structure of Zn(II)-Schiff base complex in the vacuum was also performed through density functional theory (DFT) method. The molecular structure for zinc(II) complex in vacuum was presented in Figure 2. The optimized structure displayed close resemblance with the crystal structure of the tetra zinc(II) compound. The

structure in vacuum also showed similar bond connectivity and structural features for the Schiff base ligand towards zinc(II) ions. The molecular bridges and coordination environment for zinc(II) ions remained almost identical. The inter-nuclear distances among the Zn(II) ions and the inter-nuclear angles were also in well agreement with the X-ray structure. The theoretical bond distances and bond angles of the optimized structure of **1** in vacuum along with the experimental crystal structure data were also compared in Table S2.

3.3. Experimental and theoretical views on the solution properties of Zn(II) complex

The structural rigidity of the tetranuclear Zn(II) compound in solution state was investigated by different analytical methods like steady-state absorption and emission study, molar conductivity, ESI mass spectral analysis. The Zn(II) compound was soluble in most of the polar solvents like ethanol, dichloromethane and water.

The UV-Vis spectrum for the Zn(II) compound in ethanolic solution at room temperature showed characteristics absorption maxima's at 233, 277 and 363 nm (Table S3). High-intensity transitions at 233 and 277 nm were principally assignable to the $\pi \rightarrow \pi^*$ and $n \rightarrow \pi^*$ electronic transitions of $-C=N-$ chromophore of Schiff base ligand in ethanolic solution [31]. These electronic transitions resembled very well with other Zn(II)-Schiff base based transitions [31]. A broad and low-intensity transition at 363 nm indicates ligand to metal centre charge transition (LMCT) in the zinc(II)-Schiff complex.

TD-DFT was also performed to determine the electronic properties of Zn(II) compound in solution. With an aim to get a better view on the nature of optical spectrum of Zn(II)-Schiff base compound, we have performed TD-DFT studies. The theoretical UV-Vis spectrum was also in well accordance with the experimental observations (Table S2). The theoretical absorption and fluorescence spectra were in accordance with the experimental results. The theoretical absorption (λ_{max}) maxima (278 nm) were very close to the experimental absorption maxima. In addition, the theoretical fluorescence spectra ($\lambda_{\text{em}} = 480$ nm) was also well corroborated the experimental findings ($\lambda_{\text{em}} = 476$ nm). The electronic transitions in HOMO \rightarrow LUMO/ HOMO+1 \rightarrow LUMO-1 (Figure 3, Table S3) provide better insights to make a statement about the electronic activity in solution. It is well known that lower the energy gap associated with HOMO & LUMO higher will be the activity and consequently lower will be the stability of a molecule.

The ESI-MS spectral analysis of **1** further confirms in favour of molecular integrity in solution for $[\text{Zn}_4(\mu_3\text{-OCH}_3)_2(\text{L})_2(\text{CH}_3\text{OH})_2]$ (**1**). ESI mass spectrum of **1** in ethanolic solution displays the base peak at m/z 517.35 for $[\text{Zn}_2(\text{L})(\text{OCH}_3)+\text{H}^+]$ (Figure S3) while another very important peak at m/z 1035.13 indicates the molecular ion peak in EtOH medium. The ESI-MS of ethanolic solution of Zn(II) compound confirms its structural integrity in favour of $[\text{Zn}_4(\mu_3\text{-OCH}_3)_2(\text{L})_2]$ species in solution.

With an aim to investigate detail insights in solution phase we further recorded molar conductance values for the Zn(II) compound in EtOH at room temperature. In order to investigate the solution stability of the zinc compound in ethanol medium, we carried out the measurement of molar conductivity at room temperature under aerobic condition. For this, we have taken solution of 1.10×10^{-3} M concentration and recorded molar conductance value as 5.7 $\text{Scm}^2\text{mol}^{-1}$. Molar conductance value of this compound strongly suggests non-electrolytic nature in ethanolic solution.

3.4. Luminescence property with lifetime decay of the Zn(II) compound

The photoluminescence spectrum of the **1** (λ_{ex} 277nm) in ethanol at 298 K was presented in Figure S1. The emission wavelength for Zn(II) compound in ethanolic solution is 476 nm (Figure S2) upon excitation on 277 nm. The excited state mean lifetime of the tetra-zinc(II) cluster was found to be 1.67 ns. Time dependent photoluminescence decay profile for this complex was given in Figure 4. It was seen that the compound was quite stable in solution and stable in its tetrameric form in solution. It could be assumed that the peak was probably derived from the $\pi^* \rightarrow n$ or $\pi^* \rightarrow \pi$ transitions. The nature of emission, in this case, indicated the possibility of ligand-to-metal charge transfer [32].

3.5. Phenoxazinone Synthase activity of the tetra-zinc(II) complex and its mechanistic inferences

The aminophenol oxidation activity by the tetra-zinc(II) cluster (**1**) was investigated using 2-aminophenol (2-AP) as a standard substrate in ethanol solvent under an aerobic condition at room temperature (25°C). To study this catalytic oxidation reaction, 1×10^{-4} M solution of Zn(II) complex was added to 1×10^{-2} M solution of 2-AP. The course of the catalytic reaction was monitored through UV-Vis spectrophotometer. After immediate mixing, a spectrophotometric scan was recorded with a time interval of 11 min for 3h. Common studies on 2-AP oxidation showed that 2-AP exhibits a high intensity single band at 267 nm [33] and we found same

results. With the progress of time in the spectrophotometric titration, it was seen that characteristic signal at 267 nm for 2-AP gradually disappeared in solution and concomitantly an initial new band with incremental absorbance at 434 nm appeared (Figure 5). The appearance of the band at 434 nm for this tetrazinc-Schiff base compound was a definite sign for the production of phenoxazinone species in solution[33].

Controlled experiments using 2-AP in ethanol solvent upto 3h under aerobic condition (Figure S4) was also performed. The yield of phenoxazinone compound under controlled experiments was too small in comparison with the yield of tetra-zinc based catalytic oxidation and thus, neglected. Under this circumstance, it was recommended that auto oxidation of 2-AP was responsible for the conversion of 2-AP to phenoxazinone in the controlled experiment.

Kinetic studies of the catalytic oxidation of 2-AP were also performed to understand the catalytic efficacy for this tetrazinc-Schiff base compound. The kinetics of oxidative coupling of 2-AP under aerobic atmosphere were carried out following the method of initial rates. The growth of the phenoxazinone species in EtOH at 434 nm was monitored as a function of time (Figure S5) [34, 36]. The concentration of the substrate versus rate constants was plotted which showed rate saturation kinetics. The kinetics was analyzed based on Michaelis-Menten approach of enzymatic kinetics. The values of the kinetics parameters for **1** are found as V_{\max} (Ms^{-1}) = 1.72×10^{-5} (Std. error = 1.63×10^{-6}); K_M (M) = 3.23×10^{-3} (Std. error = 5.98×10^{-4}); k_{cat} (h^{-1}) = 6.19×10^2 . We didn't find a single tetra-zinc(II) complex in the scientific literature that exhibits aminophenol oxidation activity under aerobic condition. To the best of our knowledge, this tetranuclear zinc(II)-Schiff base complex would be the first and only example till date that catalyzed the oxidative coupling of 2-aminophenol to aminophenoxazino compound under normal atmosphere with a significant turnover number. For this cause, we couldn't present a comparison of phenoxazinone synthase activity between our zinc-Schiff base complex with the few reported tetranuclear Zn(II)-Schiff base complex. The catalytic efficiency of the zinc complex for aminophenol oxidation was found high, $k_{\text{cat}}/K_M = 1.91 \times 10^5$ and indicative of very good catalytic efficacy for this oxidation reaction.

Large number of scientific literatures were reviewed to explore the mechanistic insights of catalytic phenoxazinone activity of this zinc(II) complex. One of the renowned scientists, P. Chaudhury *et al.*[36a] modeled a tetra-copper complex for the mimicking of catalytic oxidation of 2-aminophenol. He proposed that an "on-off" catalytic aspects of the radical in association with redox behaviour of the metal centers play most significant role during six-electron oxidative coupling of 2-AP in the catalytic oxidative coupling of 2-AP. Furthermore, another renowned

scientist, T. P. Begley *et al.*[36b,c,d] recommended that catalytic function for the synthesis of 2-aminophenoxazinone proceeds through a sequential three consecutive 2-electron aminophenol oxidations.

It was quite unprecedented that zinc complexes containing Schiff-base ligands displayed similar functional activities like a copper(II) based metalloenzyme, phenoxazinone synthase. Generally, it was seen that zinc ions were involved in the redox process with the two-electron transfer. So in order to elucidate the reason favoring aminophenol oxidation activity exhibited by this Zn(II)-Schiff base complex, EPR study was carried out. The X-band EPR spectra for the solutions containing tetra-zinc(II) complex in presence and absence of 2-AP were separately recorded in CH₂Cl₂ at 298 K. The EPR spectra for the tetra-zinc cluster in presence of 2-AP are presented in Figure 6. Both of the EPR spectra for this Zn(II)-Schiff base complex and 2-AP under aerobic condition at 298 K remains silent and the compounds were considered as EPR inactive. Even mixing of different zinc(II) salts with 2-AP didn't produce any signal in the EPR spectrum (Figure S6). The EPR spectra were recorded promptly upon mixing of Zn^{II} complex with 2-AP in an inert atmosphere after 10 min, and 30 min time intervals. A nearly isotropic EPR signal at $g \approx 2.01$ was found in the solution mixture and shown in Figure 6. A control experiment, under identical experimental condition, was also performed and no characteristic signal for organic radical was detected from the mixture between different zinc(II) salts and 2-AP. Thus, EPR signal, which recommends the presence of radical species/species in solution, was a definite signature to confirm the generation of radical, only in presence of Zn(II)-Schiff base complex. Hence, the course of catalysis proceeds through the participation of ligand-centered radical species in solution. Therefore, generation of radical in the catalytic cycle was most likely responsible for that oxidative coupling of 2-aminophenol. To confirm this observation, the catalytic oxidation reaction was performed using a radical scavenger, TEMPO (TEMPO = 2,2,6,6-tetramethylpiperidinoxyl). Addition of two equivalent of TEMPO to the ethanolic solution of catalyst stopped the catalytic conversion from 2-AP to APX. This investigation provided further consolidated that catalytic oxidation for 2-AP substrate only proceeded through generation of ligand centric radical in solution, only in presence of this tetra-Zn^{II} complex. It was further observed that no catalytic oxidation reactions occurred in an inert atmosphere and no formation of APX was detected. However, exposure of the reaction mixture in aerobic atmosphere, formation of APX was noticed immediately. This particular observation helped us to predict that molecular oxygen remained one of the active reactants in the catalytic cycle. In the

catalytic cycle, 2-AP was converted into the imino-benzoquinone radical in the first step of catalysis. In the next step, the release of APX was occurred with subsequent regeneration of the active catalyst.

Survey of scientific literatures on phenoxazinone synthase activity by different metal complexes showed that the oxidative coupling product of 2-AP, in general, proceeded through 6e oxidation or radical generation pathway. However, in reality, in two or three cases, scientists were able to trap the radicals in the course of catalysis. Radical detection in solution was very difficult and this might probably due to faster disproportionate of the radical in solution. However, not a single zinc complex was reported earlier that shows such catalytic oxidative coupling of 2-AP under normal condition through radical generation in solution. We were lucky enough in this regards to able to detect the radical in the course of catalysis.

In order to gain further insight in this catalytic oxidation reaction in a solution state, ESI-MS spectra of a 1:100 mixture of complex **1** and 2-AP in ethanol solvent were also recorded. The spectrum (Figure S7) exhibited a base peak at $m/z = 212.35$ (100%) that was assignable to the quinone-sodium aggregate, $[2\text{-AP-H}^+]^+$. The peak at $m/z = 1252.61$ corroborated the formation of substrate-catalyst adduct, $[\text{Zn}_4(\text{L})_2(\mu\text{-OCH}_3)_2(2\text{-AP})_2]$ species as an intermediate (Figure S7).

Another important structural aspect for this tetra-zinc(II) cluster was also investigated. To study photo-stability for the zinc(II) complex, molar conductance value was recorded for 1×10^{-4} M ethanolic solution keeping the solution in UV-Vis cuvette with passing of UV light for 120 mins. Under this condition, the molar conductance value was found to be $11 \text{ Scm}^2\text{mol}^{-1}$ for **1**. The photo-stability of the complex in presence of the substrate (2-AP) was also studied. During the spectrophotometric titration for 120 mins, we have collected the ethanolic solution of the mixture (catalyst with the substrate) from UV-Vis cuvette and recorded the molar conductance values for the compound. The molar conductance value for the mixture was found to be $17 \text{ Scm}^2\text{mol}^{-1}$ for **1**. All these conductance values corresponded to the non-electrolyte nature of the solution. The molar conductance values at room temperature helped us to predict that the pure tetra-zinc(II)-Schiff base cluster were photo-stable in dry ethanol. We also tried to recycle this tetra-zinc(II) catalyst after the course of catalysis and were able to isolate the zinc catalyst in the form of tetra-metallic core. ESI-MS and UV-Vis spectra (Figures S8 & S9) in ethanolic medium further attested the confirmation about the structural solidity of the tetra-zinc cluster in solution. So, the recycled catalyst was found in its original form except the loss of terminal coordinated methanol molecules.

From the EPR titration, *in situ* measurement of ESI-MS spectrum for the zinc complex in presence of 2-AP substrate, now we were in a position to propose a mechanistic route through which the catalytic cycles were moving on. In order to detect the by product, we were able to detect I_3^- through spectrophotometrically and found the development of the characteristic I_3^- band at 353 nm (Figure S10). Therefore, the course of catalysis indicated that substrate, at first, bound with catalyst (zinc-Schiff base complex) and formed a Catalyst-Substrate adduct. This adduct actually generated iminobenzoquinone radical employing imine chromophore of Schiff base ligand which consequently took part in oxidative coupling with another unit of 2-AP couple under aerobic atmosphere and produced phenoxazinone species in major amount with hydrogen peroxide.

4. Conclusion

In summary, a novel tetranuclear zinc(II)-Schiff base complex, $[Zn_4(L)_2(\mu_3-OCH_3)_2(CH_3OH)_2] \cdot 2CH_3OH$ (**1**) in the form of single crystals was synthesized. Single crystal X-ray structural analysis revealed that **1** crystallized in monoclinic system with $P2_1/c$ space group and exhibited stimulating structural features. This was the first zinc(II)-Schiff base compound where methanol solvent contributed significantly in assembling tetrazinc(II) core covering with diverse coordination aspects as terminal coordinator (CH_3OH), bridging(μ_3-CH_3OH) ligand and solvent for crystallization. This tetrazinc(II) structure was on the centre of inversion and three different molecular bridges (methoxido-, alkoxido- and phenoxido-) simultaneously coexist in the structure. The compound showed good photo-stability and excellent luminescence property with higher lifetime at transition state in ethanol. The compound showed good photoluminescence property with higher lifetime (1.67 ns) at transition state in ethanol medium. This zinc(II) complex was also evaluated as an effective catalytic system towards oxidation of 2-aminophenol (2-AP) in ethanol. The tetrazinc(II) complex displayed good phenoxazinone synthase like activity with significant turn over, $k_{cat}(h^{-1}) = 6.19 \times 10^2$ in ethanol under aerobic condition. ESI-MS and EPR spectral analysis of the reaction mixture between Zn(II) complex and 2-AP recommended that the course of catalysis proceeded through substrate-catalyst adduct formation and generation of radical was the driving force for oxidative coupling of 2-AP. Most importantly, iminobenzoquinone radicals were very fast to disproportionate and extremely difficult to detect. In the true sense, this was the first and only example where a tetrazinc(II)-Schiff base cluster exhibited catalytic oxidation of 2-AP through ligand centred radical activity. Further, DFT outcomes results were in well agreement with the experimental observations.

Supplementary data

Supplementary crystallographic data are available free of charge from The Director, CCDC, 12 Union Road, Cambridge, CB2 1EZ, UK (fax: +44-1223-336033; E-mail: deposit@ccdc.cam.ac.uk or www: <http://www.ccdc.cam.ac.uk>) upon request, quoting deposition number CCDC 1840633. Experimental information such IR, UV-Vis & photo-luminescence spectra, ESI mass spectra, rate vs. [substrate] plot, bond distance, & bond angle parameters are given here.

Acknowledgement

The work is financially supported by SERB, India under the FAST TRACK SCHEME for YOUNG SCIENTIST (No. SB/FT/CS-088/2013 dtd. 21/05/2014). ARC thanks to the Department of Chemical Sciences, IISER Mohali for single crystal X-ray diffraction data collection. The authors are also indebted to the reviewers for their valuable comments and suggestions.

References

- [1] R. H. Prince, in *Comprehensive Coordination Chemistry*, ed. G. Wilkinson, Gillard, G. A. McCleverty, Pergamon, Oxford 5 (1987) 925-1045.
- [2] (a) P. Mahapatra, S. Ghosh, S. Giri, V. Rane, R. Kadam, M. Drew and A. Ghosh, *Inorg. Chem.* 56 (2017) 5105-5121; (b) D. Dey, A. De, H. R. Yadav, P. S. Guin, A. R. Choudhury, N. Kole, B. Biswas, *ChemistrySelect*, 1 (2016) 1910-1916.
- [3] (a) C. Gerdemann, C. Eicken and B. Krebs, *Acc. Chem. Res.*, 35 (2002) 183-191; (b) R. K. Parashar, R. C. Sharma, A. Kumar and G. Mohan, *Inorg. Chim. Acta.*, 151 (1988) 201-208.
- [4] (a) L. I. Simándi, in *Catalytic Activation of Dioxygen by Metal Complexes*, Kluwer Academic Publishers, Dordrecht, Boston, London, 1992; (b) W. Kaim, B. Schwederski, *Bioanorganische Chemie*, Teubner, Stuttgart, 1991; *Bioinorganic Catalysis* (Ed.: J. Reedijk), Marcel Dekker, New York, 1993; (c) B. Biswas, N. Kole, M. Patra, S. Dutta and M. Ganguly, *J. Chem. Sci.* 125 (2013) 1445-1453; (c) I. Majumder, P. Chakraborty, J. Adhikary, H. Kara, E. Zangrando, A. Bauza, A. Frontera and D. Das, *ChemistrySelect*, 3 (2016) 615-625.
- [5] (a) B. Biswas, M. Mitra, J. Adhikary, G. R. Krishna, P. P. Bag, C. M. Reddy, N. Aliaga-Alcalde, T. Chattopadhyay, D. Das and R. Ghosh, *Polyhedron*, 53 (2013) 264-268; (b) S. Ghosh, C. J. Gomez Garcia, J. M. Clemente-Juan and A. Ghosh, *Magnetochem.*, 2 (2016) 2.

- (c) B. Biswas, A. Pal, G. R. Krishna, C. M. Reddy, F. Tuna, R. Ghosh, *Polyhedron*, 30 (2011) 2032-2037.
- [6] (a) A. Banerje, S. Ganguly, T. Chattopadhyay, K. S. Banu, A. Patra, S. Bhattacharya, E. Zangrando and D. Das, *Inorg. Chem.*, 48 (2009) 8695-8702; (b) B. Biswas, A. Al-Hunaiti, M. T. Räsänen, S. Ansalone, M. Leskelä, T. Repo, Y. -T. Chen, H. -L. Tsai, A. D. Naik, A. P. Railliet, Y. Garcia, R. Ghosh and N. Kole, *Eur. J. Inorg. Chem.* (2012) 4479-4485.
- [7] (a) B. L. Vallee, *Zinc Enzymes*, ed. T. G. Spiro, Wiley, New York, (1983) 1-24; (b) I. Bertini, C. Luchinat, M. S. Viezzoli, *Zinc Enzymes*, ed. I. Bertini, C. Luchinat, W. Maret, M. Zeppezauer, Birkhäuser, Boston, (1986) 27-47.
- [8] E. L. Hegg and L. Que, Jr., *Eur. J. Biochem.* 250 (1997) 625-629.
- [9] W. N. Lipscomb and N. Straeter, *Chem. Rev.*, 96 (1996) 2375-2433.
- [10] (a) N. V. Kaminskaia, B. Spingler and S. J. Lippard, *J. Am. Chem. Soc.*, 122 (2000) 6411-6422; (b) P. Seth, S. Giri and A. Ghosh, *Dalton Trans.*, 44 (2015) 12863-12870.
- [11] T. W. Reid, I. B. Wilson, in *The Enzymes* (3rd ed.), Vol. 4, Ed.: P.D. Boyer, Academic Press, New York, 1971, 373.
- [12] (a) S. R. Seidel and P. J. Stang, *Acc. Chem. Res.*, 35 (2002) 972-983.
- [13] (a) N. Periasamy, *Fluorescence Spectroscopy and Its Applications*, Indian Academy of Science, 2007; (b) D. Dey, G. Kaur, M. Patra, A. R. Choudhury, N. Kole and B. Biswas, *Inorg. Chim. Acta.*, 421 (2014) 335-341; (c) R. Sanyal, X. Zhang, P. Kundu, T. Chattopadhyay, C. Zhao, F. A. Mautner and D. Das, *Inorg. Chem.*, 54 (2015) 2315-2324.
- [14] J. Chen, X. Wang, Y. Zhu, J. Lin, X. Yang, Y. Li, Y. Lu and Z. Guo, *Inorg. Chem.*, 44 (2005) 3422-3430.
- [15] (a) C. Metcalfe and J. A. Thomas, *Chem. Soc. Rev.*, 32 (2003) 215-224; (b) H. Zhang, C. -S. Liu, X. -H. Bu, M. Yang, *Inorg. Biochem.*, 99 (2005) 1119-1125.
- [16] (a) G. Parkin, *Chem. Rev.*, 104 (2004) 699-767; (b) H. Vahrenkamp, *Dalton Trans.* (2007) 4751-4759.
- [17] (a) H. Sakiyama, R. Mochizuki, A. Sugawara, M. Sakamoto, Y. Nishida, M. Yamasaki, *J. Chem. Soc., Dalton Trans.* (1999) 997-1000; (b) N. V. Kaminskaia, B. Spingler and S. J. Lippard, *J. Am. Chem. Soc.*, 122 (2000) 6411-6422; (c) N. Mitiae, S. J. Smith, A. Neves, L. W. Guddat, L. R. Gahan and G. Schenk, *Chem. Rev.*, 106 (2006) 3338-3363; (d) A. Tamilselvi, M. Nethaji and G. Mugesh, *Chem. Eur. J.*, 12 (2006) 7797-7806.

- [18] (a) L. Que, Jr. and R. Y. N. Ho, *Chem. Rev.*, 96 (1996) 2607-2624; (b) M. Merkel, M. Pascaly, and B. Krebs, *Inorg. Chem.*, 44 (2005) 7582-7589.
- [19] S. Pal, B. Chowdhury, M. Patra, M. Maji and B. Biswas, *Spectrochim. Acta Part A: Mol. Biomol. Spectro.*, 144 (2015) 148-154.
- [20] (a) G. M. Sheldrick. *Acta Crystallogr. A*64 (2008) 112-122; (b) O. V. Dolomanov, L. J. Bourhis, R. J. Gildea, J. A. K Howard and H. J. Puschmann, *Appl. Cryst.*, 42 (2009) 339-341.
- [21] (a) CrystalClear 2.0; Rigaku Corporation: Tokyo, Japan; (b) L. J. Farrugia, *J. Appl. Cryst.*, 45 (2012) 849-85.
- [22] (a) P. Mahapatra, S. Ghosh, S. Giri, V. Rane, R. Kadam, M. Drew, A. Ghosh, *Inorg. Chem.* 56 (2017) 5105-5121; (b) D. Dey, S. Das, H. R. Yadav, A. Ranjani, L. Gyathri, S. Roy, P. S. Guin, D. Dhanasekaran, A. R. Choudhury, M. A. Akbarsha and B. Biswas, *Polyhedron*, 106 (2016) 106-114.
- [23] (a) J. C. Freeman, P. G. Nayar, T. P. Begley and J. J. Villafranca, *Biochemistry*, 32 (1993) 4826-4830; (b) R. E. Mirams, S. J. Smith, K. S. Hadler, D. L. Ollis, G. Schenk and L. R. Gahan, *J. Biol. Inorg. Chem.*, 13 (2008) 1065-1072.
- [24] M. J. Frisch, G. W. Trucks, H. B. Schlegel, G. E. Scuseria, M. A. Robb, J. R. Cheeseman, G. Scalmani, V. Barone, B. Mennucci, G. A. Petersson, H. Nakatsuji, M. Caricato, X. Li, H. P. Hratchian, A. F. Izmaylov, J. Bloino, G. Zheng, J. L. Sonnenberg, M. Hada, M. Ehara, K. Toyota, R. Fukuda, J. Hasegawa, M. Ishida, T. Nakajima, Y. Honda, O. Kitao, H. Nakai, T. Vreven, J. A. Montgomery, J. E. Peralta Jr., F. Ogliaro, M. Bearpark, J. J. Heyd, E. Brothers, K. N. Kudin, V. N. Staroverov, R. Kobayashi, J. Normand, K. Raghavachari, A. Rendell, J. C. Burant, S. S. Iyengar, J. Tomasi, M. Cossi, N. Rega, J. M. Millam, M. Klene, J. E. Knox, J. B. Cross, V. Bakken, C. Adamo, J. Jaramillo, R. Gomperts, R. E. Stratmann, O. Yazyev, A. J. Austin, R. Cammi, C. Pomelli, J. W. Ochterski, R. L. Martin, K. Morokuma, V. G. Zakrzewski, G. A. Voth, P. Salvador, J. J. Dannenberg, S. Dapprich, A. D. Daniels, O. Farkas, J. B. Foresman, J. V. Ortiz, J. Cioslowski, D. J. Fox, *Gaussian 09 (Revision A.02)*, Gaussian, Inc., Wallingford, CT, 2009.
- [25] Y. Zhao, D. G. Truhlar, *J. Chem. Phys.* 125 (2006) 194101-194118.
- [26] S. Paul, M. Karar, S. Mitra, S. A. S. Shah, T. Majumdar, A. Mallick, *ChemistrySelect*, 1 (2016) 5547-5553.

- [27] (a) B. Mennucci, E. Cances and J. Tomasi, *J. Phys. Chem. B.*, 101 (1997) 10506-10517; (b) Cances, B. Mennucci and J. Tomasi, *J. Chem. Phys.*, 107 (1997) 3032-3041; (c) R. Cammi and J. Tomasi, *J. Comput. Chem.*, 16 (1995) 1449-1458; (d) S. Miertus, E. Scrocco and J. Tomasi, *Chem. Phys.*, 55 (1981) 117-129.
- [28] T. Lu and F. Chen, *J. Comput. Chem.*, 33 (2012) 580-592.
- [29] (a) S. Paul, A. Mallick and T. Majumdar, *Chem. Phys. Lett.*, 634 (2015) 29-36; (b) A. De, A. Sahu, S. Paul, M. Joshi, A. R. Choudhury, B. Biswas, *J. Mol. Struct.*, 1167 (2018) 187-193.
- [30] (a) W. Sun, X.-T. Qin, G. -N. Zhang, S. Ding, Y. -Q. Wang, Z. -L. Liu, *Inorg. Chem. Commun.*, 40 (2014) 190-193; (b) B. Yu, Y. -X. Sun, C. -J. Yang, J. -Q. Guo, J. Li, Z. Anorg. Allg. Chem. 643 (2017) 689-698; (c) L. Jiang, D. Y. Zhang, J. J. Suo, W. Gu, J. L. Tian, X. Liu, S. P. Yan, *Dalton Trans.*, 45 (2016) 10233-10248.
- [31] J. G. Sole, L. E. Bausa, D. Jaque, *An Introduction to the Optical Spectroscopy Inorganic Solids*, John Wiley & Sons, New York, 2005.
- [32] N. Chattopadhyay, A. Mallick and S. Sengupta, *J. Photochem. Photobiol. A.*, 177 (2005) 55-60.
- [23] (a) M. H. Lee and C. R. Dawson, *Arch. Biochem. Biophys.*, 191 (1978) 119-124; (b) F. Ely, K. S. Hadler, L. R. Gahan, L. W. Guddat, D. L. Ollisand and G. Schenk, *J. Biochem.*, 432 (2010) 565-573.
- [34] (a) A. M. Ramadan, J. M. C. Sala and T. N. Parac-Vogt, *Dalton Trans.*, 40 (2011) 1230-1232; (b) M. Garai, D. Dey, H. R. Yadav, A. R. Choudhury, M. Maji B. Biswas, *ChemistrySelect*, 2 (2017) 11040-11047.
- [35] C. E. Barry, P. G. Nayar, T. P. Begley, *Biochemistry*, 28 (1989) 6323-6333.
- [36] (a) C. Mukherjee, T. Weyhermueller, E. Bothe, E. Rentschler and P. Chaudhuri, *Inorg. Chem.*, 46 (2007) 9895-9905; (b) C. E. Barry III, P. G. Nayar and T. P. Begley, *Biochemistry*, 28 (1989) 6323-6333; (c) C. E. Barry III, P. G. Nayar and T. P. Begley, *J. Am. Chem. Soc.*, 110 (1988) 3333-3334; (d) J. C. Freeman, P. G. Nayar, T. P. Begley, J. J. Villafranca, *Biochemistry*, 32 (1993) 4826-4830.

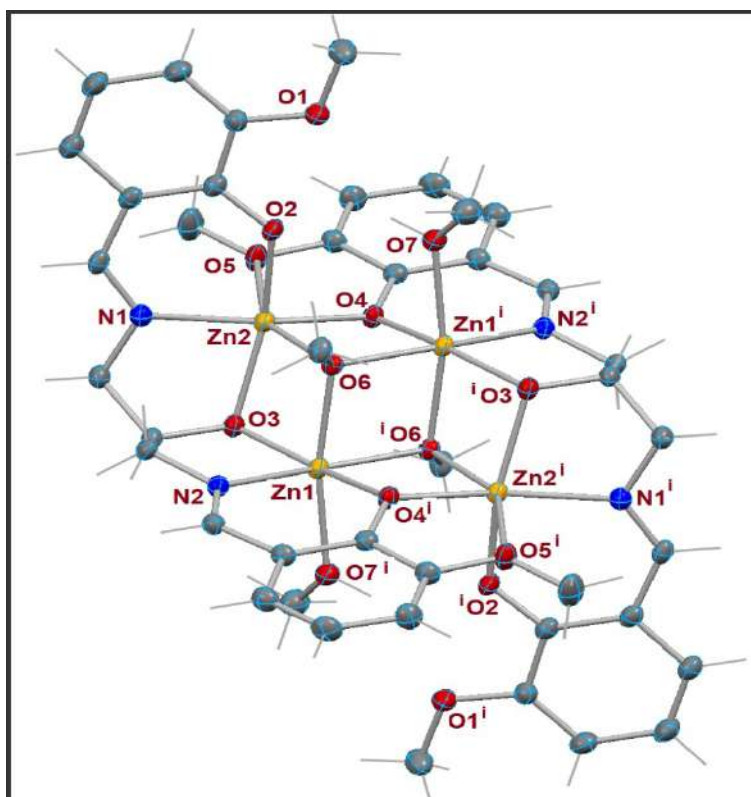


Fig.1. An ellipsoid plot (30% probability) of $[\text{Zn}_4(\text{L})_2(\mu_3\text{-OCH}_3)_2(\text{CH}_3\text{OH})_2] \cdot 2\text{CH}_3\text{OH}$ (1) with atom numbering scheme.

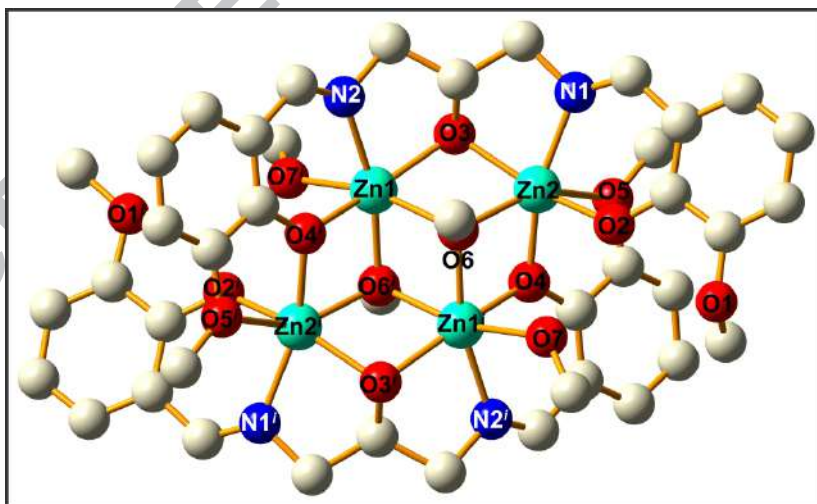


Fig.2. Optimized molecular structure of $[\text{Zn}_4(\text{L})_2(\mu_3\text{-OCH}_3)_2(\text{CH}_3\text{OH})_2]$ in vacuum using DFT/B3LYP/6-311G theoretical model.

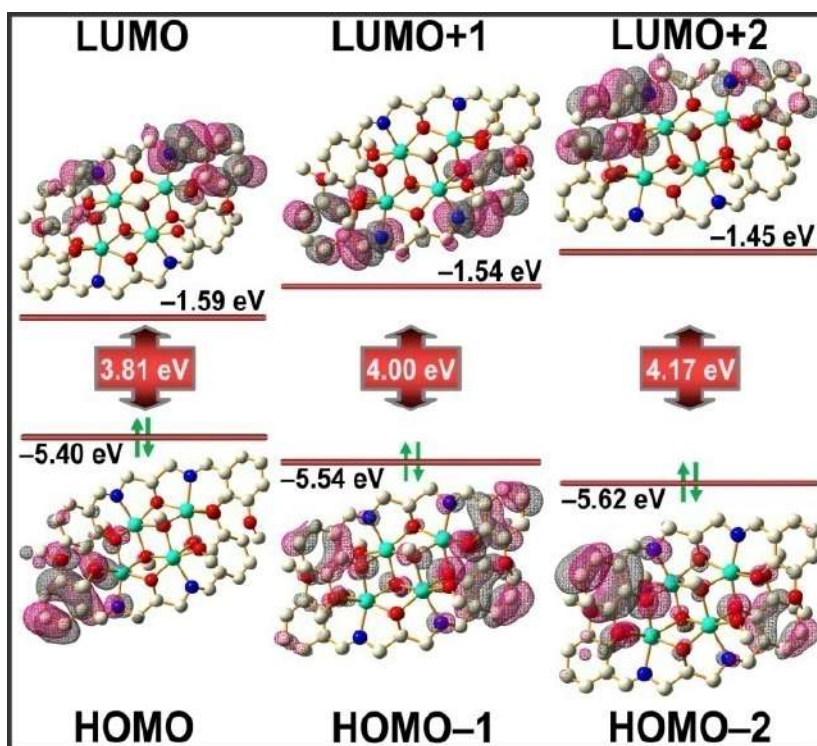


Fig.3. Images of the frontier molecular orbital's of **1** computed using B3LYP/6-311G theoretical method and IEFPCM/ethanol solvent model.

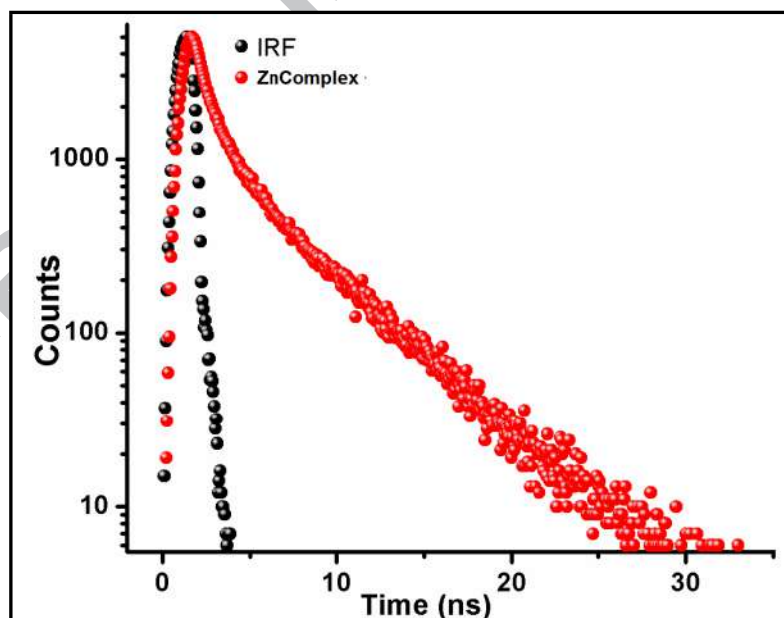


Fig.4. Time dependent photoluminescence decay profile for zinc(II) complex in EtOH

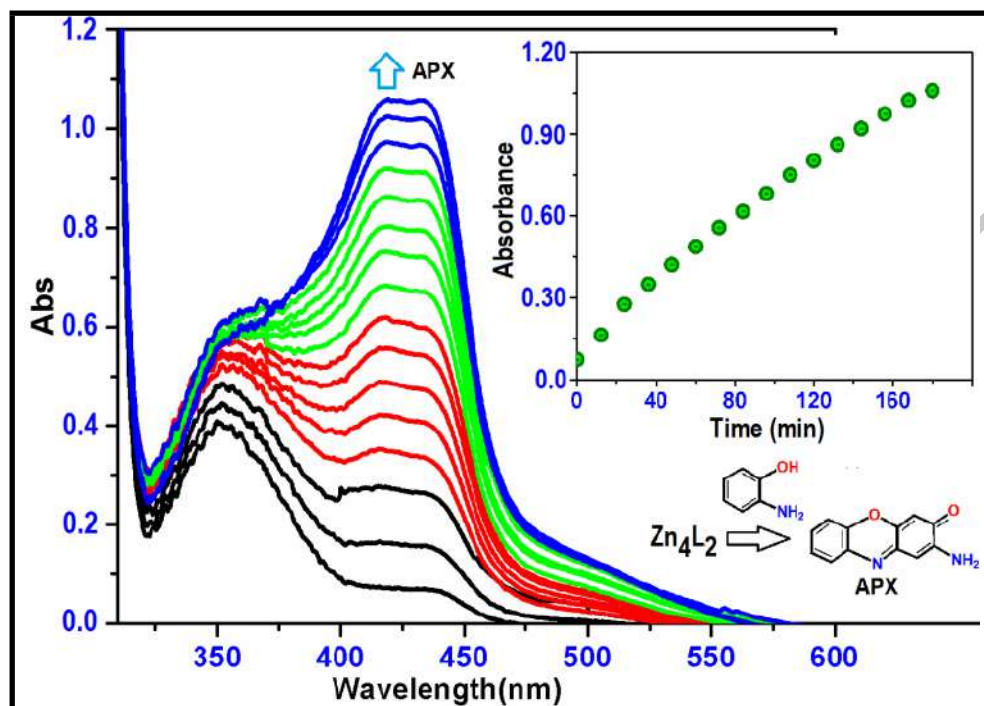


Fig.5. Growth of phenoxazinone species at 434 nm upon addition of 10^{-4} M zinc complex (1) to 100 equivalents of 2-AP under aerobic condition in ethanol at 25 °C. The spectra were recorded after every 11 min. Inset: Time vs Absorbance plot.

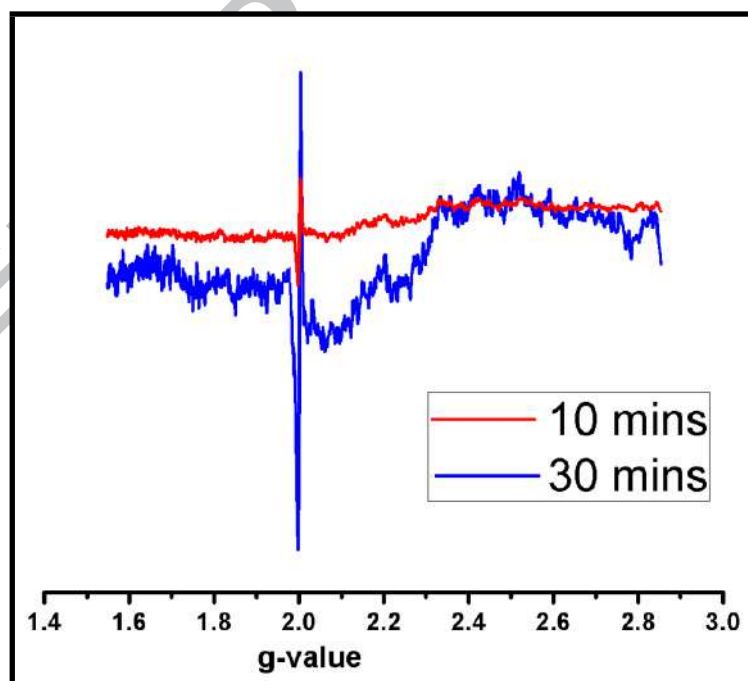


Fig.6. X-band EPR spectra of Zn-Schiff base complex in mixing with 2-AP at 10 min & 30 min in CH_2Cl_2 solution at 298 K.



Source details

[Feedback >](#) [Compare sources >](#)

Polyhedron

Formerly known as: [Journal of Inorganic and Nuclear Chemistry](#)

Formerly known as: [Inorganic and Nuclear Chemistry Letters](#)

Scopus coverage years: from 1982 to Present

Publisher: Elsevier

ISSN: 0277-5387

Subject area: [Chemistry: Inorganic Chemistry](#) [Materials Science: Materials Chemistry](#) [Chemistry: Physical and Theoretical Chemistry](#)

Source type: Journal

[View all documents >](#)[Set document alert](#)[Save to source list](#)

CiteScore 2022

5.4



SJR 2022

0.400



SNIP 2022

0.635

[CiteScore](#)[CiteScore rank & trend](#)[Scopus content coverage](#)